RECENT ADVANCES AND APPLICATIONS OF SEISMIC ISOLATION AND ENERGY DISSIPATION DEVICES

EDITED BY: Dario De Domenico, Enrico Tubaldi, Izuru Takewaki, Theodore Karavasilis, Andrea Dall'Asta and Oren Lavan

PUBLISHED IN: Frontiers in Built Environment

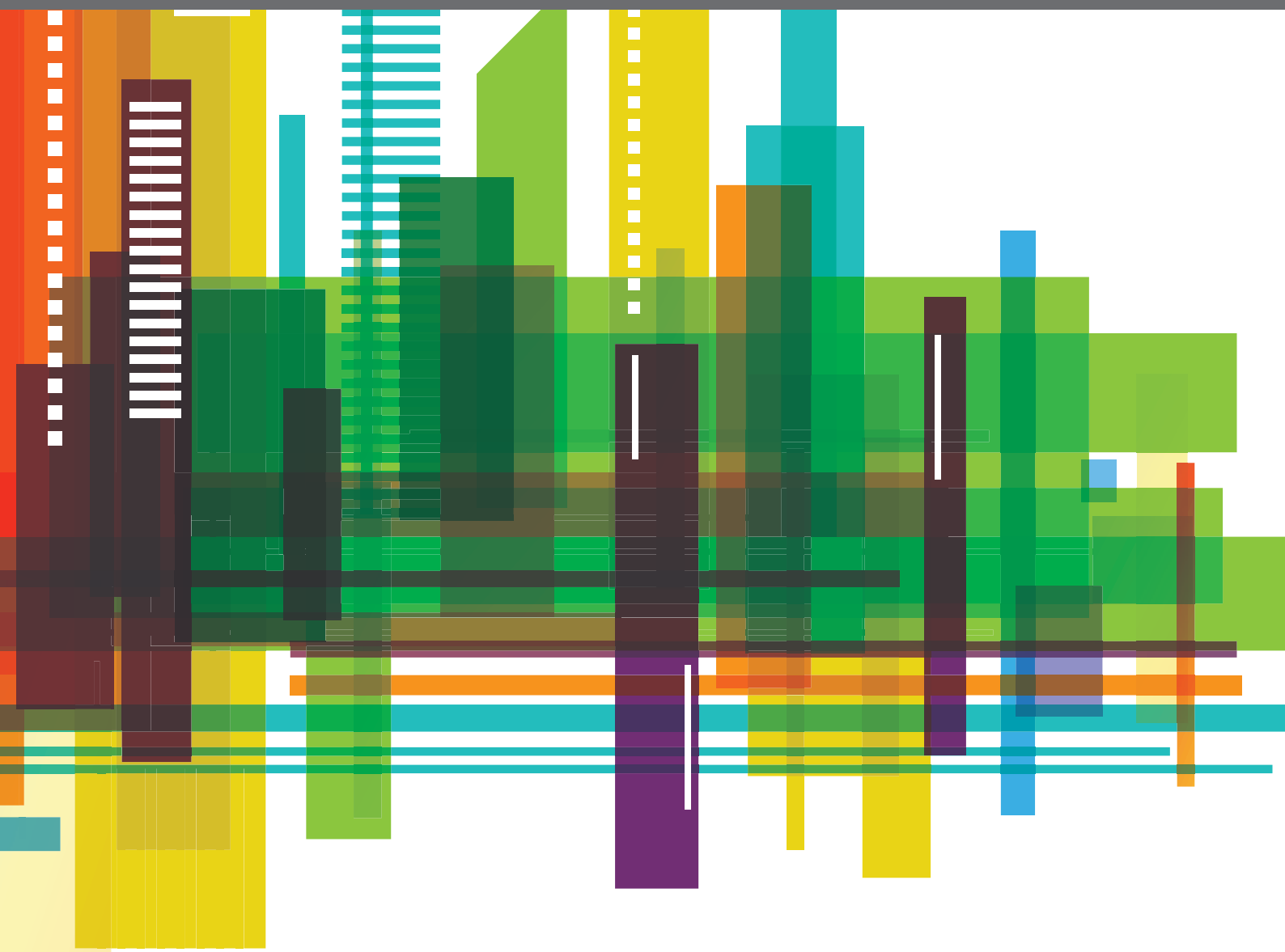

frontiers Research Topics

ISSN 1664-8714
ISBN 978-2-88966-072-8
DOI 10.3389/978-2-88966-072-8

About Frontiers

Frontiers is more than just an open-access publisher of scholarly articles: it is a pioneering approach to the world of academia, radically improving the way scholarly research is managed. The grand vision of Frontiers is a world where all people have an equal opportunity to seek, share and generate knowledge. Frontiers provides immediate and permanent online open access to all its publications, but this alone is not enough to realize our grand goals.

Frontiers Journal Series

The Frontiers Journal Series is a multi-tier and interdisciplinary set of open-access, online journals, promising a paradigm shift from the current review, selection and dissemination processes in academic publishing. All Frontiers journals are driven by researchers for researchers; therefore, they constitute a service to the scholarly community. At the same time, the Frontiers Journal Series operates on a revolutionary invention, the tiered publishing system, initially addressing specific communities of scholars, and gradually climbing up to broader public understanding, thus serving the interests of the lay society, too.

Dedication to Quality

Each Frontiers article is a landmark of the highest quality, thanks to genuinely collaborative interactions between authors and review editors, who include some of the world's best academicians. Research must be certified by peers before entering a stream of knowledge that may eventually reach the public - and shape society; therefore, Frontiers only applies the most rigorous and unbiased reviews.
Frontiers revolutionizes research publishing by freely delivering the most outstanding research, evaluated with no bias from both the academic and social point of view. By applying the most advanced information technologies, Frontiers is catapulting scholarly publishing into a new generation.

What are Frontiers Research Topics?

Frontiers Research Topics are very popular trademarks of the Frontiers Journals Series: they are collections of at least ten articles, all centered on a particular subject. With their unique mix of varied contributions from Original Research to Review Articles, Frontiers Research Topics unify the most influential researchers, the latest key findings and historical advances in a hot research area! Find out more on how to host your own Frontiers Research Topic or contribute to one as an author by contacting the Frontiers Editorial Office: researchtopics@frontiersin.org

RECENT ADVANCES AND APPLICATIONS OF SEISMIC ISOLATION AND ENERGY DISSIPATION DEVICES

Topic Editors:
Dario De Domenico, University of Messina, Italy
Enrico Tubaldi, University of Strathclyde, United Kingdom
Izuru Takewaki, Kyoto University, Japan
Theodore Karavasilis, University of Patras, Greece
Andrea Dall'Asta, University of Camerino, Italy
Oren Lavan, Technion Israel Institute of Technology, Israel

Citation: Domenico, D. D., Tubaldi, E., Takewaki, I., Karavasilis, T., Dall'Asta, A., Lavan, O., eds. (2020). Recent Advances and Applications of Seismic Isolation and Energy Dissipation Devices. Lausanne: Frontiers Media SA.
doi: 10.3389/978-2-88966-072-8

Table of Contents

frontiers in Built Environment

EDITORIAL
published: 18 August 2020
doi: 10.3389/fbuil.2020.00126

Editorial: Recent Advances and Applications of Seismic Isolation and Energy Dissipation Devices

Dario De Domenico [1], Enrico Tubaldi [2], Izuru Takewaki [3], Theodore Karavasilis [4], Andrea Dall'Asta [5] and Oren Lavan [6]*

[1] Department of Engineering, University of Messina, Messina, Italy, [2] Department of Civil and Environmental Engineering, University of Strathclyde, Glasgow, United Kingdom, [3] Department of Architecture and Architectural Engineering, Kyoto University, Kyoto, Japan, [4] Department of Civil Engineering, University of Patras, Patras, Greece, [5] School of Architecture and Design, University of Camerino, Ascoli Piceno, Italy, [6] Faculty of Civil and Environmental Engineering, Technion-Israel Institute of Technology, Haifa, Israel

Keywords: seismic base isolation, energy dissipation devices, tuned mass damper, performance-based seismic engineering, reliability-based design, dampers, damper optimization, earthquake-resistant structures

Editorial on the Research Topic

Recent Advances and Applications of Seismic Isolation and Energy Dissipation Devices

One of the major (and oldest) challenges in the earthquake engineering field has been and still continues to be the conceptualization, development, and implementation of innovative earthquake-resistant systems for reducing the vulnerability of structures and infrastructures and improving the seismic performance and resilience, while keeping construction costs reasonable. There is no doubt that seismic isolation and energy dissipation devices belong to such class of systems. The effectiveness of these technologies in protecting structural elements and non-structural components under seismic action has been proven by many theoretical and numerical studies in the literature, shake-table test results, as well as by experimental evidence on how they actually behaved during real earthquakes. A traditional earthquake-resistant design philosophy is mainly focused on the "life-safety" performance level, which implies that the structure undergoes significant damage but does not collapse during a major earthquake, so that the occupants can evacuate safely. This is certainly adequate (and somehow reasonable from economic perspectives) for ordinary structures. In contrast, a design strategy using energy dissipation devices and/or seismic isolation aims at a more challenging "functionality" performance level even under strong earthquakes. This is accomplished in a twofold manner: (1) by supplemental damping mechanisms engaged in a limited number of elements or "fuse components," which can be easily replaced or whose accumulated plastic deformations can be recovered after the earthquake; (2) by limiting the transmission of seismic energy via low lateral stiffness devices interposed between the main structure and the ground. Overall, both these strategies result in a low-damage structural system, wherein the structure can be designed to remain in an elastic or, at least, in a quasi-elastic range of the response. Until some years ago, this "high-performance level" design was deemed necessary for *strategic* structures requiring minimal downtime after the seismic event due to resulting economic and social impact (hospitals, police stations, power plants, communication centers, etc.). Nowadays, the implementation of seismic isolation (including elastomeric bearings, lead rubber bearings, sliding friction pendulum and adaptive isolation devices) and energy dissipation devices (including metallic, viscous, viscoelastic, friction, rotational and inertial dampers, tuned mass dampers and tuned liquid dampers) has become more and more common, not only for the aforementioned critical structures, but also for *ordinary* structures, and particularly those needing retrofitting.

OPEN ACCESS

Edited by:
Massimo Latour, University of Salerno, Italy

Reviewed by:
Carmine Galasso, University College London, United Kingdom

****Correspondence:***
Dario De Domenico
dario.dedomenico@unime.it

Specialty section:
This article was submitted to Earthquake Engineering, a section of the journal Frontiers in Built Environment

Received: *29 June 2020*
Accepted: *10 July 2020*
Published: *18 August 2020*

Citation:
De Domenico D, Tubaldi E, Takewaki I, Karavasilis T, Dall'Asta A and Lavan O (2020) Editorial: Recent Advances and Applications of Seismic Isolation and Energy Dissipation Devices. Front. Built Environ. 6:126. doi: 10.3389/fbuil.2020.00126

Seismic isolation and energy dissipation devices are quite mature technologies. After being studied and used for many decades, the theoretical concepts and working mechanisms underlying these systems are today well-established. Therefore, the reasons for launching a Research Topic addressing the "Recent Advances" in this field might appear questionable. Nevertheless, the use of advanced reliability-based or performance-based strategies capable of dealing with uncertainties inherent to the device behavior and to the response of the protected structures, are relatively modern research lines. Moreover, in recent years the design of such devices has benefitted from fast-changing improvements of numerical algorithms and optimization solvers, so that optimally configured devices implemented in real engineering projects can more easily and more accurately be obtained. Additionally, there is an ever-growing computational ability of advanced numerical models for the simulation of the mechanical behavior of these devices vis-à-vis the experimental one. Many complex non-linear phenomena significantly affecting their hysteretic behavior can be nowadays more truthfully incorporated in such models. Finally, the development of new classes of isolation devices, dissipative elements and hybrid systems for seismic control has gained momentum in recent years, encouraged by concurrent progress achieved in material science and mechanical engineering.

Following these motivations, in this Research Topic 18 high-quality papers have been selected and published following a detailed peer-review. These papers address a range of topics, including discussion of prototype tests from laboratory findings on devices available in the market, numerical studies on innovative techniques for seismic isolation or energy dissipation, case studies or benchmark projects of implemented isolation/dissipation technologies, and advanced design methodologies. In the Editors' opinion, each selected paper presents undisputable scientific novelty from various viewpoints (analytical, numerical, experimental, conceptual, implementation issues), proposes emblematic engineering projects, and represents a major contribution in the field. The Editors hope that this Research Topic can somehow contribute, even if modestly, to broadening the state of knowledge and the state of development of current and emerging mitigation strategies against the earthquake risk. An overview of the various papers gathered in this article collection is given below.

In the first paper, Pucinotti and Fiordaliso present an emblematic case study project concerning a steel-concrete bridge equipped with different energy dissipation devices, such as fluid viscous dampers and shock transmitting units integrated with the bearings. The project involves different complexities related not only to irregular altimetric and planimetric conformation, but also to the large number of devices required to guarantee the structural integrity of piers during severe design earthquakes. The proposed design procedure assisted by testing makes it possible to achieve good matching between numerical model and real dynamic response of the bridge (assessed by operational modal analysis of ambient vibrations). The proposed study represents a valid example of the most advanced structural design methods of bridges equipped with energy dissipation devices.

In the second paper, De Domenico et al. present an experimental investigation on the thermo-mechanical coupled response of friction pendulum isolators, with particular emphasis on the effect of frictional heating at the sliding interface. A series of full-scale experimental tests on a prototype isolator equipped with eight thermocouples are carried out, with an extensive testing protocol including different axial loads and sliding velocities. Temperature measurements are critically analyzed in view of the associated heat fluxes at the sliding interface. This physical phenomenon, often neglected in calculations and in building codes, produces a reduction of the energy dissipation capability of the isolator due to temperature-induced friction degradation, which in turn implies higher displacements of the isolated superstructure. The punctual temperature measurements of the eight thermocouples are useful to calibrate and validate sophisticated thermo-mechanical coupled finite element models that explicitly solve the thermal problem and the mechanical problem in an interconnected manner.

Another emblematic case study project is presented by Gandelli et al., namely the seismic retrofit of a hospital located in Southern Italy. The retrofitting intervention incorporates a series of hysteretic dissipative bracing systems. Emphasis is placed on the seismic protection of acceleration-sensitive and drift-sensitive non-structural components of the hospital, which represents a major issue due to the economic and social implications resulting from their failure. Different failure scenarios related to various intensity levels of the earthquake excitation are analyzed, in line with current performance-based design approaches. While the adopted hysteretic dampers are effective to reduce structural damage under severe design earthquakes, unacceptable peak floor accelerations during frequent design earthquakes occur, which cause serious damage to critical components like elevators and false ceilings, thus impairing the desired hospital functionality after the seismic event.

In the fourth paper, Ponzo et al. present a displacement-based design procedure for promising post-tensioned timber framed buildings coupled with hysteretic dissipative bracing systems. The numerical procedure aims at protecting both structural and non-structural elements, by identifying appropriate design force, strength, and stiffness of the post-tensioning system and of the dissipative braces. The equivalent force-displacement relation of the braced post-tensioned frame is represented by a flag-shaped hysteretic behavior, which combines the equivalent bare post-tensioned frame with the equivalent elastic perfectly-plastic dissipative behavior of the bracing system. The effectiveness of the proposed system and the accuracy of the developed design procedure are verified by refined non-linear dynamic analyses and by shaking table test results carried out on 2/3 scaled prototype model, and excellent agreement is found.

Effective numerical approaches for the optimal design and placement of viscous dampers in building structures accounting for uncertainties in the fault rupture slip mechanism and in the seismic input are investigated by Kondo and Takewaki, Tubaldi et al., and Navarra et al.. In particular, Kondo and Takewaki present a simultaneous treatment of the critical fault rupture slip distribution problem, via a sequential quadratic

programming method, and the optimal damper placement problem for the critical ground motion, via a sensitivity-based method. The robustness of the maximum interstory drift in building structures under the uncertainty in fault-rupture slip distribution is analyzed by an appropriate robustness function. The analysis of the critical ground motion scenario leads to the most unfavorable structural response, so that the proposed method represents a promising tool for resilient building design. A practical design method for viscous dampers connecting adjacent structures is presented by Tubaldi et al.. The method is based on a reduced order model of the coupled system, and the typical non-linear power law force-velocity behavior of the dampers is incorporated in the design process by the stochastic linearization technique. The effectiveness of the linearized reduced order model and of the overall design strategy is assessed via numerical analyses of two adjacent buildings with shear-type behavior connected by linear or non-linear fluid viscous dampers and subjected to Gaussian stochastic base acceleration. Critical analysis and comparison of the numerical results reveals a series of useful conclusions regarding the use of linear or non-linear viscous dampers depending on the seismic intensity level, and the most convenient damper placement in relationship to the target response indicator of the adjacent structures. Along a similar research line and exploiting a similar stochastic framework, Navarra et al. develop an efficient design procedure for fluid viscous dampers implemented in building structures. The procedure aims to minimize the damper cost subjected to a constraint on the structural performance. The proposed method takes advantage of some convenient closed-form expressions of the power spectral density function of the seismic input that is consistent with the pseudo-acceleration response spectrum of the installation site (expressed in a general, four-branch form valid for most of the building codes). In this way, the proposed design method is of practical connotation, as the obtained optimal design of the fluid viscous damper is coherent with the provisions of current seismic building codes.

Enhanced isolation strategies are presented by Di Matteo et al. and Zhu et al. to reduce the displacement demand of base-isolated structures and to improve the isolation performance, respectively. In particular, Di Matteo et al. comparatively investigate the performance of three unconventional hybrid isolation strategies, consisting in the combination of the base isolation (BI) with: (1) a tuned mass damper (TMD) on the basement of the structure; (2) a new TMD with a dashpot located in between the secondary mass and the ground; (3) a tuned liquid column damper (TLCD). The performance is analyzed in terms of base displacement, acceleration, and stroke of the devices. It is found that the new TMD is more effective that the other two analyzed passive devices due to the higher dissipative forces, and can represent an effective system to reduce the displacement response of base-isolated structures. Zhu et al. propose a semi-active non-linear damping-based building isolation system under seismic loadings. A two-degree-of-freedom (2-DOF) scaled building model is developed for simulation studies. Calibrated and validated against experimental results, the 2-DOF model is then used to carry out the optimal design of the non-linear damping parameter to minimize the acceleration and the inter-story drift of the building.

Another emblematic case study project concerning a seismic retrofitting intervention with hysteretic damped braces is presented by Mazza and Imbrogno. The peculiarity of this study is that the authors analyze a reinforced concrete (RC) school in Southern Italy under a critical scenario in which such structure is damaged by a fire. Different extents of damage are related to different durations of heating and cooling phases, and two fire scenarios (related to the extension of the fire compartment) are studied. A displacement-based design procedure of the hysteretic dampers is adopted to obtain a retrofitted structure globally regular with regard to stiffness and strength, by balancing the degradation of fire-exposed RC frame members. Therefore, the proposed procedure fully accounts for the damaged properties of the RC cross sections due to fire, and represents a valuable numerical tool to account for concurrent risk scenarios (earthquake and fire) when designing retrofitting interventions.

A comprehensive computer-aided seismic design tool for both new and existing structures equipped with hysteretic dampers is presented by Nuzzo et al.. This computational tool, named DIBRAST (design of Dissipative BRAced Structures), underlies a specific displacement-based design procedure developed by the same authors. Unlike other articulated procedures that require iterative steps at the design stage, the proposed methodology is implemented in a closed-form analytical variant wherein the required iterations are automated by the software, thus significantly reducing computational times. The code calculates the mechanical properties of the dissipative system, in terms of yielding force and elastic stiffness, which are able to meet the target performance objective in terms of displacement. The codes proves to be a promising computational tool aiming at simplifying the (sometimes intricate) design procedures of structures equipped with hysteretic dampers.

An innovative structural control system for high-rise buildings under pulse-type and long-duration earthquake ground motions is developed by Kawai et al.. In particular, a damping layer is inserted between two stiff cores, a sub-frame upper strong-back core and a sub-frame lower strong-back core, so that the deformation is concentrated in the connection point of the cores. The behavior of the proposed damping configuration is investigated by analyzing the resulting mode shapes with different damping levels. Then, a simplified model is proposed to allow a direct investigation of the control performance. The comparison between the simplified and full models is also provided. Finally, different types of inputs (i.e., transient-like inputs and seismic excitation) are considered to evaluate the control effectiveness. The optimal damping coefficient allows to achieve quite good response reductions when subjected to far field, near-fault pulse-like, and long-period earthquakes.

In the paper by Furinghetti et al., a hybrid simulation technique is implemented in order to assess the effectiveness of a curved surface slider in reducing the seismic response of a base isolated building. In particular, while the dynamic behavior of the superstructure is investigated by a numerical model, an isolation device (representative of the whole set of isolators) is physically

tested and both outcomes are considered together in a hybrid testing framework. The response from the hybrid simulation is compared with the response obtained with a full numerical building model in which the non-linear isolator cyclic response is implemented, and very good agreement is found. The proposed hybrid simulation technique is able to overcome the difficulties that an experimental test of a full-scale base isolated building could entail and, at the same time, allows capturing the essential dynamical characteristics of the system under investigation.

Another emblematic case study project is presented by Dall'Asta et al.. In particular, this paper presents the seismic design of the new Camerino University Research Center (Italy). The building consists of a steel braced superstructure with pinned joints and RC sub-structures able to fit the complex morphology of the installation area. In order to enhance the seismic performance of the building under different earthquake intensity levels concerning both serviceability and ultimate limit states, a hybrid base-isolation system consisting of high-damping rubber bearings and low-friction flat sliders, with a high period of isolation, is designed. A resilience and robustness oriented design procedure, based on a probabilistic seismic hazard analysis for the building site, is developed. The seismic performance is analyzed by a specific risk analysis and results are presented in terms of hazard curves for different return periods of the earthquake excitation relevant to both the isolation system and the super-structure. The results demonstrate a high level of safety and robustness of the building as well as a high level of resilience, thus making the proposed case study a representative example of earthquake-resilient building design.

Scale effects are of paramount importance in experimental tests to investigate the hysteretic behavior of isolation devices. Using scaled devices would allow cheaper and more feasible characterization, but the validity of the obtained results against the real-scale isolator may be questionable. The interesting contribution by Murota and Mori deals with such scale effects on a high damping rubber bearing. In particular, experimental tests are carried out on two types of isolators: full-scale isolators (with 1,000 mm diameter) requiring large capacity testing equipment, and scaled isolators (with 225 mm diameter) requiring smaller testing equipment and implying reduced costs. Shear-strain dependence tests and frequency dependence tests are performed on both the isolators; then, repeated loading tests are performed on the scaled model isolator. Finite element analysis is also carried out to simulate the repeated loading test on isolators with larger dimensions. Results show that, although the absolute values of the equivalent shear properties of the two bearings are different, the normalized variation trends as a function of the frequency and of the strain amplitude are relatively similar. Furthermore, repeated loading tests show that the history dependence and temperature dependence effects are remarkable and lead to a progressive loss of the shear stiffness and dissipation capacity of the bearing. Finally, the finite element analysis demonstrates that the loss rate with increasing number of cycles depends on the internal temperature increment and, hence, is strictly related to the isolator dimensions.

Ground motions with velocity pulses caused by near-fault directivity have received a great deal of attention from engineers and seismologists because of their potential to cause severe damage to structures, especially for flexible structures. Three papers of the Research Topic by Anajafi et al., Elias et al., and Hashizume and Takewaki specifically address this aspect. In particular, in the paper by Anajafi et al., the effectiveness of base isolation for long-period structures is assessed. A preliminary numerical study on inelastic displacement spectra is presented to investigate the effectiveness of seismic isolation for flexible structures. Despite the common belief that this solution is detrimental for such structures, some beneficial effects are highlighted in this study, for both far-fault (FF) and near-fault (NF) seismic events. Then, an emblematic case study project concerning the Rudshur Bridge (Iran) is analyzed. This bridge is a composite steel box girder bridge with long piers and long periods, placed in an area prone to NF excitations but designed for FF earthquakes. It is found that the seismic isolation can be effective even for this long-period bridge under both FF and NF excitation, with a reduction of both base shear and pier drift. Since the deck may undergo large displacements under NF (the larger the strength reduction, the larger the deck displacements), an optimum value of yield strength-to-weight ratio is identified. From another perspective, the use of TMD schemes is commonly discouraged for structures subjected to short-duration, pulse-like ground motions such as the aforementioned near-field earthquake excitations. While the efficiency of TMDs on structures under far-field earthquakes has been demonstrated, the convenience of its employment against near-fault earthquakes is still under discussion. The paper by Elias et al. investigates the response mitigation of a reinforced concrete chimney subjected to pulse-like near-fault ground motions with different TMD schemes, namely single TMD (SMTD), multiple TMD having equal stiffness (w-MTMDs) and multiple TMD having equal masses (e-MTMTs). Based on time-history analyses under 69 pulse-like ground motions, it is found that the pulse period of ground motion plays a very important role in how effective the TMD control schemes are. In particular, the e-MTMDs schemes prove to be effective in reducing the response of the chimney while subjected to earthquakes having dominant periods close to higher order periods, whereas the STMD is quite effective for controlling the fundamental period. Finally, in the paper by Hashizume and Takewaki, a new viscous-hysteretic hybrid (HVH) damping system is proposed for seismic control against long-period pulse-type earthquake ground motions of large amplitude. The proposed system includes a viscous damper and a hysteretic damper with a gap mechanism in parallel. In the proposed damper system, the viscous damper allows controlling the broad-amplitude range vibration whereas the hysteretic damper with a gap mechanism is expected to act as a stopper for large-amplitude range vibration. The proposed HVH damper system is a promising control system for reducing the response of long-period structures (e.g., high-rise buildings and base-isolated buildings) under pulse-type ground motions of large amplitude, without implying large residual deformation (which is an advantage compared to alternative dual hysteretic damper systems).

AUTHOR CONTRIBUTIONS

All authors listed have made a substantial, direct and intellectual contribution to the work, and approved it for publication.

ACKNOWLEDGMENTS

We would like to thank all authors for their valuable contributions, the many dedicated reviewers for their useful guidance to improve the papers, and the Editorial Team of Frontiers in Built Environment (Earthquake Engineering Section) for the professional assistance and for the valuable opportunity to launch this Research Topic.

Conflict of Interest: The authors declare that the research was conducted in the absence of any commercial or financial relationships that could be construed as a potential conflict of interest.

frontiers in Built Environment

ORIGINAL RESEARCH
published: 04 June 2019
doi: 10.3389/fbuil.2019.00074

Frictional Heating in Double Curved Surface Sliders and Its Effects on the Hysteretic Behavior: An Experimental Study

Dario De Domenico[1]*, *Giuseppe Ricciardi*[1], *Samuele Infanti*[2] and *Gianmario Benzoni*[3]

[1] Department of Engineering, University of Messina, Messina, Italy, [2] FIP Mec S.p.A., Selvazzano Dentro, Italy, [3] Department of Structural Engineering, University of California, San Diego, San Diego, CA, United States

The hysteretic behavior of friction isolators is affected by the variability of the friction coefficient caused by heating phenomena at the sliding interface. The aim of this paper is to investigate such heating phenomena through a series of full-scale experimental tests on a double curved surface slider. The prototype isolator is equipped with eight thermocouples placed in different points of the isolator, which are embedded in the sliding plate. The probes of the thermocouples are in contact with the stainless steel sheet covering the sliding plate, in such a manner that their measurements are representative of the temperature rise occurring at the sliding interface. By investigating different axial loads and sliding velocities, we discuss the measured temperature rise and its implications on the hysteretic behavior of the prototype isolator. Friction variation is observed in the cyclic response of the isolator, which reduces the energy dissipated per cycle and, consequently, may lead to some underestimations of the displacements occurring during real seismic events if a constant friction coefficient is assumed. The proposed data can be helpful to calibrate sophisticated thermo-mechanical finite element models, which is the object of ongoing research.

Keywords: curved surface slider, friction pendulum isolator, heating phenomena, friction variation, temperature measurements

OPEN ACCESS

Edited by:
Massimo Latour,
University of Salerno, Italy

Reviewed by:
Yutaka Nakamura,
Shimane University, Japan
Raffaele Laguardia,
Sapienza University of Rome, Italy

***Correspondence:**
Dario De Domenico
dario.dedomenico@unime.it

Specialty section:
This article was submitted to Earthquake Engineering, a section of the journal Frontiers in Built Environment

Received: *11 April 2019*
Accepted: *20 May 2019*
Published: *04 June 2019*

Citation:
De Domenico D, Ricciardi G, Infanti S and Benzoni G (2019) Frictional Heating in Double Curved Surface Sliders and Its Effects on the Hysteretic Behavior: An Experimental Study. Front. Built Environ. 5:74. doi: 10.3389/fbuil.2019.00074

INTRODUCTION

Curved surface sliders (CSS), also known as friction pendulum isolators, are seismic isolation devices that have been increasingly used as effective earthquake protection strategy of buildings and bridges. The pendulum operating principle is offered by an articulated slider moving along a concave surface, and the restoring capability is due to the curved geometry of the sliding surface itself. The popularity of these devices is mainly due to the large displacement capability, besides the compact shape, especially for improved versions with multiple sliding surfaces like double (Fenz and Constantinou, 2006), triple pendulum system (Sarlis and Constantinou, 2013), and the lower thickness in comparison with the elastomeric devices. The imposed natural period of vibration is controlled by the sliding surface radius, thus it is not affected by the supported mass, which results in an ideal coincidence of the center of mass and center of stiffness. The energy dissipation is uniquely dependent upon the tribological properties of the sliding materials. Typical materials employed in practice include Polytetrafluoroethylene (PTFE) composites, Ultra High Molecular Weight Polyethylene (UHMWPE), and Polyammide (PA).

Experimental findings reveal that the friction coefficient of these isolators is far from being constant during an earthquake event (i.e., complying with the Coulomb's law of friction). In reality, the friction coefficient is variable, and it may be considered as a complex function of axial load, sliding velocity, and heating phenomena at the sliding interface, which may lead to significant friction variation. The friction properties may strongly affect the seismic performance of base-isolated structures (Castaldo and Tubaldi, 2015). Among the above effects, the primary and most important source of variation of the friction coefficient is the temperature rise arising at the sliding surfaces. Friction-induced temperature rise and consequent variation of the friction coefficient are two interconnected phenomena that affect one another and that, consequently, should be carefully considered to assess the actual hysteretic characteristics of these isolation devices. Nevertheless, experimental investigations focused on the mutual interaction between mechanical and thermal behavior are very few (Constantinou et al., 2007; Quaglini et al., 2014). Moreover, available experimental results refer to just few excitation scenarios (not exploring the variability of the temperature rise with different sliding velocity and axial loads) and are limited to single CSS. Additional experimental results that correlate the temperature rise at the sliding interface with the corresponding hysteretic behavior are desirable for a proper understanding of the complex thermo-mechanical response of friction isolators.

The aim of this paper is to complement the previous experimental studies by considering a more general testing scenario. In this work, a double curved surface slider (DCSS) is tested under different monodirectional excitations (including five sliding velocities and two levels of vertical load) at the laboratory CERISI of the University of Messina, Italy. In line with previous experimental campaigns, temperature measurements are obtained through eight thermocouples embedded into the upper plate of the device, at a certain depth below the sliding interface. The mechanical and thermal response of this device is monitored experimentally. The recorded force-displacement curves and the thermocouple registrations could be useful to calibrate new thermo-mechanical models (for instance, based on finite elements) or to validate existing analytical/numerical models available in the literature (Lomiento et al., 2013a,b; Kumar et al., 2015; De Domenico et al., 2018; Furinghetti et al., 2019; Gandelli et al., 2019) against experimental findings, which is left for future research work.

PRELIMINARY CONCEPTS ON THE HYSTERETIC BEHAVIOR OF FRICTION ISOLATORS

We here recall the basics of the mechanical behavior of friction isolators focusing the attention on the frictional performance. A sketch of a DCSS is shown in **Figure 1** along with a schematic diagram of the corresponding force-displacement response. The device consists of a slider (typically made of steel), whose external surfaces are convex and equipped with two pads of a specific sliding material. The most widely used sliding materials are polytetrafluoroethylene (PTFE), PTFE-based composites enhanced with fillers, or self-lubricating polymers with high-bearing capacity such as ultra-high-molecular-weight polyethylene (UHMWPE). Above and below the slider there are two steel plates, whose internal surfaces are concave with the same curvature radius as the inner pads and are covered by a sheet of polished stainless steel (typically 2.5 mm thick).

When the slider departs from the original (equilibrium) position, the sliding motion along with the curvature of the surfaces give rise to a resisting force F. In particular, the mechanical behavior of the device is controlled by two main characteristics: (1) the curvature radius R of the two opposed pairs of curved surfaces (one concave and one convex); (2) the tribological properties of the sliding materials at the interface. Indeed, the curvature radius R affects the re-centering properties of the device according to the pendulum principle (re-centering force F_r), in relationship with the value of the axial load N (i.e., the gravity load of the supported mass) and the entity of the displacement magnitude u. On the other hand, the frictional force F_f arises due to the sliding motion and is ideally independent on the value of the displacement, but mainly related to the friction coefficient μ and to the signum of the sliding velocity v. The mathematical model describing the idealized bilinear hysteretic behavior shown in **Figure 1** is the following (Zayas et al., 1990).

$$F = F_r + F_f = \frac{W}{R}u + \mu W \,\mathrm{sign}(v) \tag{1}$$

where W is the applied vertical load acting on the device, $K_r = W/R$ represents the restoring stiffness and sign(·) is the signum function. According to Equation 1 that assumes a constant friction coefficient, the frictional force is $F_f = \pm\mu W$ depending on whether the sliding velocity is positive or negative, respectively. Therefore, the bilinear hysteretic behavior of the device stems from the sum of two contributions, the restoring force F_r and the frictional force F_f.

In contrast to the assumption of constant friction coefficient underlying Equation 1, the value of μ evolves during a real seismic event as observed in experiments. In order to highlight the real variability of the friction coefficient due to different effects, the restoring force F_r can be subtracted by experimental measures of the total force of the device F, and the resulting friction force (evolving during the test) can be divided by the vertical load W to obtain the value of μ. Relevant results obtained at the CALTRANS SRMD laboratory at the University of California San Diego are depicted in **Figure 2** for two different testing pressures, namely 15 and 30 MPa.

The Coulomb friction model would lead to a rectangular friction coefficient-displacement cycle, whereas the experimental loop departs significantly from this idealized rectangular shape. The main sources of variability of the friction coefficients are ascribed to the following aspects:

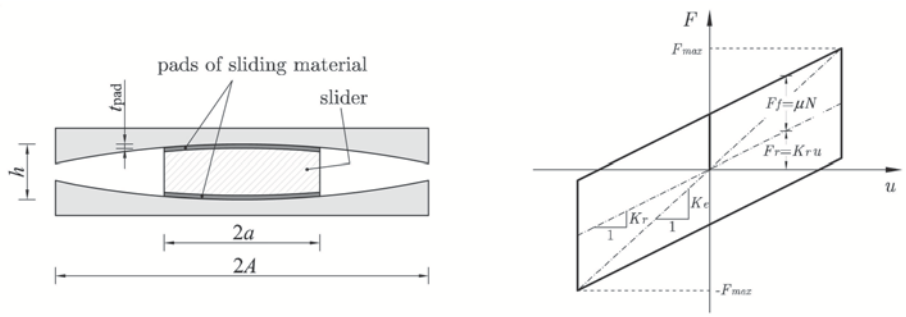

FIGURE 1 | Sketch of a double curved surface slider **(Left)** and schematic force-displacement response **(Right)**.

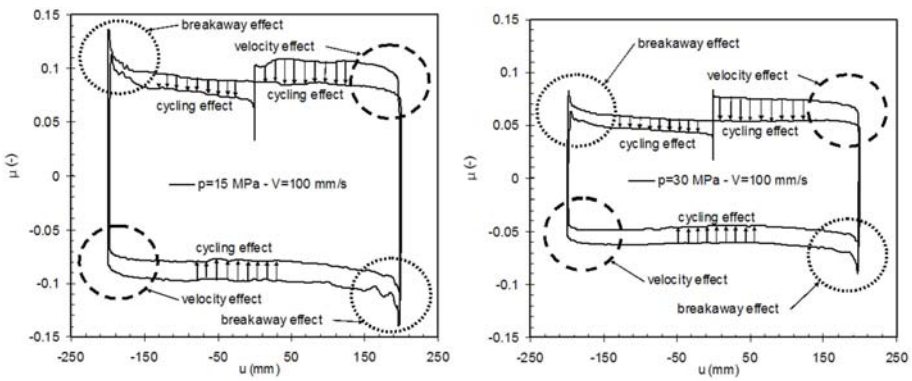

FIGURE 2 | Variability of friction coefficient with pressure, velocity, and cyclic effects (from Lomiento et al., 2012).

- *Breakaway effects* due to the transitions between the static and dynamic values of the friction coefficients that occur at the beginning of motion and at each motion reversal;
- *Pressure effects* as the friction coefficient decreases with increasing vertical loads; for instance, the two values of applied pressures lead to friction coefficients of around 0.08 (for $p = 15$ MPa) and 0.05 (for $p = 30$ MPa);
- *Velocity effects* as the friction coefficient is related to the velocity of motion; it decreases with reduction of speed and this can be observed before the motion reversals by inspection of the rounded shape of the cycle near the attainment of the peak displacement values, wherein the velocity decreases down to zero;
- *Cycling effects* as the friction coefficient decreases with repetition of cycles; this is due to heating phenomena arising at the sliding interface that induce temperature rise and friction variation. This work is mainly focused on the cycling effects, which are significant especially for high-velocity tests and for high contact pressures.

Based on these experimental observations, the frictional force F_f entering Equation 1 should be considered as a complex function of vertical load, sliding velocity, and temperature rise at the sliding interface as follows

$$F_f = \mu W \, \mathrm{sign}(v) \quad with \; \mu = \mu(W, v, T) \tag{2}$$

Such a model can only be calibrated based on extensive experimental data that investigate the temperature rise at the sliding interface for different vertical loads and sliding velocities. The present experimental work aims to provide a series of test results (temperature measurements and force-displacement loops) for a full-scale DCSS prototype that can be helpful to develop such complex models of friction variability.

DESCRIPTION OF THE EXPERIMENTAL CAMPAIGN

A full-scale prototype of double curved surface slider has been tested at the laboratory CERISI of the University of Messina, Italy (see **Figure 3**), whose main geometrical and mechanical characteristics are summarized in Failla et al. (2015).

The main geometrical properties of the device are listed in **Table 1**. The design load for the isolator is, according to the manufacturer's specifications, equal to 4,357 kN, which corresponds to the highest value of load used in the testing protocol. The sliding material is a particular type of UHMWPE

FIGURE 3 | Photograph of the laboratory CERISI, University of Messina, Italy.

TABLE 1 | Geometrical data of the analyzed double curved surface slider.

Geometric dimension	Symbol (ref. to Figure 1)	Length [mm]
Radius of the steel plate	A	765/2 = 382.5
Radius of the slider	a	415/2 = 206.5
Radius of curvature	R	3,216/2 = 1,608
Height of the slider	h	95
Thickness of the pads	t_{pad}	8

developed by the company FIP Mec S.p.A., whose trademark name is FFM (Fip Friction Material) type M (medium friction, corresponding to a minimum friction coefficient of 5.5%), which is characterized by high compressive strength, excellent wear resistance and good stability and durability properties. The material is used in a non-lubricated variant and, compared to PTFE alternatives, exhibits negligible stick-slip phenomena and is characterized by a very low ratio between the breakaway and the dynamic friction coefficient. The absence of significant breakaway phenomena at the beginning of motion has also been verified in a series of slow (quasi-static) tests performed at the laboratory CERISI on the DCSS prototype of the present experimental campaign, using triangular wave forms with constant velocity of 0.1 mm/s, in accordance with EN15129:2009 standards (CEN Comité Européen de normalisation TC 340, 2009) (whose results are not reported here for the sake of brevity). Other characteristics may be found in the manufacturer website https://www.fipindustriale.it/.

Before the tests, the upper plate of the DCSS prototype is CNC (computer numerical control) machined to create a set of holes that allow the installation of eight thermocouples, as documented in **Figure 4**. The drawings of the holes and photographs of the final configuration of the DCSS prototype are shown in **Figure 5**.

J-type thermocouples are used with conductors having dimensions 1/0.3 mm, tolerance in accordance with IEC 584 Class 2 and temperature range from −60°C to +350°C. The eight thermocouples are labeled from 0 to 7, which corresponds to the numbers of channels (CH) used for the acquisition of the temperature registrations. The thermocouples are installed in contact with the underlying polished stainless steel sheet of 2.5 mm thickness; therefore, their depth with respect to the sliding surface is exactly 2.5 mm, whereas their depth with respect to the top surface of the overlying steel plate depends on the considered thermocouple, and is 22.28 mm for thermocouple 4 (central), 23.04 mm for thermocouples 2, 3, and 5 (lying on a radius of 50 mm from the center), 25.31 mm for thermocouples 0, 1, and 6 (lying on a radius of 100 mm from the center) and 30.28 mm for thermocouple 7 (lying on a radius of 150 mm from the center). The difference in the thermocouple depths is due to the spherical curvature of the sliding surface, which is related to the radius 1,608 mm as reported in **Table 1**.

As shown in **Figure 5**, the thermocouples are embedded into the upper plate of the DCSS prototype and then special care has been taken in order to allow their conductors to come out from the device via two properly realized routes. The device is then installed in the testing equipment as can be seen in the photographs of **Figure 6**. The two routes through which the conductors pass are deep enough to prevent breakage of the wires when the upper plate is in contact with the overlying girder steel beam of the testing equipment and subject to the vertical load.

The testing protocol, listed in **Table 2**, comprises two bearing pressures (15 and 30 MPa) and five different sliding velocities. More specifically, the tests 1–10 consists of a sinusoidal displacement input of the form $u(t) = u_{\max} \sin(2\pi f_0)$ where f_0 is the frequency and $u_{\max}$ the maximum displacement. These tests have a maximum velocity $v_{\max} = 2\pi f_0 u_{\max}$ and an average velocity over a cycle $v_{av} = 4 f_0 u_{\max}$. The range of sliding velocities of the present experimental campaign has been chosen in line with similar research papers from the relevant literature (Furinghetti et al., 2019; Gandelli et al., 2019), considering the typical values of sliding velocities of commonly used devices and also the recommendations from the manufacturer of the DCSS prototype. Following (Gandelli et al., 2019), one cycle at low velocity ($v_{\max} \leq 25$ mm/s), two cycles in the medium velocity ($40 \leq v_{\max} \leq 100$ mm/s) and two cycles in the high velocity range ($v_{\max} \geq 200$ mm/s) are included in the testing protocol. The same sliding velocities investigated in Furinghetti et al. (2019) for a similar experimental work have been adopted, namely 10, 40, 100, 200, 400 mm/s. These tests have allowed us to investigate the heating phenomena for different testing scenarios ranging from small contact pressures in conjunction with slow sliding motion up to more severe excitations associated with higher contact pressured in combination with higher sliding velocities. It is reasonably expected that the temperature rise is more pronounced for the latter testing conditions, as the heat flux q (power dissipated per unit area) can be ideally expressed by the following formula (Lomiento et al., 2013b; De Domenico et al., 2018).

$$q = \frac{\mu W |v|}{\pi a^2} \tag{3}$$

thus increasing linearly with the vertical load W and the sliding velocity v.

FIGURE 4 | CNC machining of the DCSS prototype to create holes and routes for the thermocouple installation.

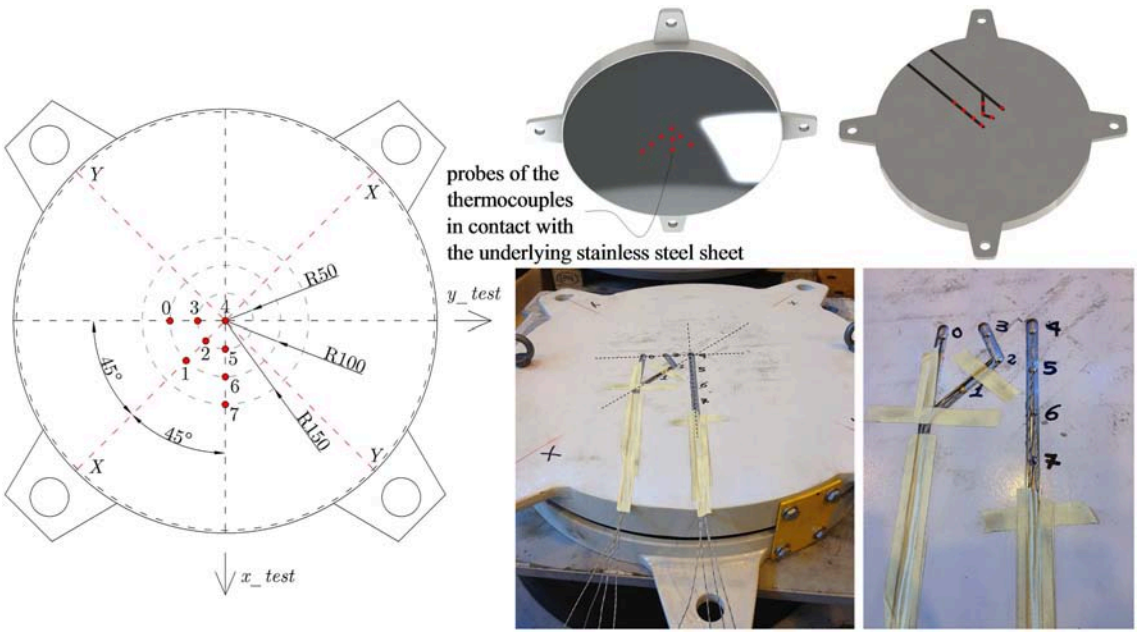

FIGURE 5 | Preparation of the DCSS prototype with eight thermocouples embedded into the upper plate.

It is worth noting that the sinusoidal displacement has been imposed along the *x_test* axis for all tests except for test #5 that has been carried along the *y_test* axis (cf. left-hand side of **Figure 5**) owing to some safety reasons on the testing equipment capabilities (related to the lower consumption of oil of the horizontal actuators along the *y_test* axis). This is important to interpret the temperature measurements of the eight thermocouples in relationship with their position in plan, since the thermocouples 4-5-6-7 are aligned with the *x_test* axis, whereas the thermocouples 4-3-0 are aligned with the *y_test* axis.

RESULTS AND DISCUSSION

For the sake of brevity, only a limited set of results of the testing protocol listed in **Table 2** are here presented and discussed. In particular, tests #2 and #7 (corresponding to maximum sliding velocities of 40 mm/s) have been selected as representative situations in which the heating phenomena are not pronounced, therefore the modest temperature rise does not lead to a significant friction variation. On the other hand, tests #5 and #8, associated with higher sliding velocities, do produce a friction variation owing to the heating phenomena occurring at the

FIGURE 6 | Installation of the DCSS prototype into the testing equipment, with thermocouple wires coming out from the two routes realized in the upper plate.

TABLE 2 | Testing protocol of the DCSS prototype.

Test #	u_{max} [mm]	W [kN]	p [MPa]	v_{max} [mm/s]	v_{av} [mm/s]	cycles [#]	f_0 [Hz]
1	300	2,178	15	10	6.4	3	0.0053
2	300	2,178	15	40	25.5	3	0.0212
3	300	2,178	15	100	63.7	3	0.0531
4	300	2,178	15	200	127.3	3	0.1061
5	300	2,178	15	400	254.6	3	0.2122
6	300	4,357	30	10	6.4	3	0.0053
7	300	4,357	30	40	25.5	3	0.0212
8	300	4,357	30	100	63.7	3	0.0531
9	300	4,357	30	200	127.3	3	0.1061
10	300	4,357	30	400	254.6	3	0.2122

sliding interface. Results from test #10 are not shown because they were affected by an experimental problem during the force recording process.

The force-displacement loops of the tests #2 and #7 are shown in **Figure 7**. As can be seen, the three cycles are almost superimposed to one another, with no significant difference between the first and third loop. This indicates that the friction coefficient is not affected by the temperature rise occurring in these tests and is quite stable during repetition of cycles (i.e., no considerable cycling effects take place). It is worth noticing some little deviations from the ideal force-displacement loop at the motion reversal (more evident in test #7). These may be ascribed to the concurrent effects of slightly varying vertical load induced by the vertical actuators (at the maximum excursion point of the slider), which are however limited to within the admissible values of the EN15129:2009 standards (CEN Comité Européen de normalisation TC 340, 2009), and the change of sliding velocity. The corresponding temperature values of the eight thermocouples are shown in **Figure 8** for both tests #2 and #7. It is observed that the maximum temperature measured during the test #2 does not exceed 35°C while the maximum temperature for test #7 is slightly higher than 42°C. The higher temperature in test #7 in comparison with test #2 (at the same maximum sliding velocity) is due to the higher contact pressure ($p = 30$ MPa in test #7 vs. $p = 15$ MPa), which corresponds to a doubled heat flux, cf. again Equation 1. However, there is a contemporaneous mechanism of "thermal control of friction," which makes the corresponding temperature rise not scaled proportionally with the heat flux (Ettles, 1986).

By inspection of the different temperature measurements of the eight channels (CH #0–CH #7), it can be noted that the highest temperature value occurs at the CH #5. The thermocouple five is indeed placed along the *x_test* axis and is probably the one associated with the more frequent sliding activity. Interestingly, the fluctuations of temperature are of short duration and therefore the corresponding temperature rise is called *flash temperature* in the relevant literature (Stachowiak and Batchelor, 2005).

Friction variation is instead observed in more severe testing excitations. In **Figure 9,** we show the force-displacement loops corresponding to test #5 and test #8. Especially for test #5, it is seen that the loops are narrowing after repetition of cycles, which is due to the friction variation induced by the temperature rise.

By examining the corresponding temperature measurements for the two tests shown in **Figure 10**, peak temperature values of around 70°C in test #5 (with maximum sliding velocity of 400 mm/s) are obtained. Once again, the thermocouple associated with the highest value of the temperature is CH #5. However, in contrast to other tests performed along the

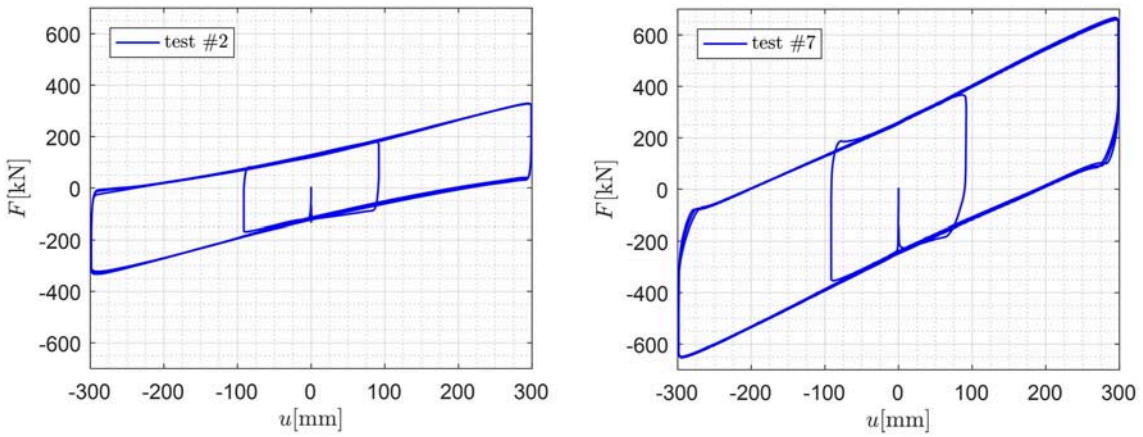

FIGURE 7 | Force-displacement loops of the DCSS prototype for test #2 **(Left)** and test #7 **(Right)**.

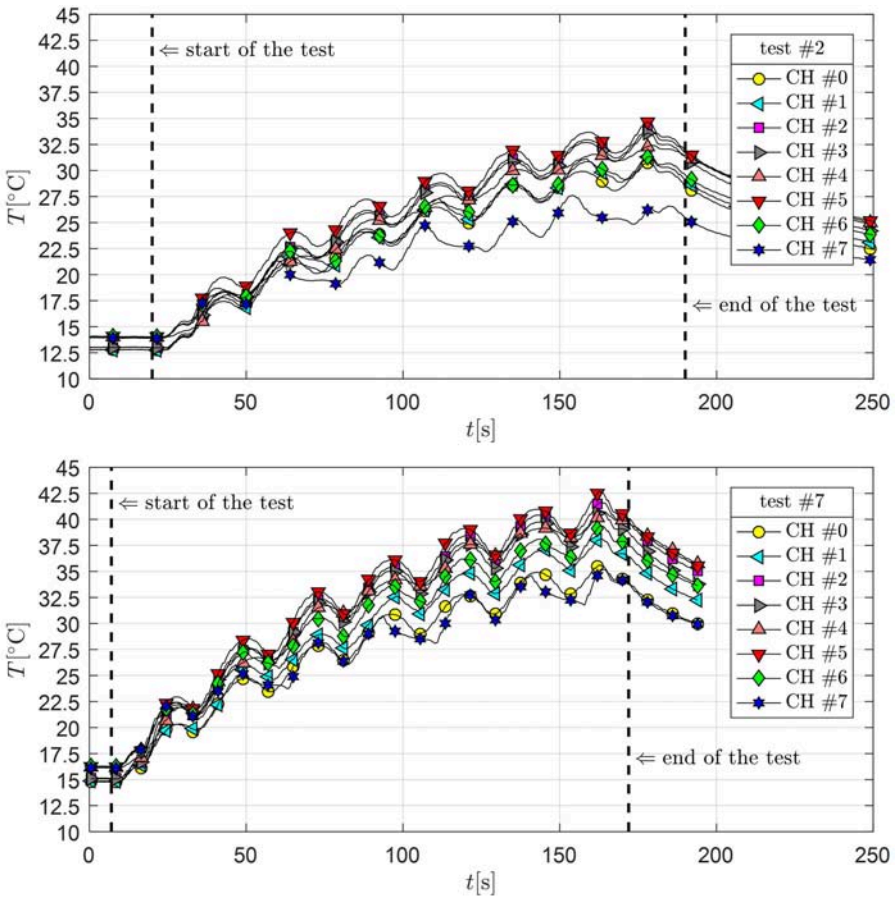

FIGURE 8 | Temperature measurements of the eight thermocouples for test #2 **(Top)** and test #7 **(Bottom)**.

x_test axis, in the test #5 the thermocouple CH #6 is associated with higher temperature values than the other tests. A possible justification is due to the fact that the sliding motion in test #5 is directed along the *y_test* axis (horizontal axis in the plan view of **Figure 5**) rather than along the *x_test* axis. Therefore, the thermocouple CH #6 is placed along the peripheral part of the slider perpendicular to the direction of the sliding motion, where the highest values of the contact pressure are expected to take

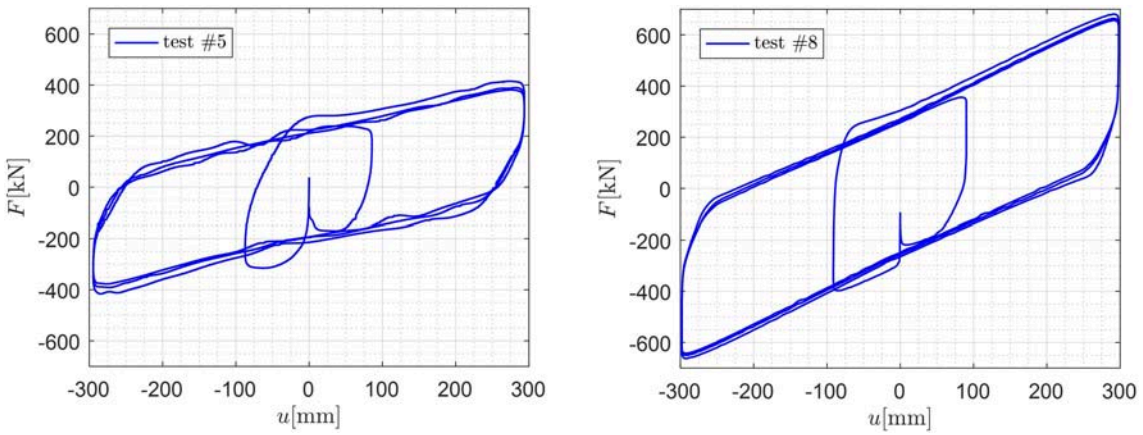

FIGURE 9 | Force-displacement loops of the DCSS prototype for test #5 **(Left)** and test #8 **(Right)**.

place. This is in line with trends of contact pressures identified in finite element analysis, cf. **Figure 11**, as well as in experimental tests through the aid of pressure-sensitive films placed between the sliding pad and the stainless steel sheet (Furinghetti et al., 2019). Moreover, the thermocouple CH #6 is crossed when the displacement of the device is zero and the corresponding velocity is maximum, therefore a large amount of heat flux (as a combination of pressure and velocity) is transferred based on Equation 1.

By observing the bottom part of **Figure 10**, the maximum temperature is slightly lower than 60°C in test #8 (with maximum sliding velocity of 100 mm/s). This fact, in combination with the previous results obtained in tests #2 and #7, indicates that the considered sliding material (UHMWPE) does not provide relevant friction variations for temperature rise up to ΔT=45°C. A summary of the maximum temperature rises (with respect to the initial value of temperature at the beginning of the test) measured by the eight channels (eight thermocouples) in the considered tests #2, #5, #7, #8 is reported in **Table 3**.

A specific proposal of analytical or numerical model accounting for the friction variation due to the heating phenomena is beyond the scope of the present paper. However, we recall that in a previous paper by the authors (De Domenico et al., 2018) a phenomenological (analytical) model was presented to capture the effects of frictional heating on the hysteretic behavior through a macroscale cycling variable. Moreover, in the same paper a thermo-mechanical coupled finite element model was also developed and validated against experimental data recorded in full-scale tests of CCS. A FORTRAN subroutine was developed to adjust the local friction coefficient based on the specific temperature value from the thermal solution. Nevertheless, in the previous work, no direct temperature measurement was performed, but the parameters of the subroutine were calibrated in an indirect fashion, based on the macroscopic force-displacement loops and, consequently, the resulting hysteretic behavior. What we aim to do in a forthcoming study is to exploit the actual temperature registrations here determined through the eight thermocouples to calibrate the above numerical model in a more consistent and physically meaningful manner.

We limit ourselves to point out the main consequences of the friction variation occurring in more severe tests (like #5 and #8) in terms of the main hysteretic parameters, namely the energy dissipated per cycle (*EDC*), and the dynamic friction coefficient per cycle μ_{dyn} computed as

$$\mu_{\mathrm{dyn}} = \frac{EDC}{4Wu_{av}} \tag{4}$$

wherein the average maximum displacement u_{av} is equal to $(u_{\max} - u_{\min})/2$, with $u_{\max}$ and $u_{\min}$ the maximum (positive) and minimum (negative) displacement in each cycle. Finally, the average maximum force F_{av} is calculated as

$$F_{av} = \frac{F_{\max} - F_{\min}}{2} \tag{5}$$

wherein $F_{\max}$ and $F_{\min}$ denote the maximum (positive) and minimum (negative) force in each cycle. Corresponding values of *EDC*, μ_{dyn} and F_{av} for the tests #5 and #8 are listed in **Table 4**, from which we note that the friction variation in test #5 leads to a reduction of 12.7% in terms of *EDC* and in terms of μ_{dyn} by comparing the first and third cycle. Similarly, the friction variation in test #8 leads to a reduction of 8.1% in terms of *EDC* and in terms of μ_{dyn} by comparing the first and third cycle. Moreover, we verify the variation of μ_{dyn} and F_{av} with respect to the mean value obtained from the three cycles by computing the variation values for the *i*th cycle as follows:

$$\Delta_{x\_i} = \frac{x_i - x_{\mathrm{mean}}}{x_{\mathrm{mean}}} \quad x_{\mathrm{mean}} = \frac{1}{3}\sum_{i=1}^{3} x_i. \tag{6}$$

with $x = EDC, F_{av}$. From the values reported in **Table 4** we notice that the DCSS prototype provided friction variations

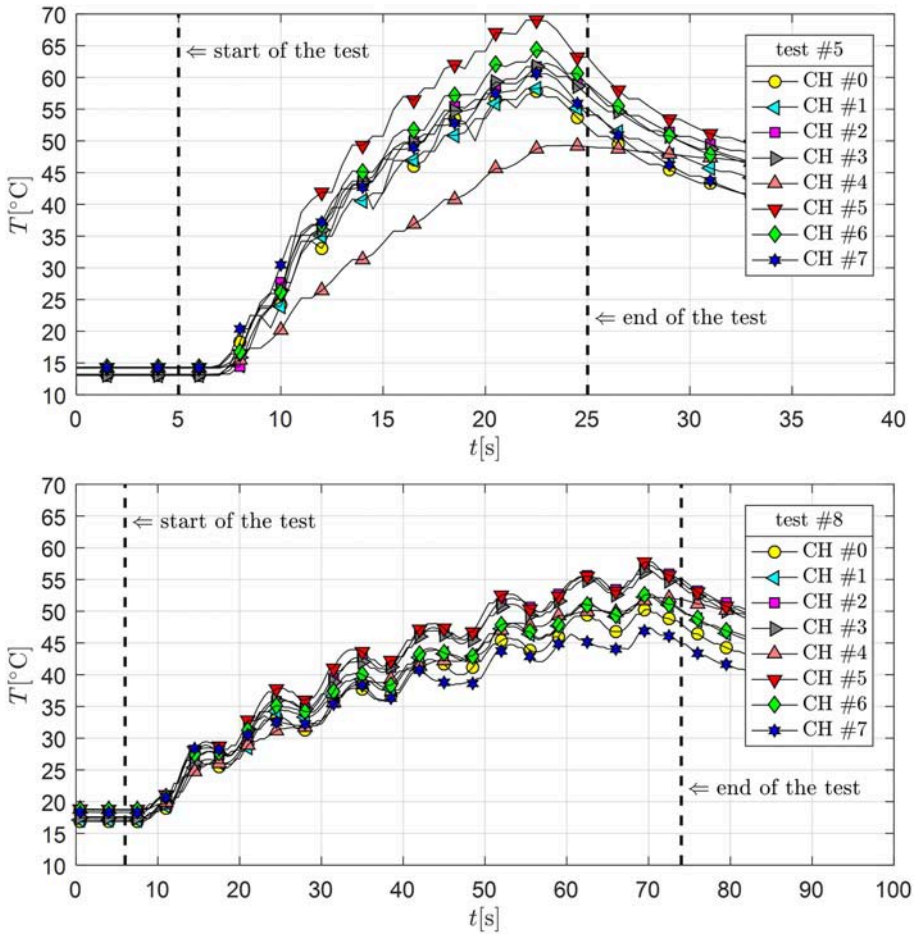

FIGURE 10 | Temperature measurements of the eight thermocouples for test #5 **(Top)** and test #8 **(Bottom)**.

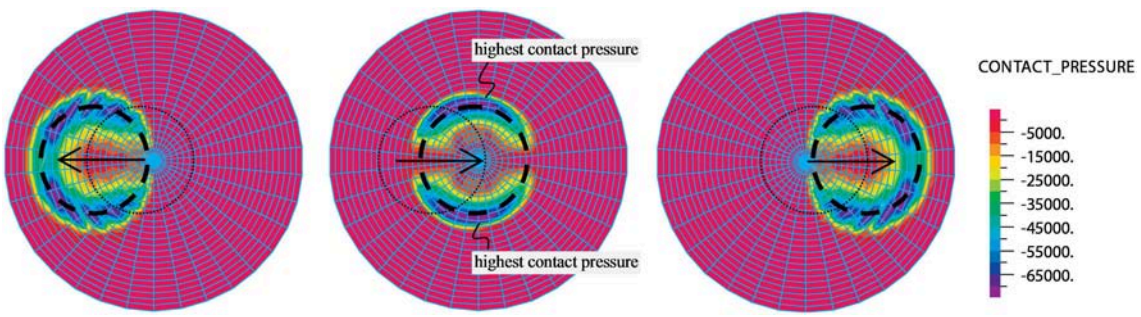

FIGURE 11 | Contour plots of contact pressure of CSS prototype analyzed in De Domenico et al. (2018).

below ±8% of the mean value. In line with the prescriptions of the EN15129:2009 standards (CEN Comité Européen de normalisation TC 340, 2009), in computing these variations only the three full cycles are considered, i.e., the starting and ending branches are excluded, although these branches are considered in the temperature measurements reported above. The presented results are useful for the calibration of a numerical model, which is the object of ongoing research.

SUMMARY AND CONCLUDING REMARKS

This paper has focused on the temperature rise of friction isolators, with particular emphasis on a double curved surface slider prototype that has been analyzed through full-scale experimental tests at the laboratory CERISI of the University of Messina, Italy. The device has been equipped with eight J-type thermocouples installed just below the stainless steel

TABLE 3 | Maximum temperature increase measured by the eight thermocouples in the tests #2, #5, #7, #8.

Test #	CH0 [°C]	CH1 [°C]	CH2 [°C]	CH3 [°C]	CH4 [°C]	CH5 [°C]*	CH6 [°C]	CH7 [°C]
2	18.1	18.7	21.2	20.9	18.6	20.8	17.4	13.7
5	44.8	45.5	49.0	48.6	35.1	54.8	50.1	46.3
7	20.8	23.3	26.5	25.7	24.6	26.4	23.1	19.1
8	33.4	35.1	39.7	38.8	33.5	39.0	34.0	29.1

** Thermocouple associated with the highest temperature.*

TABLE 4 | Hysteretic parameters corresponding to two tests with friction variation.

Test #	cycle *n*.	*EDC* [kJ]	μ_{dyn} [%]	Δ_{μ_dyn} [%]	F_{av} [kN]	Δ_{F_av} [%]
5	1	256.73	10.06	+7.84	415.3	+5.20
	2	233.41	9.15	−1.92	390.0	−1.22
	3	223.75	8.78	−5.92	379.1	−3.98
8	1	333.96	6.42	+4.67	671.6	+1.87
	2	316.39	6.09	−0.83	656.7	−0.38
	3	306.74	5.90	−3.84	649.4	−1.49

sheet in order to capture the temperature rise at the sliding interface. The thermocouples are placed on specific holes realized by a numerical control machine on the upper plate of the device. Five values of sliding velocities (in the range 10–400 mm/s) and two values of contact pressures (15 and 30 MPa) have been considered, in order to explore different thermo-mechanical responses of the DCSS prototype under a series of testing scenarios.

The results presented in this paper confirms that the temperature rise ΔT and the consequent cycling effects may affect the overall hysteretic behavior of full-scale friction isolators. However, the sliding material of the DCSS prototype used in the present experimental campaign, namely UHMWPE, is not significantly affected by temperature rise up to $\Delta T = 45°C$, at least for the tests conducted in this experimental campaign. Values of peak temperature of around 70°C have led to a certain reduction of the force-displacement loops, with a consequent reduction of the *EDC* and of the friction coefficient of a bit more than 12% when comparing the third cycle with the first cycle under imposed sinusoidal displacement tests. These variations are, however, modest (not significant) if compared to the implied uncertainties of the mechanical behavior of DCSS, the manufacturers' accuracy in defining the friction coefficient, and the approximate formulas used in the seismic codes. It is worth noting that the conclusions drawn here are limited to the employed UHMWPE as sliding material. Experimental force-displacement curves relevant to similar testing conditions (i.e., comparable sliding velocity and contact pressure) performed on a DCSS prototype with PTFE as sliding material (in place of UHMWPE of the present experimental campaign) showed significantly more marked reductions of the force-displacement curves (Furinghetti et al., 2019) than the ones reported in this paper and, by inference, a more pronounced influence of the heating phenomena on the friction coefficient. Finally, in tests involving slow sliding velocities or less severe combinations of sliding velocities and contact pressures, associated with temperature rise ΔT in the range from 25 to 45°C, no friction variation at all has been observed and the force-displacement loops are quite similar during repetition of cycles.

In the authors' opinion, the experimental findings of the present campaign can be useful to calibrate analytical models (like phenomenological models) that account for the friction variation via variables that are only indirectly related to the temperature rise (Lomiento et al., 2013b; Furinghetti et al., 2019; Gandelli et al., 2019). Additionally, the punctual temperature measurements of the eight thermocouples may be important to calibrate and validate more sophisticated thermo-mechanical coupled finite element models that explicitly solve the thermal problem and the mechanical problem in an interconnected manner (Pantuso et al., 2000; Quaglini et al., 2014; De Domenico et al., 2018), which is left for future research work.

DATA AVAILABILITY

All datasets generated for this study are included in the manuscript and/or the supplementary files.

AUTHOR CONTRIBUTIONS

DD carried out the experimental tests, post-processed the results, and wrote the paper. GR planned the CNC machining activities and the experimental tests. SI reviewed the manuscript and contributed to integrating section Results and Discussion. GB supervised the entire research work.

ACKNOWLEDGMENTS

DD and GR would like to express their gratitude to the company FIP MEC for providing the DCSS prototype used for the present experimental campaign.

REFERENCES

Castaldo, P., and Tubaldi, E. (2015). Influence of FPS bearing properties on the seismic performance of base-isolated structures. *Earth Eng. Struct. Dyn.* 44, 2817–2836. doi: 10.1002/eqe.2610

CEN Comité Européen de normalisation TC 340 (2009). *European Code UNI EN 15129:2009 Anti-seismic Devices*. Brussels: European Committee for Standardization.

Constantinou, M. C., Whittaker, A. S., Kalpakidis, Y., Fenz, D. M., and Warn, G. P. (2007). *Performance of Seismic Isolation Hardware Under Service and Seismic Loading [Report MCEER-07-0012]*. Buffalo, NY.

De Domenico, D., Ricciardi, G., and Benzoni, G. (2018). Analytical and finite element investigation on the thermo-mechanical coupled response of friction isolators under bidirectional excitation. *Soil Dyn. Earthq. Eng.* 106, 131–147. doi: 10.1016/j.soildyn.2017.12.019

Ettles, C. M. M. (1986). Polymer and elastomer friction in the thermal control regime. *ASME J. Tribol.* 108, 98–104. doi: 10.1115/1.3261151

Failla, I., Fazzari, B., Ricciardi, G., and Stella, A. (2015). "The Eurolab anti-seismic device (ASD) test facility at the University of Messina – Italy," in *Proceedings of the 14th World Conference on Seismic Isolation (14WCSI)* (San Diego, CA).

Fenz, D. M., and Constantinou, M. C. (2006). Behaviour of the double concave friction pendulum bearing. *Earthq. Eng. Struct. Dyn.* 35, 1403–1424. doi: 10.1002/eqe.589

Furinghetti, M., Pavese, A., Quaglini, V., and Dubini, P. (2019). Experimental investigation of the cyclic response of double curved surface sliders subjected to radial and bidirectional sliding motions. *Soil Dyn. Earthq. Eng.* 117, 190–202. doi: 10.1016/j.soildyn.2018.11.020

Gandelli, E., Penati, M., Quaglini, V., Lomiento, G., Miglio, E., and Benzoni, G. M. (2019). A novel OpenSees element for single curved surface sliding isolators. *Soil Dyn. Earthq. Eng.* 119, 433–453. doi: 10.1016/j.soildyn.2018.01.044

Kumar, M., Whittaker, A. S., and Constantinou, M. C. (2015). Characterizing friction in sliding isolation bearings. *Earthq. Eng. Struct. Dyn.* 44, 1409–1425. doi: 10.1002/eqe.2524

Lomiento, G., Bonessio, N., and Benzoni, G. (2012). "Effects of loading characteristics on the performance of sliding isolation devices," in *Proceedings of the 15th World Conference on Earthquake Engineering*.

Lomiento, G., Bonessio, N., and Benzoni, G. (2013a). Concave sliding isolator's performance under multi-directional excitation. *Ingegneria Sismica* 30, 17–32.

Lomiento, G., Bonessio, N., and Benzoni, G. (2013b). Friction model for sliding bearings under seismic excitation. *J. Earthq. Eng.* 17, 1162–1191. doi: 10.1080/13632469.2013.814611

Pantuso, D., Bathe, K. J., and Bouzinov, P. A. (2000). A finite element procedure for the analysis of thermo-mechanical solids in contact. *Comput. Struct.* 75, 551–573. doi: 10.1016/S0045-7949(99)00212-6

Quaglini, V., Bocciarelli, M., Gandelli, E., and Dubini, P. (2014). Numerical assessment of frictional heating in sliding bearings for seismic isolation. *J. Earthq. Eng.* 18, 1198–1216. doi: 10.1080/13632469.2014.924890

Sarlis, A. A., and Constantinou, M. C. (2013). *Model of Triple Friction Pendulum Bearing for General Geometric and Frictional Parameters and for Uplift Conditions [Report MCEER-13-0010]*. Buffalo, NY.

Stachowiak, G. W., and Batchelor, A. W. (2005). *Engineering Tribology*. Dordrecht: Elsevier Butteworth-Heinemann.

Zayas, V., Low, S., and Mahin, S. A. (1990). A simple pendulum technique for achieving seismic isolation. *Earthq. Spectra* 6, 317–333. doi: 10.1193/1.1585573

Conflict of Interest Statement: SI is employed by company Fip Mec S.p.A.

The remaining authors declare that the research was conducted in the absence of any commercial or financial relationships that could be construed as a potential conflict of interest.

frontiers in Built Environment

ORIGINAL RESEARCH
published: 12 June 2019
doi: 10.3389/fbuil.2019.00072

Multi-Span Steel–Concrete Bridges With Anti-Seismic Devices: A Case Study

Raffaele Pucinotti[1]* *and Giovanni Fiordaliso*[2]

[1] Department of PAU, Mediterranean University of Reggio Calabria, Reggio Calabria, Italy, [2] Structural Designer in Reggio Calabria, Reggio Calabria, Italy

Seismic protection for structures in general, and bridges in particular, is very complex. Indeed, any analysis of bridges with fluid viscous dampers and shock transmitting devices must be completed using a sophisticated finite element (FE) model. Furthermore, a large number of factors must be accurately considered and followed in order to effectively and efficiently protect human life. When dealing with complex structures, as is the case of the viaduct under examination, which contains numerous devices, the starting point is an assessment of the consistency of fluid-viscous dampers and shock transmitters integrated with bearings. This paper, a case study of design and static-dynamic testing procedures on multi-span steel–concrete viaduct provided with fluid viscous dampers and shock transmitters devices, deals directly with this process. To these ends, the FE modeling of the viaduct required an updating procedure model to ensure optimization. Those viaducts built during the "Caltagirone Project," can be defined as works of great interest due both to the construction methods adopted and to the techniques of stress control during the seismic stage. The design process allowed a rectification of those seismic issues deriving from structural irregularities (altimetric and planimetric), as well as from the high seismicity of the area. The analyses were carried out using a Capacity Design approach, employing non-linear seismic dissipative devices integrated as supports while validating that the substructures are maintained substantially elastic. For this reason, the piers were modeled on their non-linear behavior using Takeda's hysteretic model. Moreover, fluid viscous dampers and shock transmitters integrated with bearings were designed in accordance with the substructures' different stiffness; this partially dissipates those stresses induced by earthquakes, in order to keep the deck and the substructures substantially elastic, establishing a Life-Safety Limit State condition (at the Ultimate Limit State—ULS). The verifications carried out demonstrated the capability of structures to withstand stresses under the Collapse Limit State (CLS) condition without damage and at the same time to ensure the curvature capability from the piers. The comparisons between experimental and numerical results together with the demanding qualification tests carried out by this study demonstrate that the hydraulic devices are an efficient solution to assess seismic stresses induced on the viaduct and in its substructures, confirming the reliability of the aforesaid devices, thus ensuring better structural safety.

Keywords: steel–concrete bridges, viaduct, shock transmitter device, seismic devices, earthquake, fluid-viscous damper device, case study

OPEN ACCESS

Edited by:
Dario De Domenico, University of Messina, Italy

Reviewed by:
Ruifu Zhang, Tongji University, China
Emanuele Gandelli, Maurer AG, Germany

***Correspondence:**
Raffaele Pucinotti
raffaele.pucinotti@unirc.it

Specialty section:
This article was submitted to Earthquake Engineering, a section of the journal Frontiers in Built Environment

Received: *10 February 2019*
Accepted: *17 May 2019*
Published: *12 June 2019*

Citation:
Pucinotti R and Fiordaliso G (2019) Multi-Span Steel–Concrete Bridges With Anti-Seismic Devices: A Case Study. Front. Built Environ. 5:72. doi: 10.3389/fbuil.2019.00072

INTRODUCTION

Steel–concrete composite bridges represent a design option whose use is increasing in areas subject to high-intensity seismic activity. In point of fact, this design option is spreading more and more in the railway and motorway sector. The rapid erection, long span capability, economics, and aesthetics of these girders make them more favorable than other structural systems in terms of stiffness, resistance, and ductility.

In Makris and Zhang (2004), the authors present a case study on the seismic response of an over-crossing motorway structure equipped with elastomeric bearings and fluid dampers at its end abutments. The paper details the seismic response of the bridge, which was equipped with response modification devices accounting for the effects of soil–structure interaction; the results were compared with a hypothetical bridge with integral abutments.

In Tian et al. (2016), the authors present a numerical evaluation of the effectiveness of shock absorber devices installed between the roller bearing and stopper with the aim of reducing viaduct damage. They detail the effectiveness of thickness and types of shock absorber devices on mitigating viaduct damage. The results showed that the devices play a very important role in reducing viaduct damage.

In De Domenico et al. (2019), the authors present an overview of the most popular methodologies from literature in the field of seismic protection of building structures. The key aspects and main characteristics of the different strategies that were identified were the optimal damping coefficients and the optimal placement of Fluid Viscous Dampers (FVDs), which were scrutinized in a comparative manner.

The Montevideo viaduct sets an interesting precedent within the relevant literature on this topic by analyzing retrofitting (Bursi et al., 2008) by means of external post-tensioning. It describes the development of a finite element (FE) 3D model of the bridge and a structural analysis by means of a modal response spectrum. This was followed by a dynamic analysis aimed at identifying in detail the characteristics of steel–concrete box-girder bridges. Notably, the FE model was validated through output-only ambient vibration tests.

This paper presents a case study of design and static-dynamic testing procedures on multi-span steel–concrete viaduct enhanced with fluid viscous dampers and shock transmitter devices. The case study describes both the construction methods adopted and the techniques of stress control under seismic activity. Moreover, an elevated number of devices were placed, at the same time, into the 15 continuous long spans of variable length that compose the viaduct.

Based on the previous considerations, this paper could also refer to the "Ippolito 1" viaduct, where both fluid viscous dampers and shock transmitters integrated with bearings, designed according to the different substructure stiffness, were applied, in order to limit and partially dissipate the stresses induced by earthquakes, so that both the deck and the substructures remain substantially elastic for Ultimate Limit State (ULS).

The viaduct was designed with the purpose of creating a stable dissipative mechanism when subjected to seismic activity. The design was defined using a high-ductility approach in accordance with the Italian code (Ministero delle Infrastrutture, 2008), which considers the dissipative behavior of the structural elements, the material inelasticity, and the geometric non-linearities. The dissipative areas were concentrated on seismic restraint devices, while non-dissipative elements were dimensioned using capacity design criterion (CEN, 2005; Ministero delle Infrastrutture, 2008, 2009).

The comparison between the overall ductility demand and ductility available was carried out on the basis of the instructions provided in Eurocode 8 (CEN, 2005). In line with the capacity design criterion, the deck, the vertical support devices, the foundation, and the abutments were designed to remain elastic. An "over-strength" factor was considered to verify the pier sections outside the plastic hinge region. The dissipative devices were designed to support, without collapsing, displacements induced by an earthquake at Collapse Limit State (CLS), while the fixed restraint devices were dimensioned according to the capacity design criterion.

STEP 1: DESIGN ASSISTED BY TESTING

Modern design codes give the possibility to apply design methodologies assisted by testing (Pucinotti et al., 2015); in fact, EN1990 (Section Comparisons and Annex D) and EN1993-1-3 (CEN, 2002, 2006) contain specific rules and guidance to the design assisted by testing. In the current case study, before the devices' installation, an accurate analysis of seismic behavior and the matching of functional curves with the design assumptions were conducted.

Structural Design

The "Ippolito 1" Viaduct (**Figure 1A**) is part of the "Caltagirone Variant" project and belongs to the fast-flowing road "Licodia Eubea" (Catania—Italy), where the morphological irregularities of soil required the construction of five large span (75 m) viaducts, including Paradiso 1 (L = 722 m), Ippolito 1 (L = 1,102 m), Ippolito 2 (L = 125 m), Ippolito 3 (L = 925 m), and Molona (L = 265 m), as schematized in the **Figure 1B**.

These elements were initially developed with consideration to the highly inhomogeneous soil, composed of different layers of blue-gray clays covered by layers of scattered yellow sand. Altimetric and geotechnical irregularities necessitated the use of piers with variable height, ranging from 10 m to a maximum of 60 m. Additionally, the project takes into account multiple planimetric curvatures along its extension, as shown in **Figure 1** (Contin et al., 2015a,b).

The composite steel–concrete viaduct Ippolito 1 is 1,102 m long and 12 m wide and consists of 15 continuous spans of variable length, more specifically 68.0 + 75.0 × 13 + 59.0 m. The viaduct consists of a concrete slab supported by two steel girders (**Figure 2A**); the slab thickness is 28 cm. The girders, spaced 7.00 m, are 2.96 m high. Torsional bracings, at a distance of 6.5 m, are composed of a horizontal (L150 × 12) beam and two inclined (L150 × 12 + L150 × 12) beams. The torsional resistance was completed by a lower cross bracing system (2L150 × 12). The viaduct is located in Caltagirone, an area seismically classified as "zone 2," according to the OPCM n.3274/2003

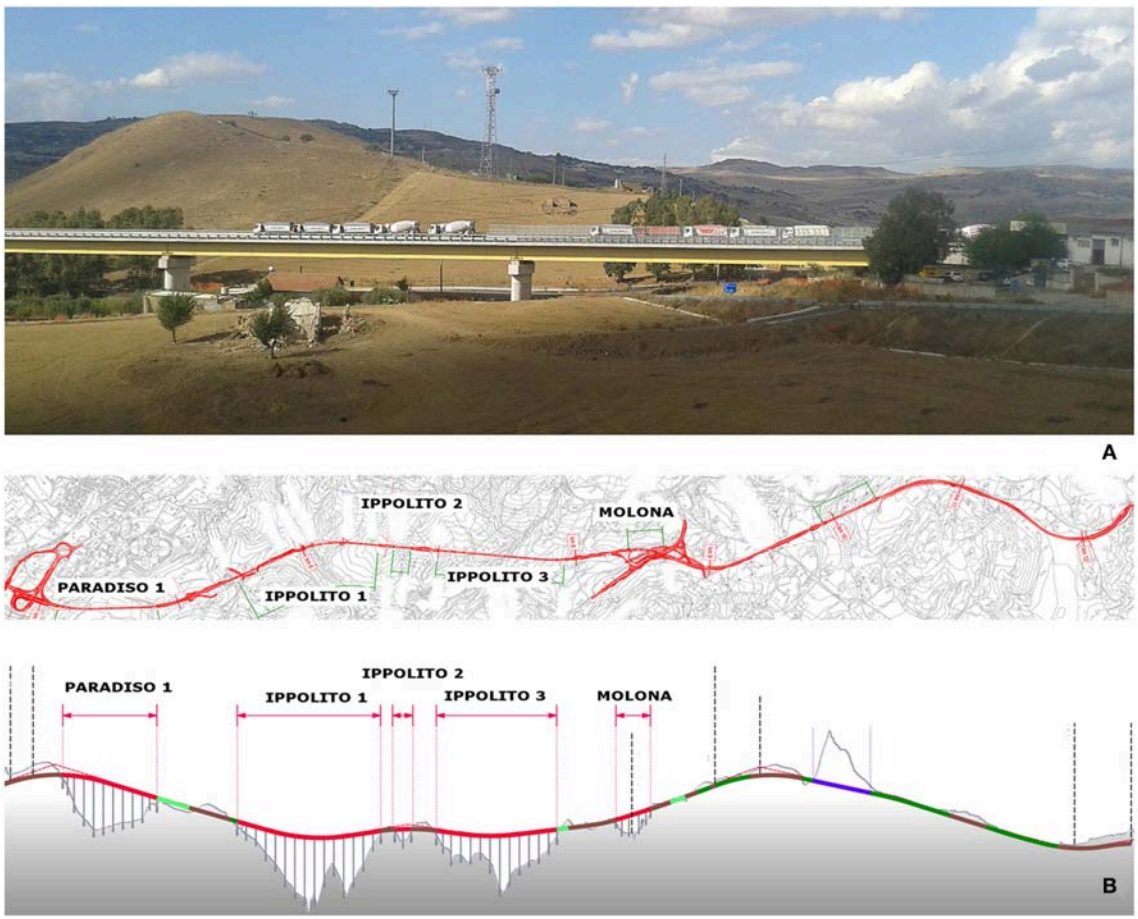

FIGURE 1 | (A) The Ippolito1 Viaduct during the load test; **(B)** "Caltagirone Variant": plant and longitudinal section of the fast-flowing road.

(OPCM 3274, 2003): a medium hazard area, where the expected ground acceleration ranges from 0.15 to 0.25 *g*.

The reference framework for seismic design structures in Italy is represented by the so-called New Code (Ministero delle Infrastrutture e dei Tasporti, 2018, 2019). While during both the design and the realization steps of the Viaduct, the reference framework for seismic designed structures were the NTC 2008 (Ministero delle Infrastrutture, 2008) and the Circular 617/2009 (Ministero delle Infrastrutture, 2009). According to both the Italian Code and Eurocode 8 (CEN, 2004; Ministero delle Infrastrutture, 2008, 2009), the seismic parameters for the case study are as follows: (i) longitude: 14.54350, latitude: 37.24318; (ii) soil type C, and (iii) return period of 950 years. The piers were made of reinforced concrete with pseudo-elliptical hollow section and have an average thickness variable between 0.30 and 0.45 m. The plinths are placed on bored piles of 1,500-mm diameter.

Class C28/35 concrete (Rck 35 MPa) was employed for piers and deck, while steel type B450C (with a yield strength of 391 Mpa) was adopted for reinforcing bars; structural steel S335J2 was used for beams and bracings. Bolts class was of 10.9 while Nelson stud connectors (S235J2G3 + C450) were employed for shear connection between concrete slab and steel beams.

Experimental tests carried out on-site showed a pile behavior in accordance with the project forecasts. The structure was dimensioned according to capacity design criterion in which dissipative zones must be concentrated on the restraint devices and at the base of piers, supporting the superstructure, the vertical support devices, and the foundations in the elastic field.

Due to the geometrical irregularities, it was necessary to couple the longitudinal oscillation of the deck with the oscillation of the piers by introducing Shock Transmitters (OT) at the top of the highest piers. These devices create a very stiff restraint against dynamic action while allowing slow movements of structures, for example, those produced by thermal variations. The lowest piers are free to oscillate, whereas the others are coupled with viscous damper devices (OTP) and thus able to control the forces directed on the underlying piers. In the transversal direction, viscous damper devices with plastic deformations (OP), and fixed restraints were employed. This allows the seismic energy to be dissipated through the possible formation of plastic hinges at the base of the piers or by means of the hysteretic behavior of the devices.

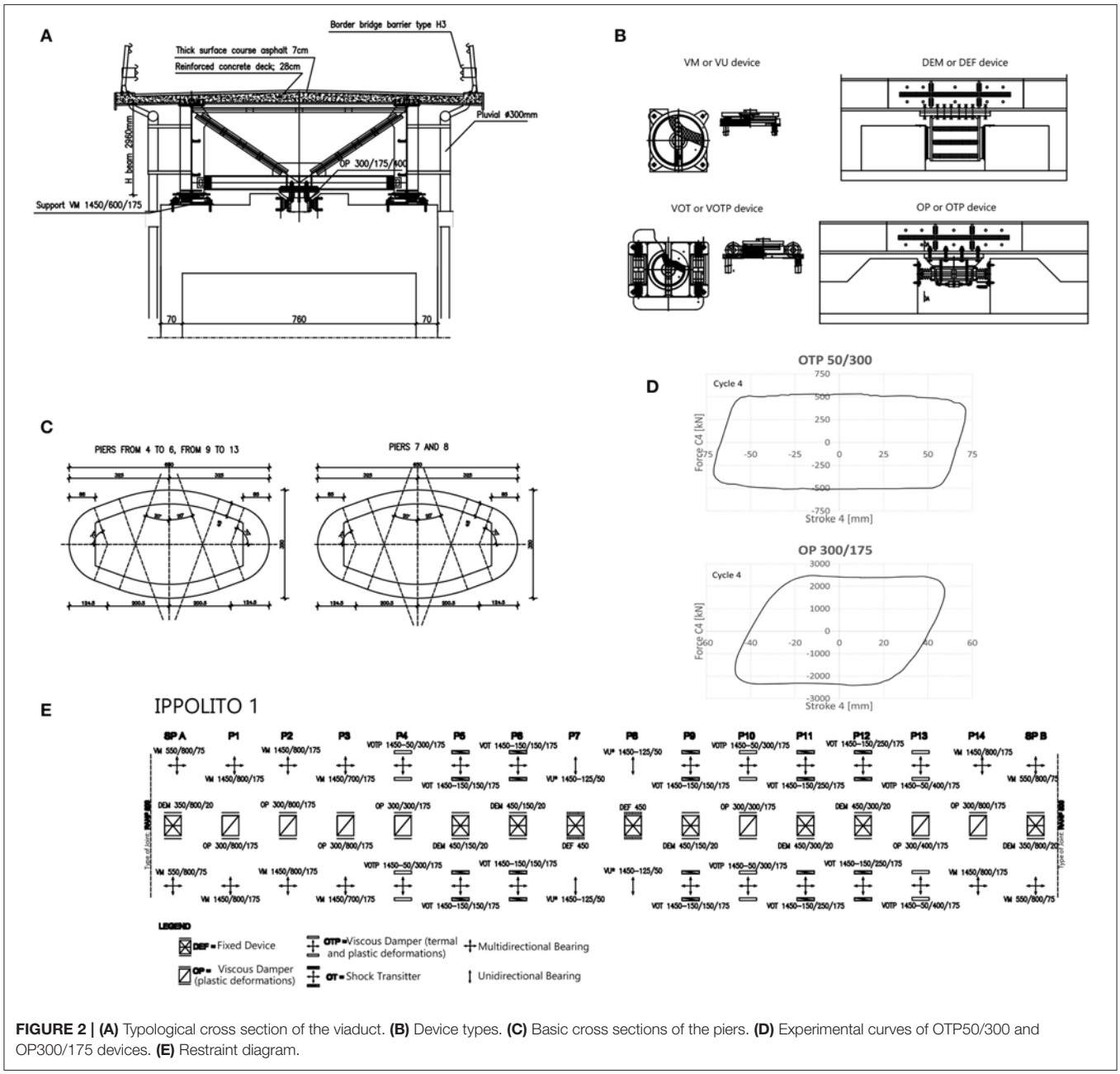

FIGURE 2 | (A) Typological cross section of the viaduct. **(B)** Device types. **(C)** Basic cross sections of the piers. **(D)** Experimental curves of OTP50/300 and OP300/175 devices. **(E)** Restraint diagram.

Figure 2 shows the typological cross section of the viaduct (**Figure 2A**), the device types adopted in the case study (**Figure 2B**), the basic cross sections of the piers (**Figure 2C**), the experimental curves of OTP50/300 and OP300/175 devices (**Figure 2D**), and the restraint diagram (**Figure 2E**). A classification scheme of the piers is reported in **Figure 3**. On the longitudinal direction, the fixed piers (P7–P8) absorb the static load due to the braking action of the vehicles and play the role of thermal center by transversal unidirectional restraint. With reference to the seismic actions, the shorter piers (P1, P2, P3, and P14 with height lower than 25 m) are free to oscillate, and the piers P3–P10–P13 (with high of about 30 m) are coupled with viscous damper devices (of OTP type) that are able to control the stress value imprinted from the deck; the remaining piers (taller than 35 m) are equipped with temporary restraining devices (shock transmitter OT). By the transversal direction, piers (P1, P2, P3, P4, P10, P13, and P14) are equipped with a multidirectional support equipped with a viscous-type damper device with plastic deformation properties (OP), while piers P5, P6, P9, P11, and P12 are equipped with a DEF-type fixed constraint (able to allow longitudinal movements). Piers P7 and P8 are equipped with a transversal unidirectional bearing device endowed with a DEF-type device. From a seismic point of view, only the piers shorter than 35 m are isolated (P1, P2, P3, P4, P10, P13, and P14).

PIER	1	2	3	4	5	6	7	8	9	10	11	12	13	14
Heigth [m]	9.25	11.8	22.9	29.8	42.5	51	56.8	56.8	38.8	29.8	50.5	41.8	28.9	11.8
Classification	LOW	LOW	LOW	MEDIUM	HIGH	HIGH	HIGH	HIGH	HIGH	MEDIUM	HIGH	HIGH	MEDIUM	LOW
Longitudinal device	VM	VM	VM	VOTP	VOT	VOT	UNI L	UNI L	VOT	VOTP	VOT	VOT	VOTP	VM
Classification	FREE	FREE	FREE	VISCOUS DAMP.	FIX	FIX	FIX	FIX	FIX	VISCOUS DAMP.	FIX	FIX	VISCOUS DAMP.	FREE
Transversal device	OP	OP	OP	OP	DEM	DEM	DEF	DEF	DEM	OP	DEM	DEM	OP	OP
Classification	VISCOUS DAMP.	VISCOUS DAMP.	VISCOUS DAMP.	VISCOUS DAMP.	FIX	FIX	FIX	FIX	FIX	VISCOUS DAMP.	FIX	FIX	VISCOUS DAMP.	VISCOUS DAMP.

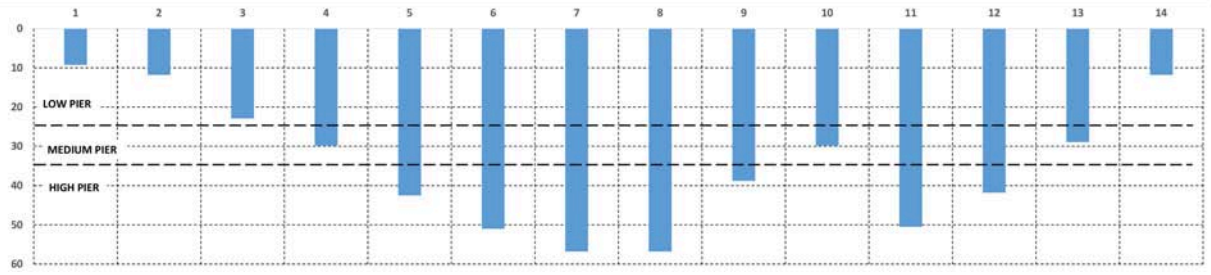

FIGURE 3 | Classification of piers.

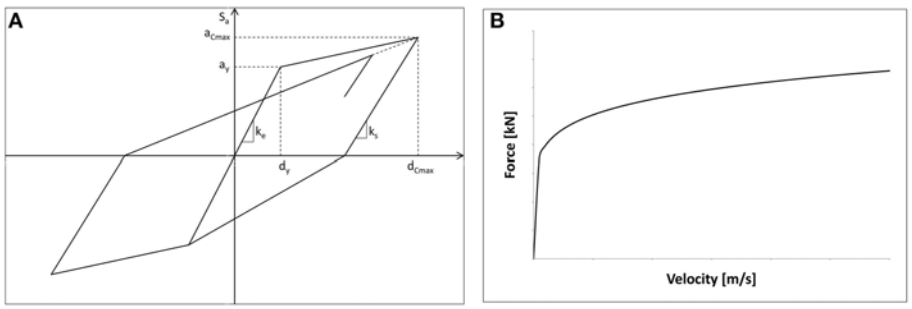

FIGURE 4 | (A) Takeda hysteresis model. **(B)** Force–velocity curve ($F = C.\ V^{\alpha}$).

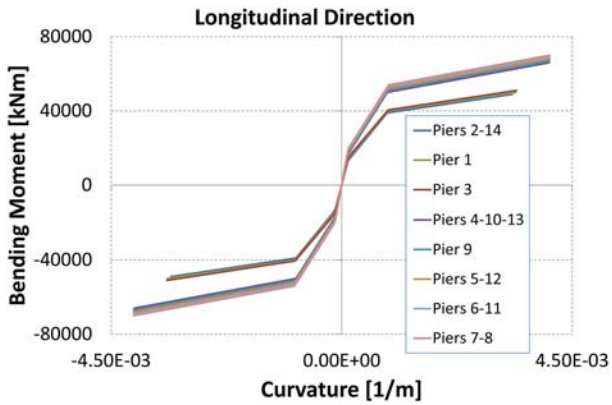

FIGURE 5 | Piers: moment–curvature diagram.

Viaduct Modeling and Analysis

A FE model of the viaduct was implemented in Strand7[1] (Strand7) that takes into account the geometric non-linearity of both the materials and the devices. The substructures were modeled with beam elements, characterized by a pseudo-elliptical hollow section with a thickness proportionally variable to height. Moreover, a moment–curvature hysteresis model (theorized by Takeda et al.) was adopted for the piers (Takeda et al., 1970) in which monotonic behavior is described through a trilinear curve (**Figure 4A**) that considers the cracking of the concrete and the yield of the rebar. Even though Takeda's hysteretic model was originally proposed for simulating the load–displacement relation of RC subassemblies, it was widely used in the description of hysteretic moment–curvature or moment–rotation relation of RC members. It is a specialized rule normally used to model reinforced concrete frame structures in non-linear transient dynamic analysis. Thus, it was possible to assess the stiffness modification of the substructures in the transitional regime by controlling the redistribution of stresses in the viaduct piers. From the model implemented, the restraint devices demonstrate the following properties:

1. Vertical supports or fixed longitudinal support; these have an almost unlimited stiffness.
2. Shock transmitters that create very stiff restraint against any dynamic action while allowing slow movements of structures, such as those produced by thermal changes without opposing significant resistance.

[1]Strand7, Release 2.4. —*Full-featured finite element analysis—Design and built for Windows.*

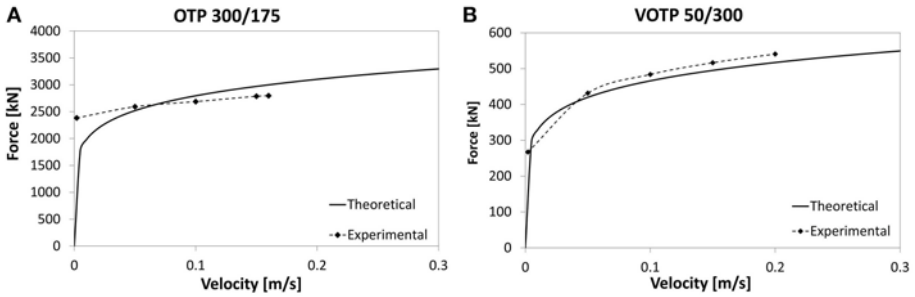

FIGURE 6 | Comparison between theoretical and experimental constitutive law for devices. **(A)** OTP 300/175 devices. **(B)** VOTP 50/300 devices.

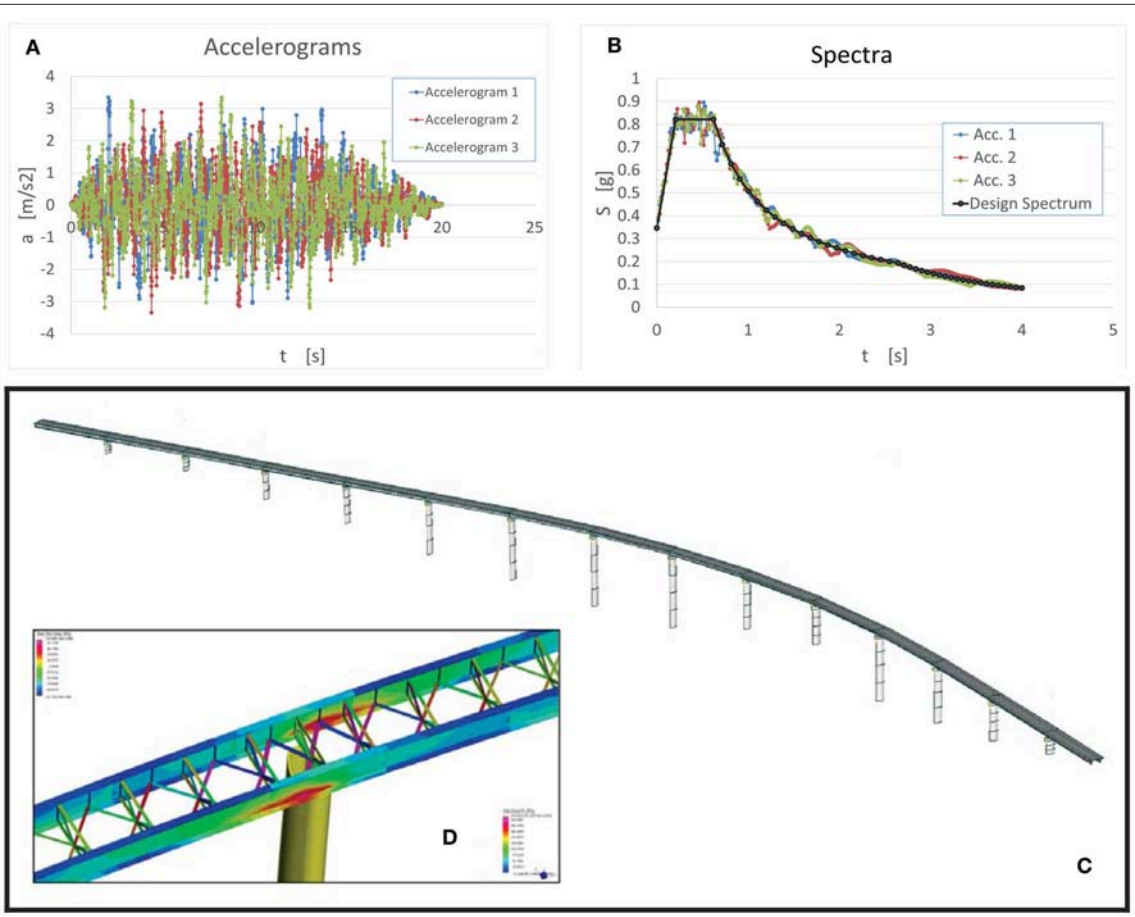

FIGURE 7 | (A) Accelerograms. **(B)** Spectra. **(C)** Finite element model of the viaduct. **(D)** Strength in the steel elements of the superstructure.

3. Fluid viscous dampers devices (OP/OTP) with a non-linear behavior; these are cylinder/piston devices that exploit the reaction force of silicon fluid forced to flow through an orifice and/or valve system. In detail, the applicable force–velocity law of (OP/OTP) is non-linear, i.e., (**Figure 4B**),

$$\mathbf{F} = \mathbf{C} \bullet \mathbf{V}^{\alpha} \quad (1)$$

where $\alpha = 0.15$, F is the force, C is the damping constant, and V is the velocity.

The dissipative devices were modeled using spring-damper elements associated with the force–velocity law as of Equation 1. The shock transmitters were modeled as truss elements with high stiffness.

Figure 5 shows the moment–curvature diagram for the piers in the longitudinal direction.

Two types of viscous damper devices were adopted:

1. OP 300/175 in the transversal direction, and
2. Double devices OTP50/300 in the longitudinal direction.

In the application of Equation 1, the damping constant C is 3,524 kN/(mm/s)$^{\alpha}$ for devices OP 300/175 and 212.5 kN/(mm/s)$^{\alpha}$ for the OTP50/300. Due to the complex orography of the land, further assessments were conducted to select FVD device parameters, with the aim of achieving a greater balance for tall piles and to protect low piles from high shear forces. Moreover, the following parameters were assigned:

- OTP50/300: Maximum design load F_d = 500 kN; (ii) Maximum design velocity V_d = 300 mm/s;
- OP 300/175: Maximum design load F_d = 3,000 kN; (ii) Maximum design velocity V_d = 200 mm/s;

Figure 6 shows the force–velocity relationship for the OP 300/175 and OTP50/300 devices; in the same figure, the comparison between theoretical and experimental constitutive law for these devices (OP and OTP) is presented. Moreover, in order to obtain further control of the results and to provide useful information on the seismic behavior, both Incremental Dynamic Analyses (IDA) and Linear Modal Analyses (LMA) were carried out (Pucinotti et al., 2015). The non-linear dynamic analysis outcomes were compared with those from the modal analysis that used a design response spectrum, in order to analyze the differences in terms of global shear force at the base of the structures.

In accordance with the Italian Code (Ministero delle Infrastrutture, 2008), the following seismic parameters were adopted: (i) rated life of the work, V_N = 50 years; (ii) use coefficient, C_U = 2; (iii) reference life of the work, V_R = 100 years; (iv) soil type C; and (v) topographic coefficient T_1 = 1. **Figures 7A,B** shows the accelerograms and the spectra, respectively. In detail, the following steps were taken:

– Non-linear time history analysis: both the Italian code (Ministero delle Infrastrutture, 2008) and Eurocode 8 (CEN, 2004, 2005) highlight three groups of accelerograms consisting of pairs of simultaneous ground motions as input for seismic structural analysis. When using artificial accelerograms, the samples used must be adequately qualified with regard to both the seismogenetic features of the sources and the soil conditions; moreover, their values must be scaled for the zone of reference. In other words, in accordance with Eurocode 8 (CEN, 2004), the following rules must be followed:

(i) A minimum of three accelerograms should be used;
(ii) The mean of the zero period spectral response acceleration values (calculated from the individual time histories) should not be smaller than the value of ag.S for the site of interest, where ag is the design ground acceleration on type A ground and S is the soil factor;
(iii) In the range of periods between 0,2T1 and 2T1, where T1 is the fundamental period of the structure in the direction where the accelerogram will be applied, no value of the mean 5% damping elastic spectrum, calculated from all time histories, should be <90% of the corresponding value of the 5% damping elastic response spectrum.

– Linear time history analysis: the results of this analysis were compared with non-linear time history analysis outcomes with the objective of selecting the appropriate behavior factor. This behavior factor "q" has been subsequently used to calculate the over-strength coefficient to be used in the assessment of non-dissipative zones.
– Modal analysis with design response spectrum (with behavior factor "q") and validation of non-linear time history analysis by comparison of the shear at the base of viaduct piers (Ministero delle Infrastrutture, 2009).

According to section 7.9.2 of the Italian Code (Ministero delle Infrastrutture, 2008, 2009), the non-dissipative elements of a viaduct are as follows: deck, supports, foundation structures and the underlying soil, abutments if they support the deck through sliding bearings, or deformable devices.

After an earthquake, the superstructure must remain in the elastic range. To these ends, in the non-linear time history analysis, the most onerous transversal displacements at the top of the piers were considered.

These results were applied to a global FEM model with the following structural elements: (i) the principal longitudinal beams and the concrete slab, modeled by 4-node shell elements; (ii) the lattice beams and bracing, modeled by beam elements; (iii) the piers and the pier caps, represented with beam elements; (iv) the seismic devices, modeled by spring-damper elements; (v) beam-to-slab connections, represented with rigid-link elements.

The model of the bridge is shown in **Figure 7C**. The set of displacements used outcomes from the time history analysis, precisely at the step relative to 13.66 s, point in time registering the maximum displacement on pier seven, about 32.46 cm. The abovementioned displacements are reported in **Table 1**.

The results of calculations and assessments show that the metal deck elements remain inside the linear elastic range (**Figure 7D**).

STEP 2: *IN SITU* STATIC AND DYNAMIC TESTING AFTER CONSTRUCTION

Static Loading Test

A static load test was performed to verify the actual structural behavior of the viaduct, compared with what was predicted under

TABLE 1 | Assigned displacements.

Pier	Displ. [cm]	Pier	Displ. [cm]	Pier	Displ. [cm]
P1	0.08	P6	24.60	P11	17.39
P2	−0.29	P7	32.46	P12	13.49
P3	−1.77	P8	21.98	P13	5.02
P4	−2.29	P9	8.85	P14	0.1
P5	7.22	P10	8.13		

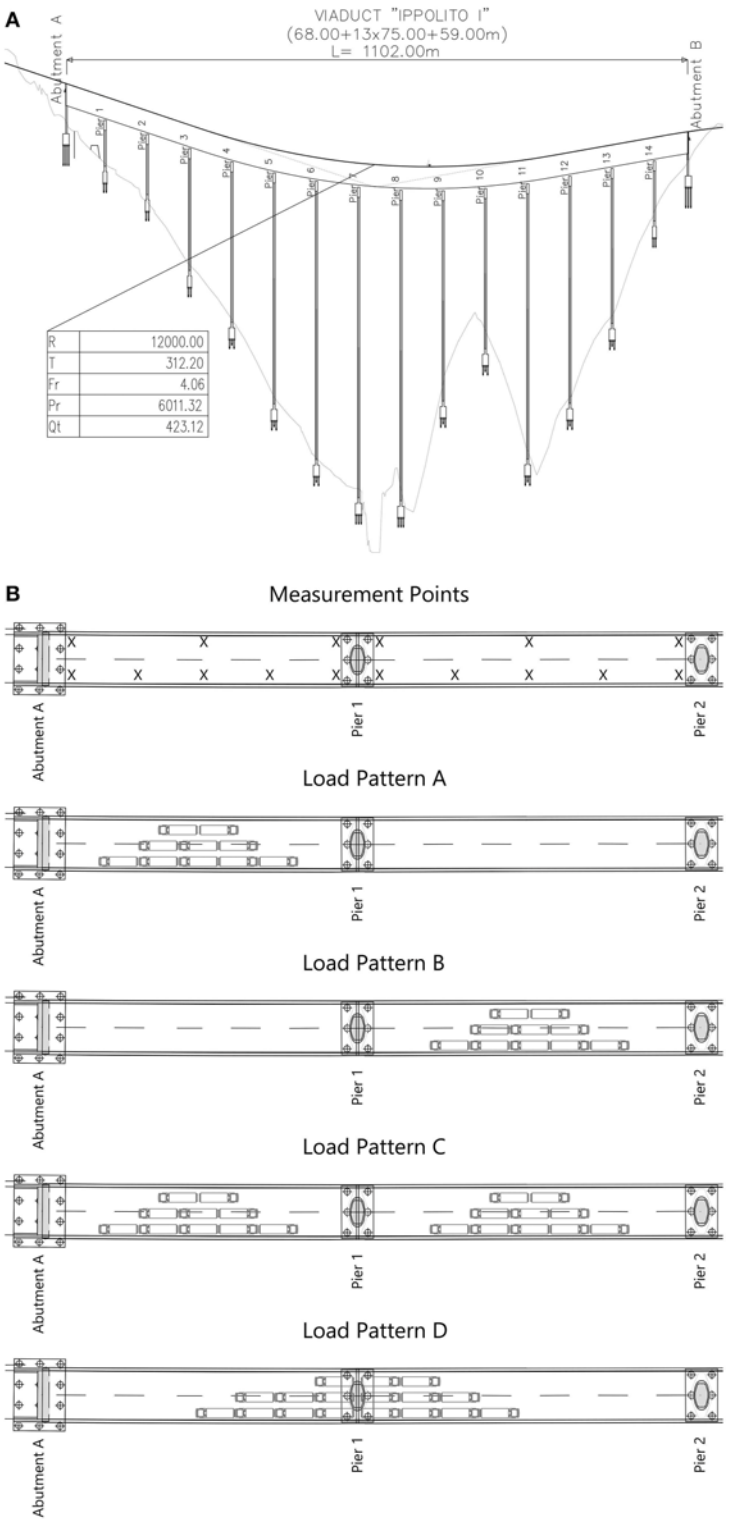

FIGURE 8 | Viaduct "Ippolito 1": **(A)** longitudinal section; **(B)** load combinations of the first and second span.

the theoretical point of view in the design step. The testing protocol envisaged the use of eight 40-ton trucks with 4 axles. The axle loads of the trucks were measured with newly calibrated, portable weighing scales. Multiple tests were carried out by loading the following spans: 1st test—spans 1, 2, and 3; 2nd test—spans 5, 6, and 7; 3rd test—spans 13, 14, and 15. **Figure 8** shows

TABLE 2 | Viaduct "Ippolito 1" — vertical displacement [experimental (white), numerical (gray)].

	Displacement [mm]												
	A1	**A2**	**A3**	**A4**	**A5**	**A6**	**A7**	**A8**	**B1**	**B2**	**B3**	**B4**	**B5**
Chainage[m]	0.00	19.70	38.30	57.10	75.70	94.50	113.10	131.70	150.80	168.00	185.00	201.70	217.70
Span 1 (Mmax) – loading patterns A	0.00	4.89	8.99	8.75	0.00	–16.65	–29.48	–31.42	0.00	53.14	79.48	60.12	0.00
	0.00	4.68	8.46	7.92	–0.09	–17.73	–32.04	–30.24	0.45	60.93	84.87	61.74	–3.42
Span 2 (Mmax) – loading patterns B	0.00	–20.67	–38.17	–37.38	0.00	76.31	109.98	72.24	0.00	–32.35	–33.27	–20.38	0.00
	–0.10	–20.30	–39.50	–36.50	0.60	82.20	117.40	77.10	0.40	–38.60	–39.50	–23.50	1.60
Pier 1(Mmin) – loadin g patterns C	0.00	–14.44	–26.52	–25.94	0.00	49.67	63.14	29.03	0.00	23.16	48.03	41.24	0.00
	0.00	–13.70	– 25.10	–23.70	0.50	56.30	73.70	37.20	0.80	33.50	59.60	48.40	–2.30
Pier 1 (Vmax) –loa ding patterns D	0.00	–3.40	–6.58	–6.76	0.00	10.30	23.88	18.11	0.00	17.21	26.05	17.03	0.00
	0.00	–3.10	–5.70	–5.50	0.10	14.20	25.80	16.90	–0.70	20.80	30.70	18.30	–0.70

TABLE 3 | Comparison between experimental and numerical frequencies.

Shape	$F_{FE,i}$ (Hz)	$F_{exp,i}$ (Hz)	Variation (%)
1.00	0.61	0.57	6.39
2.00	0.80	0.76	5.38
3.00	0.87	0.97	11.15
4.00	1.06	1.12	5.94
5.00	1.07	1.06	0.56
6.00	1.110	1.113	0.27

the load patterns for the static tests with reference to the 1st and 2nd span.

The measurement period for each load pattern was ∼20 min. The overall time for the entire static load test was ∼8 h. The vertical displacements of the bridge deck were measured using biaxial inclinometer and temperature recorders (Capetti WSD15TIIDRO); measurement points are shown as crosses (X) in **Figure 8B**.

The four main loading patterns A to D show truck positions on the bridge. As observed, the trucks were positioned back to back in order to provide symmetric loading and a maximum load effect. **Table 2** shows the comparison between the theoretical (highlighted with a gray color) and experimental results for the case study.

Dynamic Test

In order to validate the FEM model for the viaduct, a dynamic test was performed. The identification of the dynamic parameters (modal frequencies, damping ratios, mode shapes, and modal participation factors) actually provides an assessment of the global response of a system. In addition, experimental techniques for the dynamic identification provide a significant contribution in connecting assumptions and the actual behavior of a structure.

In the Identifying Structural Dynamics Analyses, techniques for experimental modal analysis (EMA) or, alternatively, operational modal analysis (OMA) can be used.

Traditional EMA uses excitation inputs while OMA aims to identify the modal properties of a structure excited by environmental sources.

Despite its usefulness, traditional EMA has some limitations; such as the following: (i) artificial excitation is normally conducted in order to measure frequency response functions (FRFs), or impulse response functions (IRFs). FRF or IRF would be very difficult or even impossible to measure using field tests and/or assessing large structures. (ii) Traditional EMA is normally conducted in a lab environment. This is at odds with real operational conditions in place in many industrial applications. (iii) Lab environments are generally suitable for individual component testing, instead of complete systems verification; furthermore, boundary conditions would need to be simulated. Therefore, the OMA technique (output only) is considered as the most suitable for important structures such as bridges or viaducts since evaluation can be performed without closing the viaduct to traffic. The campaign of dynamic surveys, which was carried out on all viaducts, were developed using

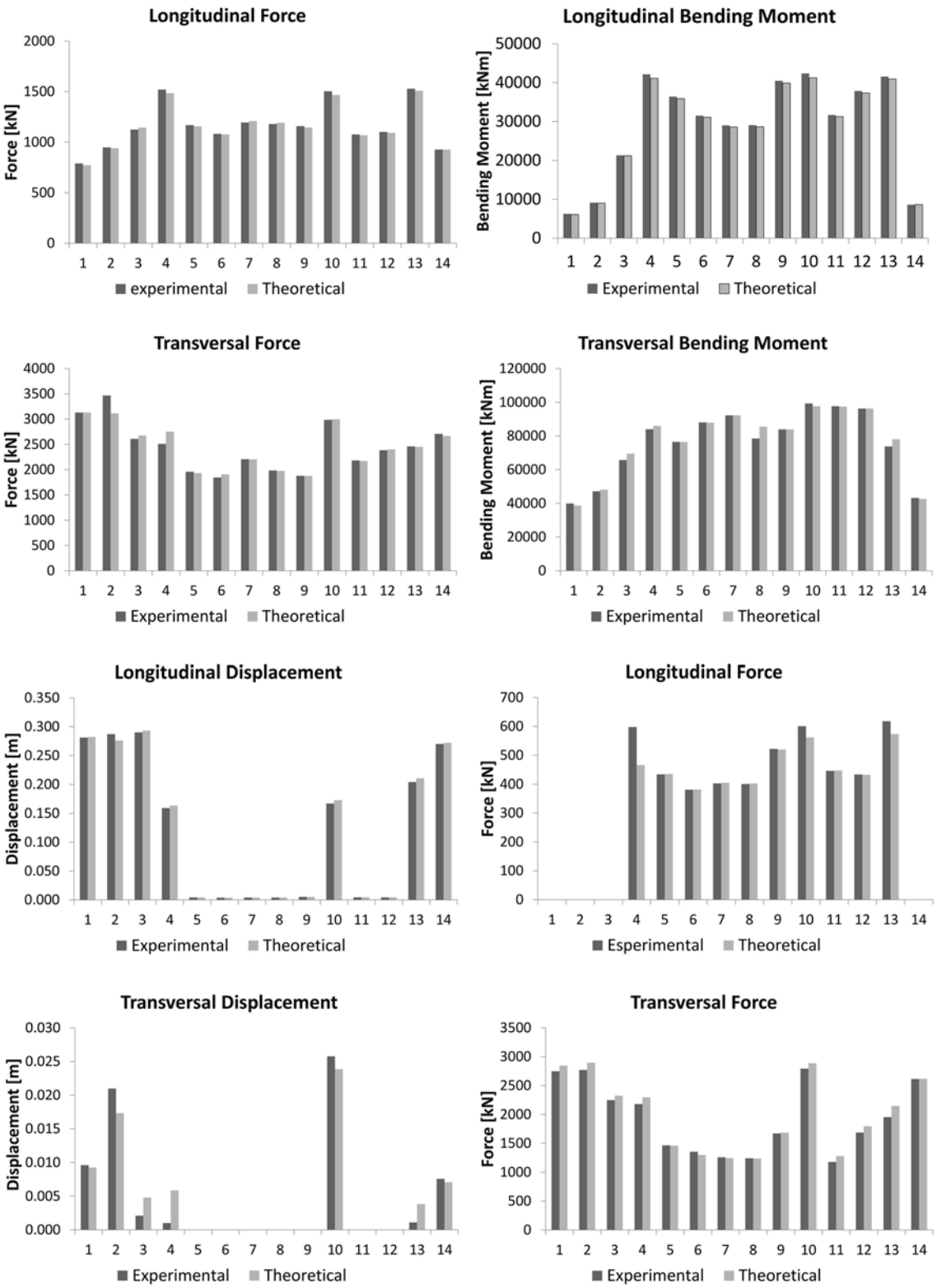

FIGURE 9 | Strength at the base of the piers and force–displacement in the devices.

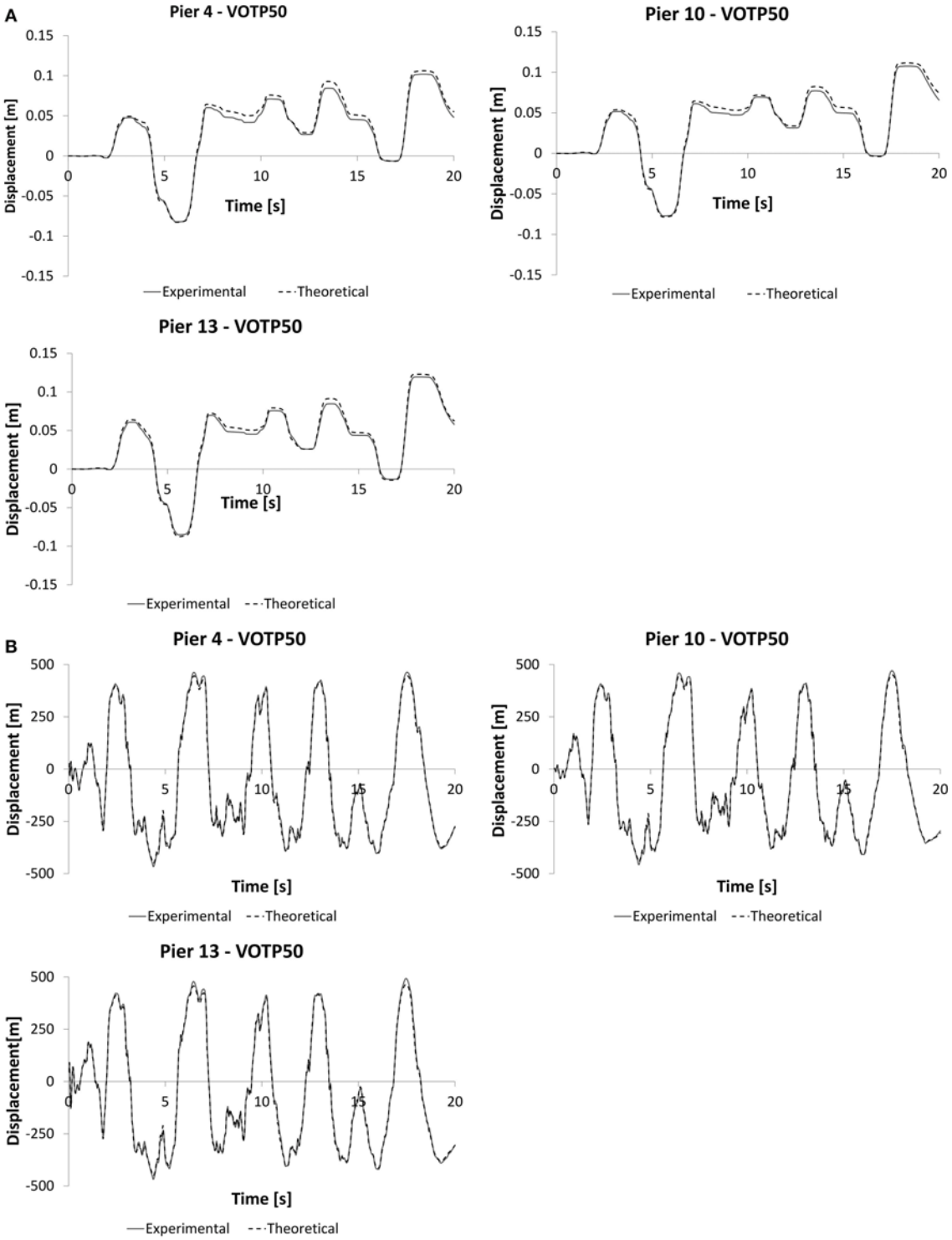

FIGURE 10 | Comparison between experimental and numerical results: **(A)** displacement vs. time curves between OTP and OTP devices; **(B)** force vs. time curves of the OTP and OTP devices.

15 accelerometers (PCB 393A03, PCB393C) connected to a 24-bit data acquisition unit with Analogic/Digital Converter (N.I. C-Daq 9172 + 4 USB9234).

The acquisitions were recorded in two different conditions; i.e., with natural excitation in the absence of vehicular traffic (wind, microsystems, etc.) and during the passage of heavy

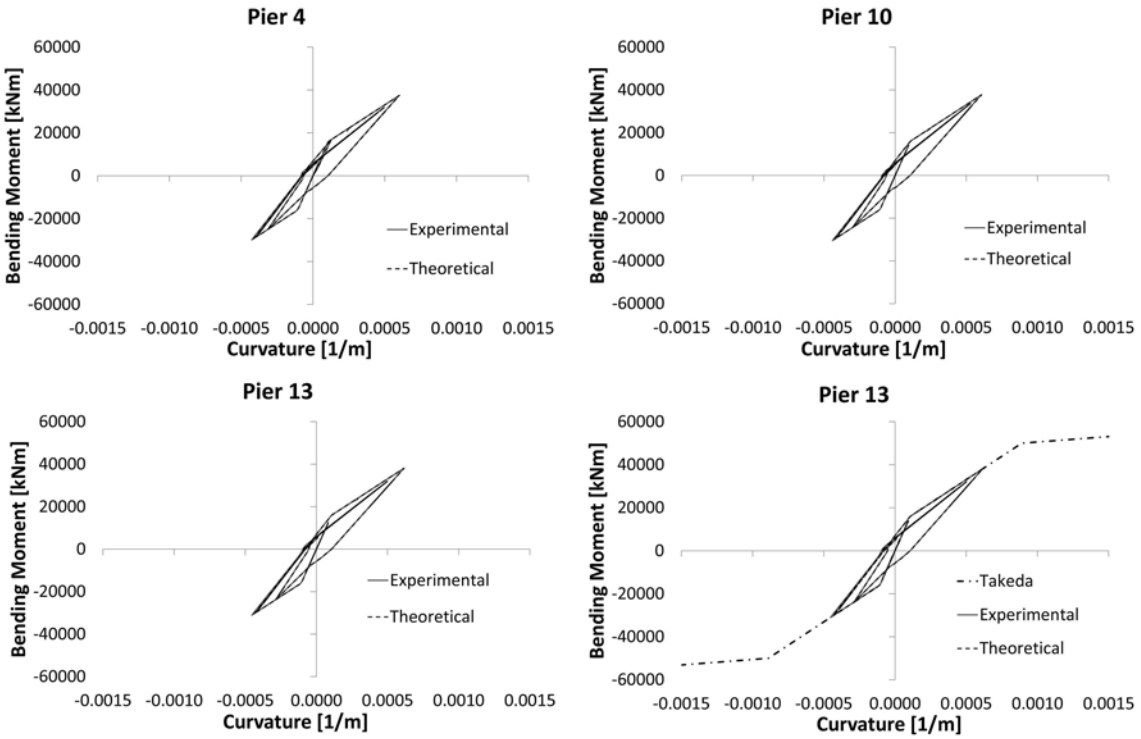

FIGURE 11 | Longitudinal moment vs. curvature diagrams at the base of the piers: comparison between experimental and numerical results.

vehicles. In the present case, where the number of available sensors (15) was lower than the desired number of DOFs, it was necessary to make more acquisitions by varying the position of the accelerometers to cover all desired measuring points. It was therefore necessary to use some reference sensors (maintaining the same position for each acquisition).

In the application of these techniques, operating in the hypothesis that the forcing (unknown) has the characteristics of a white noise, it is necessary to carefully select the total length of recordings. Generally, the duration of acquisitions is set equal to 1,000 ÷ 2,000 times for the first period of vibration on the structure. Another criterion is provided by the UNI 10985, which provides some guidelines to perform dynamic testing: the size (N) of each time sequence and the sampling step Δt must be fixed in order to obtain an adequate frequency resolution. Within the total registration period, the percent error in both auto-spectra and cross-spectra estimation is approximately equal to $1/\sqrt{\text{Nd}}$.

This means that in order to obtain an auto-spectra estimation with an error lower than 10%, it becomes necessary to set up a signal long enough to be divided in $\text{Nd} = 100$ temporal sequences; assuming an operation with $\Delta t = 0.01$ s (about 0.025 Hz), where no temporal sequences overlap, more than 68 min of acquisition is needed. If during the definition of the temporal sequences, we accept an overlap of 50% of the signal, the total duration of the registration can be reduced to 33 min.

In the case study, temporal histories of 2,400 s (40 min) with a sampling step of $t = 0.005$ s (200 Hz or freq. Nyquist 100 Hz) were chosen. Analysis was conducted as OMA, output only, as specified above. The identification of the modal parameters of the viaduct was developed using the frequency domain decomposition, enhanced frequency domain decomposition, and curve-fit frequency domain decomposition. This allowed us to validate the results obtained.

STEP 3: MODEL UPDATING

The correlation between an initial FEM and experimental data is often poor. This is due to inadequate FEM or inaccurate experimental data. The factors that can determine low accuracy of FEMs are as follows: (i) poor modeling of the structural elements and (ii) poor modeling components, e.g., the omission of interaction among components like structural joints.

Another potential source of error is represented by changes in the values of physical parameters and material properties. These can significantly change FEM predictions. Model updating procedure can improve the correlation between the FEM modal analysis and experimental results. In this paper, model updating was used to minimize the "difference" between FEA and reference test data (UNI 10985, 2002; Bursi et al., 2008).

In the model updating, the following procedure was performed:

- estimation of initial parameters, $P_{o,j}$
- computation of the sensitivity matrix $[S_{ij}]$ in order to construct the equation $\Delta R_i = [S_{ij}]\Delta P_j$, where ΔR_i is the residual

TABLE 4 | Shear stress at the base of the piers (in kN) and estimation of the behavior factor.

	P1	P2	P3	P4	P5	P6	P7	P8	P9	P10	P11	P12	P13	P14	Tot	q
Non-linear analysis	772	939	1,143	1,484	1,156	1,076	1,208	1,192	1,144	1,466	1,068	1,092	1,508	926	16,173	1.5
Linear analysis	685	850	1,138	2,554	2,274	1,608	1,437	1,417	2,580	2,551	1,560	2,206	2,482	900	24,544	

difference between the ith predicted and experimental modal data, and ΔP_j is the jth selected updating parameter;

- solving forΔP_j: $\Delta P_j = [S_{ij}]^+ \Delta R_i$, where $[S_{ij}]^+$ is the pseudo-inverse matrix of $[S_{ij}]$;
- introduction of the resulting parameter changes ΔP_j into the model and re-computation of the modal parameters;
- procedure repetition until convergence criterion satisfaction.

In detail, as a first step, the first five experimental frequencies were considered as experimental modal data and the sensitivity matrix was numerically estimated as:

$$\Delta R_i = \begin{Bmatrix} \frac{f_{\exp,1} - f_{FE,1}}{f_{\exp,1}} \\ \frac{f_{\exp,2} - f_{FE,2}}{f_{\exp,i}} \\ \cdots \\ \frac{f_{\exp,i} - f_{FE,i}}{f_{\exp,i}} \end{Bmatrix}, \ \Delta P_J = \begin{Bmatrix} \frac{p_{new,1} - p_{old,1}}{p_{old,1}} \\ \frac{p_{new,2} - p_{old,2}}{p_{old,2}} \\ \cdots \\ \frac{p_{new,j} - p_{old,j}}{p_{old,j}} \end{Bmatrix}, \ [S_{ij}] = \begin{Bmatrix} \frac{\partial f_{FE,1}}{\partial p_1} & \cdots & \frac{\partial f_{FE,1}}{\partial p_j} \\ \frac{\partial f_{FE,2}}{\partial p_1} & \cdots & \frac{\partial f_{FE,2}}{\partial p_j} \\ \cdots & \cdots & \cdots \\ \frac{\partial f_{\exp,i}}{\partial p_1} & \cdots & \frac{\partial f_{FE,i}}{\partial p_j} \end{Bmatrix}, \quad (2)$$

The parameters initially chosen for model updating were:

- Young's Modulus for concrete;
- Young's Modulus for steel;
- sidewalk thickness;
- span length;
- slab thickness;
- inferior plate thickness of the box girder.

The number of parameters to which the model is effectively sensitive corresponds to the rank of the sensitivity matrix. The valuation of this rank happens through the valuation of the single value decomposition of the sensitivity matrix. The rank of the sensitivity matrix is four. Afterwards, sensitivity analyses on the five parameters meant the following parameters could be adopted:

- Sidewalk thickness;
- Span length of the bridge;
- Slab thickness;
- Inferior plate thickness of the box girder.

At the same time, in the FEM, the experimental elastic modulus of the actual materials (steel and concrete) was introduced.

COMPARISONS

A summary of the acquisitions (setup), recorded in two different conditions (i.e., with natural excitation in the absence of vehicular traffic—wind, microsystems, etc.—and during the passage of heavy vehicles), were subsequently processed using a modal analysis software, as follows:

a) Acquisition in the absence of vehicular traffic—natural excitation:

— Number of spans investigated: 15;
— Number of setup: 16;
— Number of recorded signals: 240;
— Sampling step: 100 Hz;
— Acquisition time: 2,400 s.

b) Acquisition at the passage of heavy vehicles:

— Number of spans investigated: 15;
— Number of setup: 16;
— Number of recorded signals: 720;
— Sampling step: 100 Hz;
— Acquisition time: 120 s.

Table 3 shows the comparison between experimental frequencies and numerical frequencies obtained using Strand7 software. The second column reports the numerical frequencies, while column 3 reports the experimental frequencies after some iteration of the model updating procedure. It is easy to verify the effectiveness of the FE model (FEM).

Figure 9 refers to dissipation devices and shows the comparison between the results of the non-linear dynamic analysis (performed using the theoretical curves) and the experimental data (derived from the laboratory tests); in fact, the response of devices was assessed by experimental laboratory tests as shown in **Figure 2D**. In this context, the term experimental must be understood as a model in which the laboratory experimental curves of the devices were used with respect to the model with the nominal law. It is possible to appreciate the substantial congruence of the two analyses in terms of forces and displacements.

Figure 10 shows the previous comparison referred to in the time history analysis. From the moment–curvature diagrams (see **Figure 11**), it is possible to check how the piers remain within the linear range (energy dissipated by the concrete cracking avoiding yield on the rebar).

The devices used are not automatically re-centering. In fact, when external actions cease, the displacements return almost to zero. If excessive displacement occurs, the re-centering is still simple. It operates by connecting the circuit of the devices to a control unit. The device in this case acts as a jack for the re-centering of the bridge. Detail on re-centering capability can be found in Quaglini et al. (2017), where the re-centering capability is recognized as a fundamental function of any effective isolation system. Furthermore, in **Figure 11**, the term experimental must be understood as a model in which the laboratory experimental curves of the devices were used with respect to the model with the nominal law; moreover, Takeda's curve for pier 13 is shown in **Figure 11**.

In **Table 4**, the results of the two analyses (linear and non-linear) in terms of shear stress at the base of the piers are compared; moreover, it shows the estimation of the behavior factor $q = 1.5$.

The behavior factor q shown in **Table 4** was assessed from the IDA (Bursi et al., 2006); it is defined as follows:

$$q = \frac{pga_u}{pga_y} \tag{3}$$

where pga_y is the peak ground acceleration corresponding to first design yielding and pga_u is the peak ground acceleration corresponding to collapse.

CONCLUSIONS

Seismic protection of structures in general, and bridges in particular, is very complex. In particular, the analysis of bridges with fluid viscous dampers and shock transmitting devices must be performed using the best possible analytical model. Indeed, a large number of factors must be treated accurately in order to increase efficiency in the preservation of human life.

For complex structures, such as the viaduct under examination, which contains numerous devices, fluid-viscous dampers, and shock transmitters integrated with bearings, design assisted by testing is a necessary procedure.

Consequently, the FE modeling of the viaduct required a model updating procedure for its optimization. In fact, the viaducts built within the "Caltagirone Project," can be fully defined as works of great interest for both the construction methods adopted and the techniques of stress control in the seismic stage.

The design process resolved seismic issues deriving from structural irregularities (altimetric and planimetric) as well as from the high seismicity of the area. The analyses were carried out using a Capacity Design approach, using non-linear seismic dissipative devices integrated to supports and checking that the substructures maintain substantial elasticity. For this reason, Takeda's model is used to simulate the hysteretic behavior of the piers.

In addition, fluid viscous dampers and shock transmitters integrated with bearings were designed in accordance with the different stiffness by the substructures, thus limiting and partially dissipating stresses induced by earthquakes, in order to keep the deck and the substructures substantially elastic for Life-Safety Limit State condition (at the ULS).

The verifications carried out have demonstrated the capability of structures to withstand the stresses under the CLS condition without damage, plus they ensure the curvature capability by piers.

The comparisons between experimental and numerical results together with the demanding qualification tests carried out in this study demonstrate that the hydraulic devices are an efficient solution to control the seismic stresses induced on the viaduct and in its substructures, confirming the reliability of the aforesaid devices that ensure greater structural safety.

AUTHOR CONTRIBUTIONS

All authors listed have made a substantial, direct and intellectual contribution to the work, and approved it for publication.

REFERENCES

Bursi, O. S., Bonelli, A., Mammino, A., Pucinotti, R., and Tondini, N. (2008). "External post-tensioning retrofitting and modelling of steel–concrete box-girder bridges," in *Proceedings of 7th International Conference on Steel Bridges Guimaraes Portugal 4-6 June*, 1st Edn., eds. P. J. S. Cruz, L. S. da Silva, and F. Schroter (Guimaraes: Steel Bridges–Advanced Solutions and Technologies–published by ECCS), 425–34.

Bursi, O. S., Zandonini, R., Salvatore, W., Caramelli, S., and Haller, M. (2006). "Seismic behavior of a 3D full-scale steel–concrete composite moment resisting frame structure," in *Proceedings of Fifth International Conference on Composite Construction in Steel and Concrete* (Kruger National Park), 641–52.

CEN (2002). *EN 1990; Base of Structural Design*. Bruxelles.

CEN (2004). *EN 1998-1-1; Design of Structures for Earthquake Resistance. Part 1: General Rules, Seismic Actions and Rules for Buildings*. Bruxelles.

CEN (2005). *EN 1998-2; Design of Structures for Earthquake Resistance. Part 2: Bridges*. Bruxelles.

CEN (2006). *EN1993-1-3; Design of Steel Structures. Part 1–3: General Rules—Supplementary Rules for Cold-Formed Members and Sheeting*. Bruxelles.

Contin, A., Fiordaliso, G., Pucinotti, R., and Soffiato, A. (2015a). "Fluid viscous dampers and shock transmitters in the realization of multi-span steel–concrete viaducts. Design, testing and commissioning according to the UNI EN 15129:2009 and Italian standard "DM14.01.2008": GENERAL ASPECTS," in *Proceedings of The Italian Steel Days, CTA* (Salero), 683–890.

Contin, A., Fiordaliso, G., Pucinotti, R., and Soffiato, A. (2015b). "Fluid viscous dampers and shock transmitters in the realization of multi-span steel–concrete viaducts: case study—The Ippolito 1 Viaduct—," in *Proceedings of The Italian Steel Days, CTA* (Salero), pp. 691–698.

De Domenico, D., Ricciardi, G., and Takewaki, I. (2019). Design strategies of viscous dampers for seismic protection of building structures: a review. *Soil Dyn. Earthquake Eng.* 118, 144–165. doi: 10.1016/j.soildyn.2018.12.024

Makris, N., and Zhang, J. (2004). Seismic response analysis of a highway overcrossing equipped with elastomeric bearings and fluid dampers. *J. Struct. Eng.* 130, 830–45. doi: 10.1061/(ASCE)0733-9445(2004)130:6(830)

Ministero delle Infrastrutture (2008). *DM 14 Gennaio 2008, Norme Tecniche per le Costruzioni*. Suppl. Ord. n.30 alla G.U. n.29 del 4/2/2008.

Ministero delle Infrastrutture (2009). *Circolare 2 Febbraio 2009, Istruzioni per L'applicazione DELLE NUOVE NORME Tecniche per le Costruzioni*. Suppl. or. n.27 alla G.U. n.47 del 26/2/2009;.

Ministero delle Infrastrutture e dei Tasporti (2018). *DM 17 Gennaio 2018, Aggiornamento delle ≪Norme tecniche per le Costruzioni≫*. Suppl. Ord. alla G. U. n. 42 del 20/02/2018.

Ministero delle Infrastrutture e dei Tasporti (2019). *Circolare 21 Gennaio 2019, Istruzioni per L'applicazione dell'≪Aggiornamento delle "Norme tecniche per le costruzioni"≫*. di cui al DM 17 gennaio 2018; Supp. Ord. alla G.U. n. 35 del 11 febbraio 2019.

OPCM 3274 (2003). *Ordinanza del Presidente del Consiglio dei Ministri del 20 marzo 2003 "Primi elementi in materia di criteri generali per la classificazione sismica del territorio nazionale e di normative tecniche per le costruzioni in zona sismica*". G.U. 8/5/2003 n 105.

Pucinotti, R., Tondini, N., Zanon, G., and Bursi, O. S. (2015). Tests and model calibration of high-strength steel tubular beam-to-column and column-base composite joints for moment-resisting structures. *Earthquake Eng. Struct. Dyn.* 44, 1471–1493. doi: 10.1002/eqe.2547

Quaglini, V., Gandelli, E., Dubini, P., Limongelli, M. P., et al. (2017). Total displacement of curved surface sliders under non-seismic and seismic actions: a parametric study. *Struct. Control Health Monit.* 24, 12:*e*2031. doi: 10.1002/stc.2031

Takeda, T., Sozen, M. A., and Norby Nielsen, N. (1970). Reinforced concrete response to simulated earthquakes. *J. Struct. Division* 96, 2557–2573.

Tian, Q., Hayashikawa, T., and Wei-Xin, R. (2016). Effectiveness of shock absorber device for damage mitigation of curved viaduct with steel bearing supports. *Eng. Struct.* 109, 61–74. doi: 10.1016/j.engstruct.2015.11.026

UNI 10985 (2002). *Vibrations on Bridges and Viaducts—General Guidelines for the Execution of Dynamic Tests and Investigations*.

Conflict of Interest Statement: The authors declare that the research was conducted in the absence of any commercial or financial relationships that could be construed as a potential conflict of interest.

frontiers in Built Environment

ORIGINAL RESEARCH
published: 20 August 2019
doi: 10.3389/fbuil.2019.00100

Seismic Retrofit of Hospitals by Means of Hysteretic Braces: Influence on Acceleration-Sensitive Non-structural Components

Emanuele Gandelli[1]*, *Andreas Taras*[2], *Johann Distl*[1] and *Virginio Quaglini*[3]

[1] R&D Department, Maurer Engineering GmbH, Munich, Germany, [2] Institute of Structural Engineering, Universität der Bundeswehr, Munich, Germany, [3] Politecnico di Milano, Department Architecture, Built Environment and Construction Engineering, Milan, Italy

The paper illustrates an investigation on the effectiveness of dissipative bracing (DB) systems for seismic retrofit of buildings with sensitive non-structural components (NSCs) and technological content (TC), such as medical centers. The "Giovanni Paolo II" hospital, located in a high seismic prone area in Southern Italy, is chosen as case-study. The retrofit intervention with hysteretic braces is designed according to the Italian Building Code. The seismic response of the hospital building is investigated by means of non-linear history analyses carried out in OpenSees FE code and, in order to verify the full-operation after the earthquake, the integrity of NSCs and TC is checked. The retrofit design, thanks to the stiffening and damping effects introduced by DB system, proves suitable to protect both the structural frame and "drift-sensitive" non-structural components and content even under severe earthquakes (PGA = 0.45 g). Nevertheless, some concerns arise about the suitability of hysteretic braces for the protection of the "acceleration-sensitive" elements of the medical complex. Indeed, during weak earthquakes (PGA = 0.17 g), failures of several of these components are detected which can substantially impair the operation of the hospital in the aftermath of the seismic event.

Keywords: seismic retrofit, hysteretic braces, hospitals, non-structural components, acceleration-sensitive elements

OPEN ACCESS

Edited by:
Dario De Domenico, University of Messina, Italy

Reviewed by:
Antonio Di Cesare, University of Basilicata, Italy
Giuseppe Ricciardi, University of Messina, Italy

***Correspondence:**
Emanuele Gandelli
e.gandelli@maurer.eu

Specialty section:
This article was submitted to Earthquake Engineering, a section of the journal Frontiers in Built Environment

Received: *20 May 2019*
Accepted: *31 July 2019*
Published: *20 August 2019*

Citation:
Gandelli E, Taras A, Distl J and Quaglini V (2019) Seismic Retrofit of Hospitals by Means of Hysteretic Braces: Influence on Acceleration-Sensitive Non-structural Components. Front. Built Environ. 5:100. doi: 10.3389/fbuil.2019.00100

INTRODUCTION

Because of their importance in the management of the emergency response, medical centers must be designed to achieve high performance levels under severe ground motions. Unfortunately hospitals have proven to be as vulnerable to earthquakes as the population they serve, and in the last decades, moderate or heavy structural damages to medical complexes were reported after ground motions in California, Japan, Iran, India and Italy (USGS - United States Geological Survey, 1996; Achour et al., 2011; Rossetto et al., 2011). Besides, past experience showed that the operation of a healthcare center as a whole depends on the integrity of all its physical components, including not only the structural frame, but also non-structural components (NSCs) and technological content (TC), such as architectural elements and utilities, and medical equipment. As an example, during the last seismic events (L'Aquila, 2009; Emilia Romagna, 2012; Central Italy, 2016) Italian hospitals reported, beside structural failures (Alexander, 2010), substantial damage to their non-structural components (Masi et al., 2014; Celano et al., 2016) which jeopardized the operation in the aftermath.

Due to the large variety of typical NSCs and TC of a medical center, an exhaustive model for the definition of relevant failure thresholds is still not available. Among various approaches, the HAZUS probabilistic method (FEMA - Federal Emergency Management Agency, 1999) allows the definition of "fragility curves" that express the probability P that the seismic demand D exceeds the capacity C of the element $P(C < D|D)$. The capacity C of the NSC and TC is modeled as a random variable:

$$C = C_m \cdot \varepsilon \tag{1}$$

where C_m is the median value of C, and ε is a log-normal distribution function (having median value equal to 1 and logarithmic standard deviation equal to β). Hence, given a certain seismic event of intensity IM, the probability of failure is:

$$\begin{aligned} P(C < D|D) &= \int_0^{IM} \frac{1}{x\beta\sqrt{2\pi}} e^{-\frac{1}{2}\left(\frac{\log(x/C_m)^2}{\beta^2}\right)} dx \\ &= \phi\left(\frac{\log(IM/C_m)}{\beta}\right) \end{aligned} \tag{2}$$

being ϕ the standard normal cumulative distribution function. Typical fragility curves are established for four damage thresholds, associated to: (1) slight damage; (2) moderate damage; (3) extensive damage; and (4) complete damage.

Although a recent study (Petrone et al., 2016) addressed to "velocity-sensitive" equipment, in design codes the typical NSCs and TC of hospital complexes are generally categorized as either "drift-sensitive" (e.g., pipelines, infills, glazed surfaces) or "acceleration-sensitive" (e.g., false ceilings, elevators, medical equipment), and failure thresholds for moderate/extensive damage level are available in literature (Lupoi et al., 2008).

The importance of performance-oriented approaches for the seismic design of new hospitals and for the retrofitting of existing ones is therefore evident. Performance Based Design (PBD) procedures were firstly formulated in New Zealand in the 80's (Priestley, 2000) and nowadays have been endorsed in the most advanced design codes. Among them, the Italian building code (CSLLPP - Consiglio Superiore dei Lavori Pubblici, 2018) establishes distinct performance requirements depending on the intensity of the design earthquake:

1. FDE ("*Frequent Design Earthquake*" with 81% probability of being exceeded over the reference time period V_R): fully-operational (OP) performance level for both non-structural and structural elements;
2. SDE ("*Serviceability Design Earthquake*" with 63% over V_R probability): immediate occupancy (IO) performance level for structural elements and moderate non-structural damages;
3. BDE ("*Basic Design Earthquake*" with 10% over V_R probability): life safety (LS) performance level for structural elements (moderate/diffused plasticization of beams and columns) and remarkable non-structural damages;
4. MCE ("*Maximum Considered Earthquake*" with 5% over V_R probability): collapse prevention (CP) performance level for structural elements (severe plasticization of beams and columns) and very severe non-structural damages.

Steel Hysteretic Dampers (SHDs) were introduced in the '70s of the last century (Skinner et al., 1974, 1980) as a mean to protect civil works from earthquakes. According to a typical layout, SHDs are inserted as a part of the bracing system of the building and dissipate the seismic energy through the plastic deformation of sacrificial mild steel components; therefore SHDs provide a response which is not (or only slightly) affected by velocity, and their force-displacement characteristic is conventionally expressed by means of bilinear hysteretic models. SHDs exploiting axial loads (Takeuchi et al., 1999), shear loads (Hitaka and Matsui, 2003), bending (Tsai et al., 1993; Medeot and Chiarorro, 1996), and torsion (Dicleli and Milani, 2016) have been developed over the years, and used in a number of application worldwide for the seismic retrofit of schools (Antonucci et al., 2006, 2007; De Domenico et al., 2019a) and for the protection of hospitals (Wada et al., 2000), because of their lower cost in comparison to other antiseismic devices like e.g., fluid viscous dampers.

In common design practice (Braga et al., 2015; Mazza and Vulcano, 2015; Di Cesare and Ponzo, 2017), SHDs are designed accounting for the seismic action at BDE level. However, use of SHDs leads to an overall increase in stiffness of the structure which may have adverse effects, like e.g., increase in peak floor accelerations (PFAs), during the occurrence of weak or moderate earthquakes with return period comparable to the service life of the construction. The latter effect is investigated in this paper. A case-study hospital located in a high seismic prone area in southern Italy is analyzed and a retrofit solution implementing SHDs is proposed according to an acknowledged design method (Di Cesare and Ponzo, 2017). Non-linear response history analyses on the retrofitted building show that, although the solution is effective to protect the structure from strong earthquakes at DBE level, excessive PFAs are expected during the occurrence of weaker FDE ground motions which lead to significant damages to "acceleration-sensitive" NSCs and hence to an impaired hospital operation in the event's aftermath.

THE CASE-STUDY HOSPITAL

The "Giovanni Paolo II" hospital of Lamezia Terme (Italy), dating to the early 1970s, is selected as case-study. Two main buildings named "Degenze" and "Piastra," featuring six and three floors respectively, are connected by two tower structures ("Torre Scala") containing the vertical conveying systems (**Figure 1**).

Since it contains the surgical division of the hospital and hence a large number of earthquake-sensitive NSCs, the "Piastra" building is considered hereafter.

A survey of the non-structural components (NSCs) and technological content (TC) of the building was conducted in previous studies (Lupoi et al., 2008; Gandelli et al., 2018). NSCs and TC were categorized as either "drift-sensitive" or "acceleration-sensitive" elements (**Table 1**) and failure thresholds were established as the median capacity ($\boldsymbol{C_m}$) of relevant fragility curves available in literature (Johnson et al., 1999; Lupoi et al., 2008; Cosenza et al., 2014).

REFERENCE SEISMIC SCENARIO AND PERFORMANCE REQUIREMENTS

In order to assess the seismic response on the "Piastra" building, non-linear history analyses were carried out considering two design earthquakes and the relevant performance requirements provided by the Italian Building code (CSLLPP - Consiglio Superiore dei Lavori Pubblici, 2018): the BDE was assumed for the design of SHDs for the retrofit of the building and hence for the assessment of the structural integrity of the reinforced-concrete frame, whereas the FDE was taken into account to verify the fulfillment of the fully-operational performance (OP) requirement for non-structural elements. Design spectra were defined considering the code's provisions (CSLLPP - Consiglio Superiore dei Lavori Pubblici, 2018) for a strategic structure (functional class *IV*, $c_u = 2.0$) located in Lamezia Terme (16.18° longitude, 38.58° latitude), topographic category T_1, and a nominal life of the building $V_N = 100$ *years* (corresponding to a reference period $V_R = c_u \bullet V_N = 200$ *years*). Based on available information (Lupoi et al., 2008), the soil at and below the foundation level is mainly composed of sand and gravel with good mechanical properties (friction angle $\varphi = 30 \div 35°$). The risk of liquefaction is negligible and a type B soil was assumed. These assumptions led to peak ground acceleration (*PGA*) values of *0.17 g* at FDE, and *0.45 g* at BDE. Seven independent ground motion were selected for either seismic design level (**Table 2**) among records with magnitude $6.0 \leq Mw \leq 8.0$ and epicentral distance $0 \leq Rep \leq 35$ *km* using the target spectrum-matching criterion for fundamental periods $T \leq 2.0$ *s*. In particular, compliant natural records were searched within the European Strong-motion Database (Ambraseys et al., 2002) by means of REXEL v3.4 beta software (Iervolino et al., 2010). Since three-dimensional compatible ground motion records could not be found in the database, only the two horizontal acceleration components were considered, whereas the vertical acceleration component was neglected.

FIGURE 1 | Side-view of the hospital complex.

SEISMIC RETROFIT INTERVENTION

"As-Built" Structural Frame

The "Piastra" is a quite regular three-story building with dimensions of *140 m* in the longitudinal direction (X-direction) and *50 m* in the transversal direction (Y-direction). The story heights are *5.1 m* (basement), *3.5 m* (ground floor), and *4.5 m* (first floor) respectively, for a total height of *13.1 m*. Foundations are located at -5.1 *m* with respect to the ground level. The structural frame consists of cast-in-place reinforced concrete beams and columns and is divided into three blocks (block A, B, and C) by separation joints at each floor. The layout of the structural grid (**Figure 2A**) is common to each block, with bays of *7.2 m* and *9.6 m* in the longitudinal (X) and transversal (Y) directions, respectively. At basement level, the building is supported by 111 primary C-P1 type columns, 71 auxiliary C-P4 type columns, and 16 auxiliary C-P5 type columns. Auxiliary columns are used at the lowest level only, while primary columns are present at each floor (111 columns

TABLE 1 | Floor distribution of non-structural components (NSCs) and pieces of technological content (TC).

Category	Component	Median capacity C_m		Basement	Ground floor	First floor
		(%)	*(g)*			
Drift-sensitive	EG diesel conduits	0.90		×		
	Pipelines	0.90		×	×	×
	Curtain walls	0.75		×	×	×
	Glass windows and doors	4.60		×	×	×
Acceleration-sensitive	False ceilings		0.50	×	×	×
	UPS battery cabinets		0.52	×		
	UPS switchboard panels		1.12	×		
	UPS distribution panels		1.75	×	×	×
	Elevators		0.20	×	×	×
	Medical gas cylinders		0.50	×		
	Consultation rooms		0.45	×	×	×
	Medical equipment		0.90		×	×
	Ductwork in suspended ceiling		0.50	×	×	×
	False ceilings		0.50	×	×	×

TABLE 2 | Ground motion records for seismic analyses at FDE and BDE.

Seismic lelel	Earthquake (Wave no.)	ID	Fault mechanism	Date (mm/dd/yy)	Mw (-)	Rep (km)	PGA-X (m/s^2)	PGA-Y (m/s^2)	SF-X (-)	SF-Y (-)
	Ano Liosia (1314)	FDE-1	Normal	07/09/99	6	17	1.171	1.066	1.422	1.561
	Ano Liosia (1713)	FDE-2	Normal	07/09/99	6	18	1.087	0.839	1.531	1.984
	Campano Lucano (291)	FDE-3	Normal	23/11/80	6.9	16	1.526	1.725	1.091	0.965
FDE	Friuli (147)	FDE-4	Thrust	15/09/76	6	14	1.384	2.319	1.208	0.718
	Montenegro (199)	FDE-5	thrust	24/05/79	6.9	16	3.680	3.557	0.452	0.468
	Montenegro (232)	FDE-6	thrust	24/05/79	6.2	20	0.560	0.543	2.973	3.069
	South Iceland (6263)	FDE-7	strike slip	17/06/00	6.5	7	6.136	5.018	0.271	0.332
	Campano Lucano (291)	BDE-1	normal	23/11/80	6.9	16	1.526	1.725	2.097	2.572
	Izmir (548)	BDE-2	strike slip	06/11/92	6	30	0.283	0.384	15.687	11.543
	Montenegro (196)	BDE-3	thrust	24/05/79	6.9	25	4.453	3.000	0.996	1.479
BDE	Montenegro (197)	BDE-4	thrust	24/05/79	6.9	24	2.880	2.361	1.540	1.878
	Montenegro (199)	BDE-5	thrust	24/05/79	6.9	16	3.680	3.557	1.205	1.247
	Montenegro (232)	BDE-6	thrust	24/05/79	6.2	20	0.560	0.543	7.921	8.175
	Umbria Marche (594)	BDE-7	normal	26/09/97	6	11	5.138	4.538	0.863	0.977

Mw, magnitude; Rep, epicentral distance; PGA, Peak Ground Acceleration; SF, Scale Factor.

per floor), with cross-section as shown in **Figure 2B**; details of secondary columns can be found in another paper (Gandelli et al., 2018). The longitudinal beams have a conventional rectangular cross-section, while the transversal beams have a channel cross-section (**Figure 2C**).

Previous studies (Lupoi et al., 2008; Gandelli et al., 2018) showed that the "as-built" building frame could suffer severe structural damage, close to collapse, under moderate earthquakes corresponding to FDE level ($PGA = 0.17\,g$), and that the "Piastra" needs to be retrofitted to achieve the safety performance level prescribed by the Code. A proposed retrofitting solution by means of DBs is described in the following section.

DB Layout

For the optimal design of the dissipative bracing (DB) layout several limitations/targets have to be taken into account, namely: (i) do not impair the distribution of medical functions within the medical center by, e.g., obstructing the passage to patients and doctors; (ii) limit at each floor the eccentricity between the center of mass and the center of lateral stiffness of the braced frame; (iii) restrain torsional motions during the seismic shaking.

In order to limit the length of the elements subjected to tension/compression and prevent their buckling, two DB units are installed in the same bay according to the "inverted V" configuration shown in **Figure 3A**. A conventional arrangement is supposed, with each DB consisting of a steel hysteretic damper (SHD) connected to the main frame by means of two rigid links (RLs).

At each floor and in either horizontal direction, the proposed DB layout envisages eight SHDs for both blocks A and B, and twelve SHDs for block C (**Figure 2A**). The units are installed on the perimeter of each block to restrain torsional motion. The nomenclature adopted to identify each DB is based on its horizontal and vertical localization; e.g. "AX2-L1" stands for block A, horizontal direction X, position 2, floor 1. **Figures 2A**, **3B** show the proposed floor and elevation layouts for the DB system, respectively. Both DBs installed in the same bay share the same tag. Owing to the small gap (10 mm) provided by the separation joints in the longitudinal (X) direction, shock transmit units (STUs) are inserted at each floor to rigidly connect adjacent blocks and avoid possible hammering during the seismic shaking (**Figure 3B**).

Since the introduction of dissipative braces (DB) induces a considerable increase of axial load in structural members, local strengthening of beams and columns adjacent to DBs is often necessary (Ponzo et al., 2010; Di Cesare et al., 2014). The primary columns of the retrofitted bays are reinforced with additional layers of steel rebar along the lateral surface (**Figure 2B**) while thick steel plates are connected to the beams by means of stud anchors (**Figure 2C**). Beams and columns not directly connected to the dissipative bracing system maintain their original structural characteristics. It is worth noting that alternative solutions to mitigate the overstressing of beam and column elements have been proposed in literature (Apostolakis and Dargush, 2009; De Domenico et al., 2019b).

Design Procedure for DBs

Design parameters of the DBs have been selected by means of a step by step procedure based on a non-linear static analysis (NLSA) of the "as-built" structure (Di Cesare and Ponzo, 2017). As first step, the equivalent SDOF system of the bare frame (F) of each block of the "Piastra" building is determined from the relevant capacity curve (F-d) calculated in a previous study (Gandelli et al., 2018). Assuming that the dynamic response of the bare frame is governed by the 1st eigen-mode, the idealized elastoplastic response (F^*-d^*) of the equivalent SDOF is defined as $F^* = \frac{F}{\Gamma}$ and $d^* = \frac{d}{\Gamma}$ (being $\Gamma = \frac{m^*}{\sum m_i \phi_i^2}$ the "first mode participation factor," m_i and ϕ_i the mass and the normalized

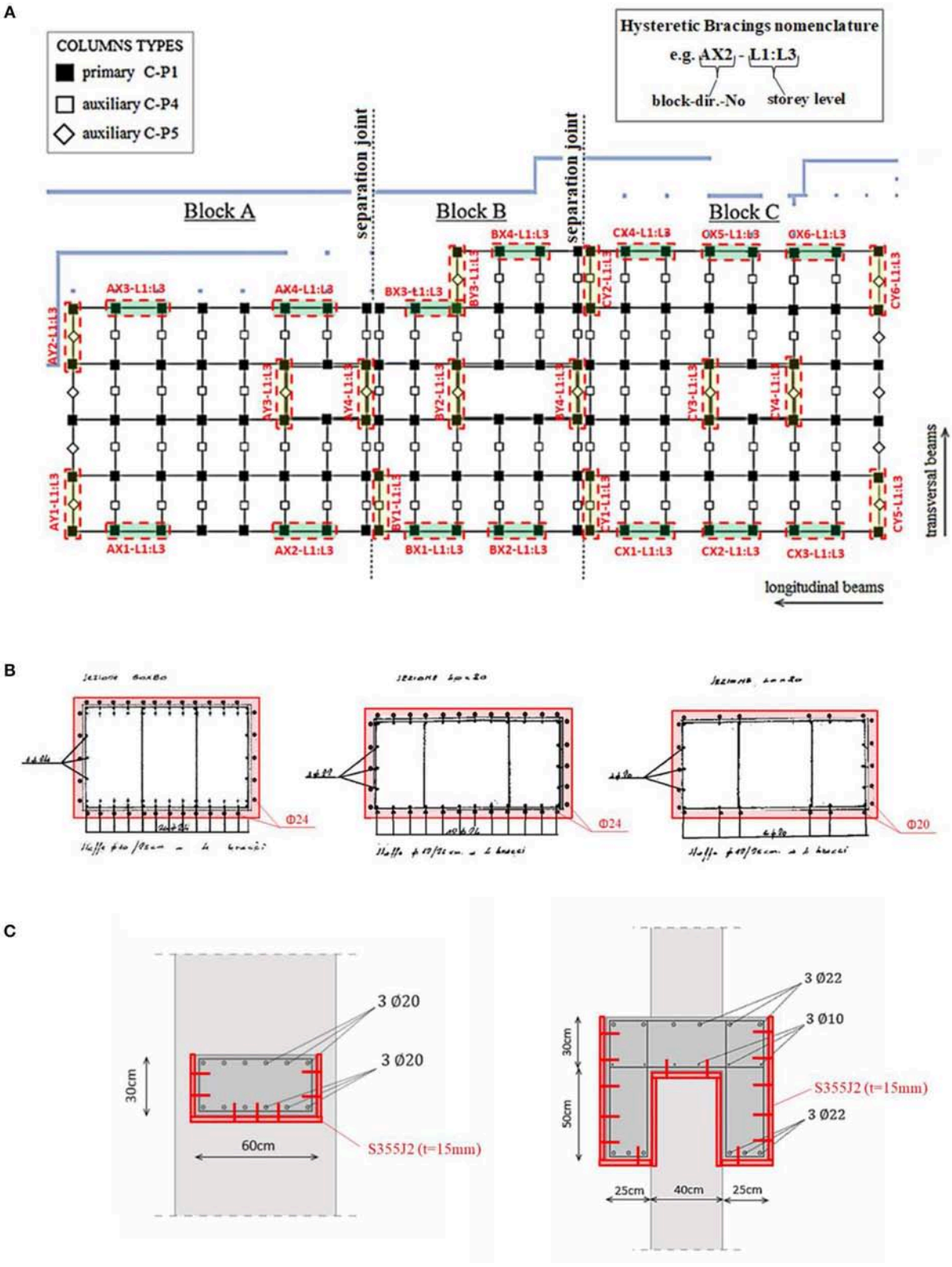

FIGURE 2 | Structural layout of the "Piastra" building. **(A)** Columns grid (in black) and plan arrangement of Dissipative Braces (in red-dashed). **(B)** Cross-section of primary columns: (left) C-P1; (center) C-P2; (right) C-P3. **(C)** Cross-section of beams in the longitudinal (left) and transversal (right) directions. Proposed strengthening is drafted in red lines, superimposed to the original layout in black/gray.

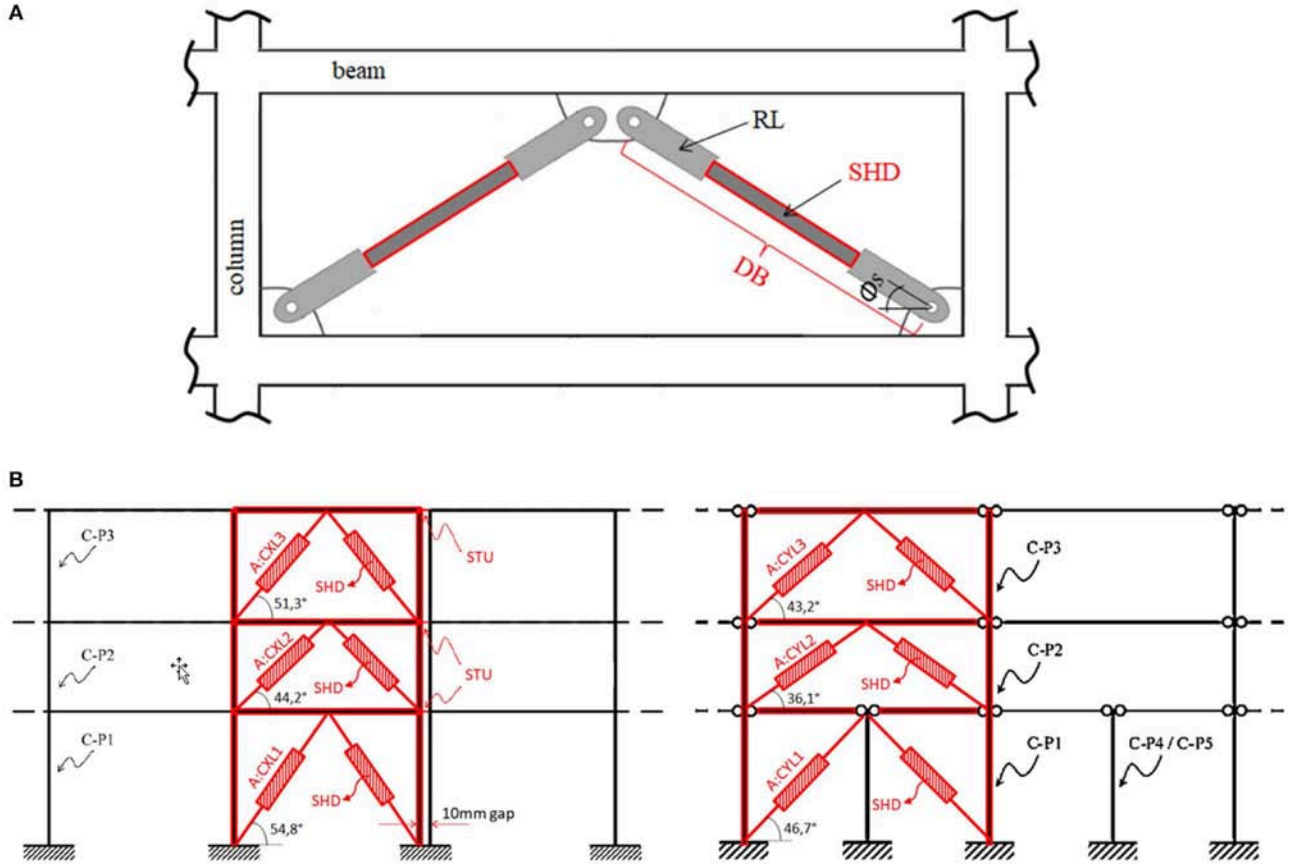

FIGURE 3 | Layout in elevation of the dissipative bracing (DB) system. **(A)** Main components of a DB: steel hysteretic damper (SHD) and rigid links (RL). **(B)** Arrangement of DBs and shock-transmit units (STU) in the longitudinal (left) and transversal (right) structural frames.

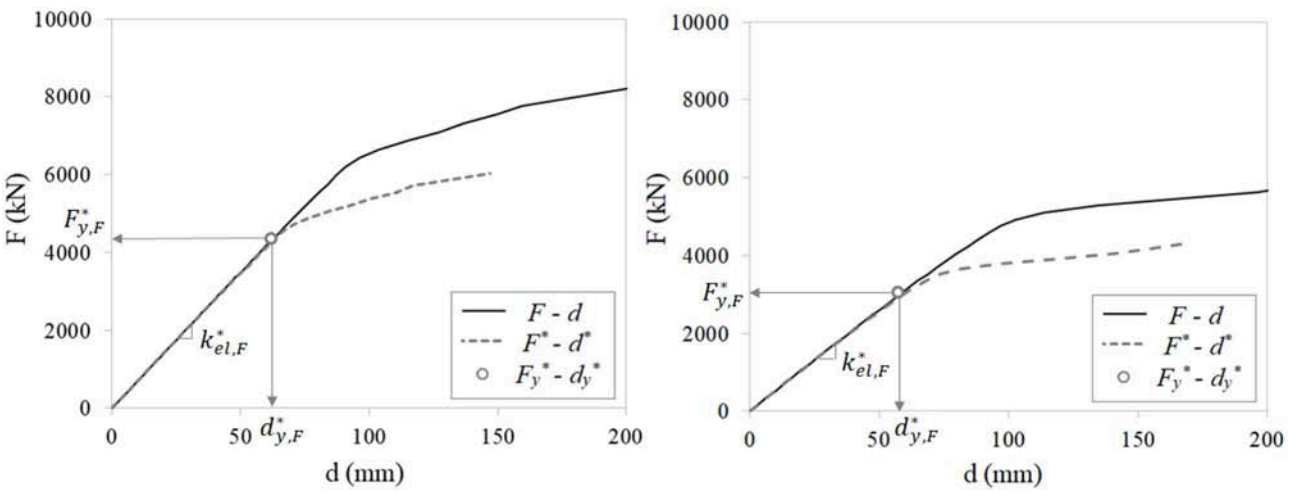

FIGURE 4 | Physical I (*F-d*) and reduced (*F*-d**) capacity curves calculated for the bare frame of block A along longitudinal (X, left) and transversal (Y, right) directions.

modal component of the ith story, respectively). As an example, **Figure 4** shows the capacity curves, both physical and reduced (equivalent SDOF), for block A along the two horizontal directions.

Eventually, the reduced mass (m^*) and the elastic stiffness ($k^*_{el,F}$) of the equivalent SDOF system are calculated as $m^* = \sum m_i \phi_i$ and $k^*_{el,F} = \frac{F^*_{y,F}}{d^*_{y,F}}$. **Table 3** provides the reduced properties

of the bare frame of the three blocks along both horizontal directions. The blocks exhibit a quite uniform behavior with close values of yielding displacement ($d^*_{y,F} \cong 60mm$) along both horizontal directions.

In the second step of the procedure the design parameters of the dissipative bracing (DB) system are determined. The force-displacement behavior of the DB system is idealized by means of an elastic perfectly-plastic SDOF system defined by the yielding force ($F^*_{y,DB}$), the elastic stiffness ($k^*_{el,DB}$), the yielding displacement ($d^*_{y,DB} = \frac{F^*_{y,DB}}{k^*_{el,DB}}$), and the ductility factor (μ^*_{DB}). In order to achieve consistent responses of the three blocks at BDE, the same target displacement for the equivalent SDOF retrofitted system (F+DB) has been assumed along both horizontal directions ($d^*_{F+DB,X} = d^*_{F+DB,Y} = d^*_{F+DB}$). This assumption additionally allows to limit the maximum force transmitted by STU units as a result of differential movements. According to well-regarded design recommendations (Vayas, 2017), the DB system is conceived in order to keep the structural members of the frame in the elastic range while the seismic energy is dissipated by the dissipative bracings only; hence the target displacement is set to $d^*_{F+DB} = 55mm$, below the yielding displacement ($d^*_{y,F}$) of each block (ranging from 60.1 to 65.5 mm, see **Table 3**). The displacement of the equivalent SDOF retrofitted system (F+DB) is hence estimated from the displacement response spectrum ($S_d(T^*_{eff,F+DB}, \xi^*_{eff,DB})$) by means of an iterative procedure. The effective period ($T^*_{eff,F+DB}$) of the equivalent SDOF system (F+DB) is calculated as:

$$T^*_{eff,F+DB} = 2\pi\sqrt{\mathbf{m}^*/(k^*_{el,F} + k^*_{eff,DB})} \tag{3}$$

being $k^*_{el,F}$ and $k^*_{eff,DB} = F^*_{y,DB}/d^*_{F+DB} = \frac{k^*_{el,DB}}{\mu^*_{DB}}$ the elastic stiffness of the frame (F) and the effective stiffness of the dissipative bracing (DB), respectively. The equivalent viscous damping of the dissipative bracing ($\xi^*_{eff,DB}$) is calculated as Dwairi et al. (2007):

$$\begin{cases} \xi^*_{eff,DB} = \left[85 + 60\left(1 - T^*_{eff,F+DB}\right)\right] \cdot \left(\frac{\mu^*_{DB}-1}{\pi\mu^*_{DB}}\right) & T^*_{eff,F+DB} < 1,0s \\ \xi^*_{eff,DB} = 85 \cdot \left(\frac{\mu^*_{DB}-1}{\pi\mu^*_{DB}}\right) & T^*_{eff,F+DB} \geq 1,0s \end{cases} \tag{4}$$

The ductility factor (μ^*_{DB}) of the dissipative bracing has been set to $\mu^*_{DB} = 10$ which is a typical value for steel hysteretic dampers (Di Cesare and Ponzo, 2017), resulting in the yielding displacement $d^*_{y,DB} = d^*_{F+DB}/\mu^*_{DB} = 5.5mm$. For the three examined blocks, convergence of the iterative procedure ($S_d\left(T^*_{eff,F+DB}, \xi^*_{eff,DB}\right) = 55 \pm 2$mm) has been reached in few iterations leading to the design parameters of the equivalent SDOF dissipative bracing (DB) summarized in **Table 4**.

In the third step of the procedure, the overall damping force ($F^*_{y,DB}$) and stiffness ($k^*_{el,DB}$) of the equivalent SDOF dissipating system are distributed along the height of the frames (**Figure 5**) proportionally to the yielding force ($F_{y,F,i}$) and the elastic stiffness ($k_{el,F,i}$) of each story. In particular, the elastic stiffness ($k_{el,DB,i}$) and the yielding force ($F_{y,DB,i}$) at the i-th level (**Table 5**) are calculated as Di Cesare and Ponzo (2017):

$$\begin{cases} k_{el,DB,i} = \left(\frac{k_{el,F,i}}{k^*_{el,F}}\right) \cdot k^*_{el,DB} \\ F_{y,DB,i} = \left(\frac{F_{y,F,i}}{F^*_{y,F}}\right) \cdot F^*_{y,DB} \end{cases} \tag{5}$$

In the last step, the elastic stiffness ($k_{el,DB,i,s}$) and the damping force ($F_{y,DB,i,s}$) of any individual dissipating brace (DB) are calculated based on the number ($n_{DB,i}$) and inclination angle (ϕ_s, **Figure 3**) of the braces at the i-th story along the considered horizontal direction:

$$\begin{cases} k_{DB,i,s} = \frac{k_{DB,i}}{(n_{DB,i} \cdot \cos^2 \phi_s)} \\ F_{y,DB,i,s} = \frac{F_{y,DB,i}}{(n_{DB,i} \cdot \cos \phi_s)} \end{cases} \tag{6}$$

The resulting design parameters of the individual DB units are reported in **Table 6**.

TABLE 3 | Equivalent SDOF parameters of the bare frames of the three blocks in both horizontal directions.

Block	Direction	Γ (-)	m^* (ton)	$F^*_{y,f}$ (kN)	$d^*_{y,f}$ (mm)	$k^*_{el,F}$ (kN/mm)
A	X	1.36	1774	4354	61.7	70.6
	Y	1.40	1795	3061	60.1	50.9
B	X	1.37	1502	3316	65.5	50.6
	Y	1.40	1520	3131	63.2	49.5
C	X	1.36	2148	4704	62.3	75.5
	Y	1.39	2176	4698	64.8	72.5

TABLE 4 | Equivalent SDOF design parameters of the DB system for the three blocks of "Piastra" buiding.

Block	Direction	$F^*_{y,DB}$ (kN)	μ^*_{DB} (-)	$k^*_{el,DB}$ (kN/mm)	$\xi^*_{eff,DB}$ (%)
A	X	6000	10	846.9	30.1
	Y	5800	10	836.5	30.1
B	X	5400	10	824.1	30.2
	Y	5200	10	822.7	30.1
C	X	7000	10	1123.8	30.1
	Y	7000	10	1080.3	29.7

TABLE 5 | Distribution in elevation of the elastic stiffness ($k_{el,DB,i}$) and the yielding force ($F_{y,DB,i}$) of the DB system.

Parameter	Level (-)	Block A		Block B		Block C	
		dir. X	dir. Y	dir. X	dir. Y	dir. X	dir. Y
$k_{el,DB,i}$ (kN/mm)	1	4514.1	6595.4	3902.2	4505.5	5261.7	6573.7
	2	1926.5	3110.6	2133.6	2176.7	2865.9	3130.7
	3	599.2	827.9	849.5	752.2	1148.6	1077.6
$F_{y,DB,i}$ (kN)	1	6199.3	7399.9	5599.3	5400.0	7198.8	7999.9
	2	4031.9	5836.9	4645.2	4263.1	5948.6	6284.6
	3	2168.2	3258.2	2498.3	2379.9	3199.0	3508.1

TABLE 6 | Design parameters of the DB units.

Parameter	Level (-)	Block A		Block B		Block C	
		dir. X	dir. Y	dir. X	dir. Y	dir. X	dir. Y
$n_{DB,i} = n_{SHD,i}$ (-)	1,2,3	8	8	8	8	12	12
$k_{el,D,B,i,s} \cong k_{el,SHD,i,s}$ (kN/mm)	1	1643.4	1373.8	1415.6	1153.0	1283.0	1019.1
	2	453.4	466.8	500.4	401.3	451.8	349.7
	3	185.4	152.6	261.9	170.4	238.0	147.9
$F_{y,DB,i,s} = F_{y,SHD,i,s}$ (kN)	1	1301.0	1057.1	1170.9	947.8	1011.8	850.6
	2	680.3	707.8	781.0	635.1	672.2	567.1
	3	419.5	437.9	481.6	393.0	414.5	350.9

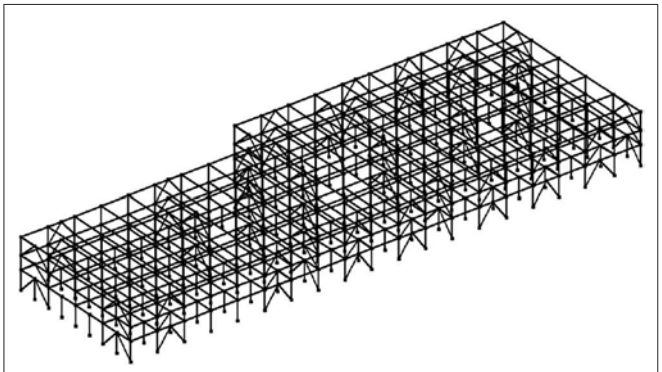

FIGURE 5 | 3D FEM model of the retrofitted "Piastra" building used in nonlinear response history analyses.

The Rigid links (RLs), provided to connect the SHDs to the r.c. frame, are sized in order to act as stiff connections that operate in their elastic field ($F_{y,RL,i,s} \gg F_{y,DB,i,s}$) and allow the overall force-displacement response of the DB system being governed by SHDs only; that is $k_{el,DB,i,s} \cong k_{el,SHD,i,s}$ (Di Cesare and Ponzo, 2017).

NUMERICAL ANALYSES

A 3D model of the retrofitted "Piastra" building (**Figure 5**) was created in the OpenSees® FEM software (McKenna et al., 2000).

To model columns and beams, non-linear "BeamWithHinges" elements (OpenSeesWiki online manual)[1], comprising two fiber sections at either end (where plastic hinges are likely to be triggered) and a linear-elastic region in the middle of the element, were used. The length of the plastic hinges (L_P) was estimated in accordance with the formula $L_P = 0.08L + 0.022f_{yd}d$, where L is the length of the beam/column member, and f_{yd} and d are the yield strength and the diameter of longitudinal steel reinforcing bars, respectively (Paulay and Priestly, 1992). The Kent-Scott-Park formulation, as modified by Karsan-Jirsa ("Concrete01-ZeroTensileStrength"), and a bilinear material law with kinematic hardening ("Steel01") were used to model concrete and steel, respectively; the relevant mechanical properties were assumed from a previous survey (Lupoi et al., 2008) as: steel elastic modulus $E = 210{,}000\ MPa$; steel yield stress $f_{yd} = 430\ MPa$; concrete elastic modulus $E = 30{,}000\ MPa$; concrete compressive strength $f_{cd} = 41\ MPa$. Softening of concrete-fibers was disregarded, while strain-parameters were set as recommended by the Italian Building Code (CSLLPP - Consiglio Superiore dei Lavori Pubblici, 2018); conservatively, hardening of steel-fibers was neglected too. A more detailed description of the modeling assumptions for r.c. elements can be found in the referred study (Gandelli et al., 2018).

The gravitational dead loads (G_k) were evaluated according to the original design report, while live loads (Q_k) were set according to the provisions of the Italian Building Code (CSLLPP - Consiglio Superiore dei Lavori Pubblici, 2018). The resulting load distributions (from bottom to upper floor) are: (1) *5.28; 5.28; 4.38 kN/m²* for dead loads, and (2) *3.00; 3.00; 0.50 kN/m²* for live loads, respectively.

The following boundary conditions were assigned to the model:

1. The nodes at foundation level were linked together and subjected to the application of "UniformExcitation" seismic inputs (OpenSeesWiki online manual)[1];
2. Vertical loads were assigned to every node according to the floor distribution of permanent (G_k) and live (Q_k) loads defined above, while relevant translational masses were evaluated as $\frac{(1.0G_k + 0.3Q_k)}{g}$;
3. A "RigidFloorDiaphragm" multi-points constraint was introduced at each floor to prevent relative displacements between nodes belonging to the same floor slab (OpenSeesWiki online manual)[1].

"Two node link" elements with a perfectly-rigid behavior along axial direction only were used to model STU devices that connect adjacent blocks, while for simplicity the DBs were modeled by means of bilinear hysteretic (material type "Steel01") trusses with a uniform behavior (axial stress-strain) over the entire length of the elements (OpenSeesWiki online manual)[1]. In order to reproduce the actual bilinear force-displacement response of the each physical DB, fictitious values of the cross-sectional area ($A_{DB,i,s}$) and the elastic modulus ($E_{DB,i,s}$) assigned at each truss element were calculated as:

$$\begin{cases} A_{DB,i,s} = F_{y,DB,i,s}/\sigma_{y,DB} \\ E_{DB,i,s} = (\sigma_{y,DB}k_{el,DB,i,s}L_{DB,i,s})/F_{y,DB,i,s} \end{cases} \quad (7)$$

being $\sigma_{y,DB} = 355MPa$ the assumed yielding stress and $L_{DB,i,s}$ the length of the i-th DB element. The stiffness hardening ratio r (i.e., the ratio of the post-yield modulus to the elastic modulus) was taken as *2.5%*, which falls in the middle of the range of typical values of r (from *0.05* to *5.0%*) reported for SHDs (Vayas, 2017). The resulting parameters of the hysteretic truss elements are reported in **Table 7**.

SEISMIC RESPONSE ASSESSMENT

According to the Italian Building Code (CSLLPP - Consiglio Superiore dei Lavori Pubblici, 2018), the seismic performance

[1] *OpenSeesWiki, online manual.* Available online at: http://opensees.berkeley.edu/wiki/index.php/Main_Page

TABLE 7 | Parameters of hysteretic truss elements for FEM analyses.

Parameter	Level (-)	Block A		Block B		Block C	
		dir. X	dir. Y	dir. X	dir. Y	dir. X	dir. Y
$L_D B, i, s(mm)$	1	6243	7004	6243	7004	6243	7004
	2	5021	5941	5021	5941	5021	5941
	3	5763	6580	5763	6580	5763	6580
$A_D B, i, s(mm^2)$	1	3665	2978	3298	2670	2850	2396
	2	1916	1994	2200	1789	1894	1598
	3	1182	1234	1357	1107	1168	988
$E_D B, i, s(MPa)$	1	$2.80 \cdot 10^6$	$3.23 \cdot 10^6$	$2.68 \cdot 10^6$	$3.02 \cdot 10^6$	$2.81 \cdot 10^6$	$2.98 \cdot 10^6$
	2	$1.19 \cdot 10^6$	$1.39 \cdot 10^6$	$1.14 \cdot 10^6$	$1.33 \cdot 10^6$	$1.20 \cdot 10^6$	$1.30 \cdot 10^6$
	3	$9.04 \cdot 10^5$	$8.14 \cdot 10^5$	$1.11 \cdot 10^6$	$1.01 \cdot 10^6$	$1.17 \cdot 10^6$	$9.84 \cdot 10^5$

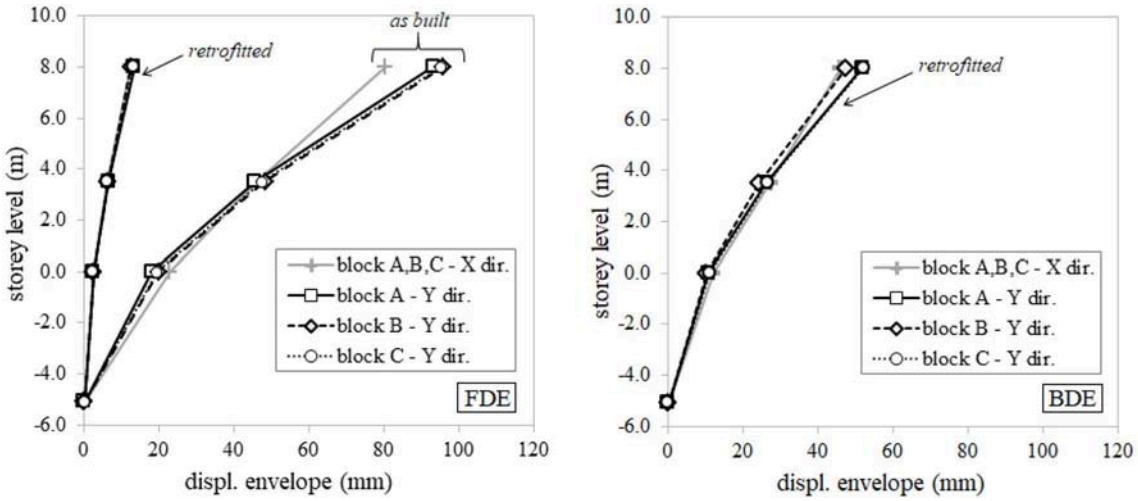

FIGURE 6 | Average displacement envelopes of the three blocks for FDE **(left)** and BDE **(right)**.

of the "Piastra" building is evaluated at both FDE and BDE considering the average response over the seven independent history analyses calculated in OpenSees FE code. The structural integrity requirement is checked at BDE while the full-operation of NSCs is verified at FDE.

In agreement with the design assumption for the DB system, the structural response of any of the three blocks is uniform along either horizontal direction at both FDE and BDE. While this outcome is quite obvious in the longitudinal (X) direction because of the STUs that act as rigid links between the adjacent frames, in the transversal (Y) direction it proves the fair tuning of effective stiffness and damping of SHDs. **Figure 6** shows the average displacement envelopes for the two considered seismic design levels. In particular, at FDE (**Figure 6**, left), the average peak displacement at roof level is 13 mm, while at BDE (**Figure 6**, right) it ranges from 46 mm to 53 mm in the longitudinal and transversal direction respectively, below the yielding threshold of the frame. Thereby the retrofitting solution permits to keep the r.c. members of the "Piastra" building in the elastic range. **Figure 6** reports also the average displacement envelope of the Bare Frame at FDE: at this intensity level the "as built" configuration of the building exhibits displacements of 81 and 95 mm in the longitudinal and transversal direction, respectively. The frame is expected to suffer structural damage at the columns of the upper story (C-P3) where plastic hinges are triggered and, as highlighted in a previous study (Gandelli, 2017), about 70% of columns' cross-sections are close to their ultimate capacity.

The response of the DB system calculated by OpenSees program is in good accordance with the results of the preliminary design. **Figure 7** shows the force-displacement loops of the SHD elements placed in the longitudinal direction of block B in position No. 1 at the three story levels (L1:L3). It can be noted that during the weak FDE-1 ground motion (**Figure 7**, left) the response of the unit at the 1st level (basement) practically remains within the elastic range, whereas the unit at the 3rd level experiences small plastic deformation (up to 5.0 mm). On the contrary, under the strong BDE-1 ground motion (**Figure 7**, right), at each story the SHD units develop large plastic deformations (up to 20 mm for the unit at the 3rd level), entailing a considerable dissipation of seismic energy.

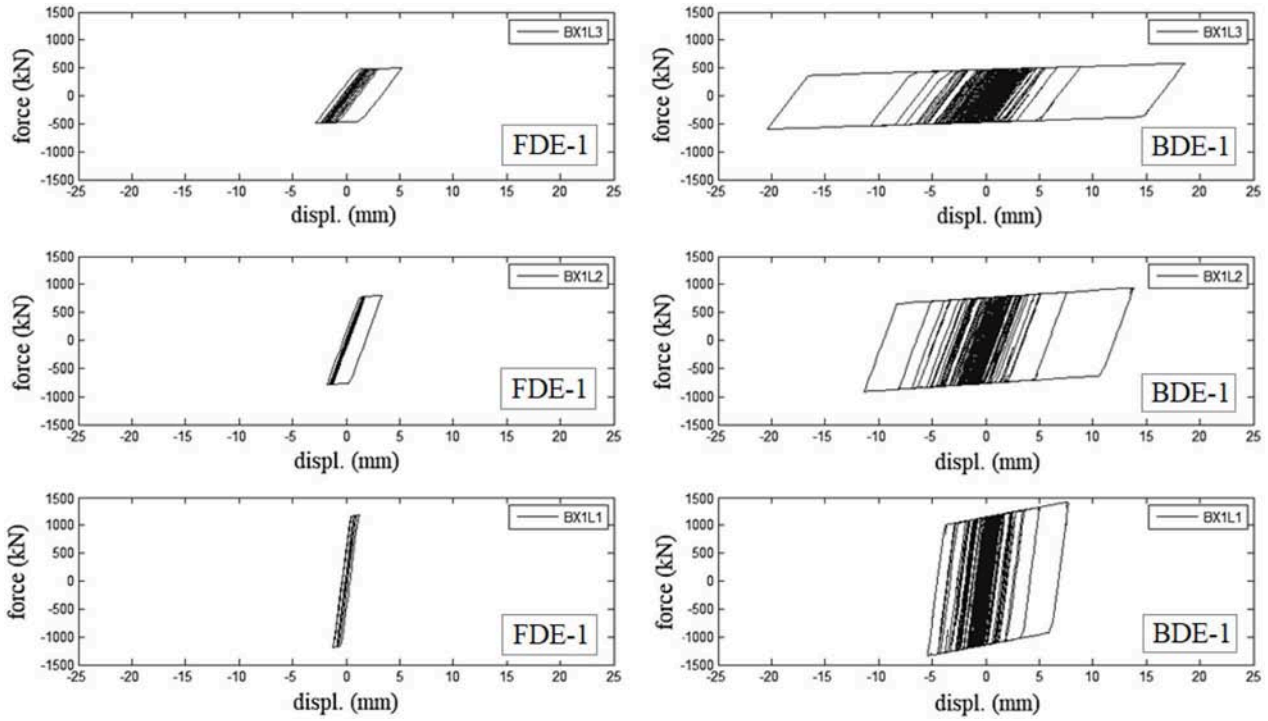

FIGURE 7 | Force-displacement response of DBs installed in position No. 1 at each story level (L1:L3) of the longitudinal frame (dir. X) of block B during FDE-1 (left) and BDE-1 (right) ground motions.

The proposed DB system proves to be a viable solution not only for the structural safety of the frame, but also for the seismic protection of "drift-sensitive" NSCs and TC. Since the failure threshold of the weakest element (0.75% for curtain walls) is not exceeded even during the most severe BDE earthquakes, the fully-operation condition is always attained from these elements. As shown in **Figures 8A,B**, the drift envelopes are indeed similar along both horizontal directions with average peak values of 0.16 and 0.53% under Frequent (FDE) and Basic Design Earthquakes (BDE), respectively. In particular for the Frequent Design Earthquake this allows a reduction of peak drifts of 79–89% along the longitudinal direction and 85–87% along the transversal one in comparison to the Bare Frame (**Figure 8A**).

However, the seismic performance of "acceleration-sensitive" elements is quite alarming, as illustrated in **Figure 8C**, where the peak floor acceleration (PFA) envelopes are compared to the failure threshold of some NSCs and TC. At FDE (**Figure 8C**, left), the following potential dysfunctions can be envisaged for the retrofitted building:

- Out of order of the elevators at every floor (resulting in slow-down in the transportation of injured patients);
- Temporary unavailability of consultation rooms at both ground and first floor levels due to possible overturning of not-restrained furniture and equipment;
- Detachment and falling of false ceilings and ductwork.

As a consequence, despite the low intensity of the seismic event, the hospital complex would not be capable to effectively manage the emergency response after the Frequent Design Earthquake, which is instead required by the Italian Building Code (CSLLPP - Consiglio Superiore dei Lavori Pubblici, 2018). This is most likely due to the stiffening effect of the DB system that, according to the design practice, is designed to constrain the displacement and protect the building during strong BDE earthquakes, but also shortens the period of vibration and increases the acceleration; since the damping introduced during FDE ground motions is small (**Figure 7**-left), the DB system appears not effective to protect "acceleration-sensitive" content. Nevertheless, it must be noted the envisaged scenario following retrofit with DBs is anyway better compared to the one expected for the "as built" structure for which higher PFA are predicted due to the negligible structural damping ($\xi = 5\%$) before the onset of plastic hinges in the columns.

Although not required by the Italian Building Code (CSLLPP - Consiglio Superiore dei Lavori Pubblici, 2018), the dynamic response of "acceleration-sensitive" NSCs and content is assessed at BDE seismic level in order to depict the potential scenario after a catastrophic earthquake (**Figure 8C**, right). In addition to the previously detected failures, also medical equipment at ground floor (e.g., computed tomography scan, magnetic resonance imaging, cardio vascular imaging, and ultrasound scan) are likely to be damaged causing a huge economic loss.

In order to limit damages to "accelerations-sensitive" non-structural components (NSCs) and content, other retrofitting techniques, like base-isolation, appear to be more suitable. The effectiveness of base isolation was indeed proven in a number

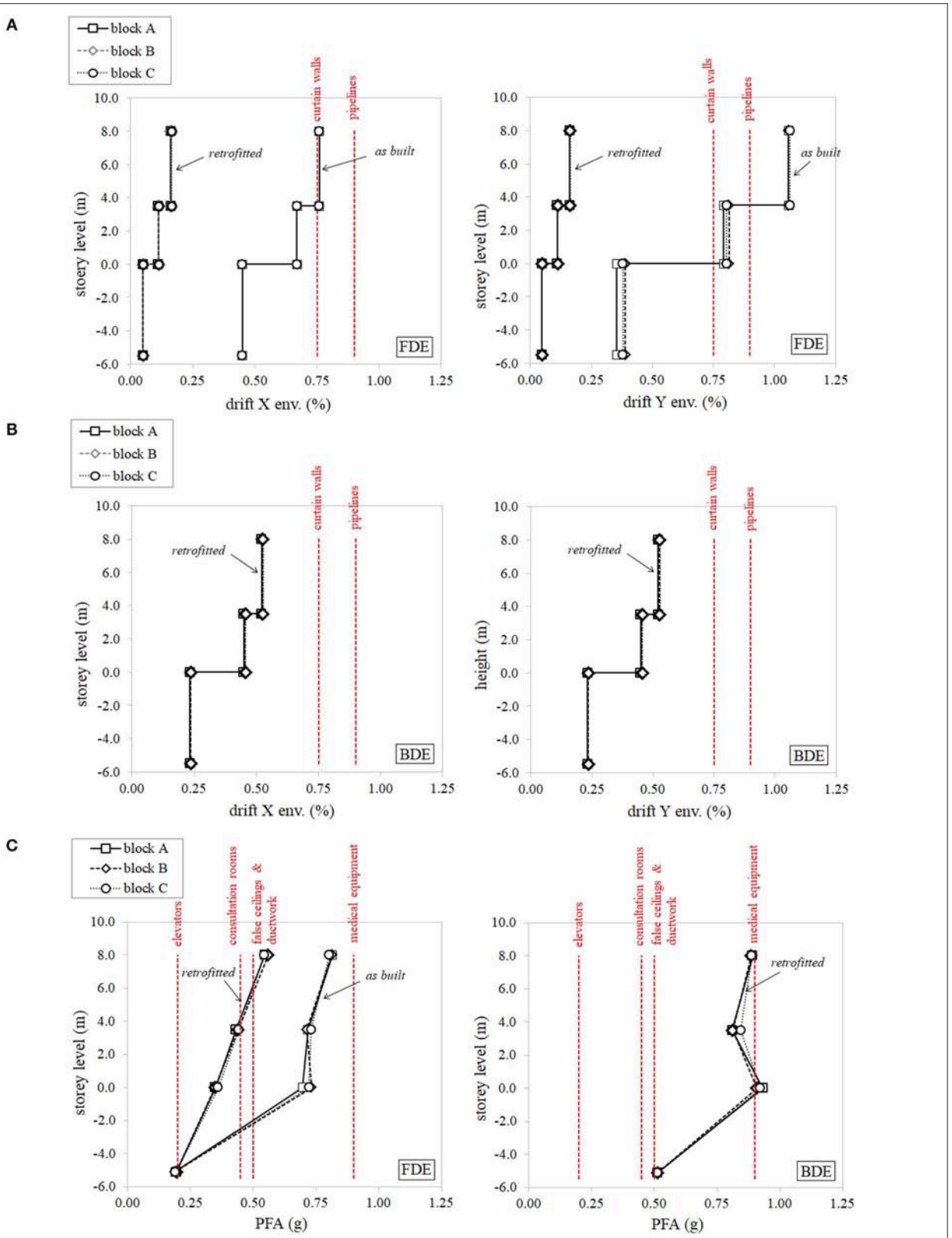

FIGURE 8 | Seismic performance of non-structural components and content (red-dashed lines represent the failure thresholds of the weakest elements). Average inter-story drift envelopes in the longitudinal (X-left) and transversal (Y-right) direction for both **(A)** FDE and **(B)** BDE levels. **(C)** Average peak floor acceleration (PFA) distributions calculated for FDE (left) and BDE (right).

of shake-table tests, as well as in real applications, e.g., from the actual response of base-isolated hospitals under real earthquakes (Nagarajaiah and Xiaohong, 2000). A design procedure for curved surface sliding isolators (CSSs) aiming at the protection of NSCs has been recently published (Gandelli et al., 2019) which allows, through a significant reduction of floor accelerations, to ensure the full operation of hospital services and the integrity of medical equipment. However, in certain cases, base isolation can be not viable due to the large seismic displacements at base level that can cause the pounding with adjacent buildings. This could be e.g., the case of the investigated case study, where the "Piastra" building, hosting the most critical surgical division of the hospital, could be base isolated, but with the risk of striking with the "Degenze" and "Torre Scala" structures. This issue can be overcome e.g., by combining the isolation system with a tuned mass damper placed over the base slab; this solution, in addition to mitigate peak floor accelerations, was proposed to limit the displacement of the isolators (De Domenico and Ricciardi, 2018).

CONCLUSIONS

The effectiveness of the intervention of seismic retrofit of hospital buildings by means of hysteretic bracing systems has been investigated in this study. The "Giovanni Paolo II" hospital of Lamezia Terme, located in a high seismic prone area in Southern Italy, is chosen as case-study. Since a previous survey demonstrated that the "Piastra" building of the medical complex could suffer heavy structural damages under moderate earthquakes, a retrofit intervention by mean of a dissipative bracing (DB) system has been designed according to the Italian Building Code (CSLLPP - Consiglio Superiore dei Lavori Pubblici, 2018). The preliminary design of the DB system is based on a non-linear static analysis whereas the seismic response of the hospital has been assessed by means of non-linear history analyses carried out in OpenSees FE code.

The proposed solution proves to be effective to protect the hospital complex from structural damage under severe BDE earthquakes (PGA = 0.45 g). The stiffening effect of the DB system has beneficial effects also for the protection of "drift-sensitive" NSCs and content. Indeed, the inter-story drift along either horizontal direction do not exceed the capacity of any NSC at FDE (PGA = 0.17 g) and, although not required by the assumed building code, even at the most demanding BDE.

On the contrary, concern arises about the suitability of hysteretic dampers for the protection of "acceleration-sensitive" elements of the medical complex. An alarming scenario can be indeed depicted after weak FDE events allowing to conclude that the hospital won't be able to manage the post-earthquake emergency. The following damages are predicted: (i) malfunction of the elevators that may slow-down the transportation of injured patients; (ii) detachment and collapse of false ceilings and supported ductwork; (iii) overturning of not-restrained furniture and equipment in medical consultation rooms leading to their temporarily unavailability.

This study, although not aiming to be exhaustive, emphasizes the potential inadequacy of conventional hysteretic bracing systems for the seismic retrofit of high-technological buildings, like hospitals, that contain a wide range of "acceleration-sensitive" elements. To overcome this issue, alternative solutions, like base-isolation and mass damping should be exploited which, thanks to mitigation of PFA, allow to ensure the full operation of hospital services after the quake.

DATA AVAILABILITY

The datasets generated for this study are available on request to the corresponding author.

AUTHOR CONTRIBUTIONS

EG and JD carried out the FEM analyses. AT and VQ supervised the calculations as technical advisors of the project. EG wrote the paper.

ACKNOWLEDGMENTS

The authors wish to thank Architect Carlo Nistico' for the support provided during the technical survey of the Giovanni Paolo II hospital of Lamezia Terme, and the Provincial Health Authority (ASP) of Catanzaro for the authorization to publish the results of the research.

REFERENCES

Achour, N., Miyajima, M., Kitaura, M., and Price, A. (2011). Earthquake induced structural and non-structural damage in hospitals. *Earthquake Spectra* 27, 617–634 doi: 10.1193/1.3604815

Alexander, D. E. (2010). The L'Aquila earthquake of 6 April 2009 and italian government policy on disaster response. *J. Nat. Resources Policy Res.* 2, 325–342. doi: 10.1080/19390459.2010.511450

Ambraseys, N., Smit, P., Sigbjornsson, R., Suhadolc, P., and Margaris, B. (2002). *Internet-Site for European Strong-Motion Data, European Commission, Research-Directorate General*. Environment and Climate Programme. Available online at: http://isesd.hi.is/ESD_Local/frameset.htm

Antonucci, R., Balducci, F., Castellano, M. G., and Don,à, F. (2006). "Pre-casted RC buildings with buckling restrained braces: the example of the new building of the faculty of engineering in Ancona," in *Proceedings of the 2nd International FIB Congress* (Napoli).

Antonucci, R., Cappanera, F., Balducci, F., and Castellano, M. G. (2007). "Adeguamento sismico del Liceo classico "Perticari" di Senigallia (AN)," in *Proceedings of the XII ANIDIS conference* (Pisa).

Apostolakis, G., and Dargush, G. F. (2009). Optimal seismic design of moment-resisting steel frames with hysteretic passive devices. *Earthquake Eng. Struc. Dyn.* 39, 355–76. doi: 10.1002/eqe.944

Braga, F., Buttarazzi, F., Dell'Asta, A., and Salvatore, W. (2015). *Protezione Sismica di Edifici in c.a. con Controventi Dissipativi in Acciaio*. Milano: Dario Flaccovio Editore.

Celano, F., Cimmino, M., Coppola, O., Magliulo, G., and Salzano, P. (2016). *Report dei Danni Registrati a Seguito Del Terremoto del Centro Italia del 24 Agosto 2016 (Release 1)*. Network ReLUIS (Rete dei Laboratori Universitari

di Ingegneria Sismica). Available online at: http://www.reluis.it/images/stories/Centre%20Italy%20earthquake%20damage%20report%20-%20R1.pdf

Cosenza, E., Di Sarno, L., Maddaloni, G., Magliulo, G., Petrone, C., and Prota, A. (2014). Shake table tests for the seismic fragility evaluation of hospital rooms. *Earthquake Eng. Struc. Dyn*. 44, 23–40. doi: 10.1002/eqe.2456

CSLLPP - Consiglio Superiore dei Lavori Pubblici (2018). *Norme Tecniche per le Costruzioni*. No. 42 of 20 February 2018. (Rome: Gazzetta Ufficiale della Repubblica Italiana).

De Domenico, D., Impollonia, N., and Ricciardi, G. (2019a). Seismic retrofitting of confined masonry-RC buildings: The case study of the university hall of residence in Messina, Italy. *Ingegneria Sismica* 36, 54–85.

De Domenico, D., and Ricciardi, G. (2018). Earthquake-resilient design of base isolated buildings with TMD at basement: application to a case study. *Soil Dyn. Earthquake Eng.* 113, 503–521. doi: 10.1016/j.soildyn.2018.06.022

De Domenico, D., Ricciardi, G., and Takewaki, I. (2019b). Design strategies of viscous dampers for seismic protection of building structures: a review. *Soil Dyn Earthquake Eng.* 118, 144–165. doi: 10.1016/j.soildyn.2018.12.024

Di Cesare, A., and Ponzo, F. C. (2017). Seismic retrofit of reinforced concrete frame buildings with hysteretic bracing systems: design procedure and behaviour factor. *Shock Vibration*. 2107. doi: 10.1155/2017/2639361

Di Cesare, A., Ponzo, F. C., and Nigro, D. (2014). Assessment of the performance of hysteretic energy dissipation bracing systems. *Bull. Earthquake Eng.* 12, 2777–2796. doi: 10.1007/s10518-014-9623-z

Dicleli, M., and Milani, A. S. (2016). *Multi-Directional Torsional Hysteretic Damper (mthd)*. US Patent No: US20120066986A.

Dwairi, H. M., Kowalsky, M. J., and Nau, J. M. (2007). Equivalent damping in support of direct displacement-based design. *J. Earthquake Eng.* 11, 512–530. doi: 10.1080/13632460601033884

FEMA - Federal Emergency Management Agency (1999). *Earthquake Loss Estimation Methodology Hazus99*. SR2: Techical Manual, Washington, DC.

Gandelli, E. (2017). *Advanced Tools for the Design of Sliding Isolation Systems for Seismic-Retrofitting of Hospitals*. [Doctoral dissertation]. Politecnico di Milan, Italy.

Gandelli, E., Dubini, P., and Quaglini, V. (2019). "A design procedure for seismic isolation retrofit of hospitals tailored to the protection of non-structural components," in *Proceedings of the 4th International Workshop on the Seismic Performance of Non-Structural Elements (SPONSE)* (Pavia), 22–23.

Gandelli, E., Quaglini, V., Dubini, P., Limongelli, M. P., and Capolongo, S. (2018). Seismic isolation retrofit of hospital buildings with focus on non-structural components. *Ingegneria Sismica Int. J. Earthquake Eng.* XXXV, 20–55.

Hitaka, T., and Matsui, C. (2003). Experimental studies of on steel shear wall with slits. *J. Struc. Eng.* 129, 586–595. doi: 10.1061/(ASCE)0733-9445(2003)129:5(586)

Iervolino, I., Galasso, C., and Cosenza, E. (2010). REXEL: computer aided record selection for code-based seismic structural analysis. *Bull. Earthquake Eng.* 8, 339–362. doi: 10.1007/s10518-009-9146-1

Johnson, G. S., Sheppard, R. E., Quilici, M. D., Eder, S. J., and Scawthorn, C. R. (1999). *Seismic Reliability Assessment of Critical Facilities: A Handbook, Supporting Documentation, and Model Code Provisions*. New York, NY: University at Buffalo. Available online at: https://ubir.buffalo.edu/xmlui/handle/10477/875

Lupoi, G., Franchin, P., Lupoi, A., Pinto, P. E., and Calvi, G. M. (2008). *Probabilistic Seismic Assessment for Hospitals and Complex-Social Systems*. ROSE Research Report No. 2008/02. IUSS Press.

Masi, A., Santarsiero, G., Gallipoli, M. R., Mucciarelli, M., Manfredi, V., Dusi, A., et al. (2014). Performance of the health facilities during the 2012 Emilia (Italy) earthquake and analysis of the Mirandola hospital case study. *Bull. Earthquake Eng.* 12, 2419–2443. doi: 10.1007/s10518-013-9518-4

Mazza, F., and Vulcano, A. (2015). Displacement-based design procedure of damped braces for the seismic retrofitting of r.c. framed buildings. *Bull Earthquake Eng.* 13, 2121–2143. doi: 10.1007/s10518-014-9709-7

McKenna, F., Fenves, G. L., and Scott, M. H. (2000). *Open System for Earthquake Engineering Simulation*. PEER Report, Berkeley, CA.

Medeot, R., and Chiarorro, R. (1996). *Multidirectional mechanic hysteresis anti-seismic device for isolating the bases of constructional systems having high mutual displacements*. US patent No. US5806250A

Nagarajaiah, S., and Xiaohong, S. (2000). Response of base-isolated USC hospital building in Northridge earthquake. *J. Struc. Eng.* 126, 1177–1186. doi: 10.1061/(ASCE)0733-9445(2000)126:10(1177)

Paulay, T., and Priestly, M. J. N. (1992). *Seismic Design of Reinforced Concrete and Masonry Buildings*. New York, NY: Wiley.

Petrone, C., Di Sarno, L., Magliulo, G., and Cosenza, E. (2016). Numerical modelling and fragility assessment of typical freestanding building conte-nts. *Bull. Earthquake Eng.* 15, 1609–1633. doi: 10.1007/s10518-016-0034-1

Ponzo, F. C., Di Cesare, A., Arleo, G., and Totaro, P. (2010). Protezione sismica di edifici esistenti con controventi dissipativi di tipo isteretico: aspetti progettuali ed esecutivi. *Progettazione Sismica* 4, 50–75.

Priestley, M. J. N. (2000). "Performance based seismic design," in *Proceedings of the 12th World Conference on Earthquake Engineering (WCEE)* (Auckland).

Rossetto, T., Peiris, N., Alarcon, J. E., So, E., Sargeant, S., Free, M., et al. (2011). Field observations from the Aquila, Italy earthquake of April 6, 2009. *Bull. Earthquake Eng.* 9, 11–37. doi: 10.1007/s10518-010-9221-7

Skinner, R. I., Kelly, J. M., and Heine, A. J. (1974). Hysteretic dampers for earthquake-resistant structures. *Earthquake Eng. Struc. Dyn.* 3, 287–296. doi: 10.1002/eqe.4290030307

Skinner, R. I., Tyler, R. G., Heine, A. J., and Robinson, W. H. (1980). Hysteretic dampers for protection of structures from earthquakes. *Bull. N. Zealand Soc. Earthquake Eng.* 13, 22–36.

Takeuchi,T., Nakamura, H., Kimura, I., Hasegawa, H., and Saeki, E., Watanabe, A. (1999). *Buckling Restrained Braces and Damping Steel Structures*. US patent No. US20050055968A1.

Tsai, K. C., Chen, H. W., Hong, C. P., and Su, Y. F. (1993). Design of steel triangular plate energy absorbers for seismic resistant construction. *Earthquake Spectra* 9, 505–528. doi: 10.1193/1.1585727

USGS - United States Geological Survey (1996). *USGS Response to an Urban Earthquake - Northridge '94*. Available online at: http://pubs.usgs.gov/of/1996/ofr-96-0263/introduc.htm#impacts

Vayas, I. (2017). *INNOSEIS Project - Valorization of INNOvative anti-SEISmic Devices*. Deliverables Available online at: http://innoseis.ntua.gr/deliverables.php?deliverable=reports

Wada, A., Huang, Y. H., and Iwata, M. (2000). Passive damping technology for buildings in Japan. *Prog. Struct. Engng Mater.* 2, 335–350. doi: 10.1002/1528-2716(200007/09)2:3M<335::AID-PSE40>3.0.CO;2-A

Conflict of Interest Statement: EG and JD are employed by the company Maurer Engineering GmbH.

The remaining authors declare that the research was conducted in the absence of any commercial or financial relationships that could be construed as a potential conflict of interest.

frontiers in Built Environment

ORIGINAL RESEARCH
published: 06 September 2019
doi: 10.3389/fbuil.2019.00104

Seismic Design and Testing of Post-tensioned Timber Buildings With Dissipative Bracing Systems

Felice Carlo Ponzo, Antonio Di Cesare, Nicla Lamarucciola and Domenico Nigro*

University of Basilicata, School of Engineering, Potenza, Italy

This paper describes a seismic design procedure for low-damage buildings composed by post-tensioned timber framed structures coupled with hysteretic dissipative bracing systems. The main goal of the design procedure is preventing or limiting earthquake-induced damage to the structural and non-structural elements. For this aim, a target design displacement is defined according to the desired performance level. Then, the corresponding design force, strength, and stiffness of the post-tensioning and of the dissipative braces are evaluated in order to size post-tensioned connections and dissipating devices. The results of shaking table testing performed at the University of Basilicata are also reported. A prototype model —2/3 scaled, three-dimensional, and three stories with a post-tensioned timber structure without and with V-inverted braces and U-shaped flexural steel dampers—has been extensively tested. During testing, the specimen was subjected to a set of seven earthquakes at different intensity levels of the peak ground acceleration. The effectiveness of the bracing system and the reliability of the proposed procedure are experimentally demonstrated. Non-linear dynamic analyses have been performed in order to simulate the experimental seismic response. The numerical model is based on a lumped plasticity approach, which combines the use of elastic elements with linear and rotational springs representing energy dissipating devices and plastic rotations of the connections. The numerical results accurately predict the non-linear behavior of the prototype model, obtaining a satisfactory matching with the target drift considered for design.

Keywords: post-tensioned timber building, dissipative bracing systems, displacement-based design, shaking table tests, non-linear dynamic analysis

OPEN ACCESS

Edited by:
Dario De Domenico,
University of Messina, Italy

Reviewed by:
Daniele Losanno,
Istituto per le tecnologie della costruzione (ITC), Italy
Marco Furinghetti,
University of Pavia, Italy

****Correspondence:***
Antonio Di Cesare
antonio.dicesare@unibas.it

Specialty section:
This article was submitted to Earthquake Engineering, a section of the journal Frontiers in Built Environment

Received: *12 July 2019*
Accepted: *21 August 2019*
Published: *06 September 2019*

Citation:
Ponzo FC, Di Cesare A, Lamarucciola N and Nigro D (2019) Seismic Design and Testing of Post-tensioned Timber Buildings With Dissipative Bracing Systems. Front. Built Environ. 5:104. doi: 10.3389/fbuil.2019.00104

INTRODUCTION

According to the current seismic code requirements, buildings are expected to provide suitable structural safety level but do not explicitly prevent structural and non-structural damages or maintain structural functionality even after strong earthquakes. The resultant seismic damages are often difficult and financially prohibitive to repair. The effects of major earthquakes have proved the inadequacy of conventional buildings in terms of suffered damages to structural and not structural elements. Further improvements in seismic design and new approaches based on low damage methodologies and cost-efficient technologies are needed (Polocoşer et al., 2018; Pu et al., 2018). The implementation of seismic protection systems, such as dissipative devices (Di Cesare and Ponzo, 2017; Mazza and Mazza, 2019) and/or rocking systems (Ponzo et al., 2012; Di Cesare et al., 2017; Wang and Zhu, 2018), reduces seismic demand and/or increases the lateral capacity

of structures, minimizing residual drift, and structural damage. It has been proved that timber structures have the capacity to withstand strong earthquakes without collapsing due to the light weight of wood material, elastic deformation capacity, and ductility of connections (Ugalde et al., 2019). Conventional wooden buildings are usually regular and the seismic resisting structures are shear walls with ductile foundation anchorages designed against the base shear force. In these cases, the maximum seismic forces are limited by the activation of inelastic deformations that could cause serious damages at predefined locations in the structure. Among the recent research on the concept of low-damage structures, post-tensioned timber-framed buildings with dissipative bracing systems can be designed to absorb energy during strong earthquakes, confining the inelastic deformations in replaceable ductile fuses while the structure returns to the initial position after severe earthquake.

The post-tensioned system is a recent technology mainly adopted in seismic areas. This technique is based on the PRESSS system, originally developed for the precast concrete frames and walls (Priestley et al., 1999), and consists of post-tensioning force combined with mass timber beam, column, and wall elements. The post-tensioned steel bars join the structural timber elements avoiding cracking of the structural members by softening the structural response elastically through rocking mechanisms (Buchanan et al., 2008). The Pres-Lam system allows the design of timber frames with wide bay lengths (8–12 m) and reduced cross-sections of structural elements (Estévez-Cimadevila et al., 2016). The use of a dissipative bracing system within a framed structure can provide significant additional stiffness and damping, reducing inelastic deformations, and internal forces. Dissipative bracing systems enable the attainment of much higher standards of seismic performance, minimizing damage after the design earthquake level, improving resilience. The system allows the devices to respond elastically at the Service Level Earthquake (SLE) and exhibit non-linear behavior at Design Basis Earthquake (DBE) (Federal Emergency Management Agency, 2012). A single-story post-tensioned frame with dissipative braces is shown in **Figure 1**. The representative model of the braced post-tensioned frame (BF) consists of the typical "flag-shaped" behavior as a combination of two components in parallel: (i) the bilinear elastic model representative of the self-centering capability of the post-tensioned bare frame (F) and (ii) the hysteretic model representative of the dissipative bracing system (DB). The replaceable steel dampers (D) of the bracing system (B) work as structural fuses that effectively reduce the forces imposed on the rest of the structural elements through the steel yielding. The ratio between elastic behavior (free rocking) of the bare post-tensioned frame and the amount of dissipation provided by the damping bracing system, represented by the β_F parameter, is the main aspect that affects the seismic response of the structure.

Regarding the seismic design of buildings with dissipative bracing systems including hysteretic dampers, several studies have been based on the Displacement Based Design (DBD) procedure (Lin et al., 2003; Zahrai and Froozanfar, 2018; Mazza and Mazza, 2019; Nuzzo et al., 2019). The base concept of DBD, originally developed by Priestley et al. (2007), consists in the approximation of a multi-degree of freedom (MDOF) structure in a single degree of freedom (SDOF) system with equivalent secant stiffness and viscous damping at the design displacement (Priestley, 2000; Priestley and Grant, 2005; Pei et al., 2012). Usually, design values are suggested within the design code depending on structural types or governed by allowable material strain limits. Recently, the application of the DBD method has been extended toward the design of timber buildings (Ugalde et al., 2019), such as CLT shear walls (Di Cesare et al., 2019a), coupled timber walls (Newcombe et al., 2011), and post-tensioned timber frames without and with the addition of dissipative rocking systems (Newcombe et al., 2010; Di Cesare et al., 2012, 2014; Pei et al., 2012). However, DBD applications to timber-framed buildings remain largely unexplored, and new techniques are still being investigated aiming to minimize residual damage induced by earthquakes.

An extensive program of shaking table tests has been developed in order to assess the effectiveness of different passive energy dissipating systems in controlling the seismic vibrations of post-tensioned timber framed buildings. The experimental campaign, carried out considering a 3D, 2/3 scaled timber frame, is part of a collaboration between the University of Basilicata (UNIBAS, Italy) and the University of Canterbury (UoC, New Zealand) (Di Cesare et al., 2012, 2017). The project aim is to evaluate the feasibility of applying jointed ductile post-tensioning technology to glue-laminated (glulam) timber (Smith et al., 2014), a more widespread engineered timber material, and to evaluate the increasing seismic performance due to the addition of various dissipative forms based on rocking mechanisms and on bracing systems.

In this paper, a DBD procedure for post-tensioned timber-framed buildings with hysteretic dissipative bracing systems is proposed. The main performance objective of the proposed method consists in preventing seismic damage to the frame elements and connections, fixing a target displacement Δ_d (or drift) and typical flag-shape parameters related to the reliable amount of dissipation of the braced post-tensioned frame under a reference level of seismic intensity. Starting from these parameters, the proposed method allows to evaluating the post-tensioning (PT) forces and the dissipative devices. The proposed procedure has been applied to design the hysteretic dampers of a three-story post-tensioned timber frame prototype model equipped with a V-inverted hysteretic dissipative bracing system, for which the preliminary results are reported in Di Cesare et al. (2019b). The effectiveness of the dissipative bracing system in control of seismic vibrations has been proved through the comparison between the experimental results of the braced frame and the results of the bare frame.

Moreover, the experimental results are endorsed by non-linear dynamic analysis, carried out in order to simulate experimental results firstly and then to validate the design results.

SEISMIC DESIGN OF POST-TENSIONED TIMBER BUILDINGS WITH DISSIPATIVE BRACING SYSTEMS

Figure 2 summarizes the proposed seismic design procedure for post-tensioned timber structures with dissipative bracing

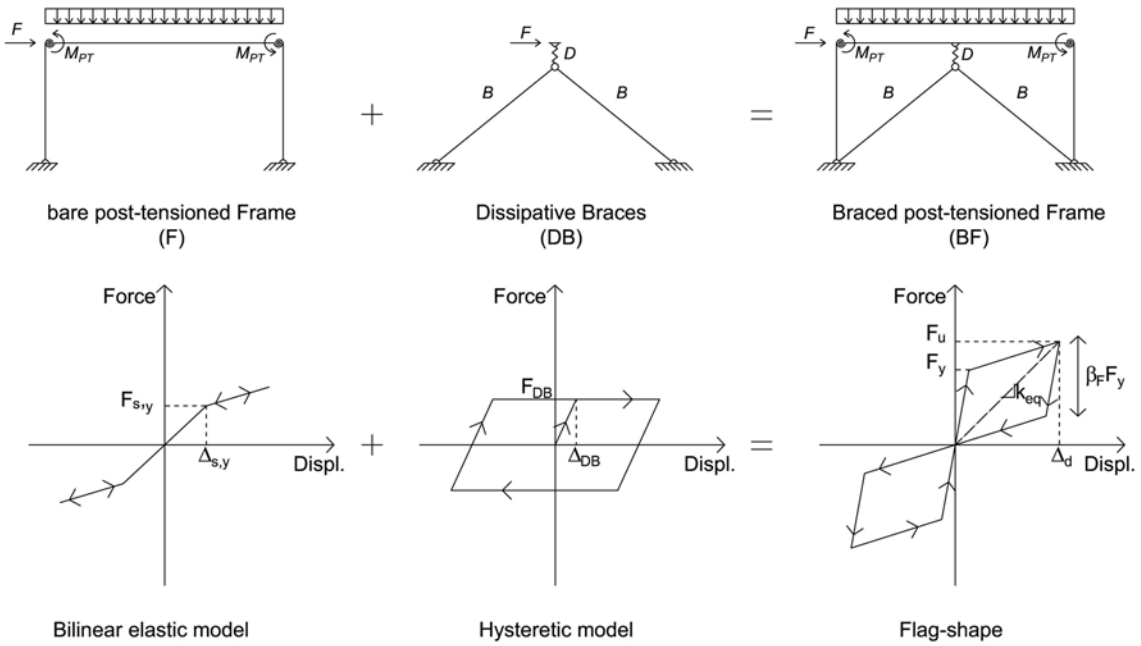

FIGURE 1 | Fundamentals of post-tensioned frame structure with dissipative bracing system.

systems. In the step-by-step procedure, the equivalent SDOF systems of the bare post-tensioned frame (F) and of the dissipative bracing system (DB) have been considered as a bilinear and hysteretic system working in parallel, providing the equivalent flag-shape response (**Figure 1**) of the combined braced post-tensioned frame (BF). The substitute SDOF structure has the same base shear F_u of the inelastic MDOF structure associated with secant stiffness k_e and equivalent viscous damping ξ_{eq} at the design displacement Δ_d or drift θ_d. The equivalent elastic properties of the SDOF system allowed the design of the MDOF structure through an elastic displacement response spectrum, reduced by ξ_{eq}. Based on the flag-shape parameters, the equivalent contributions of the bare structure and of the dissipative bracing systems can be evaluated and distributed at each story. Finally, the design assumption must be verified and the design completed.

Step 1. Define design displacement. The procedure starts defining a design displacement Δ_d at the design basis earthquake (DBE) corresponding to a target drift. The range of target drift for post-tensioned timber buildings varies between $\theta_d = 1.5 \div 2.5\%$ based on non-structural elements and their connections and anchorages (Structural Timber Innovation Company Inc, 2013).

Step 2. Assume flag shape design parameters. The equivalent force-displacement of the braced post-tensioned frame consists in the flag-shaped hysteretic behavior (**Figure 3C**), which combines the equivalent bare post-tensioned frame (**Figure 3A**) with the equivalent dissipative bracing system (**Figure 3B**). The design parameters of the flag-shape of the equivalent SDOF system are the post-yield stiffness ratio r, the displacement ductility μ, and the re-centering ratio of the global system β_F (flag loop parameter)—suggested values are $\beta_F = 0.6 \div 1.0$; $\mu = 1.5 \div 3$; $r = 0.1 \div 0.3$ (Pei et al., 2012).

Step 3. Evaluate equivalent damping. The equivalent damping ξ_{eq} of the SDOF of the braced post-tensioned frame is evaluated as the sum of energy dissipated by viscous damping $\xi_{eq,v}$ of the bare timber frame and inelastic hysteresis $\xi_{eq,h,v}$ of the dissipative bracing system. In order to account for the random nature of earthquakes, a reduction factor k should be used to correct the hysteretic damping contribution (Priestley et al., 2007)—the suggested range is $k = 0.6 \div 1$—as a function of the specific hysteretic models, ductility levels, and periods (Ponzo et al., 2018; Di Cesare et al., 2019b). Using the general DBD methodology (Priestley et al., 2007), the equivalent damping is calculated as Equation (1).

$$\xi_{eq} = \xi_{eq,v} + k \cdot \xi_{eq,h,v} \tag{1}$$

A value of viscous damping $\xi_{eq,v} = 2 \div 5\%$ is considered acceptable for timber structures (Di Cesare et al., 2019a). The equivalent hysteretic damping related to the DB $\xi_{eq,h,v}$ can be estimated by the following Equation (2) (Priestley and Grant, 2005).

$$\xi_{eq,h,v} = \frac{\beta_F(\mu - 1)}{\mu\pi[1 + r(\mu - 1)]} \tag{2}$$

Step 4. Determine the equivalent SDOF. The equivalent parameters of the SDOF system, in terms of design displacement Δ_d and equivalent mass m_e at the effective height H_e, are determined according to the fundamental mode, assuming a linear displacement profile of the i^{th}-story Δ_i of the structure, as

Equations (3), where m_i and H_i are the story masses and story heights (Priestley et al., 2007).

$$\Delta_d = \frac{\sum_{i=1}^{n}(m_i\Delta_i^2)}{\sum_{i=1}^{n}(m_i\Delta_i)};\ m_e = \frac{\sum_{i=1}^{n}(m_i\Delta_i)}{\Delta_d};\ H_e = \frac{\sum_{i=1}^{n}(m_i\Delta_i H_i)}{\sum_{i=1}^{n}(m_i\Delta_i)} \quad (3)$$

From the target displacement Δ_d, the equivalent period T_e and stiffness K_e of the SDOF system shall be calculated by direct transformation of the design acceleration response spectrum $S_d(T_e)$, as defined by Equations (4)[1].

$$S_D(T_e) = S_d(T_e)\cdot\left(\frac{T_e}{2\pi}\right)^2;\ K_e = m_e\cdot\left(\frac{2\pi}{T_e}\right)^2 \quad (4)$$

The ultimate force capacity F_u (maximum base shear) can be evaluated at the target design displacement (Priestley et al., 2007); then, based on the flag-shaped model reported in **Figure 3C**, the yielding force F_y of the equivalent SDOF system can be obtained by Equations (5).

$$F_u = K_e\cdot\Delta_d;\ F_y = \frac{F_u}{1+r(\mu-1)} \quad (5)$$

Step 5. Calculate equivalent contributions. The equivalent contributions of post-tensioning and the dissipative bracing system can be evaluated on the base of the flag-shape model (**Figure 3C**). The hysteretic contribution of the dissipative bracing system (DB) is idealized as an elasto-plastic system (**Figure 3B**). Assuming the design ductility μ_{DB} of the equivalent SDOF of the dissipative system, the yield force F_{DB}, the yield displacement $\Delta_{DB,y}$, and the elastic stiffness k_{DB} are defined as Equations (6).

$$F_{DB} = \frac{\beta_F}{2}\cdot F_y;\ \Delta_{DB,y} = \frac{\Delta_d}{\mu_{DB}};\ k_{DB} = \frac{F_{DB}}{\Delta_{DB,y}} \quad (6)$$

The ultimate $F_{S,u}$ and yielding $F_{S,y}$ forces as well as the yield displacement $\Delta_{S,y}$ on the bare post-tensioned structure can be calculated as Equations (7), where μ_S and k_S, evaluated as $k_0 = k_S + k_{DB}$, are the ductility and the initial stiffness of the equivalent bare structure, respectively (**Figure 3A**).

$$F_{S,u} = F_u - F_{DB};\ F_{S,y} = k_S\cdot\Delta_{S,y};\ \Delta_{y,S} = \frac{F_{S,u} - rk_0\Delta_d}{k_{S,0} - rk_0} \quad (7)$$

Step 6. Design members and joint connections.

6.1 Determine PT force (MMBA procedure). The post-tensioning force has been designed applying the Modified Monolithic Beam Analogy (MMBA) procedure (Structural

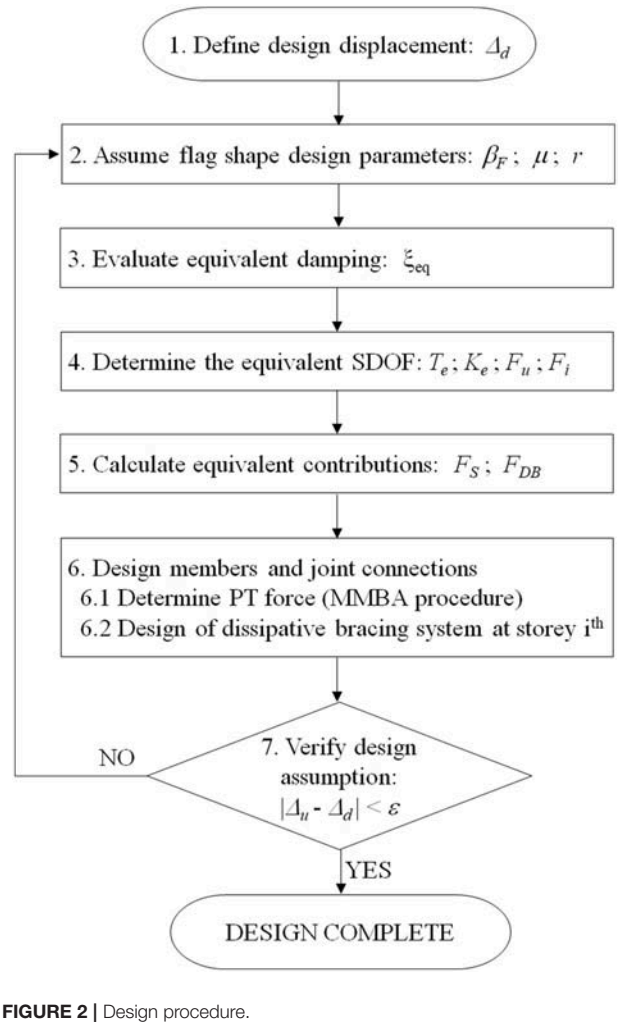

FIGURE 2 | Design procedure.

[1]EN 1998-1. (2003). *Design of Structures for Earthquake Resistance - Part 1: General Rules, Seismic Actions and Rules for Buildings*. European Committee for Standardization.

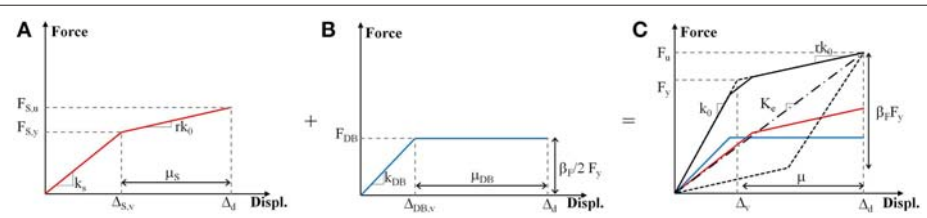

FIGURE 3 | Equivalent SDOF systems of **(A)** Bilinear elastic model of the bare post-tensioned frame F; **(B)** Hysteretic model of dissipative bracing system DB; **(C)** Flag-shape of braced post-tensioned frame BF.

Timber Innovation Company Inc, 2013). For the sake of brevity, this procedure is not reported in this paper—for details please refer to Newcombe et al. (2008). The beam to column connections are sized based on the moment demand associated with the ultimate force $F_{S,u}$ and ductility μ_S on the bare post-tensioned frame (Di Cesare et al., 2012).

6.2 Design of dissipative bracing system at i^{th} story. The characteristics of the equivalent SDOF dissipating system (F_{DB}, $\Delta_{DB,y}$, k_{DB}), determined in Step 5, are distributed up to the building story following the design procedure proposed by Di Cesare and Ponzo (2017). The stiffness $k_{DB,}$ of the equivalent bracing of the i^{th} story is determined hypothesizing that the ratio between the stiffness at the i^{th} story of the relative bracing $k_{DB,i}$ and that of the bare structure $k_{S,i}$ is proportional to the ratio r_k between the elastic stiffness of the bracing systems k_{DB} and the elastic stiffness of the equivalent bare structure $k_{S,0}$, as shown by Equation (8). The stiffness of the story i^{th} of the bare structure $k_{S,i}$ can be calculated from the inter-story displacement $\Delta s_{,i}$ generated by linear static analysis (LSA) applying to each story the distribution of horizontal seismic forces F_i (Di Cesare and Ponzo, 2017).

$$k_{DB,i} = r_k k_{S,i};\ r_k = \frac{k_{DB}}{k_{S,0}};\ k_{S,i} = \frac{1}{\Delta s_i}\sum_i F_i;\ F_i = F_u \cdot \frac{m_i \Delta_i}{\sum_{i=1}^{n}(m_i \Delta_i)} \quad (8)$$

In the same way, the yield force $F_{DB,}$ of the equivalent bracing at the i^{th} story is determined in the hypothesis that the ratio between the yield force at each floor of the bare structure $F_{Sy,i}$ and that of relative bracing $F_{DB,}$ is distributed proportionally to the ratio r_F between the strength of equivalent bracing F_{DB} systems and the strength of equivalent bare structure $F_{S,y}$ (Equations 9). The yield force of the bare structure $F_{S,y,i}$ at the i^{th} story can be calculated in a simplified manner starting from the displacements at the elastic limits $\Delta_{Sy,i}$. This is determined by redistributing the displacement at the elastic limit of the bare structure $\Delta_{S,y}$ as a function of the ratio between the inter-story displacement Δs_i and the total elastic displacement S_{TOT} calculated by means of Linear static analysis (Di Cesare and Ponzo, 2017).

$$F_{DB,i} = r_F F_{S,y,i};\ r_F = \frac{F_{DB}}{F_{S,y}};\ F_{S,y,i} = k_{S,i}\Delta_{S,y,i};\ \Delta_{S,y,i} = \frac{\Delta s_i}{s_{TOT}}\ \Delta_{S,y} \quad (9)$$

The elastic stiffness $k_{DB,i,j}$ and the yield force $F_{DB,i,j}$ of the single j^{th} dissipating brace at the i^{th} story are defined starting from the equivalent dissipative bracing system as a function of the number of dissipative braces at the i^{th} story $n_{DB,i}$, as in the following Equations (10) (Nuzzo et al., 2019).

$$k_{DB,i,j} = \frac{k_{DB,i}}{n_{DB,i}};\ F_{DB,i,j} = \frac{F_{DB,i}}{n_{DB,i}} \quad (10)$$

At this point, the mechanical characteristics of each damper (D) and brace (B) can be evaluated depending on the dissipative bracing system adopted. The stiffness $k_{D,i,j}$ and the yield force $F_{Di,j}$ of the single hysteretic damper at the i^{th} story are related to the stiffness $k_{B,i,j}$ of the elastic bracing rods and to the yield force $F_{DB,i,j}$ of the dissipative brace. Generally, the dissipative brace stiffness $k_{DB,i,j}$ can be determined as a series composition of rigid brace and damper (Equations 11) (Di Cesare and Ponzo, 2017; Nuzzo et al., 2019).

$$k_{DB,i,j} = \frac{k_{D,i,j} \cdot k_{B,i,j}}{k_{D,i,j} + k_{B,i,j}};\ F_{D,i,j} = F_{DB,i,j} \quad (11)$$

Step 7. Verify design assumption. Finally, the analysis of the MDOF structure can be performed, and the resultant ultimate displacement Δ_u or drift θ_u, evaluated performing static or dynamic non-linear analysis, is compared with the design value Δ_d or θ_d (assumed in the *Step 1*) (Ponzo et al., 2018; Di Cesare et al., 2019b). Considering a suitable modeling of the braced post-tensioned structure and assuming a tolerance value ε, if $|\Delta_u - \Delta_d|$ (or $|\theta_u - \theta_d| < \varepsilon$), the design procedure is complete, otherwise repeat the procedure from Step 2 assuming different values of the design parameters.

DESIGN OF EXPERIMENTAL PROTOTYPE MODEL

Experimental Model

The proposed DBD procedure has been applied to design a three-dimensional experimental prototype model of a braced post-tensioned timber framed building, 2/3 scaled, with three stories (height of story 2 m, total height 6 m) and a single bay in both directions (dimension in plant 4 × 3 m). The beams and columns of the frame are made of Glulam timber GL32h[2]. The floors have been designed according to Eurocode[1] for office utilization, at intermediate levels (live load of Q = 3 kN/m^2) and a rooftop garden at the third floor (Q = 2 kN/m^2). The flooring panels spanned in both directions have been made by a series of deep

FIGURE 4 | (A) Experimental model of post-tensioned timber frame building with dissipative V-inverted bracing systems. Details of bracing connections to **(B)** beam-column joint; **(C)** UFP and beam; **(D)** foundation.

[2]CNR-DT 206 R1/2018. *Istruzioni per la Progettazione.* l'Esecuzione ed il Controllo delle Strutture di Legno.

Glulam beams turned on their sides. Proper scaling factors have been applied according to the Cauchy-Froude mass similitude laws (Krawinkler and Moncarz, 1981). The post-tensioning has been applied in both directions with steel bars crossing at the beam-column joints (**Figure 4B**).

In order to assess for the influence of different amounts of energy dissipated by additional systems on the seismic response, the experimental model has been designed, and tested in different configurations (Di Cesare et al., 2017), varying the re-centering ratio: (i) $\beta_F = 0$ bare post-tensioned frame (F); (ii) $\beta_F = 0.4$ with dissipative rocking mechanisms (D) at beam-column and column-foundation connections; and (iii) $\beta_F = 0.8$ with dissipative bracing systems (F+DB = BF). In this paper the results of the bare post-tensioned frame (F), related to the free-rocking condition, and of the braced post-tensioned frame (BF) are compared. More details on the results of the dissipative rocking (D) configuration are reported in Di Cesare et al. (2014).

The dissipative bracing system selected for the experimental model consisted of two V-inverted dissipative braces for each story, installed within the bays of the two parallel frames along the testing direction, as shown in **Figure 4A**. The connection details of the bracing system are shown in **Figures 4B–D**.

The design spectrum has been defined considering a peak ground acceleration PGA of 0.44 g and medium soil class according to Eurocode[1]. The seismic inputs consisted of seven spectra-compatible earthquakes selected from the *European strong motion database* (**Figure 6**). The testing program of all configurations is summarized in **Table 1**.

The seismic response of the experimental model has been recorded by real-time monitoring through a combination of 54 instruments, including displacement potentiometers, load cells, and accelerometers. Displacement potentiometers and load cells have been used for monitoring the force-displacement behavior of all UFP dampers at each story for both sides of the braced model. During the experimental campaign, the intensity of the seismic inputs was progressively increased in acceleration for earthquakes 1,228, 196, and 535, from 10 to 100% of PGA, in order to provide additional information about the seismic performance frame response at varying levels of ground shaking (**Table 1**). In the case of braced post-tensioned frame configuration (BF) one UFP damper at the first story of the bracing system (UFP1) reached the failure condition during testing ID 187 at 100% of PGA level due to cyclic fatigue after almost 40 tests and more than 150 cycles to ductility $\mu_{DB} > 2$ sustained by the device (Ponzo et al., 2019). For the bare frame configuration (F) the PGA level was increased up to 75% because an imposed interlock of 2.5% of maximum inter-story drift was reached, except for the weaker earthquake input 1,228, at 100% of PGA (see **Table 1**).

Numerical Model

The non-linear numerical model of the test frame has been implemented using SAP2000 finite element software based on the lumped plasticity approach, which uses elastic timber elements connected with non-linear elements representing plastic connections of the system (**Figure 6**). The constitutive laws of connections elements are represented in **Figure 6**.

The beam to column joints was modeled combining two rotational springs in parallel (detail A of **Figure 6**), representative of the flexibility of the joint panel (elements 1 of **Figure 6**), and the post-tensioning (elements 2 of **Figure 6**). The non-linear force-displacement hysteretic behavior of the UFP dampers was modeled by using non-linear shear link elements connecting the elastic beam and V-inverted braces (detail B of **Figure 6**) characterized by the Bouc-Wen cyclic laws (element 3 of **Figure 6**; Bouc, 1967; Wen, 1980). Three rotational springs have been implemented at the column to base connections (detail C of **Figure 6**), representative of the moment resistance due to gravity load (elements 4 of **Figure 6**), seismic load (elements 5 of **Figure 6**), and dissipative steel angles (elements 3 of **Figure 6**). More details about numerical modeling of the bare and braced frame are reported in Ponzo et al. (2018) and Di Cesare et al. (2019b).

Design of Dissipative Bracing System

A step by step design procedure has been applied for the design of the experimental post-tensioned braced model.

Step 1. The design procedure at the design considered earthquake (PGA 100%) starts from the assumption

ID Code	Location	Date	M_W	PGA (g)	Scale Factor
1228	Izmit, Turkey	17/08/1999	7.6	0.357	1.5
196	Montenegro Serbia	15/04/1979	6.9	0.454	1
535	Erzican Turkey	13/03/1992	6.6	0.769	1.5
187	Tabas, Iran	16/09/1978	7.3	0.926	1
291	Campano Lucano, IT	23/11/1980	6.9	0.264	1.5
4673	South Iceland	17/06/2000	6.5	0.716	1.5
4677	South Iceland	17/06/2000	6.5	0.227	1

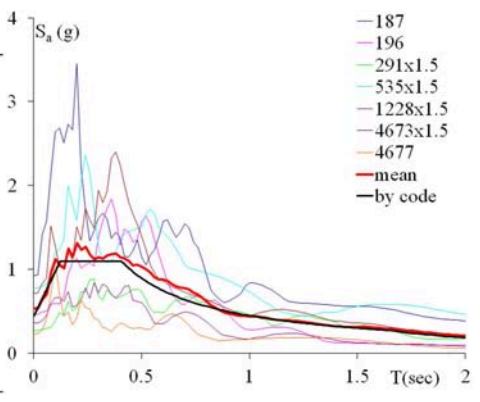

FIGURE 5 | Main characteristics of selected earthquakes.

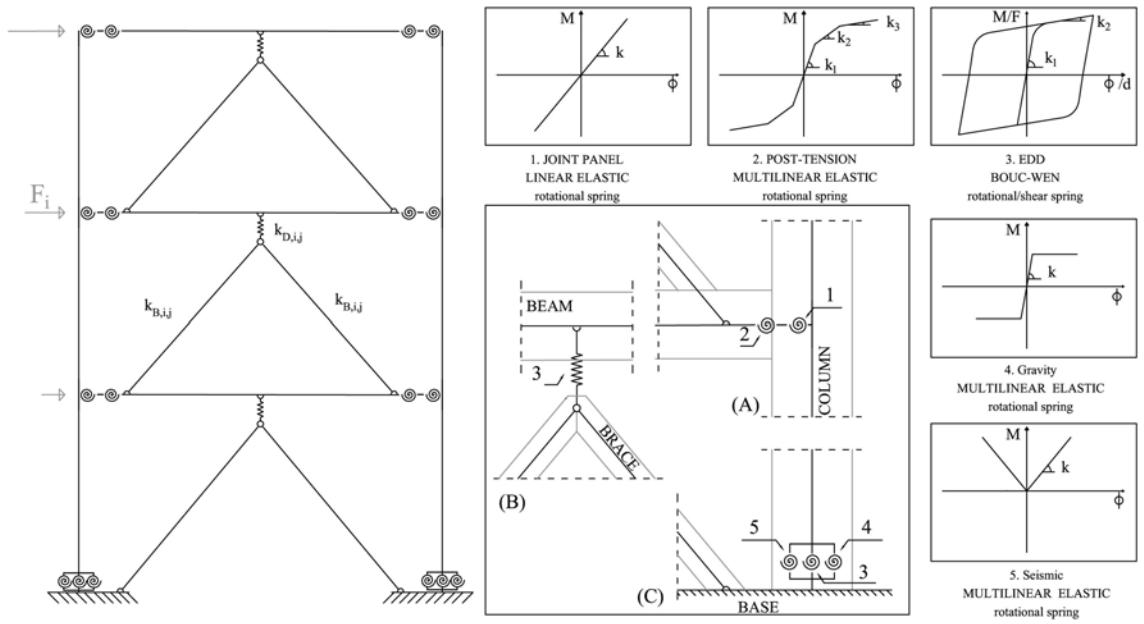

FIGURE 6 | Numerical modeling of the braced post-tensioned frame and details adopted for rocking connections (beam-column and column-foundation) and for dissipative bracing systems.

TABLE 1 | Testing program of bare frame (F), with dissipative rocking (D), and with dissipative braces (BF).

(%)	Seismic inputs						
	1228	**196**	**535**	**187**	**291**	**4673**	**4677**
10	F, D, BF	F, D, BF	F, D, BF	–	–	–	–
25	F, D, BF	F, D, BF	F, D, BF	–	–	–	–
50	F, D, BF	F, D, BF	F, D, BF	F, BF	F, BF	F, BF	F, BF
75	F, D, BF	F, D, BF	F, D, BF	–	–	–	–
100	F, D, BF	D, BF	D, BF	D, BF	D	D	D

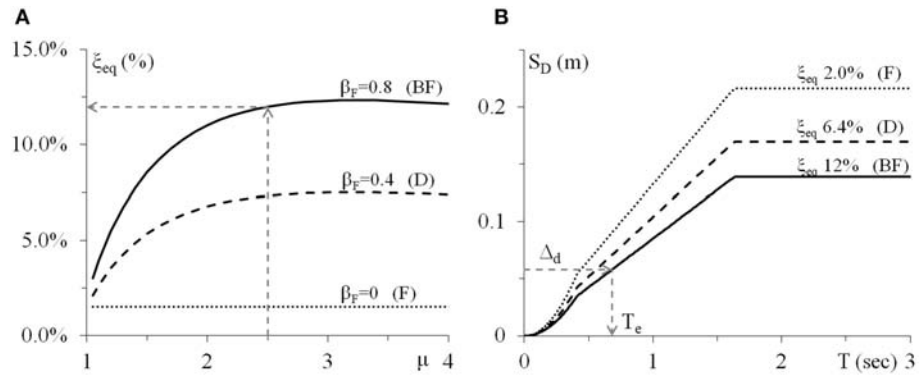

FIGURE 7 | (A) Equivalent viscous damping vs. ductility of post-tensioned timber structures for different re-centering ratios; **(B)** Design displacement response spectrum.

of the design displacement $\Delta_u = 58\,\text{mm}$ or drift $\theta_d = 1.25\%$.

Step 2. The post-yield stiffness ratio $r = 0.2$, the displacement ductility $\mu = 2.5$ and the re-centering ratio of the braced system $\beta_F = 0.8$ have been assumed in order to define the basic flag-shape system.

Step 3. The equivalent viscous damping ξ_{eq}vs. displacement ductility μ is plotted in **Figure 7A** considering an elastic viscous

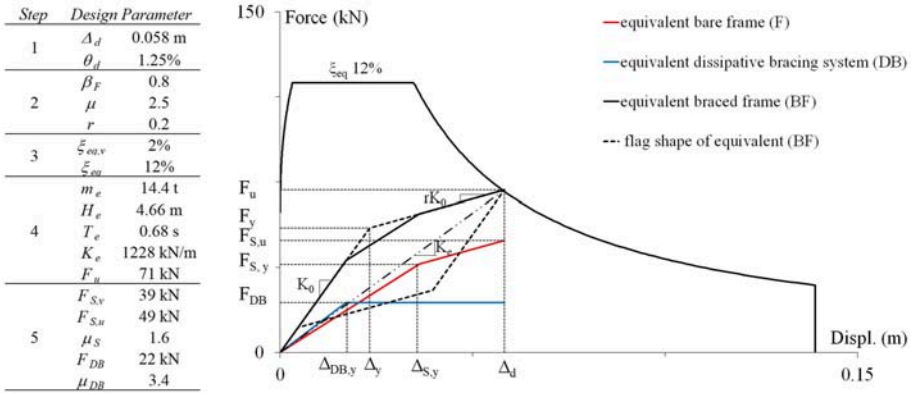

FIGURE 8 | Results of the design procedure applied to the Pres-Lam experimental model with dissipative bracing systems.

TABLE 2A | Characteristics of the braced post-tensioned frame.

Story	m_i (t)	Δ_i (mm)	F_i (kN)	Δs_i (mm)	$F_{S,y,i}$ (kN)	$k_{S,i}$ (kN/mm)	$F_{DB,i}$ (kN)	$k_{DB,i}$ (kN/mm)	$F_{DB,i,j}$ (kN)	$k_{DB,i,j}$ (kN/mm)	b_u (mm)
1	5.6	25	12	15.3	53	4.7	30	5.5	15.0	2.8	60
2	5.6	50	24	33.2	44	3.3	25	3.9	12.5	2.0	40
3	5.5	75	36	48.7	26	2.3	15	2.7	7.5	1.4	30

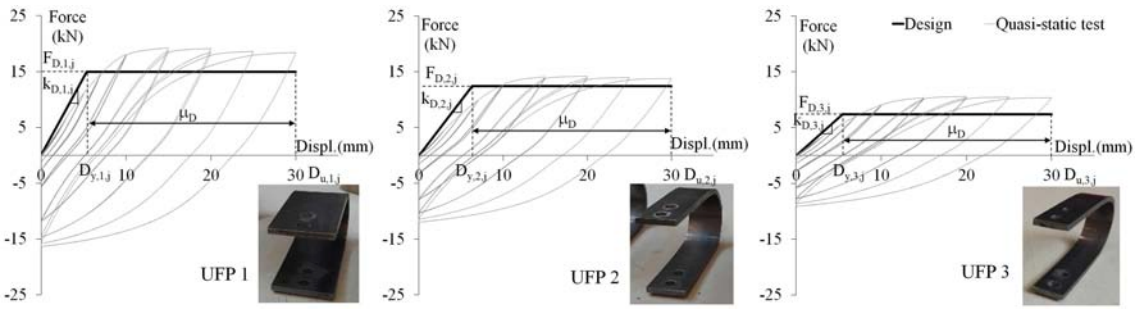

FIGURE 9 | Force-displacement of the UFP dampers at the three story.

damping $\xi_{eq,v} = 2\%$ and a reduction factor $k = 0.85$ for the hysteretic damping $\xi_{eq,h,v}$.

Step 4. The equivalent period T_e of the SDOF braced frame can be derived from the design displacement response spectrum (**Figure 7B**) reduced by the damping correction factor $\eta = \sqrt{\frac{10}{(5+\xi_{eq})}}$[3]. As highlighted, when equivalent viscous damping increased from the post-tensioned frame to the braced frame, the design displacement substantially reduced. The equivalent stiffness K_e, the yield force F_y and ultimate force F_u of the structure have been evaluated by Equation (5).

Step 5. From the flag-shape behavior, the characteristics of the equivalent bare frame and of the equivalent dissipative bracing system have been calculated using Equation (6) and Equation (7). The main design results from step 1 to step 5 are summarized in **Figure 8** in terms of force-displacement of the equivalent SDOF systems compared with the seismic design demand.

Step 6.1. The equivalent force and stiffness of the bare frame (F) have been distributed up to the stories ($k_{S,i}$, $F_{S,y,i}$) and the post-tensioning resistant moments M_{PT} have been evaluated through the MMBA method (Newcombe et al., 2008). For the experimental model the design of post-tensioning force was 100 kN for the primary direction and 50 kN for the secondary direction. The section sizes of columns were 200 × 320 mm while primary and secondary beams were 200 × 305 mm and 200 × 240 mm, respectively (Ponzo et al., 2012).

Step 6.2. Two V-inverted chevron braces for each story ($n_{DB,i} = 2$) both compounded by two linear elastic timber braces (B) in series with the elasto-plastic damper (D) composed the DB system, see **Figure 6**. The force and stiffness of the equivalent DB system have been distributed

[3]D.M. 17/01/2018. *Norme Tecniche per le Costruzioni (NTC 2018).* Gazzetta Ufficiale, n. 42 del 20/02/2018, Supplemento ordinario n.8.

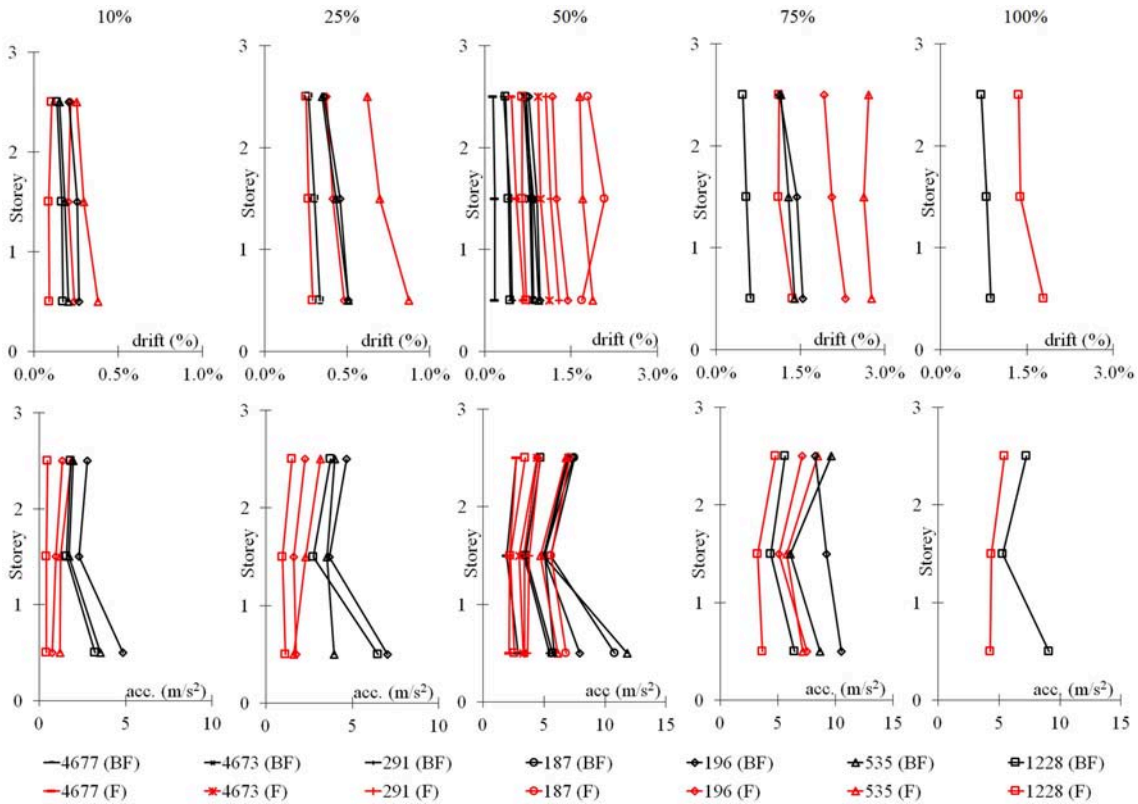

FIGURE 10 | Maximum inter-story drift and maximum acceleration at each story from all experimental tests.

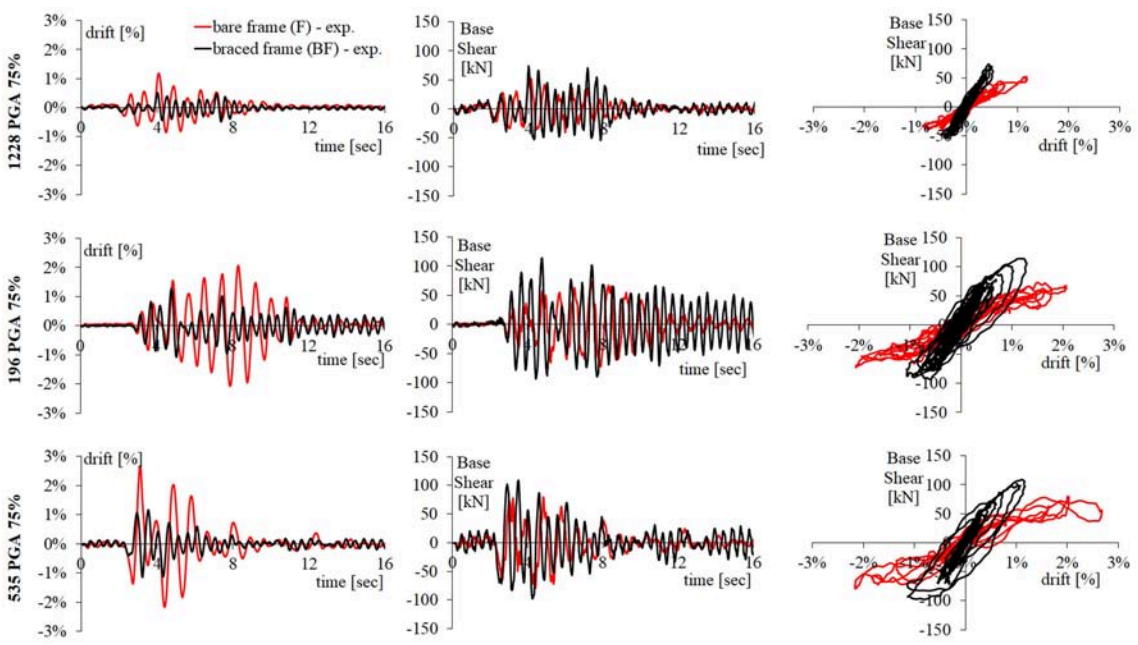

FIGURE 11 | Experimental results for (F) and (BF) obtained for seismic inputs 1228, 196, and 535 at 75% of PGA: time-histories of base shear and total drift and base shear vs. total drift.

up to the stories ($k_{DB,i}$, $F_{DB,i}$) and in the plan, then the characteristics of the single dissipating brace $k_{DB,i,j}$, $F_{DB,i,j}$ were defined. The main results of the design are summarized in **Table 2A**.

U-shaped Flexural steel Plates (UFPs) have been selected as dampers in order to comply with the force requirement at each story without changing the gravity load distribution on beams and columns and reducing the influence on the post-tensioned beam-column joints.

Each elasto-plastic damper (D) is composed of two UFPs placed between the bottom surface of the principal beam and the supporting timber rods (B) having a cross section of 160 × 180 mm (**Figure 4C**).

In the hypothesis of rigid bracing truss and flexural UFP dampers ($k_{B,i,j} >> k_{D,i,j}$), the stiffness $k_{Di,j}$ of the damper corresponds to the stiffness $k_{DB,i,j}$ of the j^{th} dissipative brace at the i^{th} story ($k_{D,i,j} \cong k_{DB,i,j}$). The design of the UFPs made of C60 stainless steel was performed by fixing geometrical diameter ($D_u = 60$ mm) and thickness ($t_u = 6$ mm) and varying the width b_u at each floor, as reported in **Table 2A**.

Quasi-static displacement controlled cyclic was performed up to the expected inter-story displacement ($\mu_D > 3$) in order

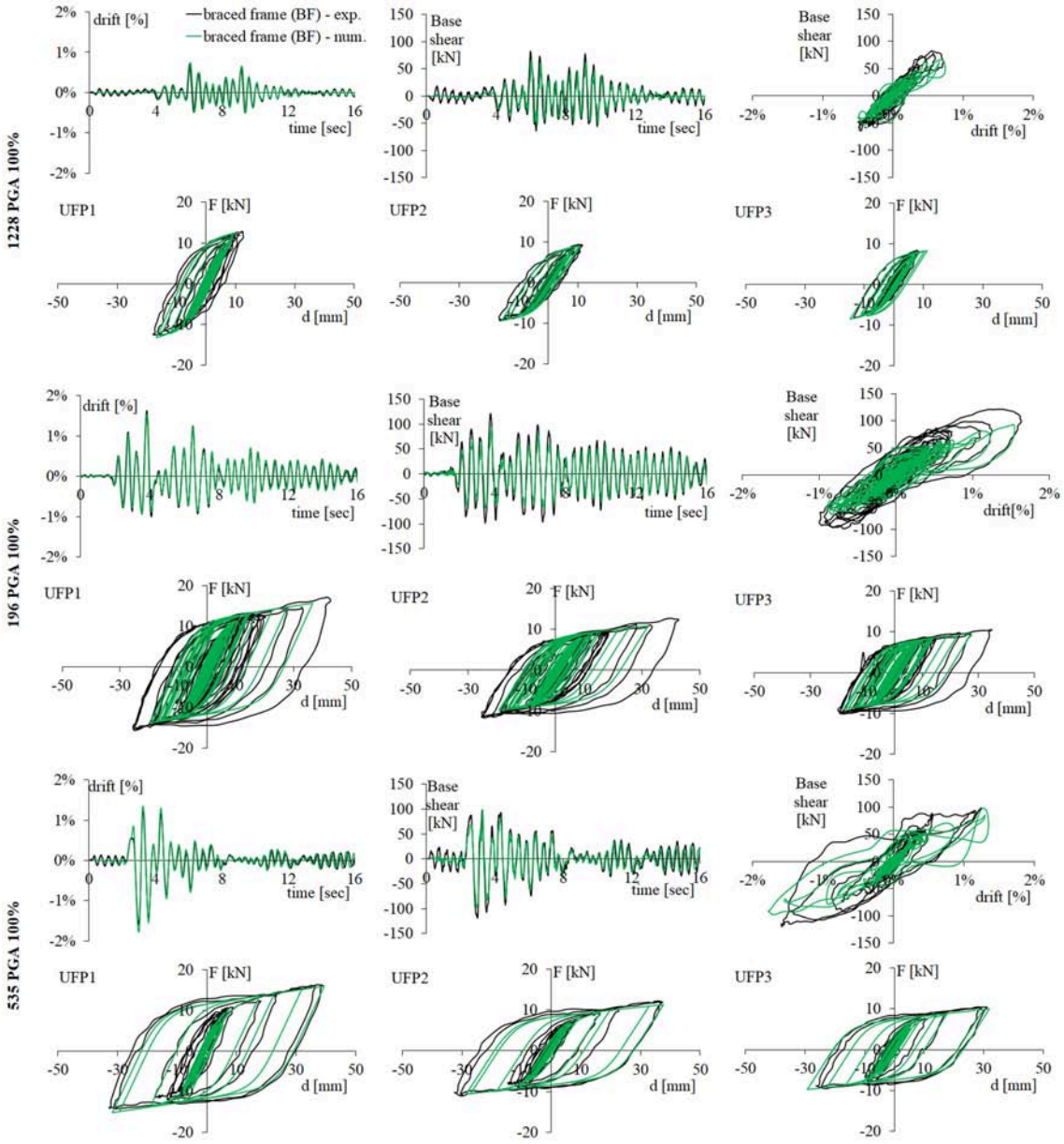

FIGURE 12 | Experimental and numerical results of BF model obtained for seismic inputs 1228, 196, and 535 at 100% of PGA: time-histories of base shear and total drift, base shear vs. total drift and hysteretic cyclic behavior of UFPs.

TABLE 2B | Experimental and numerical results at PGA 100%.

	Total drift (%)		Base shear (kN)		Equivalent damping (%)	
	Num.	Exp.	Num.	Exp.	Num.	Exp.
1228 PGA 100%	0.74	0.72	66	62	11.5	11.9
196 PGA 100%	1.54	1.60	93	98	11.8	11.4
535 PGA 100%	1.76	1.63	98	114	17.5	17.4

to characterize the UFP dampers' behavior. **Figure 9** shows the force-displacement behavior of experimental quasi-static tests performed on the UFP dampers designed and installed at each story of the braced frame compared with the results of the design procedure. The experimental results show that the design assumptions are consistent with the actual UFP dampers' behavior. Stable hysteretic behavior, without any sign of failure, has been observed during cyclic loading, maintaining almost the same energy dissipation capability. For more details about the design and testing of UFP dampers, please refer to Ponzo et al. (2019). The proposed procedure is valid also for shear link devices, such as those proposed by Nuzzo et al. (2018), as an alternative to UFP dampers if they do not modify the pattern of vertical loads in the beam. The design assumptions have been verified through non-linear time history analyses performed considering the numerical model of **Figure 6** and the input motions of **Figure 5**, as reported in the following paragraph.

RESULTS AND VALIDATION OF THE DESIGN PROCEDURE

In **Figure 10**, the comparison between experimental tests performed on the bare frame (F) and braced frame (BF) is shown in terms of maximum story drifts and maximum story accelerations for all PGA intensity levels. The values of drift of the BF at higher PGA levels (50, 75, 100%) are significantly reduced in respect to the bare frame (F), while at lower PGA intensities (10, 25%), especially for seismic inputs 1228 and 196, similar values have been experienced. The maximum accelerations of BF show some increase, in particular at the first floor, compared to the F configuration. Generally, the introduction of the hysteretic DB system allows the reduction of the total drift with a slight increase of story acceleration.

In order to show the effectiveness of the DB system, the experimental global results of the BF model have been compared with the results of F for seismic inputs 1228, 196, and 535 at 75% of the PGA level. **Figure 11** shows the time histories of base shear and total drift and of total drift vs. corresponding base shear. As can be observed, the global flag shape behavior of both models (F and BF) is highlighted for stronger earthquakes 196 and 535. Due to the stiffening contribution of the dissipative bracing system, the values of base shear increase when DB is added to the bare frame at about 30%, as assumed in the design procedure (**Figure 8**).

In order to simulate the experimental results of BF, non-linear dynamic analyses at 100% of PGA level have been carried out for the complete set of the seismic inputs. The comparisons between numerical and experimental results obtained for seismic inputs 1228, 196, and 535 are reported in **Figure 12** in terms of global behavior and local response of UFP dampers at each story. The numerical simulations are in good agreement with experimental results, and the UFPs' cyclic behaviors were reliably predicted. Only a few discrepancies can be observed on the peak values of base shear and on the maximum ductility of UFPs in the case of seismic input 196. The comparison between experimental and numerical results of the braced frame tested at 100% of PGA is summarized in **Table 2B**. The values of equivalent damping have been estimated as a fraction of the critical damping, as reported in Smith et al. (2014).

The design assumptions used for the BF model (**Figure 8**) have been validated through comparison with the experimental and numerical outcomes. The equivalent SDOF system obtained from design procedure of F and BF models compared with the acceleration-drift response spectrum format are plotted in **Figure 13**. The experimental total drift (i.e., maximum top displacement normalized by height of the structure) vs. corresponding accelerations (i.e., base shear divided by the equivalent mass) recorded at different PGA levels are reported in **Figure 13A** for the F model and in **Figure 13B** for the BF model.

The numerical results of non-linear dynamic analyses carried out on the BF model for all seismic inputs at 100% of PGA level have been compared with the target displacement Δ_d or drift θ_d assumed in the design procedure (dashed vertical line at 1.25%) in **Figure 13B**.

As can be observed, the mean value of numerical drift (averaged on seven earthquakes) was accurately predicted by the design target drift θ_d, as a verification of the design procedure (Step 7 of design method). From **Figure 13** it can be pointed out that the seismic response of the BF model at the DBE (100% of PGA) reduces the inter-story drift θ_d more than twice if compared with the response of model F (from 3 to 1.25%). This effect is mainly due to the increase of the equivalent damping ξ_{eq} (from 2 to 12%) and of the equivalent stiffness K_e (from 513 to 1228 kN/m). Moreover, the drift increase with an increasing PGA level of seismic inputs and the equivalent SDOF systems provides a reliable representation of the experimental results in both configurations (F and BF models).

CONCLUSIONS

In this paper, a displacement-based design procedure for post-tensioned timber framed buildings with dissipative-bracing systems has been described and applied to a three-dimensional, 2/3 scaled, three-story prototype experimental model. Several shaking table tests have been performed at the structural laboratory of the University of Basilicata (Italy) on different configurations of the experimental model: bare frame (F) and braced frame (BF). The dissipating bracing (BD) system considered in this application consisted of V-inverted braces

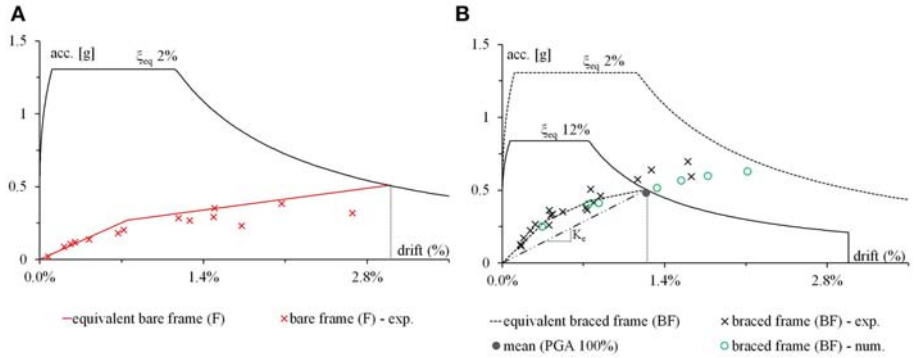

FIGURE 13 | Comparison between design results and experimental peak values in **(A)** free-rocking configuration and **(B)** dissipative bracing configuration of Pres-Lam experimental model.

(B) composed of two timber rods and a hysteretic damper (D) realized with two UFPs, with two braces for each story.

In order to investigate the effectiveness of the energy dissipating bracing system on controlling the seismic response of the post-tensioned timber frame, the experimental results of the braced frame (BF) and the bare frame (F) have been compared. The bare frame (F) and the braced frame (BF) performed as expected with the global flag-shaped behavior observed at the design levels of seismic inputs. The dissipative bracing system improved the seismic response of the experimental model by reducing to 1.25% the experimental maximum drift at the design seismic level, ∼60% less than the bare frame with an increase of 30% of the base shear. Moreover, the braced frame increases the secant stiffness more than 2-fold and the total equivalent viscous damping from 2 to 12%, in good agreement with the experimental and numerical damping estimations. No damage occurred to the structural elements throughout testing, with the application of almost 80 earthquakes in both configurations.

In order to validate the design procedure, the design assumptions have been compared with the shaking table test results and non-linear dynamic analysis carried out on the braced frame (BF) at PGA level of 100%. The numerical seismic response of the BF model and the local behavior of UFP dampers at each story have shown good agreement with experimental tests. The mean value of numerical drift (averaged on seven earthquake inputs) was very close to the design assumption, showing the reliability of the design procedure.

DATA AVAILABILITY

The datasets generated for this study are available on request to the corresponding author.

AUTHOR CONTRIBUTIONS

FP has contributed to the construction technology development and to the international collaboration with other research institutions. AD has designed the experimental specimen and the testing apparatus. DN has organized the experimental shaking table tests. NL has performed the numerical analyses and processed analytical results. All authors have contributed to manuscript revision, read, and approved the submitted version.

ACKNOWLEDGMENTS

The authors would like to acknowledge the financial support of the RELUIS 2014-2018 project, funded by the Italian Civil Protection Department, and Prof. Stefano Pampanin from University of Canterbury, Christchurch, NZ for his contribute to the research study.

REFERENCES

Bouc, R. (1967). "Forced vibration of mechanical system with hysteresis," in *4th Conference on Nonlinear Oscillations* (Prague).

Buchanan, A. H., Deam, B., Fragiacomo, M., Pampanin, S., and Palermo, A. (2008). Multi-story prestressed timber buildings in New Zealand. *J. Int. Assoc. Bridge Struct. Eng.* 18, 166–173. doi: 10.2749/101686608784218635

Di Cesare, A., Ponzo F. C., Nigro, D., Dolce, M., and Moroni, C. (2012). Experimental and numerical behaviour of hysteretic and visco-recentring energy dissipating bracing systems. *Bull. Earthquake Eng.* 10,1585–1607. doi: 10.1007/s10518-012-9363-x

Di Cesare, A., and Ponzo, F. C. (2017). Seismic retrofit of reinforced concrete frame buildings with hysteretic bracing systems: design procedure and behaviour factor. *Shock Vibr.* 2017:2639361. doi: 10.1155/2017/2639361

Di Cesare, A., Ponzo, F. C., Lamarucciola, N., and Nigro, D. (2019b). "Modelling of post-tensioned timber framed buildings with hysteretic bracing system: preliminary analysis," in *IOP Conference Series: Earth and Environmental Science, Vol. 233* (IOP Publishing), 022026. doi: 10.1088/1755-1315/233/2/022026

Di Cesare, A., Ponzo, F. C., and Nigro, D. (2014). Assessment of the performance of hysteretic energy dissipation bracing systems. *Bull. Earthquake Eng.* 12, 2777–2796. doi: 10.1007/s10518-014-9623-z

Di Cesare, A., Ponzo, F. C., Nigro, D., Pampanin, S., and Smith, T. (2017). Shaking table testing of post-tensioned timber frame building with passive energy dissipation systems. *Bull. Earthquake Eng.* 15, 4475–4498. doi: 10.1007/s10518-017-0115-9

Di Cesare, A., Ponzo, F. C., Pampanin, S., Smith, T., Nigro, D., and Lamarucciola, N. (2019a). Displacement based design of post-tensioned timber framed

buildings with dissipative rocking mechanism. *Soil Dynamics Earthquake Eng.* 116, 317–330. doi: 10.1016/j.soildyn.2018.10.019

Estévez-Cimadevila, J., Otero-Chans, D., Martín-Gutiérrez, E., and Suárez-Riestra, F. (2016). Long-span wooden structural floors with self-tensioning system: performance under asymmetrical loads. *Adv. Mater. Scie. Eng.* 2016:3696025. doi: 10.1155/2016/3696025

Federal Emergency Management Agency (2012). *Seismic Performance Assessment of Buildings Vol. 1—Methodology*. Technical report FEMA-P58, Washington, DC.

Krawinkler, H., and Moncarz, P. D. (1981). *Theory and Application of Experimental Model Analysis in Earthquake Engineering*. Standford, CA: NASA STI/Recon Technical Report N 82.

Lin, Y. Y., Tsai, M. H., Hwang, J. S., and Chang, K. C. (2003). Direct displacement-based design for building with passive energy dissipation systems. *Eng. Struct.* 25, 25–37. doi: 10.1016/S0141-0296(02)00099-8

Mazza, F., and Mazza, M. (2019). Seismic retrofitting of gravity-loads designed rc framed buildings combining CFRP and hysteretic damped braces. *Bull. Earthquake Eng.* 13, 1–23. doi: 10.1007/s10518-019-00593-5

Newcombe, M. P., Marriott, D., Kam, W. Y., Pampanin, S., and Buchanan, A. H. (2011). "Design of UFP-coupled post-tensioned timber shear walls," in *9th Pacific Conference on Earthquake Engineering* (Auckland).

Newcombe, M. P., Pampanin, S., Buchanan, A., and Palermo, A. (2008). Section analysis and cyclic behavior of post-tensioned jointed ductile connections for multi-story timber buildings. *J. Earthquake Eng.* 12, 83–110. doi: 10.1080/13632460801925632

Newcombe, M. P., Pampanin, S., and Buchanan, A. H. (2010). "Design, fabrication and assembly of a two-story post-tensioned timber building," in *Proc. World Conference on Timber Engineering* (Riva del Garda), 3092–3100.

Nuzzo, I., Losanno, D., and Caterino, N. (2019). Seismic design and retrofit of frame structures with hysteretic dampers: a simplified displacement-based procedure. *Bull. Earthquake Eng.* 17, 1–33. doi: 10.1007/s10518-019-00558-8

Nuzzo, I., Losanno, D., Caterino, N., Serino, G., and Rotondo, L. M. B. (2018). Experimental and analytical characterization of steel shear links for seismic energy dissipation. *Eng. Struct.* 172, 405–418. doi: 10.1016/j.engstruct.2018.06.005

Pei, S., Popovski, M., van de Lindt, J. W. (2012). "Performance based design and force modification factors for CLT structures," in *Proceeding of the 45th Meeting, International Council for Research and Innovation in Building and Construction, Working Commission W18 – Timber Structures, CIB-W18* (Växjö), 2012.

Polocoşer, T., Leimcke, J., and Kasal, B. (2018). Report on the seismic performance of three-dimensional moment-resisting timber frames with frictional damping in beam-to-column connections. *Adv. Struct. Eng.* 21, 1652–1663. doi: 10.1177/1369433217753695

Ponzo, F. C., Di Cesare, A., and Lamarucciola, N. (2018). Modelling of post-tensioned timber-framed buildings with seismic rocking mechanismat the column-foundation connections. *Int. J. Comput. Methods Exp. Meas.* 5, 966–978. doi: 10.2495/CMEM-V5-N6-9 66-978

Ponzo, F. C., Di Cesare, A., Lamarucciola, N., and Nigro, D. (2019). *Testing requirements of hysteretic energy dissipating devices according to the new Italian seismic code.* Compdyn 2019, 24-26 June, Crete, Greece.

Ponzo, F. C., Smith, T., Di Cesare, A., Pampanin, S., Carradine, D., and Nigro, D. (2012). "Shaking table test of a multistory post-tensioned glulam building: design and construction," in *World Conference on Timber Engineering WCTE* (Auckland), 44–52.

Priestley, M. J. N. (2000). *Performance-Based Seismic Design.* Keynote Address, 12-WCEE, Auckland, p. 22.

Priestley, M. J. N., Calvi, G. M., and Kowalsky, M. J. (2007). *Displacement-Based Seismic Design of Structures*. Pavia: IUSS Press, 670.

Priestley, M. J. N., and Grant, D. N. (2005). Viscous damping in seismic design and analysis. *J. Earthquake Eng.* 9, 229–255. doi: 10.1142/S1363246905002365

Priestley, N., Sritharan, S., Conley, J., and Pampanin, S. (1999). Preliminary results and conclusions, PRESSS five-story precast concrete test building. *PCI J.* 44, 42–67. doi: 10.15554/pcij.11011999.42.67

Pu, W., Liu, C., and Dai, F. (2018). Optimum hysteretic damper design for multi-story timber structures represented by an improved pinching model. *Bull. Earthquake Eng.* 16, 6221–6241. doi: 10.1007/s10518-018-0437-2

Smith, T., Ponzo, F. C., Di Cesare, A., Pampanin, S., Carradine, D., Buchanan, A. H., et al. (2014). Post-tensioned glulam beam-column joints with advanced damping systems: testing and numerical analysis. *J. Earthquake Eng.* 18, 147–167. doi: 10.1080/13632469.2013.835291

Structural Timber Innovation Company Inc (2013). *Post-Tensioned Timber Buildings - Design Guide, Structural Timber Innovation Company*. Christchurch.

Ugalde, D., Almazán, J. L., Santa María, H., and Guindos, P. (2019). Seismic protection technologies for timber structures: a review. *Eur. J. Wood Wood Prod.* 77, 173–194. doi: 10.1007/s00107-019-01389-9

Wang, B., and Zhu, S. (2018). Seismic behavior of self-centering reinforced concrete wall enabled by superelastic shape memory alloy bars. *Bull. Earthquake Eng.* 16, 479–502. doi: 10.1007/s10518-017-0213-8

Wen, Y. K. (1980). Equivalent linearization for hysteretic systems under random excitation. *J. Appl. Mech.* 47, 150–154. doi: 10.1115/1.3153594

Zahrai, S. M., and Froozanfar, M. (2018). Improving seismic behavior of MRFs by U-shaped hysteretic damper along diagonal brace. *Int. J. Steel Struct.* 19, 543–548. doi: 10.1007/s13296-018-0139-2

Conflict of Interest Statement: The authors declare that the research was conducted in the absence of any commercial or financial relationships that could be construed as a potential conflict of interest.

frontiers in Built Environment

ORIGINAL RESEARCH
published: 24 October 2019
doi: 10.3389/fbuil.2019.00126

Simultaneous Approach to Critical Fault Rupture Slip Distribution and Optimal Damper Placement for Resilient Building Design

*Kyoichiro Kondo and Izuru Takewaki**

Department of Architecture and Architectural Engineering, Graduate School of Engineering, Kyoto University, Kyoto, Japan

The uncertainties in ground motions may result from several factors, e.g., (i) the fault rupture process, (ii) the wave propagation, (iii) the site amplification from the earthquake bedrock to the ground surface. The uncertainty in the fault rupture slip is taken as a main factor of uncertainties in the present paper and the critical fault rupture slip distribution causing the maximum structural response is found by using the stochastic Green's function method as a generator of ground motions. Then, a multi-degree-of-freedom (MDOF) building structure is introduced as a model structure and an optimal damper placement problem is discussed for the critical ground motion. The main topic in this paper is the simultaneous determination of the critical fault rupture slip distribution and the optimal damper placement. The sequential quadratic programming method is used in the problem of critical fault rupture slip distribution and a sensitivity-based method is introduced in the optimal damper placement problem. Furthermore, the robustness for the maximum interstory drift in MDOF building structures under the uncertainty in fault rupture slip distributions is presented for resilient building design by using the robustness function. Since the critical case leads to the most unfavorable structural response, the proposed method can provide structural designers with a promising tool for resilient building design.

Keywords: critical ground motion, worst input, stochastic Green's function method, fault rupture, wave propagation, optimal damper placement, robustness, resilience

OPEN ACCESS

Edited by:
Nawawi Chouw,
The University of Auckland,
New Zealand

Reviewed by:
Dario De Domenico,
University of Messina, Italy
M Shadi Mohamed,
Heriot-Watt University,
United Kingdom

****Correspondence:***
Izuru Takewaki
takewaki@archi.kyoto-u.ac.jp

Specialty section:
This article was submitted to Earthquake Engineering, a section of the journal Frontiers in Built Environment

Received: *11 August 2019*
Accepted: *07 October 2019*
Published: *24 October 2019*

Citation:
Kondo K and Takewaki I (2019) Simultaneous Approach to Critical Fault Rupture Slip Distribution and Optimal Damper Placement for Resilient Building Design. Front. Built Environ. 5:126. doi: 10.3389/fbuil.2019.00126

INTRODUCTION

It is well-accepted that earthquake ground motions exhibit diverse aspects, as observed, for example, in Mexico (1985), Northridge (1994), Kobe (1995), Chi-chi (1999), Tohoku (2011), Kumamoto (2016). Several models have been introduced to model these ground motions taking into account their occurrence mechanisms. Recently the main stream of investigations on the process of ground motion generation is composed of the following three components, (i) the fault rupture, (ii) the wave propagation to the earthquake bedrock, (iii) the site amplification to the ground surface. To include these modeling stages, four approaches have been developed in general, (a) the theoretical approach, (b) the numerical analysis approach, (c) the semi-empirical approach and (d) the hybrid approach. It is understood that, while the theoretical and numerical analysis approaches (finite difference method as a representative; see Day, 1982; Makita et al., 2019) are

appropriate for producing directivity pulses and surface waves with the predominant period longer than 1–2 s (Bouchon, 1981; Hisada and Bielak, 2003; Yoshimura et al., 2003; Nickman et al., 2013), the semi-empirical approach is appropriate for ground motions with the predominant period shorter than 1–2 s. The empirical Green's function (Wennerberg, 1990) and the stochastic Green's function (Hisada, 2008) are frequently incorporated into the semi-empirical approach. In the hybrid approach, the shorter period ground motions are combined with the longer period waves through a matching filter.

Due to lack of sufficient observed data and intrinsic variability of characteristics in underground, it is usually recommended to treat several parameters as uncertain numbers (aleatory or epistemic) (Abrahamson et al., 1998; Lawrence Livermore National Laboratory, 2002; Morikawa et al., 2008; Cotton et al., 2013).

To investigate the effect of uncertainties in ground motions on structural response variability, Makita et al. (2018a) treated a base-isolated, building-connected hybrid structural system (Murase et al., 2013, 2014; Kasagi et al., 2016; Fukumoto and Takewaki, 2017) and tackled the effect of the uncertainty in site amplification. They dealt with the fault as a point source. On the other hand, the uncertainty in fault rupture slip is considered in the present paper and a recent one (Makita et al., 2018b). In modeling the wave propagation to the earthquake bedrock, the stochastic Green's function method is used (Irikura, 1986; Yokoi and Irikura, 1991). The Fourier amplitude of ground motions at the earthquake bedrock caused by rupture at a fault element is represented by the Boore's model (Boore, 1983) and the phase angle is represented by the phase difference method (Yamane and Nagahashi, 2008).

In this paper, the uncertainty in the fault rupture slip is taken as a main factor of uncertainty in the ground motion generation and the critical fault rupture slip distribution is found by using the stochastic Green's function method as a generator of ground motions. Then, a multi-degree-of-freedom (MDOF) building structure is introduced as a model structure and an optimal damper placement problem is discussed for the critical ground motion causing the maximum response (Drenick, 1970; Takewaki, 2007). The main topic in this paper is the simultaneous determination of the critical fault rupture slip distribution and the optimal damper placement (see Domenico et al., 2019 as a recent review paper). The sequential quadratic programming method is used in the problem of critical fault rupture slip distributions and a sensitivity-based method is introduced in the optimal damper placement problem. Furthermore, the robustness for the maximum interstory drift in MDOF building structures under the uncertainty in fault rupture slip distribution is presented for resilient building design by using the robustness function (Ben-Haim, 2006). Since the critical case leads to the most unfavorable structural response, the proposed method can provide structural designers with a promising tool for resilient building design.

STOCHASTIC GREEN'S FUNCTION METHOD FOR GROUND MOTION GENERATION

The present paper uses the stochastic Green's function method based on a plane-source model of the fault rupture to produce ground motions. Since the detailed explanation was provided in the reference (Makita et al., 2018b), a concise summary is presented in this section.

Generation of Ground Motion Using Small Ground Motions From Sub-fault Elements

The fault plane is divided into multiple fault elements and taking into account the delay of the fault element rupture initiation.

The fault plane is assumed to consist of $N_L \times N_W$ fault elements (N_L: number of divisions in the longitudinal direction, N_W: number of divisions in the width direction) and the slip action in one fault element is assumed to be composed of N_D slips. Due to Irikura (1983), the ground displacement $U_{ij}(t)$ from one fault element is produced by N_D slips $u_{ij}(t)$.

$$U_{ij}(t) = f(t) * u_{ij}(t) = \sum_{k=1}^{N_D} u_{ij}\left(t - \left(k-1\right)\frac{\tau_{ij}}{N_D}\right) \tag{1}$$

where ij refers to the ij sub-element in one fault element and τ_{ij} is the rise time of the ij sub-element. Let $f(t)$ denote the slip correction function expressed by

$$f(t) = \sum_{k=1}^{N_D} \delta\left(t - \left(k-1\right)\frac{\tau_{ij}}{N_D}\right) \tag{2}$$

where $\delta(t)$ is the Dirac delta function.

The ground displacement $U(t)$ resulting from the whole fault may then be given by

$$\begin{aligned} U(t) &= \sum_{i=1}^{N_W}\sum_{j=1}^{N_L} f\left(t - t_{ij}\right) * u_{ij}(t) \\ &= \sum_{i=1}^{N_W}\sum_{j=1}^{N_L}\sum_{k=1}^{N_D} u_{ij}\left(t - t_{ij} - \left(k-1\right)\frac{\tau_{ij}}{N_D}\right) \end{aligned} \tag{3}$$

In this paper, the following slip correction function $f(t)$ is used (Irikura, 1986; Yokoi and Irikura, 1991).

$$f(t) = \delta(t) + \frac{1}{n'}\sum_{k=1}^{(N_D-1)n'} u_{ij}\left(t - \frac{\left(k-1\right)\tau}{\left(N_D-1\right)n'}\right) \tag{4}$$

The number n' of re-division was introduced by Irikura (1986) to remove the effect of artificial periodicity. Irikura (1994) introduced the following constraint for n'.

$$\frac{n'N_D}{\tau} > 2f_H \ (f_H : \text{upper bound of the effective frequency}) \tag{5}$$

The ground displacement $U(t)$ resulting from the whole fault can finally be given by

$$U(t) = \sum_{i}^{N_L}\sum_{j}^{N_W} u_{ij}\left(t - t_{ij}\right) + \sum_{i}^{N_L}\sum_{j}^{N_W}\sum_{k}^{(N_D-1)n'} \frac{1}{n'} u_{ij}\left(t - t_{ij} - \frac{(k-1)\tau}{(N_D-1)n'}\right) \quad (6)$$

The concept of the stochastic Green's function method used in the present study is illustrated in **Figure 1A**.

For simplicity, it is assumed here that the fault rupture propagates concentrically. t_{ij} can then be expressed by

$$t_{ij} = t_{p\,ij} + t_{r\,ij} = \frac{r_{ij}}{\beta} + \frac{\eta_{ij}}{V_r} \quad (7)$$

where β: the shear wave velocity of the ground, V_r: the slip propagation speed in the fault, t_{pij}: the propagation time from the fault element to the recording point, t_{rij}: the slip initiation time in the fault element, r_{ij}: the distance between the fault element and the recording point, η_{ij}: the distance between the slip initiation point in the whole fault and the fault element.

In the present paper, it is assumed that the slip front parameters (slip initiation time t_{rij} and rise time τ_{ij}) are regarded

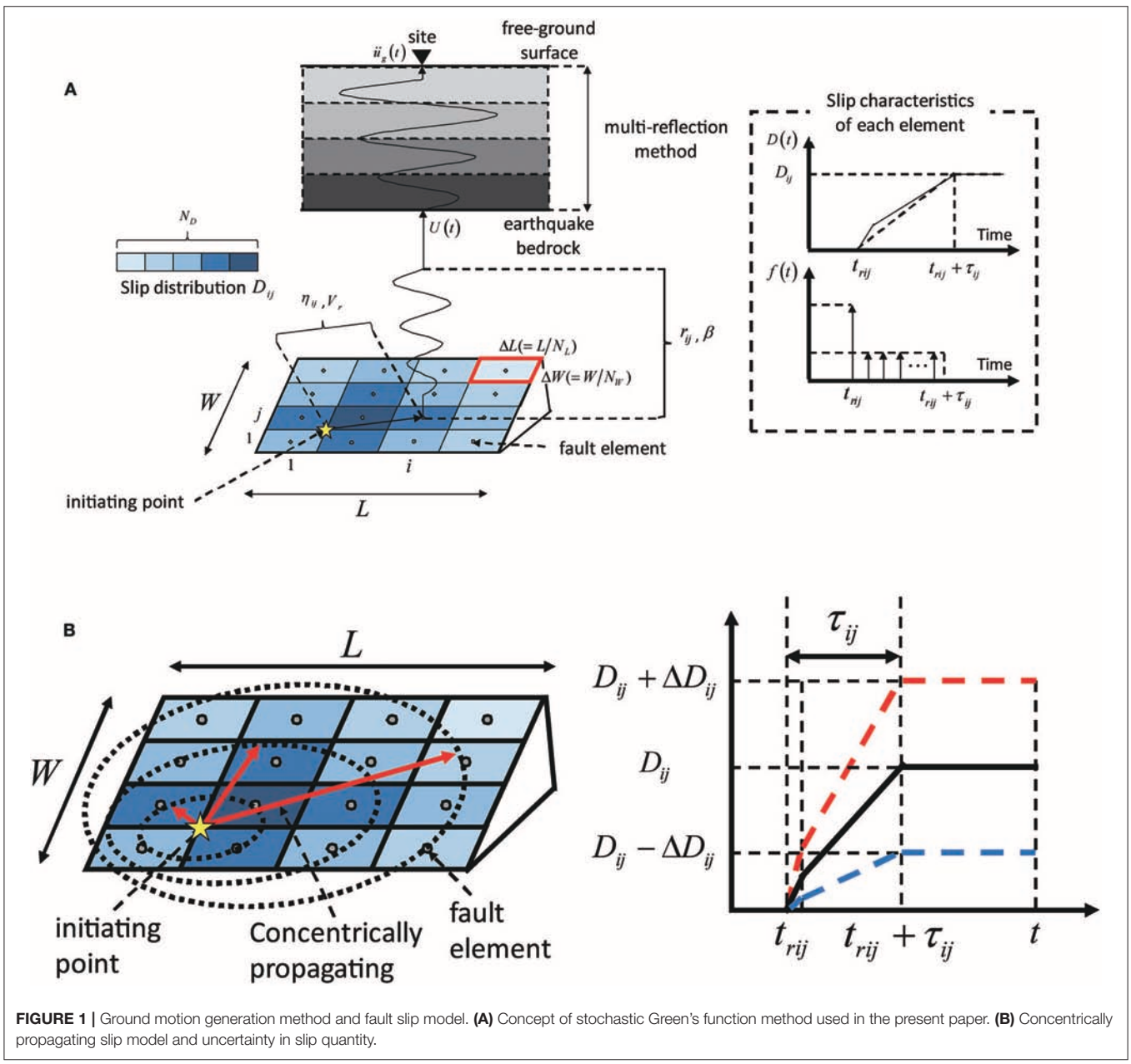

FIGURE 1 | Ground motion generation method and fault slip model. **(A)** Concept of stochastic Green's function method used in the present paper. **(B)** Concentrically propagating slip model and uncertainty in slip quantity.

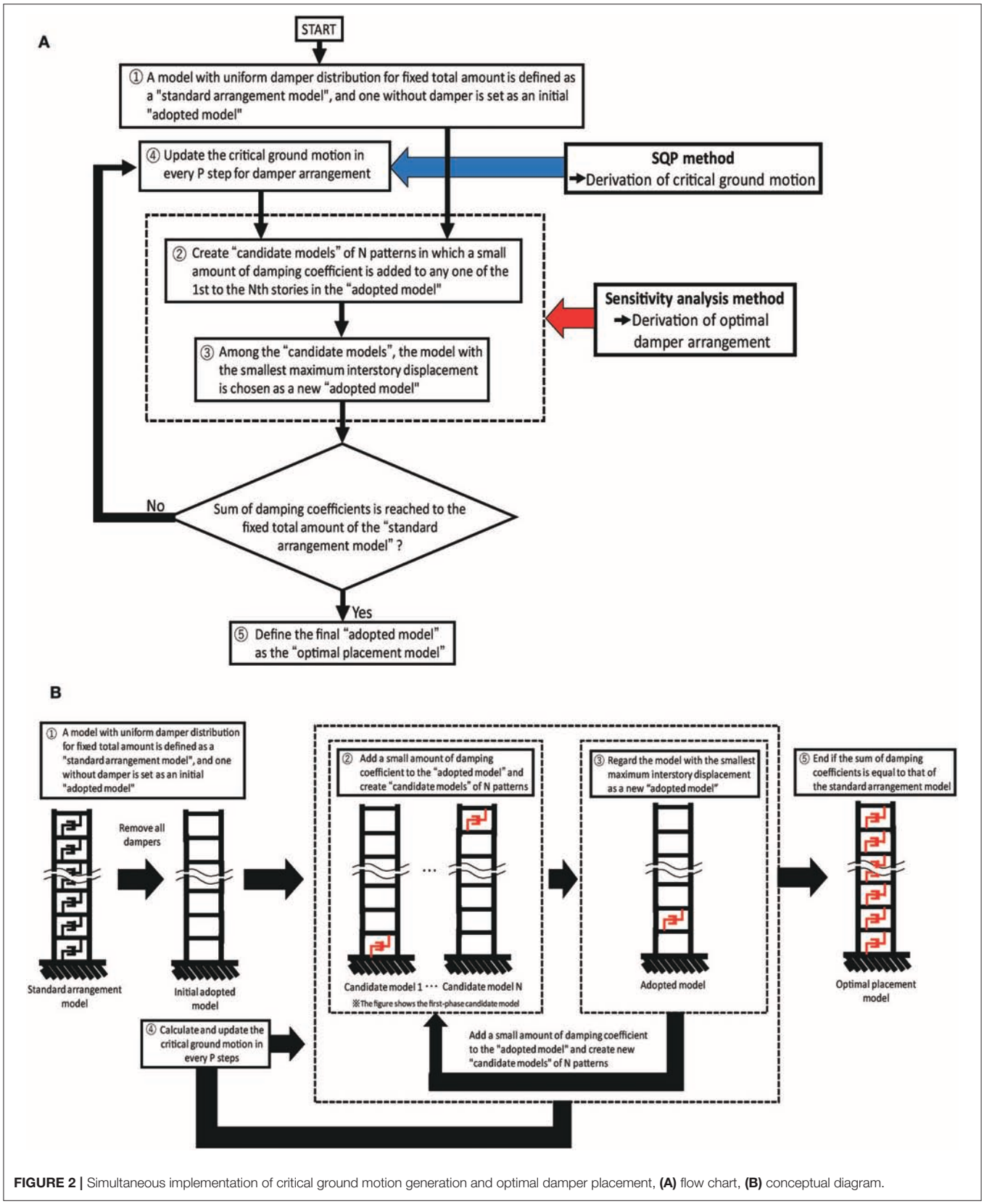

FIGURE 2 | Simultaneous implementation of critical ground motion generation and optimal damper placement, **(A)** flow chart, **(B)** conceptual diagram.

as certain parameters and the fault slip distribution is treated as a set of uncertain parameters. The model is explained conceptually in **Figure 1B**.

Small Ground Motion From Element Fault

A small ground acceleration at the earthquake bedrock resulting from the slip of a fault element can be obtained by locating a

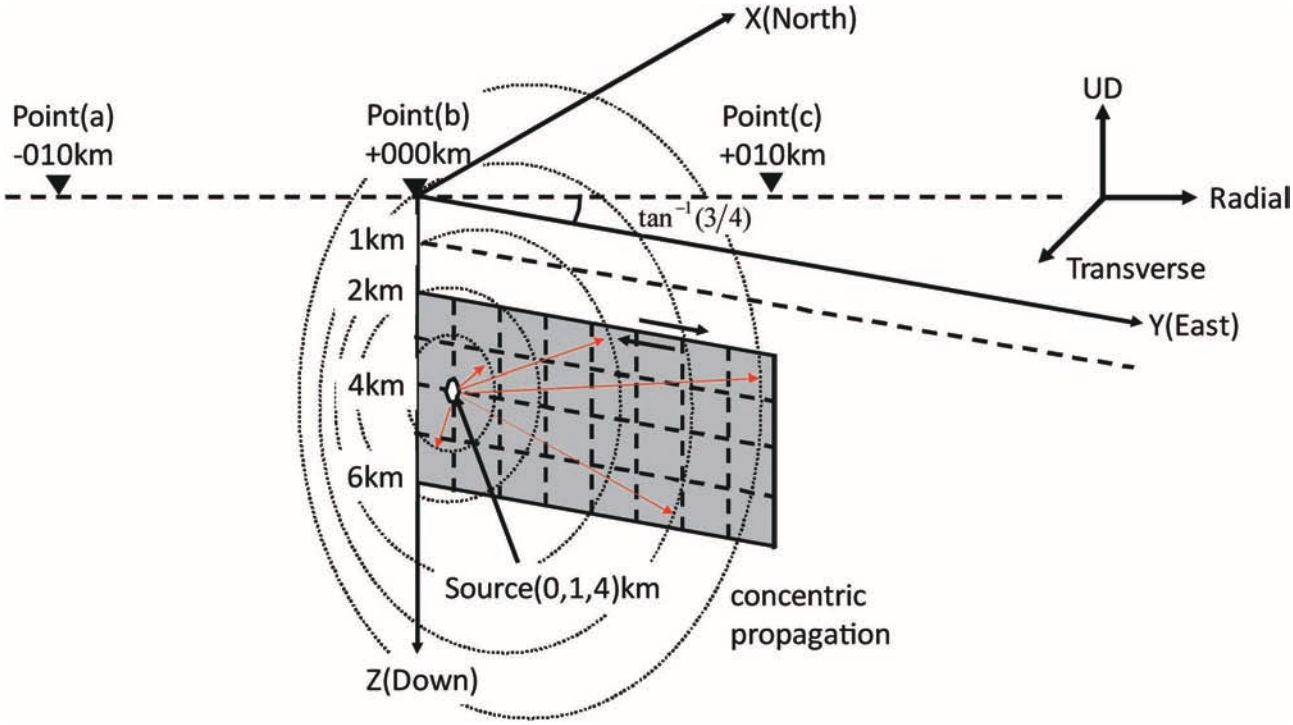

FIGURE 3 | Fault plane and three recording points (replotted based on Kato et al., 2011).

TABLE 1 | Soil conditions and source parameters.

(A) Soil conditions

Layer	Thickness H (m)	Shear wave velocity V_s (m/s)	Mass density ρ (kg/m^3)	Q-value Q (−)
1	1,000	2,000	2,600	-
2 (half-space)	-	3,464	2,700	$70f^{1.0}$

(B) Source parameters

Scaling parameters	
Along the Fault Width Direction N_W	4
Along the Fault Length Direction N_L	8
Along the slip N_D	6

Fault parameters		**Fault element parameters**	
Fault length W	4 km	Area of fault element S_S	1 km^2
Fault width L	8 km	Seismic moment M_{0S}	5.40×10^{15} Nm
Area of fault plane S	32 km^2	Slip D_S	0.167 m
Earthquake focal depth	4 km	Stress drop $\Delta\sigma_S$	13.95 Mpa
Seismic moment M_0	1.04×10^{18}Nm	Radiation pattern $R_{\theta\phi}$	0.63
Slip D	1 m	Cutoff frequency f_m	6 Hz
Stress drop $\Delta\sigma_L$	13.95 Mpa		
Rupture velocity V_r	3, 000 m/s		

TABLE 2 | Parameters in building structures.

	2-story model	5-story model	10-story model	20-story model
N	2	5	10	20
Mass per story ($\times 10^3$kg)	1,000	1,000	1,000	1,000
Fundamental natural period [s]	0.25	0.5	1.0	2.0
Structural damping ratio	5%	5%	5%	5%
Total added damping coefficient [Ns/m]	0.5×10^8	2.8×10^8	9.6×10^8	3.6×10^9

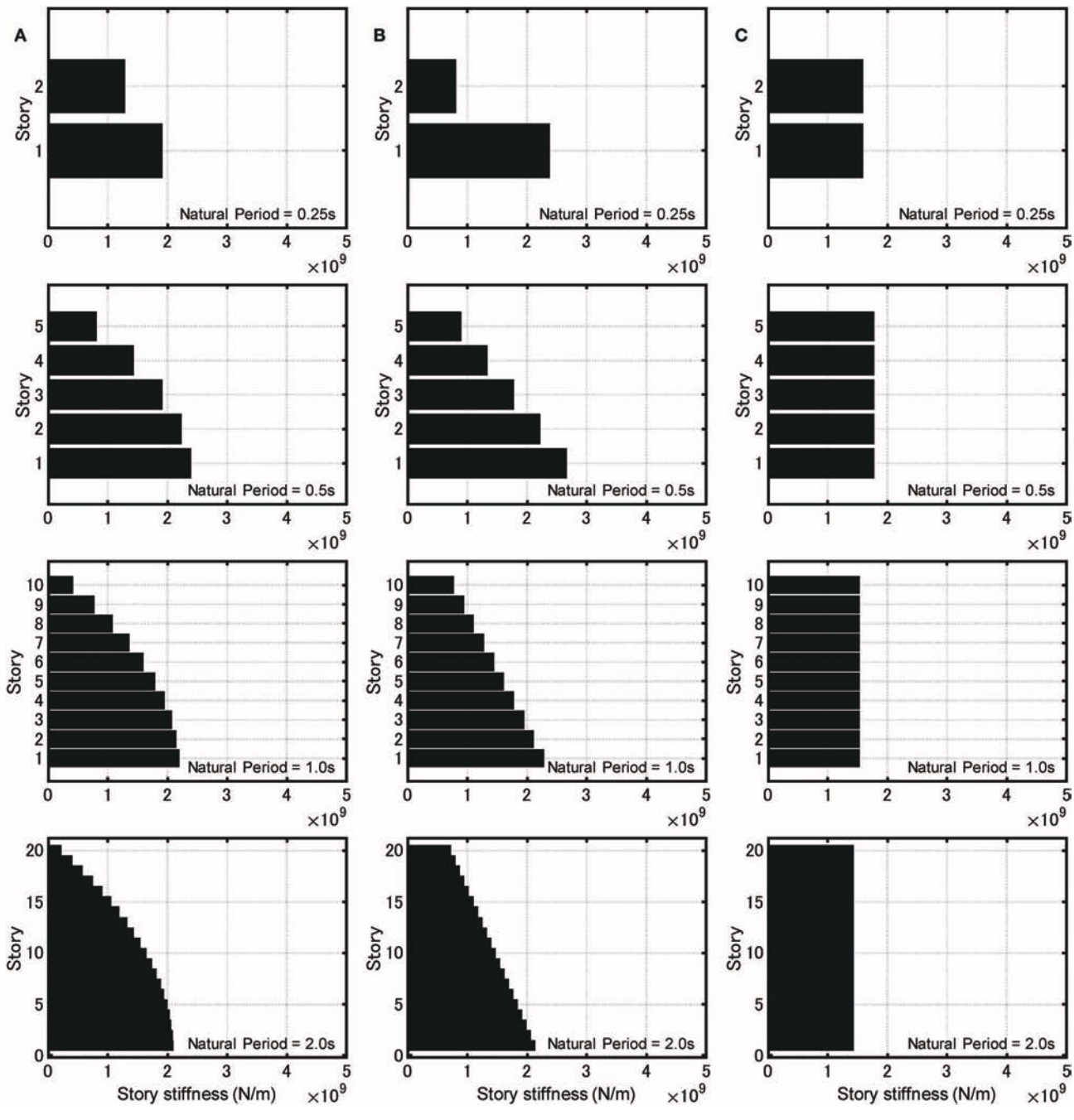

FIGURE 4 | Story stiffness distributions of three building structures. **(A)** Model with straight lowest natural mode. **(B)** Model with trapezoidal stiffness distribution. **(C)** Model with uniform stiffness distribution.

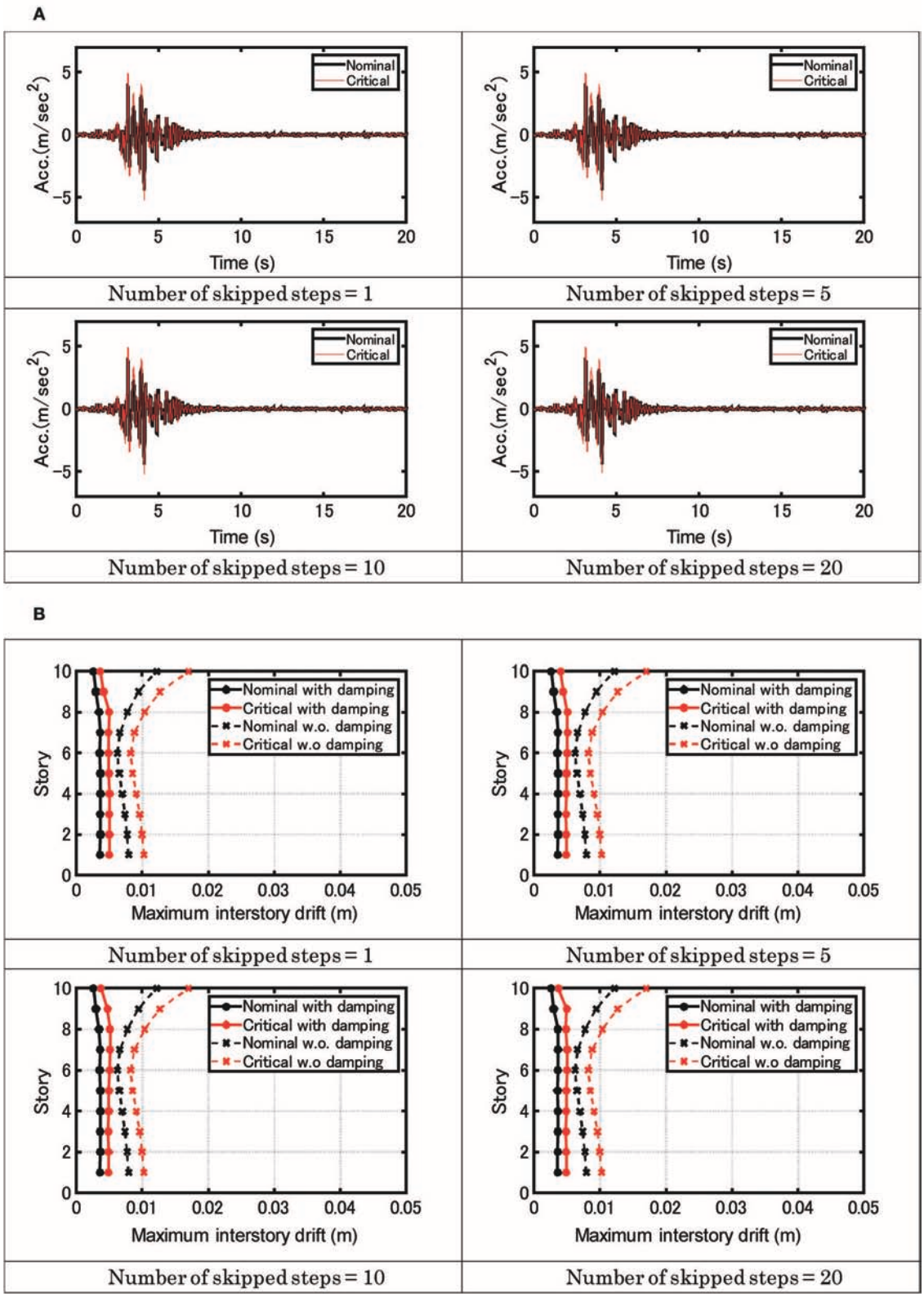

FIGURE 5 | Influence of number of skipped steps. **(A)** Acceleration of ground motions for four numbers of skipped steps. **(B)** Maximum interstory drift of MDOF model for four numbers of skipped steps.

point source at the center of the fault element (Boore, 1983). The Fourier amplitude spectrum of the acceleration at the earthquake bedrock can be given by

$$\left|F_{ij}{}^{S}(\omega)\right| = S(\omega)\cdot P(\omega) \tag{8}$$

where $S(\omega)$: parameter related to the source (fault), $P(\omega)$: parameter related to the wave attenuation in the wave passage from the fault element to the earthquake bedrock.

In this paper, $S(\omega)$ and $P(\omega)$ are from Boore (1983) (see Makita et al., 2018b). Since the phase is not given by Boore (1983), the phase difference method is introduced for expressing the phase of ground motion (Yamane and Nagahashi, 2008). The standard deviation of the phase difference resulting from the fault element *ij*can be given by

$$\sigma_{ij}/\pi = 0.06 + 0.0003 r_{ij} \tag{9}$$

This relation was derived for inland earthquakes (Makita et al., 2018a). The near-fault ground motion is assumed here in which the influence of the rupture directivity is small. In the case where the influence of the rupture directivity is not small, the relations $\sigma_{ij}/\pi = 0.05 + 0.0003 r_{ij}$ (in the direction of rupture propagation) and $\sigma_{ij}/\pi = 0.08 + 0.0003 r_{ij}$ (in the orthogonal direction of rupture propagation) are recommended (Yamane and Nagahashi, 2008). The phase spectrum is then expressed by

$$\begin{aligned} \phi_{k+1\ ij} &= \phi_{k\ ij} + \Delta\phi_{k\ ij} \quad (k = 1, 2, \ldots, N/2 - 1) \\ \Delta\phi_{ij} &= -\left(\mu + s\cdot\sigma_{ij}\right) \end{aligned} \tag{10}$$

where $\phi_{k\ ij}$: the k-th phase spectrum of the fault element, $\Delta\phi_{k\ ij}$: the k-th phase difference spectrum of the fault element ij, N: the number of adopted frequencies, μ: the mean phase difference, s: the Gaussian random number (mean = 0, standard deviation = 1). A constant value of μ is assumed here in all the fault elements.

The Fourier transform $F_{ij}{}^{S}(\omega)$ of the acceleration at the earthquake bedrock resulting from the fault element ij can be described by

$$F_{ij}{}^{S}(\omega) = \left|F_{ij}{}^{S}(\omega)\right| \cdot e^{i\phi_{ij}(\omega)} \tag{11}$$

The inverse Fourier transform of $F_{ij}{}^{S}(\omega)$ provides the acceleration at the earthquake bedrock resulting from the fault element ij. The substitution of this into Equation (6) finally provides the acceleration at the earthquake bedrock resulting from the whole fault. It is noted that the difference of displacement and acceleration does not matter.

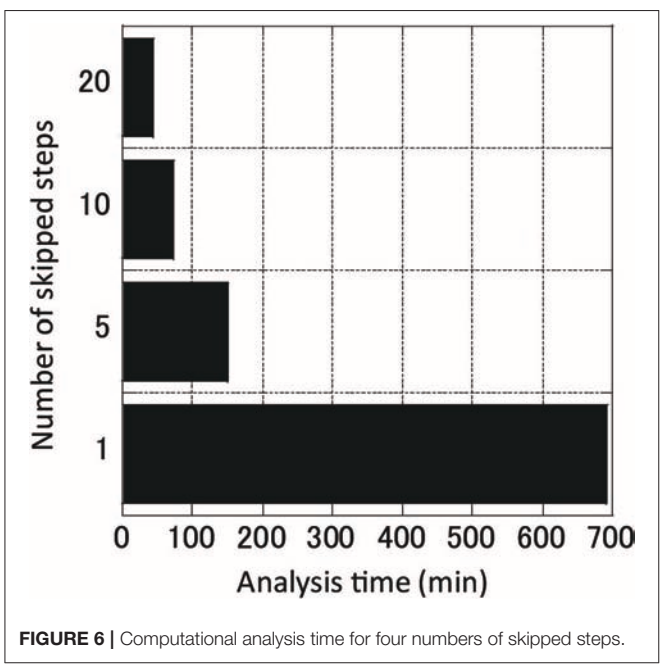

FIGURE 6 | Computational analysis time for four numbers of skipped steps.

CRITICAL SLIP DISTRIBUTION IN FAULT PLANE MAXIMIZING THE STRUCTURAL RESPONSE

The sequential quadratic programming method is used in the problem of critical fault rupture slip distributions maximizing the structural response.

Let $\mathbf{x}$ and $f(\mathbf{x})$ denote the uncertain parameters (slip quantities of fault elements) and the maximum interstory drift with respect to the total duration of building response and all stories. The problem of critical fault slip distribution can be described as

$$\begin{array}{ll} \text{Find} & \mathbf{x} \\ \text{which maximizes} & f(\mathbf{x}) \\ \text{subject to} & \mathbf{x}_{lb} \le \mathbf{x} \le \mathbf{x}_{ub} \end{array} \tag{12}$$

where $\mathbf{x}_{lb}$ and $\mathbf{x}_{ub}$ are the lower and upper bounds of uncertain parameters (slips).

In the present paper, viscous dampers are added in the building. Let c_{di} and $\bar{W}_c$ denote the viscous damping coefficient in the i-th story and the upper limit of the total quantity of damping coefficients. The problem of critical fault slip distribution for a building with added dampers can be described as

$$\begin{array}{ll} \text{Find} & \mathbf{x} \\ \text{which maximizes} & f(\mathbf{x}, \mathbf{c}_d) \\ \text{subject to} & \mathbf{x}_{lb} \le \mathbf{x} \le \mathbf{x}_{ub} \\ & \sum_{i=1}^{N} c_{di} \le \bar{W}_c, c_{di} \ge 0 \end{array} \tag{13}$$

A further criterion has to be introduced to determine the damper distribution. For this purpose, the following problem of minimizing the maximum interstory drift is posed.

$$\begin{array}{ll} \text{Find} & \mathbf{x}, \mathbf{c}_d \\ \text{which} \underset{\mathbf{c}_d}{\text{minimize}} \underset{\mathbf{x}}{\text{maximize}} & f(\mathbf{x}, \mathbf{c}_d) \end{array}$$

subject to

$$\mathbf{x}_{lb} \leq \mathbf{x} \leq \mathbf{x}_{ub}$$
$$\sum_{i=1}^{N} c_{di} \leq \bar{W}_c, c_{di} \geq 0 \qquad (14)$$

A solution procedure of this problem will be presented in the following section.

SIMULTANEOUS DETERMINATION OF CRITICAL SLIP DISTRIBUTION IN FAULT PLANE AND OPTIMAL DAMPER DISTRIBUTION

The solution procedure of the above final problem may be stated as follows:

① A model with uniform damper distribution for fixed total amount is defined as a "standard arrangement model," and one without damper is set as an initial "adopted model".

② Create "candidate models" of N patterns in which a small amount of damping coefficient is added to any one of the first to the Nth stories in the "adopted model" by using a sensitivity-based method.

③ Among the "candidate models," the model with the smallest maximum interstory displacement is chosen as a new "adopted model" by using a sensitivity-based method.

④ Update the critical ground motion in every P step for damper arrangement by using the SQP method.

⑤ Define the final "adopted model" as the "optimal placement model".

The flow chart and conceptual diagram are shown in **Figure 2**.

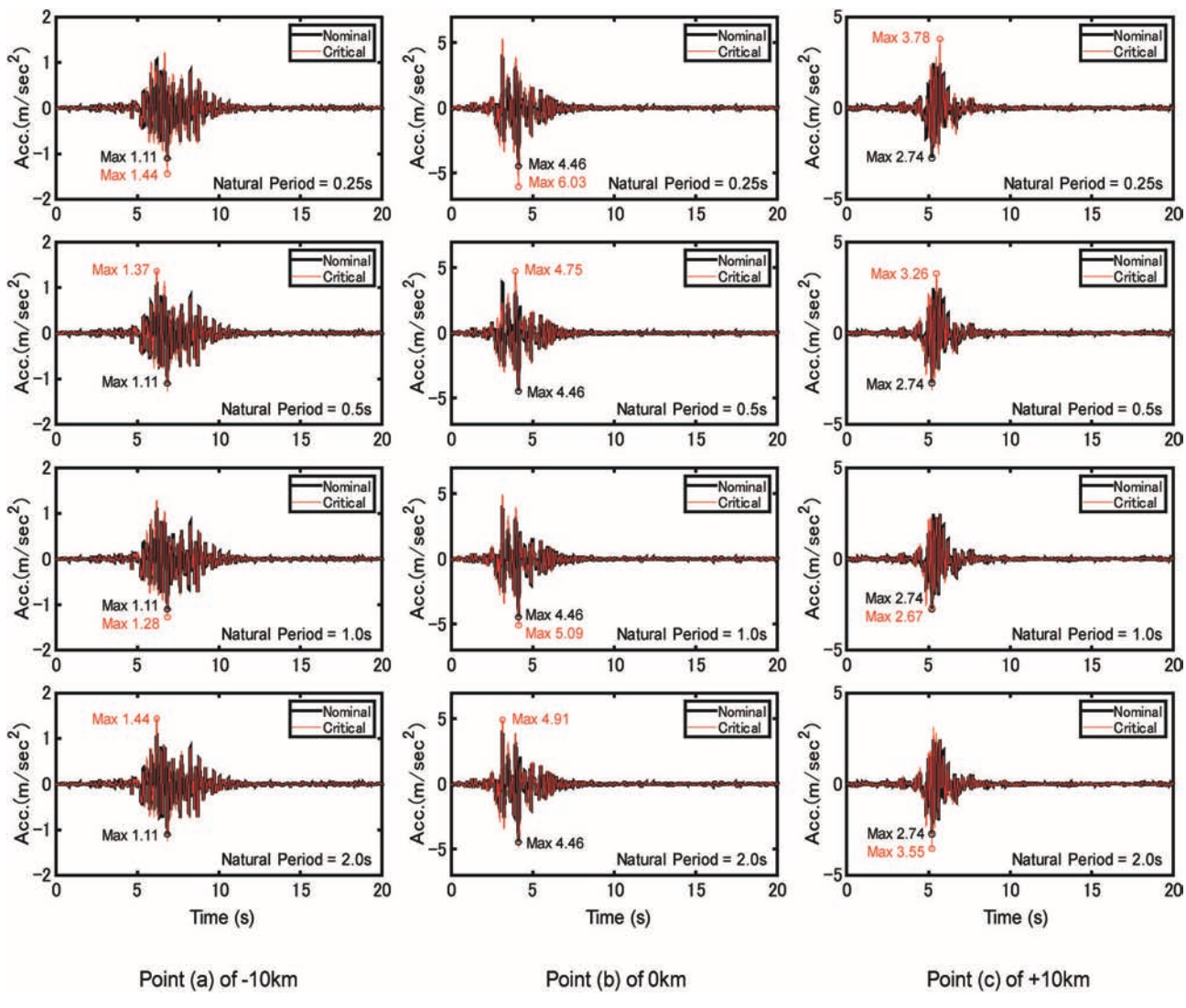

FIGURE 7 | Nominal and critical ground surface accelerations of four MDOF models with different number of stories ($T_1 = 0.25\,s$, $0.5\,s$, $1.0\,s$, $2.0\,s$) at three points (Straight lowest natural mode).

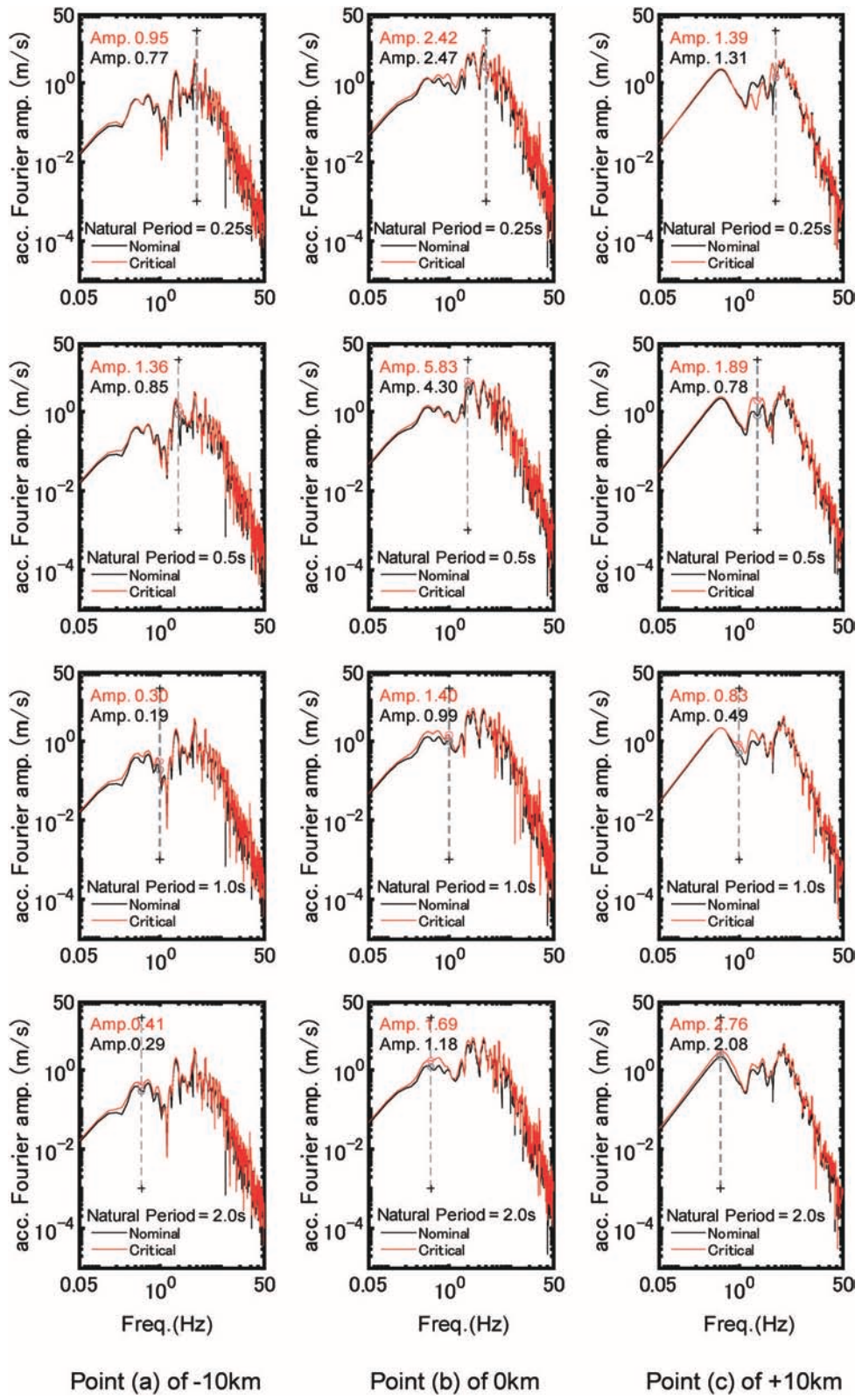

FIGURE 8 | Fourier amplitude spectra of nominal and critical ground surface accelerations of four MDOF models with different number of stories ($T_1 = 0.25\,s, 0.5\,s, 1.0\,s, 2.0\,s$) at three points (Straight lowest natural mode).

NUMERICAL EXAMPLES

Fault Model, Soil Conditions, and Recording Points

The model S21 in the benchmark test by Kato et al. (2011) was used for verification of accuracy and reliability of the method for ground motion generation employed in the present paper. The result of the verification is shown in Makita et al. (2018b). While the benchmark test uses an empirical envelope function of acceleration time histories, the method used in Makita et al. (2018b) and this paper employs the phase difference method for expressing the phase. Since the same fault model is used in the present paper, the fault model, soil conditions, and recording points are explained here again.

The fault plane and three recording points used in the reference (Kato et al., 2011) are shown in **Figure 3**. The number of fault elements (N_L, N_W) follows (Kato et al., 2011). Several convergence investigations on the number of fault elements were done in the previous research (Irikura, 1994; Kato et al., 2011) together with the consideration of reasonable analysis time. The well-known scaling law (Irikura, 1983; Makita et al., 2018b) provides the suggestion on the selection of N_L, N_W, N_D. It seems interesting to investigate how the critical fault distribution can be affected by the number of fault elements. However, this requires further computation which cannot be achieved in the framework of the present paper. This investigation will be conducted in the future. The recording points are three points (a), (b), (c). The point (b) corresponds to the epicenter. It is assumed that the

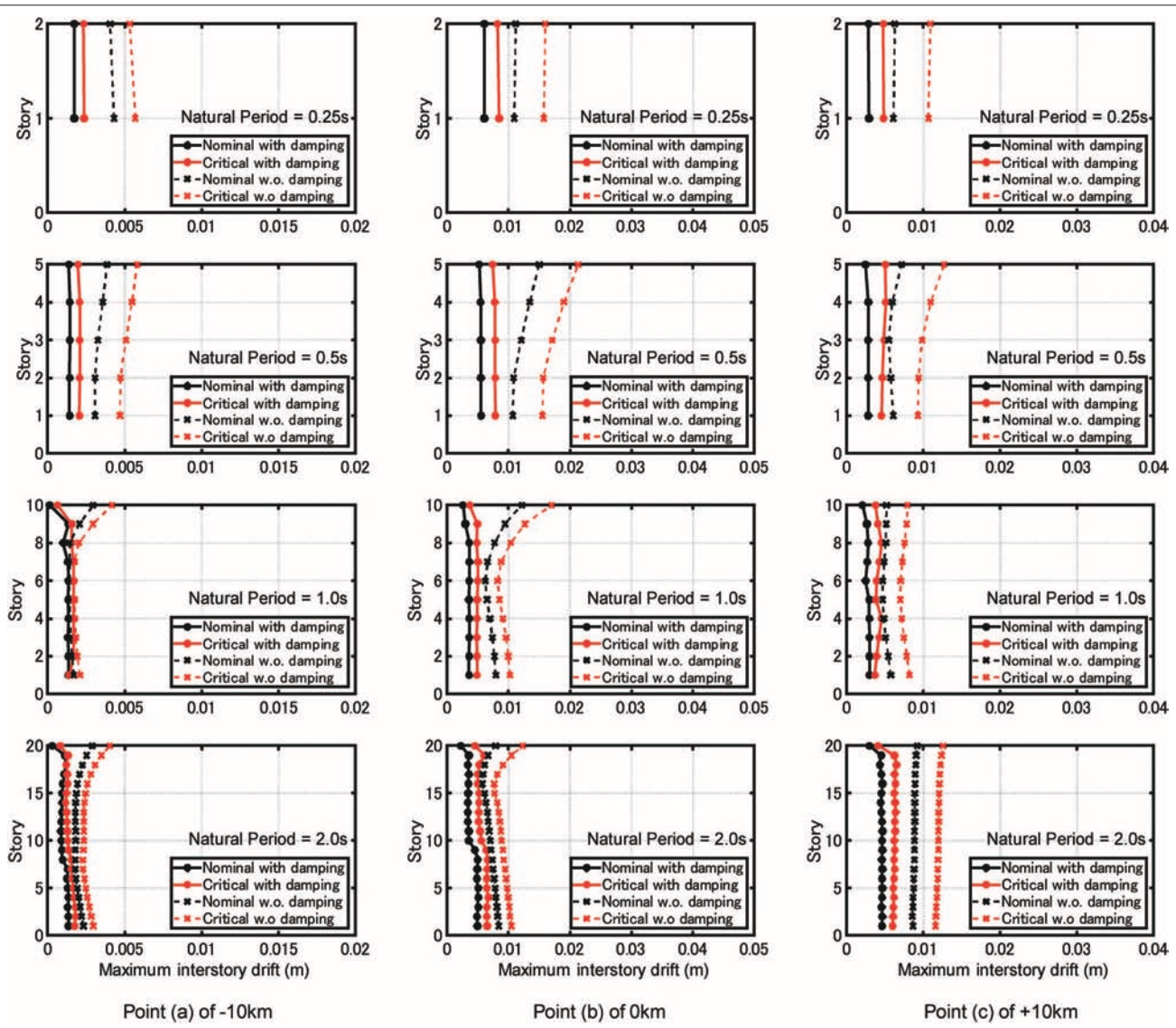

FIGURE 9 | Nominal and critical maximum interstory drift distributions of four MDOF models with different number of stories ($T_1 = 0.25\,s$, $0.5\,s$, $1.0\,s$, $2.0\,s$) at three points (Straight lowest natural mode).

fault plane is vertical and the fault type is the right-lateral strike-slip fault. The detailed fault parameters are as follows: the fault length = 8,000 m, width = 4,000 m, slip = 1 m, seismic moment $=M_0 = 1.04 \times 10^{18} Nm$, strike, dip, and rake angles are $\theta = 90^\circ$, $\delta = 90^\circ$, and $\lambda = 180^\circ$, respectively. The hypocenter is located at the point (0, 1,000 m, 4,000 m) and the fault rupture propagates concentrically with rupture velocity $V_r = 3,000$ (m/s). The hypocenter of each sub-fault is assumed to be located at its center.

Following the investigations by Somerville et al. (1999), Eshelby (1957), and Brune (1970), it is assumed that the stress drop $\Delta\sigma$ of large earthquakes and the corner frequency f_c are given by the following equations:

$$\Delta\sigma = \frac{7}{16}\frac{M_0}{R^3} \times 10^{-14} \tag{15}$$

$$f_c = 4.9 \cdot 10^6 V_s \left(\frac{\Delta\sigma}{M_0}\right)^{1/3} \tag{16}$$

where R (km) is the effective radius of the fault ($S = \pi R^2$, S : fault area). In these equations, the unit of V_s is km/s, that of $\Delta\sigma$ is bar and that of M_0 is dyne-cm.

From Equations (15), (16), $\Delta\sigma = 13.95$ (Mpa) and $f_c = 0.404$ (Hz) are derived. In this case, $\tau = 2/f_c \approx 5.0$ (s) is obtained from Boore (1983). The soil conditions are shown in **Table 1A** and the amplification of ground motion is described by one-dimensional wave propagation theory.

The division of the fault plane is $N_W \times N_L$, i.e., $N_W = 4$: fault width direction and $N_L = 8$: fault length direction. The area of sub-fault is given by $S_S = 1\,(\mathrm{km}^2)$. The seismic moment in each fault element (M_{0S}) is 5.40×10^{15}Nm and the stress drop ($\Delta\sigma_S$) in each fault element is assumed to be 13.95 (Mpa). The slip D_S of each sub-fault is given by 0.167 (m) from $M_{0S} = \mu S_S D_S$ and $N_D = 6$ from the ratio of fault plane to sub-fault (1 m/0.167 m). The seismic moment after superimposing the small earthquakes (M_0') is calculated as $M_0' = N_W \cdot N_L \cdot N_D \cdot M_{0S} \approx 1.04 \times 10^{18}$ (Nm), which is the same as M_0. The corner frequency $f_{cS} = 2.33$ Hz (Equation 16). As for the phase angle, the standard deviation of phase differences (σ_{ij}/π) are obtained from Equation (10) and its mean μ/π in each point is given by -0.140 at Point (a), -0.125 at Point (b) and -0.130 at Point (c). It is assumed that the horizontal component of superimposing wave is considered and only the SH wave is generated. Each small earthquake is produced by disassembling into the

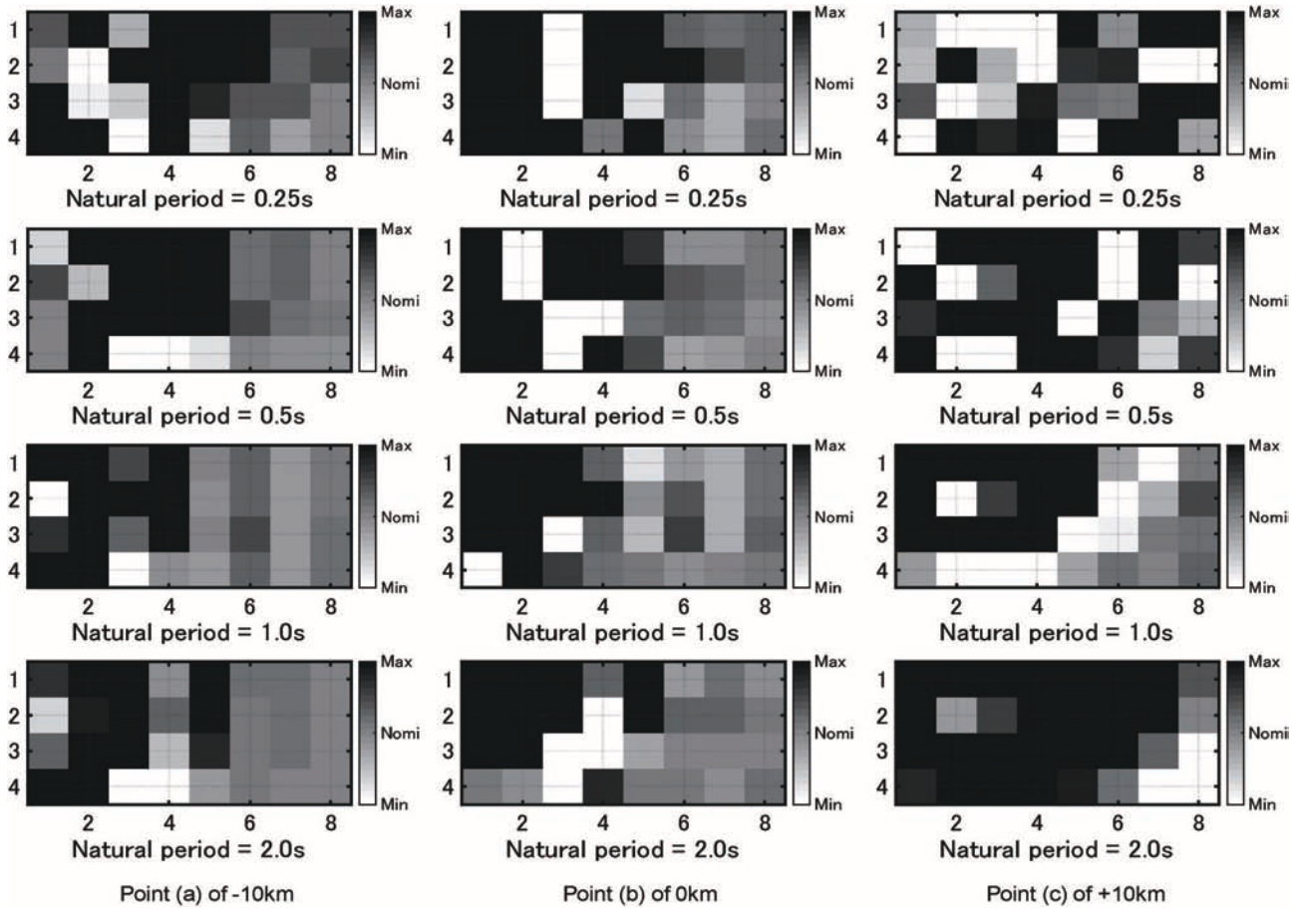

FIGURE 10 | Critical fault slip distribution of four MDOF models with different number of stories ($T_1 = 0.25s$, $0.5s$, $1.0s$, $2.0s$) at three points (Straight lowest natural mode).

NS direction component and the EW direction component. **Table 1B** indicates the source parameters of the fault plane and sub-faults.

It seems interesting to investigate the relation between the number of slips N_D and the number of fault elements and the balance between the slips size and the elements size as well as between them and the slip initiation and rise times (Irikura, 1994; Kato et al., 2011). If necessary, the influence of the introduction of re-division of fault elements may be possible by using the condition on the expressibility of fault rupture processes (Irikura, 1994; Kato et al., 2011). However, these requires further computation which cannot be achieved in the framework of the present paper.

Setting of Uncertain Fault Slip Distribution

Let regard the fault slip distribution **D** as a set of uncertain parameters. If the nominal value of **D**, the base quantities of variation of **D** (toward decreasing side and increasing side) and the degree of variability are denoted by ${D_{ij}}^C$, $\Delta \underline{D}_{ij}$, $\Delta \bar{D}_{ij}$, and α, the interval parameter expression can be given by

$$\mathbf{D}^I = \left\{ \left[{D_{ij}}^C - \alpha \Delta \underline{D}_{ij}, {D_{ij}}^C + \alpha \Delta \bar{D}_{ij} \right] \right\} \quad \left(i = 1, \cdots NW,\ j = 1, \cdots NL \right) \tag{17}$$

In this paper, $\alpha = 0.3$, $\Delta \underline{D}_{ij} = \Delta \bar{D}_{ij} = {D_{ij}}^C$ are given.

Setting of Building Structures

A shear-type building structure is employed as the super building model. 2-, 5-, 10-, and 20-story buildings are considered. The floor mass, fundamental natural period, structural damping ratio and total added damping coefficient are shown in **Table 2**. The total damping coefficient corresponds approximately to the damping ratio 0.2. Three story stiffness distributions are treated, i.e., model with straight lowest natural mode, model with trapezoidal stiffness distribution, model with uniform stiffness distribution. These story stiffness distributions are shown in **Figure 4**.

Computational Time Saving by Skipping the Procedure for Updating Critical Fault Slip Distribution and Its Accuracy Verification

The sequential quadratic programming method for the problem of critical fault slip and the sensitivity-based method for the problem of optimal damper placement are time-consuming. Especially, the sequential quadratic programming method for the problem of critical fault slip needs a lot of computational time. Therefore, a method for reducing the computational load is desired. For this purpose, a method of skipping some steps for updating the critical fault slip in simultaneous analysis of critical fault slip and optimal damper placement is proposed here which was explained in **Figure 2**.

Figure 5 shows the influence of number of skipped steps on the results of the 10-story MDOF model with straight lowest natural mode. **Figure 5A** indicates accelerations of ground motions for four numbers of skipped steps (1, 5, 10, 20) and **Figure 5B** presents the maximum interstory drift. In these figures, the nominal case and critical case are treated. In **Figure 5B**, both the model with damping and the model without damping are investigated. It can be observed that no obvious difference can be seen in case that the number of skipped steps is smaller than 20. This means that the number of skipped steps smaller than 20 can save the computational time without deterioration of accuracy.

Figure 6 shows the computational analysis time for four numbers of skipped steps. The computer system is CPU: Core

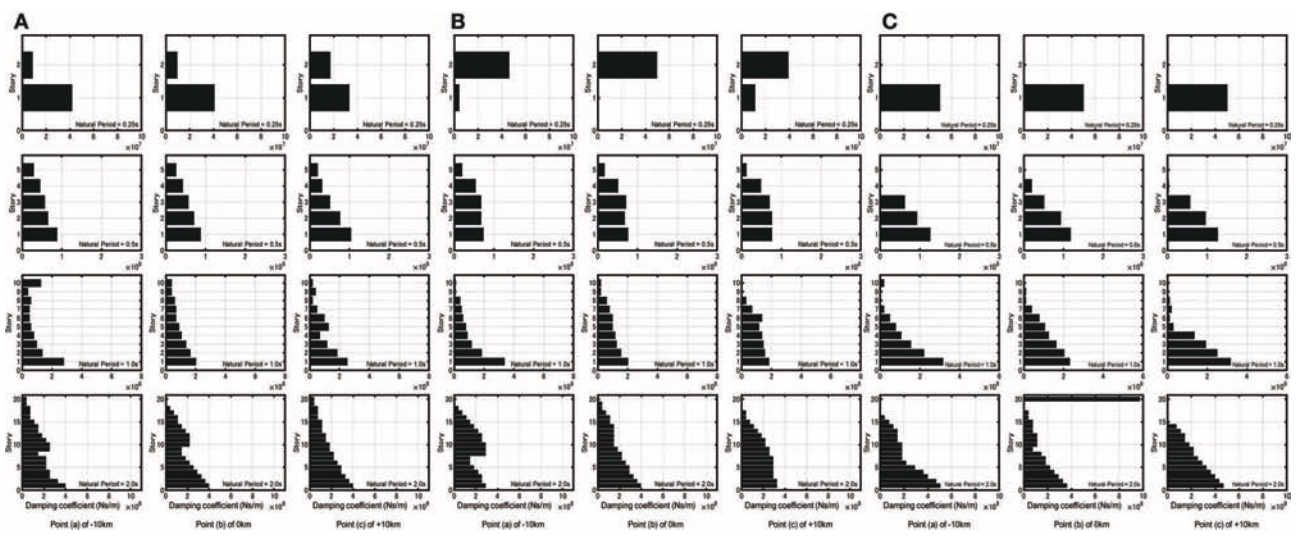

FIGURE 11 | Critical damping coefficient distributions of four MDOF models with different number of stories ($T_1 = 0.25\,s$, $0.5\,s$, $1.0\,s$, $2.0\,s$) at three points. **(A)** Model with straight lowest natural mode. **(B)** Model with trapezoidal stiffness distribution. **(C)** Model with uniform stiffness distribution.

i5-6500 (3.2 GHz), RAM: 32.0 GB (DDR4-2132), OS: Windows 10 Pro (64 bit). It can be found that remarkable reduction of analysis time is possible by skipping some steps for updating the critical fault slip. For example, in the case where the fault rupture distribution is fixed (uncertainty level $\alpha = 0$ in the robustness function analysis explained later), the computational time only for optimization with respect to viscous damper distribution is 3 min. This is 1/14 of the overall computational time (43 min in **Figure 6** for 20 skipped steps) including the robustness function analysis ($\alpha = 0, 0.1, 0.2, 0.3$).

Analysis Results

Figure 7 shows the nominal and critical ground surface accelerations of four MDOF models with different number of stories, 2, 5, 10, 20 [fundamental natural period, $T_1 = 0.25, 0.5, 1.0, 2.0$ (s)] at three points (a), (b), (c) (stiffness distribution: Straight lowest natural mode). It can be observed that the ground motion accelerations corresponding to the critical case are larger than those corresponding to the nominal case. The same observation was found for other models (trapezoidal stiffness distribution, uniform stiffness distribution).

Figure 8 presents the Fourier amplitude spectra of nominal and critical ground surface accelerations of four MDOF models with different number of stories, 2, 5, 10, 20 [$T_1 = 0.25, 0.5, 1.0, 2.0$ (s)] at three points (Straight lowest natural mode). It can also be observed that the Fourier amplitudes of ground motion accelerations corresponding to the critical case are larger than those corresponding to the nominal case.

Figure 9 indicates the nominal and critical maximum interstory drift distributions of four MDOF models with different number of stories, 2, 5, 10, 20 [$T_1 = 0.25, 0.5, 1.0, 2.0$ (s)] at three points (Straight lowest natural mode). For comparison, the cases without damper and with damper are shown. It can be found that the viscous dampers are extremely effective for the response reduction and the larger maximum interstory drifts in upper stories are well-reduced by the effect of viscous dampers. The structural response (interstory drift) at the point (b) (above the fault plane) is the maximum with an exception. Therefore, the optimal damper distribution for the point (b) is recommended only from the present result. Of course, when this distribution is adopted for other points (a), (c), the responses will become larger than those obtained for the model with the respective optimal damper distribution. On the other hand, if the optimal damper distribution adopted for the point (a) or (c) is used for the model at the point (b), the maximum interstory drift becomes larger than that evaluated for the optimal damper distribution determined for the point (b). This indicates the preference of selection of the optimal damper distribution at the point (b). Further investigation will be necessary to search the best damper distribution for guaranteeing the response constraints at all the points.

Figure 10 shows the critical fault slip distribution of four MDOF models with different number of stories, 2, 5, 10, 20 [$T_1 = 0.25, 0.5, 1.0, 2.0$ (s)] at three points (Straight lowest natural mode). It can be understood that, in the critical case, the large slips are concentrated to the upper side of the fault plane which is near to the recording point.

Figure 11A presents the critical damping coefficient distributions of four MDOF models with different number of stories, 2, 5, 10, 20 [$T_1 = 0.25, 0.5, 1.0, 2.0$ (s)] at three points (Building model: Straight lowest natural mode). Similarly,

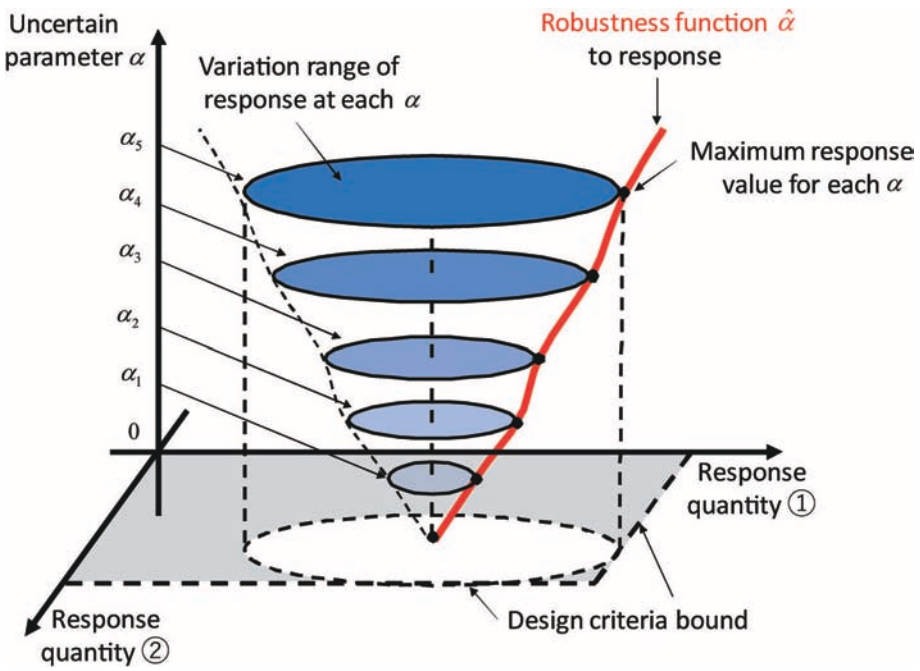

FIGURE 12 | Robustness function $\hat{\alpha}$ for various uncertainty levels.

Figure 11B indicates those for the building model with trapezoidal stiffness distribution and **Figure 11C** shows those for the building model with uniform stiffness distribution. It can be found that the damping coefficients are generally concentrated to the stories exhibiting larger maximum interstory drifts, i.e., the upper part for the model with straight lowest natural mode, the middle part for the model with trapezoidal stiffness distribution, the lower part for the model with uniform stiffness distribution. However, some exceptions exist in 2-story models. Because of the space problem (number of figures), the distribution of the maximum interstory drifts is shown in **Figure 9** only for the model with straight lowest natural mode. However,

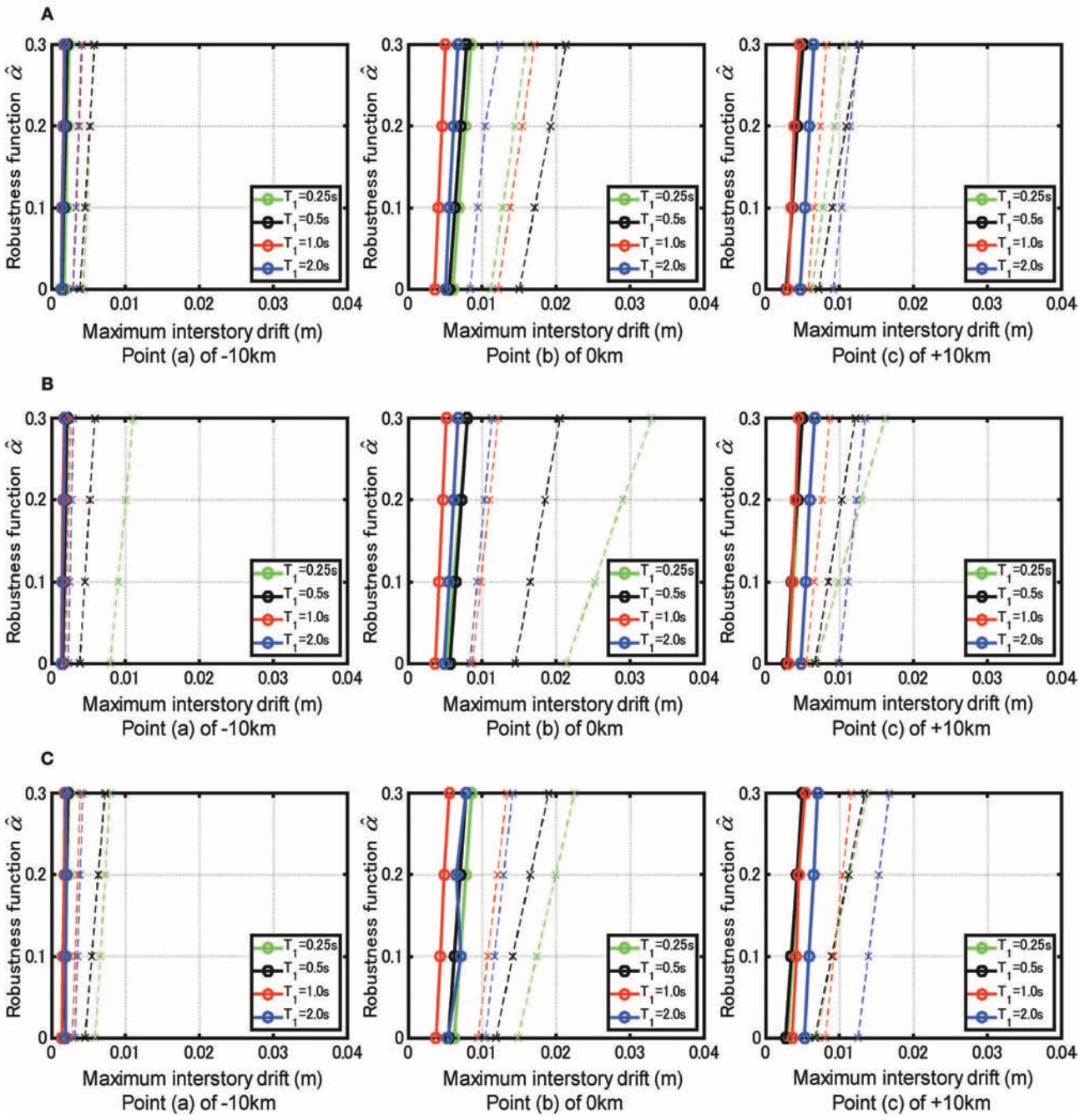

FIGURE 13 | Robustness function $\hat{\alpha}$ with respect to the maximum interstory drift of four MDOF models with different numbers of stories ($T_1 = 0.25\,s, 0.5\,s,$ $1.0\,s,\ 2.0\,s$) at three points. **(A)** Model with straight lowest natural mode. **(B)** Model with trapezoidal stiffness distribution. **(C)** Model with uniform stiffness distribution (solid line: with damper, broken line: without damper).

the distribution of the maximum interstory drifts has been derived also for the models with trapezoidal stiffness distribution and with uniform stiffness distribution. These distributions demonstrate the conclusion derived just above.

Robustness Evaluation for Uncertain Fault Slip Distribution Using Robustness Function

To evaluate the robustness of building structures for uncertain fault slip distribution, the robustness function proposed by Ben-Haim (2006) is used. Let f_c, $\mathbf{x}^I$, $\mathbf{x}(\alpha)$ denote the specified limit value of the maximum interstory drift, the interval parameters (fault slip distribution **D**) and the admissible fault slip distribution for a specified uncertainty level α. $\mathbf{x}(\alpha)$ is defined in Equation (17). The robustness function can be expressed by

$$\hat{\alpha}(\overline{\mathbf{x}}, f_c) = \max\left\{\alpha \;\middle|\; \max\left\{f(\mathbf{x}^I)|\mathbf{x}^I \in \mathbf{x}(\alpha)\right\} < f_c\right\} \qquad (18)$$

where over-bar denotes the nominal parameter. The conceptual diagram of the robustness function $\hat{\alpha}$ for various uncertainty levels is shown in **Figure 12**.

Figure 13A shows the robustness function $\hat{\alpha}$ with respect to the maximum interstory drift of the MDOF model with straight lowest natural mode for uncertain fault slip. These figures show the results for three recording points (a), (b), (c). Once the value $\hat{\alpha}$ in the vertical axis is fixed, the corresponding maximum interstory drift of the MDOF model in the horizontal axis indicates the maximum value for varied possible uncertain parameters (quantity of fault rupture slip) prescribed by $\hat{\alpha}$. It can be observed that the robustness becomes the smallest for the model at Point (b) (epicenter). This is because the response of the MDOF model is the largest at Point (b). The slope of the robustness function indicates the degree of the robustness. As the slope becomes steeper, the model becomes more robust (this indicates that the structural response is insensitive to change of fault rupture slip).

Figure 13B presents similar ones for the model with trapezoidal stiffness distribution and **Figure 13C** indicates those for the model with uniform stiffness distribution.

Since the robustness is closely related to the resilience, the presented method using the robustness function seems useful for the evaluation of resilience of buildings against uncertain fault slip distribution.

CONCLUSIONS

The uncertainty in the fault rupture slip was taken as a main source of uncertainty in the present paper and the critical fault rupture slip distribution producing the maximum structural response was found by using the stochastic Green's function method as a generator of ground motions. A multi-degree-of-freedom (MDOF) building structure was introduced as a model structure and an optimal damper placement problem was investigated for the critical ground motion. The main feature of this paper is the simultaneous treatment of the critical fault rupture slip distribution problem and the optimal damper placement problem. The sequential quadratic programming method was used in the problem of critical fault rupture slip distributions and a sensitivity-based method was introduced in the optimal damper placement problem. The robustness for the maximum interstory drift in MDOF building structures under the uncertainty in fault rupture slip distributions was presented for resilient building design by using the robustness function. The main results obtained in this paper may be summarized as follows.

(1) The ground motion accelerations corresponding to the critical case are larger than those corresponding to the nominal case. This can also be confirmed from the Fourier amplitudes of ground motion accelerations.
(2) In the critical case, the large slips are concentrated to the upper side of the fault plane which is near to the recording point.
(3) The ground surface acceleration at the epicenter becomes larger than that at other recording point. The maximum interstory drift of the super building at the epicenter also exhibits the largest value.
(4) Since the sequential quadratic programming method for the problem of critical fault slip and the sensitivity-based method for the problem of optimal damper placement are time-consuming, update of the critical fault slip distribution in each step of optimal damper placement may be unreasonable. Remarkable reduction of analysis time is possible by skipping some steps for updating the critical fault slip distribution.
(5) The viscous dampers are extremely effective for the response reduction and the larger maximum interstory drifts in upper stories are well-reduced by the effect of viscous dampers. The optimal damper distribution exhibits different properties depending on the stiffness distribution of super buildings. Large damper quantities are allocated to the stories exhibiting large interstory drifts, although some exceptions exist in two-story models. However, the point, at which the building is set, does not affect so much the optimal damper distribution.
(6) From the relation of the robustness function with the maximum interstory drift, the designers can find the level of potential robustness with respect to uncertain parameters for a specified level of the maximum interstory drift.

Even in the case where linear viscous dampers are used, the simultaneous extremization with respect to fault rupture distribution and viscous damper distribution requires many computational cycles and time. Therefore, the extension to non-linear viscous dampers appears to be the next step of research.

DATA AVAILABILITY STATEMENT

All datasets generated for this study are included in the manuscript/supplementary files.

AUTHOR CONTRIBUTIONS

KK formulated the problem, conducted the computation, and wrote the paper. IT supervised the research and wrote the paper.

FUNDING

Part of the present work was supported by KAKENHI of Japan Society for the Promotion of Science (Nos. 17K18922, 18H01584). This support was greatly appreciated.

REFERENCES

Abrahamson, N., Ashford, S., Elgamal, A., Kramer, S., Seible, F., and Somerville, P. (1998). *Proceedings of the 1st PEER Workshop on Characterization of Special Source Effects* (San Diego, CA: Pacific Earthquake Engineering Research Center, University of California).

Ben-Haim, Y. (2006). *Info-Gap Decision Theory: Decisions Under Severe Uncertainty*, 2nd Edn. London: Academic Press.

Boore, D. M. (1983). Stochastic simulation of high-frequency ground motions based on seismological models of the radiated spectra. *Bull. Seism. Soc. Am.* 73, 1865–1894.

Bouchon, M. (1981). A simple method to calculate Green's functions for elastic layered media. *Bull. Seism*. Soc. *Am.* 71, 959–971.

Brune, J. N. (1970). Tectonic stress and the spectra of seismic shear waves from earthquakes. *J. Geophys. Res.* 75, 4997–5009. doi: 10.1029/JB075i026p04997

Cotton, F., Archuleta, R., and Causse, M. (2013). What is sigma of the stress drop? *Seism. Res. Lett.* 84, 42–48. doi: 10.1785/0220120087

Day, S. M. (1982). Three-dimensional finite difference simulation of fault dynamics: rectangular fault with fixed rupture velocity. *Bull. Seism. Soc. Am.* 72, 83–96.

Domenico, D. D., Ricciardi, G., and Takewaki, I. (2019). Design strategies of viscous dampers for seismic protection of building structures: a review. *Soil Dyn. Earthquake Eng.* 118, 144–165. doi: 10.1016/j.soildyn.2018.12.024

Drenick, R. F. (1970). Model-free design of aseismic structures. *J. Eng. Mech. Div. ASCE* 96, 483–493.

Eshelby, J. D. (1957). The determination of the elastic field of an ellipsoidal inclusion and related problems. *Proc. R. Soc. A* 241, 376–396. doi: 10.1098/rspa.1957.0133

Fukumoto, Y., and Takewaki, I. (2017). Dual control high-rise building for robuster earthquake performance. *Front. Built Environ.* 3:12. doi: 10.3389/fbuil.2017.00012

Hisada, Y. (2008). Broadband strong motion simulation in layered half-space using stochastic Green's function technique. *J. Seismol.* 12, 265–279. doi: 10.1007/s10950-008-9090-6

Hisada, Y., and Bielak, J. (2003). A theoretical method for computing near-fault ground motions in layered half-spaces considering static offset due to surface faulting with a physical interpretation of fling step and rupture directivity. *Bull. Seism. Soc. Am.* 93, 1154–1168. doi: 10.1785/0120020165

Irikura, K. (1983). Semi-empirical estimation of strong ground motions during large earthquakes. *Bull. Disast. Prev. Res. Inst. Kyoto Univ*. 33, 63–104.

Irikura, K. (1986). "Prediction of strong acceleration motions using empirical Green's function," in *Proceedings of the 7th Japan Earthquake Engineering Symposium* (Tokyo), 151–156.

Irikura, K. (1994). Earthquake source modeling for strong motion prediction. *J. Seism. Soc. Jap. Second Ser.* 46, 495–512. doi: 10.4294/zisin1948.46.4_495

Kasagi, M., Fujita, K., Tsuji, M., and Takewaki, I. (2016). Automatic generation of smart earthquake-resistant building system: hybrid system of base-isolation and building-connection. *Heliyon* 2:2. doi: 10.1016/j.heliyon.2016.e00069

Kato, K., Hisada, Y., Kawabe, H., Ohno, S., Nozu, A., Nobata, A., et al. (2011). Benchmark tests for strong ground motion prediction methods: case for stochastic Green's function method (Part1). *J. Technol. Design* 17, 49–54. doi: 10.3130/aijt.17.49

Lawrence Livermore National Laboratory (2002). *Guidance for performing Probabilistic Seismic Hazard Analysis for a Nuclear Plant Site: Example Application to the Southeastern United States*. NUREG/CR-6607, UCRL-ID-133494.

Makita, K., Kondo, K., and Takewaki, I. (2018b). Critical ground motion for resilient building design considering uncertainty of fault rupture slip. *Front. Built Environ.* 4:64. doi: 10.3389/fbuil.2018.00064

Makita, K., Kondo, K., and Takewaki, I. (2019). Finite difference method-based critical ground motion and robustness evaluation for long-period building structures under uncertainty in fault rupture. *Front. Built Environ.* 5:2. doi: 10.3389/fbuil.2019.00002

Makita, K., Murase, M., Kondo, K., and Takewaki, I. (2018a). Robustness evaluation of base-isolation building-connection hybrid controlled building structures considering uncertainties in deep ground. *Front. Built Environ.* 4:16. doi: 10.3389/fbuil.2018.00016

Morikawa, N., Kanno, T., Narita, A., Fujiwara, H., Okumura, T., Fukushima, Y., et al. (2008). Strong motion uncertainty determined from observed records by dense network in Japan. *J. Seismol.* 12, 529–546. doi: 10.1007/s10950-008-9106-2

Murase, M., Tsuji, M., and Takewaki, I. (2013). Smart passive control of buildings with higher redundancy and robustness using base-isolation and inter-connection. *Earthquakes Struct.* 4, 649–670. doi: 10.12989/eas.2013.4.6.649

Murase, M., Tsuji, M., and Takewaki, I. (2014). Hybrid system of base isolation and building connection for control robust for broad type of earthquake ground motions. *J. Struct. Eng.* 60B, 413–422.

Nickman, A., Hosseini, A., Hamidi, J. H., and Barkhordari, M. A. (2013). Reproducing fling-step and forward directivity at near source site using of multi-objective particle swarm optimization and multi taper. *Earthquake Eng. Eng. Vibration* 12, 529–540. doi: 10.1007/s11803-013-0194-9

Somerville, P., Irikura, K., Graves, R., Sawada, S., Wald, D., Anderson, N., et al. (1999). Characterizing crustal earthquake slip models for the prediction of strong ground motion. *Seism. Res. Lett.* 70, 59–80. doi: 10.1785/gssrl.70.1.59

Takewaki, I. (2007). *Critical Excitation Methods in Earthquake Engineering*, 2nd edition. London: Elsevier.

Wennerberg, L. (1990). Stochastic summation of empirical Green's functions. *Bull. Seism. Soc. Am.* 80, 1418–1432.

Yamane, T., and Nagahashi, S. (2008). "A generation method of simulated earthquake ground motion considering phase difference characteristics," in *Proceedings of the 14th World Conference on Earthquake Engineering* (Beijing).

Yokoi, T., and Irikura, K. (1991). Empirical green's function technique based on the scaling law of source spectra. *J. Seism. Soc. Jap. Second Ser.* 44, 109–122. doi: 10.4294/zisin1948.44.2_109

Yoshimura, C., Bielak, J., Hisada, Y., and Fernandez, A. (2003). Domain reduction method for three-dimensional earthquake modeling in localized regions, part II: verification and applications. *Bull. Seism. Soc. Am.* 93, 825–840. doi: 10.1785/0120010252

Conflict of Interest: The authors declare that the research was conducted in the absence of any commercial or financial relationships that could be construed as a potential conflict of interest.

The reviewer DD declared a past co-authorship with one of the authors IT to the handling editor.

frontiers in Built Environment

ORIGINAL RESEARCH
published: 13 November 2019
doi: 10.3389/fbuil.2019.00132

Hybrid Passive Control Strategies for Reducing the Displacements at the Base of Seismic Isolated Structures

Alberto Di Matteo[1]*, *Chiara Masnata*[1] and *Antonina Pirrotta*[1,2]

[1] Dipartimento di Ingegneria Civile, Ambientale, Aerospaziale, dei Materiali, Università degli Studi di Palermo, Palermo, Italy,
[2] Department of Mathematical Sciences, University of Liverpool, Liverpool, United Kingdom

In this paper, the use of hybrid passive control strategies to mitigate the seismic response of a base-isolated structure is examined. The control performance of three different types of devices used for reducing base displacements of isolated buildings is investigated. Specifically, the Tuned Mass Damper (TMD), the New Tuned Mass Damper (New TMD) and the Tuned Liquid Column Damper (TLCD), each one associated to a Base Isolated structure (BI), have been considered. The seismic induced vibration control of base-isolated structures equipped with the TMD, New TMD or the TLCD is examined and compared with that of the base-isolated system without devices, using real recorded seismic signals as external input. Data show that the New TMD is the most effective in controlling the response of base-isolated structures so that it can be considered as a practical and appealing means to mitigate the dynamic response of base-isolated structures.

Keywords: hybrid structural control, base isolation, optimal design, tuned mass damper, inerter

OPEN ACCESS

Edited by:
Dario De Domenico,
University of Messina, Italy

Reviewed by:
Said Elias Rahimi,
University of Iceland, Iceland
Qinhua Wang,
Shantou University, China

***Correspondence:**
Alberto Di Matteo
alberto.dimatteo@unipa.it

Specialty section:
This article was submitted to Earthquake Engineering, a section of the journal Frontiers in Built Environment

Received: *31 July 2019*
Accepted: *24 October 2019*
Published: *13 November 2019*

Citation:
Di Matteo A, Masnata C and Pirrotta A (2019) Hybrid Passive Control Strategies for Reducing the Displacements at the Base of Seismic Isolated Structures. Front. Built Environ. 5:132. doi: 10.3389/fbuil.2019.00132

INTRODUCTION

In the context of passive vibration control, the base isolation (BI) is recognized as a valid strategy in preserving buildings from damage and collapse due to earthquakes, especially for those structures located in high hazard seismic areas and with strategic importance.

Undoubtedly, one of the advantages deriving from the installation of seismic isolators is the considerable reduction of the inter-story drift which leads to a quasi-rigid motion of the superstructure.

The effectiveness of the base isolation technique motivated many researchers to focus on its optimization limiting its detrimental features. Specifically, particular attention should be paid in a design phase to the displacements which elastomeric bearings can be subjected to. In this regard, these devices can undergo considerable deformations because of their low lateral stiffness; accordingly, some issues could arise: large displacements could cause adjacent buildings to collide; further, the need to adapt utilities and connection systems at the interface between the super-structure and the sub-structure should be considered; and finally, irreversible damage could occur in the isolators that lose their functionality.

Among several alternatives analyzed in literature for improving BI system performance, one is related to the addition of some linear viscous dampers to the BI system, or to the increase of its damping (Kelly, 1990, 1999). However, although it has been demonstrated that higher values of damping in the BI system lead to smaller deformations at the base, other drawbacks, such as the increase of both inter-story drifts and floor accelerations of the main structure, may arise (Kelly, 1999).

The idea to combine the BI system with other types of passive control systems, generally used individually in a unique control system, was proposed in Yang et al. (1991), where a structure isolated by rubber bearings and equipped with a Tuned Mass Damper placed on the base has been considered. Further, the effectiveness of such hybrid strategy has been demonstrated on the basis of numerical analysis carried out on a 20-DOFs building.

Notably, this idea arose by observing essentially two phenomena:

- through the installation of the isolation system, the frequency of total structure drops and the structure is dominated mainly by only one mode shape.
- the Tuned Mass Dampers (TMDs) reliability on suppressing structural vibrations and preventing resonance behavior in structures characterized by a prevalent vibration mode (Den Hartog, 1956).

In this regard, the coupling between the base isolation and the Tuned Mass Damper (BI+TMD) was also analyzed in Palazzo and Petti (1994, 1999), where the validity of this system in limiting the deformations at the base has been proved.

The factors influencing the performance of the TMD on the structural response of base isolated structures, such as the input frequency, the choice of the optimum tuning frequency and the damping ratio of the TMD, have been investigated in Tsai (1995). Specifically, it has been demonstrated that TMDs increase the damping of the total structure and consequently the response after the first seconds of the seismic input. In order to attenuate the structural response during the first phase of excitation, the concept of a possible efficient accelerated TMD has been proposed, but it remained only a mathematical suggestion, hardly to be realized.

As far as the position of the TMD is concerned, the effect of varying the placement of the TMD on different floor levels has been studied in Stanikzai et al. (2019) and it has been found that for low-rise buildings, the placement of TMD mass has no significant role in reducing the response of the buildings.

The need to consider larger masses to improve the efficiency of the TMD has led to consider the possibility to place multiple TMDs (MTMDs) or distributed MTMDs (d-MTMDs) along the height of buildings (Stanikzai et al., 2018). The use of multiple TMDs can represent a more robust solution also when variation of soil parameters is taken into account in the soil-structure interaction. Indeed, as demonstrated in Elias and Matsagar (2017) for the case of the combination of the TMDs with base isolated bridges, the soil type can affects the performance of the TMD, and the installation of multiple TMDs compared to a single TMD, are more effective in controlling the structural response.

Furthermore, as demonstrated in Stanikzai et al. (2018), the use of MTMDs or d-MTMDs represents an effective solution to tune the devices to higher modal frequencies too, and in order to avoid detuning effects of a single TMD with the main frequency of the structure.

However, in real cases, it could result more convenient to attach the TMD in correspondence of the level of the isolation system as detailed in Melkumyan (2012).

A practical implementation of the seismic base isolation in conjunction with a TMD, placed at the basement, to a real case study, has been examined in De Domenico and Ricciardi (2018a,b). Aiming at improving the seismic performance of a reinforced concrete building, it has been proposed to insert a TMD at the center of the basement of the building, built as a box filled with aggregate concrete, attached below the isolation floor. In this case, the role of the TMD damper and spring is supposed to be played by additional isolators which connect the TMD to the base, while the TMD is disconnected from the ground by means of sliding elements.

On this base, it can be clearly argued that the base displacement demand of isolated structure can be reduced through the use of a traditional TMD, depending on the TMD mass itself. Specifically, bigger TMD masses could lead to a greater reduction of the response of the seismic bearings.

On the other hand, the presence of a TMD on the basement may also yield some drawbacks which need to be considered: firstly, the big mass that should be added to the system; secondly, the TMD's stroke that should be taken into account in the design of the spaces for its location.

To deal with these limitations, some variants of the classic TMD have been studied; for instance, a TMD with non-linear characteristics has been proposed in Nissen et al. (1985), Natsiavas (1992), and Vakakis et al. (2003) and it has been demonstrated to be effective in minimizing deformations of the isolators despite the instability phenomena related to the non-linearities.

Another type of TMD, referred to as New TMD or non-traditional TMD, has been introduced by in Ren (2001), and in Cheung and Wong (2011) and Xiang and Nishitani (2014) the optimization of the New TMD combined with the base isolation (BI + New TMD) has been discussed.

Compared to the traditional TMD, the New TMD alters the position of the dampers. Specifically, in the New TMD, a dashpot is located between the TMD mass and the ground, rather than the TMD mass and the base of the BI system, as in a traditional TMD.

Notably, from a theoretical point of view, the installation of the New TMD involves higher dissipative forces and could attenuate the TMD stroke, consequently, it needs less space for its placing.

Among the strategies which couple passive control devices with base isolation systems, the BI + TMD and its variants are certainly the most investigated in the literature. In this context, an enhanced version of the TMD has been explored in De Domenico and Ricciardi (2018a,b) and references therein), and in De Angelis et al. (2019), by endowing the TMD with a mechanical device, called inerter, providing additional rotational inertia to the device. However, recently other solutions have been considered.

In this regard, Tuned Liquid Column Dampers (TLCDs) have been proposed as possible alternative to the TMD also in the field of hybrid control systems. Specifically, the TLCD, which consists of a U-shaped vessel filled with a certain amount of liquid, generally water, is placed on the base of the structure and, unlike TMDs, does not need mechanical components. Recently, some contributions regarding the TLCD optimization

and experimentation have been presented in Di Matteo et al. (2017a,b), where it has been shown that the effectiveness of the TLCD, if carefully designed, could be comparable or slightly lower than the TMD one. Moreover, compared to the TMD, the use of TLCDs is often preferable because of its easier installation. Further, it is cheaper and it could be employed as a water reserve in case of fire, so it represents an appealing and convenient solution.

Nevertheless, equations of motion of the TLCD may involve computationally expensive calculations due to the presence of non-linear terms and the identification of dynamic parameters that characterize this device is not so immediate.

In order to overcome these drawbacks, a simpler equivalent linear system has been introduced (Gao and Kwok, 1997; Chang, 1999; Yalla and Kareem, 2000; Wu et al., 2009), and the determination of the optimal design parameters has been studied by employing statistical linearization techniques (SLT) (Sakai et al., 1989; Di Matteo et al., 2017a,b).

Recently in Di Matteo et al. (2017a), a direct method has been developed to optimize the dynamic parameters of a TLCD attached to an isolated building, supposing a Gaussian white noise process as external input. Results derived from this approach show a good agreement with those obtained by applying the classical statistical linearization technique (SLT) which involves longer computational time (Roberts and Spanos, 1990).

On the base of this conspectus, this paper aims at comparing and investigating on the most promising strategy, among the main passive control devices coupled with the BI system, to minimize the base displacements of isolated buildings, preserving the benefits of the BI system (small inter-story drifts and accelerations).

Specifically, the analyzed hybrid systems (**Figure 1A**), are:

- BI + TMD (shown in **Figure 1B**);
- BI + New TMD (shown in **Figure 1C**);
- BI + TLCD (shown in **Figure 1D**).

In this study, the mass of each considered device is intended to be placed on the basement of isolated structure. To the best of the authors' knowledge, although several studies exist in the literature about the different types of the aforementioned absorbers, few of them consider the TLCD at the base of isolated structure and the comparison of such a device with the New TMD has not been analyzed.

In passing, it is noted that the term "New TMD" mentioned throughout the paper refers to the device proposed in Xiang and Nishitani (2014). Thus, no new device has been introduced in this paper, and readers interested on some specific insights on this control systems are referred to Xiang and Nishitani (2014) and references therein.

PROBLEM FORMULATION

In this section the equations of motion of all the exanimated systems (BI, BI + TMD, BI + New TMD, and BI + TLCD systems) in the time domain are presented, and relations in the frequency domain are also introduced. In particular, the displacement transfer functions, relating the base displacement of each system to the input force, have been determined for a full understanding of the dynamic behavior of all the systems.

BI System

Consider a BI plane frame structure, with n+1 *degrees of freedom*, excited by a horizontal earthquake ground acceleration $\ddot{x}_g(t)$ (**Figure 1A**). Let m_b, K_b, C_b denote mass, the stiffness and damping coefficient of the base isolation story in the BI model, assumed as a linear system. The displacement of mass m_b relative to the ground is denoted as $x_b(t)$. The superstructure has n degrees of freedom. The i^{th} superstructural degree of freedom has lumped mass M_i.

The corresponding displacement component $x_i(t)$ represents the superstructural displacement relative to the base. The total mass is:

$$M_{tot} = m_b + \sum_{i=1}^{n} M_i \tag{1}$$

In the time domain, the response of the isolated structure is governed by the following n+1 equations of motion:

$$\begin{cases} M_{tot}\ddot{x}_b(t) + \sum_{i=1}^{n} M_i\ddot{x}_i(t) + C_b\dot{x}_b(t) + K_b x_b(t) = -M_{tot}\ddot{x}_g(t) \\ M_i\ddot{x}_b(t) + M_i\ddot{x}_i(t) + \sum_{j=1}^{n} C_{i,j}\dot{x}_j(t) + \sum_{j=1}^{n} K_{i,j}x_j(t) = -M_i\ddot{x}_g(t) \end{cases} \tag{2}$$

$(i = 1, \ldots, n)$

In which $C_{i,j}$ and $K_{i,j}$ are the entries of the damping and stiffness matrices of the superstructure.

When dealing with a main structure having a Single Degree Of Freedom (SDOF), i.e., $n = 1$, the equations of motion are given by:

$$\begin{cases} \ddot{x}_b(t) + \mu_b\ddot{x}_1(t) + 2\omega_b\zeta_b\dot{x}_b(t) + {\omega_b}^2 x_b(t) = -\ddot{x}_g(t) \\ \ddot{x}_b(t) + \ddot{x}_1(t) + 2\omega_1\zeta_1\dot{x}_1(t) + {\omega_1}^2 x_1(t) = -\ddot{x}_g(t) \end{cases} \tag{3}$$

Where $\mu_b = M_1/M_{tot}$ represents the mass ratio; $\omega_b = \sqrt{k_b/M_{tot}}$ and $\zeta_b = C_b/(2\omega_b M_{tot})$ are the natural frequency and damping ratio of the base isolation system respectively; $\omega_1 = \sqrt{K_1/M_1}$ and $\zeta_1 = C_1/(2\omega_1 M_1)$ are the natural frequency and damping ratio of the SDOF main structure.

In the frequency domain, the Fourier transform of system (3) leads to:

$$\begin{cases} X_b(\omega)\left[-\omega^2 + 2i\omega\omega_b\zeta_b + {\omega_b}^2\right] = \omega^2\mu_b X_1(\omega) - X_g(\omega) \\ X_1(\omega)\left[-\omega^2 + 2i\omega\omega_1\zeta_1 + {\omega_1}^2\right] = \omega^2 X_b(\omega) - X_g(\omega) \end{cases} \tag{4}$$

The transfer function of the base displacement $\left(H_b(\omega) = X_b(\omega)/\ddot{X}_g(\omega)\right)$ can be written as:

$$H_b(\omega) = \frac{1 + \frac{\omega^2\mu_b}{a(\omega)}}{-b(\omega) + \frac{\omega^4\mu_b}{a(\omega)}} \tag{5}$$

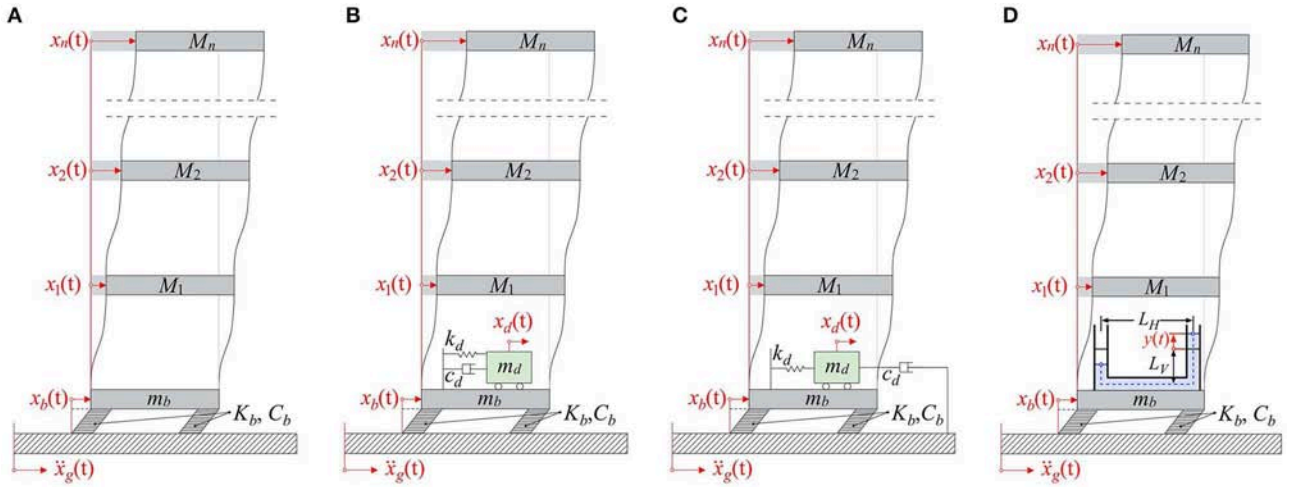

FIGURE 1 | (A) BI; **(B)** BI+TMD ; **(C)** BI+ New TMD; **(D)** BI+TLCD.

The transfer function of the displacement at the top of the superstructure$\left(H_{X_1}(\omega) = X_1(\omega)/\ddot{X}_g(\omega)\right)$ is:

$$H_{X_1}(\omega) = \frac{1}{a(\omega)}\left[-1 + \omega^2 H_b(\omega)\right] \tag{6}$$

where:

$$a(\omega) = -\omega^2 + 2i\omega\zeta_1\omega_1 + \omega_1^2 \tag{7a}$$
$$b(\omega) = -\omega^2 + 2i\omega\zeta_b\omega_b + \omega_b^2 \tag{7b}$$

Aiming at reducing the displacement occurring within the BI system, consider now the case of the above described base isolated structure in which the BI system is connected to an additional passive dissipation mechanism (such as the TMD, the TLCD or the New TMD).

Hybrid Strategy 1—BI +TMD

The hybrid control strategy combining classical TMD device with base isolation system (BI + TMD) is shown in **Figure 1B**. The TMD is modeled as a SDOF linear system with mass m_d, stiffness k_d and damping c_d. The displacement of the TMD relative to the base is denoted as $x_d(t)$. The n+2 equations of motion of a base isolated building equipped with a TMD can be written as:

$$\begin{cases} (M_{tot} + m_d)\ddot{x}_b(t) + m_d\ddot{x}_d(t) + \sum_{i=1}^{n} M_i\ddot{x}_i(t) + C_b\dot{x}_b + \\ K_b x_b(t) = -(M_{tot} + m_d)\ddot{x}_g(t) \\ m_d\ddot{x}_b(t) + m_d\ddot{x}_d(t) + c_d\dot{x}_d + k_d x_d(t) = -m_d\ddot{x}_g(t) \\ M_i\ddot{x}_b(t) + M_i\ddot{x}_i(t) + \sum_{j=1}^{n} C_{i,j}\dot{x}_j(t) + \sum_{j=1}^{n} K_{i,j}x_j(t) = \\ -M_i\ddot{x}_g(t) \end{cases} \tag{8}$$

For a SDOF main structure ($n = 1$), equations of motion are particularized as:

$$\begin{cases} (1+\mu_d)\ddot{x}_b(t) + \mu_b\ddot{x}_1(t) + \mu_d\ddot{x}_d(t) + 2\zeta_b\omega_b\dot{x}_b(t) + \\ \omega^2{}_b x_b(t) = -(1+\mu_d)\ddot{x}_g(t) \\ \ddot{x}_b(t) + \ddot{x}_d(t) + 2\zeta_d\omega_d\dot{x}_d(t) + \omega^2{}_d x_d(t) = -\ddot{x}_g(t) \\ \ddot{x}_b(t) + \ddot{x}_1(t) + 2\zeta_1\omega_1\dot{x}_1(t) + \omega^2{}_1 x_1(t) = -\ddot{x}_g(t) \end{cases} \tag{9}$$

where $\omega_d = \sqrt{k_d/m_d}$ and $\zeta_d = c_d/(2\omega_d m_d)$ are the natural frequency and damping ratio of the TMD and the other symbols have the same meaning of those defined in section BI System.

In the frequency domain, the Fourier transform of system (9) leads to:

$$\begin{cases} X_b(\omega)\left[-\omega^2(1+\mu_d) + 2i\omega\,\zeta_b\omega_b + \omega_b^2\right] - \omega^2\mu_d X_d(\omega) \\ -\omega^2\mu_b X_1(\omega) = -(1+\mu_d)\ddot{X}_g(\omega) \\ -\omega^2 X_b(\omega) + X_d(\omega)\left[-\omega^2 + 2i\omega\,\zeta_d\omega_d + \omega_d^2\right] = \\ -\ddot{X}_g(\omega) \\ -\omega^2 X_b(\omega) + X_1(\omega)\left[-\omega^2 + 2i\omega\,\zeta_1\omega_1 + \omega_1^2\right] = -\ddot{X}_g(\omega) \end{cases} \tag{10}$$

Therefore, the base-isolation displacement transfer function $\left(H_b(\omega) = X_b(\omega)/\ddot{X}_g(\omega)\right)$ can be written as

$$H_b(\omega) = \frac{(1+\mu_d) + \frac{\omega^2\mu_d}{c(\omega)} + \frac{\omega^2\mu_b}{a(\omega)}}{-b(\omega) + \frac{\omega^4\mu_d}{c(\omega)} + \frac{\omega^4\mu_b}{a(\omega)}} \tag{11}$$

while the main structure displacement transfer function $\left(H_{X_1}(\omega) = X_1(\omega)/\ddot{X}_g(\omega)\right)$ and the TMD displacement transfer function $\left(H_d(\omega) = X_d(\omega)/\ddot{X}_g(\omega)\right)$ respectively are:

$$H_{X_1}(\omega) = \frac{1}{a(\omega)}\left[-1 + \omega^2 H_b(\omega)\right] \tag{12a}$$
$$H_d(\omega) = \frac{1}{c(\omega)}\left[-1 + \omega^2 H_b(\omega)\right] \tag{12b}$$

in which

$$a(\omega) = -\omega^2 + 2i\omega\zeta_1\omega_1 + \omega_1^2 \quad (13a)$$

$$b(\omega) = -\omega^2(1+\mu_d) + 2i\omega\zeta_b\omega_b + \omega_b^2 \quad (13b)$$

$$c(\omega) = -\omega^2 + 2i\omega\zeta_d\omega_d + \omega_d^2 \quad (13c)$$

Hybrid Strategy 2—BI + New TMD

The hybrid control strategy coupling the so called New TMD or non-traditional TMD with the base isolation system (BI + New TMD) is shown in **Figure 1C**.

The New Tuned Mass Damper is modeled similarly to the TMD but, unlike the TMD, the New TMD is directly connected to the ground by a dashpot. From a theoretical point of view, this condition leads to higher damping forces compared to the traditional TMD.

The n+2 equations of motion of a base isolated building equipped with a New TMD can be written as:

$$\begin{cases} M_{tot}\ddot{x}_b(t) + \sum_{i=1}^{n} M_i\ddot{x}_i(t) + C_b\dot{x}_b + K_b x_b(t) - k_d x_d(t) \\ = -M_{tot}\ddot{x}_g(t) \\ m_d\ddot{x}_b(t) + m_d\ddot{x}_d(t) + c_d\dot{x}_d + c_d\dot{x}_b + k_d x_d(t) = -m_d \\ \ddot{x}_g(t) \\ M_i\ddot{x}_b(t) + M_i\ddot{x}_i(t) + \sum_{j=1}^{n} C_{i,j}\dot{x}_j(t) + \sum_{j=1}^{n} K_{i,j}x_j(t) = -M_i \\ \ddot{x}_g(t) \end{cases} \quad (14)$$

As it can be seen in the second line of Equation (14), the particular configuration of the New TMD, endowed with a dashpot directly connected to the ground, leads to a dissipative force $F_d = c_d\dot{x}_d + c_d\dot{x}_b$, which is larger than that related to the traditional TMD ($F_d = c_d\dot{x}_d$, see Equation (8)] since it is proportional to both the velocities of the device and the BI system.

For a SDOF main structure ($n = 1$), equations of motion are particularized as:

$$\begin{cases} \ddot{x}_b(t) + \mu_b\ddot{x}_1(t) + 2\zeta_b\omega_b\dot{x}_b(t) + \omega^2{}_b x_b(t) - \mu_d\omega^2{}_d x_d(t) \\ = -\ddot{x}_g(t) \\ \ddot{x}_b(t) + \ddot{x}_d(t) + 2\zeta_d\omega_d\dot{x}_d(t) + 2\zeta_d\omega_d\dot{x}_b(t) + \omega^2{}_d x_d(t) \\ = -\ddot{x}_g(t) \\ \ddot{x}_b(t) + \ddot{x}_1(t) + 2\zeta_1\omega_1\dot{x}_1(t) + \omega^2{}_1 x_1(t) = -\ddot{x}_g(t) \end{cases} \quad (15)$$

Where the symbols have the known meaning of those defined in the section Hybrid strategy 1—BI +TMD for the traditional TMD.

Considering the system in the frequency domain, the Fourier transform of system (15) leads to:

$$\begin{cases} X_b(\omega)\left[-\omega^2 + 2i\omega\,\zeta_b\omega_b + \omega_b^2\right] - \omega_d^2\mu_d X_d(\omega) - \omega^2\mu_b X_1(\omega) \\ = -\ddot{X}_g(\omega) \\ -\omega^2 X_b(\omega) + 2i\omega\,\zeta_d\omega_d X_b(\omega) + X_d(\omega) \\ \left[-\omega^2 + 2i\omega\,\zeta_d\omega_d + \omega_d^2\right] = -\ddot{X}_g(\omega) \\ -\omega^2 X_b(\omega) + X_1(\omega)\left[-\omega^2 + 2i\omega\,\zeta_1\omega_1 + \omega_1^2\right] = -\ddot{X}_g(\omega) \end{cases} \quad (16)$$

Therefore, the base-isolation displacement transfer function $\left(H_b(\omega) = X_b(\omega)/\ddot{X}_g(\omega)\right)$ can be written as

$$H_b(\omega) = \frac{1 + \frac{\omega^2\mu_d}{c(\omega)} + \frac{\omega^2\mu_b}{a(\omega)}}{-b(\omega) + \frac{\omega^4\mu_d}{c(\omega)} + \frac{\omega^4\mu_b}{a(\omega)} + \frac{2i\omega^3\mu_d\zeta_d\omega_d}{c(\omega)}} \quad (17)$$

while the main structure displacement transfer function $\left(H_{X_1}(\omega) = X_1(\omega)/\ddot{X}_g(\omega)\right)$ and the New TMD displacement transfer function $\left(H_d(\omega) = X_d(\omega)/\ddot{X}_g(\omega)\right)$, respectively are:

$$H_{X_1}(\omega) = \frac{1}{a(\omega)}\left[-1 + \omega^2 H_b(\omega)\right] \quad (18a)$$

$$H_d(\omega) = \frac{1}{c(\omega)}\left[-1 + 2i\omega\zeta_d\omega_d H_b(\omega) + \omega^2 H_b(\omega)\right] \quad (18b)$$

in which

$$a(\omega) = -\omega^2 + 2i\omega\zeta_1\omega_1 + \omega_1^2 \quad (19a)$$

$$b(\omega) = -\omega^2 + 2i\omega\zeta_b\omega_b + \omega_b^2 \quad (19b)$$

$$c(\omega) = -\omega^2 + 2i\omega\zeta_d\omega_d + \omega_d^2 \quad (19c)$$

Hybrid Strategy 3—BI+TLCD

Another means to control the seismic response of base isolated structure consists of the use of TLCD located on the basement of the main structure (BI+TLCD) (**Figure 1D**). Denoting with g the gravitational acceleration, L_v and L_h the vertical and horizontal liquid length, respectively, $L = L_h + 2L_v$ the total length of the liquid column inside the TLCD, the n+2 dimensional system of equations can be expressed by:

$$\begin{cases} (M_{tot} + m)\ddot{x}_b(t) + m_h\ddot{y} + \sum_{i=1}^{n} M_i\ddot{x}_i(t) + C_b\dot{x}_b + K_b x_b(t) \\ = -(M_{tot} + m)\ddot{x}_g(t) \\ m_h\ddot{x}_b(t) + m\ddot{y}(t) + \frac{m}{2L}\xi\left|\dot{y}(t)\right|\dot{y}(t) + 2\frac{m}{L}g y(t) = \\ -m_h\ddot{x}_g(t) \\ M_i\ddot{x}_b(t) + M_i\ddot{x}_i(t) + \sum_{j=1}^{n} C_{i,j}\dot{x}_j(t) + \sum_{j=1}^{n} K_{i,j}x_j(t) = \\ -M_i\ddot{x}_g(t) \end{cases} \quad (20)$$

Here $\alpha = L_h/L$ is the so called length ratio and describes the fraction of effectively moving liquid in horizontal direction $m_h = \alpha m$, to the total liquid mass m inside the tube, $y(t)$ is the vertical liquid displacement and ξ is a head loss factor dependent on the type of flow and its interaction with container wall or on the presence of orifice inside the TLCD. When $n = 1$ (SDOF main structure), equations of motion can be written as:

$$\begin{cases} (1+\mu_2)\ddot{x}_b(t) + \alpha\mu_2\ddot{y}(t) + \mu_b\ddot{x}_1(t) + 2\zeta_b\omega_b\dot{x}_b(t) \\ +\omega^2{}_b x_b(t) = -(1+\mu_2)\ddot{x}_g(t) \\ \alpha\ddot{x}_b(t) + \ddot{y}(t) + \frac{1}{2L}\xi\left|\dot{y}(t)\right|\dot{y}(t) + \omega^2{}_l y(t) = -\alpha\ddot{x}_g(t) \\ \ddot{x}_b(t) + \ddot{x}_1(t) + 2\zeta_1\omega_1\dot{x}_1(t) + \omega^2{}_1 x_1(t) = -\ddot{x}_g(t) \end{cases} \quad (21)$$

Where, $\mu_2 = m/M_{tot}$ is the liquid mass ratio and $\omega_l = \sqrt{2g/L}$ is the frequency associated with the liquid inside the TLCD (Hochrainer and Ziegler, 2006).

It is worth noting that, unlike traditional TMDs, the TLCD response is non-linear due to the presence of term $\frac{1}{2L}\xi\left|\dot{y}\left(t\right)\right|\dot{y}\left(t\right)$ in the second equation of the system (21) (Di Matteo et al., 2012, 2014a,b).

However, in order to avoid onerous calculus and complex optimization procedure due to the presence of the non-linear damping term, the original non-linear system (21) usually is replaced by a linear equivalent one. Using the "Statistical Linearization Technique" (SLT), the equations of the BI + TLCD system can be written in the following form:

$$\begin{cases} \left(1+\mu_2\right)\ddot{x}_b\left(t\right)+\alpha\mu_2\ddot{y}+\mu_b\ddot{x}_1\left(t\right)+2\zeta_b\omega_b\dot{x}_b\left(t\right) \\ +\omega_b^2 x_b\left(t\right)=-\left(1+\mu_2\right)\ddot{x}_g\left(t\right) \\ \alpha\ddot{x}_b\left(t\right)+\ddot{y}\left(t\right)+2\zeta_2\omega_2\dot{y}\left(t\right)+\omega_2^2 y\left(t\right)=-\alpha\ddot{x}_g\left(t\right) \\ \ddot{x}_b\left(t\right)+\ddot{x}_1\left(t\right)+2\zeta_1\omega_1\dot{x}_1\left(t\right)+\omega_1^2 x_1\left(t\right)=-\ddot{x}_g\left(t\right) \end{cases} \tag{22}$$

where ζ_2 is the equivalent damping ratio, which can be calculated through a direct optimization procedure of the TLCD design parameters performed in Di Matteo et al. (2014a,b, 2015, 2017a,b) and explained in the **Appendix**. Specifically, following the analysis in Roberts and Spanos (1990), Di Matteo et al. (2014a), the relationship between ζ_2 and ξ is:

$$\zeta_2=\frac{\xi}{2L\,\omega_2}\sqrt{\frac{2}{\pi}}\sigma_{\dot{Y}} \tag{23}$$

where $\sigma_{\dot{Y}}$ is the standard deviation of the velocity of the liquid inside in the TLCD (see **Appendix A** for further details).

In the frequency domain, the Fourier transform of system Equation (22) leads to:

$$\begin{cases} X_b\left(\omega\right)\left[-\omega^2\left(1+\mu_2\right)+2i\omega\,\zeta_b\omega_b+\omega_b^2\right]-\omega^2\alpha\mu_2 Y\left(\omega\right) \\ -\omega^2\mu_b X_1\left(\omega\right)=-\left(1+\mu_2\right)\ddot{X}_g\left(\omega\right) \\ -\omega^2\alpha X_b\left(\omega\right)+Y\left(\omega\right)\left[-\omega^2+2i\omega\,\zeta_2\omega_2+\omega_2^2\right]= \\ -\alpha\ddot{X}_g\left(\omega\right) \\ -\omega^2 X_b\left(\omega\right)+X\left(\omega\right)\left[-\omega^2+2i\omega\,\zeta_1\omega_1+\omega_1^2\right]=-\ddot{X}_g\left(\omega\right) \end{cases} \tag{24}$$

Therefore, the base-isolation displacement transfer function $\left(H_b\left(\omega\right)=X_b\left(\omega\right)/\ddot{X}_g\left(\omega\right)\right)$ can be written as

$$H_b\left(\omega\right)=\frac{\left(1+\mu_2\right)+\frac{\omega^2\alpha^2\mu_2}{c(\omega)}+\frac{\omega^2\mu_b}{a(\omega)}}{-b\left(\omega\right)+\frac{\omega^4\alpha^2\mu_2}{c(\omega)}+\frac{\omega^2\mu_b}{a(\omega)}} \tag{25}$$

while the main structure displacement transfer function $\left(H_{X_1}\left(\omega\right)=X_1\left(\omega\right)/\ddot{X}_g\left(\omega\right)\right)$ and the fluid displacement transfer function, respectively, are

$$H_{X_1}\left(\omega\right)=\frac{1}{a\left(\omega\right)}\left[-1+\omega^2 H_b\left(\omega\right)\right] \tag{26a}$$

$$H_Y\left(\omega\right)=\frac{\alpha}{c\left(\omega\right)}\left[-1+\omega^2 H_b\left(\omega\right)\right] \tag{26b}$$

In which

$$a\left(\omega\right)=-\omega^2+2i\omega\zeta_1\omega_1+\omega_1^2 \tag{27a}$$

$$b\left(\omega\right)=-\omega^2\left(1+\mu_2\right)+2i\omega\zeta_b\omega_b+\omega_b^2 \tag{27b}$$

$$c\left(\omega\right)=-\omega^2+2i\omega\zeta_2\omega_2+\omega_2^2 \tag{27c}$$

The aforementioned closed form solutions to evaluate the frequency response functions (FRFs) of the systems have been directly considered to carry out the frequency analysis in the following.

ANALYSIS OF THE CONTROL PERFORMANCE

In order to investigate on the efficacy of the proposed hybrid strategies to reduce the base displacement and acceleration without increasing other structural quantities (such as roof displacements and accelerations), here a numerical example, involving two different main systems, has been developed.

The first structural system is a SDOF base isolated structure model, while the second one is a MDOF base isolated structure model. Both structures have been analyzed equipped each time with the aforementioned passive vibration control devices (TMD, TLCD, and New TMD) and subjected to selected recorded accelerograms, to take into account the influence of the non-stationary nature of real earthquakes.

Specifically, the San Fernando and the Chi-Chi recorded earthquakes have been used as input forces (**Figures 2A,B**), taken by the FEMA P-695-FF (FEMA P-695, 2009), a collection of ground motions with a magnitude between 6.5 and 7.6 recorded on NEHRP site classes C (soft rock) and D (stiff soil).

Note that these two earthquakes records present quite different characteristics since the first has high impulsive content in the first instants of motion, which is known to be an unfavorable condition for the efficiency of control devices.

The analysis has been carried out both in the time and in the frequency domain.

In the following numerical simulations carried out on the SDOF base isolated structure, controlled by a passive control device, the FRFs have been found using the closed form solutions reported in section Problem Formulation. For the multi-degree of freedom (MDOF) superstructure, the FRFs have been computed by means of the *fft* function in MatLab, which computes the discrete Fourier transform of a signal using a Fast Fourier Transform (FFT) algorithm (Frigo and Johnson, 1998).

Analysis of the Control Performance of a SDOF Base-Isolated Structure

In this section the control performance of the BI system equipped with the TMD, the New TMD and the TLCD is investigated in terms of base displacement, acceleration, and roof displacement time-histories. The analysis has been firstly carried out in the time domain and then in the frequency domain.

The benchmark structure used for the numerical analysis is a base-isolated SDOF building ($n=1$) as reported in Xiang and Nishitani (2014). The superstructure has a mass story $M_1 = 1\cdot10^6$ kg, an elastic story stiffness $K_1 = 3.94\cdot10^4$ kN/m, and a damping coefficient $C_1 = 2.51\cdot10^2$ kNs/m (corresponding to a damping ratio of $\zeta_1 = 0.01$).

As far as the base-isolation system is concerned, its mass is $M_b = 5\cdot10^4$ kg, while stiffness and damping coefficient are assumed to be $K_b = 2.59\cdot10^3$ kN/m (corresponding to a natural

frequency $\omega_b = 1.57\,\text{rad/s}$) and $C_b = 1.64 \cdot 10^2\,\text{kN s/m}$ (corresponding to a damping ratio $\zeta_b = 0.05$), respectively.

As far as the passive control devices are concerned, the mass ratio is supposed to be the same for all the considered systems. Hence, the TLCD incorporated to the BI system has a mass ratio $\mu_2 = 5\%$ equal to the TMD mass ratio $\mu_d = 5\%$ and to the New TMD mass ratio $\mu_d = 5\%$.

The specific dynamic parameters of the considered devices coupled with the BI system have been chosen on the basis of some optimization procedures reported in **Appendix A**.

The TLCD placed on the BI system has a length ratio $\alpha = 0.6$, and the frequency ratio $\nu_{opt} = 0.943$ and the head loss coefficient $\xi_{opt} = 10.427$ have been determined from the optimization procedure proposed in Di Matteo et al. (2017a) and described in **Appendix A**.

The TMD frequency ratio and damping coefficient are $\nu_{opt} = 0.94$ and $\zeta_{d,opt} = 0.11$ respectively, found using the TMD optimization technique proposed in Di Matteo et al. (2019).

Finally, the New TMD parameters are: the frequency ratio $\nu_{opt} = 4.47$ and damping coefficient $\zeta_{d,opt} = 0.393$, found using the optimal New TMD parameters computed as described in Xiang and Nishitani (2014).

For sake of simplicity, the main structure and the base-isolation subsystem have been supposed to be linear systems.

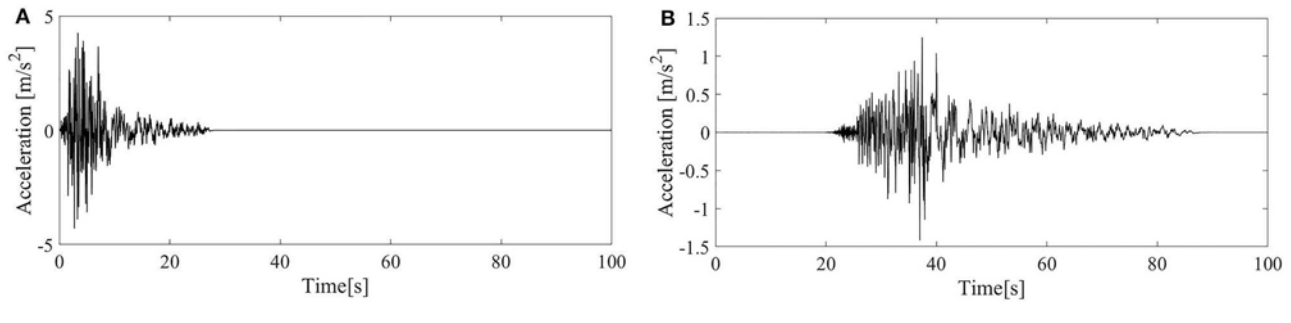

FIGURE 2 | Earthquake records: **(A)** San Fernando earthquake; **(B)** Chi-Chi earthquake.

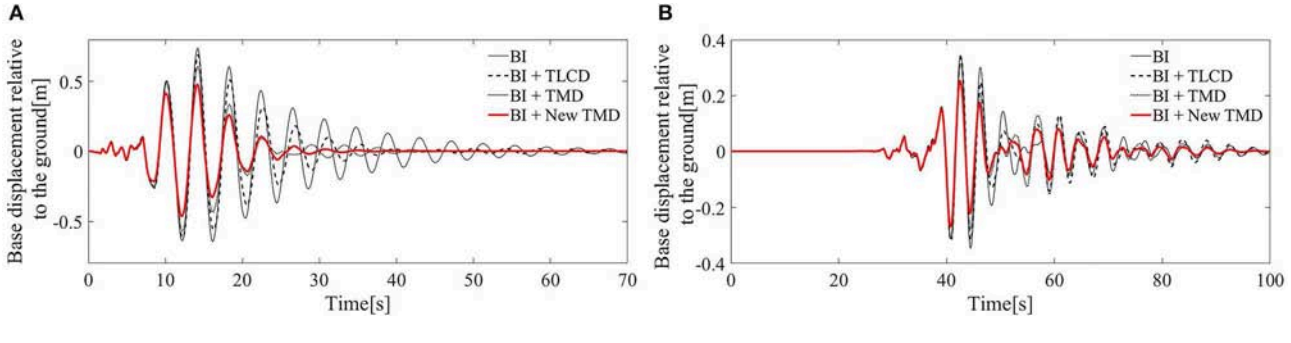

FIGURE 3 | Base isolation displacements relative to the ground: **(A)** Response to the San Fernando earthquake. **(B)** Response to the Chi-Chi earthquake. BI system, black line; BI system with the TLCD, black dashed line; BI system with the TMD, black dotted line; BI system with the New TMD, red thick line.

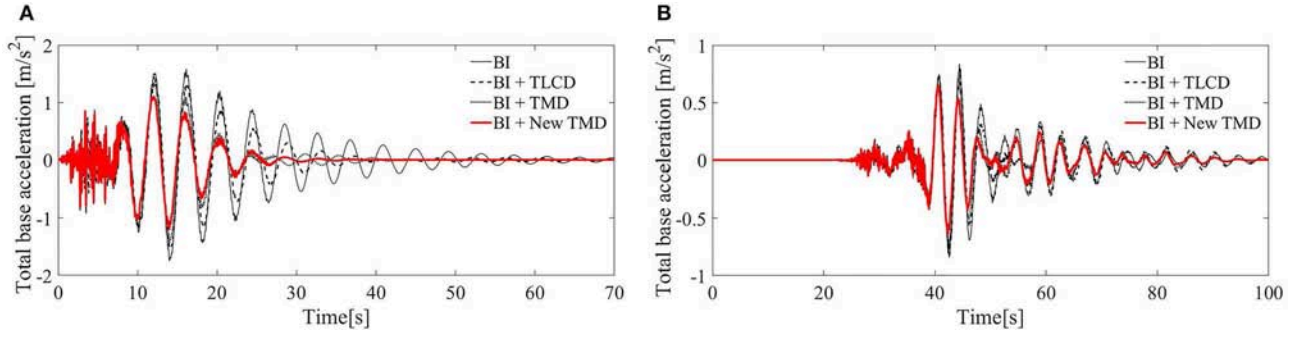

FIGURE 4 | Total base accelerations: **(A)** Response to the San Fernando earthquake. **(B)** Response to the Chi-Chi earthquake; BI system, black line; BI system with the TLCD, black dashed line; BI system with the TMD, black dotted line; BI system with the New TMD, red thick line.

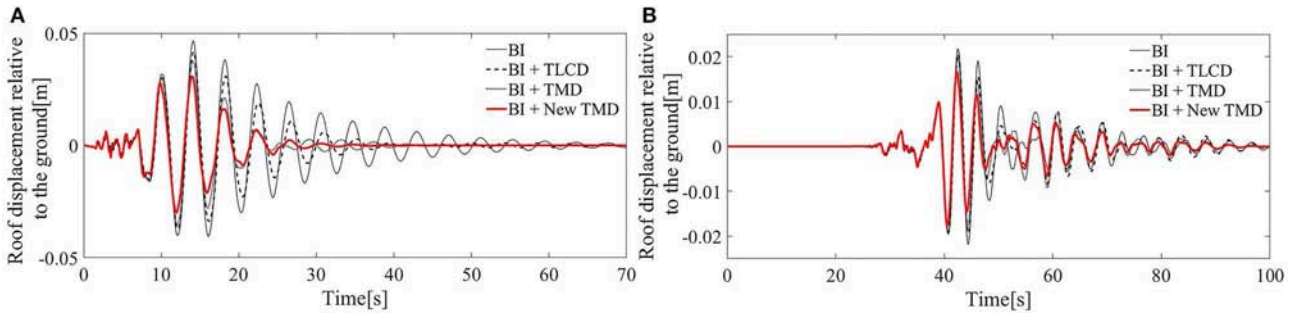

FIGURE 5 | Roof displacements relative to the ground: **(A)** Response to the San Fernando earthquake. **(B)** Response to the Chi-Chi earthquake; BI system, black line; BI system with the TLCD, black dashed line; BI system with the TMD, black dotted line; BI system with the New TMD, red thick line.

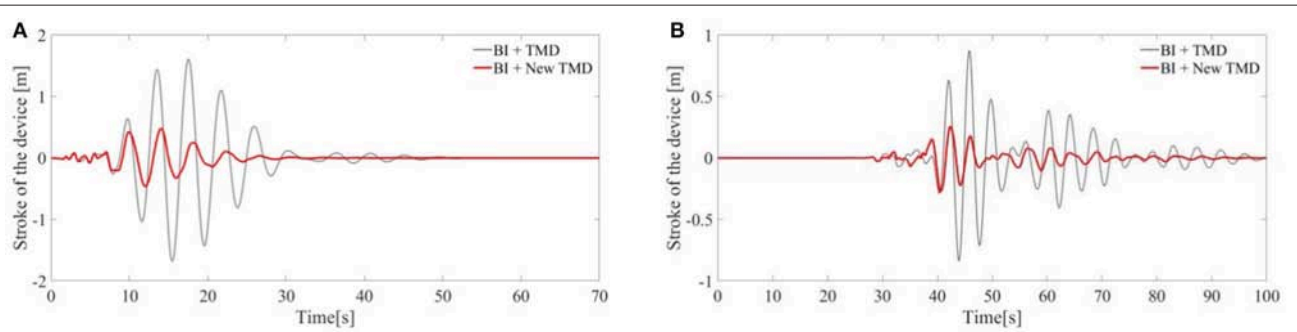

FIGURE 6 | Stroke of the device: **(A)** Response to the San Fernando earthquake. **(B)** Response to the Chi-Chi earthquake; BI system with the TMD, black dotted line; BI system with the New TMD, red thick line.

Clearly, many real base-isolation systems may show characteristic non-linear features. In De Domenico et al. (2018), for instance, an improved response spectrum analysis taking into account a more realistic non-linear behavior of the BI system, has been developed.

The corresponding response time histories of the base-isolated reference structure with and without control devices are shown in **Figures 3**–**5**, respectively.

Figures 3A,B show that for both the seismic ground motions, the New TMD device incorporated to a BI system (red thick line), is the most efficient strategy in terms of reducing of peak base deformation (with a decrease of almost 37% for the San Fernando record and 26% for the Chi-Chi record). From **Figures 4**, **5** it emerges the New TMD can reduce base acceleration (49% for the San Fernando record and 36% for the Chi-Chi record) (**Figures 4A,B**) and top floor displacements too (**Figures 5A,B**).

Finally, the stroke of the New TMD and TMD, defined as $x_b(t) - x_d(t)$, is plotted in **Figure 6**. Note that, the displacement of the TLCD device is not shown since, being represented by the vertical displacement of the liquid inside the device, as depicted in **Figure 1D**, it is not directly comparable to the horizontal displacement of the TMD and New TMD (**Figures 1B,C**).

As it can be seen, the New TMD design yields smaller displacements compared to the traditional TMD for the two considered inputs. This is due to the particular configuration of the dashpot in the device New TMD which leads to larger dissipative forces compared to the TMD. This result is in agreement with results described in Xiang and Nishitani (2014).

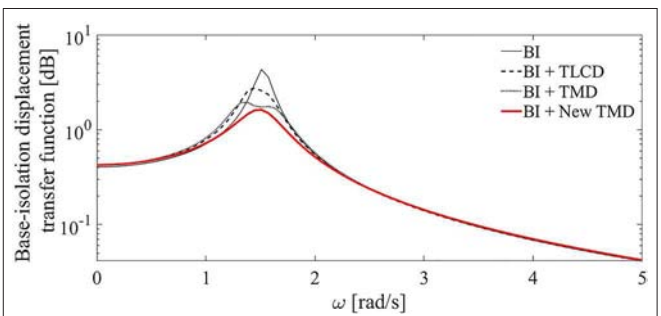

FIGURE 7 | Magnitudes of the base-isolation displacement transfer function of the BI system (black line), BI system with the TLCD (black dashed line), BI system with the TMD (black dotted line), and BI system with the New TMD (red thick line).

Notably, this aspect can be particularly advantageous in practical cases where the space designed to host the device is limited.

Once introduced the FRFs of each hybrid strategy, a frequency analysis is developed in order to understand the dynamic behavior of each system in the frequency domain.

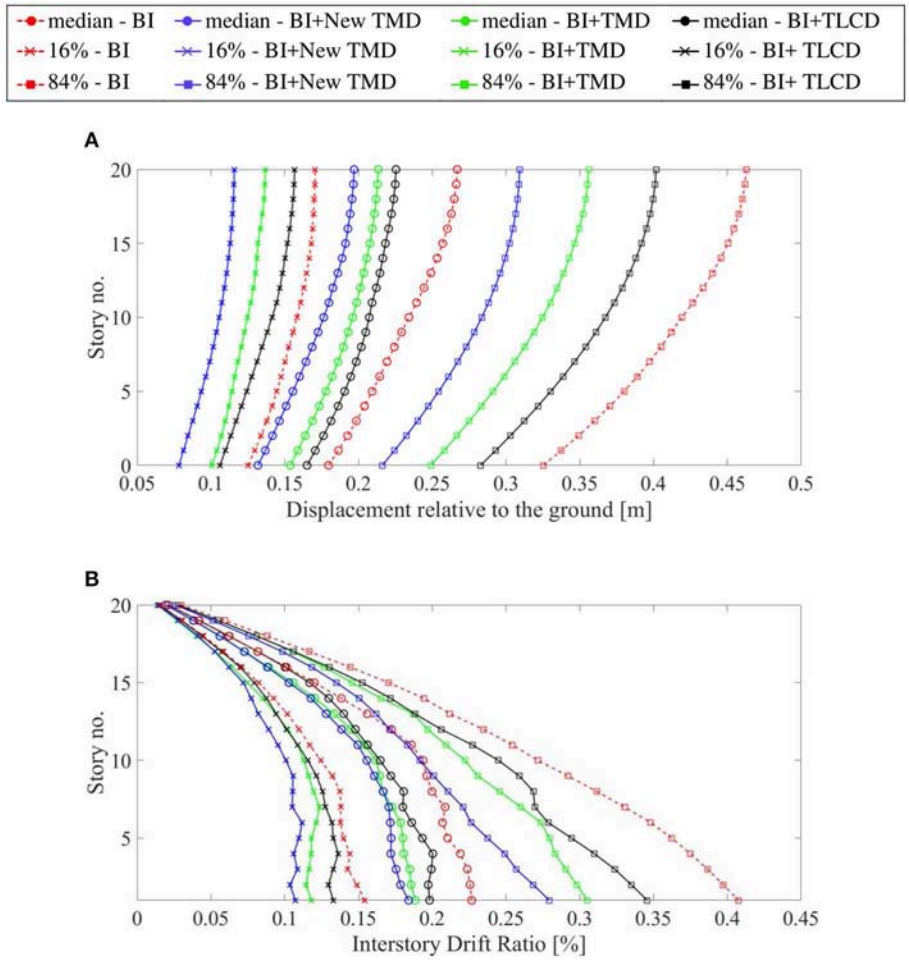

FIGURE 8 | Response profiles for hybrid controlled structure with TLCD (black solid line), with TMD (green solid line), with New TMD (blue solid line) and base-isolated structure (red dashed line) subjected to the 44 FEMA P-695-FF records: circles, median; crosses, 16th percentile; squares, 84th percentiles. **(A)** In terms of peak floor displacement relative to the ground. **(B)** In terms of peak floor displacement interstorey drift ratio.

The base-isolation displacement transfer function of the simple BI system is compared to that of the base isolated one equipped with the TMD, the New TMD and the TLCD, respectively, as shown in **Figure 7**.

As it can be seen, the presence of a passive control device reduces the amplitude of the frequency response of the BI system (black line). Again, according to the frequency analysis, the New TMD (red thick line), achieves the best control of the structural response.

Analysis of the Control Performance of a MDOF-Story Base-Isolated Structure

In this section the analysis of the control performance of the BI system equipped with the TMD, New TMD or the TLCD is extended to the case of a MDOF superstructure, both in the time and in the frequency domain, to take into account also the case of tall structures.

In order to investigate the influence of the non-stationary nature of real ground motions, the control performances of the base-isolated structure equipped with each device has been examined in the time domain by using 44 different selected recorded accelerograms extracted by data of the recorded far-field ground motions of the FEMA P-695-FF set described in FEMA P-695 (2009).

The superstructure used for the numerical analysis is a base-isolated 20-story building ($n = 20$) (Yang et al., 1991).

The structural properties of each story unit are as follows: story mass $M_i = 3 \cdot 10^5$ kg, elastic story stiffness $K_i = 10^6$ kN/m, damping coefficient $C_i = 2261$ kN s/m (corresponding to a damping ratio of the first mode $\zeta_1 = 0.005$), and height of each story $h_i = 3.0$ m. As far as the base-isolation system is concerned, its mass is $M_b = 4 \cdot 10^5$ kg, while stiffness and damping coefficient are assumed to be $K_b = 4 \cdot 10^4$ kN/m (corresponding to a natural frequency $\omega_b = 2.5$ rad/s) and $C_b = 320$ kN s/m (corresponding to a damping ratio $\zeta_b = 0.01$), respectively.

The TLCD incorporated to the BI system has a mass ratio $\mu_2 = 5\%$ and length ratio $\alpha = 0.6$, the frequency ratio is $\nu_{opt} =$

0.96 and the head loss coefficient is $\xi_{opt} = 6.71$, obtained on the basis of Di Matteo et al. (2017a) and as described in **Appendix A**.

The TMD parameters are: mass ratio $\mu_d = 5\%$, the frequency ratio $\nu_{opt} = 0.94$ and damping coefficient $\zeta_{d,opt} = 0.11$, found using the TMD optimization procedure proposed in Di Matteo et al. (2019).

Finally, the New TMD parameters are: mass ratio $\mu_d = 5\%$, the frequency ratio $\nu_{opt} = 4.47$ and damping coefficient $\zeta_{d,opt} = 0.397$, found using the New TMD optimization procedure proposed in Xiang and Nishitani (2014). Also in this case, the basic hypotheses suppose the linearity of the main structure and of the base-isolation subsystem.

For each of the FEMA P-695-FF 44 records, the displacement relative to the ground (**Figure 8A**) and interstorey drift ratio (**Figure 8B**) of the base-isolation subsystem and of the main structure are determined for the base-isolated structure and the base-isolated structure controlled by the TMD, TLCD and the New TMD.

In this regard, **Figure 8** show the profiles (median, 16 and 84th percentiles) of the peak response quantities of the base-isolated structure without devices (red dashed line), with TLCD

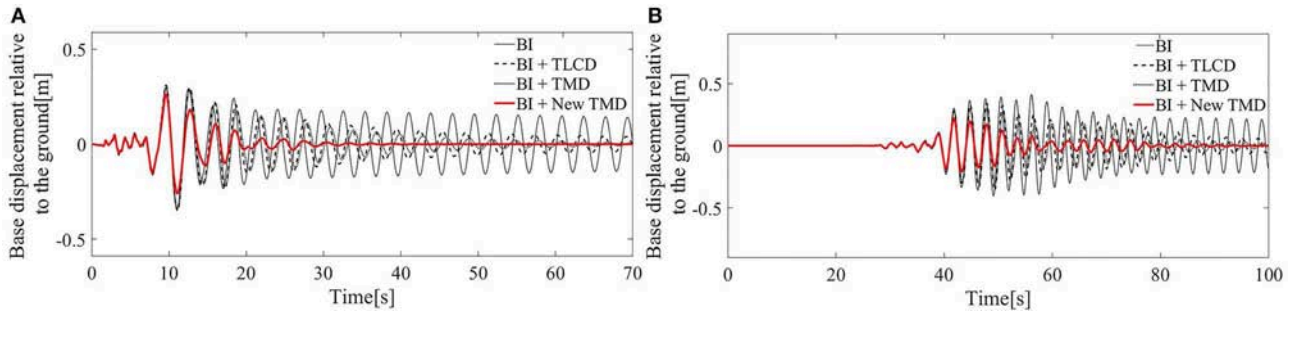

FIGURE 9 | Base isolation displacements relative to the ground: **(A)** Response to the San Fernando earthquake. **(B)** Response to the Chi-Chi earthquake; BI system, black line; BI system with the TLCD, black dashed line; BI system with the TMD—black dotted line; BI system with the New TMD, red thick line.

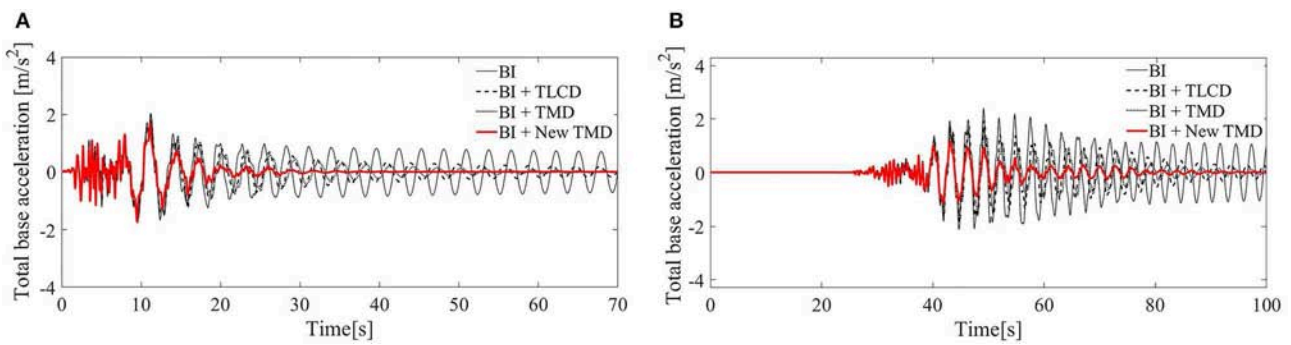

FIGURE 10 | Total base accelerations: **(A)** Response to the San Fernando earthquake. **(B)** Response to the Chi-Chi earthquake; BI system, black line; BI system with the TLCD, black dashed line; BI system with the TMD, black dotted line; BI system with the New TMD, red thick line.

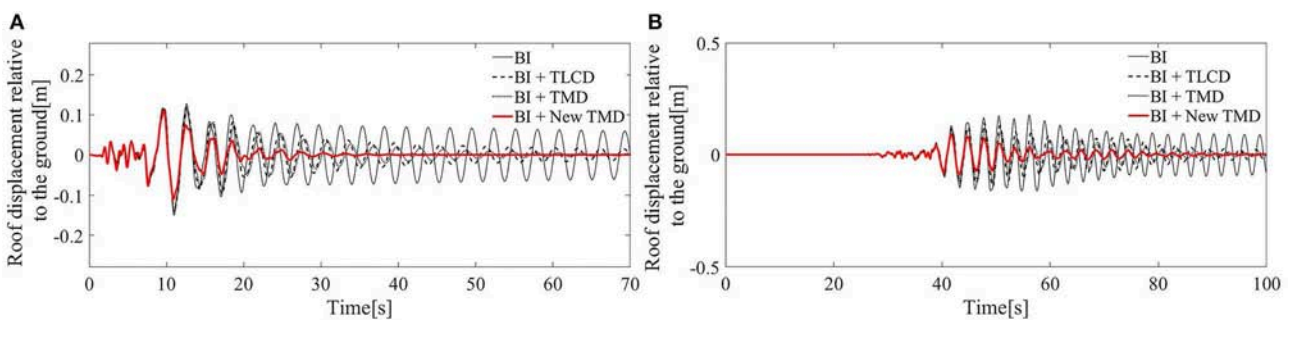

FIGURE 11 | Roof displacements relative to the ground: **(A)** Response to the San Fernando earthquake. **(B)** Response to the Chi-Chi earthquake; BI system, black line; BI system with the TLCD, black dashed line; BI system with the TMD, black dotted line; BI system with the New TMD, red thick line.

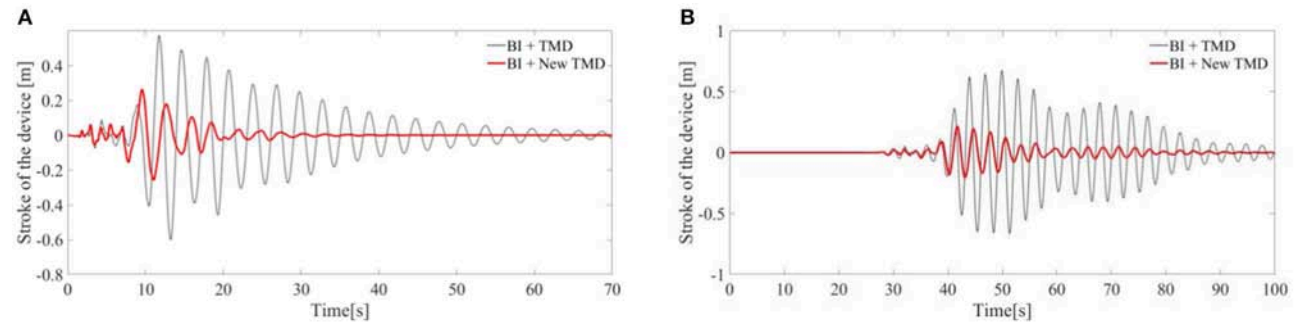

FIGURE 12 | Stroke of the device: **(A)** Response to the San Fernando earthquake. **(B)** Response to the Chi-Chi earthquake; BI system with the TMD, black dotted line; BI system with the New TMD, red thick line.

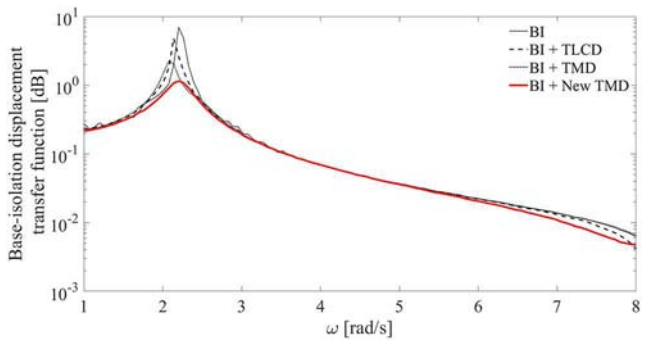

FIGURE 13 | Magnitudes of the base displacement transfer function of the BI system (black line), BI system with the TLCD (black dashed line), BI system with the TMD (black dotted line), and BI system with the NEW TMD (red thick line).

(black solid line), TMD (green solid line), and New TMD (blue solid line).

As can be seen in **Figure 8**, the New TMD device in combination with the base-isolation subsystem outperforms the other devices in reducing the structural responses.

Specifically, results for the same recorded accelerograms (the San Fernando and Chi-Chi earthquakes) of the section Analysis of the control performance of a SDOF base-isolated structure as the external inputs.

The corresponding response time histories of the base-isolated reference structure with and without control devices are shown in **Figures 9–11**, respectively.

It emerges that, for the San Fernando seismic action, the New TMD device incorporated to a BI system (red thick line), can reduce the base deformation (with a decrease of the peak base deformation of almost 16 %) (**Figure 9A**), base acceleration (20%) (**Figure 11A**) and top floor displacements (58%) (**Figure 11A**).

Moreover, the New TMD can achieve greater reductions for the Chi-Chi earthquake: the maximum peak of the base displacement can be reduced of almost 80%, while of almost 60% with the BI + TMD system and 41% with the BI + TLCD system (**Figure 9B**).

Furthermore, although TMDs, as well as the New TMDs and TLCDs cannot mitigate the structural responses in the first seconds of the excitation, since in this cases, the use of an active system device or a sort of accelerated TMD could be necessary (Tsai and Lin, 1993; Tsai, 1995; Yalla and Kareem, 2003; Hochrainer and Ziegler, 2006), the overall effect of such a passive control device on the BI system is a significant decrease of all the response quantities, as shown in **Figures 9–11**.

Moreover, as it can be seen from **Figure 12**, the stroke length of the New TMD is greatly reduced compared with the traditional TMD for both the considered earthquakes. In this regard, the New TMD may represent an advantageous solution in real cases when the space designed to host the device is limited.

It emerges that the New TMD device, compared to the traditional TMD and to the TLCD, yields a higher dissipation of the structural vibrations.

As far as the analysis in the frequency domain is concerned, the results of a frequency analysis on the 20-DOFs base isolated structure equipped with an energy dissipation mechanism are shown in the following considering the mean of the FRFs obtained for each of the FEMA P-695-FF 44 records. Here the FRFs have been obtained numerically by using MatLab built-in function FFT—Fast Fourier Transform (Frigo and Johnson, 1998). Specifically, in **Figure 13** it can be observed the New TMD (red thick line), similarly to the TMD (black dotted line), is more effective in reducing the peak of the frequency transfer function of the base displacement of the BI system (black line).

CONCLUSION

In this study the dynamic behavior of base-isolated buildings equipped with several types of passive control systems is investigated. In particular, strategies which combine the Base Isolation with the Tuned Mass Damper, the New Tuned Mass Damper and the Tuned Liquid Column Damper have been examined. The effectiveness of each device in reducing the dynamic response of base isolated structure is stressed by comparison with the response of the simple base isolated structure.

Mathematical formulations of the all above described hybrid strategies have been given in the time and in the frequency domain. Moreover, the control performance of each device connected to the base-isolated structure has been examined considering firstly a SDOF base-isolated shear-type frame structure subjected to two specific recorded accelerograms with different features. Numerical simulations show that the New TMD is particularly effective in controlling the base isolated displacement demand (with a significantly reduction of the maximum base displacement value of almost 80% in the case of a MDOF isolated building under the Chi-Chi earthquake), compared to the base-isolated structure without any passive control device. Finally, results suggest that the New TMD can further reduce relative base-isolation displacements and the other response quantities, such as the base acceleration, the top floor displacement, the stroke of the device, and the amplitude of the base displacement frequency transfer function, even compared to the most common devices such as the TMD and the TLCD.

Although results may be influenced by several parameters such as the typology of the structure, the considered accelerograms and soil type, the analyses, carried out on a 20-story base-isolated shear-type frame structure by using a set of 44 different ground motions with different magnitudes and taking into account several soil site classes (between soft and stiff soil), confirm that the design of the New TMD parameters is quite reliable for different types of earthquakes and that the New TMD can represent an effective means to reduce the response of base-isolated structures.

DATA AVAILABILITY STATEMENT

The datasets generated for this study are available on request to the corresponding author.

AUTHOR CONTRIBUTIONS

All authors listed have made a substantial, direct and intellectual contribution to the work, and approved it for publication.

ACKNOWLEDGMENTS

The authors gratefully acknowledge financial support from the Italian Ministry of Education, University and Research (MIUR) under the Prin 2017 grant Multiscale Innovative Materials and Structures.

SUPPLEMENTARY MATERIAL

The Supplementary Material for this article can be found online at: https://www.frontiersin.org/articles/10.3389/fbuil.2019.00132/full#supplementary-material

REFERENCES

Bakre, S. V., and Jangid, R. S. (2007). Optimum parameters of tuned mass damper for damped main system. *Struc. Control Health Monit.* 14, 448–470. doi: 10.1002/stc.166

Chang, C. C. (1999). Mass dampers and their optimal designs for building vibration control. *Eng. Struct.* 21, 454–463. doi: 10.1016/S0141-0296(97)00213-7

Cheung, Y. L., and Wong, W. O. (2011). Optimization of a non-traditional dynamic vibration absorber for vibration control of structures under random force excitation. *J. Sound Vibration* 330, 1039–1044. doi: 10.1016/j.jsv.2010.10.031

De Angelis, M., Giaralis, A., Petrini, F., and Pietrosanti, D. (2019). Optimal tuning and assessment of inertial dampers with grounded inerter for vibration control of seismically excited base-isolated systems. *Eng. Struct.* 196:109250. doi: 10.1016/j.engstruct.2019.05.091

De Domenico, D., Falsone, G., and Ricciardi, G. (2018). Improved response-spectrum analysis of base-isolated buildings: a substructure-based response spectrum method. *Eng. Struct.* 162, 198–212. doi: 10.1016/j.engstruct.2018.02.037

De Domenico, D., and Ricciardi, G. (2018a). Earthquake-resilient design of base isolated buildings with TMD at basement: application to a case study. *Soil Dyn. Earthquake Eng.* 113, 503–521. doi: 10.1016/j.soildyn.2018.06.022

De Domenico, D., and Ricciardi, G. (2018b). An enhanced base isolation system equipped with optimal tuned mass damper inerter (TMDI). *Earthquake Eng. Struct. Dyn.* 47, 1169–1192. doi: 10.1002/eqe.3011

Den Hartog, J. P. (1956). *Mechanical Vibrations*. New York, NY: McGraw-Hil.

Di Matteo, A., Furtmuller, T., Adam, C., and Pirrotta, A. (2017a). Optimal design of tuned liquid column dampers for seismic response control of base-isolated structures. *Acta Mechanica* 229:437–454. doi: 10.1007/s00707-017-1980-7

Di Matteo, A., Furtmuller, T., Adam, C., and Pirrotta, A. (2017b). Earthquake excited base-isolated structures protected by tuned liquid column dampers: design approach and experimental verification. *Proc. Eng.* 199, 1574–1579. doi: 10.1016/j.proeng.2017.09.060

Di Matteo, A., Lo Iacono, F., Navarra, G., and Pirrotta, A. (2012). "The TLCD passive control: numerical investigations vs experimental results," in *ASME 2012 InternationalMechanical Engineering Congress and Exposition Dynamics, Control and Uncertainty*, Vol. 4 (New York, NY: ASME), 1283–1290. doi: 10.1115/IMECE2012-86568

Di Matteo, A., Lo Iacono, F., Navarra, G., and Pirrotta, A. (2014a). Direct evaluation of the equivalent linear damping for TLCD systems in random vibration for pre-design purposes. *Int. J. Nonlinear Mech.* 63, 19–30. doi: 10.1016/j.ijnonlinmec.2014.03.009

Di Matteo, A., Lo Iacono, F., Navarra, G., and Pirrotta, A. (2014b). Experimental validation of a direct pre-design formula for TLCD. *Eng. Struct.* 75, 528–538. doi: 10.1016/j.engstruct.2014.05.045

Di Matteo, A., Lo Iacono, F., Navarra, G., and Pirrotta, A. (2015). Optimal tuning of tuned liquid column damper systems in random vibration by means of an approximate formulation. *Meccanica* 50, 795–808. doi: 10.1007/s11012-014-0051-6

Di Matteo, A., Masnata, C., and Pirrotta, A. (2019). Simplified analytical solution for the optimal design of tuned mass damper inerter for base isolated structures. *Mech. Syst. Signal. Proc.* 134C: 106337. doi: 10.1016/j.ymssp.2019.106337

Elias, S., and Matsagar, V. A. (2017). Effectiveness of tuned mass dampers in seismic response control of isolated bridges including soil-structure interaction. *Latin Am. J. Solids Struct.* 14, 2324–2341. doi: 10.1590/1679-78253893

FEMA P-695 (2009). *Quantification of Building Seismic Performance Factors Technical Representative Federal Emergency Agency*. Washington, DC.

Frigo, M., and Johnson, S. G. (1998). "FFTW: an Adaptive Software Architecture for the FFT," in *Proceedings of the International Conference on Acoustics, Speech, and Signal Processing* (Seattle, WA), 1381–1384. doi: 10.1109/ICASSP.1998.681704

Gao, H., and Kwok, K. C. S. (1997). Optimization of tuned liquid column dampers. *Eng. Struct.* 19, 476–486. doi: 10.1016/S0141-0296(96)00099-5

Hochrainer, M. J., and Ziegler, F. (2006). Control of tall building vibrations by sealed tuned liquid column dampers. *Struct. Control. Health Monit.* 13, 980–1002. doi: 10.1002/stc.90

Kelly, J. M. (1990). Base isolation: linear theory and design. *J. Earthquake Spectra* 6, 223–244. doi: 10.1193/1.1585566

Kelly, J. M. (1999). The role of damping in seismic isolation. *Earthquake Eng. Struct. Dyn.* 28, 3–20.

Melkumyan, M. G. (2012). "New concept of a dynamic damper to restrict the displacements of seismically isolated buildings," *Conference: International Conference on Advances in Materials Science and Engineering*, Seoul, Korea.

Natsiavas, S. (1992). Steady state oscillations and stability of non-linear dynamic vibration absorbers. *J. Sound Vibration* 156, 227–245. doi: 10.1016/0022-460X(92)90695-T

Nissen, J. C., Popp, K., and Schmalhorst, B. (1985). Optimization of a non-linear dynamic vibration absorber. *J. Sound Vibration* 99, 149–154. doi: 10.1016/0022-460X(85)90454-7

Palazzo, B., and Petti, L. (1994). "Seismic Response Control in Base Isolated Systems Using Tuned Mass Dampers," in *Proceedings of First World Conference on Structural Control*, Los Angeles, California.

Palazzo, B., and Petti, L. (1999). Combined control strategy: based isolation and tuned mass damping. *ISET J. Earthquake Technol.* 36, 121–137.

Perez, R., and Behdinan, K. (2007). Particle swarm approach for structural design optimization. *Comput. Struct.* 85, 1579–88. doi: 10.1016/j.compstruc.2006.10.013

Ren, M. Z. (2001). A variant design of the dynamic vibration absorber. *J. Sound Vibration* 245, 762–770. doi: 10.1006/jsvi.2001.3564

Roberts, J. B., and Spanos, P. D. (1990). *Random Vibration and Statistical Linearization*. New York, NY: Wiley.

Sakai, F., Takeda, S., and Tamaki, T. (1989). "Tuned Liquid Column Damper-New Type Device for Suppression of Building Vibration," in *Proceedings of the International Conference on Highrise Buildings* (Nanjing), 926–931.

Stanikzai, M. H., Elias, S., Matsagar, V. A., and Jain, A. K. (2018). Seismic response control of base-isolated buildings using multiple tuned mass dampers. *Struct. Design Tall Special Build.* 28:e1576. doi: 10.1002/tal.1576

Stanikzai, M. H., Elias, S., Matsagar, V. A., and Jain, A. K. (2019). Seismic response control of base-isolated buildings using tuned mass damper. *Aust. J. Struct. Eng.* doi: 10.1080/13287982.2019.1635307. [Epub ahead of print].

Tsai, H.-C., and Lin, G. C. (1993). Optimum tuned-mass dampers for minimizing steady-state response of supportexcited and damped structures. *Earthquake Eng. Struct. Dyn.* 22, 957–913. doi: 10.1002/eqe.4290221104

Tsai, H. C. (1995). The effect of tuned-mass damper on the seismic response of base-isolated structures. *Int. J. Solids Struct.* 32, 1195–1210. doi: 10.1016/0020-7683(94)00150-U

Vakakis, A. F., Manevitch, L. I., Gendelman, O., and Bergman, L. A. (2003). Dynamics of linear discrete systems connected to local, essentially non-linear attachments. *J. Sound Vibration* 264, 559–577. doi: 10.1016/S0022-460X(02)01207-5

Wu, J. C., Chang, C. H., and Lin, Y. Y. (2009). Optimal design of non-uniform tuned liquid column dampers in horizontal motion. *J. Sound Vibration* 326, 104–122. doi: 10.1016/j.jsv.2009.04.027

Xiang, P., and Nishitani, A. (2014). Optimum design for more effective tuned mass damper system and its application to base-isolated buildings. *Struct. Control Health Monit.* 21, 98–114. doi: 10.1002/stc.1556

Yalla, S., and Kareem, A. (2000). Optimum absorber parameters for tuned liquid column dampers. *J. Struct. Eng.* 126, 906–915. doi: 10.1061/(ASCE)0733-9445(2000)126:8(906)

Yalla, S. K., and Kareem, A. (2003). Semiactive tuned liquid column dampers: experimental study. *J. Struct. Eng.* 129, 960–971. doi: 10.1061/(ASCE)0733-9445(2003)129:7(960)

Yang, J. N., Danielians, A., and Liu, S. C. (1991). Aseismic hybrid control systems for building structures. *J. Eng. Mech.* 117, 836–853. doi: 10.1061/(ASCE)0733-9399(1991)117:4(836)

Conflict of Interest: The authors declare that the research was conducted in the absence of any commercial or financial relationships that could be construed as a potential conflict of interest.

frontiers in Built Environment

ORIGINAL RESEARCH
published: 03 December 2019
doi: 10.3389/fbuil.2019.00141

Effects of Fire Duration on the Seismic Retrofitting With Hysteretic Damped Braces of r.c. School Buildings

Fabio Mazza and Giovanna Imbrogno*

Department of Civil Engineering, University of Calabria, Cosenza, Italy

School buildings are susceptible to high incidents of fire because of carelessness, faulty electrical installation and arson, raising the attention on their seismic retrofitting after fire exposure. Hot and residual mechanical properties of a reinforced concrete (r.c.) structure exposed to fire depend on duration of the heating and cooling phases. As a consequence, seismic retrofitting of a fire-damaged framed structure may not be effective when the peak temperature during a fire is considered. For a successful retrofit, ultimate capacity resulting from residual properties after cooling needs to be taken into account. To this end, the state secondary school Collina-Castello of Bisignano (Cosenza, Italy), a three-story r.c. framed structure designed in a medium-risk seismic region to comply with a former Italian seismic code, is considered as test structure. Thermal analysis of r.c. frame members is preliminarily carried out for two fire scenarios, on the assumption that the fire compartment is confined to the ground (F0) and first (F1) levels. Moreover, four fire-damage cases are examined, considering only the heating phase, at 30 (i.e., F1) and 45 (i.e., F0) minutes of fire resistance, and the overall fire cycle, for fast, medium and slow phases of cooling. Afterwards, the school is supposed to be retrofitted with hysteretic damped braces (HYDBs), in order to achieve the performance levels imposed by current Italian code in a high-risk seismic zone. Non-linear static and dynamic analyses of the unbraced and damped braced structures are carried out, with reference to the degradation of r.c. frame members for different fire durations in the design procedure of the HYDBs.

Keywords: r.c. school buildings, fire damage, duration of heating and cooling phases, hysteretic damped braces, thermal analysis, seismic retrofitting, non-linear seismic analysis

OPEN ACCESS

Edited by:
Panagiotis Mergos, City University of London, United Kingdom

Reviewed by:
Ehsan Noroozinejad Farsangi, Graduate University of Advanced Technology, Iran
Chrysanthos Maraveas, University of Liège, Belgium
Emanuele Brunesi, Fondazione Eucentre, Italy
Gloria Terenzi, University of Florence, Italy

****Correspondence:***
Fabio Mazza
fabio.mazza@unical.it

Specialty section:
This article was submitted to Earthquake Engineering, a section of the journal Frontiers in Built Environment

Received: *13 August 2019*
Accepted: *11 November 2019*
Published: *03 December 2019*

Citation:
Mazza F and Imbrogno G (2019) Effects of Fire Duration on the Seismic Retrofitting With Hysteretic Damped Braces of r.c. School Buildings. Front. Built Environ. 5:141. doi: 10.3389/fbuil.2019.00141

INTRODUCTION

Fires have heating and cooling phases, yet the effects of the latter on temperature distribution and residual mechanical properties are generally not considered when evaluating structural behavior. However, recent experimental (e.g., Gernay, 2019) and computational (e.g., Behnam, 2017) studies, characterizing detrimental effects of the cooling phase, have highlighted the possibility of a further decrease in the carrying capacity of reinforced concrete (r.c.) members even after maximum fire temperature has been reached. Specifically, degradation of the mechanical properties of r.c. structures may continue when the fire cools slowly because of the delayed increase of temperature in the inner layers due to thermal inertia of concrete (Dimia et al., 2011; Mazza and Alesina, 2019).

Concrete does not recover strength (i.e., thermal decohesion) and stiffness (i.e., thermal damage) after fire and its heat properties are progressively reduced as function of the duration of the heating and cooling phases (Lee et al., 2008; Maraveas and Vrakas, 2014). Progressive and explosive spalling are also evident in high and ultra-high strength concrete rather than in normal one, on account of low permeability (i.e., hydraulic spalling) and restrained thermal dilation (i.e., thermal spalling) of the zone near the heated surface produced by the cooler inner layers of concrete (Maraveas and Vrakas, 2014). Moreover, the residual compressive strength of the concrete is significantly influenced by the cooling method, with an additional strength reduction of 38% for quenching but not for spraying (Botte and Caspeele, 2017). On the other hand, reinforcing steel bars recover most of their initial properties provided that maximum temperature during fire remains below a critical value (Felicetti et al., 2009). Specifically, mild- and high-strength and stainless steels regain at least 75% of their initial mechanical properties after exposure to fire temperatures above 600°C (Maraveas et al., 2017). As a result, the assessment of fire damage to the structure upon cooling is necessary to establish whether the residual capacity should be increased by retrofitting. However, the simplified 500°C isotherm method, proposed by Eurocode 2 (European Committee for Standardization, EC 2.1-2, 2004b) for assessing the fire resistance of r.c. frame members, applies in the case of thermal profiles inside the member similar to those induced by a standard fire, but it fails in the case of natural fire when the external layers undergo cooling while the internal ones remain hot. In a realistic fire scenario, thermal analysis of the r.c. cross-sections should be performed in the time domain considering the intensity and duration of the fire, because verification at the maximum temperature is not always a sufficient precaution.

On the basis of the above, the seismic retrofitting of r.c. structures damaged by a fire can be a serious problem because an earthquake after a fire can find a different, more vulnerable, condition with respect to the hot stage related to the maximum gas temperature (Mazza, 2015). Damped bracing systems represent a cost-effective strategy which can simultaneously add damping and increase strength (e.g., Christopoulos and Filiatrault, 2006), thereby limiting structural damage without changing the existing structural components. As a matter of fact, the use of dissipative braces also provides significant additional stiffness in the structure, that usually affects maximum base shear and sometimes floor accelerations adversely. But this problem loses its relevance for post-fire resistance because a significant decrease in stiffness and strength is confirmed in the structural members exposed to fire, in comparison with the no-fire condition (Mazza and Alesina, 2019), thus stiffer and stronger damped braces can be inserted in the fire-damaged level; these will be able to restore the corresponding initial values at that level. As final remark, many design procedures of damped braces have been developed according to the performance-based design philosophy (Mazza et al., 2015; Sorace et al., 2016), in parallel to the notable improvement in damper technology, although specific seismic code provisions are still lacking.

The present work shows how to retrofit school buildings damaged from fire, taking into account effects of different fire durations. The Collina-Castello school building in Bisignano (Italy), a three-story r.c. framed structure designed in a medium-risk seismic region to comply with a former Italian code (Italian Ministry of Public Works, 1975), is considered as test structure. Two fire scenarios are assumed considering the fire compartment confined to the area of the ground (F0) and first (F1) levels, with the parametric time-temperature fire curves evaluated in accordance with Eurocode 1 (European Committee for Standardization, EC 1.1-2, 2004a). Four fire cases are investigated: i.e., only the heating phase, at 30 (i.e., F1) and 45 (i.e., F0) minutes of fire resistance; the overall fire duration, in cases of fast, medium and slow cooling. Residual strength and stiffness properties of r.c. frame members after fire are evaluated by experimental results, taking into account the fact that when concrete (Chang et al., 2006) and steel rebars (Slowanski et al., 1971) have cooled down an additional decrease in their performance may occur. Then, the fire-damaged school is retrofitted with hysteretic damped braces (HYDBs) on the basis of a displacement-based design procedure (Mazza et al., 2015) modified in order to recover structural regularity compromised by fire. Finally, in order to check the effectiveness of the proposed retrofitting criterion, non-linear static and dynamic analyses of the unbraced and damped braced fire-damaged structures are carried out.

THE COLLINA-CASTELLO SCHOOL BUILDING

Layout and Design

The school building Collina-Castello in Bisignano (Cosenza, Italy), monitored since 2004 within the Italian network of the Seismic Observatory of Structures is considered for the numerical study (**Figure 1A**). The three-story reinforced concrete (r.c.) structure was constructed in 1983; it is made of four plane frames along the principal in-plan X direction (**Figure 1C**). Only perimeter frames are placed along the short side (**Figure 1D**), lacking interior beams in parallel with the floor slab direction. In plan orientation of columns, having a 0.4 m × 0.5 m cross-section, and typologies of the longitudinal (0.4 m × 0.6 m) and transversal (0.5 m × 0.4 m) beams are also reported in **Figure 1B**. The r.c. structure was designed to comply with the admissible tension method, in compliance with a former Italian seismic code (Italian Ministry of Public Works, 1975), assuming a medium-risk seismic region (coefficient of seismic intensity $C = 0.07$) and a medium subsoil class (coefficient of subsoil $\varepsilon = 1.0$). In 2004, the Department of Civil Protection (D.C.P.) carried out a geometrical survey and material controls of the building. A cylindrical compressive strength of 20.4 MPa and an elastic secant modulus $E_c = 25{,}140$ MPa, for concrete, and a yield strength of 375 MPa for steel are assumed. The strengths of concrete and steel are divided by a confidence factor valued at 1.2, corresponding to a suitable level of knowledge of the building as provided by the current Italian seismic code (Italian Ministry of the Infrastructures, 2018). The gravity loads are represented by: dead loads of 5.52 and 5.00 kN/m^2 on the first and second floor, respectively, and 6.78 kN/m^2 on the top floor, assigning the

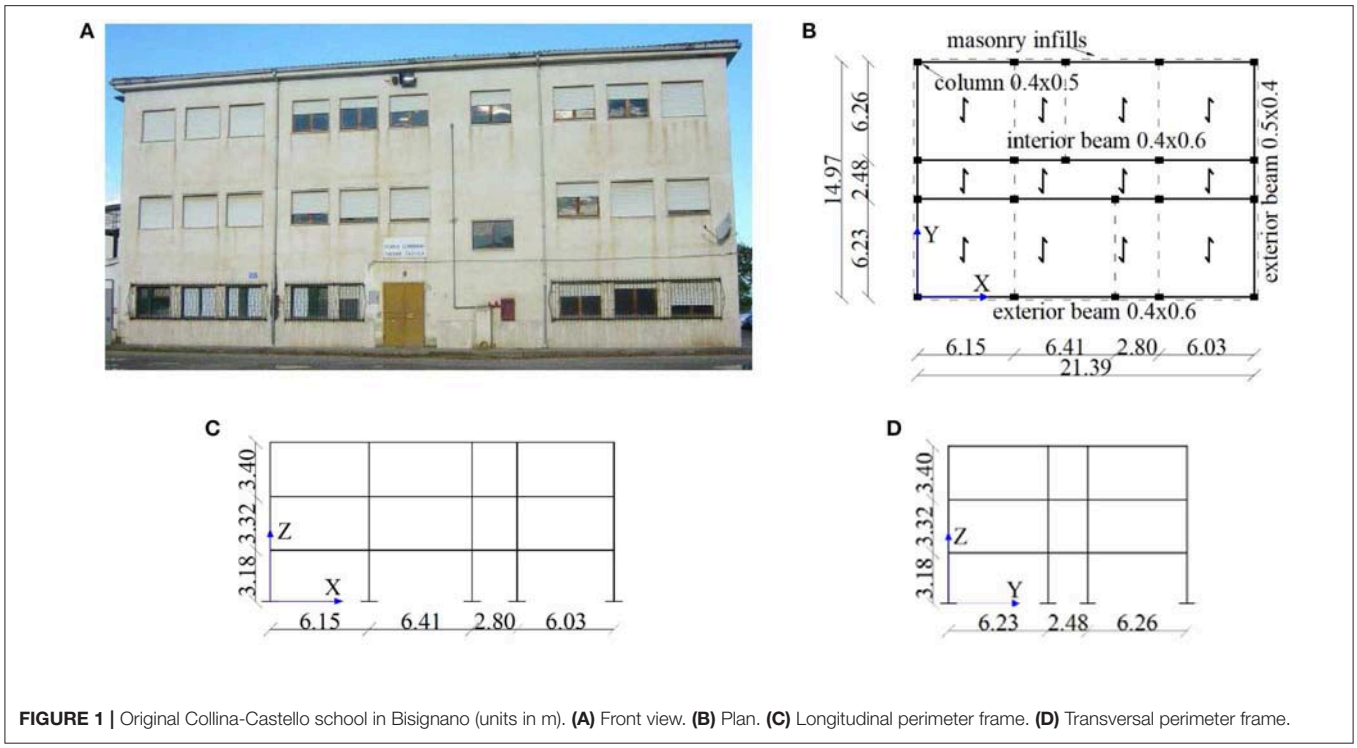

FIGURE 1 | Original Collina-Castello school in Bisignano (units in m). **(A)** Front view. **(B)** Plan. **(C)** Longitudinal perimeter frame. **(D)** Transversal perimeter frame.

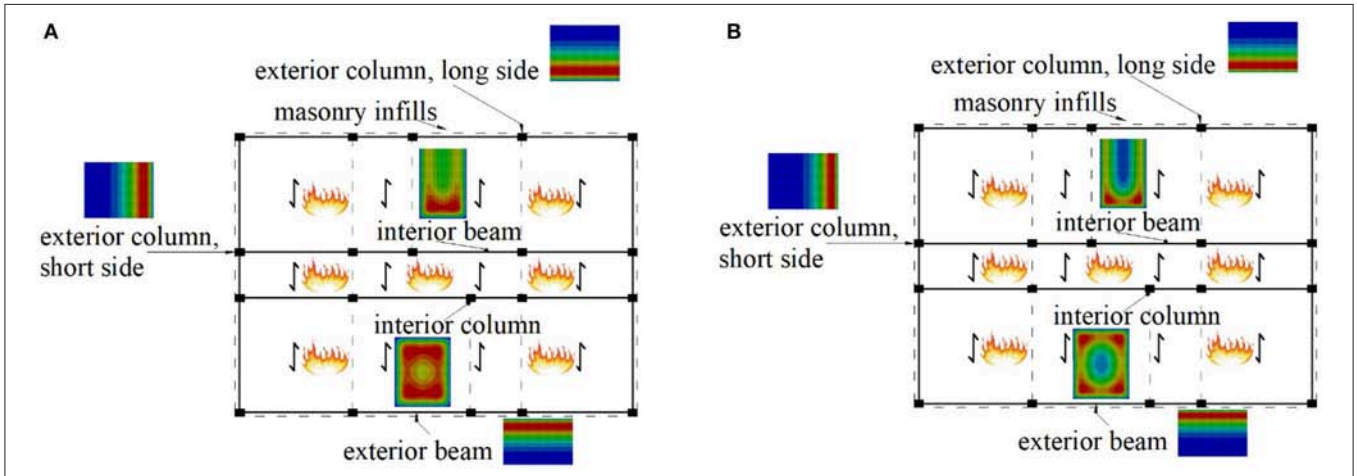

FIGURE 2 | Fire compartments for the Collina-Castello school. **(A)** Fire scenario F0. **(B)** Fire scenario F1.

weight of the roof at the third level; live loads of 3.0 kN/m^2 on the first two floors and 0.5 kN/m^2 on the top floor, omitting the snow load on the roof in the seismic load combination. Masonry-infills regularly distributed in elevation are placed along the perimeter, assuming a weight of 11 kN/m^3. Additional details on the steel reinforcement of columns and beams, constant along the height of the building, are reported in other works (Mazza and Vulcano, 2014a; Sorace and Terenzi, 2014).

TABLE 1 | Design parameters of the fire load (EC 1-1.2).

Fire case	Fire resistance	$Q_{f,k}$ [MJ]	$q_{f,d}$ [MJ/m^2]	$q_{t,d}$ [MJ/m^2]	A_f [m^2]	A_t [m^2]
F0	R45	167,015	520.3	190.8	321	875
F1	R30	117,276	365.3	134.0	321	875

Design of the Fire Scenarios

Ground and first floor levels of the Collina-Castello school are used for offices and classrooms, respectively, producing two different fire scenarios (i.e., F0 and F1) with a uniform temperature extended to the whole floor area (**Figure 2**). Fire involves four and three sides of the interior columns and beams,

TABLE 2 | Design parameters of the cooling phase.

Fire case	Fire resistance	O [$m^{1/2}$]	b [J/m^{2}s$^{1/2}$K]	θ_{max} [°C]	t^*_{max} [min]	$t_{cooling}$ [min]
F0	R_{SC}	0.020		835	105	416
	R_{MC}	0.028	1177	882	80	257
	R_{FC}	0.063		1,003	36	100
F1	R_{SC}	0.025		815	64	265
	R_{MC}	0.034	1177	858	46	160
	R_{FC}	0.066		955	24	71

respectively, and one side for all the exterior elements. The design value of the fire load density is function of the combustible contents of the compartment (EC 1.1-2):

$$q_{t,d} = q_{f,d} \cdot A_f / A_t \tag{1}$$

related to A_t, the total area of enclosure (i.e., walls, ceiling, and floor, including openings), and $q_{f,d}$. The latter is the value corresponding to the surface area of the floor (A_f)

$$q_{f,d} = \delta_{q1} \cdot \delta_{q2} \cdot \delta_n \cdot Q_{f,k} / A_f \tag{2}$$

being: $Q_{f,k}$ the characteristic fire load; δ_{q1} and δ_{q2} partial factors related to the risk of fire; δ_n differentiation factor depending on the active fire prevention measures. With reference to 30 min (R30) and 45 min (R45) of exposure, the design parameters of the fire load for the two levels of the test structure are shown in **Table 1**.

Many time-temperature curves are available in order to simulate post-flashover fully developed fires (Ariyanayagam and Mahendran, 2014). The EC 1.1-2 expression of the gas temperature θ_g(°C) during the heating phase takes into account size, thermal properties, and ventilation conditions of the fire compartment by using the following equation

$$\theta_g = 20 + 1325 \cdot \left(1 - 0.324e^{-0.2t^*} - 0.204e^{-1.7t^*} - 0.472e^{-19t^*}\right) \tag{3}$$

where the actual duration of the fire is determined by considering fictitious time t^* given by time t (in hours) multiplied by a dimensionless parameter equal to

$$\Gamma = \left(O/b\right)^2 / (0.04/1160)^2 \tag{4}$$

where O is an opening factor related to A_v, area of vertical openings, h_{eq}, weighted average of vertical openings, and A_t, total area of enclosure

$$O = A_v {h_{eq}}^{0.5} / A_t \tag{5}$$

and b is the thermal inertia of all enclosure surfaces of the compartment. The gas temperature in the cooling phase is evaluated as

$$\begin{aligned} \theta_g &= \theta_{\max} - 625\left(t^* - t^*_{\max}\right), \; t^*_{\max} \le 0.5\,h \\ \theta_g &= \theta_{\max} - 250\left(3 - t^*_{\max}\right)\left(t^* - t^*_{\max}\right), \; 0.5\,h < t^*_{\max} < 2\,h \\ \theta_g &= \theta_{\max} - 250\left(t^* - t^*_{\max}\right), \; t^*_{\max} \ge 2\,h \end{aligned} \tag{6}$$

where the maximum temperature θ_{max} in the heating phase lasts for

$$t^*_{\max} = \max\left(0.2 \cdot 10^{-3} q_{t,d}/O, t_{\lim}\right) \tag{7}$$

being t_{lim}=25, 20, and 15 min in the case of slow, medium and fast fire growth, respectively. This parametric curve shall apply to compartments with mainly cellulosic type fuel loads, floor area up to 500 m^2 and thermal inertia $100 \le b \le 2{,}200$ J/m^{2}s$^{1/2}$K and opening factor $0.02 \le O \le 0.2$ m$^{1/2}$. It is interesting to note that the duration of the cooling phase is unaffected by the fuel load density while it increases for decreasing values of the opening factor and increasing values of thermal inertia. In particular, **Table 2** reports the above mentioned parameters defining the final instant of the cooling phase ($t_{cooling}$). Three cooling laws are assumed for the F0 (**Figure 3A**) and F1 (**Figure 3B**) fire scenarios, corresponding to different final instants to recovery the ambient temperature of 20°C: i.e., fast (R_{FC}), medium (R_{MC}), and slow (R_{SC}) cooling.

The standard ISO-834 curve (ISO 834, 1999) is also reported in **Figure 3**, representing the heating phase with fire temperature depending on the elapsed time only. The combination of the design parameters results in an increase of maximum temperature and a concurrent reduction of duration of the heating and cooling phases when increasing values of the opening factor are assumed.

Next, the temperature distribution in the r.c. frame members is evaluated considering boundary conditions on the heat flow derived from the parametric time-temperature curves proposed by EC 1.1-2. Specifically, quadratic 8-node quadrilateral elements, with a mesh size equal to 1 cm, are assumed for two-dimensional uncoupled heat transfer transient finite element analysis of r.c. cross-sections (ABAQUS, 2014). The unexposed cross-section sides are assumed to be at ambient temperature of 20°C, while temperature is considered constant along the longitudinal axis of each frame member. Thermal parameters used for concrete (c) and steel (s) are as follows: thermal conductivity, $k_c = 2$ W/mK and $k_s = 50$ W/mK; specific heat, $c_{p,c} = 900$ J/kgK and $c_{p,s} = 450$ J/kgK; density, $\rho_c = 2{,}300$ kg/m^3 and $\rho_s = 7{,}850$ kg/m^3. Finally, a heat convection factor equal to 35 W/m^{2}K and radiation emissivity equal to 0.56 are assumed for the concrete of surfaces exposed to fire, while 9 W/m^{2}K is selected as convection factor for the surfaces not exposed.

With regard to the interior beams and columns on the ground level of the Collina-Castello school, thermal mappings of r.c. cross sections are shown in **Figures 4A–D,E–H**, respectively, considering thermal diffusion in the part of beams included in the floor slab. The internal distribution of temperature during the heating phase, after 45 min of fire exposure (R45), is compared with that evaluated at the end of fast (R_{FC}), medium (R_{MC}), and slow (R_{SC}) phases of cooling for the F0 fire scenario. Note that for decreasing decay rates of the cooling phase (**Figures 4B–D,F–H**), the internal layers show higher temperatures than the exterior ones. This behavior depends on the delayed increase in temperature in the internal layers due to thermal inertia of internal concrete, while the external layers cool

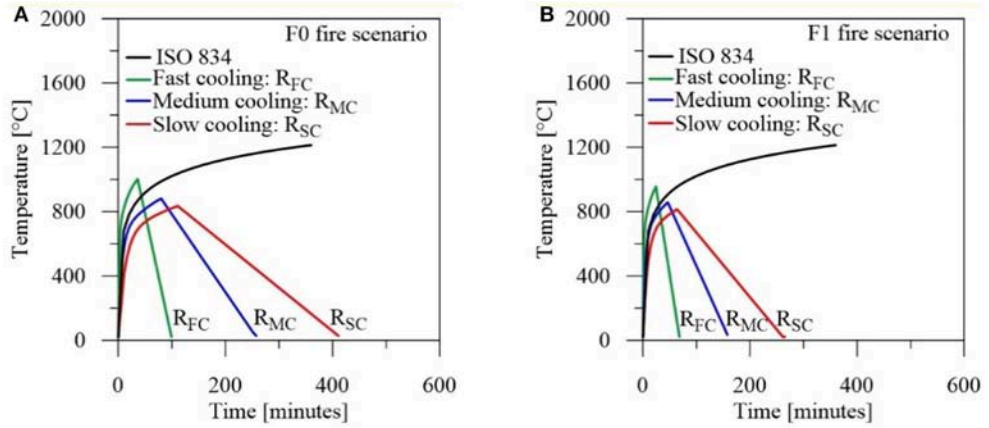

FIGURE 3 | Time-temperature curves for the Collina-Castello school. **(A)** F0 fire scenario. **(B)** F1 fire scenario.

down. On the other hand, during the heating phase the external layers are heated to temperatures much higher than those of the internal layers (**Figures 4A,E**). Finally, a close relation between duration of the cooling phase and maximum temperature and extension of the damaged part of the cross-section is observed, while the number of sides exposed to fire is the main parameter when the heating phase is considered.

Specifically, the most heated areas are found to be the corners (**Figures 4B,F**), edges (**Figures 4C,G**), and center (**Figures 4D–H**) when R_{FC}, R_{MC}, and R_{SC} are considered, respectively. Similar results, omitted for the sake of brevity, are obtained for the exterior columns, with a short and long side exposed to fire, and beams, with the most headed areas parallel to the side exposed to fire.

Residual Properties of r.c. Frame Members After a Fire

The residual values of the stiffness, strength, and ductility properties of r.c. frame members exposed to fire are evaluted by a variable isotherm method, on the assumption that the temperature is constant along their longitudinal axis. To a specific duration of the heating (t^*_{max}) and cooling ($t_{cooling}$-t^*_{max}) phases of a fire, the r.c. cross-section is divided into an appropriate number of concentric subsections, each of which is further subdivided in a number of subelements corresponding to the exposed sides. Discretization of the cross-sections of r.c. frame members is shown in **Figure 5**, distinguishing interior columns (**Figure 5A**) and beams (**Figure 5B**) and exterior columns (**Figure 5C**) and beams (**Figure 5D**). Specifically, the temperature in the center of the i-th subelement is considered and simmetry is used in the case of opposite sides exposed to fire (e.g., $T_{bottom,i} = T_{top,i}$ and $T_{left,i} = T_{right,i}$, for an interior column, and $T_{left,i} = T_{right,i}$, for an interior beam). It should be noted that the innermost subelement (see blue edge) has an equal temperature on all sides.

As an example, time-temperature profiles for the cross-section of r.c. interior columns at the ground (i.e., F0 scenario) and first (i.e., F1 scenario) levels of the school are plotted in **Figure 6**, starting from the border and ending at the center along the horizontal direction. Temperatures in the center of five concrete concentrically layers are shown, with reference to the slow (**Figures 6A,D**), medium (**Figures 6B,E**), and fast (**Figures 6C,F**) cooling rates. Note that the temperature evolution in the concentric layers is different during the heating and cooling phases and more marked differences are observed for decreasing values of the cooling rate. Moreover, maximum temperature in the outer layers is reached before t^*_{max} for all rates of cooling, while this occurs during or at the end of the cooling phase for the inner ones. Finally, temperature variations are more evident for the F0 scenario characterized by the highest temperature during fire, while the temperature of the internal layers does not recover the ambient value at the end of the time-temperature curves ($t_{cooling}$) reported in **Table 2**.

Two approaches are applied to evaluate the residual capacity of the cross-sections subjected to different fire scenarios and decay rates: (i) the 500°C isotherm method proposed by EC 2.1-2, combined with R30 and R45 fire resistances in the heating phase; (ii) the proposed variable isotherm method, using time-temperature profiles of the internal layers during the cooling phase. For this purpose, reduction factors of the compressive strength, $\alpha_{fc} = f_{c\theta}/f_{c20}$, and elastic modulus, $\alpha_{Ec} = E_{c\theta}/E_{c20}$, for concrete (Chang et al., 2006) and the yield strength, $\alpha_{fy} = f_{y\theta}/f_{y20}$, for steel (Slowanski et al., 1971) are reported in **Figure 7**, with reference to the hot (**Figure 7A**) and cold (**Figure 7B**) conditions.

Note that notable reduction of the residual strength of the concrete is observed during the cooling phase due to thermal inertia of the inner layers, contrary to the EC 2.1-2 where concrete exceeding the temperature of 500°C is not considered. The situation is quite different for the yield strength of steel highlighting an almost complete recovery after cooling, differently from the EC 2.1-2 where a notable reduction is hypothesized referring to the maximum temperature during the heating phase.

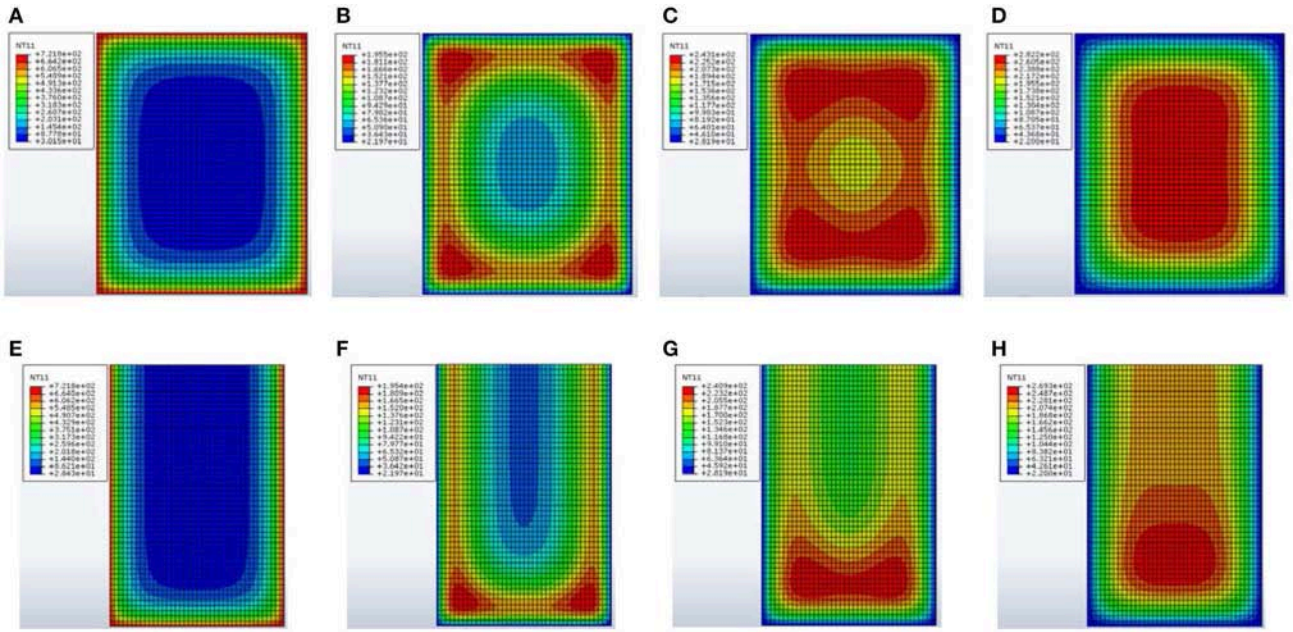

FIGURE 4 | Thermal mappings of interior r.c. frame members for the F0 fire scenario. **(A)** R45: columns. **(B)** R_{FC}: columns. **(C)** R_{MC}: columns. **(D)** R_{SC}: columns. **(E)** R45: beams. **(F)** R_{FC}: beams. **(G)** R_{MC}: beams. **(H)** R_{SC}: beams.

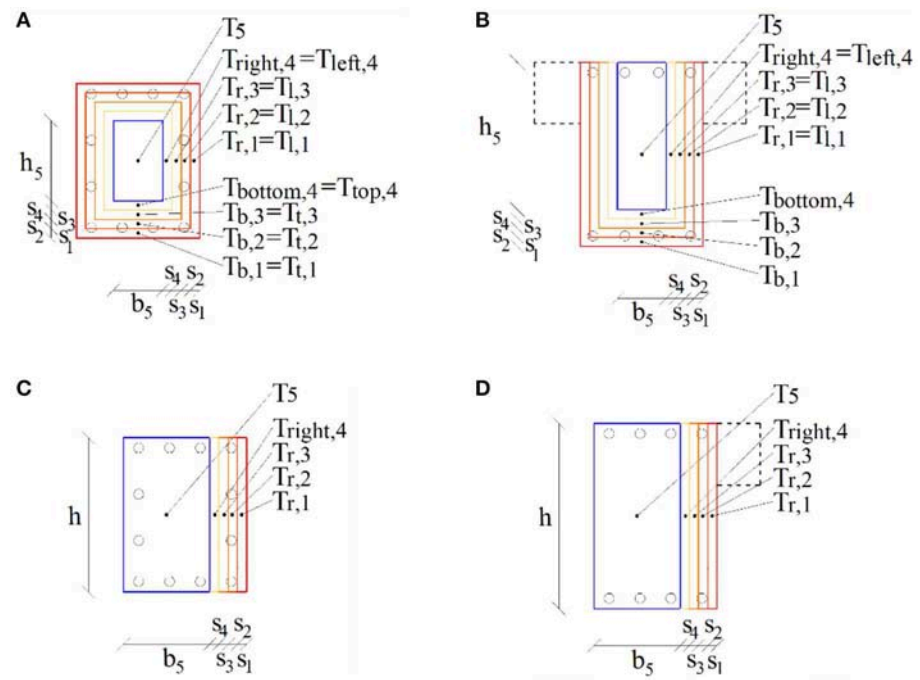

FIGURE 5 | Discretization of an r.c. cross-section with the variable isotherm method. **(A)** Interior column. **(B)** Interior beam. **(C)** Exterior column. **(D)** Exterior beam.

For the sake of brevity, only post-fire mechanical properties of the interior columns along the main local axis of the cross-section are reported in **Figure 8**, with reference to the first (**Figures 8A,C,E**) and second (**Figures 8B,D,F**) levels of the Collina Castello school. The influence of the duration of the cooling phase is investigated by comparing slow (R_{SC}), medium (R_{MC}), and fast (R_{FC}) cooling processes with results at the R30 (i.e., F1) and R45 (i.e., F0) fire resistances and the no fire

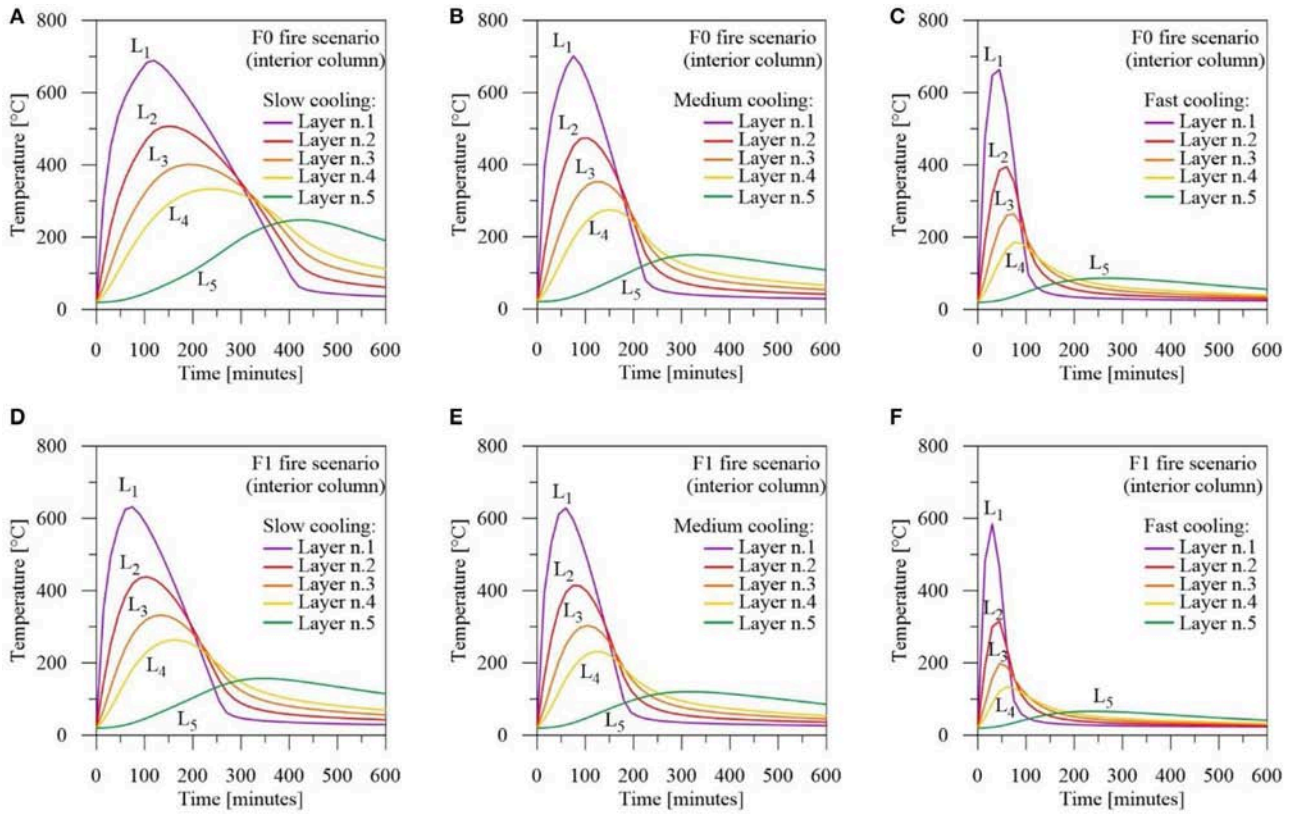

FIGURE 6 | Time-temperature profiles for the cross-section of an interior column exposed to fire at the ground **(A,B,C)** and first **(D,E,F)** level of the Collina-Castello school.

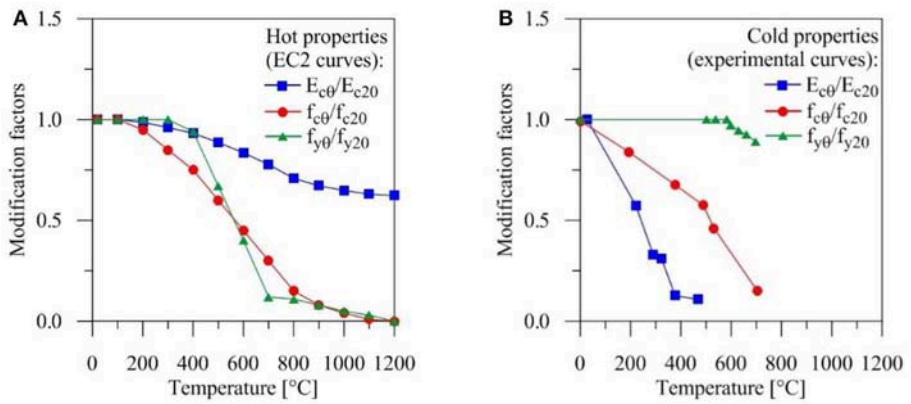

FIGURE 7 | Modification factors of mechanical properties for r.c. frame members during heating and cooling phase: hot **(A)** and cold **(B)** properties.

condition (i.e., $T = 20°C$). In particular, the axial load (N_{Rd}) and bending moment (M_{Rd}) ultimate interaction domain narrows for decreasing values of the cooling rate (**Figures 8A,B**), especially when the balanced compressive load is exceeded.

Moreover, the notable reduction of the flexural stiffness after heating and cooling (**Figures 8C,D**) leads to a different distribution of the seismic loads between the exterior and interior columns of the fire compartment, compared to the heating (i.e., R30 and R45) and no fire conditions. Finally, only limited fire effects are found on the ultimate ductility corresponding to the axial force due to the gravity loads (**Figures 8E,F**).

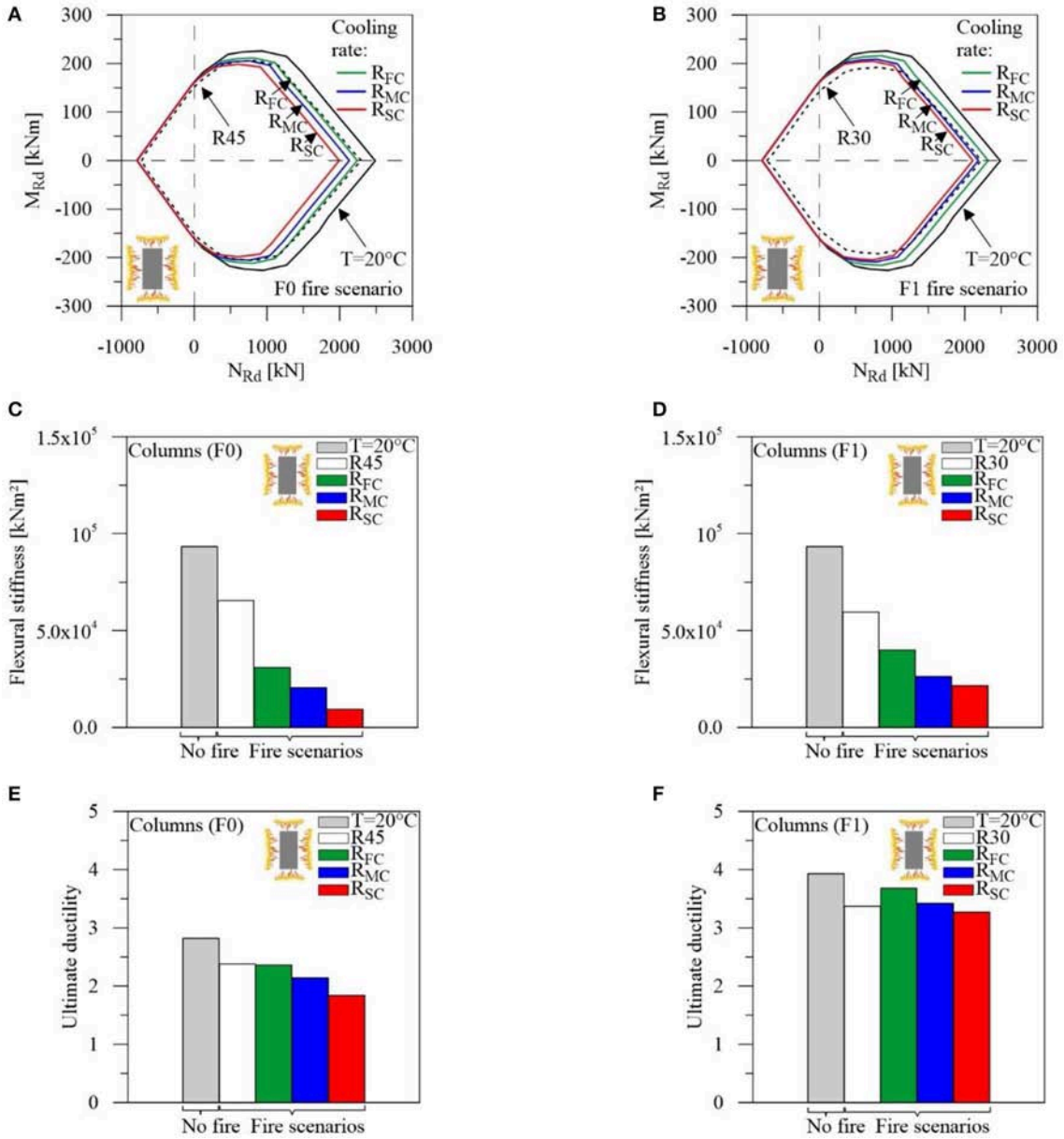

FIGURE 8 | Residual properties for interior columns of the Collina-Castello school: F0 **(A,C,E)** and F1 **(B,D,F)** fire scenarios.

Seismic Retrofitting With Hysteretic Damped Braces

The non-linear static (pushover) analysis of the school is carried out before and after fire, along the in-plan X and Y principal axes. The inelastic behavior of the r.c. frame members is modeled with plastic hinges lumped at both ends, assuming an elastic-plastic moment-curvature law with linear hardening (i.e., hardening ratio $r_F = 3\%$). A three-step algorithm, based on the Haar–Kàrmàn principle, and the arc-length method are adopted to evaluate the capacity curve (Mazza and Mazza, 2010; Mazza, 2014a). Invariant lateral force distributions are considered for the non-linear static analysis, varying the intensity proportionally to the floor masses with ("modal type") or without ("uniform type") the fundamental vibration mode. The pushover analyses are terminated once the ultimate value of the curvature ductility demand is attained at critical sections of frame members (see NTC18 provisions for existing buildings). As an example, normalized base shear (i.e., V_b/W_{tot}, W_{tot} being the total seismic weight) and horizontal top displacement (i.e., u_{top}/H_{tot}, H_{tot} being the total height) of the structure, along the X and Y directions, are plotted in **Figure 9** with and without fire.

The capacity curves along the X direction are plotted in **Figures 9A–D** with reference to the F0 and F1 fire scenarios, respectively. In detail, results obtained for fast (R_{FC}), medium

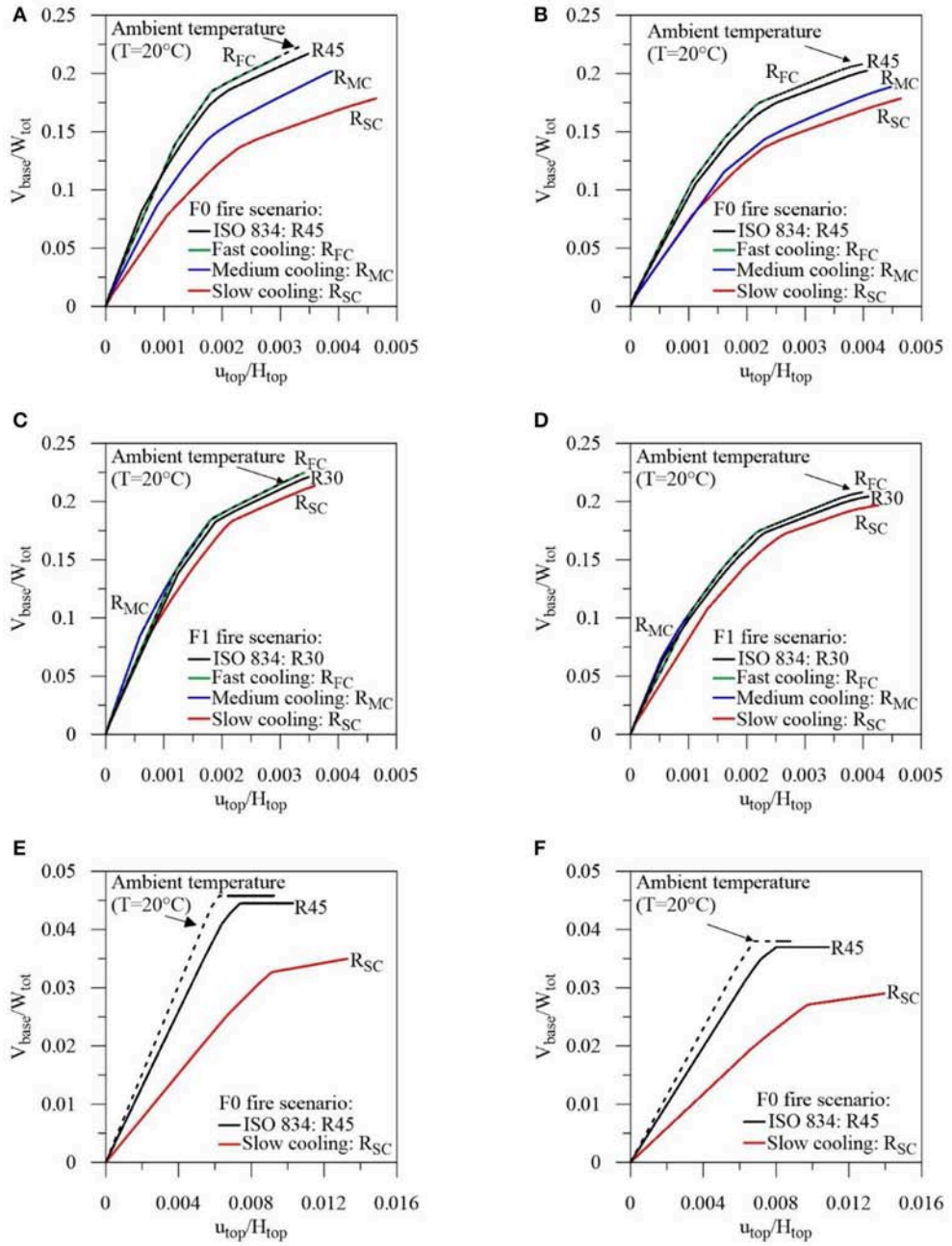

FIGURE 9 | Comparison of pushovers curves for the Collina-Castello school before retrofitting, with and without fire at ground (F0) and first (F1) level. **(A)** Uniform pattern in the X direction: F0 scenario. **(B)** Modal pattern in the X direction: F0 scenario. **(C)** Uniform pattern in the X direction: F1 scenario. **(D)** Modal pattern in the X direction: F1 scenario. **(E)** Uniform pattern in the Y direction: F0 scenario. **(F)** Modal pattern in the Y direction: F0 scenario.

(R_{MC}) and slow (R_{SC}) cooling phases are compared with those corresponding to the ISO-834 curve with R45 and R30 fire resistances, respectively. Pushover curves corresponding to the "uniform" (**Figures 9A,C**) and "modal" (**Figures 9B,D**) load distributions are more restrictive in terms of displacement and shear, respectively. Moreover, the significant decrease of stiffness and strength in the structural elements exposed to the F0 fire scenario corresponds to an increase of displacement and reduction of shear in comparison with the no-fire condition, when an increasing fire duration is considered (**Figures 9A,B**). Little difference is found with results obtained for ambient temperature for the F1 fire scenario (**Figures 9C,D**). This may be justified by the fact that capacity curves corresponding to different fire conditions depend on undamaged columns at the ground level when fire at the first level is assumed. Finally, central columns at the ground level affect the ultimate behavior in the no

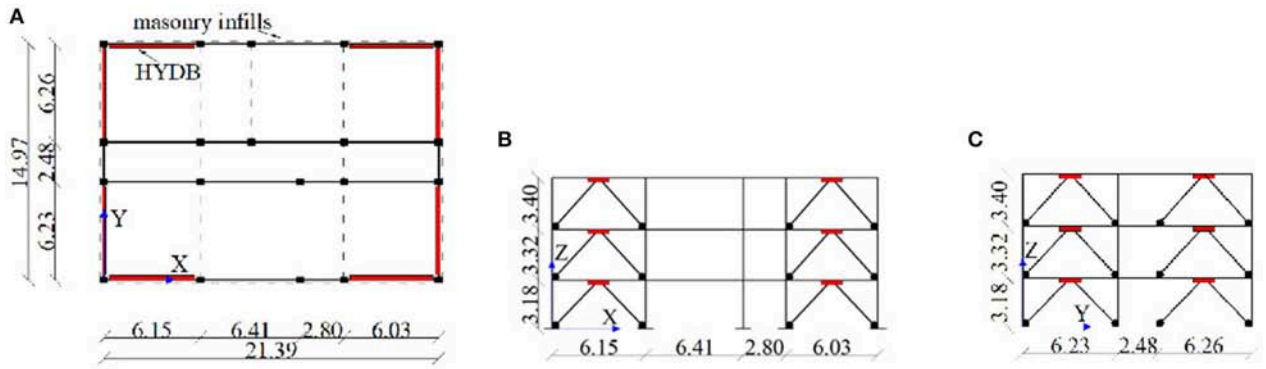

FIGURE 10 | Retrofitted Collina-Castello school in Bisignano (units in m). **(A)** Plan. **(B)** Longitudinal perimeter frame. **(C)** Transversal perimeter frame.

TABLE 3A | Stiffness (kN/m) and strength (kN) of the HYDBs (case A, LS limit state).

X direction	$\mu_{Fd} = 1.3$		$\mu_{Fd} = 1.5$	
Story	K_{DB}	$N_{y,DB}$	K_{DB}	$N_{y,DB}$
1	4,320,170	343	3,417,667	309
2	1,655,221	280	1,291,708	252
3	406,074	159	269,074	143
Y direction	$\mu_{Fd} = 1.1$		$\mu_{Fd} = 1.3$	
1	521,340	120	365,708	98
2	245,141	98	182,110	80
3	21,494	55	0	0

TABLE 3B | Stiffness (kN/m) and strength (kN) of the HYDBs (case A, CP limit state).

X direction	$\mu_{Fd} = 1.3$		$\mu_{Fd} = 1.5$	
Story	K_{DB}	$N_{y,DB}$	K_{DB}	$N_{y,DB}$
1	5,570,490	448	2,188,083	425
2	2,163,601	366	2,397,345	328
3	595,872	208	2,173,574	169
Y direction	$\mu_{Fd} = 1.1$		$\mu_{Fd} = 1.3$	
1	894,265	208	632,565	172
2	396,176	169	290,187	141
3	78,105	96	38,378	80

fire condition, while exterior columns collapse when the F0 fire scenario is considered. Similar curves are plotted in **Figures 9E,F** referring to pushover curves of the undamaged and R45 and R_{SC} fire-damaged structures in the F0 scenario. As can be seen, top displacement in the Y direction is greater than in the X direction, due to the lack of interior beams in parallel with the floor slab direction, but the opposite occurs in terms of base shear depending on the in-plan orientation of the cross-sections of all columns (see **Figure 1B**).

In order to carry out seismic retrofitting of the school building in line with the provisions imposed by NTC18, a steel chevron bracing system with hysteretic dampers (HYDBs) is inserted in the exterior bays of the perimeter frames at all three stories (**Figure 10**). The coordinates of the seismic zone (longitude 16.17° and latitude 39.31°) correspond to peak ground accelerations on rock equal to 0.323 and 0.426 g at the life safety (LS) and collapse prevention (CP) limit states, respectively, and medium subsoil class (subsoil parameter equal to 1 and 1.08 at LS and CP, respectively).

The Displacement-Based-Design (DBD) procedure of HYDBs already proposed by the authors (Mazza, 2014b; Mazza and Vulcano, 2014b; Mazza et al., 2015) is applied to in-elevation irregularity due to fire. The distribution criterion of the HYDBs

TABLE 3C | Stiffness (kN/m) and strength (kN) of the HYDBs (case B, LS limit state).

X direction	$\mu_{Fd} = 1.3$		$\mu_{Fd} = 1.5$	
Story	K_{DB}	$N_{y,DB}$	K_{DB}	$N_{y,DB}$
1	2,001,244	330	1,559,924	297
2	2,192,637	254	1,709,111	229
3	1,987,974	131	1,549,581	118
Y direction	$\mu_{Fd} = 1.1$		$\mu_{Fd} = 1.3$	
1	378,892	119	262,542	98
2	247,345	99	171,391	81
3	180,341	55	124,962	45

is aimed to obtain a retrofitted structure globally regular with regard to stiffness and strength, by balancing the degradation of fire-exposed r.c. frame members. In detail, the stiffness distribution of the HYDBs is selected assuming the same value of the drift ratio at each story of the irregularly fire damaged building (i.e., case A). Moreover, the strength distribution of the HYDBs is assumed so that their activation tends to occur at

TABLE 3D | Stiffness (kN/m) and strength (kN) of the HYDBs (case B, CP limit state).

X direction	$\mu_{Fd} = 1.3$		$\mu_{Fd} = 1.5$	
Story	K_{DB}	$N_{y,DB}$	K_{DB}	$N_{y,DB}$
1	2,612,369	431	2,221,280	425
2	2,862,208	332	2,449,962	328
3	2,595,046	172	2,221,280	169
Y direction	$\mu_{Fd} = 1.1$		$\mu_{Fd} = 1.3$	
1	657,855	207	462,241	172
2	429,455	172	301,756	143
3	313,120	95	220,013	79

each story simultaneously, before reaching the shear resistance of the r.c. frame members. A proportional stiffness criterion (i.e., case B) is also applied, assuming that mode shapes of the fire-damaged structure remain practically the same after the insertion of HYDBs. The distribution of the lateral loads supported by the damped braces at the yielding point is assumed proportional to the stiffness distribution. This criterion is preferable in the case of an in-elevation regular structure, because the stress distribution in the frame members remains practically unchanged after retrofitting, but it may be misleading in the case of vertical irregularity due to fire. Stiffness (K_{DB}) and yield-load ($N_{y,DB}$) values of the HYDBs for the A and B cases described above are reported in **Tables 3A–D**, respectively, for the in-plan X and Y directions.

The design of the HYDBs is carried out to prevent brittle failure mechanisms of the original structure. To this end, different values of the design frame ductility are assumed at the LS and CP limit states (i.e., $\mu_{Fd} = 1.3$ and 1.5 in the *X* direction; $\mu_{Fd} = 1.1$ and 1.3 in the *Y* direction) combined with a constant design value of ductility for the HYDs (i.e., $\mu_D = 20$). It should be noted that the flexibility of the supporting steel brace connecting the damper to the frame is not considered (i.e., brace stiffness $K_B \rightarrow \infty$), so that the lateral stiffnesses of the HYDBs (K_{DB}) and HYDs (K_D) are assumed equal as well as the corresponding stiffness hardening ratios (i.e., $r_{DB} = r_D = 3\%$).

NUMERICAL RESULTS

A numerical study is performed to investigate the effectiveness of the new DBD procedure of the HYDBs and their distribution over the height of the building (i.e., cases A and B). To this end, non-linear static and dynamic analysis of the fire-damaged unbraced (UF) and damped braced (DBF) frames are carried out. The focus is mainly on the slow cooling phase (i.e., R_{SC}) that corresponds to the most severe fire in relation to duration, even if maximum temperature less than that observed for medium (i.e., R_{MC}) and fast (i.e., R_{FC}) cooling occurs (see **Figure 3**). Reduced stiffness, strength and ductility of the frame members at the ground and first levels, where the F0 and F1 fire compartments are localized, are evaluated by means of the variable isotherm method. Columns are assumed to behave elastically under axial forces, accounting for the interaction with bending moment in the yield condition, while axial strains are not considered in the beams; shear deformations are neglected in all the r.c. frame members. The hysteretic behavior of the HYDBs is simulated with a bilinear law, to prevent yielding and buckling of the steel braces. The non-linear static and dynamic responses are evaluated by an incremental step-by-step procedure (see Mazza, 2014a, 2015). At each step of the analysis, the incremental elastic response is evaluated as function of the known initial state and given nodal displacements; then, the elastic-plastic flexural solution is obtained by an initial stress iterative procedure. A Rayleigh damping matrix is assumed in the analysis of the test structures, imparting a viscous damping ratio equal to 5% to the first and third modes of the UF and DBF structures in the selected horizontal direction, so covering those modes important to the response.

Firstly, capacity curves are plotted in **Figures 11A–D** with reference to the X and Y directions, to evaluate the seismic vulnerability of the UF and DBF structures, assuming constant drift ratio (i.e., DBF.A in **Figures 11A,C**) and proportional stiffness (i.e., DBF.B in **Figures 11B,D**) design criteria. Stiffness and yield strength properties of the HYDBs are evaluated for both the displacement response spectra at the LS and CP limit states. The non-linear static analysis of the DBF.A and DBF.B structures is terminated once the ultimate value of damper ductility, assumed equal for all the examined cases (i.e., $\mu_{Du} = 20$), is attained. Checks of the ultimate limit state for ductile mechanism have also been carried out for the r.c. elements, for both unbraced and damped braced frames. As shown, the seismic retrofitting with HYDBs has proved to be more effective for the X direction rather than the Y, the latter exhibiting high deformability and low strength of the original structure due to the lack of interior beams. Moreover, the increase of lateral stiffness due to the insertion of the HYDBs produces a more marked increase of seismic loads in the Y direction characterized by the highest value of the fundamental vibration period. Note that the displacement capacity of the DBF.A (**Figures 11A,C**) is greater than that obtained for the DBF.B structures (**Figures 11B,D**), while comparable values of total base shear are obtained. As expected, the optimal design solutions are obtained when the CP limit state (see green lines) is combined to the lowest design values of the frame ductility along the X (i.e., $\mu_{Fd} = 1.3$) and Y (i.e., $\mu_{Fd} = 1.1$) directions.

Afterwards, in order to evaluate the effects of the retrofitting criteria of the HYDBs (i.e., DBF.A and DBF.B) on the seismic response of the school, non-linear dynamic analyses are carried out to consider two sets of horizontal accelerograms, corresponding to the LS and CP limit states. In accordance with the minimum number of artificial motions imposed by NTC18, three accelerograms, each with a duration of the stationary part equal to 10 s and a total duration of 25 s, are generated for each set of motions using the computer code (Seismoartif, 2018). The elastic response spectra of the artificial accelerograms match, on average, NTC18 elastic response spectra in the range of vibration periods 0.05–4 s. Specifically, local damage in terms of the ductility demand of

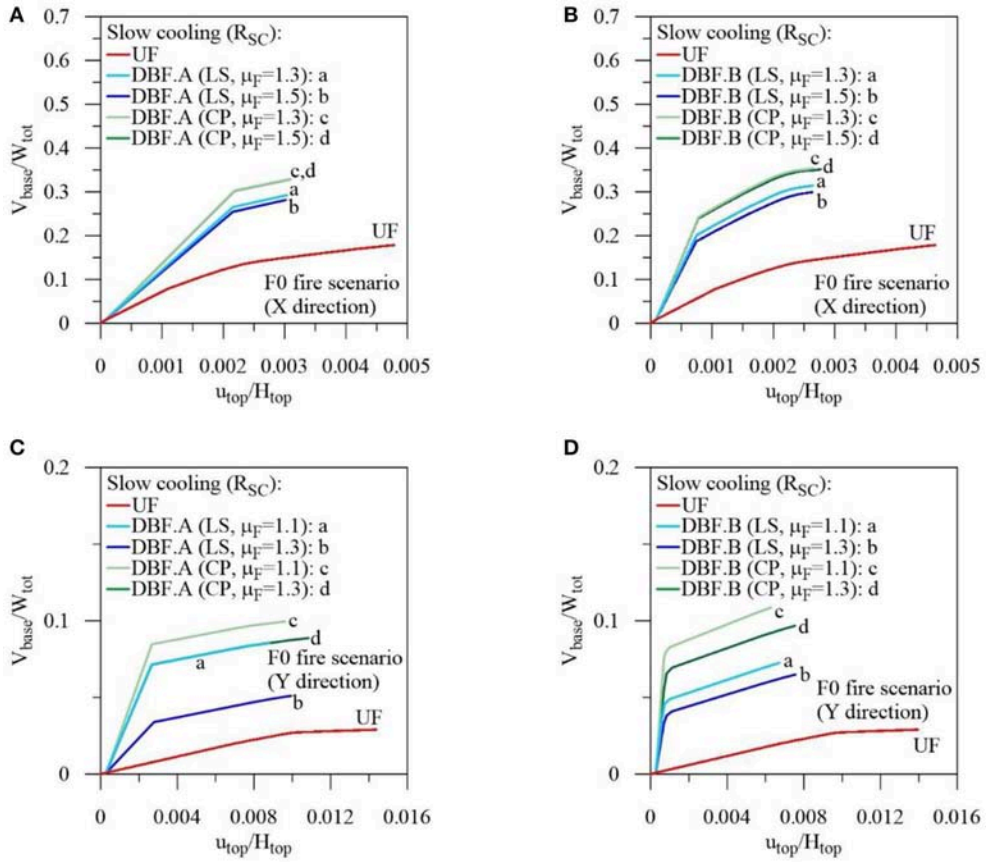

FIGURE 11 | Comparison of pushovers curves along the in-plan X and Y directions for the retrofitted Collina-Castello school, at LS and CP limit states. **(A)** Constant drift ratio criterion: X direction. **(B)** Proportional stiffness criterion: X direction. **(C)** Constant drift ratio criterion: Y direction. **(D)** Proportional stiffness criterion: Y direction.

beams and columns is reported in **Figures 12A–D**, respectively, evaluated as mean values of the maximum ductility demand obtained for the three artificial earthquakes considered at the LS limit state. Two retrofitting solutions are considered for the F0 fire scenario, assuming X (**Figures 12A,C**) and Y (**Figures 12B,D**) directions. For a comparison, the results of the original structure in the no fire and fire-damaged conditions are also presented.

Moreover, a time ratio α_t, defined as the ratio between the time corresponding to the ultimate curvature of a critical section of the r.c. members (t_{max}) and the total duration of the artificial motions (i.e., $t_{tot} = 25$ s), is evaluated. Note that the analysis is terminated early for the UF at ambient temperature (i.e., $\alpha_{t,X} = 0.170$ and $\alpha_{t,Y} = 0.158$) and even before for slow cooling after fire (i.e., $\alpha_{t,X} = 0.142$ and $\alpha_{t,Y} = 0.073$), while α_t equal to 1.0 is always obtained for the retrofitted structures. As can be observed, a "strong column-weak beam" mechanism is obtained by the insertion of HYDBs, with the DBF.A ensuring more effective damage control of the beams than the DBF.B, especially at the lower stories. Graphs similar to the previous ones, omitted for the sake of brevity, are obtained with reference to earthquakes at the CP limit state. As expected, the analyses of the original structure are interrupted before of what occurred at the LS limit state (i.e., $\alpha_{t,X} = 0.084$ and $\alpha_{t,Y} = 0.043$, at ambient temperature; $\alpha_{t,X} = 0.075$ and $\alpha_{t,Y} = 0.045$ after slow cooling). On the other hand, similar results are obtained for the DBF.A and DBF.B structures, but a premature collapse of the DBF.B occurs (i.e., $\alpha_{t,X} = 0.08$ and $\alpha_{t,Y} = 0.16$).

To check the effectiveness of the DBD procedure in involving most of the HYDBs in the energy dissipation, the vertical distribution of maximum ductility demand of the HYDBs is plotted in **Figures 12E,F** at the LS and CP limit states, respectively. At each story, comparison between constant drift (case A) and proportional stiffness (case B) criteria is made for the HYDBs placed along the in-plan X and Y directions where $\mu_{Fd} = 1.5$ and $\mu_{Fd} = 1.3$ are assumed, respectively. Note that distribution of HYDB ductility demand is fairly uniform for the DBF.B and maximum values at the second (X direction) and third (Y direction) levels generally take place. However, it is not surprising that the maximum value evaluated along the Y direction occurs at the LS instead of the CP limit state, given that the final instant for the latter is $t_{max} = 4.0$ s (i.e., $\alpha_{t,Y} = 0.16$). On the contrary, quite an irregular distribution of the ductility demand along the building height is obtained for HYDBs of the DBF.A structure, in both principal directions, with maximum values at the ground level where the F0 scenario is

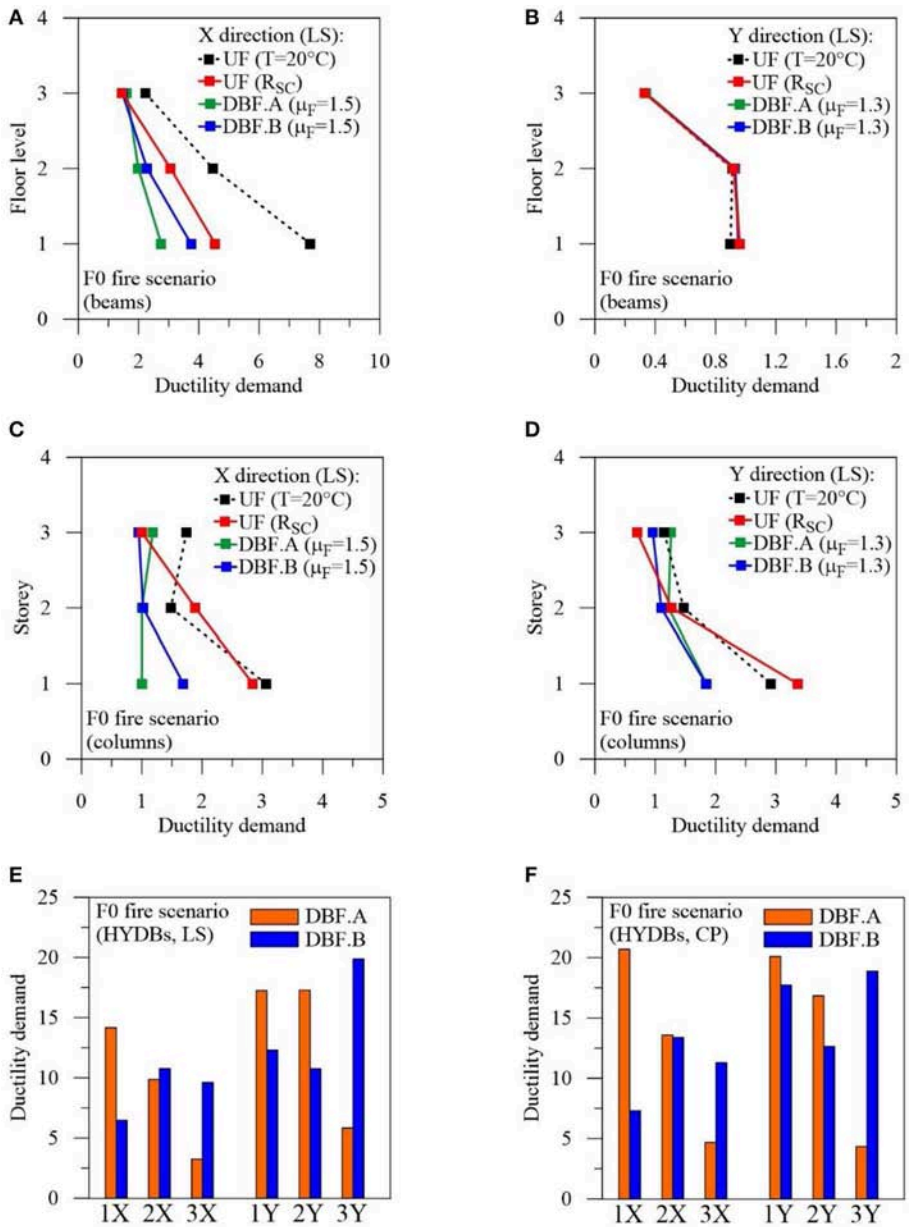

FIGURE 12 | Ductility demand of r.c. frame members and HYDBs for the Collina-Castello school. **(A)** Beams (X direction, LS). **(B)** Beams (Y direction, LS). **(C)** Columns (X direction, LS). **(D)** Columns (Y direction, LS). **(E)** HYDBs (X and Y directions, LS). **(F)** HYDBs (X and Y directions, CP).

assumed. This result confirms the fact that the constant drift criterion is the best choice for reducing the seismic vulnerability of structures exposed to fire by acting mainly on the floor where fire damage occurs.

CONCLUSIONS

Effects of duration of a fire on the seismic retrofitting of school buildings by means of HYDBs is studied for increasing values of the opening factor, corresponding to increase of maximum temperature and reduction of duration of the heating and cooling phases. First, thermal analysis is carried out on an actual building represented by the Collina-Castello school in Bisignano (Italy), evaluating the distribution of temperature in the cross sections of fire exposed r.c. structural members. Fast, medium and slow cooling laws are assumed for the F0 and F1 fire scenarios corresponding to fire compartment confined to the area of the ground and first floor, respectively. A close relation between duration of the cooling phase and maximum temperature and extension of the damaged part of the cross-section is observed. In particular, the internal layers show higher temperatures than the exterior ones for decreasing decay rates of the cooling phase, while during the heating phase the external layers are heated to temperatures much higher than those of the internal layers. Then,

a variable isotherm method is proposed for evaluating residual properties of r.c. frame members after the cooling phase of a fire, as an alternative to the simplified 500°C isotherm method proposed by EC 2.1-2. To this end, time-temperature profiles of concentrically layers of r.c. cross-sections are evaluated, highlighting that the temperature difference between the free surface and internal layers of a structural element varies during the heating and cooling phases and increases for decreasing values of cooling rate.

Afterwards, non-linear static analysis of the original school is carried out before and after fire, showing that the significant decrease of stiffness and strength in the r.c. structural elements exposed to fire corresponds to an increase of displacement and reduction of shear in comparison with the no-fire condition, especially when an increasing fire duration is considered for the F0 fire scenario. Stiffness and strength distributions of the HYDBs are evaluated with a criterion aiming to obtain a damped braced structure which can be considered globally regular after the degradation of fire-exposed r.c. frame members (i.e., case DBF.A). A proportional stiffness criterion is also applied, assuming that mode shapes of the fire-damaged structure remain practically the same after the insertion of HYDBs (i.e., case DBF.B). Results from non-linear static analysis highlight that the displacement capacity of the DBF.A structures is greater than that obtained for the DBF.B, while comparable values of total base shear are obtained. The effectiveness of the HYDBs is confirmed by non-linear dynamic analysis, forced to stop early for the UF structure, unlike for the retrofitted structures. A "strong column-weak beam" mechanism is obtained by the insertion of HYDBs, with the DBF.A ensuring more effective damage control of the beams than the DBF.B, especially at the lower stories. A rather irregular distribution of ductility demand along the building height is obtained for HYDBs of the DBF.A structure, acting mainly on the floor where fire damage occurs.

DATA AVAILABILITY STATEMENT

The datasets generated for this study are available on request to the corresponding author.

AUTHOR CONTRIBUTIONS

FM and GI contributed to conception and design of the study, numerical results, first draft of the manuscript, manuscript revision and read the submitted version.

FUNDING

The present work was financed by ReLUIS (Italian network of university laboratories of earthquake engineering), in accordance with the Convenzione DPC-ReLUIS 2019-2021, WP15, Code Revisions for Isolation and Dissipation.

REFERENCES

ABAQUS (2014). *Computer Software, Dassault Systems. Users and Theory Manual Version 6.14*. Johnston, RI: ABAQUS Inc.

Ariyanayagam, A. D., and Mahendran, M. (2014). Development of realistic design fire time-temperature curves for the testing of cold-formed steel wall systems. *Front. Struct. Civil Eng.* 8, 427–447. doi: 10.1007/s11709-014-0279-1

Behnam, B. (2017). On the interaction between span length and opening ratio of RC frames under natural fires. *Proc. Inst. Civil Eng. Struct. Build.* 171, 472–486. doi: 10.1680/jstbu.17.00044

Botte, W., and Caspeele, R. (2017). Post-cooling properties of concrete exposed to fire. *Fire Saf. J.* 92, 142–150. doi: 10.1016/j.firesaf.2017.06.010

Chang, Y. F., Chen, Y. H., Sheu, M. S., and Yao, G. C. (2006). Residual stress-strain relationship for concrete after exposure to high temperatures. *Cement Concr. Res.* 36, 1999–2005. doi: 10.1016/j.cemconres.2006.05.029

Christopoulos, C., and Filiatrault, A. (2006). *Principles of Passive Supplemental Damping and Seismic Isolation*. Pavia: IUSS Press.

Dimia, M. S., Guenfoud, M., Gernay, T., and Franssen, J.-M. (2011). Collapse of concrete columns during and after the cooling phase of a fire. *J. Fire Protect. Eng.* 21, 245–263. doi: 10.1177/1042391511423451

European Committee for Standardization, EC 1.1-2 (2004a). *Eurocode 1: Actions on Structures - Part 1-2: General Actions - Actions on Structures Exposed to Fire. ENV* 1991-1-2, 2004. Brussels.

European Committee for Standardization, EC 2.1-2 (2004b). *Eurocode 2: Design of Concrete Structures - Part 1–2: General Rules - Structural Fire Design. ENV* 1992-1-2, 2004. Brussels.

Felicetti, R., Gambarova, P. G., and Meda, A. (2009). Residual behavior of steel rebars and R/C sections after a fire. *Constr. Build. Mater.* 23, 3546–3555. doi: 10.1016/j.conbuildmat.2009.06.050

Gernay, T. (2019). Fire resistance and burnout resistance of reinforced concrete columns. *Fire Saf. J.* doi: 10.1016/j.firesaf.2019.01.007

ISO 834 (1999). *International Standard, Fire Resistance Tests, ISO834-1 Test Conditions*. Geneva.

Italian Ministry of Public Works (1975). *Norme tecniche per le costruzioni in zone sismiche (DM75)*, D.M. 08-04-1975 (in Italian).

Italian Ministry of the Infrastructures (2018). *Technical Regulations for the Constructions (NTC18),* D.M. 17-01-2018. Rome (in Italian).

Lee, J., Xi, Y., and William, K. (2008). Properties of concrete after high-temperature heating and cooling. *ACI Mater. J.* 105, 334–341. doi: 10.14359/19894

Maraveas, C., Fasoulakis, Z., and Tsavdaridis, K. D. (2017). Post-fire assessment and reinstatement of steel structures. *J. Struct. Fire Eng.* 8, 181–201. doi: 10.1108/JSFE-03-2017-0028

Maraveas, C., and Vrakas, A. A. (2014). Design of concrete tunnel linings for fire safety. *Struct. Eng. Int.* 24, 319–329. doi: 10.2749/101686614X13830790993041

Mazza, F. (2014a). Modelling and nonlinear static analysis of reinforced concrete framed buildings irregular in plan. *Eng. Struct.* 80, 98–108. doi: 10.1016/j.engstruct.2014.08.026

Mazza, F. (2014b). Displacement-based seismic design of hysteretic damped braces for retrofitting in-plan irregular r.c. framed structures. *Soil Dyn. Earthq. Eng.* 66, 231–240. doi: 10.1016/j.soildyn.2014.07.001

Mazza, F. (2015). Seismic vulnerability and retrofitting by damped braces of fire-damaged r.c. framed buildings. *Eng. Struct.* 101, 179–192. doi: 10.1016/j.engstruct.2015.07.027

Mazza, F., and Alesina, F. (2019). Fragility analysis of R.C. seismically-isolated structures with residual mechanical properties after fire exposure. *Soil Dyn. Earthq. Eng.* 121, 383–398. doi: 10.1016/j.soildyn.2019.03.020

Mazza, F., and Mazza, M. (2010). Nonlinear analysis of spatial framed structures by a lumped plasticity model based on the Haar-Kàrmàn principle. *Comput. Mech.* 45, 647–664. doi: 10.1007/s00466-010-0478-0

Mazza, F., Mazza, M., and Vulcano, A. (2015). Displacement-based seismic design of hysteretic damped braces for retrofitting in-elevation irregular r.c. framed structures. *Soil Dyn. Earthq. Eng.* 69, 115–124. doi: 10.1016/j.soildyn.2014.10.029

Mazza, F., and Vulcano, A. (2014a). Equivalent viscous damping for displacement-based seismic design of hysteretic damped braces for retrofitting framed buildings. *Bull. Earthq. Eng.* 12, 2797–2819. doi: 10.1007/s10518-014-9601-5

Mazza, F., and Vulcano, A. (2014b). Design of hysteretic damped braces to improve the seismic performance of steel and r.c. framed structures. *Ingegneria Sismica* 31, 5–16.

Seismoartif (2018). *Seismosoft, Earthquake Engineering Software Solutions*. Available online at: www.seismosoft.com/seismoartif

Slowanski, L., Grabowski, J., and Kosiorek, M. (1971). The influence of temperature on mechanical properties of reinforcing steel 34GS. *Inżynieria i Budownictwo* 4, 157–161.

Sorace, S., and Terenzi, G. (2014). Motion control-based seismic retrofit solutions for a R/C school building designed with earlier Technical Standards. *Bull. Earthq. Eng.* 12, 2723–2744. doi: 10.1007/s10518-014-9616-y

Sorace, S., Terenzi, G., and Mori, C. (2016). Passive energy dissipation-based retrofit strategies for R/C frame water storage tanks. *Eng. Struct.* 106, 385–398. doi: 10.1016/j.engstruct.2015.10.038

Conflict of Interest: The authors declare that the research was conducted in the absence of any commercial or financial relationships that could be construed as a potential conflict of interest.

frontiers in Built Environment

ORIGINAL RESEARCH
published: 21 February 2020
doi: 10.3389/fbuil.2020.00013

DIBRAST: A Computer-Aided Seismic Design Procedure for Frame Structures Equipped With Hysteretic Devices

Iolanda Nuzzo[1], Francesca Ciliento[2] and Nicola Caterino[2,3]*

[1] Construction Technologies Institute, National Research Council of Italy, Naples, Italy, [2] Department of Engineering, University of Naples Parthenope, Naples, Italy, [3] Construction Technologies Institute, National Research Council of Italy, San Giuliano Milanese, Italy

This paper describes a comprehensive computer-aided seismic design approach for both new and existing frame structures equipped with hysteretic dampers. Despite continuous advancements in the state of the art demonstrating the effectiveness of these devices in mitigating seismic hazard, non-linearities involved in the problem and the articulated nature of most of the available design procedures often make them quite difficult to be implemented for real complex structures. To promote widespread use of hysteretic dampers, we present a thorough design approach that includes the application of a specific displacement-based design procedure by means of a computer-aided support tool developed in a Visual Basic environment and named *DIBRAST*. The software is realized to drive the designer through the dissipative system's design. Required iterations are automated, thus significantly reducing the processing time. As its final output, it delivers the mechanical properties of the damping braces in order to meet a specific performance objective. In order to further support practitioners in the geometrical characterization of actual design dampers, authors developed an additional Visual Basic tool—the *Shear Link Non-Linear Model*—that is able to provide yielding force and elastic stiffness of a specific type of hysteretic device according to its geometry and material. In addition, geometric details of each device can be preliminary determined by means of newly proposed design charts, presented herein, that allow us to take into account the buckling issue too. Both developed tools are freely available online. A case study is provided to demonstrate the effectiveness of the proposed design approach and tools.

Keywords: computer-aided design approach, hysteretic dampers, braced structures, SL devices, design charts

OPEN ACCESS

Edited by:
Dario De Domenico, University of Messina, Italy

Reviewed by:
Antonio Di Cesare, University of Basilicata, Italy
Fabio Mazza, University of Calabria, Italy

****Correspondence:***
Iolanda Nuzzo
nuzzo@itc.cnr.it

Specialty section:
This article was submitted to Earthquake Engineering, a section of the journal Frontiers in Built Environment

Received: *16 December 2019*
Accepted: *31 January 2020*
Published: *21 February 2020*

Citation:
Nuzzo I, Ciliento F and Caterino N (2020) DIBRAST: A Computer-Aided Seismic Design Procedure for Frame Structures Equipped With Hysteretic Devices. Front. Built Environ. 6:13. doi: 10.3389/fbuil.2020.00013

INTRODUCTION

In recent years, the earthquake engineering research community has made a huge effort to develop structural vibration control systems for seismic hazard mitigation of new or existing structures. Nowadays, base isolation systems and energy dissipation devices represent a well-known solution to reduce the response of structures subjected to dynamic loads. Their proper functioning, within the family of passive control systems, does not require an external power supply or control algorithm, which is different to active or semi-active devices.

In this paper, the main focus is on metallic hysteretic dampers whose role, when embedded within the superstructure, is to absorb a portion of the seismic input energy through a mechanism involving the plastic deformation of their constitutive material. In this way, the inelastic demand on the principal framing system is reduced along with its damage, which is meant to be concentrated in the dampers. The idea of installing metallic dampers for seismic structural control was at first introduced by Kelly et al. (1972). Over the years, many authors have proposed various devices that have differing in shape and dissipative mechanisms (Javanmardi et al., 2019). Among them, Bergman and Goel (1987) and Whittaker et al. (1991) developed the Added Damping and Stiffness (ADAS) system; its dissipation capacity is based upon flexural deformation of X-shaped metallic plates connected at the top and bottom end to a rigid element, which thus does not allow for rotation. Based on the same functioning principle of ADAS, Tsai et al. (1993) proposed the Triangular-plate Added Damping and Stiffness (TADAS). Subjected to a lateral perpendicular force, triangular parallel metallic plates undergo uniform yielding along their height. Both ADAS and TADAS are commonly installed throughout moment-resisting frames on chevron brace supports. A rhombic ADAS damper was developed by Shin and Sung (2005) using low-yield strength steel with hinge supports at both ends. Kobori et al. (1992) introduced a honeycomb steel damper (or "panel system") to increase energy absorption in high-rise buildings. It consists of a steel plate characterized by a honeycomb-shaped opening in the central part subjected to loads acting in its own plane. The buckling-restrained brace (BRB) is composed of an unbounded thin steel core encased in a concrete-filled steel tube (Watanabe et al., 1988; Clark et al., 1999). Energy dissipation is provided by axial deformation of the internal steel core while buckling is avoided by the external casing. BRBs exhibit their dissipation capacity even for a low displacement demand since they are able to yield for displacements of a few millimeters. The result is thus that they are suitable even for seismic retrofitting of stiff structures (De Domenico et al., 2019). Di Cesare et al. (2014) proposed the Hysteretic Damper (HD), whose dissipation capacity is based upon flexural deformation of low-carbon steel plates of a particular shape. Generally installed on chevron braces supports, the HD provides additional lateral strength and stiffness, thus contributing to limiting interstory drifts. A wide range of mechanical properties can be obtained by simply varying the dimensions of the thin steel plates. At first investigated at the University of Girona, Spain, by Cahís et al. (1997), Bozzo et al. (1998), Bozzo and Barbat (1999), Cahís (2000) the Shear Link (SL) consists of a steel panel with variable thickness along its height, and it can undergo significant inelastic shear deformations.

Despite the advancements in the state of the art, the use of hysteretic dampers as a seismic control system is not yet widely spread due to the lack of proper guidelines providing support for the design of structures equipped with hysteretic dampers. The European Standard for Anti-Seismic Devices (EN 15129, 2009) has established that the type of analysis, response spectrum, or time-history analysis, should be chosen according to the type of device. Despite this, no indications are provided for the definition of an appropriate response factor. At the same time, it strongly recommends performing a dynamic non-linear analysis when the equivalent damping ratio is higher than 15%. This threshold can actually be easily overcome in the case of hysteretic dampers due to their significant non-linear behavior. Certainly, a non-linear analysis can better predict the structural inelastic performances, particularly when performed by adopting sophisticated hysteresis models (Vaiana et al., 2018, 2019a; Mazza, 2019a) and numerical methods (Greco et al., 2018; Vaiana et al., 2019b). Nevertheless, it cannot be considered a practical tool for preliminary sizing of the dissipative system. To this aim, various authors have proposed many design procedures, often consisting of performance-based approaches. Special effort was also devoted to including the influence of the finite stiffness of the supporting braces on the overall response of both viscous and hysteretic dampers (Losanno et al., 2015, 2018, 2019). Kim and Choi (2004) proposed a methodology providing the required effective damping of BRBs at the target displacement. Bergami and Nuti (2013) developed an iterative procedure where a target damping ratio was defined according to a fixed displacement demand. Mazza and Vulcano (2015) proposed a framework to design the dissipative system according to a target deformation. Based on non-linear static analysis, Di Cesare and Ponzo (2017) introduced a design approach for the evaluation of the mechanical properties of dissipative systems that are given a target top displacement and are able to regularize strength and stiffness distributions along the height of the braced structure when necessary. In addition, the authors proposed an analytical formulation of the behavior factor of braced structures as a result of a wide parametric analysis. Ponzo et al. (2019) proposed a design approach for low-damage braced post-tensioned timber frames providing the mechanical properties of both post-tensioned and the hysteretic dissipative brace systems at the target displacement to achieve a reference level of seismic intensity. Mazza (2019b) developed a displacement-based design procedure to size hysteretic damped braces according to a target performance level, accounting for the degrading cyclic response of r.c. frame members by means of a combined plastic-damage hysteretic model (Mazza, 2019a). Nuzzo et al. (2019) introduced a comprehensive displacement-based design approach with a direct reference to effective parameters of the damping braces in a way that is suitable for professional applications. However, non-linearity involved in the problem and the iterative nature of most of the mentioned procedures often make them articulated and lacking in promptness, and it is thus of little attraction for practitioners. In order to promote the diffusion of hysteretic dampers as seismic control strategy for both new and existing structures, the authors believe that the development of a free online design tool, supplied with a user manual, may be decisive. It should be easily applicable, driving practitioners toward the implementation of a design procedure suitable for real applications. In particular, required input data should be clearly defined, while design output should allow for the effective size of the dissipative braces. In this perspective, the displacement-based design method proposed by Nuzzo et al. (2019) is believed to be suitable to this aim. Indeed, though it is still an iterative procedure, the authors demonstrated that the steps and iterations

require only analytical computations and do not involve any iterative numerical structural analysis. This makes the procedure implementable within a computer-aided tool, thus supporting designers in the fulfillment of the several phases of the procedure. In the present study, a significant effort was undertaken by the authors in order to develop *DIBRAST*—DIssipative BRAced STructures—a tool in the Visual Basic environment. Its structure, described in this paper, directly revokes the steps of the design procedure previously proposed by the same authors (Nuzzo et al., 2019). The software automates the required iterations, finally providing the dissipative system's mechanical properties needed in order to achieve the desired structural performance. Input parameters and the output of the software are outlined in next sections. Namely, a modal analysis and a pushover curve of the bare frame are required at the beginning in order to determine the equivalent capacity curve. After providing input seismic hazard parameters at the site of interest, the tool is able to build the design response spectrum with consideration for the equivalent damping ratio provided by the added hysteretic dissipation system at target displacement. During the application, some assumptions concerning the dissipative system's ductility capacity and post-yielding-to-elastic stiffness ratio have to be made. Thereafter, the equivalent damped brace capacity curve is determined as the difference between the dissipative system and bare frame ones. The final output of the software consists of the dissipative system mechanical properties along each damped bay and story. Successively, the effective design dampers and braces can be easily tuned introducing mechanical properties of commercial devices, which are commonly available on the market.

A similar contribution was provided by DISIPA-SLB (Bozzo et al., 2019), a plugin for CSI and ETABS (2016) structural analysis software, implementing two iterative design procedures based on simplified linear analysis. This tool, despite being able to iterate autonomously the design procedure, gives the user little control over the target interstory drift, which has to be checked from the analysis at each iteration. Moreover, it was demonstrated that linear analysis overestimates shear forces in the dampers and, consequently, leads to the excessive oversizing of their supporting element (Ciliento, 2019).

Once the mechanical design properties of the added hysteretic damping system are defined, a practical design approach should also allow for the definition of the corresponding device's geometry. This makes the procedure effective, complete, and, therefore, of interest to practitioners. At a preliminary design stage, the use of an analytical approach is preferable since it is suitable for the prompt association of a specific geometry to defined mechanical properties. It strongly depends on the typology of the adopted control device and needs to be defined as a function of it. As an additional achievement of this work, authors proposed a design approach to properly associate the mechanical properties of a specific type of damper, in particular the SL device previously introduced, to its geometry. Therefore, a further Visual Basic tool has been developed with the aim of determining SL elastic stiffness and yielding force as a function of its material and geometrical properties as well as boundary conditions. The analytical model besides the proposed tool has been developed in a previous work by the same authors (Nuzzo et al., 2019). Moreover, in order to further support the designer in the selection of the damper's geometry, new design charts are proposed herein. Their description and mode of use are described.

A TOOL TO DESIGN DISSIPATIVE BRACED STRUCTURES: *DIBRAST*

To promote the adoption of metallic dampers as a seismic protection system, Nuzzo et al. (2019), proposed a comprehensive displacement-based design procedure that is suitable for both new and existing structures. The method is based on a closed-form analytical procedure and allows us to obtain a preliminary sizing of the dissipative system in few iterations. Besides modal and pushover analysis of the bare frame (F system) required at the beginning, further structural analyses are not necessary to achieve the final result. Its main objective is to provide the desired force–displacement capacity curve of the equivalent braced frame (BF system) given in **Figure 1**, i.e., the frame equipped with the damped brace system (DB system), according to a fixed performance point. The latter is evaluated starting from the target displacement of the bare frame, chosen according to the type of building (new or existing one) and its class of importance (ordinary or mission critical structure), and defining the corresponding level of force, taking into account the equivalent damping ratio provided by the hysteretic behavior of the dampers. All steps of the procedure are thoroughly described in Nuzzo et al. (2019). In this paper, authors propose *DIBRAST*, a practical tool developed in Visual Basic environment, given as a support in the application of the displacement-based design framework. The software is freely available online[1], and it is accompanied by a related user manual. It implements all steps of the procedure, finally providing the desired mechanical properties of the dissipative braces in order to meet the performance objective. The user is guided on data to be input at each step in the only editable cells through pop-up notes, moving the cursor in correspondence with the input columns.

In order to implement the design framework with the support of *DIBRAST*, there are several piece of information the user should input:

- Target displacement;
- F system capacity curve;
- Seismic hazard parameters;
- Number of bays to brace with dissipative systems at each story.

The tool will provide valuable information as its output:

- Identification of the Performance Point (PP);
- Capacity curves of BF and DB systems, plotted in the ADRS space together with those from the F system;

[1]http://www.ingegneria.uniparthenope.it/ricerca/index.php?page=software2

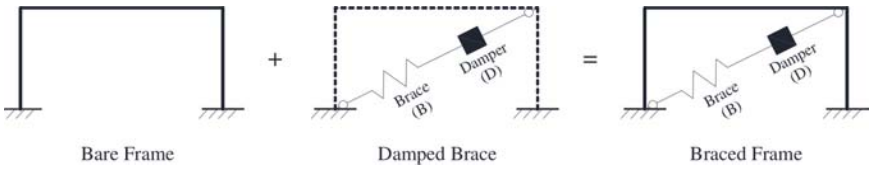

FIGURE 1 | Schematization of the bare frame, damped brace, and braced frame systems.

- Mechanical properties of each dissipative system in terms of yielding force and elastic stiffness;
- Ductility check of the j-th damper at i-th story.

The design procedure requires two different types of iteration to be implemented. The first is needed in order to determine PP: it is automatically and autonomously solved by *DIBRAST* and does not require any particular action from the user. The second type of iteration must be performed at the end of the procedure in order to verify initial assumptions relative to DB system mechanical properties, as this will be clarified in the following sections. In this case, *DIBRAST* checks if the iteration is needed and, if this is the case, suggests the new values to be implemented by the user through a warning box until convergence is achieved. Although it involves the user, also this type of iteration is significantly simplified and reduces processing time.

DIBRAST software is divided into four sections, given that steps 2–3 and steps 5–6 of the design procedure are processed together, as shown in **Figure 2** and as described in the following sections.

Step 1: Bare Frame Behavior

In section 1 of the software, a linear or non-linear configuration for the bare frame (F system) has to be chosen, and the target displacement will be set accordingly. Namely, F could be dissipative, partially dissipative, or elastic. In case of dissipative or partially dissipative behavior, a target interstory drift (θ_d) can be set considering the maximum allowable plastic hinge rotation according to code provisions or reparability issues, respectively. Alternatively, for elastic behavior, θ_d can be defined in order to limit damage to non-structural elements. Once the pushover curve of the F system is known, the shear force distribution along the height ($V_{F,i}$) and the absolute story displacements ($d_{abs,i}$) in correspondence of the target displacement have to be defined in the editable cells along with the first modal shape (Ψ_i). Also, seismic masses are input by arranging permanent and live loads in a seismic combination. Modal participation factor (Γ) and equivalent mass (m^*) are given automatically as an output, allowing to determine the F single-degree-of-freedom (SDOF) system capacity curve. A further action is required by the user in order to determine the F system bilinear capacity curve.

Steps 2–3: Evaluation of the Performance Point and Design Capacity Curves for BF and DB Systems

Section 2–3 of the tool implements the analytical procedure for the evaluation of the performance point described by the following equations (Mazza and Vulcano, 2015; Nuzzo et al., 2019):

$$\xi_{eq,BF} = \xi_{v,F} + \frac{\xi_{h,F} \cdot V^*_{PP,F} + \xi_{h,DB} \cdot V^*_{PP,DB}}{V^*_{PP,F} + V^*_{PP,DB}} \quad (1)$$

$$\xi_{h,F} = k\left[63.7 \cdot \frac{(\mu^*_F - 1) \cdot (1 - r^*_F)}{\mu^*_F \cdot [1 + r^*_F \cdot (\mu^*_F - 1)]}\right] \quad (2)$$

$$\xi_{h,DB} = k\left[63.7 \cdot \frac{(\mu^*_{DB} - 1) \cdot (1 - r^*_{DB})}{\mu^*_{DB} \cdot [1 + r^*_{DB} \cdot (\mu^*_{DB} - 1)]}\right] \quad (3)$$

$$V^*_{PP,DB} = V^*_{PP,BF} - V^*_{PP,F} \quad (4)$$

In the above equations, the bare frame parameters, namely ductility demand μ^*_F, post-to-pre yielding stiffnesses ratio r^*_F, needed to get the hysteretic damping ratio $\xi_{h,F}$ (Eq. 2, Dwairi et al., 2007), and the base shear at PP ($V^*_{PP,F}$) are known from step 1. The F system viscous damping ratio $\xi_{v,F}$ shall be supposed according to the structural typology. Differently, in order to evaluate the DB hysteretic damping ratio $\xi_{h,DB}$ (Eq. 3), ductility and post-to-pre yielding stiffnesses ratio, μ^*_{DB} and r^*_{DB}, initially unknown, have to be supposed at this point and will be checked by the end of the procedure. Moreover, k is a reduction factor that accounts for cyclic degradation (ATC, 1996).

The solutions of Eqs (1) and (4), concerning the equivalent BF damping ratio ($\xi_{eq,BF}$) and the equivalent DB base shear at PP ($V^*_{PP,DB}$), respectively, depend on each other. Consequently, in order to apply Eq. (4), the user must give a first trial value of the equivalent base shear of the braced frame system ($V^*_{PP,BF}$) that is greater than $V^*_{PP,F}$. Hence, the software automatically implements some iterations until convergence is reached, giving, as a result, $V^*_{PP,BF}$ and $\xi_{eq,BF}$. Once the performance point is determined, the desired capacity curve of the global equivalent structure (BF system) is evaluated by solving Eqs (5–7), the latter only in the case of non-linear F systems:

$$K^*_{BF} = (\alpha + 1) \cdot K^*_F \quad (5)$$

$$K^*_{BF,py,1} = (1 + r^*_{DB} \cdot \alpha) \cdot K^*_F \quad (6)$$

$$K^*_{BF,py,2} = (r^*_F + r^*_{DB} \cdot \alpha) \cdot K^*_F \quad (7)$$

where K^*_{BF}, $K^*_{BF,py,1}$ and $K^*_{BF,py,2}$ are the equivalent BF elastic and post-yielding stiffnesses, K^*_F is the F system elastic stiffness, and α is the DB-to-F elastic stiffnesses ratio, which can be analytically determined (Nuzzo et al., 2019).

Then, the equivalent damped brace capacity curve is obtained as a difference between BF and F. Thereby, by the end of

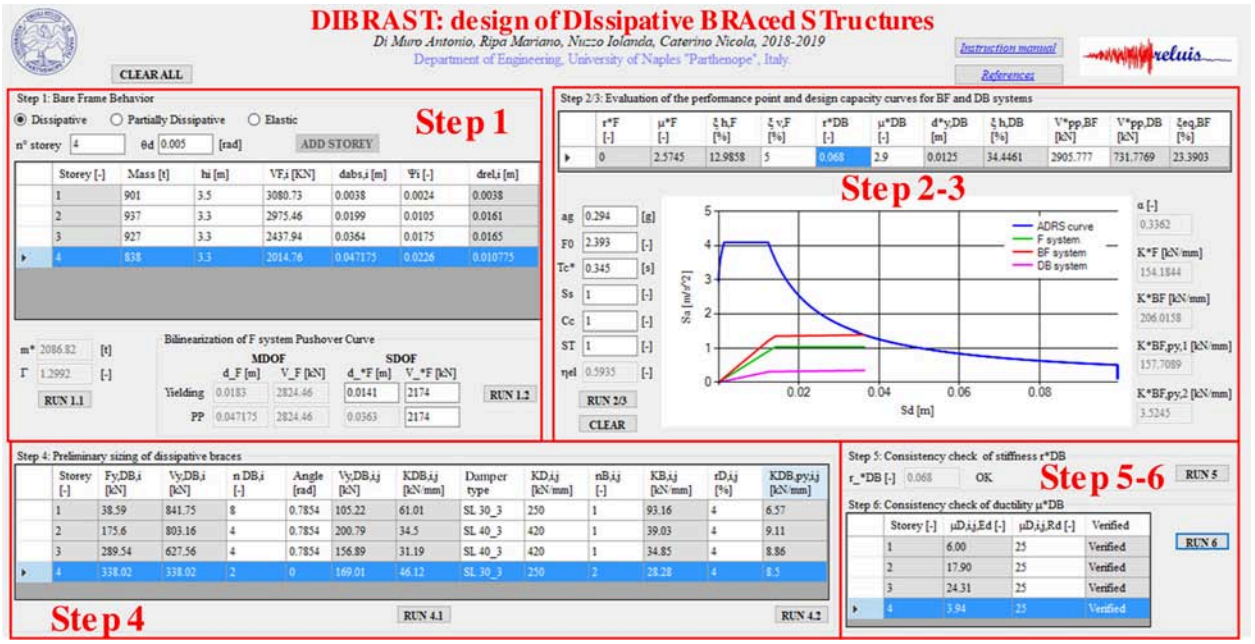

FIGURE 2 | Screenshot of *DIBRAST*: a tool for preliminary sizing of dissipative systems.

steps 2–3, capacity curves of F, DB, and BF systems are known and plotted together with the design Acceleration Displacement Response Spectrum (ADRS), i.e., they reduced by the equivalent damping ratio (**Figure 3**). In this section, the ADRS curve is defined with reference to the Italian design NTC code (Ministry of Infrastructures, 2018). However, any response spectrum according to international codes can be uploaded by defining equivalent parameters.

Step 4: Preliminary Sizing of Dissipative Braces

At step 4, the software delivers the required dissipative braces yielding force and elastic stiffness ($V_{y,DB,i}$ and $K_{DB,i}$) for each i-th story, assuming a proportionality criterion with respect to the modal behavior. Consequently, by only setting the number of braces at each level, the tool distributes the corresponding mechanical properties, finally providing a design-yielding force and elastic stiffness for each j-th dissipative brace at each story, $V_{y,DB,i,j}$ and $K_{DB,i,j}$. At this point, effective properties of dampers have to be specified by the user. To this aim, hysteretic devices can be designed according to a force criterion: known $V_{y,DB,i,j}$ is the demanding shear force in each j-th dissipative system at i-th story, and the damper is chosen so that its yielding force matches the design force. Finally, once the elastic stiffness of the j-th damper at i-th story is known and input in *DIBRAST* ($K_{D,i,j}$), the software provides the required elastic stiffness of the supporting element by solving the following equation:

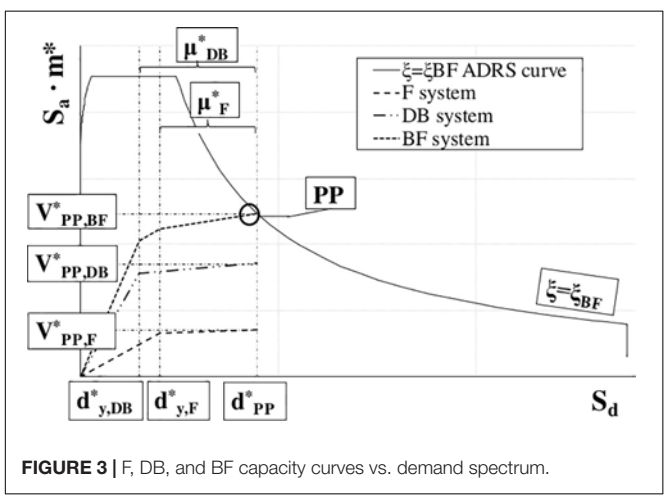

FIGURE 3 | F, DB, and BF capacity curves vs. demand spectrum.

$$\frac{1}{K_{B,i,j}} = \frac{1}{K_{DB,i,j}} - \frac{1}{K_{D,i,j}} \tag{8}$$

Consequently, it is possible to size the support element, that may be given by steel elements, such as diagonal or chevron braces (**Figure 4**). This makes the procedure of significant impact for professional applications since it is characterized by high practicality.

As an additional feature, *DIBRAST* provides the post-yielding stiffness of the dissipative brace ($K_{DB,py,i,j}$), once the damper's post-yielding-to-elastic stiffness ratio is defined ($r_{D,i,j}$). The latter parameter should be known for a specific hysteretic device from its experimental characterization. The provision of $K_{DB,py,i,j}$ can be helpful when performing non-linear time-history simulations.

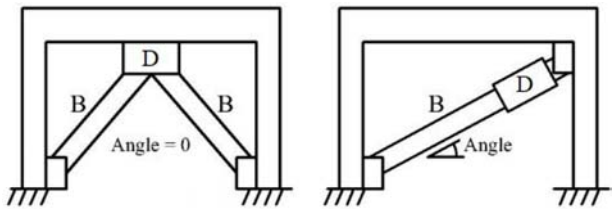

FIGURE 4 | Supporting brace configuration (B = brace; D = damper).

Step 5–6: Consistency Check on r^*_{DB} and μ^*_{DB}

Consistency check of DB post-to-pre yielding stiffness r^*_{DB} takes place at step 5. *DIBRAST* analytically determines r^*_{DB} value for the defined dissipative braces, and successively compares it to the initial assumption at step 2. If the results are not verified, a warning message box suggests the new value to be used to implement again the procedure from step 2. Each new iteration can be performed by simply running the successive steps of the tool. Finally, at step 6, the ductility demand $\mu^*_{DB,i,j}$ for each dissipative brace is checked for compatibility with its capacity, and the latter is user defined.

ADDITIONAL DESIGN TOOLS FOR SL PRELIMINARY SIZING

The definition of dampers geometry according to design mechanical properties may often result in a demanding procedure, requiring time-consuming blind numerical simulations. Differently, an analytical approach is suitable for a prompt, preliminary sizing, driving the designer toward the correct order of magnitude of the required damper's dimensions. In the state of the art, several typologies of hysteretic devices exist, and each is characterized by a different geometry and a specific working rule. Consequently, it is not possible to determine a design procedure available for a generic hysteretic damper, since a specific analytical model is needed for each of them. In the present work, authors developed a design tool with reference to the SL device. It consists of a metallic hysteretic damper realized from a hot laminated steel plate modeled as to obtain an I-shape (Nuzzo et al., 2015, 2018), shown in **Figure 5**. Top and bottom flanges represent the stiffer parts and are employed to realize the connection to other structural elements, while energy dissipation is concentrated in the web, corresponding with so-called dissipative windows. The latter are manufactured with a reduced thickness through a milling process, thus avoiding welding procedure. On the top part, the damper is provided of slotted holes to avoid axial forces from the upper beam due to gravitational loads.

Several generations of SL dampers have been developed in an attempt to enhance their dissipative performances assessed through several experimental campaigns. Investigations were first carried out at ISMES S.p.A in Bergamo (Italy) (Franchioni et al., 2001) and later on at the University of Girona (Hurtado and Bozzo, 2005; Hurtado, 2006; Hurtado and Bozzo, 2008). More recently, further tests were performed at the University of Naples (Nuzzo et al., 2018), showing quite stable hysteretic behavior of the damper under cyclic loading. Successively, Nuzzo et al. (2019) developed an analytical model to determine SL yielding force and elastic stiffness given its geometry, boundary conditions, and material. In particular, the yielding force is determined considering a pure shear behavior, knowing the material yielding shear stress and the web's transversal area. On the other hand, the elastic stiffness has been evaluated through the principal of virtual works and accounting for both the shear and flexural behavior of the damper. In particular, the SL is modeled as a frame element characterized by different sections along its height. Two configurations have been considered, namely Fixed-Fixed (FF) and Fixed-Not Fixed (FNF) depending on whether upper bolts are fully tightened or not, thus accounting for the role of boundary conditions in the mechanical response of the device. The resulting analytical expressions characterizing the SL elastic stiffness can be find in Nuzzo et al. (2019), where the model's accuracy was demonstrated through experimental comparison. In order to provide further support to the designer who wants to properly characterize a SL damper, the above analytical models, which result in long and unfriendly expressions, have been implemented in a Visual Basic environment, thus developing a *Shear Link Non-Linear Model* tool, given in **Figure 6**. The software is freely available online[2], and this is accompanied by a relevant user manual. The required input parameters concern different areas:

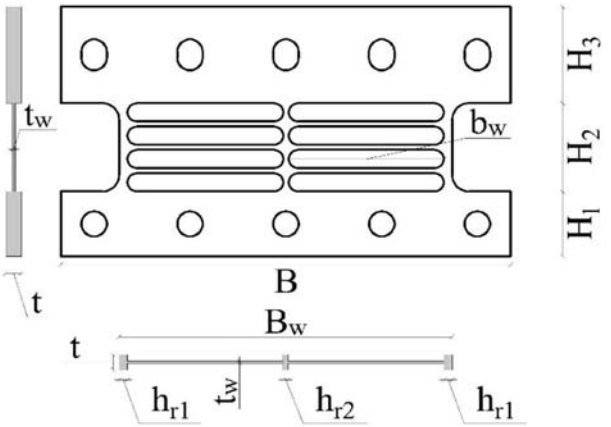

FIGURE 5 | Shear Link damper.

- essential geometric dimensions, described in the representation of the device within the tool, which can be selected from a dropdown list or are *user defined*;
- the type of material that can be selected among European commercial ones with precompiled mechanical properties or can be *user defined*;
- boundary conditions, which are directly represented in the tool.

[2]http://www.ingegneria.uniparthenope.it/ricerca/index.php?page=software1

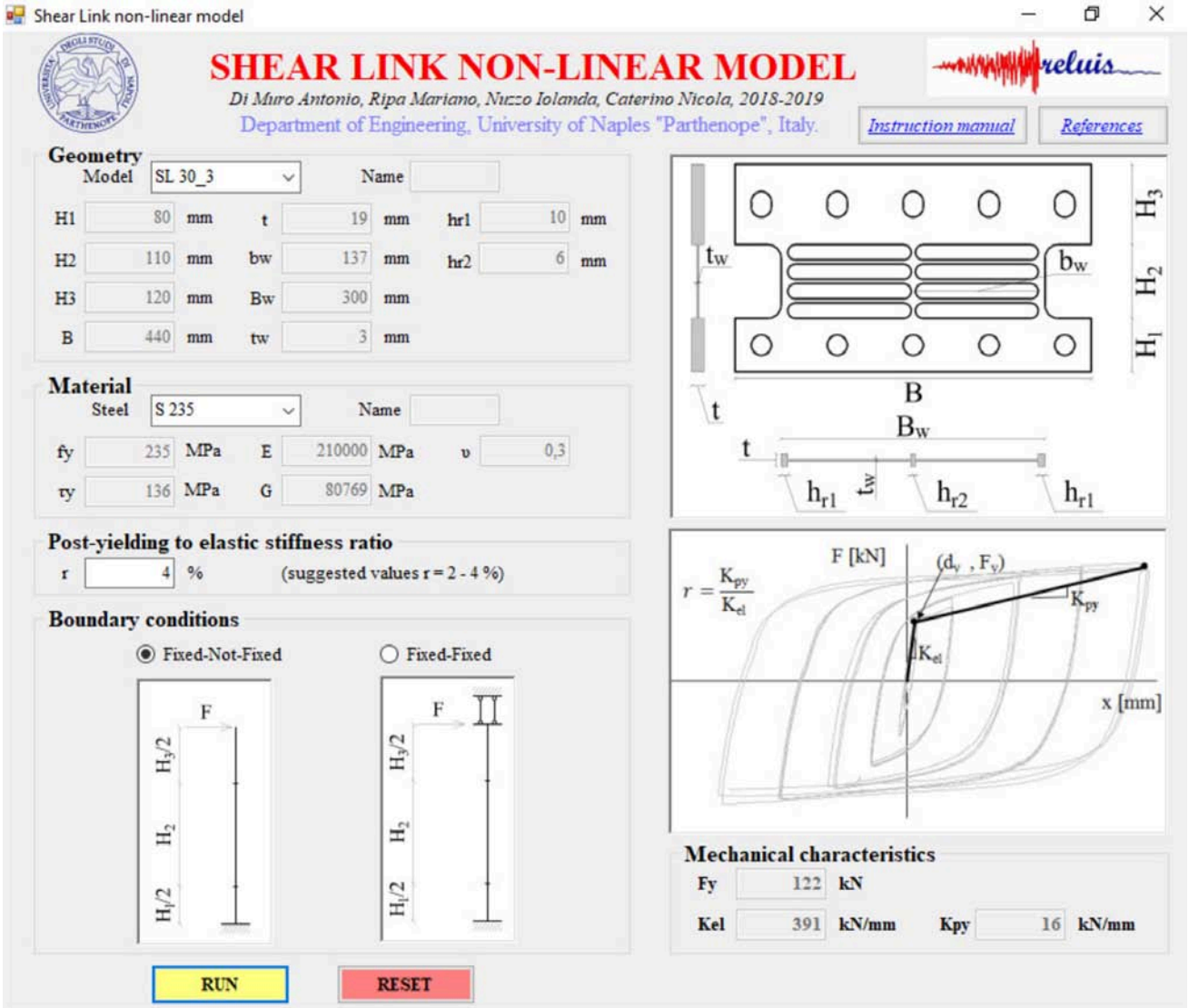

FIGURE 6 | Screenshot of the Visual Basic tool to calibrate SL mechanical properties.

The software implements the analytical model specifically developed for the SL damper, providing output in the form of estimated yielding force and elastic stiffness.

The use of the tool can be very handy for SL sizing, but it would still require a blind—though fast—design through iterative assessments. For this reason, the authors investigated the influence of SL geometry on the mechanical characteristics of interest, i.e., yielding force and elastic stiffness. In particular, a parametric study was developed varying the dissipative web's thickness (t_w), width (B_w), and height (H_2). The results of this investigation have been arranged in new design charts, presented from **Figure 7** to **Figure 9**, where the SL yielding force and elastic stiffness nomenclature are condensed as F_y and K_{el}.

The following charts have been developed considering the FNF configuration and given that, from authors experience, it represents the most commonly adopted solution. European S235, S275, and S355 standard steel grades have been considered.

The design chart is comprehensive of three different parts:

- in the left part, the yielding force is given as a function of t_w, fixing B_w in different curves;
- the central plot describes the relation between the three investigated geometric dimensions, namely t_w, B_w, and H_2, providing the maximum limit of the web's height avoiding buckling mechanism (Nuzzo et al., 2019);
- on the right side, the elastic stiffness is associated to t_w, B_w, and H_2. In addition, for different combinations of B_w and H_2 parameters, corresponding to several curves (from a to e), the upper bound values of t_w generating buckling (black dots in the right-side charts of **Figures 7–9**) have been determined. Thus, the dashed

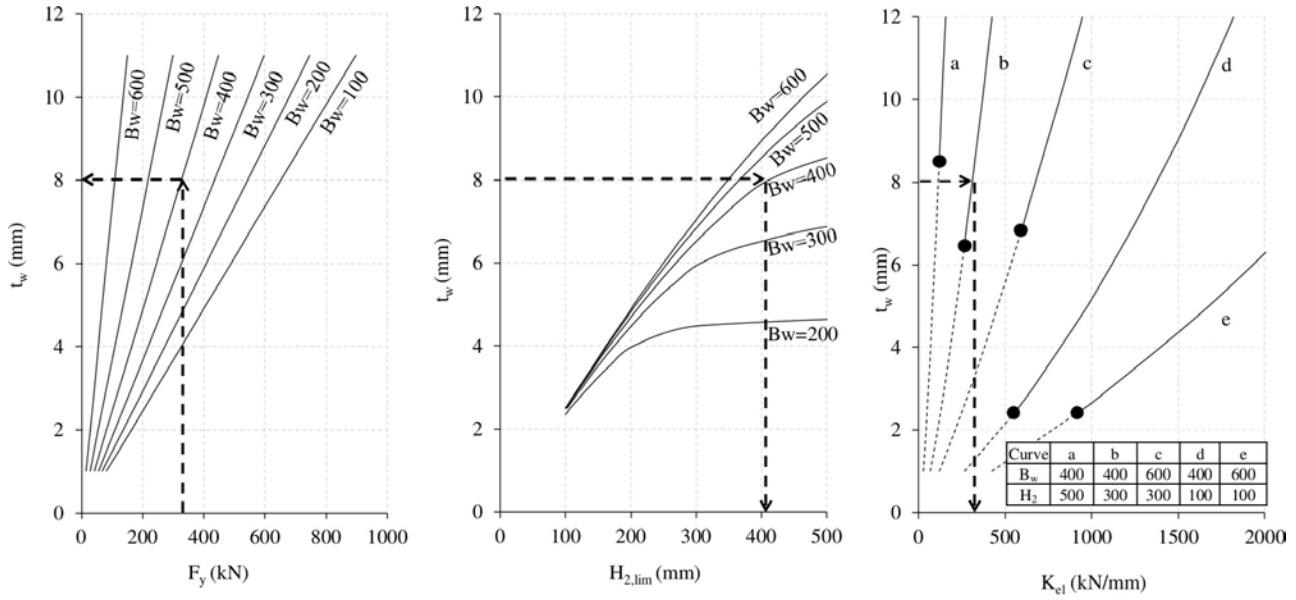

FIGURE 7 | Preliminary design chart of SL devices (S235 steel grade; B_w and H_2 expressed in mm).

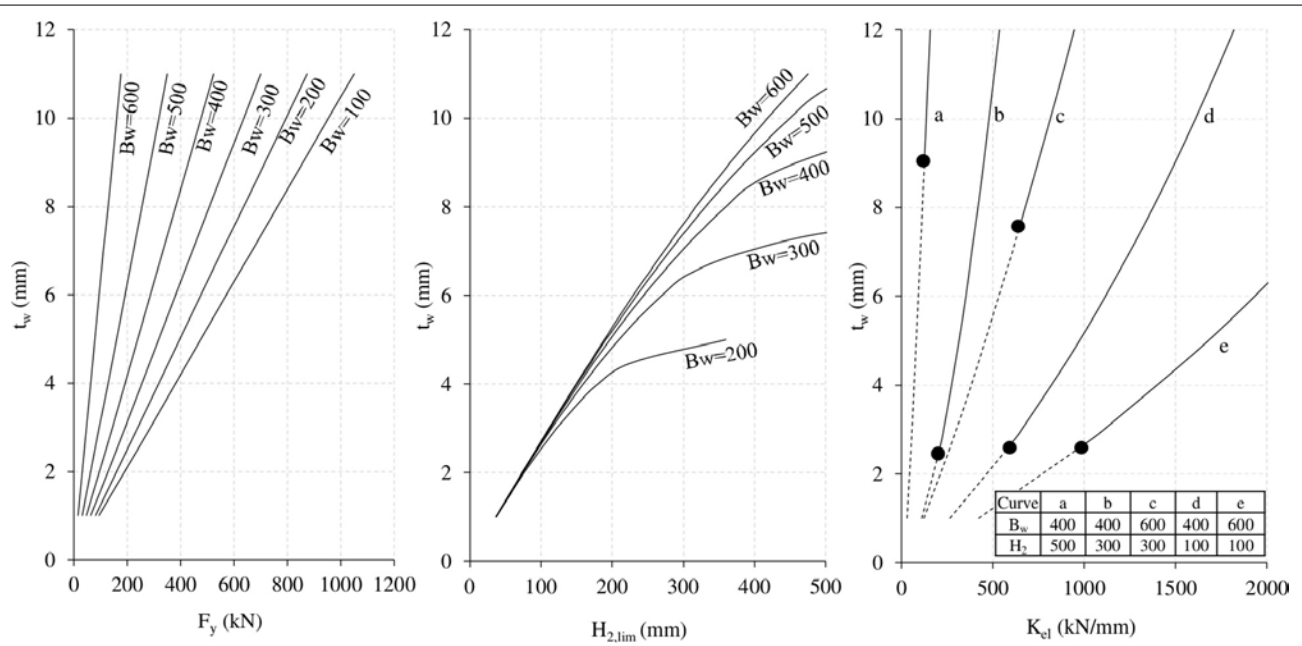

FIGURE 8 | Preliminary design chart of SL devices (S275 steel grade; B_w and H_2 expressed in mm).

lines correspond to geometrical combinations which generate buckling, whereas the continuous lines represent suitable geometries.

An applicative example of the use of the proposed design charts is provided in **Figure 7**. It starts from the assumption that the SL yielding force is known. It can be assumed as the demanding yielding shear force ($V_{y,DB,i,j}$) of the j-th dissipative system at i-th story output of step 4 from the *DIBRAST* tool. Therefore, it is possible to enter in the left part of the design chart with the required F_y level and read the corresponding SL optimal t_w after selecting B_w. The minimum possible value of the web's width, compatible with the choice of a limited dimension of the web's thickness, should be selected. In this way it is possible to optimize the device's weight and cost, also simplifying the assembly procedure. Moreover, further issues that may influence the correct choice of B_w are the connection system and specific architectural requirements. Furthermore, in order to

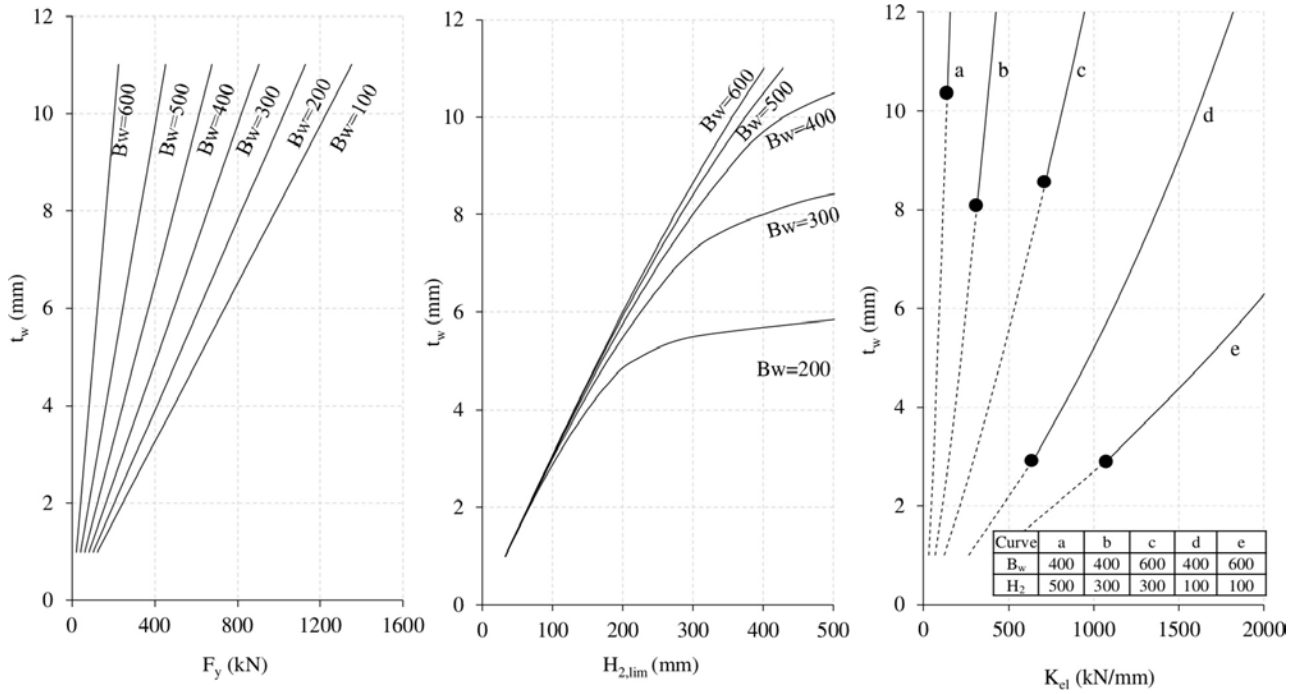

FIGURE 9 | Preliminary design chart of SL devices (S355 steel grade; B_w and H_2 expressed in mm).

avoid buckling mechanism, a maximum B_w value of 600 mm is suggested, together with a minimum t_w value of 3 mm (Nuzzo et al., 2019). At this point, entering in the central design chart in correspondence of selected t_w and B_w values, the H_2 upper limit preventing buckling mechanism can be read. Authors suggest considering a lower bound for H_2 equal to 100 mm, in order to allow for the proper placement of the dissipative windows within the web. Finally, once H_2 has been selected within the above range, entering the right side plot the designer can easily detect damper's K_{el}. In addition, this chart allows to further check SL geometry with regards to buckling phenomenon, verifying it to be outside of the gray area.

CASE STUDY: SEISMIC UPGRADE OF A RC STRUCTURE BY MEANS OF HYSTERETIC DAMPERS

The design framework proposed herein has been applied to the case study of an existing RC frame structure (**Figure 10**) situated in Norcia (central Italy). This structure was already assumed as a case study by the Italian Laboratories University Network of seismic engineering (ReLUIS) within a research project (2017–2018) investigating the application of different seismic control strategies. The building, designed and built in the early 1960s, hosts a public school and consists of three floors and a semi-underground level. The dimensions in the plan are 12.8 m × 58.9 m, while the interstory height is 3.5 m at the lowest floor and 3.3 m for the other levels for a maximum height of 16 m considering the sloping roof. Arranging permanent and live loads in seismic combination, seismic masses of 907 tons, 937 tons, and 838 tons have been defined for levels 1, levels 2–3, and for the top level, respectively.

The seismic behavior of the as-built existing structure (F system) has been assessed in X direction through pushover analysis (CSI and SAP2000, 2019) according to NTC2018 (Ministry of Infrastructures, 2018), resulting in a satisfactory Life Safety (LS) limit state. The numerical 3D FEM model of the structure included clay-bricks infill walls modeled in compression as equivalent stiff braces with brittle post-yield behavior (Bergami and Nuti, 2015). The fundamental vibrational period is 0.71 s, corresponding to translational mode in X direction (**Figure 10**). However, in the perspective of reducing earthquake-induced damage to structural and non-structural elements at LS limit state, a maximum allowable interstory drift ratio of 0.5% is imposed under events characterized by a return period T_R = 712 years (10% of probability of being exceeded in 75 years). In order to meet this target performance, which is quite challenging for an existing building, a retrofitting strategy consisting of the installation of dissipative systems, i.e., diagonal and chevron braces arranged with SL dampers, is adopted along longitudinal frames (X direction). In this way it is possible to increase the lateral stiffness of the structure, providing, at the same time, added energy dissipation capacity. The retrofitted strategy is meant to concentrate damage mostly in the dampers, thus ensuring structural integrity and decreasing repairing costs in the aftermath of a seismic event. The design of the damping braces, to be installed only along X direction, is developed with the support of *DIBRAST*, while SL devices are defined through the use of

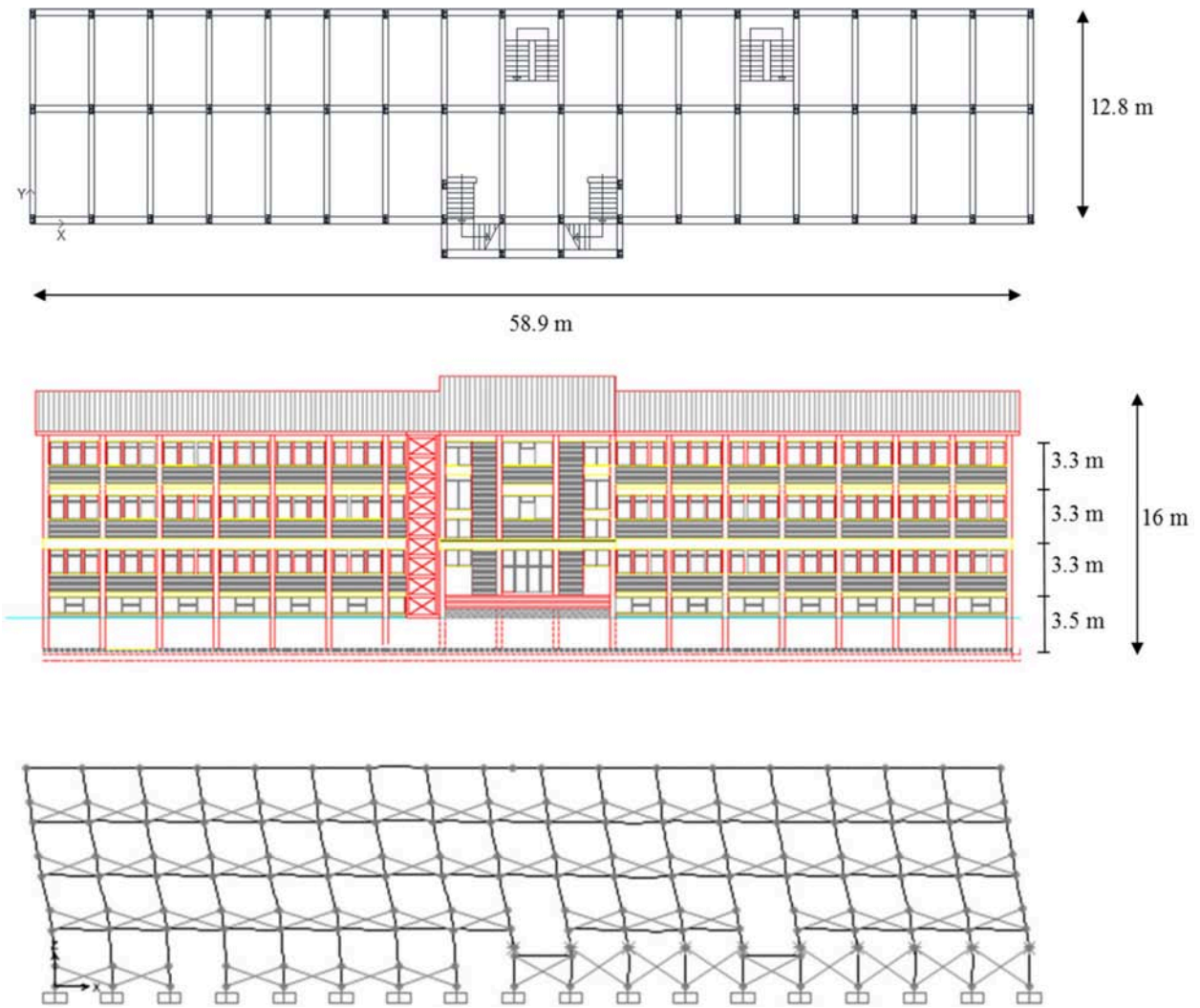

FIGURE 10 | Plan and elevation views of the case study and first modal shape in x–z plane.

proposed design charts and assessed by means of *Shear Link Non-Linear Model*.

Design of Dissipative Braces Through DIBRAST

The dissipative system has been designed through the displacement-based design framework proposed by Nuzzo et al. (2019) with the support of a *DIBRAST* tool. In order to run the software, some information from the bare frame modal and pushover analysis are required. It is highlighted that the mentioned analyses have been previously performed for seismic assessment of the existing structure. Main steps of the design procedure are summarized in the following section, and final results are displayed in **Figure 11**.

After having identified F system behavior as *dissipative*, F properties at the target displacement θ_D = 0.5% have been defined. Namely, shear forces at each story and corresponding absolute displacements at target performance have been evaluated and inputted at step 1, along with first modal shape and seismic masses. Modal participation factor (Γ = 1.3) and equivalent mass (m^* = 2095t) have been given as output for the determination of the F equivalent SDOF system capacity curve. At this point, the bilinear F system capacity curve has been constructed (**Figure 12**), determining base shear $V^*_{F,y} = V^*_{F,PP}$ = 2174 kN and top yielding displacement $d^*_{F,y}$ = 0.014 m, while d^*_{PP} is automatically determined by the tool (d^*_{PP} = 0.036 m).

According to step 2 of the design framework, the performance point is univocally determined once the viscous damping ratio of the equivalent F system, ductility, and post-yielding to elastic stiffness ratio of the dissipative system are defined. At this point, first trial values for the latter parameters have been initially considered equal to 3 and 0.4 respectively, whereas $\xi_{v,F}$ has been set to 5%. At the same time, first trial equivalent base shear at performance point of the BF system has been specified greater than the F system one (i.e., 2500 kN > 2174 kN).

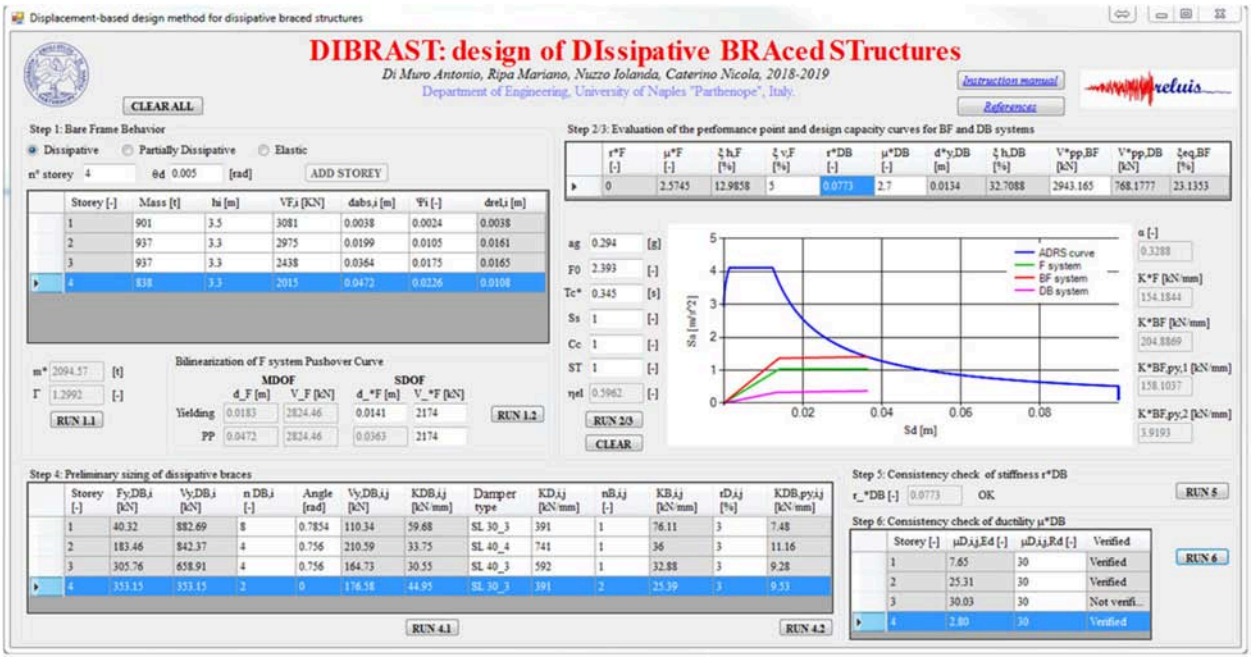

FIGURE 11 | Damping braces design by means of *DIBRAST*.

Consequently, the equivalent damping ratio of the BF system has been automatically determined as an output by *DIBRAST*, and it is around 23%. Additionally, the final value of BF system at PP is $V^*_{BF,PP}$ = 2943 kN. Seismic hazard parameters according to the Italian NTC2018 code in correspondence with the specific site and LS limit state are given in the input. At the end of step 3, *DIBRAST* provides the ADRS design curve for $\xi_{eq,BF}$, plotted together with F capacity curve and desired BF and DB capacity curves.

Knowing the equivalent damped brace system capacity curve, mechanical properties of the dissipative system in correspondence of each story can be read as an output of step 4. Thereby, after specifying the number of dampers at the i-th story, the tool provides the optimal stiffness ($K_{DB,i,j}$) and yielding force ($V_{y,DB,i,j}$) of the j-th dissipative system at i-th story to converge on the desired result.

Dissipative braces composed of SL dampers arranged with steel diagonals are supposed to be installed at all levels. In particular, dissipative braces are installed only on perimetral frames along X direction, which resulted in them being more flexible than transversal ones. A total number of 8, 4, and 2 dampers are employed at first, second/third and fourth story, respectively (**Figure 13**). It is worth highlighting that the damped braces configuration is chosen in order to reduce the transmission of detrimental shear action in correspondence of columns. After defining the number of dampers at each story, the software provides the required mechanical properties at each braced bay. At this point, dimensioning of SLs and supporting braces can be performed and are addressed to the next section.

Successively, *DIBRAST* also provides required stiffness of supporting elements by solving Eq. 8. Thus, proper steel diagonals dimensions have been chosen from commercial catalogs according to required mechanical properties.

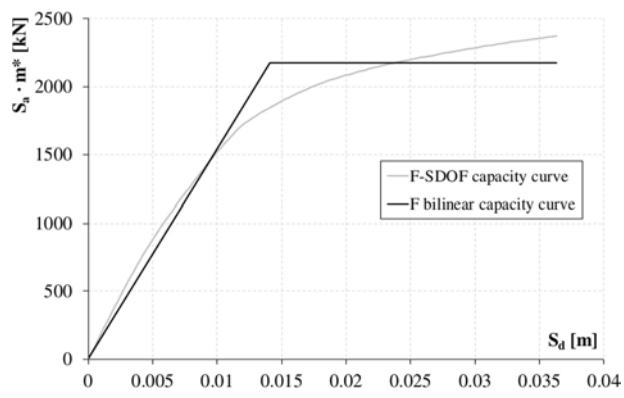

FIGURE 12 | F system capacity curve.

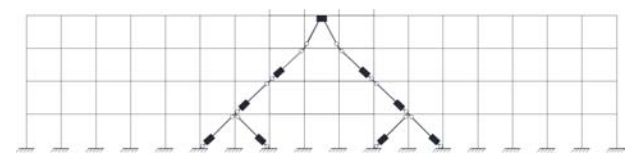

FIGURE 13 | Dissipative braces configuration.

In addition, SL devices post-yielding-to-elastic stiffness ratio ($r_{D,i,j}$) has been set to 3%, obtaining the damped braces post-yielding stiffness distribution throughout the height.

After having designed the dissipative system, the equivalent post-yielding-to-elastic stiffnesses ratio r^*_{DB} has to be checked to be consistent with the value initially set at step 2. Hence, the procedure is autonomously iterated until convergence is reached for r^*_{DB} equal to 0.08. Finally, prompt ductility checks on each damper have been performed at the final step of the tool, considering SL ductility capacity equal to 30.

Design of SL Dampers According to Required Performance

Knowing the required mechanical properties for each dissipative brace, the SL dampers have been designed through the design chart and the additional *Shear Link Non-Linear Model* tool presented in this paper.

Although various geometrical combinations may correspond to required mechanical properties, an attempt was made to limit the variability of dimensions to facilitate supply and on-site assembly operations. After selecting S275 steel grade and setting the SL yielding force (F_y) equal to the demanding shear force ($V_{y,DB,i,j}$) output from *DIBRAST*, the design chart of **Figure 8** was adopted for the preliminary design of SL dampers. The value of B_w was restricted in the range of 300–400 mm, thus determining optimal t_w values from the left-side plot of the design chart equal to 3 or 4 mm. Consequently, in the perspective of avoiding buckling phenomenon of the web, maximum height within stable behavior was detected from the central plot of the chart. Giving $H_{2,lim}$ as the upper bound, H_2 equal to 110 mm was considered for all devices. Finally, knowing t_w, B_w, and H_2 for each device, SL elastic stiffness was determined from the right-side plot of the design chart. This approach led to the design of three types of SL devices, SL 30_3 for the first and last story, SL 40_4 at the second story, and SL 40_3 for the third one. The adopted SL geometries have been implemented in *Shear Link Non-linear Model* additional tool, thus further assessing the corresponding mechanical properties and accurately reading their values. Consequently, it is possible to determine the supporting brace section, knowing its required elastic stiffness in output from *DIBRAST* tool. Steel tubular elements have been selected from commercial catalogs and are characterized by a diagonal cross section and thickness dimensions in the range of 139.7 × 4 mm to 219.1 × 5.9 mm. Finally, the actual mechanical properties of dissipative braces, i.e., corresponding to real SL and brace-adopted design elements, have been determined and compared to required values output from *DIBRAST* (**Table 1**), evidencing a satisfactory matching.

Assessment of the Design Approach Through Non-linear Analysis

In order to assess effectiveness of the proposed design approach, a static non-linear analysis was performed. In this way, SL devices with inelastic behavior were properly considered. In the 3D FEM model, damping braces have been modeled as non-linear Bouc-Wen link elements, adopting actual values of the mechanical parameters of dissipative braces (**Table 1**). The resulting pushover curve was converted into the equivalent SDOF system one, and the corresponding bilinear curve was determined. Comparing it to the desired retrofitted capacity curve (**Figure 14**), output from *DIBRAST*, a very satisfactory matching was observed. The desired DB capacity curve according to *DIBRAST* is shown as well, proving its adequateness in enhancing the as-built system and achieving the performance goal. At the performance point, the displacement demand on dampers resulted in containment in the range of 5–17 mm, which is thus lower than the displacement capacity of the SL dampers.

TABLE 1 | Required vs. actual performance for single dissipative brace in horizontal direction.

	Required performance for single dissipative brace		Actual performance for single dissipative brace	
Story (-)	**Yielding force (kN)**	**Elastic stiffness (kN/mm)**	**Yielding force (kN)**	**Elastic stiffness (kN/mm)**
1	110	60	101	64
2	210	34	185	34
3	164	31	139	33
4	176	45	143	50

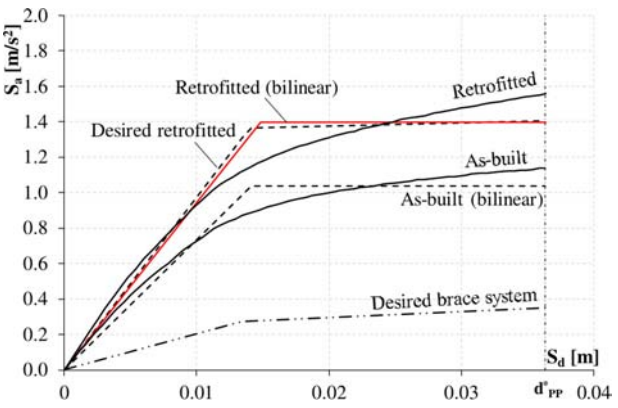

FIGURE 14 | As-built and retrofitted capacity curves.

CONCLUSION

This paper has provided a comprehensive computer-aided seismic design procedure for structures equipped with hysteretic devices. As a matter of fact, despite several experimental works in literature highlighting the effectiveness of these devices for seismic hazard mitigation, their employment is not yet widespread due to a lack of design guidelines and prompt methodologies suitable for real structures. In fact, although various design procedures have been proposed, their quite articulated and iterative nature often make them unappealing for professional applications. For the above reasons, in the attempt of promoting the broad use of metallic hysteretic dampers as seismic protection systems, authors firmly believe

in the need to support designers with a computer-aided tool able to drive them in the fulfillment of all steps of a specific displacement-based design procedure previously developed by the same authors. This specific methodology has been chosen because of its closed-form analytical nature, not involving further numerical structural analysis. Moreover, it is able to directly provide output-effective design parameters of dissipative system, resulting in it being suitable for professional applications. In this perspective, the *DIBRAST*—design of DIssipative BRAced Structures—tool has been developed, revoking the several phases of the framework. Required iterations are automated by the software, thus significantly reducing processing time. Input data are clearly identified and include bare frame properties along with the definition of the target displacement, to be given as a function of bare frame linear or non-linear behavior. In particular, modal and pushover analyses of the bare frame have to be performed at the beginning to determine its capacity curve as well as the first modal shape. Output effectively allow us to size the dissipative system, providing its mechanical properties, in terms of yielding force and elastic stiffness, are able to meet the performance objective. The computer-aided *DIBRAST* tool proposed herein is designed to be suitable for a wide variety of metallic hysteretic dampers. This work provides a complete how-to-use description of the software, which is freely available online.

Furthermore, to provide additional support to the designer in the geometrical characterization of hysteretic devices, analytical models, specifically developed for a particular damper, i.e., the SL, have been implemented in Visual Basic environment, thus developing *Shear Link Non-Linear Model* tool. This second software can be freely downloaded as well. The software delivers SL mechanical characteristics in terms of yielding force and elastic stiffness once the user inputs essential geometric dimensions, the type of material, and the boundary conditions. Although this allows us to get SL properties in an easy and prompt way, this tool still requires an initial blind design of the damper in order for it to be iteratively assessed. For this reason, authors further investigated on the influence of SL geometry on the mechanical characteristics of interest and, based on results of this study, new design charts have been proposed herein. In particular, the plots guide the designer in the detection of damper's web optimal dimensions according to the desired yielding force, output from *DIBRAST*, also accounting for the possible web's buckling phenomenon.

The effectiveness of the newly proposed design tools has been assessed with reference to the RC case study structure, located in central Italy, that was seismically upgraded by means of SL dampers. Using the *DIBRAST* tool, the optimal mechanical properties of damped braces at each of the four stories have been calculated. The overall performance objective was low structural damage thanks to the high dissipation provided by the hysteretic devices. Geometric details of each device were determined first using the newly proposed design charts and then through assessing them by means of the additional *Shear Link Non-Linear Model* tool. Finally, a non-linear static analysis of the retrofitted structure was performed, showing the achievement of the desired goals.

DATA AVAILABILITY STATEMENT

All datasets generated for this study are included in the article/supplementary material.

AUTHOR CONTRIBUTIONS

IN developed the seismic design approach in the Visual Basic environment with the assistance of the other two authors. FC applied the whole procedure to the case-study by means of the proposed softwares, then validated the outcomes through non-linear analyses. NC produced the charts for sizing the devices, and coordinated and supervised the overall work. All authors contributed to revising the manuscript and to approving the submitted version.

FUNDING

The research activity has been developed in the framework of the ReLUIS research project 2019–2021 funded by the Italian Department for Civil Protection. The above support is gratefully acknowledged.

ACKNOWLEDGMENTS

The authors would like to thank Eng. Antonio Di Muro and Eng. Mariano Ripa for their great support and collaboration in the realization of the Visual Basic tools.

REFERENCES

ATC (1996). *Seismic Evaluation and Retrofit of Concrete Buildings, ATC*-40. Redwood City, CA: Applied Technology Council.

Bergami, A. V., and Nuti, C. (2013). A design procedure of dissipative braces for seismic upgrading. *Earthq. Struct.* 4, 85–108. doi: 10.12989/eas.2013.4.1.085

Bergami, A. V., and Nuti, C. (2015). Experimental tests and global modeling of masonry infilled frames. *Earthq. Struct.* 9, 281–303. doi: 10.12989/eas.2015.9.2.281

Bergman, D. M., and Goel, S. C. (1987). *Evaluation of Cyclic Testing of Steel-Plate Devices for Added Damping and Stiffness*. Ann Arbor, MI: Department of Civil Engineering, University of Michigan.

Bozzo, L. M., and Barbat, A. H. (1999). *Diseño Sismorresistente de Edificios. Técnicas Convencionales y Avanzadas (in Spanish)*. Barcelona: Editorial Reverte.

Bozzo, L. M., Cahís, X., and Torres, L. A. (1998). "Shear type energy dissipator for the protection of masonry infill walls," in *Proceedings of the 6th US National Conference on Earthquake Engineering*, Seattle, WA.

Bozzo, L. M., Gonzales, H., Pantoja Medina, M., Munoz, E., and Ramirez, J. (2019). "Modeling, analysis and seismic design of structures using energy dissipators SLB," in *Proceedings of the International Symposium on Earthquake Engineering*, Lima

Cahís, X. (2000). *Desarrollo de un Nuevo Disipador de Energía Para Diseño Sismorresistente. Análisis Numérico y Validación Experimental de su Comportamiento*. Ph.D. thesis, Universitat Politècnica de Catalunya, Barcelona.

Cahís, X., Bozzo, L. M., Torres, L., and Foti, D. (1997). "An energy dissipating device for seismic protection of masonry infill walls," in *Proceedings of the 8 Convegno Nazionale ANIDIS*, Taormina.

Ciliento, F. (2019). *Development of Seismic Design Procedures for Building Structures Equipped with SLB Metallic Hysteretic Devices*. Ph. D. thesis, University of Naples Federico II, Naple.

Clark, P., Aiken, I., Kasai, K., Ko, E., and Kimura, E. (1999). "Design procedures for buildings incorporating hysteretic damping devices," in *Proceedings, 68th Annual Convention, Santa Barbara, California Structural Engineers Association of California, SEAOC*, Santa Barbara, 355–371.

CSI and ETABS (2016). *Structural Software for Building Analysis and Design*. Berkeley, CA: Computers and Structures Inc.

CSI and SAP2000 (2019). *Integrated Software for Structural Analysis and Design*. Berkeley, CA: Computer and Structures Inc.

De Domenico, D., Impollonia, N., and Ricciardi, G. (2019). Seismic retrofitting of confined masonry-RC buildings: the case study of the university hall of residence in Messina. *Italy Ingegneria Sismica.* 36, 54–84.

Di Cesare, A., and Ponzo, F. C. (2017). Seismic retrofit of reinforced concrete frame buildings with hysteretic bracing systems: design procedure and behaviour factor. *Shock Vib.* 2017:2639361. doi: 10.1155/2017/2639361

Di Cesare, A., Ponzo, F. C., and Nigro, D. (2014). Assessment of the performance of hysteretic energy dissipation bracing systems. *Bull. Earthq. Eng.* 12, 2777–2796. doi: 10.1007/s10518-014-9623-z

Dwairi, H. M., Kowlsky, M. J., and Nau, J. M. (2007). Equivalent damping in support of direct displacement-based design. *Earthq. Eng.* 11, 512–530. doi: 10.1080/13632460601033884

EN 15129 (2009). *European Standard, Anti-seismic devices*. Brussels: European Committee for Standardization.

Franchioni, G., Severn, R. T., and Bairrao, R. (2001). *Experimental Investigations on Semiactive and Passive Systems for Seismic Risk Mitigation.* Report No. 7, ECOEST2 & ICONS.

Greco, F., Rosati, L., Serino, G., and Vaiana, N. (2018). A mixed explicit-implicit time integration approach for nonlinear analysis of base-isolated structures. *Ann. Solid Struct. Mech.* 10, 17–29. doi: 10.1007/s12356-017-0051-z

Hurtado, F. (2006). *Propuesta de Disipador Genérico "SL" Para Edificios y su Diseño Sismorresistente*. Ph. D. thesis, Universitat Politécnica de Catalunya, Barcelona.

Hurtado, F., and Bozzo, L. M. (2005). Un disipador Shear Link (SL) generalizado para diseño sismorresistente (in Spanish). *Hormigón Y Acero.* 235, 53–68.

Hurtado, F., and Bozzo, L. M. (2008). "Numerical and experimental analysis of a shear-link energy dissipator for seismic protection of buildings," in *Proceedings of the 14th World Conference on Earthquake Engineering*, Beijing.

Javanmardi, A., Ibrahim, Z., Ghaedi, K., Ghadim, H. B., and Hanif, M. U. (2019). State-of-the-art review of metallic dampers: testing, development and implementation. *Arch. Comput. Methods Eng.*

Kelly, J. M., Skinner, R. I, and Heine, A. J. (1972). Mechanisms of energy absorption in special devices for use in earthquake resistant structures. *Bull. N. Z. Soc. Earthq. Eng.* 5, 63–88.

Kim, J., and Choi, H. (2004). Behavior and design of structures with buckling-restrained braces. *Eng. Struct.* 26, 693–706. doi: 10.1016/j.engstruct.2003.09.010

Kobori, T., Miura, Y., and Fukuzawa, E. (1992). "Development and application of hysteresis steel dampers," in *Proceedings of the 10th World Conference on Earthquake Engineering*, Rotterdam, 2341–2346.

Losanno, D., Londono, J. M., Zinno, S., and Serino, G. (2018). Effective damping and frequencies of viscous damper braced structures considering the supports flexibility. *Comput. Struct.* 207, 121–131. doi: 10.1016/j.compstruc.2017.07.022

Losanno, D., Spizzuoco, M., and Serino, G. (2015). An optimal design procedure for a simple frame equipped with elastic-deformable dissipative braces. *Eng. Struct.* 101, 677–697. doi: 10.1016/j.engstruct.2015.07.055

Losanno, D., Spizzuoco, M., and Serino, G. (2019). Design and retrofit of multi-story frames with elastic-deformable viscous damping braces. *J. Earthq. Eng.* 23, 1441–1464. doi: 10.1080/13632469.2017.1387193

Mazza, F. (2019a). A plastic-damage hysteretic model to reproduce strength stiffness degradation. *Bull. Earthq. Eng.* 17, 3517–3544. doi: 10.1007/s10518-019-00606-3

Mazza, F. (2019b). A simplified retrofitting method based on seismic damage of a SDOF system equivalent to a damped braced building. *Eng. Struct.* 200:109712. doi: 10.1016/j.engstruct.2019.109712

Mazza, F., and Vulcano, A. (2015). Displacement-based design procedure of damped braces for the seismic retrofitting of r.c. framed buildings. *Bull. Earthq. Eng.* 13, 2121–2143. doi: 10.1007/s10518-014-9709-7

Ministry of Infrastructures (2018). *NTC Technical Regulations for the Constructions (in Italian)*.

Nuzzo, I., Losanno, D., and Caterino, N. (2019). Seismic design and retrofit of frame structures with hysteretic dampers: a simplified displacement-based procedure. *Bull. Earthq. Eng.* 17, 2787–2819. doi: 10.1007/s10518-019-00558-8

Nuzzo, I., Losanno, D., Caterino, N., Serino, G., and Bozzo Rotondo, L. M. (2018). Experimental and analytical characterization of steel shear links for seismic energy dissipation. *Eng. Struct.* 172, 405–418. doi: 10.1016/j.engstruct.2018.06.005

Nuzzo, I., Losanno, D., Serino, G., and Bozzo, L. M. (2015). "Simplified nonlinear analysis: application to damper-braced structures," in *Proceedings of the 15th International Conference on Civil, Structural and Environmental Engineering Computing*, Prague.

Ponzo, F. C., Di Cesare, A., Lamarucciola, N., and Nigro, D. (2019). Seismic design and testing of post-tensioned timber buildings with dissipative bracing systems. *Front. Built Environ.* 5, 1–13. doi: 10.3389/fbuil.2019.00104

Shin, M. H., and Sung, W. P. (2005). A model for hysteretic behaviour of rhombic low yield strength steel added damping and stiffness. *Comput. Struct.* 83, 895–908. doi: 10.1016/j.compstruc.2004.11.012

Tsai, K. C., Chen, H. W., Hong, C. P., and Su, Y. F. (1993). Design of steel triangular plate energy absorbers for seismic-resistant construction. *Earthq. Spectra* 9, 505–528. doi: 10.1193/1.1585727

Vaiana, N., Sessa, S., Marmo, F., and Rosati, L. (2018). A class of uniaxial phenomenological models for simulating hysteretic phenomena in rate-independent mechanical systems and materials. *Nonlinear Dyn.* 93, 1647–1669. doi: 10.1007/s11071-018-4282-2

Vaiana, N., Sessa, S., Marmo, F., and Rosati, L. (2019a). An accurate and computationally efficient uniaxial phenomenological model for steel and fiber reinforced elastomeric bearings. *Compos. Struct.* 211, 196–212. doi: 10.1016/j.compstruct.2018.12.017

Vaiana, N., Sessa, S., Marmo, F., and Rosati, L. (2019b). Nonlinear dynamic analysis of hysteretic mechanical systems by combining a novel rate-independent model and an explicit time integration method. *Nonlinear Dyn.* 98, 2879–2901. doi: 10.1007/s11071-019-05022-5

Watanabe, A., Hitomi, Y., Saeki, E., Wada, A., and Fujimoto, M. (1988). "Properties of brace encased in buckling-restraining concrete and steel tube," in *Proceedings of 9 th World Conference on Earthquake Engineering*, Tokyo–Kyoto.

Whittaker, A. S., Bertero, V. V., Thompson, C. L., and Alonso, L. J. (1991). Seismic testing of steel plate energy dissipation devices. *Earthq. Spectra* 7, 563–604. doi: 10.1193/1.1585644

Conflict of Interest: The authors declare that the research was conducted in the absence of any commercial or financial relationships that could be construed as a potential conflict of interest.

frontiers in Built Environment

ORIGINAL RESEARCH
published: 26 February 2020
doi: 10.3389/fbuil.2020.00019

Semi-actively Implemented Non-linear Damping for Building Isolation Under Seismic Loadings

Yun-Peng Zhu[1], *Zi-Qiang Lang*[1]*, *Yosuke Kawanishi*[2] *and Masayuki Kohiyama*[3]

[1] Department of Automatic Control and Systems Engineering, University of Sheffield, Sheffield, United Kingdom, [2] Formerly, Graduate School of Science and Technology, Keio University, Hiyoshi, Japan, [3] Department of System Design Engineering, Keio University, Hiyoshi, Japan

It is well-known that semi-active solution can achieve building isolation with much less energy requirements than active solutions. Also, it has been shown in previous studies that compared to linear damping, non-linear damping performs better for building isolation under sinusoidal ground motions. The present study is concerned with the extension of the application of the semi-actively implemented non-linear damping to building isolation under seismic loadings. A two-degree-of-freedom (2-DOF) scaled building model is used for simulation studies. Experimental tests on a physical building model have been used to validate the effectiveness of the 2-DOF scaled building model in representing the behaviors of a physical building structure. The optimal design of the semi-actively implemented non-linear damping for building isolation under design seismic motions is then carried out using the 2-DOF scaled building model based on simulation studies. The results show that an optimal design of semi-actively implemented non-linear damping can improve the performance of building isolation under design seismic motions in terms of both absolute acceleration and inter-story drift.

Keywords: building, isolation, semi-active, non-linear damping, seismic loadings

OPEN ACCESS

Edited by:
Luigi Di Sarno,
University of Sannio, Italy

Reviewed by:
Dario De Domenico,
University of Messina, Italy
Kohei Fujita,
Kyoto University, Japan
Miao Yu,
Chongqing University, China

***Correspondence:**
Zi-Qiang Lang
z.lang@sheffield.ac.uk

Specialty section:
This article was submitted to Earthquake Engineering, a section of the journal Frontiers in Built Environment

Received: *13 October 2019*
Accepted: *11 February 2020*
Published: *26 February 2020*

Citation:
Zhu Y-P, Lang Z-Q, Kawanishi Y and Kohiyama M (2020) Semi-actively Implemented Non-linear Damping for Building Isolation Under Seismic Loadings. Front. Built Environ. 6:19. doi: 10.3389/fbuil.2020.00019

INTRODUCTION

Building isolation systems are important for protecting buildings during earthquakes (Fujita et al., 2016; Hayashi et al., 2018). Traditional building isolation systems are designed using low horizontal-stiffness bearings to achieve low resonant frequencies so as to isolate earthquake loadings over a wide range of frequencies (Naeim, 1989). However, during some recent earthquakes, e.g., the 2011 Tohoku earthquake in Japan, long period ground motion with low frequencies were recorded, which was close to the resonance frequencies of some high-rise and base-isolated buildings (Takewaki et al., 2011; Kasai et al., 2013), indicating that traditional solutions may not provide desired isolation performance in these cases. Although some traditional isolation devices such as tuned mass damper (TMD) (Taniguchi et al., 2008) or enhanced variants with the inerter as tuned mass damper inerter (TMDI) (De Domenico et al., 2019) have been discussed and applied in building isolation systems, expensive costs, and sensitive adjustment to the dynamic property are required in these devices of a constructed building (Dan and Kohiyama, 2013).

The vibration around the resonant frequencies can be reduced by introducing a linear damping into the building isolation system, but this can be detrimental to the building isolation over non-resonance frequency ranges (Soong, 1990; Amini et al., 2015). Large supplemental damping combined with seismic isolation is detrimental because it increases the higher-mode response, thus

having a negative effect on the superstructure acceleration and inter story drift (Kelly, 1999; De Domenico and Ricciardi, 2018). To resolve this issue, many active control techniques including the actively implemented Linear–quadratic– Gaussian (LQG) control (Liu and Wu, 2013; Wang and Dyke, 2013) have been applied to improve the building isolation performance. However, the active control techniques require large power supply and high maintenance cost (Sims et al., 1999), and the stability of the actively controlled building isolation system would also be a concern (Taniguchi et al., 2016). Recently, it has been shown that these problems can be circumvented by using a non-linear damping based isolator that can reduce transmitted vibrations over both resonant and non-resonant frequencies (Peng et al., 2010, 2011; Guo et al., 2012; Lang et al., 2013). For example, Peng et al. (2010, 2011) has shown that non-linear damping can reduce the force transmissibilities over all frequency ranges of concern for both single-degree-of-freedom (SDOF) and multi-degree-of-freedom (MDOF) systems subject to sinusoidal loadings.

In practice, a non-linear damping can be realized by using, e.g., viscous fluid dampers or friction dampers, to dissipate seismic energies for building isolation (Symans et al., 2008). However, these are usually difficult to design and implement in practice to achieve a desired damping characteristic, and a semi-active solution is considered to be an ideal solution to this problem (Guyomar and Badel, 2006; Ebrahimi et al., 2008; Laalej et al., 2012; Weber, 2014; Ho et al., 2018). For example, Laalej et al. (2012) studied the use of an MR (Magneto-Rheological) damper in an isolation system to semi-actively implement the power law non-linear damping characteristics. Ebrahimi et al. (2008) investigated the implementation of non-linear vibration absorbers using the eddy current damper.

The properties of the semi-actively implemented non-linear-damping-based building isolation system have been investigated by the authors for the cases where the seismic loadings are sinusoidal (Weber, 2014). The results indicated that the non-linear damping can provide a desired isolation performance under sinusoidal loadings. However, in practice, the seismic loadings are usually complex bandwidth or random signals, where different frequencies are interacted in the isolation system. It is significant to clarify the isolation performance of semi-active control damping subject to seismic loadings before applying the device into a building system. In the present study, the work will be extended to investigate the design and semi-active implementation of non-linear damping for building isolation under seismic loadings.

The paper is organized as follows. The performance of a semi-actively implemented non-linear-damping-based building isolation system for a laboratory physical building model under sinusoidal loadings is analyzed in section The Non-linear Damping-Based Semi-active Building Isolation System. Then, in Section Design of Non-linear Damping-Based Building Isolation System Under Seismic Ground Motions, the extension of the application of the non-linear damping technique to the cases where the building model is subject to seismic ground motions is investigated. Finally, conclusions are reached in section Conclusions.

THE NON-LINEAR DAMPING-BASED SEMI-ACTIVE BUILDING ISOLATION SYSTEM

A Scaled 2-DOF Building Model With a Semi-active Isolator

In laboratory studies, in order to investigate the performance of a building isolation system, the building system is often simplified to a mass-stiffness-damping MDOF system and then further scaled down to a 2-DOF system as shown in **Figure 1** (Wang and Dyke, 2013; Amini et al., 2015; Hayashi et al., 2018; Ho et al., 2018), where the lower and upper masses represent the floor slab above the isolation layer and the superstructure of the target building, respectively. In **Figure 1**, m_1 and m_2 are the masses of the 2-DOF system, k_1 and k_2 are the stiffness parameters, c_1 and c_2 are damping parameters, x_1 and x_2 are the 1st and 2nd floor displacements relative to the ground motion z, respectively.

The 2-DOF building system is protected by a semi-active isolator producing a damping force determined by the ground motion acceleration $\ddot{z}$ and the first floor displacement x_1. The motion equation of the 2-DOF system with this semi-active isolator can be written as

$$\boldsymbol{M}\ddot{\boldsymbol{x}} + \boldsymbol{C}\dot{\boldsymbol{x}} + \boldsymbol{K}\boldsymbol{x} = \boldsymbol{E}u_{\text{con}} + \boldsymbol{F}\ddot{z} \tag{1}$$

where

$$x = [x_1,\ x_2]^{\mathrm{T}};\ \boldsymbol{M} = \begin{bmatrix} m_1 & 0 \\ 0 & m_2 \end{bmatrix};\ \boldsymbol{C} = \begin{bmatrix} c_1 + c_2 & -c_2 \\ -c_2 & c_2 \end{bmatrix};$$
$$\boldsymbol{K} = \begin{bmatrix} k_1 + k_2 & -k_2 \\ -k_2 & k_2 \end{bmatrix};\ \boldsymbol{E} = [1,\ 0]^{\mathrm{T}};\ \boldsymbol{F} = [-m_1,\ -m_2]^{\mathrm{T}}$$

and $u_{\text{con}} = F_d(x_1)$ represents the damping force produced by the semi-active isolator, $F_d(x_1)$ is a function dependent on x_1.

The Non-linear Damping-Based Semi-active Isolator

Consider the case where the semi-active isolator is implemented by a linear damper with three variable coefficients c_{p1}, c_{p2}

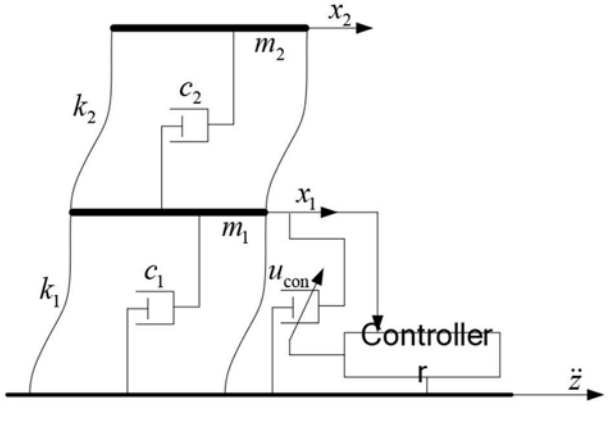

FIGURE 1 | The scaled 2-DOF building model.

and c_{p3} as shown in **Figure 2**. The maximum damping c_{p3} is realized by closing the bottom valve and opening the top valve, the middle damping c_{p2} is obtained by closing the top valve and opening the bottom valve, and the minimum damping c_{p1} is generated by opening both the bottom and top valves. In addition, the damping force from the isolator is produced such that:

$$u_{\text{con}} = F_d(x_1) = -c_s(t)\,\dot{x}_1 \tag{2}$$

where

$$c_s(t) = \begin{cases} c_{p1}, & \text{for } u_d/\dot{x}_1 \le (c_{p1}+c_{p2})/2 \\ c_{p2}, & \text{for } (c_{p1}+c_{p2})/2 < u_d/\dot{x}_1 \le (c_{p2}+c_{p3})/2 \\ c_{p3}, & \text{for } u_d/\dot{x}_1 > (c_{p2}+c_{p3})/2 \end{cases} \tag{3}$$

and u_d is the desired damping force.

Figure 3A shows the MATLAB Simulink realization of a non-linear damping-based semi-active isolator where the desired force u_d is determined as a power law damping such that $u_d = -c_{n3}\dot{x}_1^3$ with c_{n3} being the non-linear damping coefficient. The dynamics of the semi-active isolator is modeled by the first order transfer function $(Ts+1)^{-1}$ where T is the time constant of the transfer function and s is the variable in the Laplace transform. The damping force u_{con} is produced to achieve the objective of $u_d = -c_{n3}\dot{x}_1^3$ by computing the selected $c_{n3}v^2$ value, which are either c_{p1}, c_{p2} or c_{p3}, times the velocity v. **Figure 3B** shows how an increase of the power law damping coefficient c_{n3} from $c_{n3,1}$ to $c_{n3,2}$ to $c_{n3,3}$ can approximately be realized by a switch between c_{p1}, c_{p2} and c_{p3} to produce an approximate of different cubic damping forces $u_{\text{con},1}$, $u_{\text{con},2}$ and $u_{\text{con},3}$, respectively. In practice, due to the mechanics of the semi-active damping device which is modeled by $(Ts+1)^{-1}$, the changing of the damping coefficients will not be a bump like **Figure 3B**, and will gradually shift between different damping coefficients.

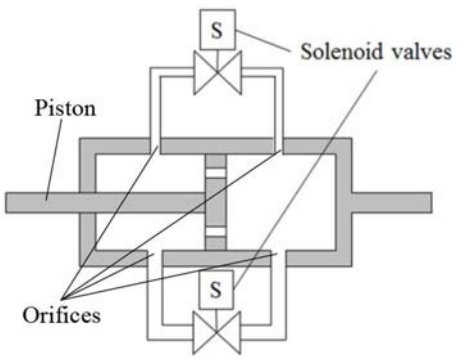

FIGURE 2 | Schematic illustration of a semi-active isolator.

Performance Under Sinusoidal Ground Motions

It has been shown in Lang et al. (2013) and Ho et al. (2018) that, under a sinusoidal ground motion given by:

$$\ddot{z} = A\sin(2\pi ft) \tag{4}$$

with A and f are excitation magnitude and frequency in ms^{-2} and Hz, respectively, by using an appropriate non-linear damping-based semi-active isolator, the force transmissibility defined by Lang et al. (2013) and Ho et al. (2018).

$$T_s(f) = \frac{\left|F\{\ddot{x}_i + \ddot{z}\}|_{\omega=2\pi f}\right|}{A},\ i = 1 \text{ or } 2 \tag{5}$$

can be significantly reduced over both the resonant and non-resonant frequency ranges of the building system. In (5), $F\{.\}$ denotes the Fourier transform operation.

For example, the parameters of a 2-DOF building model obtained by scaling down the 10-story Sosokan building model at Keio University in Japan are:

$$\begin{aligned} m_1 &= 3.672\text{ kg},\ m_2 = 1.696\text{ Kg}; \\ k_1 &= 1036\text{ N/m}\ ,\ k_2 = 5868.7\text{ N/m}; \\ c_1 &= 0.0856\text{ Ns/m}\ ,\ c_2 = 0.5367\text{ Ns/m}; \end{aligned} \tag{6}$$

Consider the case where the three coefficients of the linear damper that implements the semi-active isolator are designed as:

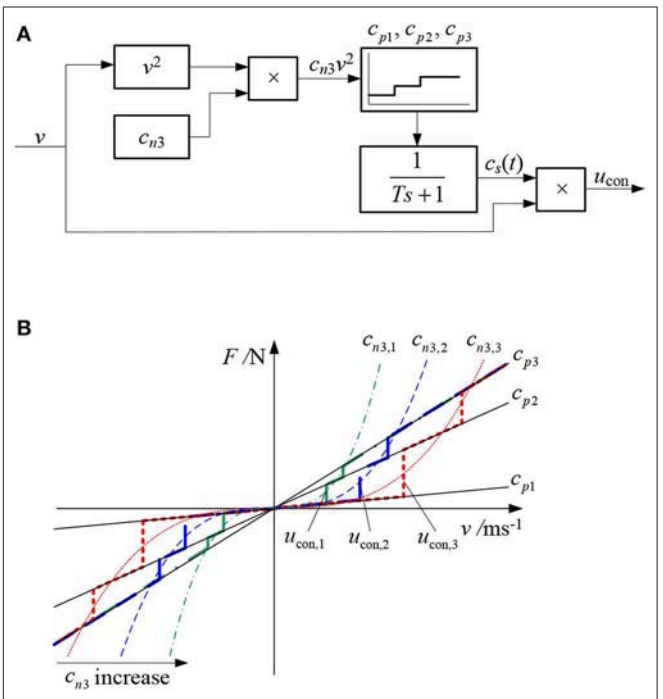

FIGURE 3 | Semi-active implementation of non-linear damping-based isolator. **(A)** An illustration of the semi-actively implemented non-linear damper. **(B)** Semi-actively implemented damping forces under different cubic non-linear damping schemes.

$$c_{p1} = 4.76\ \text{Ns/m}\ ;\ c_{p2} = 39.8\ \text{Ns/m}\ ;\ c_{p3} = 55.9\ \text{Ns/m} \quad (7)$$

and the time constant with the damper is $T = 0.155\,\text{s}$ (Nakamichi, 2018).

The transmissibility (5) on the first floor of the 2-DOF building model under sinusoidal input (4) with $A = 1\ \text{ms}^{-2}$ and $f \in (0, 15]$ Hz is shown in **Figure 4**, indicating the isolation performance under the non-linear damping-based semi-active isolator with $c_{n3} = 3 \times 10^4\ \text{Ns}^3/\text{m}^3$ and the performance under three linear damping-based semi-active isolators with $c_s(t) = c_{p1}$, c_{p2} and c_{p3}, respectively.

From **Figure 4**, the advantage of non-linear damping over linear damping when the building system is subject to harmonic loadings can clearly be observed. These phenomena have been investigated in the previous studies (Lang et al., 2013) but there is still no result on the performance of the non-linear damping-based semi-active building isolation system when the system is subject to seismic ground motions.

In the following, the design and evaluation of the non-linear damping-based semi-active building isolation system will be extended to the case of a 2-DOF laboratory building model subject to seismic ground motion loadings.

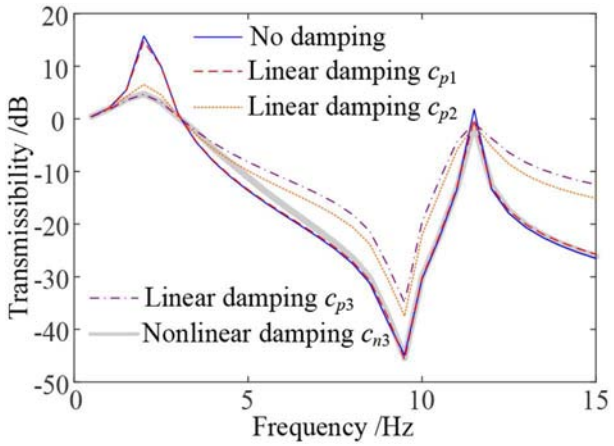

FIGURE 4 | Force transmissibility under linear and non-linear damping-based semi-active isolators.

DESIGN OF NON-LINEAR DAMPING-BASED BUILDING ISOLATION SYSTEM UNDER SEISMIC GROUND MOTIONS

Comparison of the Output Response of the 2-DOF System and the Response of a Laboratory Physical Building Model to Seismic Ground Motions

Generally speaking, the seismic ground motions are random signals that contain a wide band of frequencies.

In this study, two different seismic waves including the hard-soil-layer (Type 1) and soft-soil-layer (Type 2) ground motions are considered. The time histories of the two ground motions that can be recorded in practice are produced according to different design response spectra shown in **Figure 5A**, where the waves were scaled down in the experiment by the scaling factor $\lambda_t = 1/5$ to the sampling time and $\lambda_m = 5$ to the magnitude as shown in **Figure 5B**.

A 2-DOF building model test rig is shown in **Figure 6**, where the first floor velocity $\dot{x}_1$ is used to control the semi-active isolator with $\dot{x}_1$ estimated by a Kalman filter using the measured acceleration data $\ddot{z}$, $\ddot{x}_1$ and $\ddot{x}_2$ (Dan et al., 2015; Nakamichi, 2018; Kohiyama et al., 2019). The parameters of the physical building model and the semi-active isolator are given in Equations (6) and (7), respectively. Therefore, the test rig is a 2-DOF scaled down physical model of the Sosokan building.

The semi-active control damper is shown in **Figure 7A**, where the structure of internal electromagnetic valve is demonstrated in **Figure 7B** (Nakamichi, 2018). The linear damping coefficient c_{p1} is achieved when two valves open, c_{p2} is achieved when one valves open, and c_{p3} is achieved when all valves close. Specifications of the damper and controller are listed in **Table 1**.

Figure 8 shows the switch-overs between the three different damping coefficients during the model simulation and experimental test on the 2-DOF scaled down building model,

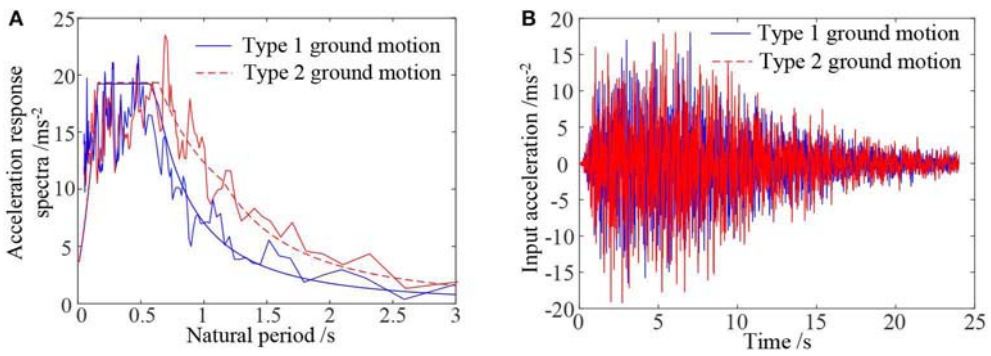

FIGURE 5 | The response spectra and corresponding time histories of seismic ground motions. **(A)** The response spectra of ground motions. **(B)** Scaled seismic ground motions.

respectively. Both the model simulation and experimental test are undertaken under Type 1 ground motion in **Figure 5A** with the coefficient of non-linear damping to be implemented chosen as $c_{n3} = 3 \times 10^4$ Ns^3/m^3. **Figure 8** shows the comparison of the simulated and experimentally obtained building acceleration responses on the first floor.

It can be seen from **Figures 8**, **9** that the simulation results are basically consistent with experimental ones, indicating that the 2-DOF system (6) and (7) can well represent the laboratory physical building model for the analysis and design of a semi-active building isolation system.

System Analysis and Design

Consider the 2-DOF scaled down building model with parameters given by Equation (6) and the semi-active isolator with three switchable damping parameters given by Equation (7). The responses of the building model to the two seismic ground motions in **Figure 5B** are obtained by simulation studies. **Figure 9** shows the maximum of the absolute acceleration and inter-story drift on the first and second floor, respectively. The results are obtained when Type 1 ground motion is applied and non-linear damping coefficients implemented by the semi-active isolator are varied over the range of $c_{n3} \in [0,\ 10] \times 10^4$ Ns^3/m^3. In addition, the responses of the building model under three

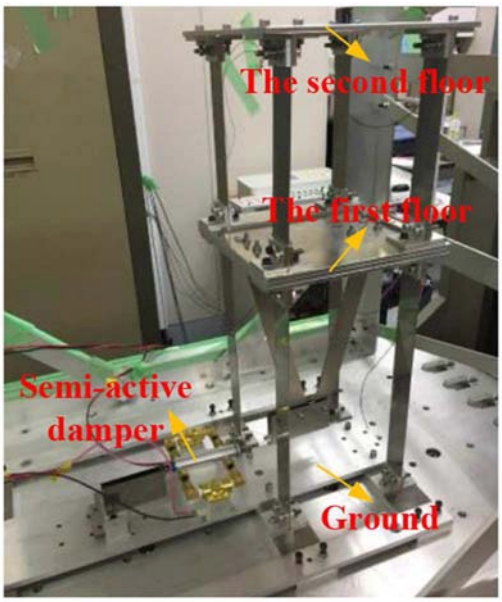

FIGURE 6 | The 2-DOF scaled down laboratory physical model of the Sosokan Building.

TABLE 1 | The specification of the semi-active control damper.

Specification	Value
Damper	
Maximum stroke	±27.5 mm
Mass	0.90 kg
Electromagnetic valve	
Diameter of orifice	2 mm
Mass	0.300 kg
Maximum working pressure difference	0.6 MPa
Rated voltage	24 V

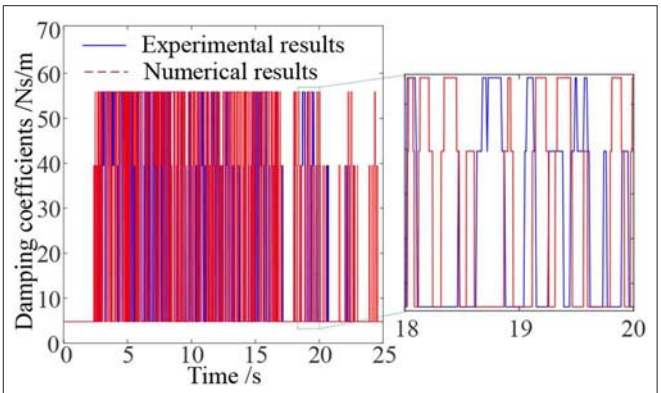

FIGURE 8 | Switch-overs of damping coefficients with semi-active isolator.

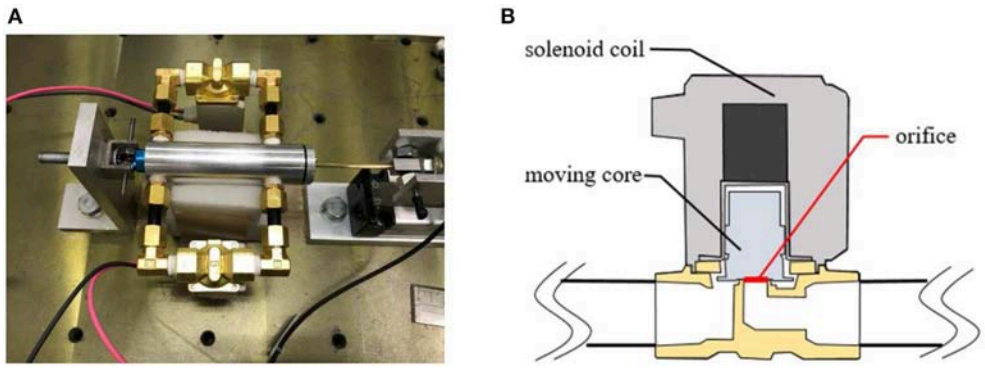

FIGURE 7 | The semi-active control damper. **(A)** The damper structure. **(B)** The internal electromagnetic valve.

linear damping-based isolations are also obtained and shown in **Figure 9** for a comparison.

It can be seen from **Figure 10** that, an increase of linear damping can reduce the maximum inter-story drift, but may increase the maximum of absolute accelerations. However, by using non-linear damping implemented by semi-active isolator, an optimal design for c_{n3} can be reached such that a desired isolation performance in terms of both maximum absolute accelerations and inter story drift can be achieved.

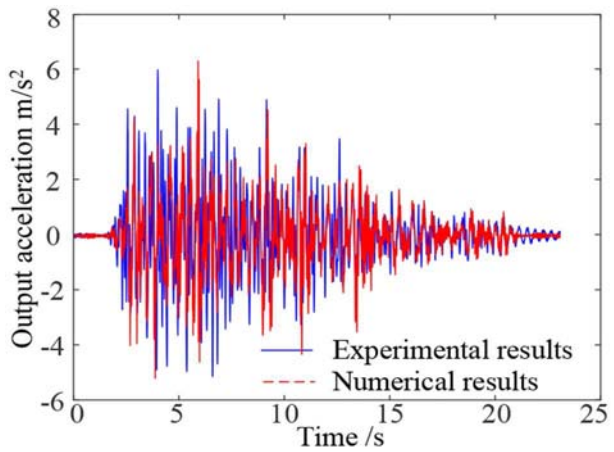

FIGURE 9 | Acceleration responses.

Figure 11 shows the same performance of the non-linear/linear damping based semi-active building isolation system but under Type 2 ground motion. Obviously, a conclusion about the optimal design of c_{n3} similar to that reached from **Figure 10** can be obtained.

Based on these observations, it is possible to find a non-linear damping parameter c_{n3} to achieve desired isolation performance including both the acceleration and displacement of all floors. The desired isolation performance is defined by the designer. For example, the issue of optimal design of non-linear damping parameter c_{n3} can be formulated under Type 1 ground motion as follows:

Find a non-linear damping coefficient $c_{n3} = \bar{c}_{n3}$, such that:

$$\bar{c}_{n3} = \max\{c_{n3}\} \tag{8}$$

subject to the constraint.

$$\begin{cases} \max(|\ddot{x}_1 + \ddot{z}|) \le 6.17\ \mathrm{m/s^2}\ ;\ \max(|x_1|) \le 0.019\ \mathrm{m}; \\ \max(|\ddot{x}_2 + \ddot{z}|) \le 9.86\ \mathrm{m/s^2}\ ;\ \max(|x_2|) \le 0.021\ \mathrm{m}; \end{cases} \tag{9}$$

The above design problem is to find the maximum value of the non-linear damping coefficient that satisfy the acceleration and displacement requirement (9). It is worth noting that the constraint (9) is only used to illustrate the design process and in practice, the optimized result may not be achieved when an inappropriate constraint is applied.

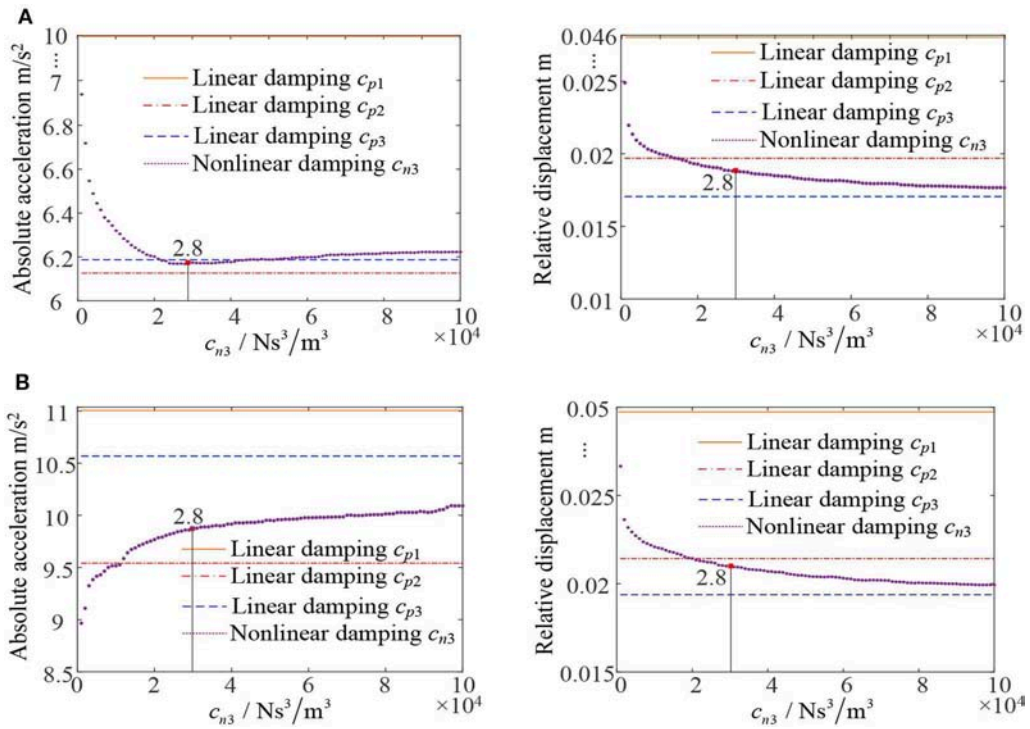

FIGURE 10 | Maximum output acceleration and inter-story drift under Type 1 ground motion. **(A)** Absolute acceleration and inter-story drift of the first floor. **(B)** Absolute acceleration and inter-story drift of the second floor.

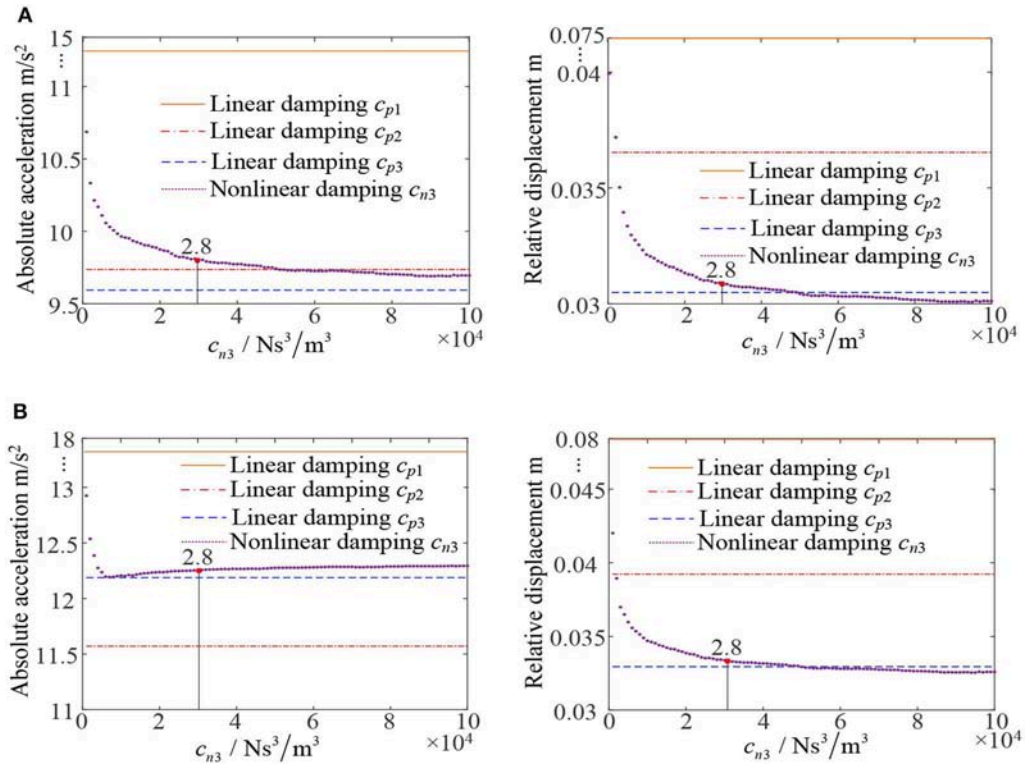

FIGURE 11 | Maximum output acceleration and inter-story drift under Type 2 ground motion. **(A)** Absolute acceleration and inter-story drift of the first floor. **(B)** Absolute acceleration and inter-story drift of the second floor.

The optimal design can be numerically achieved as:

$$c_{n3} = 2.8 \times 10^4 \ \mathrm{Ns^3/m^3} \tag{10}$$

which is illustrated in **Figures 10**, **11**.

It can be seen from **Figures 10**, **11** that, by using the optimal design (10) so as to satisfy the design requirement under Type 1 ground motion, an ideal maximum absolute acceleration and inter-story drift can also be achieved when the building system is subject to loadings represented by Type 2 ground motion.

CONCLUSIONS

The semi-active non-linear-damping-based building isolation has previously been introduced under sinusoidal ground motions to achieve low force transmissibilities over the whole frequency range of concern. However, most seismic loadings in practice are bandwidth and random signals, which are more complex than the sinusoidal loading case and there is not much researches focused on the application of semi-active damping isolation system in these scenarios before. In the present study, the base isolation under seismic ground motions and the design of the semi-active base isolation system have been studied to extend the application of the semi-active non-linear damping-based building isolation to more complicated scenarios.

A 2-DOF building model, which is a scaled down representation of the Sosokan building in Keio University in Japan, is used for the analysis and design of the semi-active non-linear damping-based building isolation system under seismic loadings. Both the acceleration and the inter-story drift of the building model have been taken into account. An optimal design of the non-linear damping parameter has been achieved numerically.

The present study shows that a desired building isolation performance under seismic loadings can be achieved by an optimally designed semi-actively implemented non-linear damping-based isolation system. Studies including the theoretical investigation and statistical design of a semi-active non-linear damping-based isolation system under various seismic ground motions will be conducted in future studies.

DATA AVAILABILITY STATEMENT

The datasets generated for this study are available on request to the corresponding author.

AUTHOR CONTRIBUTIONS

All authors listed have made a substantial, direct and intellectual contribution to the work, and approved it for publication.

ACKNOWLEDGMENTS

The research work was partly supported by the UK Royal Society (Grant number IE150298).

REFERENCES

Amini, F., Mohajeri, S. A., and Javanbakht, M. (2015). Semi-active control of isolated and damaged structures using online damage detection. *Smart Mater. Struct.* 24:105002. doi: 10.1088/0964-1726/24/10/105002

Dan, M., Ishizawa, Y., Tanaka, S., Nakahara, S., Wakayama, S., and Kohiyama, M. (2015). Vibration characteristics change of a base-isolated building with semi-active dampers before, during, and after the 2011 Great East Japan earthquake. *Earthq. Struct.* 8, 889–913. doi: 10.12989/eas.2015.8.4.889

Dan, M., and Kohiyama, M. (2013). "Simultaneous optimization of structural shape and control system of large-scale space frame," in *9th World Conference on Earthquake Resistant Engineering Structures, ERES 2013,* A Coruña, 169–178. doi: 10.2495/ERES130141

De Domenico, D., Deastra, P., Ricciardi, G., Sims, N. D., and Wagg, D. J. (2019). Novel fluid inerter based tuned mass dampers for optimised structural control of base-isolated buildings. *J. Franklin Inst.* 356, 7626–7649. doi: 10.1016/j.jfranklin.2018.11.012

De Domenico, D., and Ricciardi, G. (2018). An enhanced base isolation system equipped with optimal tuned mass damper inerter (TMDI). *Earthq. Eng. Struct. Dyn.* 47, 1169–1192. doi: 10.1002/eqe.3011

Ebrahimi, B., Khamesee, M. B., and Golnaraghi, M. F. (2008). Design and modeling of a magnetic shock absorber based on eddy current damping effect. *J. Sound Vib.* 315, 875–889. doi: 10.1016/j.jsv.2008.02.022

Fujita, K., Miura, T., Tsuji, M., and Takewaki, I. (2016). Experimental study on influence of hardening of isolator in multiple isolation building. *Front. Built Environ.* 2:12. doi: 10.3389/fbuil.2016.00012

Guo, P. F., Lang, Z. Q., and Peng, Z. K. (2012). Analysis and design of the force and displacement transmissibility of non-linear viscous damper based vibration isolation systems. *Nonlin. Dyn.* 67, 2671–2687. doi: 10.1007/s11071-011-0180-6

Guyomar, D., and Badel, A. (2006). Non-linear semi-passive multimodal vibration damping: an efficient probabilistic approach. *J. Sound Vib.* 294, 249–268. doi: 10.1016/j.jsv.2005.11.010

Hayashi, K., Fujita, K., Tsuji, M., and Takewaki, I. (2018). A simple response evaluation method for base-isolation building-connection hybrid structural system under long-period and long-duration ground motion. *Front. Built Environ.* 4:2. doi: 10.3389/fbuil.2018.00002

Ho, C., Zhu, Y., Lang, Z. Q., Billings, S. A., Kohiyama, M., and Wakayama, S. (2018). Non-linear damping based semi-active building isolation system. *J. Sound Vib.* 424, 302–317. doi: 10.1016/j.jsv.2018.03.023

Kasai, K., Mita, A., Kitamura, H., Matsuda, K., Morgan, T. A., and Taylor, A. W. (2013). Performance of seismic protection technologies during the 2011 Tohoku-Oki earthquake. *Earthq. Spectra* 29, S265–S293. doi: 10.1193/1.4000131

Kelly, J. M. (1999). The role of damping in seismic isolation. *Earthq. Eng. Struct. Dyn.* 28, 3–20. doi: 10.1002/(SICI)1096-9845(199901)28:1<3::AID-EQE801>3.0.CO;2-D

Kohiyama, M., Omura, M., Takahashi, M., Yoshida, O., and Nakatsuka, K. (2019). Update of control parameters for semi-actively controlled base-isolated building to improve seismic performance. *Jap. Archit. Rev.* 2, 226–237. doi: 10.1002/2475-8876.12090

Laalej, H., Lang, Z. Q., Sapinski, B., and Martynowicz, P. (2012). MR damper based implementation of non-linear damping for a pitch plane suspension system. *Smart Mater. Struct.* 21:045006. doi: 10.1088/0964-1726/21/4/045006

Lang, Z. Q., Guo, P. F., and Takewaki, I. (2013). Output frequency response function based design of additional non-linear viscousdampers for vibration control of multi-degree-of-freedom systems. *J. Sound Vib.* 332, 4461–4481. doi: 10.1016/j.jsv.2013.04.001

Liu, Y. H., and Wu, W. H. (2013). Active vibration isolation using a voice coil actuator with absolute velocity feedback control. *Int. J. Autom. Smart Technol.* 3, 221–226. doi: 10.5875/ausmt.v3i4.215

Naeim, F. (1989). The seismic design handbook. New York, NY: Springer Science and Business Media. doi: 10.1007/978-1-4615-9753-7

Nakamichi, F. (2018). Control of semi-active oil damper using local sensor for reducing equipment response (master thesis). Keio University, Hiyoshi, Japan.

Peng, Z. K., Lang, Z. Q., Jing, X. J., Billings, S. A., Tomlinson, G. R., and Guo, L. Z. (2010). The transmissibility of vibration isolators with a non-linear antisymmetric damping characteristic. *J. Vib. Acoust.* 132:014501. doi: 10.1115/1.4000476

Peng, Z. K., Lang, Z. Q., Zhao, L., Billings, S. A., Tomlinson, G. R., and Guo, P. F. (2011). The force transmissibility of MDOF structures with a non-linear viscous damping device. *Int. J. Non-Lin Mech.* 46, 1305–14. doi: 10.1016/j.ijnonlinmec.2011.06.009

Sims, N. D., Stanway, R., Peel, D. J., Bullough, W. A., and Johnson, A. R. (1999). Controllable viscous damping: an experimental study of an electrorheological long-stroke damper under proportional feedback control. *Smart Mater. Struct.* 8:601. doi: 10.1088/0964-1726/8/5/311

Soong, T. (1990). *Active Structural Control: Theory and Practice, Ser. Longman Structural Engineering and Structural Mechanics Series*. London, UK: Addison-Wesley London

Symans, M. D., Charney, F. A., Whittaker, A. S., Constantinou, M. C., Kircher, C. A., Johnson, M. W., et al. (2008). Energy dissipation systems for seismic applications: current practice and recent developments. *J. Struct. Eng.* 134, 3–21. doi: 10.1061/(ASCE)0733-9445(2008)134:1(3)

Takewaki, I., Murakami, S., Fujita, K., Yoshitomi, S., and Tsuji, M. (2011). The 2011 off the Pacific coast of Tohoku earthquake and response of high-rise buildings under long-period ground motions. *Soil Dyn. Earthq. Eng.* 31, 1511–1528. doi: 10.1016/j.soildyn.2011.06.001

Taniguchi, M., Fujita, K., Tsuji, M., and Takewaki, I. (2016). Hybrid control system for greater resilience using multiple isolation and building connection. *Front. Built Environ.* 2:26. doi: 10.3389/fbuil.2016.00026

Taniguchi, T., Der Kiureghian, A., and Melkumyan, M. (2008). Effect of tuned mass damper on displacement demand of base-isolated structures. *Eng. Struct.* 30, 3478–3488. doi: 10.1016/j.engstruct.2008.05.027

Wang, Y., and Dyke, S. (2013). Modal-based LQG for smart base isolation system design in seismic response control. *Struct. Control Health Monitor.* 20, 753–768. doi: 10.1002/stc.1490

Weber, F. (2014). Semi-active vibration absorber based on real-time controlled MR damper. *Mech. Syst. Signal Process.* 46, 272–288. doi: 10.1016/j.ymssp.2014.01.017

Conflict of Interest: The authors declare that the research was conducted in the absence of any commercial or financial relationships that could be construed as a potential conflict of interest.

frontiers in Built Environment

ORIGINAL RESEARCH
published: 19 March 2020
doi: 10.3389/fbuil.2020.00029

Smart Seismic Control System for High-Rise Buildings Using Large-Stroke Viscous Dampers Through Connection to Strong-Back Core Frame

Akira Kawai[1], *Tatsuhiko Maeda*[1,2] *and Izuru Takewaki*[1]*

[1] Department of Architecture and Architectural Engineering, Graduate School of Engineering, Kyoto University, Kyotodaigaku-Katsura, Kyoto, Japan, [2] Structural Design Division, Takenaka Co., Osaka, Japan

An innovative structural control system is proposed for high-rise buildings. A damping layer is provided between a stiff upper core frame suspended from the top of the main building and a stiff lower core frame connected to the building foundation. As the ratio of stiffness of both core frames to that of the main building becomes larger, the relative displacement in the damping layer (damper deformation) approaches to the top floor displacement of the main building. The large displacement of the top floor displacement of the main building is taken full advantage in the proposed control system as most of the total displacement of the main building results from the damper deformation instead of interstory drift. Transformation of the multi-degree-of-freedom (MDOF) model into the single-degree-of-freedom (SDOF) model enables a simplified but rather accurate response evaluation for pulse-type and long-duration earthquake ground motions. The results of the time history response analysis of buildings including this control system are presented for various recorded ground motions. Finally, the effectiveness of the proposed structural control system is discussed from the viewpoint of earthquake input energy.

Keywords: passive damper, viscous damper, building connection, double impulse, multi impulse, pulse-type motion, long-duration motion, input energy

OPEN ACCESS

Edited by:
Yoshikazu Araki,
Nagoya University, Japan

Reviewed by:
Chia-Ming Chang,
National Taiwan University, Taiwan
Michele Palermo,
University of Bologna, Italy
Barbara Gwynne Simpson,
Oregon State University, United States

***Correspondence:**
Izuru Takewaki
takewaki@archi.kyoto-u.ac.jp

Specialty section:
This article was submitted to Earthquake Engineering, a section of the journal Frontiers in Built Environment

Received: *10 January 2020*
Accepted: *28 February 2020*
Published: *19 March 2020*

Citation:
Kawai A, Maeda T and Takewaki I (2020) Smart Seismic Control System for High-Rise Buildings Using Large-Stroke Viscous Dampers Through Connection to Strong-Back Core Frame. Front. Built Environ. 6:29. doi: 10.3389/fbuil.2020.00029

INTRODUCTION

After emerging in the 1980s and 1990s (Leipholz, 1980; Leipholz and Abdel-Rohman, 1986; Housner et al., 1997), the technique of structural control using active and passive control mechanisms has become main stream in structural engineering for tall and special buildings, e.g., base-isolated buildings (Hanson and Soong, 2001; Christopoulos and Filiatrault, 2006; Takewaki, 2009; Lagaros et al., 2012; Domenico et al., 2019). For civil and building structures, passive control plays a central role. This is because of increased demand for taller buildings and the introduction of new construction materials, accelerating the development of new techniques in the field of passive structural control (for example, Takewaki, 1997; Garcia, 2001; Lavan and Levy, 2005; Aydin et al., 2007; Silvestri and Trombetti, 2007; Whittle et al., 2012). However, the characteristics of near-fault and long-duration ground motions can have a significant effect on tall building response. The effects of near-fault ground motions and long-duration/long-period ground motions on tall and base-isolated buildings have been investigated in detail (Hall et al., 1995; Takewaki et al., 2011). The advantage of passive control systems is that they are robust to unexpected disturbances (Takewaki, 2007, 2009).

Various passive structural control systems exist for tall buildings (Takewaki, 2009; Lagaros et al., 2012; Fukumoto and Takewaki, 2015, 2017; Tani et al., 2017; Domenico et al., 2019). The most popular includes the interstory-type (Takewaki, 2009; Lagaros et al., 2012; Domenico et al., 2019) and soft first story-type (Tani et al., 2017). However, passive structural control systems, able to respond to both near-fault ground motions and long-duration/ long-period ground motions, are very limited (Murase et al., 2013; Fukumoto and Takewaki, 2015, 2017; Hayashi et al., 2018). Structural control via passive control devices is difficult for near-fault ground motions because the earthquake energy input is made during very short time interval. For near-fault ground motions, base-isolation system attaining an un-resonant state can be an effective technique. However, base-isolation system requires large site areas to prevent impact to retaining walls and increases construction cost. Moreover, base-isolation systems are vulnerable to resonant long-duration/long-period ground motions.

In this paper, a new structural control system is proposed for high-rise buildings. In this system, a sub core frame is located along a main building and a damping layer is provided between a stiff upper core frame suspended from the top of the main building and a stiff lower core frame (strong-back core frame) attached to the building foundation. Although, the concept is not the same, the strong-back core frame system was investigated in the past (Lai and Mahin, 2015; Palermo et al., 2018). The previous strong-back core frame system aimed at avoiding the plastic deformation concentrations in a few stories by distributing the frame deformations to many stories. The large displacement of the top floor displacement of the main building is taken full advantage in the proposed control system. Transformation of the multi-degree-of-freedom (MDOF) model into the single-degree-of-freedom (SDOF) model enables a simplified but rather accurate response evaluation for pulse-type and long-duration earthquake ground motions which are represented by the double impulse and the multi impulse, respectively. While passive viscous dampers are effective for long-duration ground motions owing to the sufficient time for energy dissipation, they are not necessarily effective for near-fault ground motions. These properties are also investigated in the proposed passive control system. The results of the time history response analysis of buildings including this control system are presented for various recorded ground motions. Finally, the effectiveness of the proposed structural control system is discussed from the viewpoint of earthquake input energy in which the original energy transfer function plays a central role (Housner, 1959, 1975; Berg and Thomaides, 1960; Housner and Jennings, 1975; Zahrah and Hall, 1984; Uang and Bertero, 1990; Ordaz et al., 2003; Takewaki, 2004a,b).

PROPOSED PASSIVE CONTROL SYSTEM USING LARGE-STROKE VISCOUS DAMPERS THROUGH CONNECTION TO STRONG-BACK CORE FRAME

System Overview

Consider a passive control system using large-stroke viscous dampers connected to a strong-back core frame, as shown in **Figure 1A**. This control system is proposed to reduce the seismic response of high-rise buildings. It is assumed that the main building is used for an apartment house and the lower strong-back core frame is used for car parking. The upper strong-back core frame is used only for the stiffness element connecting the top of the main frame to the lower strong-back core frame. To enable the efficient use of passive dampers, a stiff core (strong-back core frame) is constructed and attached to the foundation. Another stiff core frame is hung from the top story stiff sub-assemblage of the main building. The height of the lower strong-back core frame is determined from the architectural user demand based on the number of parked cars. Because this lower strong-back core frame is made of a wall-type reinforced concrete structure with relatively small mass, the horizontal force demand is not significant. Since deformation, or story drift demand, is concentrated in the connecting story, a large stroke is required for viscous dampers. Oil dampers of large stroke typically used usually for base-isolation systems are employed in this system.

Simplification of Controlled Building System Into MDOF Model

The building structure including the proposed control system can be represented by a linear MDOF system as shown in **Figure 1B**. The main building structure is a reinforced concrete structure of 35 stories. The subsystem consists of two subassemblages, i.e., the lower strong-back core frame and the upper strong-back core frame as shown in **Figure 1A**. Since a sub frame of large stiffness is required in the upper strong-back, braced systems were used for the upper strong-back. Large-stroke viscous dampers (oil dampers) were installed at the connection layer of the lower and upper strong-back core frames, as shown in **Figure 1A**. The total damping coefficient of those large-stroke viscous dampers is denoted by C_d. The fundamental natural period of the total system by complex eigenvalue analysis was 2.24(s). It is possible to decompose the overall system into three subassemblages with fixed boundaries to characterize the component properties, as shown in **Figure 1B**. This division was made for defining the stiffnessses of three parts. The masses of the main building and the strong-back core frames were determined from the data of a project building. The fundamental natural periods of these three subassemblages (main building, lower strong-back core frame and upper strong-back core frame) are 2.20, 1.06, 0.51(s). The structural damping is considered only in the main building and the damping ratio is 0.03. Eight oil dampers of 2500[kNs/m]-class are installed and the damping coefficients C_d=0 $\sim$ 5.0 $\times$ 10^7[Ns/m] are considered for parametric analysis. This model is treated as the original model. Because the stiffness of the upper and lower strong-back core frames affects the control performance of the proposed passive damper control system, another model with stiffer lower and upper strong-back core frames (10 times larger than the original) is used in later section for comparison (sections Seismic Response of Buildings Including Proposed Passive Control System and Its Simplified Evaluation Method and Earthquake Input Energy and Energy Transfer Function). The original model is described as "the Original Model" and the other model is called "the Stiffer Model."

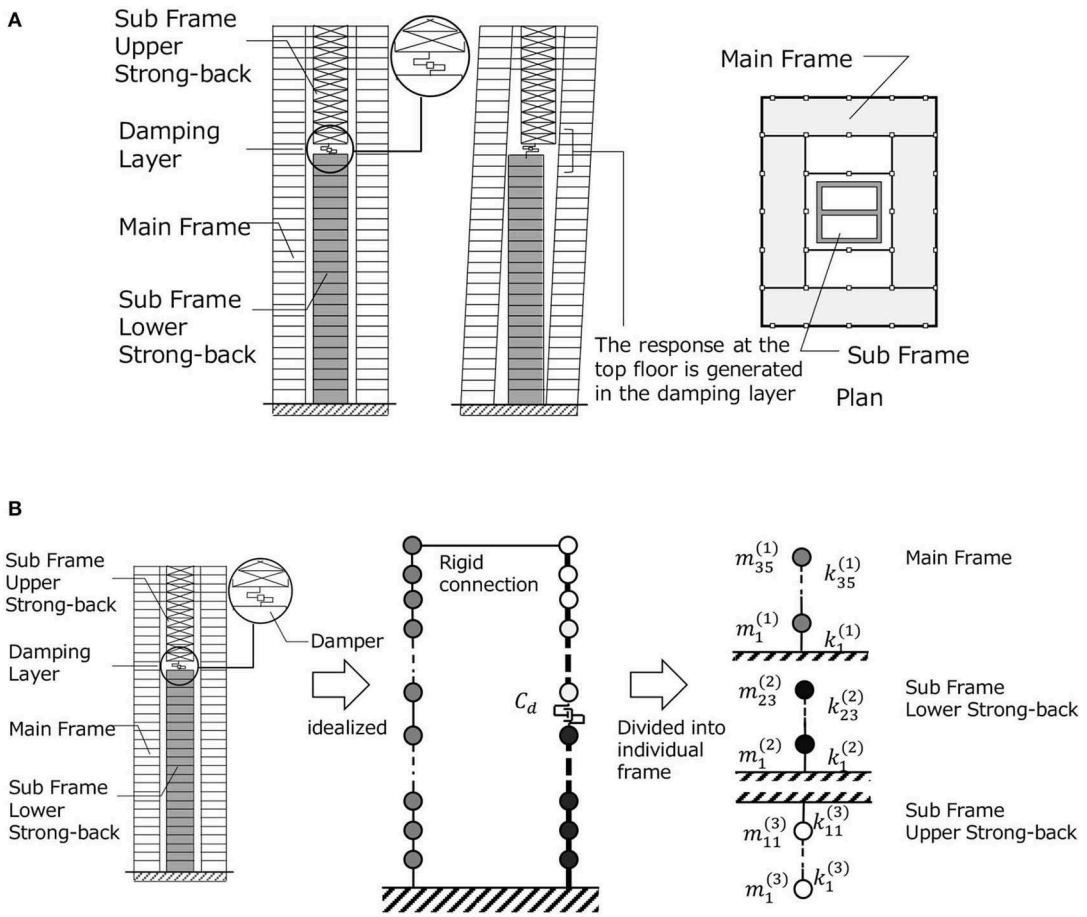

FIGURE 1 | Proposed control system using large-stroke viscous dampers through connection to strong-back core frame. **(A)** Overview of building with control system and **(B)** Simplification of controlled building system into MDOF model and decomposition into subassemblage models.

Eigenvalue Analysis of MDOF Model of Controlled Building System

Since the main building and the strong-back core frames have structural damping proportional to the stiffness and the passive viscous damper has an independent damping coefficient, the overall system has non-proportional damping. Complex eigenvalue analysis was performed for this model. **Figure 2A** shows the lowest-mode complex mode vector multiplied by the corresponding complex participation factor for three viscous damper damping coefficients for the Original Model. In upper figures, the absolute value, the real value and the imaginary values are plotted. In lower figures, the amplitudes and the phase angles of the lowest-mode complex mode vector at three points (top of the main frame, point just above the damper and point just below the damper) are shown. The distance between the point just above the damper and point just below the damper indicates the damper stroke. **Figure 2B** illustrates the lowest-mode complex eigenvector multiplied by the corresponding complex participation factor for three viscous damper damping coefficients for the Stiffer Model. It can be observed that the absolute value of the displacement of the subsystem becomes smaller as the damping coefficient becomes larger. In addition, the absolute value of the deformation of the connecting story becomes smaller after it becomes larger for some damper damping coefficient. This means that there exists an optimal damper damping coefficient that effectively reduces the deformation of the main building.

REDUCTION OF MDOF MODEL INTO SDOF MODEL USING CORRECTION FACTOR ON DAMPER DAMPING COEFFICIENT

Since the MDOF model requires complex computation for the idealized inputs (double impulse for near-fault ground motion and multi impulse for long-duration ground motion) and recorded ground motions, a simple SDOF model is introduced to clarify the intrinsic earthquake response properties of the buildings including the proposed control system. The response evaluation method using this SDOF model is called "a simplified evaluation method".

Let M_{main}, k_{main}, and c_{main} denote the total mass of the main building, stiffness of the main building and structural damping coefficient of the main building as an SDOF model.

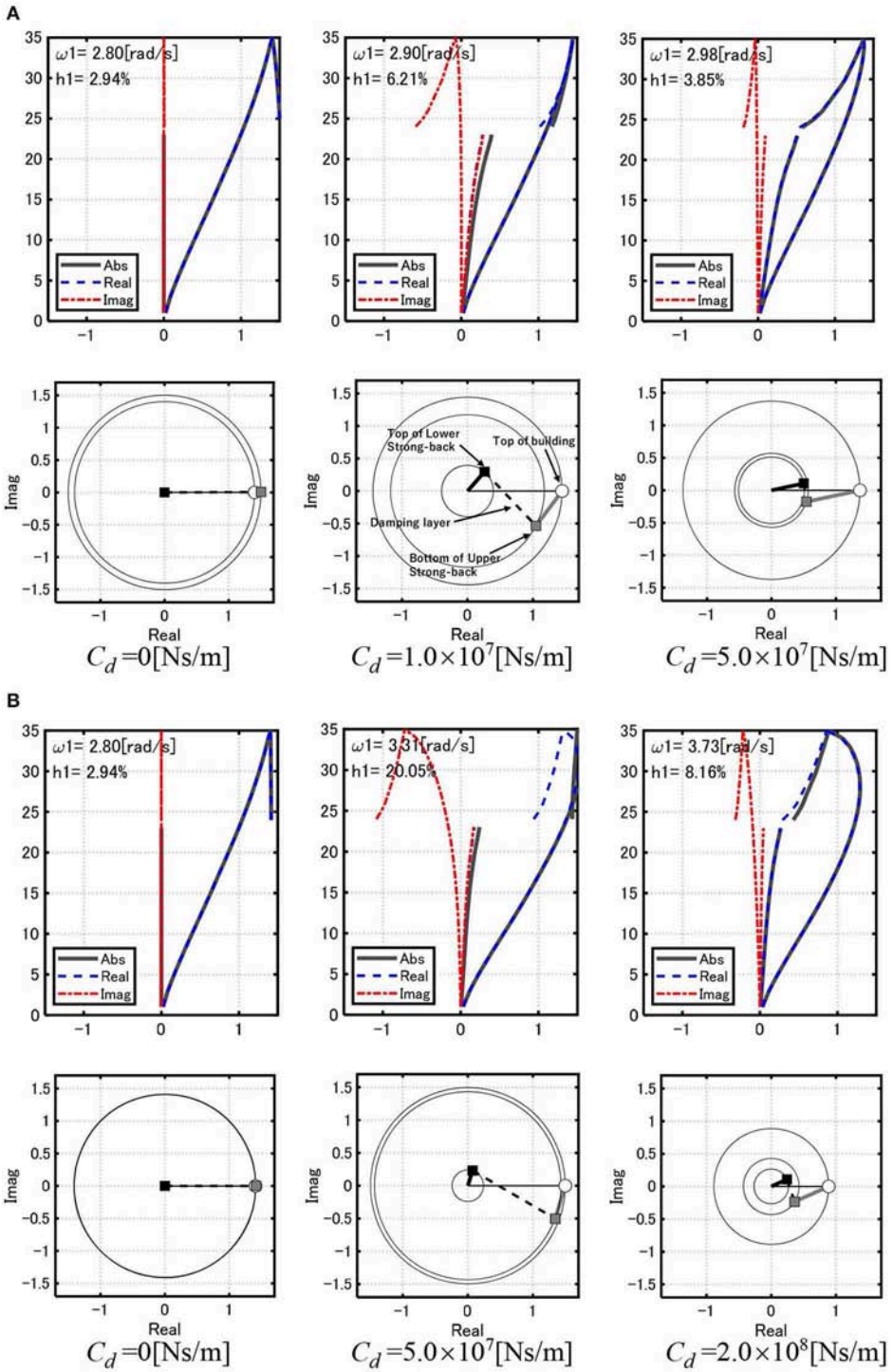

FIGURE 2 | Lowest-mode complex eigenvector multiplied by complex participation factor for three viscous damper damping coefficients. **(A)** Original Model and **(B)** Stiffer Model.

In addition, let M_{upper}, k_{upper}, k_{lower} denote the mass of the upper strong-back core frame, stiffness of the upper strong-back core frame, and stiffness of the lower strong-back core frame. The MDOF model is reduced to an equivalent SDOF model using the correction factor β on the damping coefficient C_d of dampers. This correction factor is introduced to account for various factors that could cause differences in damper behavior in the MDOF and SDOF models. A similar procedure was adopted

in the reference (Hayashi et al., 2018). Let $C_d^*(=\beta C_d)$ denote the corrected damping coefficient. At first, a transformation method from the MDOF model into an equivalent SDOF model with a Maxwell-type spring-dashpot model was introduced as shown in **Figure 3** with the help of the correction factor. The stiffness k_{sub} of the sub frame can be derived assuming that k_{upper} and k_{lower} are in series. Then, the Maxwell-type spring-dashpot model is reduced to a Kelvin-Voigt model as shown in **Figure 3**. It was confirmed that, since a large deformation occurs at the connection between the upper core frame and the lower core frame and the mass of the main frame is much larger than both core frames, it is reasonable to disregard the mass of the lower core frame and regard the lower core frame as a spring. **Table 1** presents the parameters of equivalent SDOF models of three subassemblages shown in **Figure 1B** for the Original Model.

In the transformation from the Maxwell-type spring-dashpot model to a Kelvin-Voigt model, the following relations on the frequency-dependent damping coefficient $c_e(\omega)$ and the frequency-dependent stiffness $k_e(\omega)$ are used.

$$c_e(\omega) = \frac{C_d^* k_{sub}^2}{\omega^2 C_d^* 2 + k_{sub}^2}, \quad k_e(\omega) = \frac{\omega^2 C_d^{*2} k_{sub}}{\omega^2 C_d^{*2} + k_{sub}^2} \qquad (1a,b)$$

$$\omega = \sqrt{(k_{main} + k_e)/(M_{main} + M_{upper})} \qquad (2)$$

Substitution of Equation (2) into Equation (1b) leads to the determination of k_e. Subsequent substitution of k_e into Equation (2) provides an approximate fundamental natural circular frequency ω_e for the total system. $k_e(\omega_e)$ and $c_e(\omega_e)$ are used subsequently for time-history response analysis.

Figure 4 shows the computation flow of the damping coefficient of the viscous damper in the equivalent SDOF model to ensure the validity of using the SDOF model in the response evaluation in relation to the MDOF model. For the appropriate comparison of damping performance with respect to varied damper damping coefficient between the SDOF and MDOF models, a damping ratio normalized by the peak value is introduced and denoted by h with an overbar. The difference between the lowest damping ratios of the SDOF model and the MDOF model is used to evaluate the correction factor β. In this process, the condition $\bar{h}'_{SDOF}(C_d^*) = \bar{h}'_1(C_d)$ is used. **Figure 5** relates the original damping coefficient C_d of the viscous damper installed at the connection of the upper and lower strong-back core frames in the MDOF model and the damping coefficient C_d^* of the corresponding viscous damper in the equivalent SDOF model for the Original Model and the Stiffer Model. The plot of the 'calculated C_d^*' was evaluated by using the equivalence of the normalized lowest damping ratios between the MDOF model and the SDOF model. The increase of damper damping coefficient does not always lead to the reduction of responses because excessively large dampers introduce often induces the addition of complex stiffness. In this case, the damping ratio exhibits a local maximum with respect to damper damping coefficient. The ratio of the damping ratio to such maximum value can be used to assess the performance of the dampers. The ratio of the damping ratio to such maximum value was introduced for the MDOF model and the SDOF model. The plot $C_d^* = \beta C_d$ was obtained by determining β at one value of C_d. The damping coefficients 8.92×10^6[Ns/m] and 3.39×10^7[Ns/m] were obtained from the MDOF and SDOF models for the Original Model such that the corresponding damping ratios attain peak values. Similarly, the damping coefficients 4.25×10^7[Ns/m] and 1.95×10^8[Ns/m] were obtained from the MDOF and SDOF models for the Stiffer Model. It can be observed that the proposed correction procedure is accurate enough. **Figure 5** also demonstrates that, if the correction factor β is not introduced, i.e., β =1, a large error occurs in the response prediction by means of the SDOF model. In other words, a prediction error in the damper damping

TABLE 1 | Parameters of equivalent SDOF models of three subassemblages for Original Model.

	Main building	Lower strong-back core frame	Upper strong-back core frame
Total mass [kg]	8.16×10^7	1.01×10^7	1.00×10^6
Natural circular frequency [rad/s]	2.86	5.91	12.4
Stiffness [N/m]	6.66×10^8	3.53×10^8	1.55×10^8
Damping coefficient [Ns/m]	1.40×10^7		

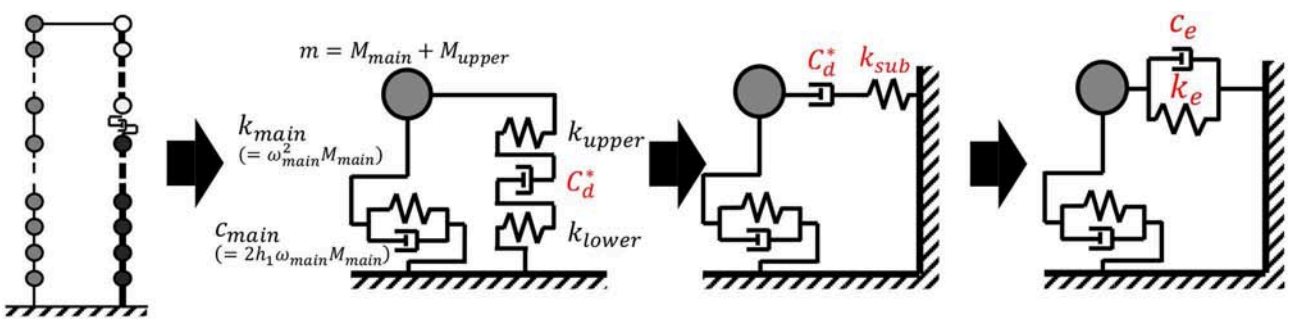

FIGURE 3 | Reduction of MDOF model into equivalent SDOF model.

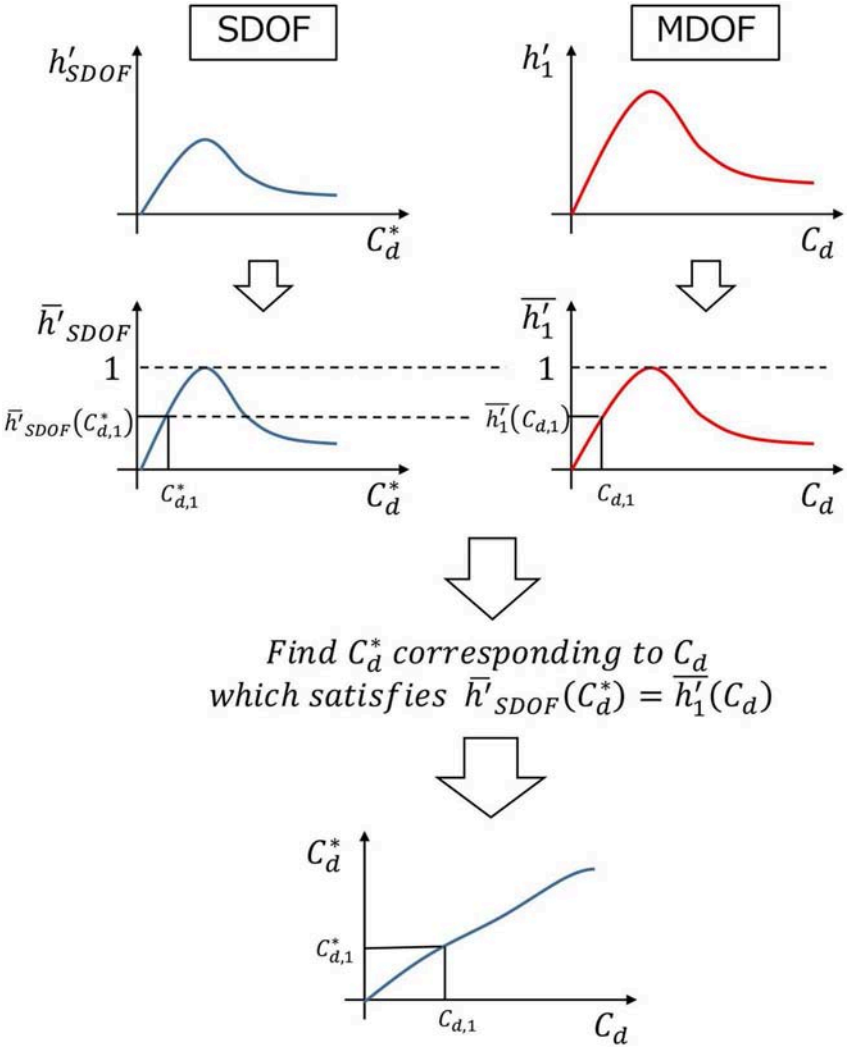

FIGURE 4 | Computation flow of damping coefficient of viscous damper in equivalent SDOF model.

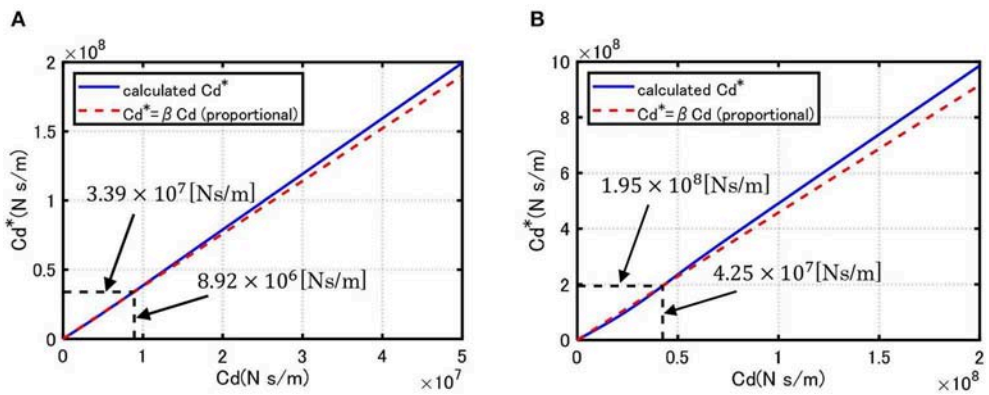

FIGURE 5 | Relation of original damping coefficient of viscous damper in MDOF model and damping coefficient of viscous damper in equivalent SDOF model. **(A)** Original Model ($\beta = 3.80$) and **(B)** Stiffer Model ($\beta = 4.58$).

coefficient, 3.80 and 4.58 times, leads to a large error in the response evaluation.

SEISMIC RESPONSE OF BUILDINGS INCLUDING PROPOSED PASSIVE CONTROL SYSTEM AND ITS SIMPLIFIED EVALUATION METHOD

In this section, the seismic response of buildings including the proposed control system under idealized ground motions and recorded ground motions is investigated through the comparison with that of the simplified SDOF model introduced in the previous section.

Kojima and Takewaki (2015a) demonstrated that one-cycle sinusoidal wave is a good representation of the main part of pulse-type near-fault ground motions. This double impulse is a simplified version of one-cycle sinusoidal input. When a SDOF is resonant to one-cycle sinusoidal input, the response to the double impulse provides a good estimate of the response to one-cycle sinusoidal input. However, when a MDOF is used, the correspondence between the responses to the double impulse and one-cycle sinusoidal input is not guaranteed, even if both inputs are resonant to the fundamental mode of the MDOF. For this reason, the comparison of the responses of the MDOF under the double impulse and one-cycle sinusoidal input is shown here.

Response of Buildings Including Proposed Control System Subjected to Double Impulse and Its Simplified Evaluation Method

Consider the seismic response of buildings including the proposed passive control system and its simplified evaluation method. As a representative of near-fault ground motions, the double impulse resonant to the building is introduced (Kojima and Takewaki, 2015a). The acceleration input of the double impulse can be expressed by

$$\ddot{u}_g^{DI}(t) = V_I\delta(t) - V_I\delta(t-t_0) \tag{3}$$

where $\delta(t)$ is the Dirac's delta function, V_I is the initial input velocity and t_0 is the time interval of two impulses. The corresponding one-cycle sine wave can be described by

$$\ddot{u}_g^{1SW}(t) = 0.5\omega_p V_{p1}\sin\left(\omega_p t\right)\ \ \left(0 \le t \le {T_1}'\right) \tag{4}$$

This one-cycle sine wave is introduced to ensure the validity of the double impulse in connection to actual near-fault ground motions. Some actual near-fault ground motions include an influential pulse-type motion which can be represented by one-cycle sine wave (see Kojima and Takewaki, 2016).

In Equation (4), $\omega_p = \pi/t_0$ is the input circular frequency and ${T_1}' = 2t_0$ is the damped fundamental natural period of the building. V_{p1} is specified as $V_{p1} = 1.2222V_I$ to guarantee the equivalence of the Fourier amplitudes of the double impulse and the one-cycle sine wave even at the first peak (Kojima et al., 2017). Let ${\omega_e}'$ and h_e denote the damped natural circular frequency and the damping ratio of the SDOF model. Since the response after the first impulse is a free vibration with zero initial displacement and initial velocity$=-V_I$, the displacement of the SDOF model after the first impulse can be expressed by

$$u_e(t) = -\frac{V_I}{{\omega_e}'}e^{-h_e\omega_e t}\sin{\omega_e}' t \tag{5}$$

The displacement of the SDOF model is equal to the sum of the damper deformation u_d and the deformation u_{sub} of the lower and upper cores:

$$u_d + u_{sub} = u_e \tag{6a}$$

Since the damper and the lower and upper core frames are in series, the force equivalence can be expressed by

$$\beta C_d\dot{u}_d = k_{sub}u_{sub} = c_e\dot{u}_e + k_e u_e \tag{6b}$$

From Equation (5), (6a, b), the damper deformation can be obtained from

$$\begin{aligned} u_d(t) &= \left(1-\frac{k_e}{k_{sub}}\right)u_e(t) - \frac{c_e}{k_{sub}}\dot{u}_e(t) \\ &= -\frac{V_I}{{\omega_e}'}e^{-h_e\omega_e t}\left\{\left(1-\frac{k_e}{k_{sub}}+\frac{h_e\omega_e c_e}{k_{sub}}\right)\sin{\omega_e}' t \right. \\ &\left. +\ \frac{{\omega_e}' c_e}{k_{sub}}\cos{\omega_e}' t\right\} \end{aligned} \tag{7}$$

The maximum displacement is obtained at time: $t_1 = \arctan(\sqrt{1-{h_e}^2}/h_e)/{\omega_e}'$ from $\dot{u}_e(t_1) = 0$ (see **Figure 6A**). The time t_2 of the maximum deformation of the damper can be derived by substituting the condition $\dot{u}_d(t_2) = 0$ into Equation (6):

$$u_d(t_2) = u_e(t_2) \tag{8a}$$

$$c_e\dot{u}_e(t_2) + k_e u_e(t_2) = 0 \tag{8b}$$

as

$$t_2 = \frac{1}{{\omega_e}'}\arctan\left(\frac{{\omega_e}' c_e}{h_e\omega_e c_e - k_e}\right) \tag{9}$$

In summary, the maximum displacement of the mass of the SDOF model and the maximum deformation of the damper can be described by $u_e(t_1)$ and $u_d(t_2) = u_e(t_2)$, respectively. Consider a critical excitation problem for maximizing the response after the second impulse where the velocity input amplitude V_I is fixed and the interval t_0 between two impulses is varied. Since the critical input of the second impulse is taken into account, the displacement of the mass of the SDOF model just before the beginning of the second impulse is 0 and its velocity is $V_I\exp(-\pi h_e\sqrt{1-{h_e}^2})$. Therefore, the vibration after the input of the second impulse corresponds to the free vibration from the initial displacement, $=0$, and the initial velocity, $=V_I\{1+\exp(-\pi h_e\sqrt{1-{h_e}^2})\}$. As a result, the maximum displacement

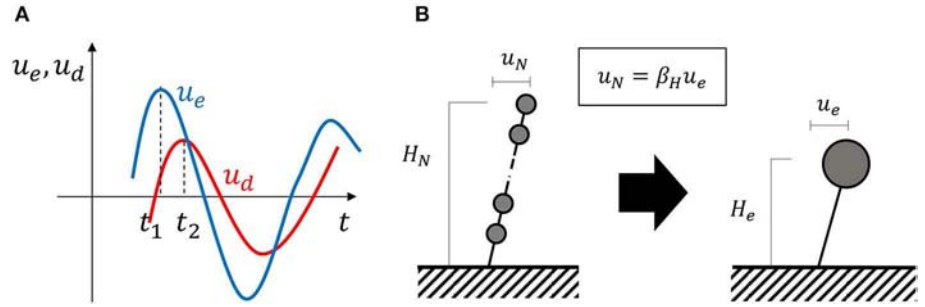

FIGURE 6 | Time-history responses and height correction in SDOF transformation. **(A)** Times at maximum displacements and **(B)** Equivalent height in equivalent SDOF model.

of the mass of the SDOF model and the maximum deformation of the damper can be derived in terms of the damper damping coefficient C_d.

$$u_e^{Max}(C_d) = \frac{V_I}{\omega_e'}\left\{1 + \exp\left(-\frac{h_e\pi}{\sqrt{1-h_e{}^2}}\right)\right\} e^{-h_e\omega_e t_1} \sin\omega_e' t_1 \tag{10a}$$

$$u_d^{Max}(C_d) = \frac{V_I}{\omega_e'}\left\{1 + \exp\left(-\frac{h_e\pi}{\sqrt{1-h_e{}^2}}\right)\right\} e^{-h_e\omega_e t_2} \sin\omega_e' t_2 \tag{10b}$$

Since the displacement of the SDOF model mass is different from the top displacement of the MDOF model (see **Figure 6B**), the maximum top displacement of the MDOF model and the maximum damper deformation can be expressed in terms of the height ratio $\beta_H = H_N/H_e$ (H_N: height of MDOF model, H_e: height of equivalent SDOF model).

Maximum top displacement of MDOF model :

$$\beta_H u^{Max}(C_d, k_{upper}, k_{lower}) \tag{11a}$$

Maximum damper deformation : $\beta_H u_d^{Max}(C_d, k_{upper}, k_{lower})$ (11b)

Figure 7 compares the maximum displacements from the closed-form expression for the SDOF model under the double impulse ($V_I = 0.10\ [m/s]$), the time-history response analysis for the MDOF model under the double impulse and the time-history response analysis for the MDOF model under the corresponding one-cycle sine wave. Two models were considered: the Original Model and the Stiffer Model. It can be observed that the response of the MDOF model under the double impulse approximates the response of the MDOF model under the corresponding one-cycle sine wave. The closed-form expression for the SDOF model underestimates the response of the MDOF model slightly. Although the displacement response reduction effect in the top displacement from the model without the damper is not remarkable in the Original Model, it is remarkable in the Stiffer Model.

Response of Buildings Including Proposed Control System Subjected to Multi Impulse and Its Simplified Evaluation Method

While the transient response was treated for the double impulse, the steady-state response is dealt with for the multi-impulse which can be used to approximate long-period, long-duration ground motion.

Consider the multi impulse expressed by

$$\ddot{u}_g^{MI}(t) = V_I\delta(t) - V_I\delta(t-t_0) + V_I\delta(t-2t_0) - \cdots \tag{12}$$

This input was introduced by Kojima and Takewaki (2015b) for approximating long-duration sinusoidal input (Takewaki et al., 2011):

$$\ddot{u}_g^{MSW}(t) = 0.5\omega_p V_{p2}\sin(\omega_p t) \quad (0 \le t \le 10T_1') \tag{13}$$

When we consider the resonant input (the impulse is input at the zero displacement), the vibrations can be described by free vibration of the initial displacement, =0, and the initial velocity:

$$\begin{aligned} V_0 &= V_I(-1)^N \sum_{i=0}^{N-1}\left\{\exp\left(-h_e\pi/\sqrt{1-h_e^2}\right)\right\}^i \\ &= V_I(-1)^N \frac{1-\left\{\exp\left(-h_e\pi/\sqrt{1-h_e^2}\right)\right\}^N}{1-\exp\left(-h_e\pi/\sqrt{1-h_e^2}\right)} \end{aligned} \tag{14a}$$

Note, when the input cycle N becomes infinity, the initial velocity at later cycles converges to

$$V_0 = \pm V_I \frac{1}{1-\exp\left(-h_e\pi/\sqrt{1-h_e^2}\right)} \tag{14b}$$

The maximum displacement of the equivalent SDOF model can be obtained as

$$u_e^{Max}(C_d) = \frac{V_I}{\omega_e'}\frac{1-\left\{\exp\left(-h_e\pi\sqrt{1-h_e^2}\right)\right\}^N}{1-\exp\left(-h_e\pi\sqrt{1-h_e^2}\right)} e^{-h_e\omega_e t_1}\sin\omega_e' t_1 \tag{15a}$$

The maximum deformation of the damper is given by

$$u_d^{Max}(C_d) = \frac{V_I}{\omega_e'} \frac{1 - \left\{\exp\left(-h_e\pi/\sqrt{1-h_e^2}\right)\right\}^N}{1 - \exp\left(-h_e\pi/\sqrt{1-h_e^2}\right)} e^{-h_e\omega_e t_2} \sin\omega_e' t_2 \quad (15b)$$

Similar to the input of the double impulse, the maximum top displacement of the MDOF model and the maximum damper deformation under the multi-impulse input can be expressed in terms of the height ratio $\beta_H = H_N/H_e$.

$$\text{Maximum top} - \text{story displacement} : \beta_H u_e^{Max}(C_d, k_{upper}, k_{lower}, N) \quad (16a)$$

$$\text{Maximum damper deformation} : \beta_H u_d^{Max}(C_d, k_{upper}, k_{lower}, N) \quad (16b)$$

Figure 8 compares the maximum displacements from the closed-form expression for the SDOF model under the multi impulse, time-history response analysis for the MDOF model under the multi impulse, and time-history response analysis for the MDOF model under a 10-cycle sine wave (N=20). As in the case under the double impulse, the Original Model and the Stiffer Model were considered. The maximum response of the MDOF model under the multi impulse approximates that of the MDOF model under the corresponding 10-cycle sine wave. The closed-form expression using the SDOF model slightly underestimates the response of the MDOF model. The response reduction effect in the top displacement from the model without damper is significant even in the Original Model compared to

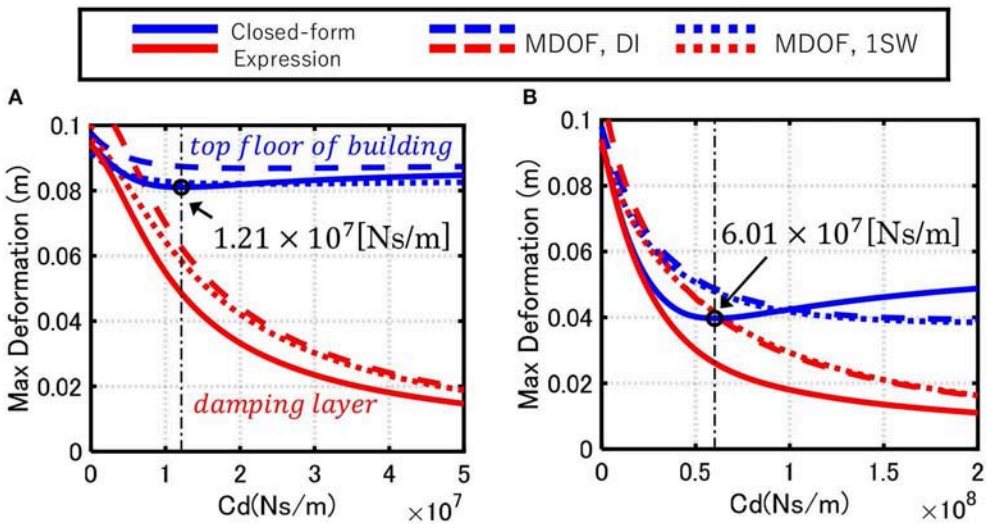

FIGURE 7 | Comparison of maximum displacements among closed-form expression for SDOF model under double impulse, time-history response analysis for MDOF model under double impulse and time-history response analysis for MDOF model under one-cycle sine wave. **(A)** Original Model and **(B)** Stiffer Model.

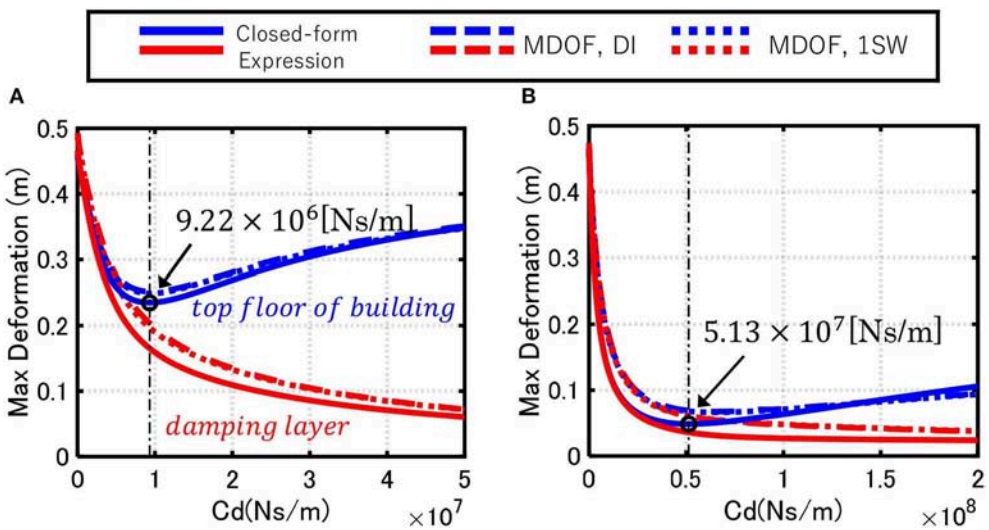

FIGURE 8 | Comparison of maximum displacements among closed-form expression for SDOF model under multi impulse, time-history response analysis for MDOF model under multi impulse and time-history response analysis for MDOF model under 10-cycle sine wave. **(A)** Original Model and **(B)** Stiffer Model.

the input of the double impulse. This characteristic is more significant in the Stiffer Model. An optimal damper damping coefficient exist in both the Original Model and the Stiffer Model. Note, the optimal damper damping coefficient can be obtained by using the SDOF model described in the next section.

Response of Buildings Including Proposed Control System Subjected to Recorded Ground Motions and Its Simplified Evaluation Method

The response characteristics of the building with the proposed control system under recorded ground motions are investigated in this section for various damper damping coefficient.

Table 2 shows the employed recorded ground motions. The corresponding velocity response spectra are shown in **Figure 9**.

Figure 10A presents the simplified evaluation of the maximum top displacement and the maximum damper deformation for the Original Model. The maximum top-story displacement and the maximum damper deformation are plotted with respect to the damper damping coefficient. **Figure 10B** indicates the corresponding evaluation for the Stiffer Model. While a slight difference exists in some ground motions, the proposed equivalent SDOF model provides a good approximate of the response of the MDOF model. Furthermore, the optimal damper damping coefficient obtained for the multi impulse (**Figure 8**) minimizes the top displacement of the main building. This phenomenon can be seen clearly under the input of OS1 (long-period, long-duration ground motion).

Figure 11A shows the maximum interstory drift angle for various damper damping coefficients for the Original Model and **Figure 11B** illustrates the corresponding one for the Stiffer Model. It can be seen that a large damper deformation is observed in the Stiffer Model. This means that the increase of stiffness of the strong-back core frame enhances the effectiveness of dampers. Furthermore, the optimal damper damping coefficient obtained for the multi impulse (**Figure 8**) reduces the maximum interstory drift angle of the main building most effectively. This phenomenon is significant for the input of OS1 (long-period, long-duration ground motion).

For the pulse-type ground motions (JMA Kobe NS, Rinaldi Sta. FN), the interstory drifts in the lower to middle stories are constant independent of the damper damping coefficients. The response reduction rates of the interstory drifts in the upper stories from the response of the model without damper are affected by the damper damping coefficients. In addition, such response reduction rates do not change much for the model with dampers larger than the optimal value. On the other hand, for the long-period, long-duration ground motion (OS1), the interstory drifts in the lower to middle stories are large and the response reduction rates of those are affected by damper quantities. The reduction rate is the largest for the optimal damper damping coefficient.

TABLE 2 | Acceleration amplitude of input recorded ground motions.

	Input ground motion	Acceleration amplitude (cm/s2)	Duration (s)
(a)	El Centro 1940 NS	341.7	53.74
(b)	Taft 1952 EW	175.9	54.38
(c)	Hachinohe 1968 NS	229.7	50.98
(d)	JMA Kobe NS	270.3	70.00
(e)	Rinaldi Sta. 1994 FN	825.5	14.965
(f)	OS1*	267.1	655.36

**Introduced by Japanese Governmental Agency for considering the long-duration/long-period ground motion which is predicted during the next Nankai-Trough earthquake.*

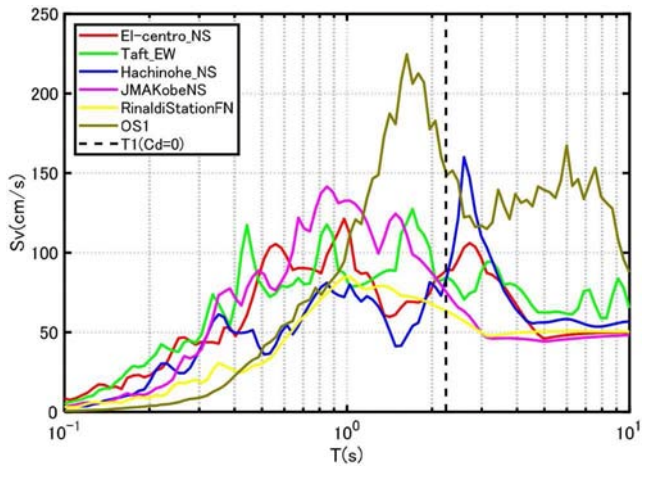

FIGURE 9 | Velocity response spectra of input recorded ground motions.

EARTHQUAKE INPUT ENERGY AND ENERGY TRANSFER FUNCTION

The earthquake input energy is an important measure for evaluating the seismic performance of structures (Housner, 1959; Uang and Bertero, 1990; Takewaki, 2004a,b). The earthquake input energy to an elastic structure can be expressed in the frequency domain (Ordaz et al., 2003; Takewaki, 2004a,b). When the Fourier transform of the ground acceleration $\ddot{u}_g(t)$ is denoted by $\ddot{U}_g(\omega)$, the total input energy to the MDOF model can be expressed by

$$E_I^{MDOF} = \int_0^\infty F^{MDOF}(\omega)\left|\ddot{U}_g(\omega)\right|^2 d\omega \tag{17}$$

where $F^{MDOF}(\omega)$ is the energy transfer function defined by

$$F^{MDOF}(\omega) = \mathrm{Re}\left[-\frac{i\omega}{\pi}\boldsymbol{H}_D^T(\omega)\mathbf{M1}\right] \tag{18}$$

In Equation (18), $\boldsymbol{H}_D(\omega)$, **M1** denote the displacement transfer function vector of the MDOF model, the mass matrix of the MDOF model, and the influence vector of 1 s, respectively. The energy dissipated by the dampers can be expressed by

$$E_D^{MDOF} = \int_0^\infty F_D^{MDOF}(\omega)\left|\ddot{U}_g(\omega)\right|^2 d\omega \tag{19}$$

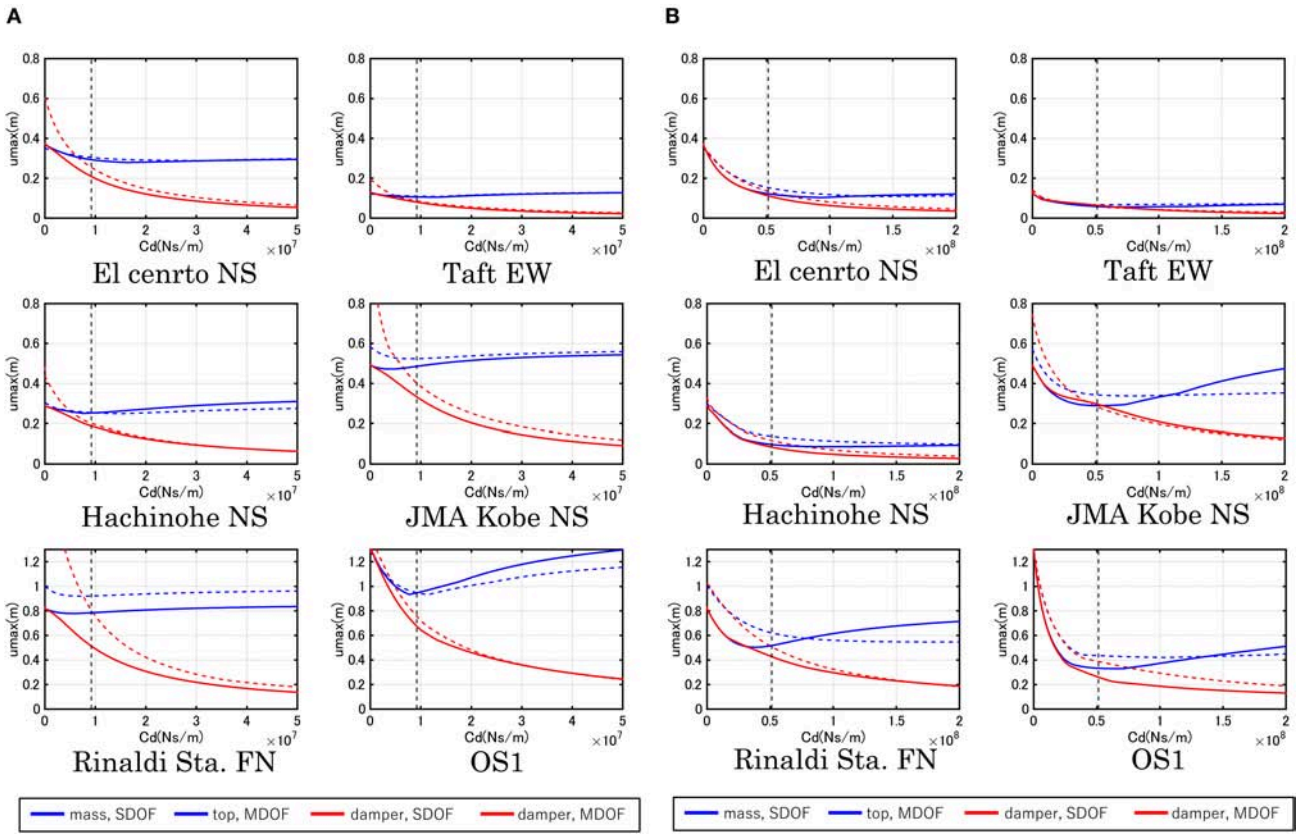

FIGURE 10 | Simplified evaluation of maximum top displacement and maximum damper deformation. **(A)** Original Model and **(B)** Stiffer Model.

where $F_D^{MDOF}(\omega)$ is the energy transfer function for dampers defined by

$$F_D^{MDOF}(\omega) = \mathrm{Re}\left[\frac{\omega^2 C_d}{\pi}\left|H_D^{Damper}(\omega)\right|^2\right] \tag{20}$$

Figure 12 shows the comparison of $F^{MDOF}(\omega)$ (total system) and $F_D^{MDOF}(\omega)$ (damper system) for the damper damping coefficient $C_d = 1.0 \times 10^7$[Ns/m]. Since the areas of $F^{MDOF}(\omega)$ and $F_D^{MDOF}(\omega)$ represent the total input energy and the damper consumption energy under the white noise-like input, the relation of the areas of $F^{MDOF}(\omega)$ and $F_D^{MDOF}(\omega)$ indicates the energy dissipation performance of the dampers. The area of the energy transfer function is meaningful for the random input and the maximum value of the energy transfer function is important for the long-duration sine wave because the Fourier spectrum of the long-duration sine wave has a sharp peak and the maximum value of the energy transfer function correlates with such a peak. Properties for the area and the maximum value of the energy transfer function for increasing damper quantities are disclosed below.

The total input energy to the equivalent SDOF model is:

$$E_I^{SDOF} = \int_0^\infty F^{SDOF}(\omega)\left|\ddot{U}_g(\omega)\right|^2 d\omega \tag{21}$$

where $F^{SDOF}(\omega)$ is the energy transfer function for the SDOF model defined by

$$F^{SDOF}(\omega) = \mathrm{Re}\left[-\frac{i\omega}{\pi}H_D^{SDOF}(\omega)(M_{main} + M_{upper})\right] \tag{22}$$

$H_D^{SDOF}(\omega)$ is derived by using the Maxwell model for the dashpot-spring model (frequency-dependent spring and damping coefficient in the Kelvin-Voigt model). The energy dissipated by the dampers in the SDOF model can be expressed by

$$E_D^{SDOF} = \int_0^\infty F_D^{SDOF}(\omega)\left|\ddot{U}_g(\omega)\right|^2 d\omega \tag{23}$$

where $F_D^{SDOF}(\omega)$ is the energy transfer function for the dampers in the SDOF model:

$$F_D^{SDOF}(\omega) = \frac{\omega^2 \beta C_d {k_{sub}}^2}{\pi(\omega^2\beta^2{C_d}^2 + {k_{sub}}^2)}\left|H_D^{SDOF}(\omega)\right|^2 \tag{24}$$

Figure 13A shows the area of the energy transfer function for the overall system and damper with respect to damper damping coefficient in the Original Model and the Stiffer Model. The area of the energy transfer function for the overall system is constant with respect to damper level regardless of the MDOF

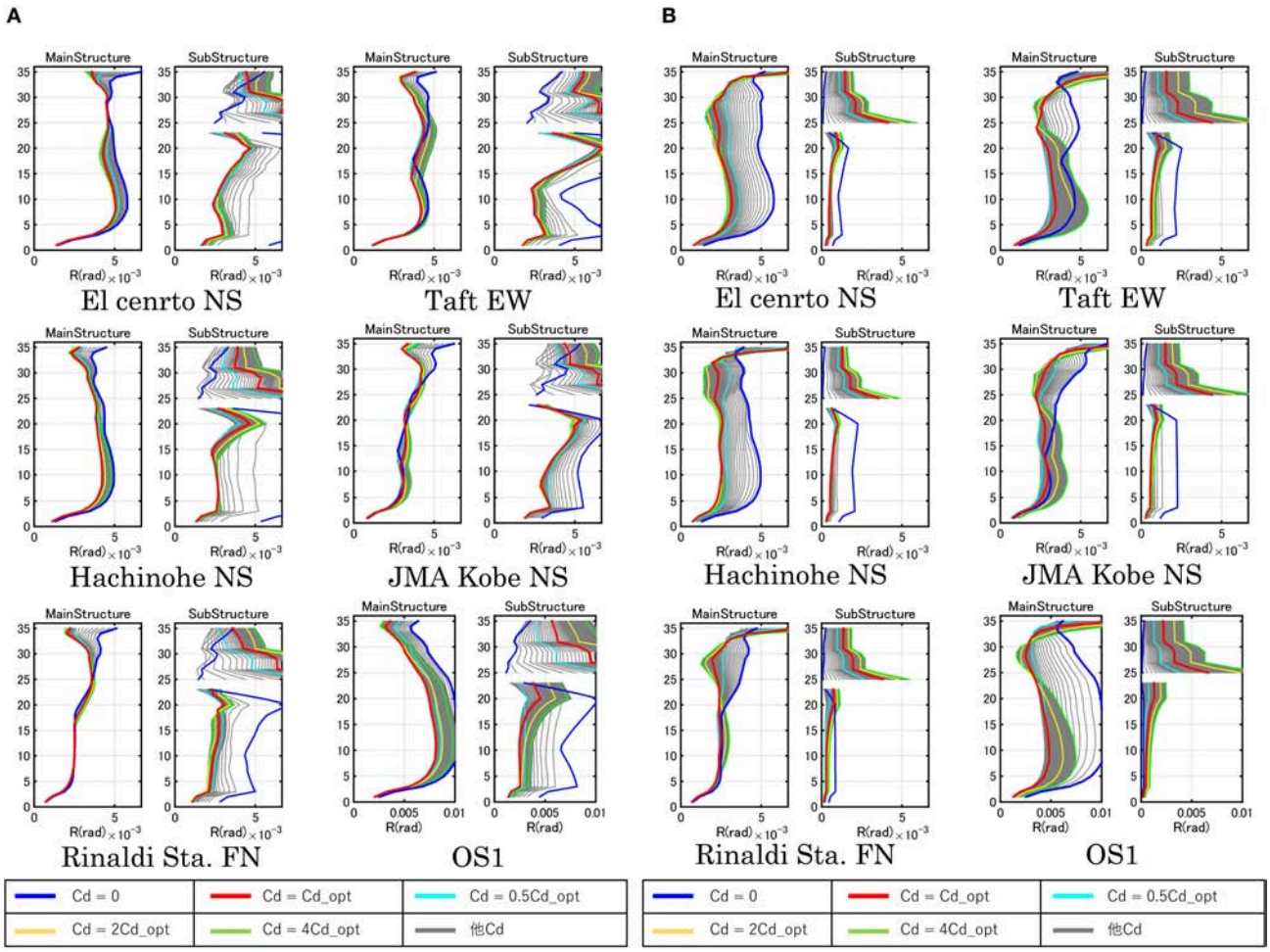

FIGURE 11 | Maximum interstory drift angle for various damper levels. **(A)** Original Model and **(B)** Stiffer Model.

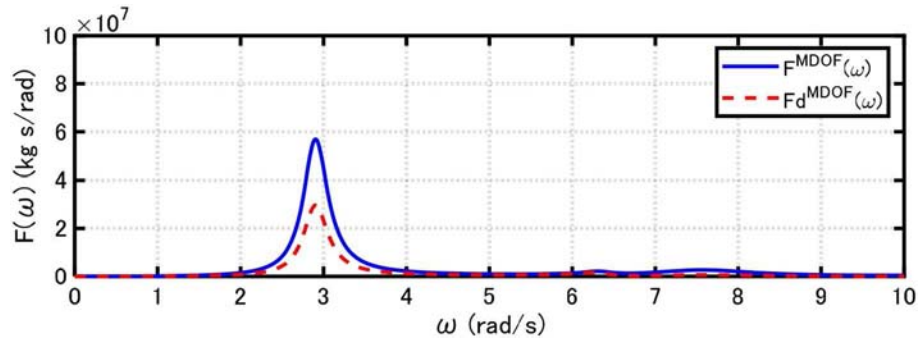

FIGURE 12 | Energy transfer functions for total system and viscous damper installed at connection point between upper and lower strong-back core frames.

model or the SDOF model (Takewaki, 2004a,b). The difference between the MDOF model and the SDOF model is due to the difference of mass (the SDOF model disregards the mass of the lower strong-back core frame). It can also be observed that, while the SDOF model underestimates the area of the energy transfer function of the total input energy in the MDOF model, it overestimates the area of the energy transfer function as an index for energy dissipation performance of the dampers in the MDOF model. There also exists an optimal damper damping coefficient maximizing the area of the energy transfer function for the damper, i.e., the most effective damper damping coefficient. Those damper quantities are shown in **Figure 13A**.

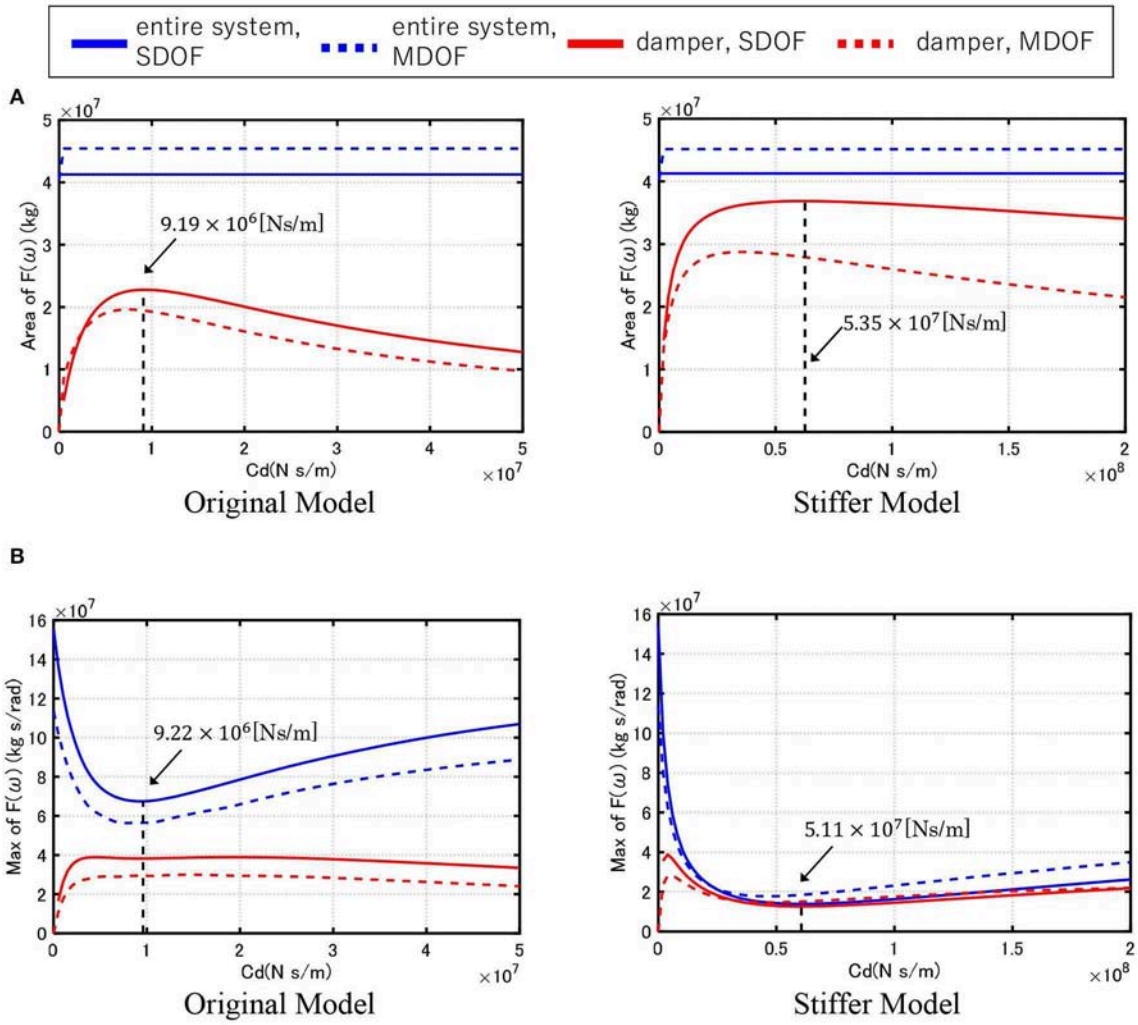

FIGURE 13 | Area and maximum value of energy transfer function with respect to damper level. **(A)** Area of energy transfer function and **(B)** Maximum value of energy transfer function.

These optimal damper damping coefficients correspond well to the optimal ones, shown in **Figure 8**, obtained for the minimum top displacement for the multi impulse.

Figure 13B presents the maximum value of the energy transfer function with respect to the damper damping coefficient in the Original Model and the Stiffer Model. The SDOF model overestimates the maximum value of the energy transfer function for the total input energy and the damper energy consumption in the MDOF model in the Original Model. As the stiffness of strong-back core frame becomes larger, the energy consumption in the dampers governs the main part of the input energy.

LIMITATIONS OF PROPOSED CONTROL SYSTEM AND SIMPLIFICATION METHOD

To investigate the limitation of the proposed control system, further numerical computation was conducted for various parameters. It was clarified that (i) the stiffness ratio of strong-back core frames to the main frame has to possess a large value, (ii) the foundation of the main frame and the lower strong-back core frame has to have sufficient stiffness, (iii) the proposed system is not effective enough for so-called long-period pulse-type motions of large velocity amplitude. As the stiffness ratio of the strong-back core frames to the main frame and the stiffness of the foundation become larger, the effectiveness of the proposed control system is enhanced. The long-period pulse-type motions of large velocity amplitude over 2.0[m/s] as recorded at Kumamoto (Japan) in 2016 are critical and could cause extremely large interstory drifts in the lower stories of the main frame. It was confirmed that the introduction of interstory-type passive control systems into lower stories of the main frame in addition to the proposed control system is effective for such critical ground motions. It was also clarified that the proposed simplification method does not work well in the cases mentioned above.

SUMMARIES AND CONCLUSIONS

A new damper deformation concentration-type structural control system has been proposed for pulse-type and long-duration earthquake ground motions. Summaries and conclusions are as follows:

(1) A transformation method from an MDOF model into an SDOF model with a Maxwell-type spring-dashpot model was proposed, including a correction factor for compensating the difference in the damper behavior of both models. Then, the Maxwell-type spring-dashpot model was reduced to a Kelvin-Voigt model for a fixed frequency. The proposed control system and simplification method have some limitations: the stiffness ratio of the strong-back core frames to the main frame has to possess a large value, the foundation of the main frame and the lower strong-back core frame has to have sufficient stiffness, and the proposed system is not effective enough for so-called long-period pulse-type motions of large velocity amplitude over 2.0 [m/s].
(2) A simplified seismic response evaluation method to estimate the maximum deformation of the dampers was proposed for the reduced SDOF model, which was subjected to a resonant double impulse to represent near-fault pulse-type ground motions and a resonant multi impulse to represent long-duration, long-period ground motions. The closed-form expression of the response under the critical double impulse and the critical multi impulse provides an accurate prediction of the response for the corresponding one-cycle and long-duration sine waves. By using this method, the maximum top-story displacement of the main building and the maximum deformation of dampers can be estimated.
(3) The optimal damper damping coefficient minimizing the response of the main building can be obtained by changing the damper damping coefficient in the simplified response evaluation method.
(4) The energy transfer functions characterizing the earthquake energy input were derived for the MDOF model and the SDOF model. The area and the maximum value of the energy transfer functions were employed to evaluate the effectiveness and efficiency of the dampers. The area and the maximum value of the energy transfer functions of the SDOF model can approximate those in the MDOF model. The optimal damper damping coefficients derived from the maximization of the area of the energy transfer function correspond well to the optimal ones obtained for the minimum top displacement for the multi impulse.
(5) The response reduction performance from the model without dampers can be enhanced greatly by increasing the stiffness of the lower strong-back core frame attached to the foundation and the upper strong-back core frame hung from the top story stiff sub-assemblage of the main building.

DATA AVAILABILITY STATEMENT

The datasets generated for this study are available on request to the corresponding author.

AUTHOR CONTRIBUTIONS

AK formulated the problem, conducted the computation, and wrote the paper. TM conducted the computation and discussed the results. IT supervised the research and wrote the paper.

FUNDING

Part of the present work is supported by the Grant-in-Aid for Scientific Research (KAKENHI) of Japan Society for the Promotion of Science (Nos. 17K18922, 18H01584) and Takenaka Co.

ACKNOWLEDGMENTS

This support was greatly appreciated. In addition, some ground motions used here were recorded by K-NET (National Research Institute for Earth Science and Disaster Resilience in Japan) and JMA (Japan Meteorological Agency).

REFERENCES

Aydin, E., Boduroglu, M. H., and Guney, D. (2007). Optimal damper distribution for seismic rehabilitation of planar building structures. *Eng. Struct.* 29, 176–185. doi: 10.1016/j.engstruct.2006.04.016

Berg, G. V., and Thomaides, T. T. (1960). "Energy consumption by structures in strong-motion earthquakes," in *Proceedings of 2nd World Conferences on Earthquake Engineering* (Tokyo; Kyoto), 681–696.

Christopoulos, C., Filiatrault, A. (2006). *Principle of Passive Supplemental Damping and Seismic Isolation*. Pavia: IUSS Press.

Domenico, D. D., Ricciardi, G., and Takewaki, I. (2019). Design strategies of viscous dampers for seismic protection of building structures: a review. *Soil Dyn. Earthquake. Eng.* 118, 144–165. doi: 10.1016/j.soildyn.2018.12.024

Fukumoto, Y., and Takewaki, I. (2015). Critical demand of earthquake input energy to connected building structures. *Earthq. Struct.* 9, 1133–1152. doi: 10.12989/eas.2015.9.6.1133

Fukumoto, Y., and Takewaki, I. (2017). Dual control high-rise building for robuster earthquake performance. *Front. Built Environ.* 3:12. doi: 10.3389/fbuil.2017.00012

Garcia, D. L. (2001). A simple method for the design of optimal damper configurations in MDOF structures. *Earthq. Spectra* 17, 387–398. doi: 10.1193/1.1586180

Hall, J. F., Heaton, T. H., Halling, M. W., and Wald, D. J. (1995). Near-source ground motion and its effects on flexible buildings. *Earthq. Spectra* 11, 569–605. doi: 10.1193/1.1585828

Hanson, R. D., and Soong, T. T. (2001). *Seismic Design With Supplemental Energy Dissipation Devices*. Oakland, CA: Earthquake Engineering Research Institute.

Hayashi, K., Fujita, K., Tsuji, M., and Takewaki, I. (2018). A simple response evaluation method for base-isolation building-connection hybrid structural system under long-period and long-duration ground motion. *Front. Built Environ.* 4:2. doi: 10.3389/fbuil.2018.00002

Housner, G. W. (1959). Behavior of structures during earthquakes. *J. Eng. Mech. Div. ASCE.* 85, 109–129.

Housner, G. W. (1975). "Measures of severity of earthquake ground shaking," in *Proceedings of the US National Conferences on Earthquake Engineering*," (Ann Arbor, MI), 25–33.

Housner, G. W., Bergman, L. A., Caughey, T. K., Chassiakos, A. G., Claus, R. O., Masri, S. F., et al. (1997). Structural control: past, present, and future. *J. Eng. Mech. ASCE.* 123, 897–971. doi: 10.1061/(ASCE)0733-9399(1997)123:9(897)

Housner, G. W., and Jennings, P. C. (1975). "The capacity of extreme earthquake motions to damage structures," in *Structural and Geotechnical Mechanics: A Volume Honoring,* eds N. M. Newmark, and W. J. Hall (Englewood Cliff, NJ: Prentice-Hall), 102–116.

Kojima, K., Saotome, Y., and Takewaki, I. (2017). Critical earthquake response of a SDOF elastic-perfectly plastic model with viscous damping under double impulse as a substitute of near-fault ground motion. *J. Struct. Construct. Eng.* 735, 643–652. doi: 10.1002/2475-8876.10019

Kojima, K., and Takewaki, I. (2015a). Critical earthquake response of elastic-plastic structures under near-fault ground motions (part 1: fling-step input), *Front. Built Environ.* 1:12. doi: 10.3389/fbuil.2015.00012

Kojima, K., and Takewaki, I. (2015b). Critical input and response of elastic-plastic structures under long-duration earthquake ground motions. *Front. Built Environ.* 1:1415. doi: 10.3389/fbuil.2015.00015

Kojima, K., and Takewaki, I. (2016). Closed-form critical earthquake response of elastic-plastic structures on compliant ground under near-fault ground motions. *Front. Built Environ.* 2:1. doi: 10.3389/fbuil.2015.00013

Lagaros, N. D., Plevris, V., and Mitropoulou, C. C. (2012). *Design Optimization of Active and Passive Structural Control Systems*. Hershey, PA: IGI Global. doi: 10.4018/978-1-4666-2029-2

Lai, J. W., and Mahin, S. A. (2015). Strongback system: a way to reduce damage concentration in steel-braced frames. *J. Struct. Eng. ASCE.* 141:04014223. doi: 10.1061/(ASCE)ST.1943-541X.0001198

Lavan, O., and Levy, R. (2005). Optimal design of supplemental viscous dampers for irregular shear-frames in the presence of yielding. *Earthq. Eng. Struct. Dyn.* 34, 889–907 doi: 10.1002/eqe.458

Leipholz, H. H. E. (1980). "Structural control," in *Proceedings of the International IUTAM Symposium on Structural Control, University of Waterloo* (New York, NY: North-Holland Publishing Company).

Leipholz, H. H. E., and Abdel-Rohman, M. (1986). *Control of Structures*. Dordrecht: Martinus Nijhoff Publishers. doi: 10.1007/978-94-009-4402-2

Murase, M., Tsuji, M., and Takewaki, I. (2013). Smart passive control of buildings with higher redundancy and robustness using base-isolation and inter-connection. *Earthq. Struct.* 4, 649–670. doi: 10.12989/eas.2013.4.6.649

Ordaz, M., Huerta, B., and Reinoso, E. (2003). Exact computation of input-energy spectra from fourier amplitude spectra. *Earthq. Eng. Struct. Dyn.* 32, 597–605. doi: 10.1002/eqe.240

Palermo, M., Laghi, V., Gasparini, G., and Trombetti, T. (2018). Coupled response of frame structures connected to a strongback. *J. Struct. Eng. ASCE*. 144:04018148. doi: 10.1061/(ASCE)ST.1943-541X.0002134

Silvestri, S., and Trombetti, T. (2007). Physical and numerical approaches for the optimal insertion of seismic viscous dampers in shear-type structures. *J. Earthquake Eng.* 11, 787–828. doi: 10.1080/13632460601034155

Takewaki, I. (1997). Optimal damper placement for minimum transfer functions. *Earthq. Eng. Struct. Dyn.* 26, 1113–1124. doi: 10.3389/fbuil.2019.00004

Takewaki, I. (2004a). Frequency domain modal analysis of earthquake input energy to highly damped passive control structures. *Earthquake Eng. Struct. Dyn.* 33, 575–590. doi: 10.1002/eqe.361

Takewaki, I. (2004b). Bound of earthquake input energy. *J. Struct. Eng. ASCE.* 130, 1289–1297. doi: 10.1061/(ASCE)0733-9445(2004)130:9(1289)

Takewaki, I., Murakami, S., Fujita, K., Yoshitomi, S., and Tsuji, M. (2011). The 2011 off the Pacific coast of Tohoku earthquake and response of high-rise buildings under long-period ground motions. *Soil Dyn. Earthq. Eng.* 31, 1511–1528. doi: 10.1016/j.soildyn.2011.06.001

Takewaki, I. (2007). *Critical Excitation Methods In Earthquake Engineering, 2nd Edn*. Amsterdam: Elsevier. doi: 10.1016/B978-008045309-5/50013-3

Takewaki, I. (2009). *Building Control With Passive Dampers: Optimal Performance-Based Design For Earthquakes*. Singapore: John Wiley and Sons. doi: 10.1002/9780470824931

Tani, T., Maseki, R., and Takewaki, I. (2017). Innovative seismic response controlled system with shear wall and concentrated dampers in lower stories. *Front. Built Environ.* 3:57. doi: 10.3389/fbuil.2017.00057

Uang, C. M., and Bertero, V. V. (1990). Evaluation of seismic energy in structures. *Earthquake Eng. Struct. Dyn.* 19, 77–90. doi: 10.1002/eqe.4290190108

Whittle, J. K., Williams, M. S., Karavasilis, T. L., and Blakeborough, A. (2012). A comparison of viscous damper placement methods for improving seismic building design. *J. Earthquake Eng.* 16, 540–560. doi: 10.1080/13632469.2011.653864

Zahrah, T. F., and Hall, W. J. (1984). Earthquake energy absorption in SDOF structures. *J. Struct. Eng. ASCE*. 110, 1757–1772. doi: 10.1061/(ASCE)0733-9445(1984)110:8(1757)

Conflict of Interest: TM was employed by the company Takenaka Corporation.

The remaining authors declare that the research was conducted in the absence of any commercial or financial relationships that could be construed as a potential conflict of interest.

The authors declare that this study received funding from Takenaka Corporation. The funder was not involved in the study design, collection, analysis, interpretation of data, the writing of this article or the decision to submit it for publication.

frontiers in Built Environment

ORIGINAL RESEARCH
published: 19 March 2020
doi: 10.3389/fbuil.2020.00025

A Design Method for Viscous Dampers Connecting Adjacent Structures

Enrico Tubaldi[1], Laura Gioiella[2], Fabrizio Scozzese[2], Laura Ragni[3] and Andrea Dall'Asta[2]*

[1] Department of Civil and Environmental Engineering, University of Strathclyde, Glasgow, United Kingdom, [2] School of Architecture and Design, University of Camerino, Ascoli Piceno, Italy, [3] Department of Civil and Building Engineering and Architecture, Polytechnic University of Marche, Ancona, Italy

This paper investigates the seismic design of fluid viscous dampers connecting adjacent structural systems. A simplified dampers design strategy is proposed, which relies on a linearized reduced order model of the coupled system. A stochastic linearization technique is adopted with the aim of extending the design method to non-linear viscous dampers. The effectiveness of the design method and of the coupling strategy are assessed via numerical analysis of two adjacent buildings with shear-type behavior connected by linear or non-linear viscous dampers and subjected to Gaussian stochastic base acceleration. Different dampers locations are analyzed. The accuracy of the reduced order model is assessed, by comparing the relevant response statistics to those provided by a refined multi degree of freedoms model. Finally, a parametric study is performed to assess the effectiveness of dissipative connection for different values of seismic intensity and dampers parameters (i.e., viscous coefficients and velocity exponents).

Keywords: non-linear viscous dampers, adjacent buildings, stochastic linearization, reduced order model, dampers design, dissipative coupling

OPEN ACCESS

Edited by:
Ehsan Noroozinejad Farsangi, Graduate University of Advanced Technology, Iran

Reviewed by:
Abbas Sivandi-Pour, Graduate University of Advanced Technology, Iran
Ersin Aydin, Nigde Ömer Halisdemir University, Turkey
Fadzli Mohamed Nazri, University of Science Malaysia, Malaysia

****Correspondence:***
Enrico Tubaldi
enrico.tubaldi@strath.ac.uk

Specialty section:
This article was submitted to Earthquake Engineering, a section of the journal Frontiers in Built Environment

Received: *13 December 2019*
Accepted: *19 February 2020*
Published: *19 March 2020*

Citation:
Tubaldi E, Gioiella L, Scozzese F, Ragni L and Dall'Asta A (2020) A Design Method for Viscous Dampers Connecting Adjacent Structures. Front. Built Environ. 6:25. doi: 10.3389/fbuil.2020.00025

INTRODUCTION

Many experimental and analytical studies have proven that the introduction of damping devices between adjacent buildings provides an efficient mean for improving the seismic performance of the two systems. The behavior of adjacent structures linked by rigid, active, or passive control devices (Soong and Spencer, 2002; Christopoulos and Filiatrault, 2006; Takewaki, 2009) has been object of study of many papers in the last decades (Xu et al., 1999; Ni et al., 2001; Kim et al., 2006; Cimellaro and Lopez-Garcia, 2007; Roh et al., 2011; Richardson and Walsh, 2012; Tubaldi et al., 2014; Tubaldi, 2015). These studies have shown that the interaction between two systems with different dynamic properties through the connecting devices allows to reduce the structural seismic responses in terms of displacements and accelerations with respect to the unconnected case. The dissipative coupling constitutes also an effective tool to mitigate the seismic pounding (Sorace and Terenzi, 2013; Abdeddaim et al., 2016; Karabork and Aydin, 2019) between adjacent buildings without sufficient seismic joint, by avoiding invasive retrofit interventions finalized to joint enlargement.

The dissipative coupling of adjacent structures also includes the case of existing structures connected to new external systems. This retrofit measure has been recently investigated in different studies (Gioiella et al., 2018a; Reggio et al., 2019), because it presents several advantages compared to other methods (e.g., dissipative braces inserted within the frames), thanks to the reduced

interferences with the existing frame and the low downtime associated with the installation of the retrofit measure. There can be different arrangements for the external protection system, which can be for example a new external reaction tower or an exoskeleton structure wrapping the building to be protected. The study reported in (Gioiella et al., 2018a), investigated the modal properties and the seismic response of an r.c. frame building coupled with an external pinned-rocking truss equipped with linear fluid viscous at its base and connected at the floor level with the building to protect. Also in (Impollonia and Palmeri, 2018) a similar system is investigated, but in this case, the external reaction towers have been equipped with non-linear devices. In (Gioiella et al., 2018b), a comparison was made in terms of efficiency between alternative external retrofitting systems, one consisting in a pinned-rocking truss with dampers at its base, and the other in a fixed base external structure with the dampers located at floor level. In (Reggio et al., 2019), the behavior of a primary structure protected by an external self-supporting exoskeleton system, rigidly connected to the inner frame is assessed.

A significant number of the studies reported above has focused on the definition of procedures or closed-form expressions for the design of the optimal damper properties of the connecting dampers. Many works have considered the simplified case of adjacent buildings modeled as single degree of freedom (SDOF) systems. In this context, Zhu and Iemura (2000) and Zhu and Xu (2005) derived analytical expressions for the optimal properties of respectively a Kelvin-type damper and a Maxwell-type connecting damper, under a white-noise ground excitation. The optimal properties have been evaluated by minimizing the averaged vibration energy of either the primary structure or the two adjacent structures. Bhaskararao and Jangid (2007) also derived closed-form expressions for the optimal linear viscous damper properties that minimize the systems' relative displacements and absolute accelerations under harmonic excitation, and the mean square responses under stationary white-noise random excitation. Hwang et al. (2007), based on complex modal analysis, proposed a closed-form expressions of the relation between the viscous constant of the linear viscous dampers and the damping factors of the adjacent connected SDOF systems. The optimal properties of hysteretic dampers were evaluated by Basili and De Angelis (2007a) by minimizing an energy performance index, i.e., the ratio of the maximum value of the energy dissipated in the device, to the corresponding maximum value of the input energy.

In general, different approaches can be followed to evaluate the optimal properties of the connecting system. Some authors (Zhang and Xu, 1999; Kim et al., 2006; Tubaldi et al., 2014), perform extensive parametric analyses, other (Basili and De Angelis, 2007a; Ok et al., 2008; Bigdeli et al., 2012) suggest optimization procedures, which are generally able to provide the optimal damper location as well. An alternative strategy could be that of looking only at the damping in correspondence of one or more vibration modes (Luco and De Barros, 1998), or reducing the model order, i.e., by transforming the multiple degree of freedom (MDOF) models into two simplified equivalent SDOF systems (Aida et al., 2001; Basili and De Angelis, 2007b; Zhu et al., 2010), and then defining the damper properties based on already available closed-form expressions or methodologies.

In this paper, the seismic response of adjacent buildings connected by energy dissipation devices is further investigated, with specific focus on the use of fluid viscous dampers (FVDs). The effectiveness for seismic protection purposes of such class of devices has been extensively analyzed in the past decades (Symans and Constantiou, 1998; Pekcan et al., 1999; Lin and Chopra, 2002; Christopoulos and Filiatrault, 2006; Takewaki, 2009), and specific issues have been also studied. These include the effect of the ground motion variability on the response of systems equipped with linear or non-linear viscous dampers (Tubaldi et al., 2015; Dall'Asta et al., 2016) and the influence of the variability of the damper properties, due to the device manufacturing process, on the seismic performance of the system (Lavan and Avishur, 2013; Dall'Asta et al., 2017; Scozzese et al., 2019).

Moreover, this study aims at developing a design strategy for fluid viscous dampers connecting adjacent buildings based on a linearized reduced order model. Starting from the knowledge of the dynamical properties of the unconnected buildings, the design method requires an assumption on the distribution of the dampers at the various floors. Once the amount of added damping necessary to protect one of the two frames is decided, the dimensions of FVDs are determined. A simplified expression for the design of the dampers, applicable in many situations, is also provided. Finally, a stochastic linearization technique is used to extend the design procedure to the case of non-linear dampers, which are diffused in design practice. In the last part of the paper, extensive analyses of various case studies are reported, in order to compare the results achieved by the MDOF systems and by the reduced order model, considering linear, and non-linear dampers, as well as different damper configurations.

PROBLEM FORMULATION

In this section, the formulation of the problem involving two adjacent MDOF structures coupled by fluid viscous dampers is presented in general terms, in section "Equation of Motion for MDOF Systems Connected by Non-Linear Viscous Dampers" with reference to non-linear devices and in section "MDOF Systems Connected by Linear FVDs and Reduced Order Model" for the case of linear ones. In this latter section, a reduced order model of the coupled systems is developed. Moreover, a simplified formula for estimating the added damping ratio is derived, which can be used for design purposes. Afterwards, in section "Non-Linear System and Linear Equivalence Based on Stochastic Response", an equivalence criterion is used to relate the properties of non-linear FVDs to linear ones, to be used along with the design approach proposed.

Equation of Motion for MDOF Systems Connected by Non-Linear Viscous Dampers

The equation of motion of two adjacent MDOF systems, A and B, coupled by viscous dampers (**Figure 1**), is:

$$\mathbf{M}\ddot{\mathbf{u}}(t) + \mathbf{C}\dot{\mathbf{u}}(t) + \mathbf{K}\mathbf{u}(t) + \mathbf{f}[\dot{\mathbf{u}}(t)] = -\mathbf{M}\mathbf{r}\ddot{u}_g(t) \quad (1)$$

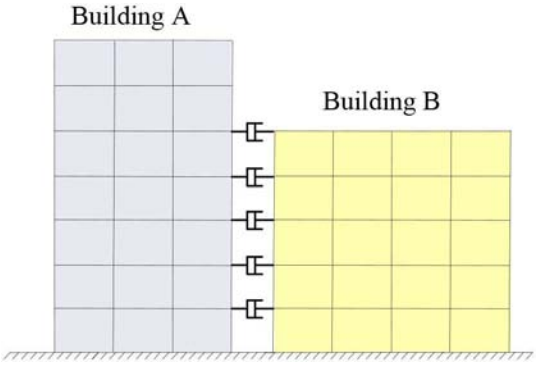

FIGURE 1 | Frame structures connected by means of fluid viscous dampers.

where $\mathbf{M}$, $\mathbf{C}$, and $\mathbf{K}$ are linear operators (i.e., matrices) describing the mass, damping and stiffness distribution in the two systems; $\mathbf{r}$ is the load distribution vector; $\ddot{u}_g(t)$ is a function describing the seismic input; $\mathbf{f}[\dot{\mathbf{u}}(t)]$ is the vector of forces due to coupling damper devices; a superposed dot denotes differentiation with respect to time. The vector $\mathbf{u}(t)$, describing the floor motion, can be split into two vectors collecting the displacements at floor level of structural system A and structural system B, i.e., $\mathbf{u} = \begin{bmatrix} \mathbf{u}_{\mathrm{A}(m)} \\ \mathbf{u}_{\mathrm{B}(n)} \end{bmatrix}$. Accordingly, the linear operators can be split into: $\mathbf{M} = \begin{bmatrix} \mathbf{M}_{\mathrm{A}(mxm)} & \mathbf{0}_{(mxn)} \\ \mathbf{0}_{(nxm)} & \mathbf{M}_{\mathrm{B}(nxn)} \end{bmatrix}$; $\mathbf{K} = \begin{bmatrix} \mathbf{K}_{\mathrm{A}(mxm)} & \mathbf{0}_{(mxn)} \\ \mathbf{0}_{(nxm)} & \mathbf{K}_{\mathrm{B}(nxn)} \end{bmatrix}$; $\mathbf{C} = \begin{bmatrix} \mathbf{C}_{\mathrm{A}(mxm)} & \mathbf{0}_{(mxn)} \\ \mathbf{0}_{(nxm)} & \mathbf{C}_{\mathrm{B}(nxn)} \end{bmatrix}$.

The vector $\mathbf{f}[\dot{\mathbf{u}}(t)]$ has the following expression:

$$\mathbf{f}[\dot{\mathbf{u}}(t)] = \begin{bmatrix} \mathbf{f}_d[\dot{\mathbf{u}}(t)]_{(n)} \\ \mathbf{0}_{(m-n)} \\ -\mathbf{f}_d[\dot{\mathbf{u}}(t)]_{(n)} \end{bmatrix} \tag{2}$$

where $\mathbf{f}_d[\dot{\mathbf{u}}(t)] = \mathbf{f}_d(t)$ is a n-dimension vector, whose j-th component is given by:

$$\begin{aligned} \mathbf{f}_{dj}[\dot{\mathbf{u}}(t)] &= c_{d,j}\left|\dot{\mathbf{u}}_j(t) - \dot{\mathbf{u}}_{j+m}(t)\right|^{\alpha} \mathrm{sgn}\left[\dot{\mathbf{u}}_j(t) - \dot{\mathbf{u}}_{j+m}(t)\right] \\ j &= 1:n \end{aligned} \tag{3}$$

where $c_{d,j}$ represents the viscous constant of the j-th damper with behavior described by the value of the constant α. When $\alpha = 1$ the behavior of the dampers is linear, instead when $\alpha < 1$ the behavior is non-linear.

MDOF Systems Connected by Linear FVDs and Reduced Order Model

In the case of linear dampers, Equation (1) can be rewritten as:

$$\mathbf{M}\ddot{\mathbf{u}}(t) + (\mathbf{C} + \mathbf{C}_d)\dot{\mathbf{u}}(t) + \mathbf{K}\mathbf{u}(t) = -\mathbf{M}\mathbf{r}\ddot{u}_g(t) \tag{4}$$

in which matrix $\mathbf{C}_d$ describes the properties and the location of the linear viscous dampers connecting the adjacent buildings. According to the previous general expression of $\mathbf{f}[\dot{\mathbf{u}}(t)]$, matrix $\mathbf{C}_d$ has the following expression:

$$\mathbf{C}_d = \begin{bmatrix} \mathbf{C}_{d0(nxn)} & \mathbf{0}_{(nx(m-n))} & -\mathbf{C}_{d0(nxn)} \\ \mathbf{0}_{((m-n)xn)} & \mathbf{0}_{((m-n)xn)} & \mathbf{0}_{((m-n)xn)} \\ -\mathbf{C}_{d0(nxn)} & \mathbf{0}_{(nx(m-n))} & \mathbf{C}_{d0(nxn)} \end{bmatrix} \tag{5}$$

where $\mathbf{C}_{d0}$ is the diagonal matrix, containing the values $c_{d0,j}$ of the viscous constants of the dampers at each connected story.

In order to simplify the problem and develop a reduced order model, suitable for the design of the dissipative system, the following decomposition of the motion is considered for the system:

$$\mathbf{u}(t) = \mathbf{\Phi}\mathbf{q}(t) \tag{6}$$

where $\mathbf{\Phi}$ is the matrix containing the undamped eigenvectors (modal shapes) of the combined system and $\mathbf{q}(t)$ is a vector of order $n+m$, containing the generalized displacements. In this case, the set of all the modal shapes consists of the two separated sets containing the modal shapes of A and the modal shapes of B.

After substituting Equation (6) into Equation (4) and premultiplying by $\mathbf{\Phi}^T$, one obtains:

$$\begin{aligned} &\mathbf{\Phi}^T\mathbf{M}\mathbf{\Phi}\ddot{\mathbf{q}}(t) + \mathbf{\Phi}^T(\mathbf{C} + \mathbf{C}_d)\mathbf{\Phi}\dot{\mathbf{q}}(t) + \mathbf{\Phi}^T\mathbf{K}\mathbf{\Phi}\mathbf{q}(t) \\ &= -\mathbf{\Phi}^T\mathbf{M}\mathbf{r}\ddot{u}_g(t) \end{aligned} \tag{7}$$

This corresponds to a system of $n+m$ coupled equations.

To develop a reduced order model capable to describe the coupled system dynamic behavior with good accuracy, at least the first undamped modes of each building alone have to be considered. Let $\boldsymbol{\varphi}_{\mathrm{A}u}$ and $\boldsymbol{\varphi}_{\mathrm{B}u}$ denote the vectors containing the first modal shapes of building A and B, respectively. Matrix $\mathbf{\Phi}$ reduces to:

$$\mathbf{\Phi} = \begin{bmatrix} \boldsymbol{\varphi}_{\mathrm{A}} & \boldsymbol{\varphi}_{\mathrm{B}} \end{bmatrix} = \begin{bmatrix} \boldsymbol{\varphi}_{\mathrm{A}u_{(m)}} & \mathbf{0}_{(m)} \\ \mathbf{0}_{(n)} & \boldsymbol{\varphi}_{\mathrm{B}u_{(n)}} \end{bmatrix} = \begin{bmatrix} \boldsymbol{\varphi}_{\mathrm{A}ud_{(m)}} & \mathbf{0}_{(n)} \\ \boldsymbol{\varphi}_{\mathrm{A}uu_{(m-n)}} & \mathbf{0}_{(m-n)} \\ \mathbf{0}_{(n)} & \boldsymbol{\varphi}_{\mathrm{B}ud_{(n)}} \end{bmatrix} \tag{8}$$

where $\boldsymbol{\varphi}_{\mathrm{B}ud} = \boldsymbol{\varphi}_{\mathrm{B}u}$ and $\boldsymbol{\varphi}_{\mathrm{A}u}$ is further split into $\boldsymbol{\varphi}_{\mathrm{A}ud}$, containing the modal displacements of building A for the first n degree of freedom, and $\boldsymbol{\varphi}_{\mathrm{A}uu}$ containing the modal displacements of building A for the upper stories, from $n+1$ to m, not connected to building B.

Under this approximation, the vector $\mathbf{q}$ contains two components only, denoted as q_A and q_B, and Equation (7) reads as follows:

$$\begin{aligned} &\boldsymbol{\varphi}_{\mathrm{A}u}{}^T\mathbf{M}_{\mathrm{A}}\boldsymbol{\varphi}_{\mathrm{A}u}\ddot{q}_{\mathrm{A}}(t) + \boldsymbol{\varphi}_{\mathrm{A}u}{}^T\mathbf{C}_{\mathrm{A}}\boldsymbol{\varphi}_{\mathrm{A}u}\dot{q}_{\mathrm{A}}(t) + \boldsymbol{\varphi}_{\mathrm{A}ud}{}^T\mathbf{C}_{d0}\boldsymbol{\varphi}_{\mathrm{A}ud}\dot{q}_{\mathrm{A}}(t) \\ &\quad -\boldsymbol{\varphi}_{\mathrm{A}ud}{}^T\mathbf{C}_{d0}\boldsymbol{\varphi}_{\mathrm{B}ud}\dot{q}_{\mathrm{B}}(t) + \\ &\quad +\boldsymbol{\varphi}_{\mathrm{A}u}{}^T\mathbf{K}_{\mathrm{A}}\boldsymbol{\varphi}_{\mathrm{A}u}q_{\mathrm{A}}(t) = -\boldsymbol{\varphi}_{\mathrm{A}u}{}^T\mathbf{M}_{\mathrm{A}}\mathbf{r}\ddot{u}_g(t) \\ &\boldsymbol{\varphi}_{\mathrm{B}u}{}^T\mathbf{M}_{\mathrm{B}}\boldsymbol{\varphi}_{\mathrm{B}u}\ddot{q}_{\mathrm{B}}(t) + \boldsymbol{\varphi}_{\mathrm{B}u}{}^T\mathbf{C}_{\mathrm{B}}\boldsymbol{\varphi}_{\mathrm{B}u}\dot{q}_{\mathrm{B}}(t) + \boldsymbol{\varphi}_{\mathrm{B}ud}{}^T\mathbf{C}_{d0}\boldsymbol{\varphi}_{\mathrm{B}ud}\dot{q}_{\mathrm{B}}(t) \\ &\quad -\boldsymbol{\varphi}_{\mathrm{B}ud}{}^T\mathbf{C}_{d0}\boldsymbol{\varphi}_{\mathrm{A}ud}\dot{q}_{\mathrm{A}}(t) + \\ &\quad +\boldsymbol{\varphi}_{\mathrm{B}u}{}^T\mathbf{K}_{\mathrm{B}}\boldsymbol{\varphi}_{\mathrm{B}u}q_{\mathrm{B}}(t) = -\boldsymbol{\varphi}_{\mathrm{B}u}{}^T\mathbf{M}_{\mathrm{B}}\mathbf{r}\ddot{u}_g(t) \end{aligned} \tag{9}$$

After posing:

$$\begin{aligned} m_i &= \boldsymbol{\varphi}_{iu}{}^T \mathbf{M}_i \boldsymbol{\varphi}_{iu} \\ c_i &= \boldsymbol{\varphi}_{iu}{}^T \mathbf{C}_i \boldsymbol{\varphi}_{iu} \\ k_i &= \boldsymbol{\varphi}_{iu}{}^T \mathbf{K}_i \boldsymbol{\varphi}_{iu} \qquad \text{for } i = \text{A, B} \\ l_{eff,i} &= \boldsymbol{\varphi}_{iu}{}^T \mathbf{M}_i \mathbf{r} \\ \gamma_i &= \frac{l_{eff,i}}{m_i} \end{aligned} \tag{10}$$

and dividing by the modal participation factor γ_i, Equation (9) can be rewritten as:

$$\begin{aligned} &\ddot{\overline{q}}_{\mathrm{A}}(t) + 2\xi_{\mathrm{A}}\omega_{\mathrm{A}}\dot{\overline{q}}_{\mathrm{A}}(t) + \frac{\boldsymbol{\varphi}_{\mathrm{A}ud}{}^T \mathbf{C}_{d0} \boldsymbol{\varphi}_{\mathrm{A}ud}}{m_{\mathrm{A}}}\dot{\overline{q}}_{\mathrm{A}}(t) \\ &\quad - \frac{\boldsymbol{\varphi}_{\mathrm{A}ud}{}^T \mathbf{C}_{d0} \boldsymbol{\varphi}_{\mathrm{B}ud}}{m_{\mathrm{A}}}\dot{\overline{q}}_{\mathrm{B}}(t) + \omega_{\mathrm{A}}^2 \overline{q}_{\mathrm{A}}(t) = -\ddot{u}_g(t) \\ &\ddot{\overline{q}}_{\mathrm{B}}(t) + 2\xi_{\mathrm{B}}\omega_{\mathrm{B}}\dot{\overline{q}}_{\mathrm{B}}(t) + \frac{\boldsymbol{\varphi}_{\mathrm{B}ud}{}^T \mathbf{C}_{d0} \boldsymbol{\varphi}_{\mathrm{B}ud}}{m_{\mathrm{B}}}\dot{\overline{q}}_{\mathrm{B}}(t) \\ &\quad - \frac{\boldsymbol{\varphi}_{\mathrm{B}ud}{}^T \mathbf{C}_{d0} \boldsymbol{\varphi}_{\mathrm{A}ud}}{m_{\mathrm{B}}}\dot{\overline{q}}_{\mathrm{A}}(t) + \omega_{\mathrm{B}}^2 \overline{q}_{\mathrm{B}}(t) = -\ddot{u}_g(t) \end{aligned} \tag{11}$$

where $\overline{q}_i(t) = \frac{q_i(t)}{\gamma_i}$, $\frac{c_i}{m_i} = 2\xi_i\omega_i$ and $\frac{k_i}{m_i} = \omega_i^2$ for $i = \text{A, B}$. This way, there is a clear correspondence between the MDOF systems and the reduced order model.

The total amount of damping due to the frame and to the dissipative connection of the equivalent 2-SDOF system can be expressed as follows:

$$\begin{aligned} \overline{\xi}_{\mathrm{A}} &= \xi_{\mathrm{A}} + \frac{\boldsymbol{\varphi}_{\mathrm{A}ud}{}^T \mathbf{C}_{d0} \boldsymbol{\varphi}_{\mathrm{A}ud}}{2m_{\mathrm{A}}\omega_{\mathrm{A}}} - \frac{\boldsymbol{\varphi}_{\mathrm{A}ud}{}^T \mathbf{C}_{d0} \boldsymbol{\varphi}_{\mathrm{B}ud}}{2m_{\mathrm{A}}\omega_{\mathrm{A}}} \\ \overline{\xi}_{\mathrm{B}} &= \xi_B + \frac{\boldsymbol{\varphi}_{\mathrm{B}ud}{}^T \mathbf{C}_{d0} \boldsymbol{\varphi}_{\mathrm{B}ud}}{2m_B\omega_B} - \frac{\boldsymbol{\varphi}_{\mathrm{B}ud}{}^T \mathbf{C}_{d0} \boldsymbol{\varphi}_{\mathrm{A}ud}}{2m_B\omega_B} \end{aligned} \tag{12}$$

In the case of a single damper with viscous constant $c_{d0,r}$ connecting story r of buildings A and B, these expressions coincide with those reported in (Aida et al., 2001):

$$\begin{aligned} \overline{\xi}_{\mathrm{A}} &= \xi_{\mathrm{A}} + \frac{c_{d0,r}}{2m_{\mathrm{A}}\omega_{\mathrm{A}}}\boldsymbol{\varphi}_{\mathrm{A}ud,r}^2 - \frac{c_{d0,r}\boldsymbol{\varphi}_{\mathrm{A}ud,r}\boldsymbol{\varphi}_{Bud,r}}{2m_{\mathrm{A}}\omega_{\mathrm{A}}} \\ \overline{\xi}_B &= \xi_B + \frac{c_{d0,r}}{2m_B\omega_B}\boldsymbol{\varphi}_{Bud,r}^2 - \frac{c_{d0,r}\boldsymbol{\varphi}_{\mathrm{A}ud,r}\boldsymbol{\varphi}_{Bud,r}}{2m_B\omega_B} \end{aligned} \tag{13}$$

In general, the system is non-classically damped (Sivandi-Pour et al., 2014, 2015) because of the non-zero term $\boldsymbol{\varphi}_{\mathrm{A}ud}{}^T \mathbf{C}_{d0} \boldsymbol{\varphi}_{\mathrm{B}ud}$. By neglecting the off-diagonal terms in Equation (12), the following approximate expressions of the damping ratio for the first two fundamental vibration modes of the coupled system can be obtained:

$$\begin{aligned} \overline{\xi}_{\mathrm{A},\,app} &= \xi_{\mathrm{A}} + \frac{\boldsymbol{\varphi}_{\mathrm{A}ud}{}^T \mathbf{C}_{d0} \boldsymbol{\varphi}_{\mathrm{A}ud}}{2m_{\mathrm{A}}\omega_{\mathrm{A}}} \\ \overline{\xi}_{\mathrm{B},\,app} &= \xi_B + \frac{\boldsymbol{\varphi}_{\mathrm{B}ud}{}^T \mathbf{C}_{d0} \boldsymbol{\varphi}_{\mathrm{B}ud}}{2m_B\omega_B} \end{aligned} \tag{14}$$

The study of Hwang et al. (Hwang et al., 2007), based on complex modal analysis of two adjacent SDOF systems connected by a viscous damper, has shown that the decoupling approximation yields very accurate results in the case of well-separated vibration frequencies of the two systems and low added damping. Usually, for ratios $\omega_{\mathrm{B}}/\omega_{\mathrm{A}} > 1.5 \div 2$, Equation (14) can be assumed to provide accurate estimates of the buildings damping ratios (Hwang et al., 2007). It is noteworthy that the dampers connecting adjacent buildings are efficient in dissipating energy only for buildings with different dynamic properties and that in the case of two identical adjacent buildings, the dampers would not be activated.

It is worth to note that, under the approximation of Equation (14) and recalling the expression of $\mathbf{C}_{d0}$, the addition of dampers between two adjacent buildings induces a mass-proportional damping in each system (Trombetti and Silvestri, 2004). Thus, the dissipation capacity of the added dampers depends on the absolute displacements of each system, rather than on the interstorey drifts (stiffness-proportional damping), and obviously is different from building to building.

Non-Linear System and Linear Equivalence Based on Stochastic Response

Non-linear devices are widely diffused, due to their ability to reduce dampers forces in case of high velocity (Tubaldi et al., 2015), and thus it is useful to establish a link between the linear formulation of section "Equation of motion for MDOF systems connected by nonlinear viscous dampers" and the non-linear one of section "MDOF systems connected by linear FVDs and reduced order model". This can be achieved by choosing an equivalence condition between the two systems and by defining the relationship between the parameters of the non-linear FVDs and the parameters of the equivalent linear FVDs. On this regard, in literature there are different linearization approaches, one of the most diffused being based on energy considerations under harmonic inputs [see Christopoulos and Filiatrault (2006)]. In this work. a stochastic linearization technique, already employed in Rüdinger and Krenk (2003), Rüdinger (2006), Rudinger (2007), Di Paola et al. (2007), Di Paola and Navarra (2009), and De Domenico and Ricciardi (2018, 2019), is chosen to identify the equivalent linear expression for non-linear devices.

For this purpose, it is assumed here that the input $\ddot{u}_g(t)$ to the non-linear system of Equation (1) is a Gaussian stochastic stationary process. Equation (1) becomes a stochastic equation and the displacement response and relevant derivatives are also stochastic quantities. The equation of the equivalent linear system is:

$$\mathbf{M}\ddot{\mathbf{U}}(t) + \left(\mathbf{C} + \mathbf{C}_d^{eq}\right)\dot{\mathbf{U}}(t) + \mathbf{K}\mathbf{U}(t) = -\mathbf{M}\mathbf{R}\ddot{u}_g(t) \tag{15}$$

where the effect of the non-linear dampers is expressed by the equivalent linear matrix $\mathbf{C}_d^{eq}$, whose terms are evaluated using a force-based equivalent criterion (De Domenico and Ricciardi, 2018, 2019). In particular, the matrix $\mathbf{C}_d^{eq}$ has the same structure of the matrix $\mathbf{C}_d$, shown in Equation (5), where $\mathbf{C}_{d0}^{eq}$ is a nxn diagonal submatrix containing the values of the equivalent viscous constant, determined as follows:

$$c_{d0,j}^{eq} = c_{d,j}^{NL}\frac{2^{1+\frac{\alpha}{2}}\Gamma\left(1+\frac{\alpha}{2}\right)}{\sqrt{2\pi}}\sigma_{\Delta\dot{\mathbf{u}}_j}^{\alpha-1} \qquad j = 1:n \tag{16}$$

where $\sigma_{\Delta\dot{\mathbf{u}}_j}$ is the standard deviation of the relative velocity between the ends of the damper at the j-th floor.

It is evident that the equivalence holds only for the assigned stationary process $\ddot{u}_g(t)$, that can be described by its power spectral density $S_{\ddot{U}_g}(\omega)$, so equivalent parameters vary by varying the input intensity and the input frequency content. In the considered case, oriented to study the seismic response, the equivalence is found by considering a Kanai-Tajimi process (Kanai, 1957; Tajimi, 1960).

Passing from the MDOF systems to the reduced order model, Equation (16) becomes:

$$c_{d0,j}^{eq} = c_{d,j}^{NL} E\left[\left|\Delta\dot{\mathbf{u}}_j\right|^{\alpha-1}\right] = \frac{2^{\alpha/2}\Gamma\left(\frac{\alpha}{2}\right)}{\sqrt{2\pi}}\sigma_{\Delta\dot{\mathbf{u}}_j}^{\alpha-1} \quad j = 1:n \tag{17}$$

where:

$$\begin{aligned}\sigma_{\Delta\dot{\mathrm{U}}_j} &= \sqrt{E\left[\Delta\dot{\mathbf{u}}_j^2\right]} \\ &= \sqrt{\boldsymbol{\varphi}_{\mathrm{A}u,j}^2 E\left[\dot{q}_{\mathrm{A}}^2\right] + \boldsymbol{\varphi}_{\mathrm{B}u,j+m}^2 E\left[\dot{q}_{\mathrm{B}}^2\right] - 2\boldsymbol{\varphi}_{\mathrm{A}u,j}\boldsymbol{\varphi}_{\mathrm{B}u,j+m} E\left[\dot{q}_{\mathrm{A}}\dot{q}_{\mathrm{B}}\right]} \\ j &= 1:n\end{aligned} \tag{18}$$

and where $\boldsymbol{\varphi}_{i,r}$ denotes the value of modal shape i at degree of freedom r.

FLUID VISCOUS DAMPERS DESIGN

The dissipative system is designed by exploiting the classically damped reduced order model.

The distribution of dampers is described by $\mathbf{C}_{d0} = \lambda\tilde{\mathbf{C}}_{d0}$, where $\tilde{\mathbf{C}}_{d0}$ is an arbitrary diagonal matrix fixed in advance and controlling the dampers' distribution story by story and λ is a scale factor controlling the global dimension of the dissipative system. The components of the matrix $\tilde{\mathbf{C}}_{d0}$ are $\tilde{c}_{d0,j}$.

The scale factor λ is determined by requiring that the damping added to one of the two frames, denoted as primary structure in the following and conventionally coinciding with system B, is equal to a target value ξ_{add}. The value of λ can be obtained from Equation (14), and its expression is the following:

$$\lambda = \frac{2m_{\mathrm{B}}\omega_{\mathrm{B}}\xi_{add}}{\boldsymbol{\varphi}_{\mathrm{B}ud}{}^{T}\tilde{\mathbf{C}}_{d0}\boldsymbol{\varphi}_{\mathrm{B}ud}} \tag{19}$$

Once λ is known, the constant of the damper connecting the j-th level is $c_{d0,j} = \lambda\tilde{c}_{d0,j}$. There can be a large number of dampers arrangements equivalent in terms of ξ_{add}; in the following examples two different arrangements of dampers, widely diffused in applications, are analyzed.

In the case of non-linear dissipative system with damping exponent α, it is possible to exploit the equivalence condition described above, but it is necessary to fix the properties of the stochastic process $\ddot{U}_g(t)$ at which the equivalent condition must hold. Many times, the frequency contents are fixed and it is only necessary to assign a scale factor related to the intensity level, as in the following application where a Kanai-Taijmi process is assumed and the scale factor of the power spectral density (PSD) describing the process is calibrated according to the intensity of the design action.

In order to assign the properties of the non-linear dampers, the MDOF linear system obtained for the previous design procedure is assumed as the equivalent linear system and the variance of the relative velocity at each story $\sigma_{\Delta\dot{\mathbf{u}}_j}$ is evaluated by using the numerical procedure described in **Appendix A**, starting from the PSD of the input.

At this point, the constants of the non-linear dampers ensuring an equivalent response for the assumed input intensity can be obtained from Equation (20).

$$c_{d,j}^{NL} = \lambda\tilde{c}_{d0,j}\frac{\sqrt{2\pi}}{2^{1+\frac{\alpha}{2}}\Gamma\left(1+\frac{\alpha}{2}\right)\sigma_{\Delta\dot{\mathbf{u}}_j}^{\alpha-1}} \quad j = 1:n \tag{20}$$

APPLICATION EXAMPLES

In this section, the proposed design method for the dampers is applied with reference to a case study, involving two planar structures of different story number. Parametric analysis is conducted, both in the case of linear and non-linear dampers, by varying the values of the viscous damping constants and of the parameter α. Two different configurations of dissipative connection are analyzed, the first one, defined as uniform distribution, considers the installation of devices with equal properties at all the stories of the lower building. The second configuration involves the installation of a single damper at the last floor of the lower structure. The response parameters monitored, both in the MDOF system and in the reduced order model, are the floor displacements, the absolute accelerations and the dampers' forces. Finally, the behavior of linear and non-linear devices is analyzed for different levels of the seismic intensity, far from the design condition.

Case Study and Seismic Input

Two coupled steel moment-resisting frame buildings with shear-type behavior are considered as case study in this application example (**Figure 1**). The properties of these buildings, assumed as deterministic, are taken from (Tubaldi et al., 2014). Building A is an 8-story frame with constant floor mass, $m_A = 454{,}540$ kg, and stiffness, $k_A = 628{,}801$ kN/m. Building B is a four-story building with constant story mass, $m_B = 454{,}540$ kg, and stiffness, $k_B = 470{,}840$ kN/m. The story heights are equal to 3.2 m. Matrices $\mathbf{C}_{\mathrm{A}}$ (with dimensions 8×8) and $\mathbf{C}_{\mathrm{B}}$ (with dimensions 4×4) describe the inherent buildings' damping. They are based on the Rayleigh model and are obtained by assuming a damping factor $\zeta_A = \zeta_B = 2\%$ for the first and last fundamental vibration modes of each system. The fundamental vibration periods of building A and B are $T_A = 0.915$ and $T_B = 0.562$ s, respectively.

The two degrees of freedom reduced order model corresponding to the adjacent buildings has the following properties: $m_A = l_{eff,\mathrm{A}} = 3113.9$ kNs^2/m, $m_{\mathrm{B}} = l_{eff,\mathrm{B}} = 1624.4$ kNs^2/m, $k_{\mathrm{A}} = 1.4669{\cdot}10^5$ kN/m, $k_{\mathrm{B}} = 2.0295{\cdot}10^5$ kN/m, $c_{\mathrm{A}} = 854.91$ kNs/m, $c_{\mathrm{B}} = 726.28$ kNs/m.

The stochastic seismic input considered in all the examples is modeled as a stationary Gaussian process whose PSD function is

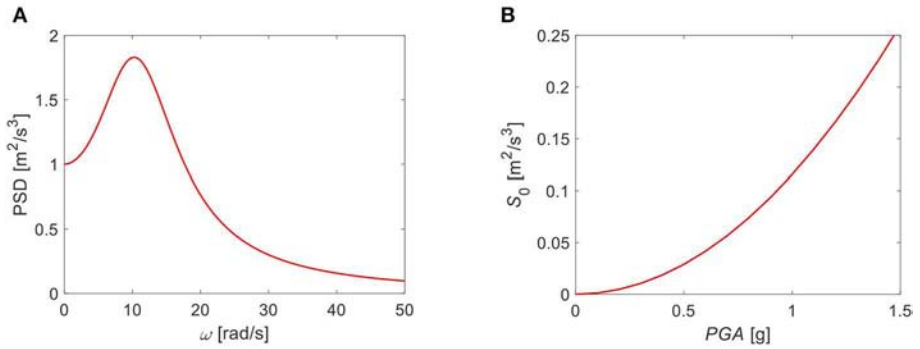

FIGURE 2 | Input ground motion: **(A)** PSD function of the seismic input process, and **(B)** relation between S_0 and *PGA*.

described by the widely-used Kanai-Tajimi model (Kanai, 1957; Tajimi, 1960) i.e.,

$$S_{KT}(\omega) = S_0 \cdot \frac{\omega_g^4 + 4 \cdot \xi_g^2 \cdot \omega^2 \cdot \omega_g^2}{\left[\omega_g^2 - \omega^2\right]^2 + 4 \cdot \xi_g^2 \cdot \omega^2 \cdot \omega_g^2} \tag{21}$$

in which: S_0 is the amplitude of the bedrock excitation spectrum, modeled as a white noise process; ω_g and ζ_g are the fundamental circular frequency and the damping factor of the soil, respectively. The following values of the parameters are used hereinafter: $\omega_g = 12.5$ rad/s, $\zeta_g = 0.6$.

Figure 2A shows the PSD function for $S_0 = 1$ m^2/s^3 whereas **Figure 2B** shows the relationship between the parameter S_0 of the Kanai-Tajimi spectrum and the average peak ground acceleration (*PGA*) at the site. This relation has been assessed empirically based on the procedure reported in Tubaldi et al. (2012).

Fluid Viscous Dampers Design

The dissipative system is designed by using the procedure described above. Two different arrangements of dampers widely diffused in applications are considered. The first refers to a uniform distribution of dampers with equal properties placed, connecting the first four floors of building A and B. In this case the shape of the damper distribution is described by $\tilde{c}_{d0,j} = 1$ and the viscous constants are:

$$c_{d0,j} = \frac{2 m_B \omega_B \xi_{add}}{\sum_{j=1}^{ndof\ B} \varphi_{B,j}^2} \tag{22}$$

The second configuration, instead, corresponds to a single damper placed between the fourth floors of building A and B, where the velocities are expected to be the highest. In this case the shape of the damper distribution is described by $\tilde{c}_{d0,j} = 0$ for $j = 1:3$, $\tilde{c}_{d0,4} = 1$ and the viscous constant at the forth level is:

$$c_{d0,4} = \frac{2 m_B \omega_B \xi_{add}}{\varphi_{B,4}^2} \tag{23}$$

The amount of added damping used for the dampers' design is $\xi_{add} = 0.10$, applied to the shorter building B (the expected value of the total damping is $\bar{\xi} = 0.12$, being $\xi = 0.02$ the amount of inherent damping).

According to the MDOFs, for the case with four dampers, the design damping constant of each device from Equation (22) is $c_{d0,j} = 1016.0\ kNs/m$; for the case of the single damper at the fourth floor the viscous damping constant from Equation (23) is $c_{d0,4} = 2357.50\ kNs/m$.

In the case of non-linear dissipative system with characteristic parameter α, the equivalence condition is applied with reference to the stationary input describing the design seismic input ($PGA_{ref} = 0.3$ g).

The values of the coefficient $c_{d,j}^{NL}$ of the equivalent linear viscous dampers depend on the value assumed for the velocity exponent α. **Figure 3** shows the variation with α of the $c_{d,j}^{NL}$ values evaluated via Equation (16), for both the cases of dampers at each floor with homogeneous properties (**Figure 3A**) and of single damper (**Figure 3B**).

Modal Properties of the Systems With Linear Dampers Before and After the Coupling

Complex modal analysis of the two uncoupled and coupled MDOF adjacent buildings is carried out and the relevant results are summarized in **Table 1**, in terms of modal vibration periods and damping factors. As expected, the coupled buildings are non-classically damped and tend to vibrate together, as a single system. However, because of the low added damping, the vibration shapes for each of the composite vibration modes are such that the displacements of a building prevail over the displacement of the other building, and thus pertinent modal shapes can be identified for each building (labeled as A if the modal displacement of A prevails, as B otherwise).

It is observed (**Table 1**) that the addition of viscous dampers does not significantly affect the vibration periods of the systems, whereas it increases significantly the modal damping factor. The increase of damping, more relevant for building B (the shorter structure), is significant only at the lower vibration modes. Moreover, the effects on the system dynamic properties are comparable between the two considered dampers configurations (single and uniform).

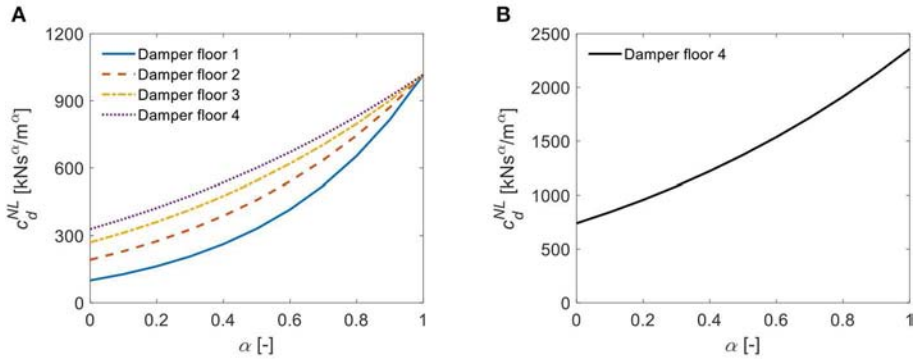

FIGURE 3 | Design equivalent viscous coefficients for non-linear dampers vs. damper exponent α : **(A)** Dampers at each floor with homogeneous properties, **(B)** Single damper.

TABLE 1 | Modal analysis results for uncoupled buildings (subscript "0") and coupled buildings (subscript "d").

Mode	Uncoupled buildings				MDOF Coupled with uniform dampers				MDOF Coupled with single damper			
	T_0 [s]		ζ_0 [–]		T_d [s]		ζ_d [–]		T_d [s]		ζ_d [–]	
	A	B	A	B	A	B	A	B	A	B	A	B
1	0.915	0.562	0.0200	0.0200	0.909	0.563	0.0532	0.1226	0.907	0.562	0.0589	0.123
2	0.309	0.195	0.0113	0.0148	0.310	0.194	0.0455	0.0599	0.309	0.195	0.0304	0.0447
3	0.189	0.127	0.0121	0.0176	0.191	0.127	0.0175	0.0406	0.190	0.128	0.0145	0.0251
4	0.140	0.104	0.0140	0.0200	0.140	0.104	0.0282	0.0386	0.140	0.114	0.0271	0.0174

Response Statistics Assessment at the Dampers Design Conditions

In the following, the performance of the MDOF coupled system, assumed as reference solution, is compared with the one of the non-classically damped reduced order model. The reduced order model equipped with linear dampers is characterized by the following damping matrix components. For what concerns the buildings coupled with dampers uniformly distributed along the first four floors one has $2\xi_A m_A \omega_A + \boldsymbol{\varphi}_{Aud}{}^T \mathbf{C}_{d0} \boldsymbol{\varphi}_{Aud} = 2321.2\ kNs/m$, $2\xi_B m_B \omega_B + \boldsymbol{\varphi}_{Bud}{}^T \mathbf{C}_{d0} \boldsymbol{\varphi}_{Bud} = 4357.5\ kNs/m$, and $\boldsymbol{\varphi}_{Aud}{}^T \mathbf{C}_{d0} \boldsymbol{\varphi}_{Bud} = \boldsymbol{\varphi}_{Bud}{}^T \mathbf{C}_{d0} \boldsymbol{\varphi}_{Aud} = 2299.6\ kNs/m$. For the case of a single damper at the fourth floor, instead, the damping parameters are $2\xi_A m_A \omega_A + \boldsymbol{\varphi}_{Aud}{}^T \mathbf{C}_{d0} \boldsymbol{\varphi}_{Aud} = 2579.6\ kNs/m$, $2\xi_B m_B \omega_B + \boldsymbol{\varphi}_{Bud}{}^T \mathbf{C}_{d0} \boldsymbol{\varphi}_{Bud} = 4357.7\ kNs/m$ and $\boldsymbol{\varphi}_{Aud}{}^T \mathbf{C}_{d0} \boldsymbol{\varphi}_{Bud} = \boldsymbol{\varphi}_{Bud}{}^T \mathbf{C}_{d0} \boldsymbol{\varphi}_{Aud} = 2502.6\ kNs/m$.

In the case of dampers at each floor, the damping factors for the first two modes of the coupled buildings are, respectively, $\overline{\xi}_A = 0.0535$ and $\overline{\xi}_B = 0.121$, in very good agreement with the corresponding values evaluated by considering the refined MDOF model (**Table 1**). In the case of a single damper connecting the two buildings, the corresponding damping factors for the first two modes of the coupled buildings are, respectively, $\overline{\xi}_A = 0.0595$ and $\overline{\xi}_B = 0.121$, again in very good agreement with the corresponding values evaluated by considering the refined model (**Table 1**).

Figure 4 compares the root mean square (RMS) stationary response (i.e., the standard deviation of the response) of both the uncoupled and coupled buildings with uniform dampers subjected to the seismic input described in the previous section. **Figure 5** compares the response for the buildings coupled by a single damper. The comparison is made in terms of RMS of floor displacements (**Figures 4A**, **5A**), floor absolute accelerations (**Figures 4B**, **5B**) and relative displacements between the first four floors (**Figures 4C**, **5C**), which are demand parameters particularly useful to describe the effectiveness of the dissipative coupling strategy in improving the performance of the buildings. Moreover, **Figures 4C**, **5C** show the relative displacement demands between the first four floors of the adjacent buildings, which is the parameter controlling the pounding probability.

In general, it is observed that the dampers are effective in reducing the displacement and acceleration response of both the buildings, as well as the relative displacements. The displacement response of building B is more damped than that of building A, as expected from the results of modal analysis of the coupled buildings. Similar trends are observed for the acceleration responses. Finally, it is noted that the reduced order model provides accurate estimates of the response in terms of displacements, being the responses of the 2SDOF model very close to those corresponding to the refined MDOF model. Higher deviations are observed between the responses in terms of RMS acceleration.

Figure 6 compares the RMS forces of the dampers. For the uniform dampers configuration (**Figure 6A**) these forces increase with increasing building height, because the absolute and relative velocities of the two buildings increase along the height. Again, a very good agreement is observed between the estimates of the reduced order and the refined model. For the case with single damper (**Figure 6B**), the agreement between the

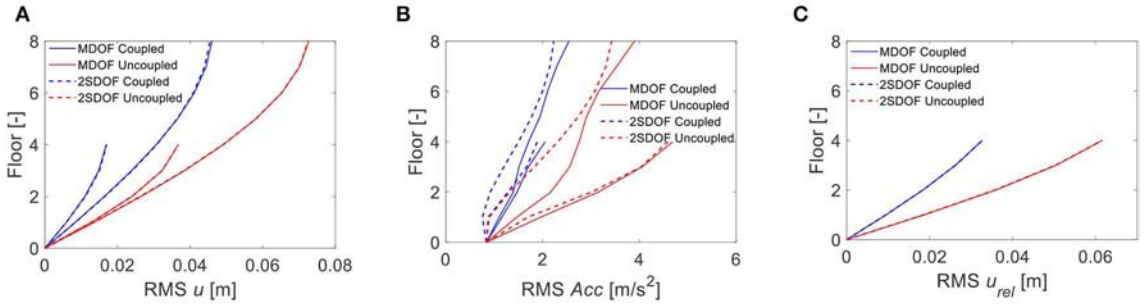

FIGURE 4 | RMS displacement **(A)**, acceleration response **(B)**, and relative displacement **(C)** of the uncoupled and coupled buildings with uniform dampers, according to the refined model (MDOF) and the reduced order model (2SDOF).

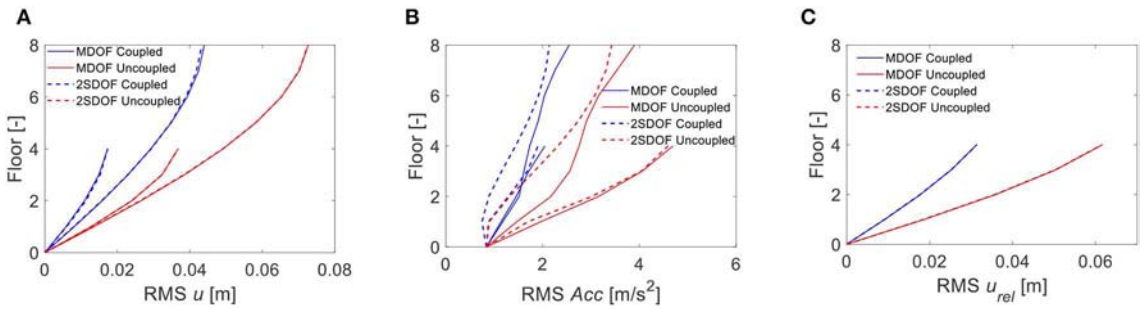

FIGURE 5 | RMS displacement **(A)**, acceleration response **(B)**, and relative displacement **(C)** of the uncoupled and coupled buildings with single damper, according to the refined model (MDOF), and the reduced order model (2SDOF).

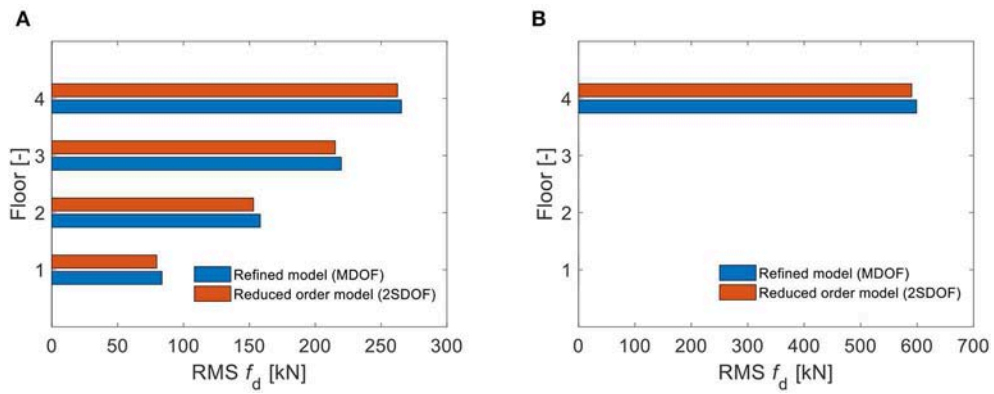

FIGURE 6 | Comparison of RMS damper forces according to the refined model (MDOF) and the reduced order model (2SDOF): **(A)** Case with uniform dampers; **(B)** Case with single damper.

results from the reduced order and the refined model is very good, too.

Furthermore, it is observed that, for a given level of added damping ratio, the sum of the forces experienced by the dampers placed according to the uniform distribution is much lower than the force of the single damper placed at the top floor of building B. This result has important effects on the costs of the retrofit strategy, being the damper cost strictly related to the damper force (Altieri et al., 2018).

Parametric Study and Response Statistics Assessment

The following subsections analyses the stochastic response sensitivity to the following parameters: the viscous coefficients

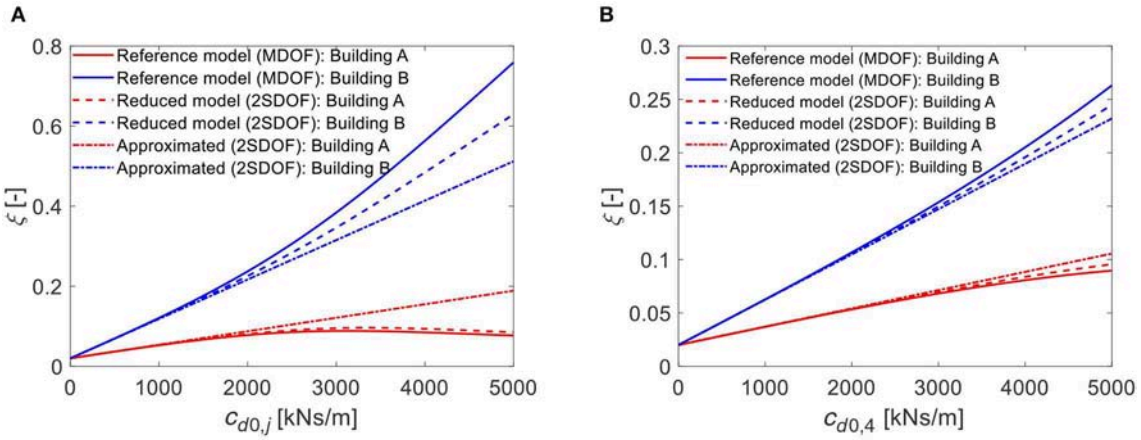

FIGURE 7 | Comparison between first two modes damping ratios evaluated by using different models: **(A)** case with uniform dampers; **(B)** case with single damper.

$c_{d0,j}$ and $c_{d0,4}$, the velocity exponent α, and the seismic input intensity.

Influence of the Viscous Coefficient

In this section, a parametric study is carried out to evaluate the effectiveness of the dampers in mitigating the building stationary responses to the previously described seismic input. This study also permits to assess the accuracy of the reduced order model for different damper properties. For this purpose, the value of the viscous coefficients $c_{d0,j}$ and $c_{d0,4}$ is varied in a range between 0.0 and 5,000 kNs/m.

Figure 7 plots and compares the damping ratios of the first two modes of the coupled system (corresponding to the modes of building A and B, respectively) for the following three different models: (1) the refined model (MDOF), (2) the reduced order model (2SDOF) with CMA, and (3) the 2SDOF model with the approximation introduced by Equation (15) (i.e., neglecting the off-diagonal terms). Curves related to building A are shown in red, those of building B in blue; solid, dashed and dotted styles are used to distinguish the results concerning the MDOF, the 2SDOF and the approximated approach, respectively. It is worth noting that the estimates obtained by using the refined model are exact, thus they are assumed as reference solution.

In general, it is noted that the addition of viscous dampers between the two adjacent buildings increases the damping factor of the second vibration mode, related to building B, rather than that of the first mode, related to the vibration of the building A. It is also observed that the three models provide equivalent results for low values of the added damping. For high values of $c_{d0,j}$ and $c_{d0,4}$, the two modal damping factors evaluated by applying complex modal analysis on the 2DOF model are still quite accurate (in particular for Building A vibration mode), whereas the damping factors evaluated by applying Equation (14) become very inaccurate for increasing values of $c_{d0,j}$ and $c_{d0,4}$. Similar results were observed in the works (Tubaldi et al., 2014) and (Tubaldi et al., 2012). A better agreement among the estimates of the different models is observed when a single damper configuration is used (**Figure 7B**).

The parametric study is also extended to evaluate the stochastic response in terms of buildings' displacements (**Figures 8A,C**) and damper forces (**Figures 8B,D**).

With reference to the arrangement with uniform dampers, it is observed that:

- For both the buildings, there exists an optimal value of the damping constant $c_{d0,j}$ that minimizes the displacement response. For values of $c_{d0,j}$ higher than 1,500 kNs/m the displacement response of building B does not change significantly, while for the building A this happens for values of $c_{d0,j}$ higher than 3,000 kNs/m.
- The dampers force always increases for increasing values of $c_{d0,j}$, although the relative velocities between the two buildings reduce.
- The reduced order model provides very accurate estimates of the building displacement response and of the damper forces for a wide range of damper properties. Its accuracy slightly decreases for increasing $c_{d0,j}$ values.

Influence of the Damper Non-Linearity

A second parametric study is performed by considering the case of non-linear viscous dampers connecting the two buildings in the same configurations already analyzed before, i.e., uniform distribution with equal properties at the first four floors and a single device at the last elevation of building B. The values of the dampers viscous constants, $c_{d0,j}$ and $c_{d0,4}$ are varied in the range between 0 and 5,000 kNs/m. The discrete values of the damper exponent considered are $\alpha = 0.3$, 0.5, 0.7, and 1, this latter for comparison purpose only. The optimal damping constant for building A and B are summarized in **Table 2**. **Figure 9** reports the stationary response in terms of building top displacements and forces of the damper at the fourth floor for different values of c_{d0} and of α.

The optimal damping constant for building A and B are summarized in **Table 2**.

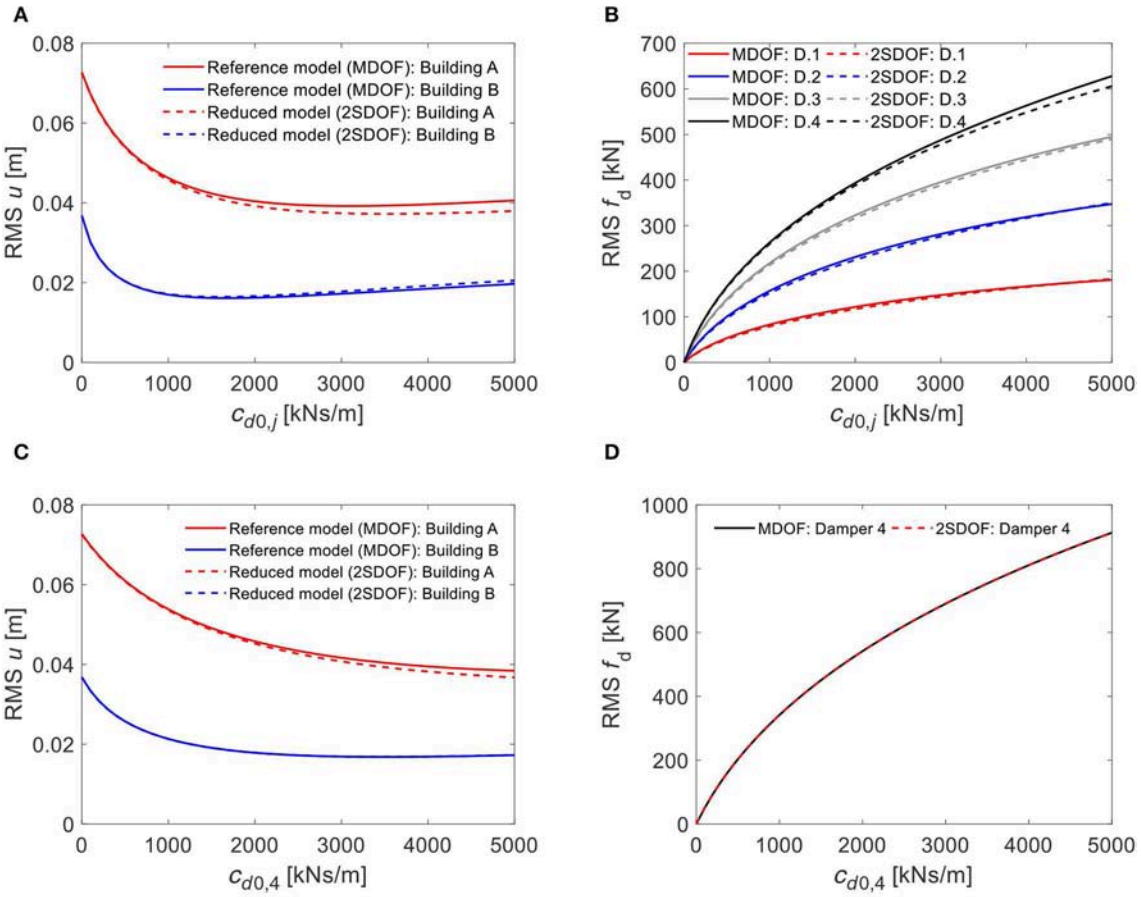

FIGURE 8 | Stationary response vs. damping viscous constant: **(A)** Top-floor displacement of building A and B (uniform dampers case), **(B)** Damper forces (uniform dampers case), **(C)** Top-floor displacement of building A and B (single damper case), **(D)** damper forces (single damper case).

TABLE 2 | Optimal damping constants for different α values and corresponding RMS building top displacements and 4th story damper force.

		Optimal $c_{d0,j}$ [kNs/m]		RMS displacements [m]		RMS damper force [kN]	
	α	A	B	A	B	A	B
Uniform dampers	1	3,100	1,700	0.0392	0.0161	495.8	359.6
	0.7	1,800	1,100	0.0394	0.0160	442.2	336.6
	0.5	1,300	800	0.0396	0.0160	446.4	318.1
	0.3	900	600	0.0397	0.0159	427.6	310.1
Single damper	1	5,500	3,500	0.0380	0.0168	912	750
	0.7	4,200	2,400	0.0379	0.0168	1,050	748
	0.5	3,050	1,900	0.0379	0.0168	1,052	760
	0.3	2,200	1,400	0.0379	0.0168	1,100	730

In **Figures 9A**, **10A** it is observed that the optimal damper viscous constant reduces significantly for decreasing α values and that the RMS displacements at the optimal damping constant value are practically insensitive to the exponent α (**Table 2**). Thus, if the properties of the non-linear viscous dampers are appropriately calibrated, the same performance in terms of response reduction of the linear viscous dampers can be achieved.

The results reported in **Figures 9B**, **10B** show that, for a given $c_{d0,j}$ value, the damper force increases for decreasing α values. However, the damper forces at the optimal $c_{d0,j}$ values evaluated for the different exponents α are comparable (**Table 2**) and

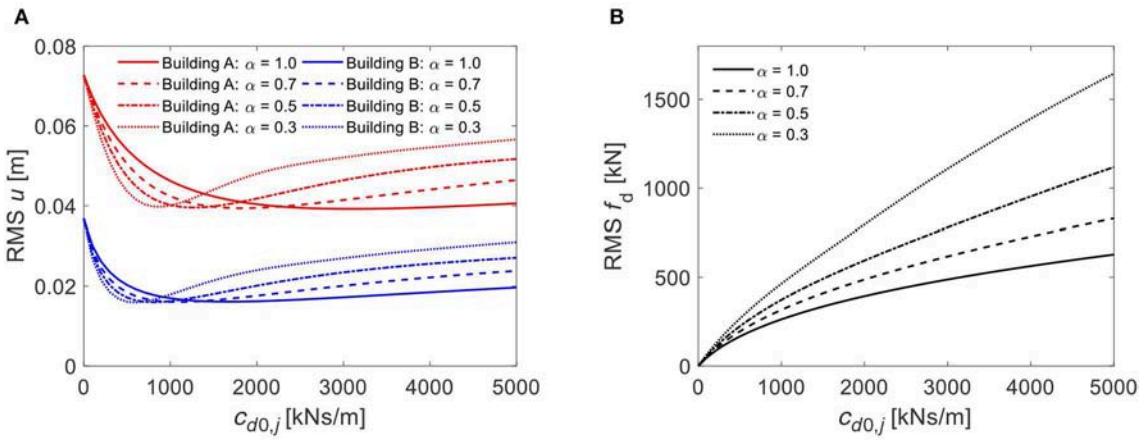

FIGURE 9 | Stationary response vs. damping viscous constant $c_{d0,j}$ for different α values: **(A)** Top-floor displacement of building A and B, **(B)** 4th floor damper force. Case with uniform dampers.

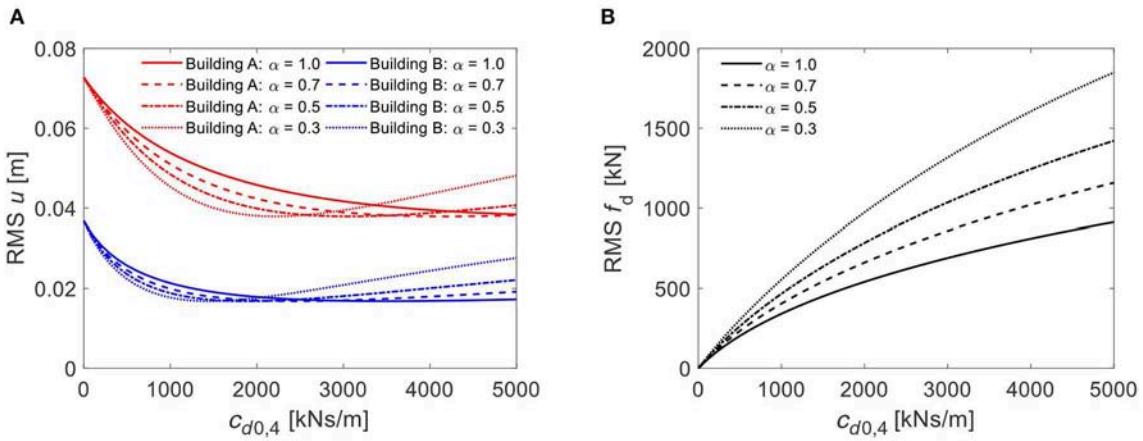

FIGURE 10 | Stationary response vs. damping viscous constant $c_{d0,4}$ for different α values: **(A)** top-floor displacement of building A and B, **(B)** 4th floor damper force. Case with single damper.

reduce only slightly for increasing α values. Thus, the non-linear viscous dampers with optimal properties exhibit a performance similar to the linear viscous dampers with optimal properties also in terms of damper forces.

Influence of the Seismic Intensity

In order to compare the efficiency of the dampers, the seismic response corresponding to the optimal damper properties obtained for building B for the different α values and for $PGA_{ref} = 0.3$ g, is evaluated by considering different seismic intensities, as described by the PGA (**Figure 11**).

The buildings coupled by the dampers with different exponents exhibit comparable displacement responses for the various seismic intensities considered. In fact, the top displacement responses of building A and B tend to increase only slightly for increasing damper non-linearity (i.e., for decreasing α values). On the other hand, the damper forces reduce significantly for decreasing α values and for *PGA* values higher than the reference design value $PGA_{\text{ref}} = 0.3$ g. This result is extremely important because the viscous damper costs depend on the design force rather than on the viscous constant (Tubaldi and Kougioumtzoglou, 2015; Altieri et al., 2018).

CONCLUSIONS

In this paper, the seismic response of adjacent buildings connected by fluid viscous dampers is analyzed. A simplified dampers design strategy is proposed, which relies on a linearized reduced order model of the coupled system. A stochastic linearization technique is adopted with the aim of extending the design method to non-linear viscous dampers. The effectiveness of the design method and of the coupling strategy is assessed via numerical analysis of two adjacent buildings with shear-type behavior connected by linear or non-linear viscous dampers and subjected to Gaussian stochastic

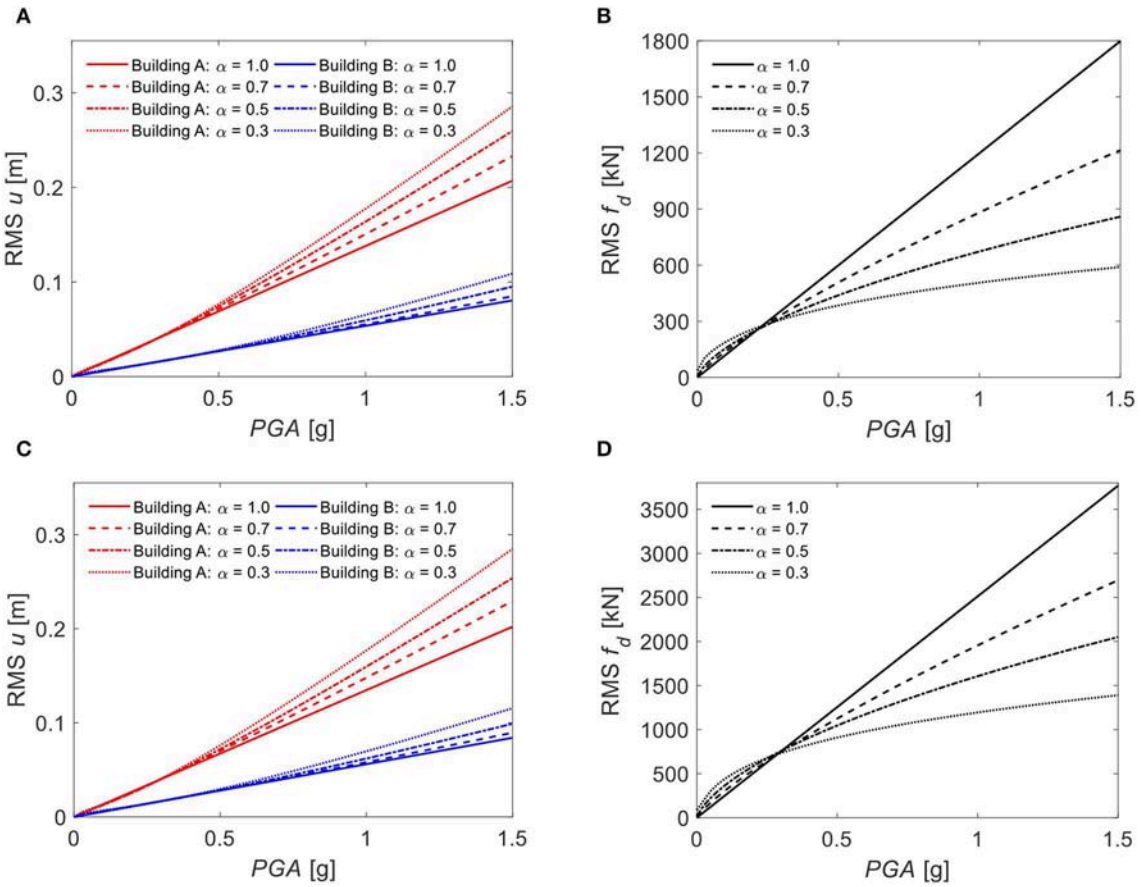

FIGURE 11 | RMS response for increasing seismic intensities: **(A)** top-floor displacement of building A and B (uniform dampers case), **(B)** 4th floor damper force (uniform dampers case), **(C)** top-floor displacement of building A and B (single damper case), **(D)** 4th floor damper force (single damper case).

base acceleration. Among the possible damper arrangements consistent to the target amount of added damping, two limit configurations are analyzed, consisting of: a uniform distribution along the height; a single damper at the last elevation of the shorter building. The performance of the coupled system is investigated by considering different response parameters including buildings' displacements and accelerations as well as dampers' forces.

The outcomes of this study show that the reduced order model provides accurate estimates of the building displacement response and of the damper forces for a wide range of damper properties. Its accuracy slightly decreases for increasing values of the viscous constants.

For what concerns the use of linear dampers, the following conclusions can be drawn:

- The use of dampers to connect the adjacent buildings can improve significantly the performance of both the buildings.
- An optimal value of the damping constant exists for both the buildings and minimizes the displacement response.
- The dampers force always increases for increasing values of the viscous constant, although the relative velocities between the two buildings reduce. The increase of the root mean square force is less than linear for both the cases of uniform dampers and single damper.
- Linear viscous dampers are more effective in damping the displacement response for seismic intensities higher than the reference seismic intensity, at the expense of significantly increased damper forces.

For what concerns the use of non-linear devices, it is concluded that:

- The configuration with a single damper placed at the fourth floor provides forces that are notably lower than the sum of the forces of the fourth viscous damper employed in the alternative arrangement. This result has important effects on the optimization of the costs associated to the retrofit of adjacent buildings with viscous dampers.
- The optimal damper viscous constant reduces significantly for decreasing α values and the displacement response in correspondence of the optimal damper constant value are insensitive to the exponent α. Thus, an appropriate calibration of the non-linear dampers provides the same performance in terms of seismic response reduction as for the case with linear devices.

To conclude, it is worth noting that the proposed damper design method is valid for a wide range of ω_B/ω_A ratios, however the results presented in this study may quantitatively change by varying the features of the buildings. More

precisely, the efficiency of the coupling strategy diminishes for systems with similar fundamental vibration periods, because of the in-phase dynamic motion experienced by the buildings.

Future developments of this work should also aim to assess the effectiveness of the dynamic coupling for mitigating seismic pounding hazard.

DATA AVAILABILITY STATEMENT

The datasets generated for this study are available on request to the corresponding author.

AUTHOR CONTRIBUTIONS

ET, LG, FS, LR, and AD wrote the formulation of the problem, performed the numerical analyses and processed the analytical results. All authors have contributed to the manuscript revision, read and approved the submitted version.

SUPPLEMENTARY MATERIAL

The Supplementary Material for this article can be found online at: https://www.frontiersin.org/articles/10.3389/fbuil.2020.00025/full#supplementary-material

REFERENCES

Abdeddaim, M., Ounis, A., Djedoui, N., and Shrimali, M. K. (2016). Pounding hazard mitigation between adjacent planar buildings using coupling strategy. *J. Civil Struct. Health Monit.* 6, 603–617. doi: 10.1007/s13349-016-0177-4

Aida, T., Aso, T., Takeshita, K., Takiuchi, T., and Fuji, T. (2001). Improvement of the structure damping performance by interconnection. *J Sound Vibration* 242, 333–53. doi: 10.1006/jsvi.2000.3349

Altieri, D., Tubaldi, E., De Angelis, M., Patelli, E., and Dall'Asta, A. (2018). Reliability-based optimal design of nonlinear viscous dampers for the seismic protection of structural systems. *Bull. Earthquake Eng.* 16, 963–982. doi: 10.1007/s10518-017-0233-4

Basili, M., and De Angelis, M. (2007a). Optimal passive control of adjacent structures interconnected with nonlinear hysteretic devices. *J. Sound Vibration* 301, 106–125. doi: 10.1016/j.jsv.2006.09.027

Basili, M., and De Angelis, M. (2007b). A reduced order model for optimal design of 2-mdof adjacent structures connected by hysteretic dampers. *J Sound Vibration* 306, 297–317. doi: 10.1016/j.jsv.2007.05.012

Bhaskararao, A. V., and Jangid, R. S. (2007). Optimum viscous damper for connecting adjacent SDOF structures for harmonic and stationary white-noise random excitations. *Earthquake Eng. Struct. Dyn.* 36, 563–571. doi: 10.1002/eqe.636

Bigdeli, K., Hare, W., and Tesfamariam, S. (2012). Configuration optimization of dampers for adjacent buildings under seismic excitations. *Eng Optimization* 12, 1491–1509. doi: 10.1080/0305215X.2012.654788

Christopoulos, C., and Filiatrault, A. (2006). *Principles of Passive Supplemental Damping and Seismic Isolation*. IUSS Press, Pavia, Italy.

Cimellaro, G. P., and Lopez-Garcia, D. (2007). "Seismic response of adjacent buildings connected by nonlinear viscous dampers," in *Forensic Engineering Conference at Structures Congress* (Long Beach, CA).

Dall'Asta, A., Scozzese, F., Ragni, L., and Tubaldi, E. (2017). Effect of the damper property variability on the seismic reliability of linear systems equipped with viscous dampers. *Bull Earthquake Eng.* 15, 5025–5053. doi: 10.1007/s10518-017-0169-8

Dall'Asta, A., Tubaldi, E., and Ragni, L. (2016). Influence of the nonlinear behaviour of viscous dampers on the seismic demand hazard of building frames. *Earthquake* 45, 149–169. doi: 10.1002/eqe.2623

De Domenico, D., and Ricciardi, G. (2018). Improved stochastic linearization technique for structures with nonlinear viscous dampers. *Soil Dyn. Earthquake Eng.* 113, 1–818. doi: 10.1016/j.soildyn.2018.06.015

De Domenico, D., and Ricciardi, G. (2019). Earthquake protection of structures with nonlinear viscous dampers optimized through an energy-based stochastic approach. *Eng. Struct.* 179, 523–539. doi: 10.1016/j.engstruct.2018.09.076

Di Paola, M., La Mendola, L., and Navarra, G. (2007). Stochastic seismic analysis of structures with nonlinear viscous dampers. *J. Struct. Eng.* 133, 1475–1478. doi: 10.1061/(ASCE)0733-9445(2007)133:10(1475)

Di Paola, M., and Navarra, G. (2009). Stochastic seismic analysis of MDOF structures with nonlinear viscous dampers. *Struct. Control Health Monit.* 16, 303–318. doi: 10.1002/stc.254

Gioiella, L., Tubaldi, E., Gara, F., Dezi, L., and Dall'Asta, A. (2018a). Modal properties and seismic behaviour of buildings equipped with external dissipative pinned rocking braced frames. *Eng. Struct.* 172, 432–439. doi: 10.1016/j.engstruct.2018.06.043

Gioiella, L., Tubaldi, E., Gara, F., Dezi, L., and Dall'Asta, A. (2018b). Stochastic seismic analysis and comparison of alternative external dissipative systems. *Shock Vibrations* 47:5403737. doi: 10.1155/2018/5403737

Hwang, J. S., Wang, S. J., Huang, Y. N., and Chen, J. F. (2007). A seismic retrofit method by connecting viscous dampers for microelectronics factories. *Earth Eng. Struct. Dyn.* 36, 1461–1480. doi: 10.1002/eqe.689

Impollonia, N., and Palmeri, A. (2018). Seismic performance of buildings retrofitted with nonlinear viscous dampers and adjacent reaction towers. *Earthquake Eng. Struct. Dyn.* 47, 1329–1351. doi: 10.1002/eqe.3020

Kanai, K. (1957). Semi-empirical formula for the seismic characteristics of the ground motion. *Bull. Earthq. Res. Inst. Univ.* 35, 309–325.

Karabork, T., and Aydin, E. (2019). Optimum design of viscous dampers to prevent pounding of adjacent structures. *Earthquakes Struct.* 16, 437–453. doi: 10.12989/eas.2019.16.4.437

Kim, K., Rye, J., and Chung, L. (2006). Seismic performance of structures connected by viscoelastic dampers. *Eng. Struct.* 28, 83–195. doi: 10.1016/j.engstruct.2005.05.014

Lavan, O., and Avishur, M. (2013). Seismic behavior of viscously damped yielding frames under structural and damping uncertainties. *Bull. Earthquake Eng.* 11, 2309–2332. doi: 10.1007/s10518-013-9479-7

Lin, W.-H., and Chopra, A. K. (2002). Earthquake response of elastic SDF systems with non-linear fluid viscous dampers. *Earthquake Eng. Struct. Dyn.* 31, 1623–1642. doi: 10.1002/eqe.179

Luco, J. E., and De Barros, F. C. P. (1998). Optimal damping between two adjacent elastic structures. *Earthquake Eng. Struct. Dyn.* 27, 649–659. doi: 10.1002/(SICI)1096-9845(199807)27:7<649::AID-EQE748>3.0.CO;2-5

Ni, Y. Q., Ko, J. M., and Ying, Z. G. (2001). Random seismic response analysis of adjacent buildings coupled with non-linear hysteretic dampers. *J. Sound Vib.* 26, 403–417. doi: 10.1006/jsvi.2001.3679

Ok, S., Song, J., and Park, K. (2008). Optimal design of hysteretic dampers connecting adjacent structures using multiobjective genetic algorithm and stochastic linearization method. *Eng. Struct.* 30, 1240–1249. doi: 10.1016/j.engstruct.2007.07.019

Pekcan, G., Mander, J. B., and Chen, S. S. (1999). "Fundamental considerations for the design of nonlinear viscous dampers. *Earthquake Eng. Struct. Dyn.* 28, 1405–1425. doi: 10.1002/(SICI)1096-9845(199911)28:11<1405::AID-EQE875>3.0.CO;2-A

Reggio, A., Restuccia, L., Martelli, L., and Ferro, G. A. (2019). Seismic performance of exoskeleton structures. *Eng. Struct.* 198. doi: 10.1016/j.engstruct.2019.109459

Richardson, A., Walsh, K. K., and Abdullah, M. M. (2012). Closed-form equations for coupling linear structures using stiffness and damping elements. *Struct. Control Health Monit.* 20, 259–281. doi: 10.1002/stc.490

Roh, H., Cimellaro, G. P., and Lopez-Garcia, D. (2011). Seismic response of adjacent steel structures connected by passive device. *Adv. Struct. Eng.* 14, 499–517. doi: 10.1260/1369-4332.14.3.499

Rüdinger, F. (2006). Optimal vibration absorber with nonlinear viscous power law damping and white noise excitation. *J. Eng. Mech*. 132, 46–53. doi: 10.1061/(ASCE)0733-9399(2006)132:1(46)

Rudinger, F. (2007). Tuned mass damper with nonlinear viscous damping. *J. Sound Vibrat.* 300, 932–948. doi: 10.1016/j.jsv.2006.09.009

Rüdinger, F., and Krenk, S. (2003). Spectral density of an oscillator with power law damping excited by white noise. *J. Sound Vib*. 261, 365–371. doi: 10.1016/S0022-460X(02)01183-5

Scozzese, F., Dall'Asta, A., and Tubaldi, E. (2019). Seismic risk sensitivity of structures equipped with anti-seismic devices with uncertain properties. *Struct. Safety* 77, 30–47. doi: 10.1016/j.strusafe.2018.10.003

Sivandi-Pour, A., Gerami, M., and Kheyroddin, A. (2015). Determination of modal damping ratios for non-classically damped rehabilitated steel structures. *Iranian J. Sci. Tech.* 39:81. doi: 10.1007/s40999-016-0003-8

Sivandi-Pour, A., Gerami, M., and Khodayarnezhad, D. (2014). Equivalent modal damping ratios for non-classically damped hybrid steel concrete buildings with transitional storey. *Struct. Eng. Mech.* 50, 383–401. doi: 10.12989/sem.2014.50.3.383

Soong, T. T., and Spencer, B. F. (2002). Supplemental energy dissipation: state-of-the-art and state-of-the-practice. *Eng. Struct.* 24, 243–259. doi: 10.1016/S0141-0296(01)00092-X

Sorace, S., and Terenzi, G. (2013). Damped interconnection-based mitigation of seismic pounding between adjacent R/C buildings. *Int. J. Eng. Tech.* 5, 406–412. doi: 10.7763/IJET.2013.V5.585

Symans, M. D., and Constantiou, M. C. (1998). Passive fluid viscous damping systems for seismic energy dissipation. *ISET J. Earthquake Tech.* 35, 185–206.

Tajimi, H. (1960). "A statistical method of determining the maximum response of a building structure during an earthquake," in *Proceedings of the 2nd WCEE, II* (Tokyo: Science Council of Japan), 781–798.

Takewaki, I. (2009). *Building Control With Passive Dampers: Optimal Performance-Based Design for Earthquakes*. Singapore: John Wiley & Sons.

Trombetti, T., and Silvestri, S. (2004). Added viscous dampers in shear-type structures: the effectiveness of mass proportional damping. *J. Earthquake Eng.* 8, 275–313. doi: 10.1080/13632460409350490

Tubaldi, E. (2015). Dynamic behavior of adjacent buildings connected by linear viscous/viscoelastic dampers. *Struct. Control Health Monit.* 22, 1086–1102. doi: 10.1002/stc.1734

Tubaldi, E., Barbato, M., and Dall'Asta, A. (2014). Performance-based seismic risk assessment for buildings equipped with linear and nonlinear viscous dampers. *Eng. Structures* 78, 90–99. doi: 10.1016/j.engstruct.2014.04.052

Tubaldi, E., Barbato, M., and Ghazizadeh, S. A. (2012). Probabilistic performance-based risk assessment approach for seismic pounding with efficient application to linear systems. *Structural Safety* 36–37:14–22. doi: 10.1016/j.strusafe.2012.01.002

Tubaldi, E., and Kougioumtzoglou, I. A. (2015). Nonstationary stochastic response of structural systems equipped with nonlinear viscous dampers under seismic excitation. *Earthquake Eng. Struct. Dyn.* 44, 121–138. doi: 10.1002/eqe.2462

Tubaldi, E., Ragni, L., and Dall'Asta, A. (2015). Probabilistic seismic response assessment of linear systems equipped with nonlinear viscous dampers. *Earthquake Eng. Struct. Dyn.* 44, 101–120. doi: 10.1002/eqe.2461

Xu, Y. L., He, Q., and Ko, J. M. (1999). Dynamic response of damper-connected adjacent buildings under earthquake excitation. *Eng. Struct.* 21, 135–48. doi: 10.1016/S0141-0296(97)00154-5

Zhang, W. S., and Xu, Y. L. (1999). Dynamic characteristics and seismic response of adjacent buildings linked by discrete dampers. *Earth Eng. Struct. Dyn.* 28, 1163–1185. doi: 10.1002/(SICI)1096-9845(199910)28:10<1163::AID-EQE860>3.0.CO;2-0

Zhu, H., Ge, D., and Huang, X. (2010). Optimum connecting dampers to reduce the seismic responses of parallel structures. *J. Sound Vibration* 330, 1931–1949. doi: 10.1016/j.jsv.2010.11.016

Zhu, H. P., and Iemura, H. (2000). A study of response control on the passive coupling element between parallel structures. *Struct. Eng. Mech.* 9, 383–396. doi: 10.12989/sem.2000.9.4.383

Zhu, H. P., and Xu, Y. L. (2005). Optimum parameters of Maxwell model-defined dampers used to link adjacent structures. *J. Sound Vibration* 279, 253–274. doi: 10.1016/j.jsv.2003.10.035

Conflict of Interest: The authors declare that the research was conducted in the absence of any commercial or financial relationships that could be construed as a potential conflict of interest.

frontiers in Built Environment

ORIGINAL RESEARCH
published: 03 April 2020
doi: 10.3389/fbuil.2020.00033

Experimental Assessment of the Seismic Response of a Base-Isolated Building Through a Hybrid Simulation Technique

Marco Furinghetti[1,2]*, *Igor Lanese*[2] *and Alberto Pavese*[1]

[1] *Department of Civil Engineering and Architecture, University of Pavia, Pavia, Italy,* [2] *European Centre for Training and Research in Earthquake Engineering, EUCENTRE, Pavia, Italy*

Base-isolated structural systems have been more and more investigated through both numerical and experimental campaigns, in order to evaluate their effective advantages, in terms of vulnerability reduction. Thanks to the lateral response of proper isolation devices, large displacement demands can be accommodated, and the overall energy of the seismic event can be dissipated, by means of hysteretic behaviors. Among the common typologies of isolators, curved surface slider devices represent a special technologic solution, with potentially high dissipative capacities, provided by innovative sliding materials. On the other hand, the overall behavior is highly non-linear, and a number of research works have been developed, aiming at the definition of the most comprehensive analytical model of such devices. The most realistic response of a base-isolated structure could be returned by a shake table test of a full-scale building. However, dimensions of the available shake tables do not allow consideration of the common load conditions, to which the isolation devices are subjected, and consequently, scaled specimens are needed, and unrealistic responses could be found. Hybrid simulations seem to solve such an issue, by accounting for an experimental substructuring, represented by a physical device tested in a testing equipment, and a numerical substructuring, consisting of a numerical model of the superstructure. Thus, a much more realistic response of the full-scale structure can be computed. In this work, the outcomes of a number of hybrid simulations have been deeply analyzed and compared to a similar numerical model. Proper non-linear constitutive laws for isolation devices have been adopted, in order to evaluate the effectiveness of design and assessment procedures, commonly adopted in real-practice applications.

Keywords: hybrid testing, base isolation, curved surface slider devices, friction coefficient, numerical and experimental substructuring

OPEN ACCESS

Edited by:
Izuru Takewaki,
Kyoto University, Japan

Reviewed by:
Giacomo Navarra,
Kore University of Enna, Italy
Fabrizio Paolacci,
Roma Tre University, Italy

***Correspondence:**
Marco Furinghetti
marco.furinghetti@unipv.it

Specialty section:
This article was submitted to Earthquake Engineering, a section of the journal Frontiers in Built Environment

Received: *13 December 2019*
Accepted: *06 March 2020*
Published: *03 April 2020*

Citation:
Furinghetti M, Lanese I and Pavese A (2020) Experimental Assessment of the Seismic Response of a Base-Isolated Building Through a Hybrid Simulation Technique. Front. Built Environ. 6:33. doi: 10.3389/fbuil.2020.00033

INTRODUCTION

Experimental testing has been always a fundamental aspect of the validation process, particularly in cases in which the structural or non-structural components under investigation show a complex non-linear dynamic behavior. Among the available experimental techniques, dynamic hybrid testing with substructuring has been identified by the authors as the most suitable testing technique

because of research peculiarities. Hybrid testing, also often referred to as hybrid simulation, or hardware-in-the-loop in mechanical and automotive fields, is one of the most advanced testing techniques, nowadays well known and recognized as a powerful and cost-effective investigation option (Pegon and Pinto, 2000; Pegon and Magonette, 2002; Calabrese et al., 2015; Bursi et al., 2017). Such a technique finds its roots in the pseudo-dynamic testing technique introduced in the late 1960s by Japanese researchers (Hakuno et al., 1969), with the aim of taking advantage of both the numerical simulation and experimental testing capabilities. Within this framework, the structure or component under investigation is split into a numerical subsystem (NS) and a complementary experimentally tested physical subsystem (PS). While NS is characterized by a well-known behavior (e.g., the deck of a bridge expected to remain in the elastic range), PS is constituted by one or more elements in which uncertainties in the numerical modeling might be relevant (e.g., elements characterized by brittle and non-linear response and rate-dependent behavior such as friction). Since the complex part of the structure is physically tested in the laboratory, an explicit model of PS is not required, thus simplifying in this respect the investigation complexity. Furthermore, since the PS to be tested is only a portion of the entire structure under investigation, a bigger and often a full-scale specimen can be considered; consequently, typical compliance problems of shake table tests of big structures can be solved, by avoiding at the same time the distortions due to geometry scaling.

The test execution time rate is a key point in hybrid testing; it differentiates between pseudo-dynamic, fast, and real-time testing, with strong influence on the achievable results. A very slow test execution, with a time scale factor of the order of $\lambda = 200$, can be considered for non-rate-dependent structures, such as steel or masonry partitions, in case relaxation and creep phenomena are not relevant. On the other hand, a real-time test execution should be considered when the PS is strictly rate dependent, which is typically the case of fluid viscous dampers, liquid-Tuned Mass Dampers (TMDs), etc. In between, the test execution can be somehow dynamic but slower than real time, which can be a suitable option for many applications, including base isolation devices (Lanese, 2012; Lanese et al., 2018).

While the combination of both numerical simulation and experimental testing capabilities is very appealing from the effectiveness and achievable results points of view, such combination produces a complex and heterogeneous environment. An effective management of the test definition, implementation, and execution requires good multidisciplinary knowledge and skills of numerical simulation, signal processing, actuation and mechanical systems control. In addition, further crucial aspects derive from the combination of such different environments, for example, the treatment of noisy experimental signals in a numerical model and in a solving algorithm that might result in progressive undesired oscillations and unstable overall response.

The algorithm managing the test execution and providing the step-by-step solution of the NS and computing the displacement increments to be applied to the PS must be necessarily different from typical methods used in pure numerical simulation. Among others, iterations cannot be considered to avoid spurious oscillation in the PS, stressing and damaging the physical specimen out of the real structural behavior meant to be represented.

A partitioned method (PM) suitable to treat and couple different sub-domains, thus fitting the hybrid simulation needs, was developed by Pegon and Magonette (2002). The method was developed starting from the well-known GC method (Gravouil and Combescure, 2001), while the operations sequence has been modified to allow for a parallel-tasks execution. Two separated parallel processes, obtained through the introduction of a forward prediction, are then carried out for NS and PS, while at each so-called coarse time step, the two sub-domains are coupled. This separation allows for an independent-tasks execution; a different time step can be considered for the PS and NS; this is often desirable since the PS needs a continuous test execution at the facility digital controller rate – typically about 1 kHz – while the NS, possibly complex and non-linear, likely needs a larger time step to provide the step-by-step solution. While a numerical model of the PS is not required, an estimation of the initial stiffness of the PS matrix is needed to implement an explicit Newmark scheme, while the numerical part is treated with a semi-implicit approach. Bonelli et al. (2008) investigated the convergence and stability characteristics of the PM, while Bursi et al. (2010) proposed an enhanced variant, that is, the PM-α, that enables the coupling of arbitrary generalized-α (G-α) schemes endowed with numerical dissipation.

In order to ensure a correct implementation through the hybrid testing technique, all critical aspects coming from both numerical and experimental sides and from their combination need to be addressed, together with a reliable implementation of proper boundary conditions at the interface between NS and PS and, finally, a robust strategy for the verification of the results reliability assessment.

In this work, a proper framework for the hybrid simulation of a base-isolated building has been defined, in order to compute the most realistic response of a case study structure, equipped with double-concave surface slider (DCSS) devices, when subjected to earthquake excitations. Outcomes have been compared to numerical results of non-linear time history analyses of single-degree-of-freedom (SDOF) and multiple-degrees-of-freedom (MDOF) oscillators, together with reference values returned by equivalent linear elastic analyses, which represent the most used design and assessment procedures in the common practice.

CASE STUDY STRUCTURE

The case study structure consists of a six-story reinforced concrete frame building, as shown in **Figure 1**: the present structural system has been deeply analyzed in recent research works, by designing all members according to Italian code-conforming provisions (D.M. 17/01/2018, 2018; Cardone et al., 2017). Plan dimensions are approximately 21 and 12 m for x and y directions, respectively, and the interstory height is 3.05 m for all the floors, but the ground one, which has a height of 3.4 m; consequently, the total height of the building is equal to 19 m.

FIGURE 1 | Case study structure.

For each floor of the building, a seismic mass approximately equal to 300 tons can be considered, with a total value of 2,080 tons. According to the implemented cross sections of both beams and columns and the mass properties, the first mode of vibration of the structure is represented by a period around 1.0 s. Modal characteristics have been deeply studied in the next sections, for the definition of the numerical substructuring of the hybrid testing framework.

DEFINITION OF THE SEISMIC INPUT

Hybrid simulations presented in this research work have been performed, by considering seven unidirectional natural seismic events (Iervolino et al., 2009; Furinghetti and Pavese, 2017). As ruled by the Italian Building Code (D.M. 17/01/2018, 2018), records have been selected according to the seismic hazard level defined for the construction site: precisely, L'Aquila has been considered as a reference location, with soil class C and topography category T1. The collapse limit state has been assumed, which corresponds to 5% probability of exceedance in the reference life of the structural system, equal to 50 years (return period 975 years). Spectrum compatibility has been checked: lower and upper bounds for the mean spectrum of the selected events have been defined according to 90 and 130%, respectively, of the code design spectrum and a period range within 0.15 and 3.0 s has been considered. Individual ground motion records have been scaled, in order to better achieve spectrum-compatibility prescriptions; moreover, scale factors have been bounded between 0.5 and 2.0, aiming at preserving the correct frequency content for the considered peak ground acceleration (PGA) values. In **Table 1**, all the selected records are listed, together with the main characteristics of the considered earthquakes.

In **Figure 2**, results of the spectrum-compatibility check are shown, in terms of individual and mean response spectra, in comparison to the target and lower- and upper-bound graphs.

It can be noted that all the individual response spectra are significantly close to the target one: consequently, the mean spectrum fairly represents the seismic hazard level of the considered construction site.

DEFINITION OF THE HYBRID TESTING FRAMEWORK

In this section, the framework for the hybrid simulations of the case study structure is defined. Precisely, the reinforced concrete frame structure has been numerically implemented, by considering the actual stiffness and mass matrices of a full three-dimensional finite element model (FEM). The base isolation system is represented through a single physical full-scale device, which is representative of the whole set of isolators: accordingly, all isolators are assumed to be subjected to the same average vertical load, which can be computed as the total weight of the structure divided by the number of bearings, and to purely translational motion, by neglecting torsional movements of the superstructure.

Experimental Substructuring

All the hybrid simulations have been performed at the Laboratory of the EUCENTRE Foundation in Pavia (Italy) (Peloso et al., 2012). For the implementation of the experimental substructuring, the bearing tester system has been used, in order to apply and monitor the response of the full-scale physical device, which represents the whole isolation system of the case study structure. In **Figure 3**, the testing setup is shown.

The device is installed on a sliding bench, which applies the unidirectional translational motion, by means of two horizontal actuators. The vertical load is applied by dynamic actuators, located underneath the sliding bench, thanks to the reaction arch, which provides vertical restraint conditions. The whole testing system is governed by the laboratory hydraulic system, which consists of eight hydraulic power supply units (total flow capacity: 1,360 l pm) with 280-bar working pressure and of five accumulators banks, each one with two 45-L piston accumulators and six 30-L gas bottles for a total piston accumulator volume of 450 L and a total bottle volume of 900 L.

The device consists of a DCSS isolator (Fenz and Constantinou, 2006; De Domenico et al., 2018), with an internal non-articulated slider. Both the sliding surfaces have the same radius of curvature (1,600 mm), and the slider height is equal to 120 mm: thus, the equivalent radius of curvature results to 3,080 mm. The implemented circular sliding pads have a diameter equal to 160 mm, and the maximum displacement capacity is equal to 325 mm (**Figure 4**).

In order to define the vertical load to be applied at the tested device, the average reaction force has been computed, as the ratio between the total weight of the superstructure and the

TABLE 1 | Selection of natural events.

Event #	Station ID	Earthquake name	Date	Mw	Fault mechanism	Epicentral distance (km)	Original PGA (g)	Scaled PGA (g)	Scale factor (#)
1	ST164(x)	Kalamata	13/09/1986	5.9	Normal	10.0	0.215	0.429	2.00
2	ST163(x)	Kalamata	13/09/1986	5.9	Normal	11.0	0.240	0.479	2.00
3	ST271(y)	Dinar	01/10/1995	6.4	Normal	8.0	0.319	0.404	1.27
4	ST561(x)	Izmit	17/08/1999	7.6	Strike-slip	47.0	0.238	0.475	2.00
5	EC04(y)	Imperial Valley	15/10/1979	6.5	Strike-slip	27.0	0.485	0.485	1.00
6	EC05(y)	Imperial Valley	15/10/1979	6.5	Strike-slip	27.7	0.519	0.519	1.00
7	ERZ(x)	Erzincan	13/03/1992	6.6	Strike-slip	9.0	0.495	0.446	0.90

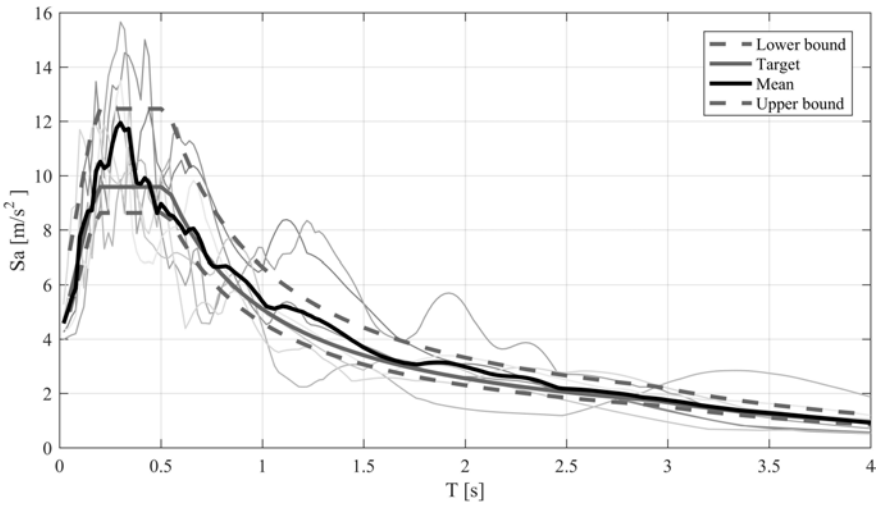

FIGURE 2 | Spectrum-compatibility graphical results.

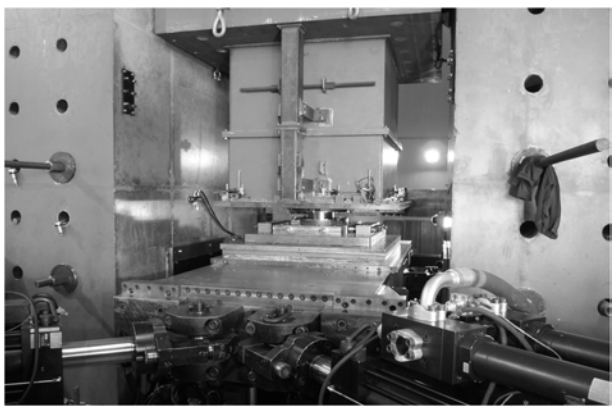

FIGURE 3 | Testing setup of the Bearing Tester System at the EUCENTRE Foundation.

number of bearings: hence with the total mass of the building at 2,080 tons and given 24 structural bearings, a vertical load of 850 kN has been computed, corresponding to 43 MPa of average contact pressure. The sliding pad consists of an innovative graded polytetrafluoroethylene (PTFE) material, filled with carbon fibers (Furinghetti et al., 2019a).

Firstly, frictional properties have been investigated, for a correct evaluation of the displacement demand of the isolation system and a correct definition of the time scale of the hybrid simulation (Mosqueda et al., 2004; Lomiento et al., 2013; Quaglini et al., 2014; Kumar et al., 2015; CEN, 2018). To this aim, dynamic tests have been performed on the device, by applying sinusoidal horizontal displacement time series with different frequencies (i.e., peak velocities), with a maximum displacement equal to 150 mm and the previously described average vertical load (850 kN). The considered velocity levels are 2.5, 10, 50, and 150 mm/s; tests at 10 and 50 mm/s have been carried out two times, in order to assess the repeatability of the computed friction properties. In **Figure 4**, the resulting characterization curve is reported, together with a best-fit curve, according to the most common analytical expression of the velocity effect for PTFE-based materials (Constantinou et al., 1990; Dolce et al., 2005; Furinghetti et al., 2019a).

As expected for PTFE-based materials, the friction coefficient value achieves an asymptotic value (8.6%) if 50 mm/s velocity

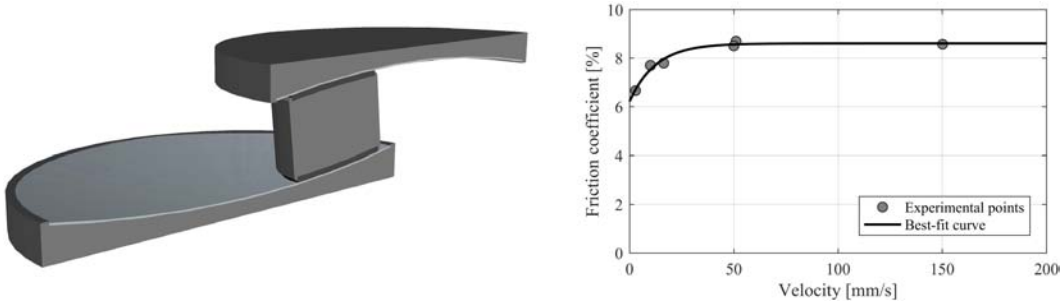

FIGURE 4 | Tested isolator and frictional characterization curve.

is exceeded. Repeated tests have provided experimental points aligned with respect to the best-fit characterization curve. Since hybrid simulations have to be carried out according to a scaled time axis and due to the just analyzed velocity effect of frictional properties, the definition of the proper time scale (TS) represents an important issue, for the correct evaluation of the response of the overall system. To this aim, an equivalent linear elastic analysis has been carried out, by considering the target acceleration displacement response spectrum (ADRS) and an equivalent linear elastic SDOF, for the computation of the seismic demands of the isolation system, in terms of maximum displacement and velocity. Such an analysis consists of an iterative procedure: initially, a numerical value of the displacement demand D_{max} is guessed, and consequently, the SDOF oscillator is characterized, by computing the following:

- the secant period of the overall isolated system:

$$T_{sec} = 2\pi \sqrt{\frac{D_{max}}{g\left(\mu + \frac{D_{max}}{R_{eq}}\right)}}$$

- the equivalent viscous damping:

$$\xi_{eq} = \frac{2}{\pi} \cdot \frac{\mu}{\mu + \frac{D_{max}}{R_{eq}}}$$

- the damping scaling factor:

$$\eta = \sqrt{\frac{10}{5 + \xi_{eq}}}$$

- and the displacement spectral coordinate:

$$D_{max} = Sd\,(T_{sec}, \eta)$$

Convergence is reached when the initial guessed displacement value becomes fairly comparable to the spectral coordinate, within an assumed tolerance. The spectral coordinate is computed as a function of the secant period and the damping scaling factor η (with lower bound of 0.55), as ruled by the Italian Building Code (D.M. 17/01/2018, 2018).

All parameters depend on the mechanical properties of the isolation system, namely, the equivalent radius of curvature R_{eq} (3.08 m) and the friction coefficient μ: at a first stage, such a parameter has been assumed equal to the asymptotic value of the characterization curve (8.6%, corresponding to a velocity higher than 50 mm/s), in order to evaluate the maximum velocity demand (i.e., the spectral velocity at convergence), for the correct definition of the time scale. By considering all the aforementioned hypotheses, maximum displacement and velocity demands returned by the equivalent linear elastic analysis are, respectively, equal to 150 mm and 447 mm/s (secant period: 2.107 s, equivalent viscous damping: 40%). Thus, in order to obtain a similar frictional response in the hybrid tests, by providing simulations as close as possible to real time, a time scale factor equal to 8 has been assumed, which corresponds to 56 mm/s peak velocity (447 mm/s divided by 8). In addition, a second set of hybrid tests have been performed, aiming at computing the response of the isolated case study structure, by considering a lower coefficient of friction: to do so, a time scale equal to 32 has been assumed, which corresponds to 14 mm/s peak velocity and, consequently, to 7.8% of friction coefficient. In **Figure 5**, graphical results for equivalent linear elastic analyses are shown, for both time scale factors 32 and 8.

In **Table 2**, numerical results are summarized.

Both the analyses have returned approximately the same peak velocity: hence, the definition of time scale 32 can be considered in agreement with the assumed frictional properties. In addition, other response parameters look similar between the considered cases; thus, the provided results of hybrid simulations can be interpreted as the evaluation of the response of the same structural system, equipped with two individual sliding materials (even though different time scales are considered).

Numerical Substructuring

The superstructure has been numerically modeled within the hybrid simulation algorithm, by considering an MDOF oscillator. Precisely, at each story location of the building, a single horizontal translational degree of freedom has been defined, referred to as the ground location. Aiming at considering the same behavior of the 3-D FEM of the superstructure, an *ad hoc* static condensation procedure has been applied and a full stiffness matrix has been computed, and consequently, the effective contribution of each column and beam is taken into account (Chopra, 1995; Furinghetti et al., 2019b). Given the full 3-D model, the location

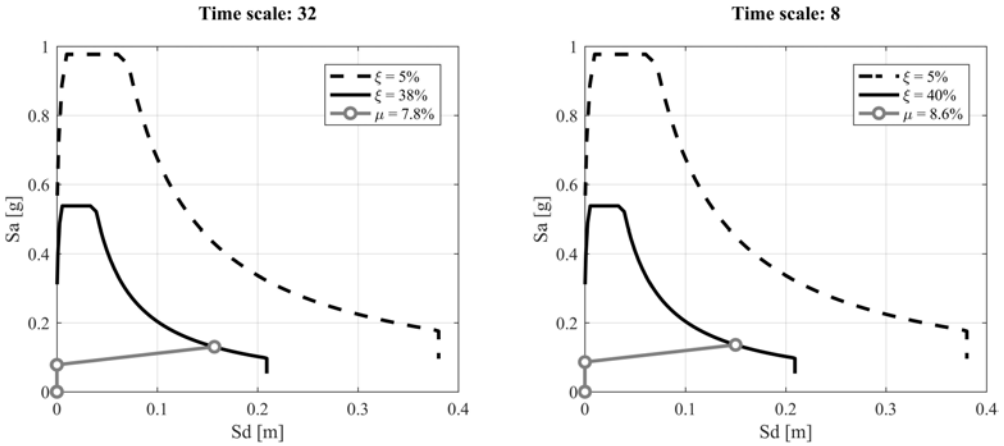

FIGURE 5 | Graphical results of equivalent linear elastic analyses.

TABLE 2 | Results of equivalent linear elastic analyses.

	D_{max} (m)	A_{max} (g)	ξ_{eq} (#)	T_{sec} (s)	V_{max} (m/s)
μ = 7.8%	0.157	0.130	38.1%	2.202	0.448
μ = 8.6%	0.150	0.136	40.3%	2.107	0.447

of the center of mass has been defined for all stories, and a master–slave strategy has been adopted, by applying a rigid diaphragm constraint to all structural points of the same floor. For the computation of the *i*th column of the stiffness matrix, a lumped horizontal force is applied to the center of mass of the *i*th floor, whereas all the other stories are restrained: numerical components are then obtained by dividing reaction forces by the horizontal displacement of the unrestrained floor.

Such a procedure allows consideration of the effective deformability of each story of the superstructure, from both the translational and torsional points of view, even though only translational degrees of freedom are considered: this is allowed, since the adopted concave surface slider devices generally reduce torsional effects in the response of the isolated superstructure. The resulting stiffness matrix consists of a full matrix, with no null components, far from an alternative definition of the commonly known three-diagonal matrix of a shear-type model. The mass diagonal matrix has been simply computed, by extracting for each level the assembled masses of all nodes of the considered story. In order to check the effectiveness of the proposed static condensation procedure, the modal analysis has been carried out on both the MDOF and the 3-D FEMs, by considering the fixed-base structure; results have been compared, in terms of vibration periods, modal participating mass ratios, and modal shapes. In **Table 3**, period and participating mass ratio values are listed for both models, whereas in **Figure 6**, modal shapes are analyzed.

As can be noted, modal analysis of the MDOF model have returned approximately the same values of both vibration periods and participating mass ratios of the 3-D FEM.

Also, modal shapes are approximately overlapped for all modes. The fifth and sixth modes only show small discrepancies between the compared modal shapes: nonetheless, participating mass ratios are very small, revealing a negligible contribution in the building seismic response.

Thus, the dynamic system implemented in the hybrid simulation algorithm can be expressed as follows:

$$\overline{\overline{M}} \cdot \begin{pmatrix} \ddot{u}_0 \\ \ddot{u}_1 \\ \ddot{u}_2 \\ \vdots \\ \ddot{u}_6 \end{pmatrix} + \overline{\overline{C}} \cdot \begin{pmatrix} \dot{u}_0 \\ \dot{u}_1 \\ \dot{u}_2 \\ \vdots \\ \dot{u}_6 \end{pmatrix} + \overline{\overline{K}} \cdot \begin{pmatrix} u_0 \\ u_1 \\ u_2 \\ \vdots \\ u_6 \end{pmatrix} + F_{is}^{exp} \cdot n_{is} \cdot \begin{pmatrix} 1 \\ 0 \\ 0 \\ \vdots \\ 0 \end{pmatrix} = -\overline{\overline{M}} \cdot \begin{pmatrix} 1 \\ 1 \\ 1 \\ \vdots \\ 1 \end{pmatrix} \cdot \ddot{x}_g$$

Where:

- $\overline{\overline{M}}$, $\overline{\overline{C}}$, and $\overline{\overline{K}}$ are the mass, damping, and stiffness matrices, respectively, of the whole base-isolated system;
- u_i is the relative translational degrees of freedom located at each level of the building with respect to the ground;
- $\ddot{x}_g$ is the considered ground motion;
- n_{is} is the number of implemented isolation bearings; and
- F_{is}^{exp} is the experimental force of the physical substructuring, that is, the DCSS device.

The damping matrix models a multimodal damping, with 5% for all vibration modes, and no damping for the first, second, and third modes. During the hybrid simulation, at each time

TABLE 3 | Modal analyses comparison: vibration periods and participating mass ratios.

	MDOF		FEM 3-D	
Mode #	***T* (s)**	**M_x (%)**	***T* (s)**	**M_x (%)**
1	0.976	82.8%	0.980	82.7%
2	0.319	11.0%	0.320	11.3%
3	0.181	3.7%	0.181	3.7%
4	0.122	1.3%	0.123	1.4%
5	0.094	0.7%	0.094	0.6%
6	0.075	0.6%	0.075	0.7%

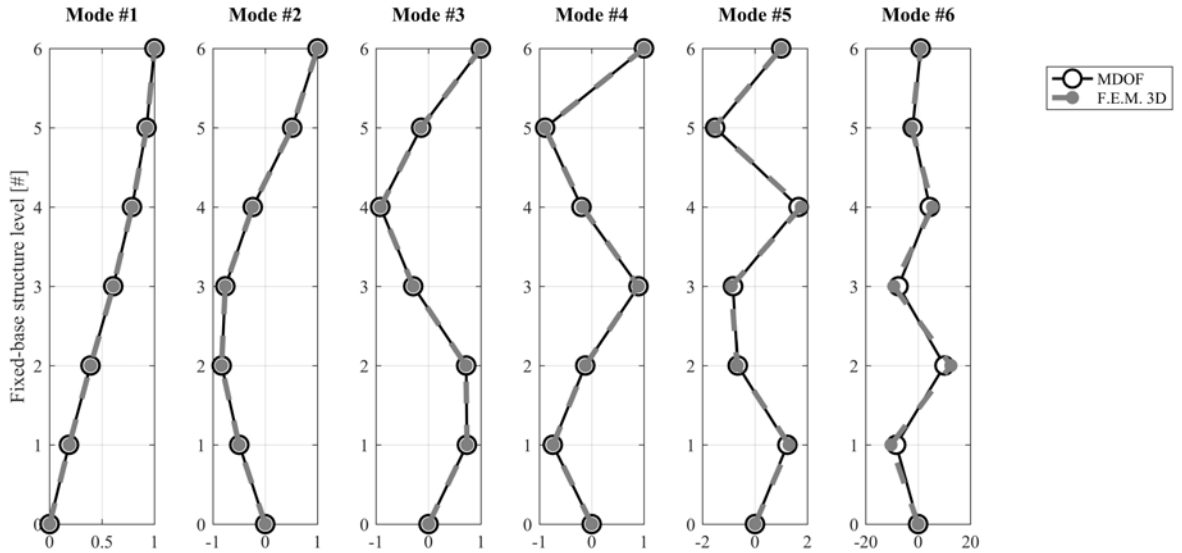

FIGURE 6 | Modal analyses comparison: modal shapes check.

step, u_0, which is the horizontal degree of freedom at the isolation level, represents the input displacement for the bearing tester system, which applies the proper deformed shape to the physical bearing: consequently, the recorded force of the full-scale tested device F_{is}^{exp} is used in the dynamic system for the computation of all degrees of freedom at all levels. According to the assumed modeling strategy, the single full-scale tested device is representative of the force response of the whole isolation system, through the proper scale factor n_{is} and by applying the average vertical load, due to static conditions. Even though this hypothesis seems to excessively simplify the overall dynamic system, reasonable results can be obtained for the considered case study structure. Precisely, in static conditions, vertical reactions have a limited variability among all the supporting points, with standard deviation of 180 kN, related to an average value of 850 kN; the adopted sliding pad diameter (160 mm) implies an average contact pressure of 43 MPa, with a consequent standard deviation of 9 MPa. Thus, the frictional response is not expected to vary among the isolators, since the implemented sliding material provides a reasonable stable value of friction coefficient at the considered contact pressure range of variation [34 ÷ 52 MPa (Furinghetti et al., 2019a)]. In addition, effects of the dynamic overturning moment generally lead to negligible variation of vertical loads at isolation devices (Pavese et al., 2019), and no vertical component of the selected seismic events have been considered.

RESULTS

In what follows, results of hybrid tests are analyzed, for both the considered time scale factors. Precisely, attention has been focused on the experimental hysteretic response, maximum displacement and velocity demands, dissipated energy of the isolation system, and interstory drift for all levels of the superstructure. Experimental outcomes are compared to the related quantities returned by the same MDOF model [eq. (1)], by implementing the isolation force response according to the following hysteretic rule:

$$F_{is}^{num} = W_{is}\left(\frac{u_0}{R_{eq}} + \mu\left(\frac{\dot{u}_0}{TS}\right)\cdot \tanh\left(\frac{\dot{u}_0}{v_s}\right)\right)$$

Where:

u_0 is the translational degree of freedom located at the isolation level;

W_{is} is the vertical load applied to the device (850 kN);

v_s is a hysteretic parameter which rules the slope of the friction coefficient trend at the transition at zero sliding velocity (the smaller the value, the sharper the transition); and

R_{eq} and $\mu\left(\frac{\dot{u}_0}{TS}\right)$ are the equivalent radius of curvature and the coefficient of fiction, respectively.

According to the characterization curve (**Figure 4**), the friction coefficient has been assumed as a function of the actual velocity of the simulation, that is, the numerical velocity divided by the considered time scale *TS*, aiming at comparing results related to the same frictional response.

In addition, performances of the isolation system have been compared also to the dynamic behavior of a non-linear SDOF oscillator, according to the following system:

$$M_{TOT} \cdot \ddot{u}_0 + F_{is}^{num} \cdot n_{is} = -M_{TOT} \cdot \ddot{x}_g$$

where M_{TOT} represents the total mass of the isolated system; the same modeling strategy of the isolation force of the MDOF system has been assumed.

Isolation Hysteretic Response

In **Figures 7**, **8**, hysteretic responses of the isolation system are shown, for time scales 32 and 8, respectively. Results are compared between hybrid simulations and numerical MDOF dynamic system integration.

All inclined horizontal lines are related to a given friction coefficient value, and the inclination is associated to the equivalent radius of curvature of the device (3.08 m): such a graphical representation of results allows analysis of the variation of the coefficient of friction during motion. It is possible to notice the velocity effect, that is, the common dependency of the friction coefficient on the sliding velocity of the simulation, which is represented by the real velocity value, divided by the time scale factor. Consequently, peak values of velocity are much lower than the real ones, and the transition phase between the slow and the fast friction coefficient parameters of the characterization curve can be better appreciated. In most cases, hysteretic loops of the purely numerical simulations fairly capture the hybrid experimental behavior of the isolation system, for both the considered time scale factors; the highest discrepancies can be detected for events #6 and #7, where the maximum displacement demand of the isolation level is overestimated by the numerical simulation. Thus, the adopted modeling strategy of the hysteretic response of the isolation system seems to lead to higher peak displacement values (maximum variation: approximately +30% for time scale 32), even though in most cases hysteretic loops are almost overlapped with an accurate prediction of the real experimental force response of the physical device.

Isolation System Peak Response Parameters

In **Figures 9–11**, the peak response of the isolation system has been analyzed, in terms of maximum values of displacement, velocity, and force, respectively. Results are provided by comparing the considered response parameters returned by the SDOF and MDOF numerical oscillators and the hybrid simulations for all events; in addition, mean values among the selected earthquakes have been highlighted, in order to assess the accuracy of the response predictions computed by the equivalent linear elastic analysis.

Concerning the displacement response, for time scales 32 and 8, the SDOF oscillator returns lower values, in comparison to both the MDOF model and the hybrid simulations, which look very similar, even though the MDOF model generally leads to higher displacement demands, as already noticed by analyzing hysteretic responses. On the other hand, if the mean value among the applied events is considered, both the numerical oscillators lead to significantly good results, especially for time scale 8. In addition, in all cases (SDOF, MDOF, and hybrid simulation), the mean displacement is lower than the reference value computed through the equivalent linear elastic analysis, according to the target spectrum provided by the standard code (approximately 150 mm): thanks to the lower bound of the damping reduction factor of both acceleration and displacement spectra, higher displacement values can be achieved, and a safe definition of the displacement capacity of isolation devices can be made.

The peak velocity response of the isolation system is fairly captured by the MDOF numerical oscillator, in comparison to the hybrid simulation, and in some cases, also the SDOF model leads to reasonably good results. In the hybrid simulation, the real peak velocity of the physical device is bounded between 10 and 24 mm/s for time scale 32 and between 45 and 96 mm/s for time scale 8: the assumed friction coefficients for the equivalent linear elastic analyses exactly correspond to average values of velocity in the aforementioned ranges. This results into a fairly good estimation of the mean peak sliding velocity among the selected events for all the simulations (numerical SDOF and MDOF and experimental hybrid simulations), in comparison the value returned by the equivalent linear elastic analysis for both the adopted time scale factors.

Finally, concerning the peak force responses, variability among the considered simulations, both numerical and experimental, is significantly lower, and approximately the same results can be found for the single-event and mean results. Even though the physical device provides a highly non-linear force response, such a behavior can be accurately described and modeled through the adopted numerical hysteretic constitutive law.

SUPERSTRUCTURE INTERSTORY DRIFT RESPONSE

In **Figure 12**, the peak interstory drift profile is shown for the single-event and mean responses of both numerical MDOF model and the experimental hybrid simulations, by considering time scales 32 and 8.

Numerical non-linear time history analyses of the MDOF model return approximately the same profiles of the hybrid simulation for both time scale factors. Mean profiles are represented by values approximately equal to 0.5%, which can be considered as an upper bound to ensure a linear elastic

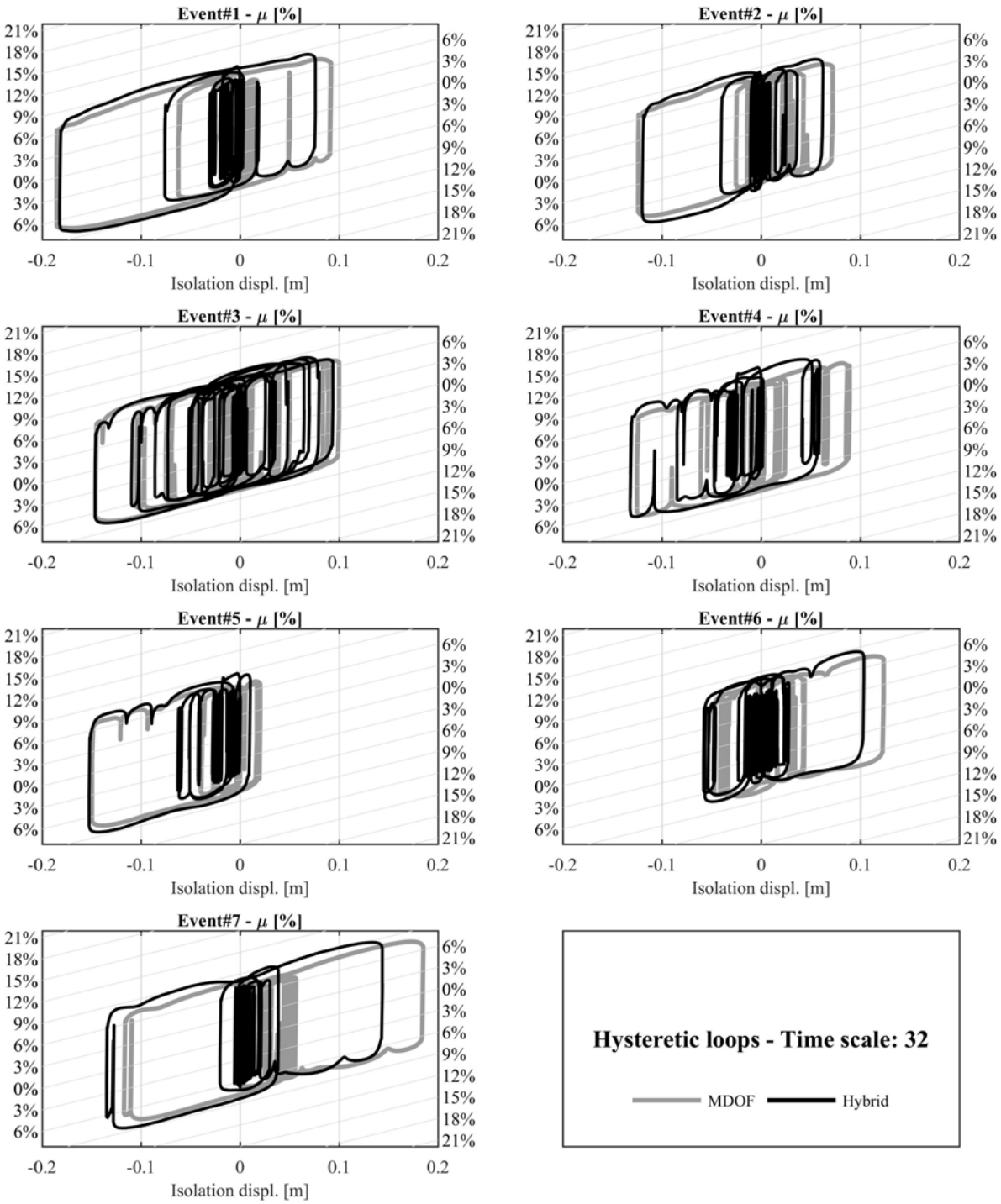

FIGURE 7 | Hysteretic response comparison—time scale 32.

behavior of the superstructure. Thus, also the overall behavior of the building in experimental hybrid simulations can be fairly approximated by assuming a proper non-linear constitutive law for the isolation level. Nonetheless, at some level of the superstructure, small variations can be detected.

CONCLUDING REMARKS

In this work, the experimental outcomes of hybrid earthquake simulations on a base-isolated building have been compared to results of purely numerical SDOF and MDOF oscillators,

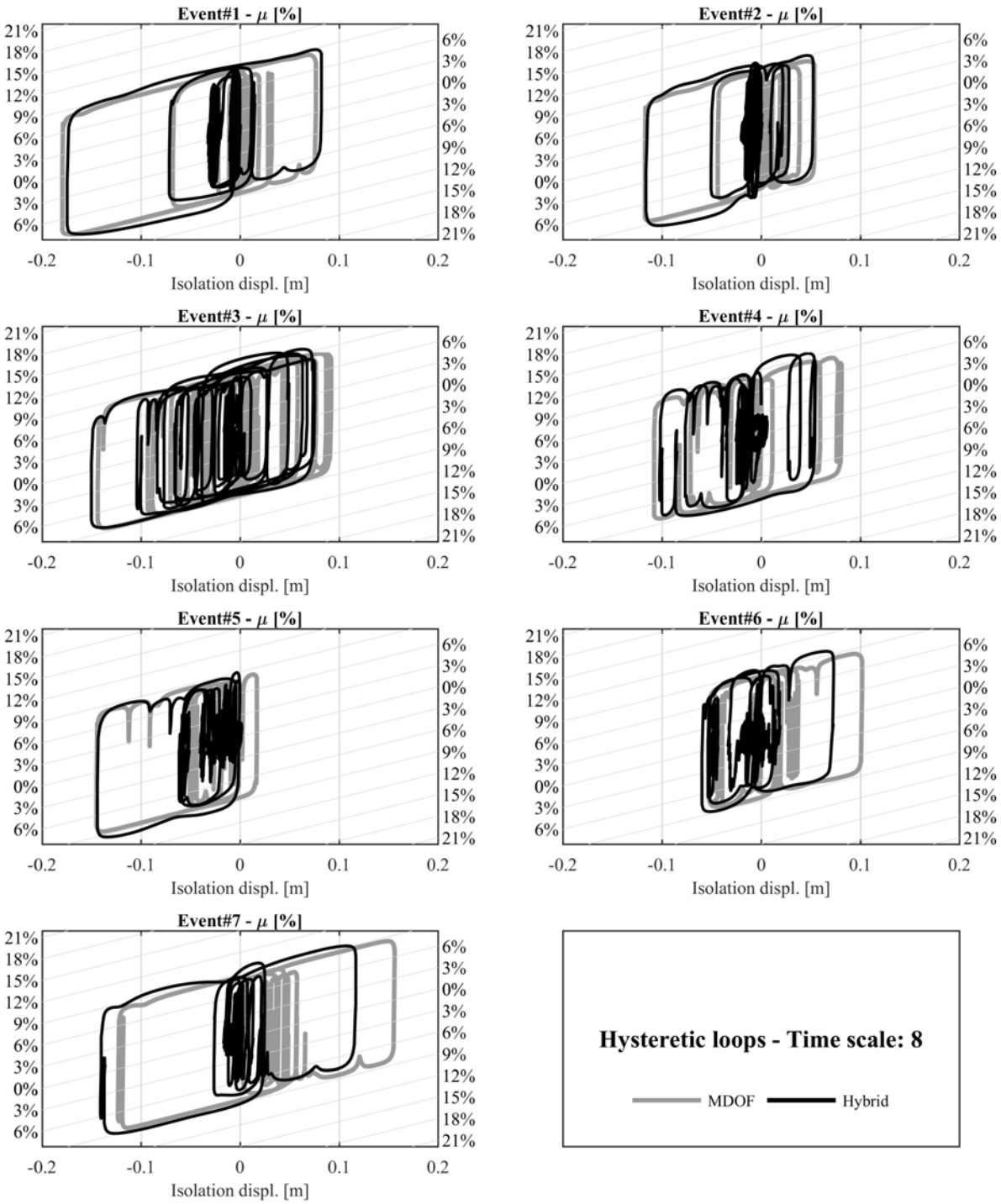

FIGURE 8 | Hysteretic response comparison—time scale 8.

which account for a proper non-linear constitutive law for the isolation system. Precisely, DCSS devices have been implemented for numerical simulations, whereas a physical device has been tested in the Bearing Tester System of the Laboratory of EUCENTRE Foundation in Pavia (Italy). Tests have been carried out with a selection of seven natural seismic events, and spectrum compatibility has been ensured, by reducing the single-event discrepancy, with respect to the target spectrum provided by the standard code. A number of improvement of hybrid testing strategies

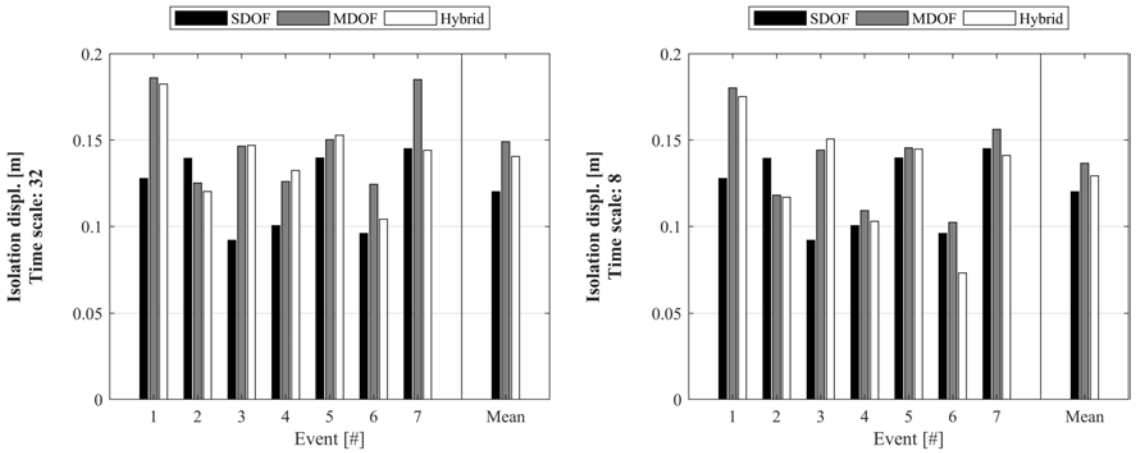

FIGURE 9 | Isolation displacement response—time scales 32 and 8.

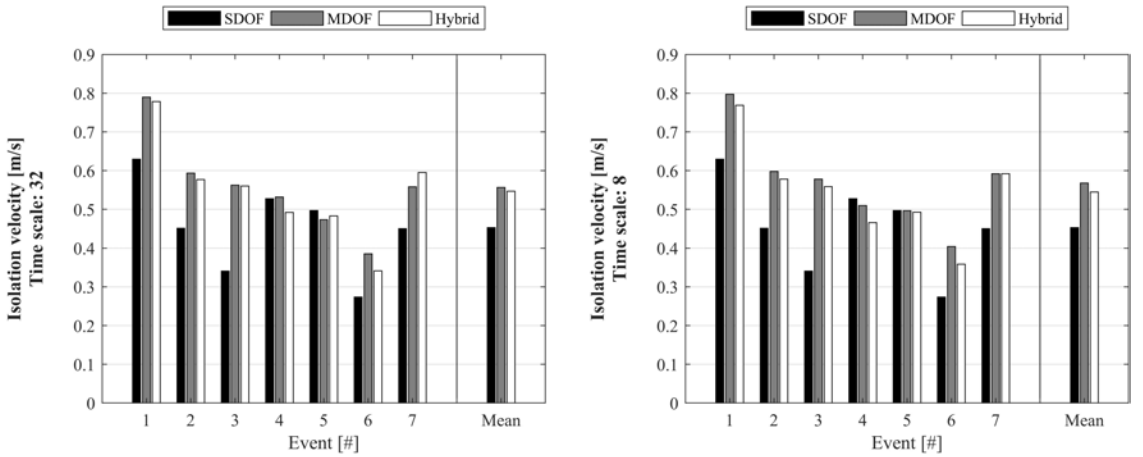

FIGURE 10 | Isolation velocity response—time scales 32 and 8.

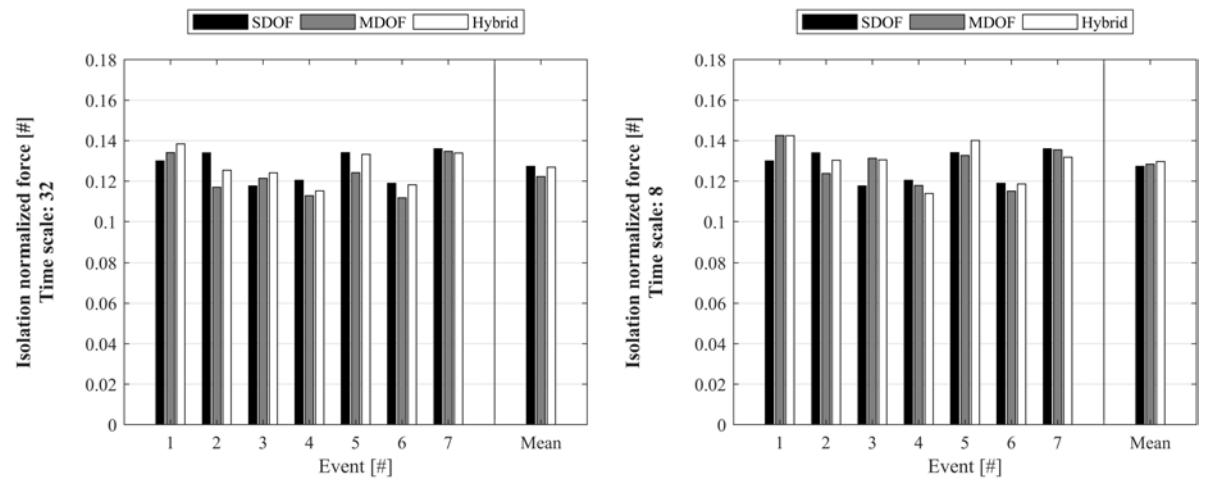

FIGURE 11 | Isolation force response—time scales 32 and 8.

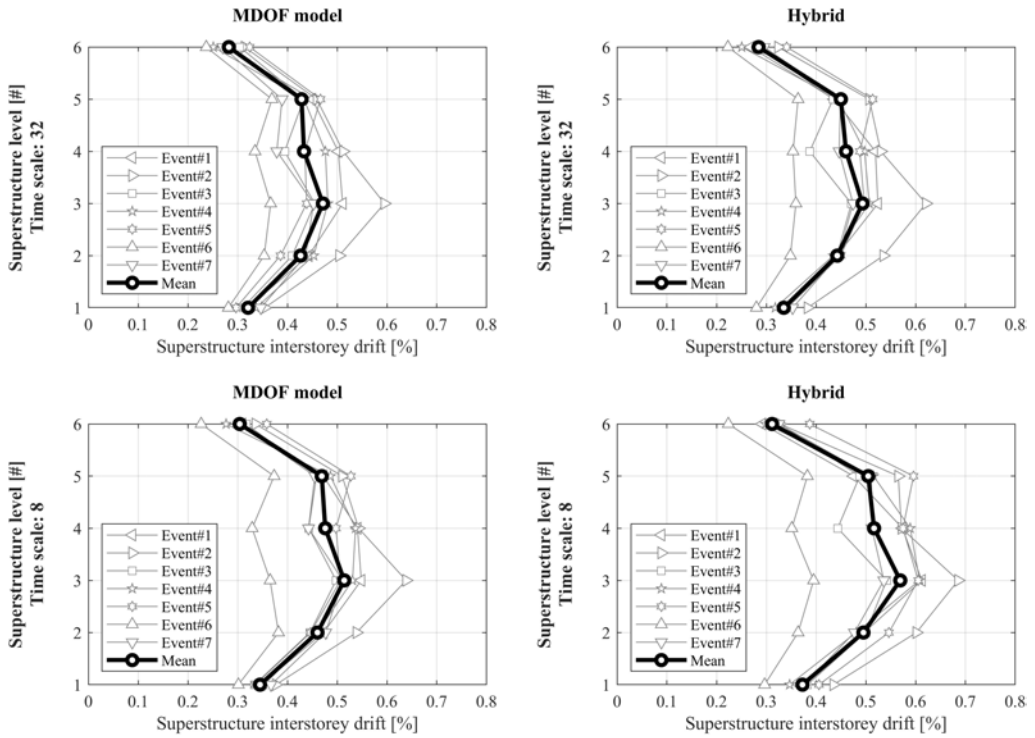

FIGURE 12 | Interstory drift response—time scales 32 and 8.

have been achieved, for the experimental assessment of base-isolated building:

- The numerical substructuring of hybrid simulations has been implemented as a statically condensed MDOF oscillator, which has the same dynamic properties as the full 3-D FEM of the case study structure, modeled by means of linear elastic structural elements;
- Hybrid simulations have been carried out by considering two individual time scale factors, namely 32 and 8, in order to investigate different regions of the characterization curve, which correspond to different frictional properties, aiming at considering configurations closer to the realistic real-time simulation.

The outcomes of hybrid tests for all the selected events have been compared to numerical results of both simplified procedures and non-linear time history analyses. Precisely, we have the following:

- A preliminary estimation of the performance of the isolation system has been computed, through an equivalent linear elastic analysis, which accounts for the effective friction coefficient, according to a characterization curve obtained from dynamic tests, which have highlighted the common dependency of frictional properties of PTFE-based sliding materials on the velocity. Results have shown that the mean response of hybrid simulations can be fairly captured by the equivalent linear elastic analysis, which consequently represents a very useful tool for design of isolation systems, even though highly non-linear behaviors are considered.
- In addition, also non-linear time history analyses have been computed, by accounting for both SDOF and MDOF numerical oscillators. Both oscillators lead to comparable peak responses, even though the SDOF system returns lower displacements values. On the other hand, the MDOF system seems to provide overestimations of the more realistic displacement demands of the hybrid simulations. Similar conclusions can be drawn for sliding velocity response, and much lower discrepancies can be detected in the peak isolation force analysis. Concerning the isolation hysteretic response, for all events, the overall force of the device is properly captured by the numerical non-linear constitutive law. Finally, the superstructure peak interstory drift profiles returned by the numerical MDOF model provide a good approximation of the more realistic maximum deformation related to hybrid tests.

The present testing campaign provides evidences that proper non-linear constitutive laws for isolation devices can effectively reproduce a realistic response of a base-isolated building, at least if the superstructure is linearly modeled; in addition, equivalent linear elastic analysis can be adopted for design purposes, in order to obtain safe estimations of the maximum displacement allowance of the implemented devices. More hybrid simulations

could be carried out, by accounting for distributed (or lumped) plasticity for all structural elements of the superstructure, with time scale factors closer to real time, aiming at comparing simpler linear elastic responses to the outcomes of one of the most realistic testing techniques for base-isolated systems.

DATA AVAILABILITY STATEMENT

All datasets generated for this study are included in the article/supplementary material.

AUTHOR CONTRIBUTIONS

MF has defined and carried out all the numerical analyses and the post-processing of experimental data, by defining the research assumptions of hybrid simulations. IL has developed the algorithm for hybrid simulations and has managed the experimental part of the work. AP has managed the definition of the overall research, from both the experimental and the numerical points of view.

FUNDING

Part of the current work has been carried out under the financial support of the Italian Civil Protection, within the frameworks of the Executive Project 2017–2019 (Project 3—Assessment of the seismic isolation of building structures through hybrid tests with numerical substructuring) and the national Research Project DPC–ReLUIS (National Network of Laboratories of Seismic Engineering) 2014–2018, Line 6—Isolation and Dissipation.

REFERENCES

Bonelli, A., Bursi, O. S., He, L., Magonette, G., and Pegon, P. (2008). Convergence analysis of a parallel inter eld method for heterogeneous simulations with dynamic substructuring. *Int. J. Num. Methods Eng.* 75, 800–825. doi: 10.1002/nme.2285

Bursi, O. S., Abbiati, G., Cazzador, E., Pegon, P., and Molina, F. J. (2017). Nonlinear heterogeneous dynamic substructuring and partitioned FETI time integration for the development of low-discrepancy simulation models. *Int. J. Num. Methods Eng.* 112, 1253–1291. doi: 10.1002/nme.5556

Bursi, O. S., He, L., Bonelli, A., and Pegon, P. (2010). Novel generalized- methods for interfield parallel integration of heterogeneous structural dynamic systems. *J. Comput. Appl. Math.* 234, 2250–2258.

Calabrese, A., Strano, S., and Terzo, M. (2015). Real-time hybrid simulations vs shaking table tests: case study of a fibre-reinforced bearings isolated building under seismic loading. *Struct. Contr. Health Monit.* 22, 535–556. doi: 10.1002/stc.1687

Cardone, D., Conte, N., Dall'Asta, A., Di Cesare, A., Flora, A., Leccese, G., et al. (2017). "RINTC project: nonlinear analyses of Italian code-conforming base-isolated buildings for risk of collapse assessment," in *COMPDYN 2017 - Proceedings of the 6th International Conference on Computational Methods in Structural Dynamics and Earthquake Engineering*, Rhodes Island

CEN (2018). *Comité Européen de Normalisation TC 340, European Code UNI EN 15129:2018 Anti-Seismic Devices*. Brussels: European Committee for Standardization.

Chopra, A. K. (1995). *Dynamics of Structures Theory and Applications to Earthquake Engineering*. Upper Saddle River, NJ: Prentice Hall.

Constantinou, M., Mokha, A., and Reinhorn, A. (1990). Teflon bearings in base isolation II: modeling. *J. Struct. Eng.* 116, 455–474. doi: 10.1061/(asce)0733-9445(1990)116:2(455)

D.M. 17/01/2018 (2018). *Norme Tecniche per le Costruzioni, D.M. 17/01/2018*. Italia: Gazzetta Ufficiale.

De Domenico, D., Ricciardi, G., and Benzoni, G. (2018). Analytical and finite element investigation on the thermo-mechanical coupled response of friction isolators under bidirectional excitation. *Soil Dyn. Earthq. Eng.* 106, 131–147. doi: 10.1016/j.soildyn.2017.12.019

Dolce, M., Cardone, D., and Croatto, F. (2005). Frictional behavior of steel-PTFE interfaces for seismic isolation. *Bull. Earthq. Eng.* 3, 75–99. doi: 10.1007/s10518-005-0187-9

Fenz, D., and Constantinou, M. C. (2006). Behaviour of the double concave friction pendulum bearing. *Earthq. Eng. Struct. Dyn.* 35, 1403–1424. doi: 10.1002/eqe.589

Furinghetti, M., and Pavese, A. (2017). Equivalent uniaxial accelerogram for CSS-based isolation systems assessment under two-components seismic events. *Mechan. Based Des. Struct. Mach.* 45, 282–295. doi: 10.1080/15397734.2017.1281145

Furinghetti, M., Pavese, A., Quaglini, V., and Dubini, P. (2019a). Experimental investigation of the cyclic response of double curved surface sliders subjected to radial and bidirectional sliding motions. *Soil Dyn. Earthq. Eng.* 117, 190–202. doi: 10.1016/j.soildyn.2018.11.020

Furinghetti, M., Pavese, A., and Rizzo Parisi, E. (2019b). "Static condensation procedure of finite element models for fast non-linear time history analyses of base-isolated structures," in *COMPDYN 2019 Proceedings of the 7th ECCOMAS Thematic Conference on Computational Methods in Structural Dynamics and Earthquake Engineering*, Crete.

Gravouil, A., and Combescure, A. (2001). Multi-time-step explicit – implicit method for non-linear structural dynamics. *Int. J. Num. Method Eng.* 50, 199–225. doi: 10.1002/1097-0207(20010110)50:1<199::aid-nme132>3.0.co;2-a

Hakuno, M., Shidawara, M., and Hara, T. (1969). Dynamic destructive test of a cantilever beam controlled by an analog computer. *Trans. Jpn. Soc. Civil Eng.* 171, 1–9. doi: 10.2208/jscej1969.1969.171_1

Iervolino, I., Galasso, C., and Cosenza, E. (2009). REXEL: computer aided record selection for code-based seismic structural analysis. *Bull. Earthq. Eng.* 8, 339–362. doi: 10.1007/s10518-009-9146-9141

Kumar, M., Whittaker, A. S., and Constantinou, M. C. (2015). Characterizing friction in sliding isolation bearings. *Earthq. Eng. Struct. Dyn.* 44, 1409–1425. doi: 10.1002/eqe.2524

Lanese, I. (2012). *Development and Implementation of an Integrated Architecture for Real-Time Dynamic Hybrid Testing in the Simulation of Seismic Isolated Structures*. Ph.D. Dissertation, Rose School, Pavia.

Lanese, I., Pavese, A., and Furinghetti, M. (2018). "Hybrid testing of seismic isolated structures: facing time and geometry scaling issues," in *Proceedings of 16th European Conference on Earthquake Engineering*, Thessaloniki.

Lomiento, G., Bonessio, N., and Benzoni, G. (2013). Concave sliding isolator's performance under multi-directional excitation. *Ingegneria Sismica* 30, 17–32.

Mosqueda, G., Whittaker, A. S., and Fenves, G. L. (2004). Characterization and modeling of friction pendulum bearings subjected to multiple components of excitation. *J. Struct. Eng.* 130, 433–442. doi: 10.1061/(asce)0733-9445(2004)130:3(433)

Pavese, A., Furinghetti, M., and Casarotti, C. (2019). Investigation of the consequences of mounting laying defects for curved surface slider devices under general seismic input. *J. Earthq. Eng.* 23, 377–403. doi: 10.1080/13632469.2017.1323046

Pegon, P., and Magonette, G. (2002). *Continuous PSD Testing with Nonlinear Substructuring: Presentation of a Stable Parallel Inter-Field Procedure*. Technical Report 1.02.167. Ispra: European Commission.

Pegon, P., and Pinto, A. (2000). Pseudo-dynamic testing with substructuring at the ELSA Laboratory. *Earthquake Eng. Struct. Dynam.* 29, 905–925. doi: 10.1002/1096-9845(200007)29:7<905::aid-eqe941>3.0.co;2-p

Peloso, S., Pavese, A., and Casarotti, C. (2012). Eucentre trees lab: laboratory for training and research in earthquake engineering and seismology. *Geotech. Geol. Earthquake Eng.* 20, 65–81. doi: 10.1007/978-94-007-1977-4_4

Quaglini, V., Bocciarelli, M., Gandelli, E., and Dubini, P. (2014). Numerical assessment of frictional heating in sliding bearings for seismic isolation. *J. Earthquake Eng.* 18, 1198–1216. doi: 10.1080/13632469.2014.924890

Conflict of Interest: The authors declare that the research was conducted in the absence of any commercial or financial relationships that could be construed as a potential conflict of interest.

frontiers in Built Environment

ORIGINAL RESEARCH
published: 07 April 2020
doi: 10.3389/fbuil.2020.00032

An Efficient Stochastic Linearisation Procedure for the Seismic Optimal Design of Passive Control Devices

Giacomo Navarra, Francesco Lo Iacono and Maria Oliva*

Faculty of Engineering and Architecture, Kore University of Enna, Enna, Italy

The seismic response of structures is often enhanced by introducing passive control devices that can operate through the dissipation of the input energy or by modifying the dynamic characteristics of the main structure. The inherent non-linearities in the constitutive laws of some of them lead to computation difficulties and have limited the large-scale use and design of these devices. In this study, a procedure for the optimal design of multi passive control devices is proposed. The general case of linear Multi-Degree-Of-Freedom (MDOF) not-classically-damped structural systems controlled by Fluid Viscous Dampers (FVD) are investigated in a stochastic framework. The procedure consists of evaluation of the device optimal pattern by minimizing an objective function related to the dampers cost and subjected to a constraint on the structural behavior. For each configuration, the complete probabilistic characterization of the response is achieved by employing random vibration theory, Stochastic Linearisation (SL) techniques and a novel analytic model which provides closed-form PSD functions of earthquakes accelerations coherent to response spectra suggested by seismic codes. Exploiting this model, a procedure to speed up the Stochastic Linearisation technique by avoiding any numerical integration is proposed. Applications on MDOF building structures have been carried out to validate the proposed approach in terms of accuracy and reduction of the computational effort and to obtain optimal pattern of the passive control device coherently with the provisions of seismic building codes.

Keywords: passive control device, stochastic linearisation technique, PSD coherent to response spectra, optimal design, spectral moments, closed-form expressions

OPEN ACCESS

Edited by:
Dario De Domenico, University of Messina, Italy

Reviewed by:
Alberto Di Matteo, University of Palermo, Italy
Afshin Moslehi Tabar, Tafresh University, Iran
Agathoklis Giaralis, City University of London, United Kingdom

****Correspondence:***
Giacomo Navarra
giacomo.navarra@unikore.it

Specialty section:
This article was submitted to Earthquake Engineering, a section of the journal Frontiers in Built Environment

Received: *14 December 2019*
Accepted: *05 March 2020*
Published: *07 April 2020*

Citation:
Navarra G, Lo Iacono F and Oliva M (2020) An Efficient Stochastic Linearisation Procedure for the Seismic Optimal Design of Passive Control Devices. Front. Built Environ. 6:32. doi: 10.3389/fbuil.2020.00032

1. INTRODUCTION

The solution of a structural design problem generally requires the evaluation of a set of parameters in order to fulfill several requirements, for instance, in terms of strength, serviceability and dynamic performance of the structural system at hand. Each requirement is usually indicated as a *limit state* and the design problem, in other words, can be expressed as the measurement of the violation of a given set of limit states (Melchers, 1999). Since there are infinite sets of design parameters that ensure the respect of the limit states, optimization techniques may be deployed, in order to choose those parameters that satisfy the requirements and, at the same time, minimize a properly defined cost function.

Most of the established design strategies define structural safety in a deterministic way, assuming that both structural parameters and applied loads are known, even if conservative values, derived from statistical studies, are utilized. This approach leads to consider only the mean response

and to neglect its dispersion. Since the uncertainties affect both structural properties and load characteristics, a more reliable analysis should be defined into a probabilistic framework. In the last decades, several methodologies have been developed for the probabilistic measure of the structural safety, in which any uncertainty about a design variable, a structural property or a load feature has to be taken into account explicitly and modeled through its respective probability density function (Melchers, 1999). Accordingly, also limit states and cost functions have to be described in terms of their probability of occurrence.

The dynamic response of structural systems subjected to seismic loads is often enhanced by introducing passive control devices, such as Fluid Viscous Dampers (FVD), Tuned Liquid Column Dampers (TLCD) or Non-linear Energy Sinks (NES). These devices operate through several different physical mechanisms by increasing the energy dissipation or by changing the dynamic characteristics of the system to which they are attached. Their use has received increasing attention in recent decades (Housner et al., 1997; Spencer and Nagarajaiah, 2003) and important applications for improving the structural performances to dynamic loads (e.g., earthquakes or winds) of new or existing building structures have been developed. The design parameters of passive control devices depend on the dynamic features of the structural system to be controlled as well as on the characteristics of the considered dynamic load. Moreover, some of the passive control devices exhibit non-linear constitutive laws and, even admitting that the primary system behaves linearly, in the controlled system a non-linear behavior may arise. This increases the computation difficulties and limits the large-scale use and design of these devices.

In fact, the probabilistic optimal design of non-linear passive control devices should be performed by means of Monte Carlo simulations, involving a very large computational effort (Oliva et al., 2017). On the other hand, in case of linear systems, the tools of random vibration theory allow for a full probabilistic characterization of the structural response, provided that a reliable stochastic model of the seismic input is available. Aiming at this, it is common to replace the non-linear equations of motion of a system equipped with a passive device with linear equivalent ones by using well-established procedures as Stochastic Linearisation (SL) techniques (Atalik and Utku, 1976; Roberts and Spanos, 1991; Elishakoff, 2000; Alibrandi and Ricciardi, 2012). The conditions of equivalence, when passing from the non-linear to the equivalent linear system, may be established in order to preserve some response quantities in statistical sense. Since the parameters of the linear equivalent system depend implicitly on response statistics, most of SL algorithms require the solution of a system of algebraic non-linear equations, although it has been found (Roberts and Spanos, 1991) that a simple recursive loop is adequate to simultaneously satisfy them. Hence, the computational burden required for the analyses increases, even if it is drastically reduced with respect to Monte Carlo simulations. Moreover, calculations are very often carried out only numerically, since analytical closed-form solutions for response statistics are available just for a limited class of problems (Artale et al., 2017). In Spanos and Miller (1994), formulae for the computation of the response spectral moments have been derived for the case of random excitations with band-limited white noise, Gaussian and Kanai-Tajimi seismic spectra. In order to overcome some limitations of the conventional SL, Fujimura and Der Kiureghian (2007) proposed an alternative method of linearisation, called "tail equivalent linearisation." This is a non-parametric method which consists in replacing the non-linear system with a linear one, so that the tail probability of the linear response above a specified threshold corresponds to the first order reliability approximation of the tail probability of the non-linear response above the same threshold. It provides superior accuracy for the distribution of the maximum response, especially in the tail region and it was mainly used for reliability purposes (Der Kiureghian and Fujimura, 2009).

Alternatively, Giaralis and Spanos (2010) defined a stochastic dynamic-based algorithm in order to estimate the seismic demand of bilinear hysteretic SDOF oscillators consistently with seismic code provisions that does not require non-linear numerical integrations. Their algorithm consists in the definition of a non-parametric RS-consistent stationary PSD function and in the use of the SL in order to define the so-called equivalent linear parameters (ELPs) and, finally, in the estimation of the peak inelastic response of the non-linear oscillator. Since the applicability of this latter approach was limited to relatively mild non linear response, an higher-order SL scheme was further proposed in Spanos and Giaralis (2013) for the treatment of a wider class of hysteretic constitutive laws with a resulting higher accuracy. Recently, Mitseas et al. (2018) proposed a novel stochastic dynamics framework to estimate the peak inelastic response of MDOF strongly non-linear system in a seismic context without undertaking non-linear step-by-step integrations of the response. The algorithm allows for the seismic demand estimation of MDOF systems without numerical integrations nor modal combination rules involved. Starting again from the definition of a non-parametric RS-consistent PSD function, SL is used in order to decouple the MDOF system into several SDOF oscillators characterized by ELPs. These oscillators are able to capture the peaks of the non-linear response for each DOF of interest directly in the geometric space. In order to achieve high accuracy, the algorithm requires an iterative scheme in which, for each DOF, the PSD is updated basing on the RS defined by damping modification factors.

Among the several passive control devices proposed and realized in the last decades, Fluid Viscous Dampers (FVDs) have received great attention and have been widely used in order to reduce the effects of wind or earthquakes on civil structures and to mitigate the vibrations due to shocks in mechanical equipment. Their appeal for use in seismic engineering derives from the low maintenance required, from their re-usability for subsequent earthquakes, but also from the fact that the forces exerted by the dampers and elastic forces are out of phase and the stress level in the structure is not increased by their presence. A great amount of research papers have been devoted to the optimal design and optimal placement of fluid viscous dampers to enhance the structural performance. The most relevant scientific literature in this field has been recently collected in a very comprehensive review paper (De Domenico et al., 2019) which allows for a comparison of the different strategies used to identify the optimal design configurations of FVDs. Nevertheless, it is

noteworthy to recall two approaches. In the first one (Tubaldi and Kougioumtzoglou, 2015), the non-stationary stochastic response of a hysteretic SDOF system equipped with FVDs is calculated by an approximate analytical technique that makes use of a modified SL scheme and allows to consider realistic seismic excitations with time-varying frequency content. In Gidaris and Taflanidis (2015) the performance assessment and optimal design of fluid viscous dampers in a probabilistic life-cycle cost framework is discussed to obtain optimal design under different seismic scenarios.

From a mathematical perspective, the procedure presented in this work belongs to the wider class of the constrained optimization problems. In particular, the optimal pattern of the device parameters is evaluated by minimizing an objective function related to the device cost and by ensuring that a constraint function based on the structural behavior is not violated. Both cost and constraint functions are defined into a probabilistic framework. For each damper configuration, the controlled system response is evaluated by using random vibration theory in conjunction with SL technique.

In order to reduce the great computational burden involved in these problems, two novelty aspects have been here proposed and introduced. Firstly, assuming that earthquake time-histories can be modeled as samples of a stationary stochastic process, an analytical representation of earthquake load Power Spectral Density (PSD) functions consistent with seismic codes Response Spectra (RS) (Barone et al., 2015, 2019) have been adopted. Secondly, an algorithm has been set up in order to obtain approximate analytical expressions of the response first spectral moments for not-classically damped Multi-degrees-of-freedom (MDOF) systems, without performing any numerical integration.

It is to remark that the more recent SL techniques for the determination of the seismic demand for hysteretic systems (Giaralis and Spanos, 2010; Spanos and Giaralis, 2013; Mitseas et al., 2018) can greatly benefit of these novelty aspects, both in terms of a significant reduction of the computational efforts in the derivation of RS-consistent PSD functions, and in accuracy, since some approximations in evaluating the response statistics can be removed without increasing the computational burden.

In the following, it will be shown how these spectral moments can be used in order to perform SL and to evaluate the optimal design of passive control systems in an efficient and accurate way. The paper is organized as in the following: in section 2 the probabilistic optimal design problem is firstly formulated in general form and then particularized for the case of n-DOF linear structural systems controlled by means of m concurrent non-linear FVDs (Di Paola et al., 2007; Di Paola and Navarra, 2009); in Section 3, in order to take advantage of the random vibration theory, the classical SL approach is described for the problem at hand and a procedure for the analytical evaluation of the response statistics, useful for SL technique, is proposed for linear n-DOF non-classically damped systems; section 4 is devoted to numerical applications in which the reduction in computational effort and the accuracy of the proposed procedure are investigated and the optimal design of FVDs is performed for a plane shear-type five-story frame and for a three-dimensional building structure. For this last application, the accuracy of the proposed procedure is further assessed in time-domain by performing a non-linear response history analysis on a set of spectrum compatible ground motion records. Finally, some conclusions are drawn. In Appendix brief details on the deriving of RS-consistent analytical PSD function and the expressions for its evaluation are provided, along with the analytical expressions that lead to the evaluation of the cross-spectral moments in modal space, once the direct spectral moments are determined.

2. PROBLEM FORMULATION

The equations of motion of a n-DOF linear structural system in its so-called *uncontrolled* state, subjected to a sample of ground motion acceleration process $\ddot{U}_g(t)$ can be expressed as:

$$\mathbf{M}\ddot{\mathbf{U}}(t) + \mathbf{C}\dot{\mathbf{U}}(t) + \mathbf{K}\mathbf{U}(t) = -\mathbf{M}\boldsymbol{\tau}\ddot{U}_g(t) \tag{1}$$

where $\mathbf{M}$, $\mathbf{C}$ and $\mathbf{K}$ are the $(n \times n)$ mass, damping and stiffness matrices, respectively, $\mathbf{U}(t)$ is the $(n \times 1)$ vector collecting the degrees of freedom of the structural system, dots means time derivatives and $\boldsymbol{\tau}$ is the $(n \times 1)$ influence vector.

Aiming at reducing the dynamic response of the uncontrolled structure, it is common to introduce in the system passive control devices. The latter, operating through different physical mechanisms, generate additional damping forces or modify the dynamic characteristics of the so-called *controlled* system. Since many of the practically used passive control devices, such as Fluid Viscous Dampers (FVD), Non-linear Energy Sinks (NES) or Tuned Liquid Column Dampers (TLCD), present non-linear constitutive relationships, the general form of the equations of motion of the controlled system can be written as:

$$\mathbf{g}\left(\ddot{\hat{\mathbf{U}}}, \dot{\hat{\mathbf{U}}}, \hat{\mathbf{U}}\right) = \mathbf{f}(t) \tag{2}$$

where $\hat{\mathbf{U}}$ is the new degree-of-freedom vector, which may differ from $\mathbf{U}(t)$ for those categories of devices that introduce additional degrees of freedom, for example passive absorbers; $g_i(\ddot{\hat{\mathbf{U}}}, \dot{\hat{\mathbf{U}}}, \hat{\mathbf{U}})$ and $f_i(t)$ are the total internal non-linear forces and the external applied loads, respectively, acting in the i-th degree-of-freedom direction.

The dynamic behavior of the controlled system and its ability in mitigating the seismic response are governed by the design variables of the control devices, which, in turn, depend on both dynamic features of the uncontrolled system and on the characteristics of the considered dynamic load.

In general, the greater the size and cost of the used control devices, the greater reductions in response may be achieved, until allowance criteria provided by building codes are satisfied. Therefore, the problem of the optimal design of passive control devices can be properly set and, since earthquakes are random in nature, it should be tackle into a probabilistic framework, as in the following:

$$\begin{gathered} \min_{\mathbf{x}} \phi(\mathbf{x}, \mathbf{r}) \\ \text{subjected to:} \\ P_s(\mathbf{x}, \mathbf{r}) - \bar{P}_s \geq 0 \\ \mathbf{x} \in \Omega \end{gathered} \tag{3}$$

where $\phi(\mathbf{x}, \mathbf{r})$ is the cost function to be minimized, $\mathbf{x}$ and $\mathbf{r}$ are the vectors collecting the design variables and the uncertain parameters, respectively, $P_s(\mathbf{x}, \mathbf{r})$ is the survival probability, $\bar{P}_s$ is the target survival probability and Ω is the feasibility domain of the design variables. Cost function and survival probability can be expressed in terms of design variables and of the response statistics, but their analytical expressions are specific for each kind of passive control device.

Generally, the uncertain parameters $\mathbf{r}$ can be divided into two categories. The first one is related to the definition of the structural model (uncertainty in mass, stiffness and damping values, or model uncertainties), whereas the second one accounts for the randomness of the load. However, in case of seismic input, it is possible to neglect the uncertainties of the structural model as they lead to smaller dispersions of the response (Pinto et al., 2007). Hereinafter, the system parameters are hence considered as deterministically known and $\mathbf{x}$ collects only the location patterns and the design variables of the control devices.

Moreover, it is assumed that earthquake acceleration time-histories may be modeled as finite time duration samples of a zero-mean Gaussian stationary stochastic process, completely defined by the knowledge of its Power Spectral Density (PSD) function. In this case, the vector $\mathbf{r}$ collects the parameters of the seismic input stochastic model, obtained by using recently proposed analytical expressions of PSDs consistent with assigned RS, that cover most of the international building codes (Barone et al., 2015, 2019). The Appendix reports further details of this PSD model along with the closed-form relationship between the RS parameters and the consistent PSD function ones. In recent studies (Giaralis and Spanos, 2010; Spanos and Giaralis, 2013), RS-consistent PSDs have been numerically derived and used also for stochastic analyses of non-linear yielding structures by the application of the SL. The joint use of such technique and an analytical model of the seismic PSD function could certainly improve the overall computational efficiency.

The solution of the problem expressed in Equation (3) requires, for each tentative set of the design variables, the stochastic analysis of a non-linear system, which is often performed by means of Monte Carlo simulations, involving very large computational efforts. On the other hand, in case of linear systems and a properly defined stochastic model of the seismic input, the probabilistic characterization of the structural response can be easily computed by means of the tools of stochastic analysis.

In the following, an optimal design problem is considered when FVDs are used as passive control devices. However, similar approaches may be addressed for other types of non linear passive control systems as, for instance, TLCDs (Di Matteo et al., 2014a,b, 2015) or NESs (Navarra et al., 2019b).

Viscous dampers have been widely used to mitigate the effects of wind or earthquakes on civil structures and in the shock and vibration isolation of equipment. Their appeal derives from the low maintenance required and their re-usability for subsequent earthquakes, but also from the fact that the forces exerted by the dampers are out of phase with respect to the elastic forces and do not increase the stress level in the structure. Moreover, they can be used for the protection of new constructions as well as for retrofitting purposes. Conversely, the major drawback in using viscous dampers consists in handling their non-linear force-velocity constitutive law.

The equations of motion of the controlled system in Equation (2), when m viscous dampers are concurrently deployed become:

$$\mathbf{M}\ddot{\mathbf{U}}(t) + \mathbf{C}\dot{\mathbf{U}}(t) + \mathbf{K}\mathbf{U}(t) + \mathbf{F}_D(t) = -\mathbf{M}\boldsymbol{\tau}\ddot{U}_g(t) \tag{4}$$

where $\mathbf{F}_D(t)$ is the vector of the non-linear forces exerted by the viscous dampers. Although in literature there are several attempts to model the constitutive law of viscous dampers by using the theory of visco-elasticity (Schwann et al., 1988) or the fractional calculus (Makris et al., 1993), most of the manufacturers currently use a force-velocity relationship, validated by several laboratory tests, expressed as:

$$f_d(\dot{Y}) = C_d |\dot{Y}|^{\alpha} \operatorname{sign}(\dot{Y}) \tag{5}$$

being C_d and α the characteristic parameters of the damper device, $\dot{Y}$ the relative velocity at the damper ends and sign $(\cdot)$ the signum function. For sesmic protection purposes, values of α between 0.15 and 0.50 are used, in order to attain quite large control forces even for small relative velocities and to have almost constant output forces for large velocity values.

The non-linear forces vector $\mathbf{F}_D(t)$ can be expressed as:

$$\mathbf{F}_D(t) = \mathbf{R}^{\mathrm{T}}\mathbf{f}_d(\dot{\mathbf{Y}}) \tag{6}$$

where $\mathbf{Y}(t)$ is a m-ranked vector that collects the relative displacements at the ends of each damper and all the response quantities whose statistics are useful for the computation of the cost function and of the survival probability. These quantities can be obtained as linear combinations of the degrees of freedom $\mathbf{U}(t)$, through the definition of a $(m \times n)$ transformation matrix $\mathbf{R}$ as:

$$\mathbf{Y}(t) = \mathbf{R}\mathbf{U}(t) \tag{7}$$

Since the selection of the degrees of freedom and of the response quantities of interest depends on the geometry of the problem and on the passive control devices locations, it is not possible to attain to a general expression of the matrix $\mathbf{R}$. However, since FVDs are usually inserted into the frame braces, from a computational point of view, it is convenient to include in $\mathbf{Y}(t)$ all the inter-story drifts of the structure. The i-th element of the vector $f_d(\dot{Y})$ is expressed as in Equation (5), taking into account that each damper may have, in general, different characteristic parameters $C_{d,i}$ and α_i. Obviously, if no dampers are deployed at the i-th inter-story, a value of $C_{d,i} = 0$ is set.

2.1. Cost Function and Survival Probability

In literature, several estimators of the cost function have been proposed (De Domenico et al., 2019). In Bahnasy and Lavan (2013), the use of the sum of the dampers constants $C_{d,i}$ at the various floors has been proposed, whereas the expected value of the sum of the peak forces of each damper has been considered in Altieri et al. (2018) and Tubaldi et al. (2016). Herein, recalling the probabilistic aspects of the proposed approach, the cost function

has been defined as the sum of the characteristic values of the peak force of each damper, that represents a reliable measure of its cost, being related to its dimensioning (Navarra et al., 2017). Hence, the cost function $\phi(\mathbf{x}, \mathbf{r})$ in Equation (3) can be written as:

$$\phi(\mathbf{x}, \mathbf{r}) = \sum_{i=1}^{m} f_{dk,i} = \sum_{i=1}^{m} C_{d,i} \left| \eta_{k,i}\, \sigma_{\dot{Y}_i} \right|^{\alpha_i} \tag{8}$$

where $f_{dk,i}$ is the characteristic value (at 95% percentile) of the peak force exterted by the i-th damper, $\sigma_{\dot{Y}_i}$ is the standard deviation of the relative velocity at the ends of the i-th damper and $\eta_{k,i}$ is the correspondent peak factor, as defined in the classical first-passage reliability theory (Vanmarcke, 1972, 1975):

$$\eta_{k,i} = \sqrt{2 \ln \left\{ \frac{2\nu_{\dot{Y}_i} T_s}{-\ln(0.95)} \left[1 - \exp\left(-q_{\dot{Y}_i}^{1,2} \sqrt{\pi \ln \left[\frac{2\nu_{\dot{Y}_i} T_s}{-\ln(0.95)} \right]} \right) \right] \right\}} \tag{9}$$

In Equation (9), T_s is the duration of the time window, $\nu_{\dot{Y}_i}$ and $q_{\dot{Y}_i}$ are the mean zero-crossing rate and the bandwidth factor, respectively, whose expressions can be evaluated in terms of the first spectral moments $\lambda_{\dot{Y}_i,j}$ of the i-th relative velocity process:

$$\nu_{\dot{Y}_i} = \frac{1}{2\pi} \sqrt{\frac{\lambda_{\dot{Y}_i,2}}{\lambda_{\dot{Y}_i,0}}}; \quad q_{\dot{Y}_i} = \sqrt{1 - \frac{\lambda_{\dot{Y}_i,1}^2}{\lambda_{\dot{Y}_i,2} \lambda_{\dot{Y}_i,0}}} \tag{10}$$

Spectral moments are defined as the geometric moments of the one-sided PSD function $G_X(\omega)$ with respect to the axis $\omega = 0$, so that the m-th order spectral moment of a generic stochastic process $X(t)$ is given by:

$$\lambda_{X,m} = \int_0^{+\infty} \omega^m\, G_X(\omega)\, \mathrm{d}\omega\,. \tag{11}$$

Spectral moments, indeed, are related to peculiar statistics of stochastic processes and allow for their characterization. For example $\lambda_{X,0}$ and $\lambda_{X,2}$ represent the variances of the processes $X(t)$ and $\dot{X}(t)$, respectively, and other quantities as central frequency and bandwidth parameter, as well as approximate solutions for the first-passage problem can be evaluated in terms of spectral moments (Vanmarcke, 1972, 1975, 1976b; Der Kiureghian, 1980; Di Paola and Muscolino, 1988).

The survival probability $P_s\left(b_{max,i}, T_s\right)$ is associated to the non occurrence of crossings, into the time window T_s, of the i-th maximum allowable inter-story drift $b_{max,i}$, computed from the actual story height and can be evaluated as:

$$P_s\left(b_{max,i}, T_s\right) = \left[1 - \exp\left(-\frac{b_{max,i}^2}{2\sigma_{\dot{Y}_i}^2} \right) \right] \exp\left(-2\tilde{\alpha}_{Y_i}\left(b_{max,i}\right) T_s \right) \tag{12}$$

where the risk function $\tilde{\alpha}_{Y_i}\left(b_{max,i}\right)$ is:

$$\tilde{\alpha}_{Y_i}\left(b_{max,i}\right) = 2\nu_{Y_i} \frac{1 - \exp\left(-\sqrt{\frac{\pi}{2}} \frac{b_{max,i}}{\sigma_{Y_i}} q_{Y_i}^{1,2} \right)}{\exp\left(\frac{b_{max,i}^2}{2\sigma_{\dot{Y}_i}^2} \right) - 1} \tag{13}$$

and the quantities ν_{Y_i}, q_{Y_i} and $\sigma_{\dot{Y}_i}^2 = \lambda_{Y_i,0}$ are the mean zero-crossing rate, the bandwidth factor and the variance of the relative displacements, respectively. Therefore, they can be computed as in Equations (10), but with reference to the process Y_i, in terms of the first spectral moments $\lambda_{Y_i,j}$. Assuming that the failure condition is attained when only one inter-story drift exceeds the allowable value, the global survival probability P_s in Equation (3) is finally obtained as:

$$P_s = \min\{P_s\left(b_{max,i}, T_s\right)\} \tag{14}$$

3. EFFICIENT STOCHASTIC LINEARISATION TECHNIQUE

Since Equation (4) is non-linear, the evaluation of the response statistics useful for solving the optimal design problems has to be performed through Monte Carlo simulations, which require heavy computational efforts. In order to overcome this difficulty, the Stochastic Linearisation (SL) technique may be an effective tool (Atalik and Utku, 1976). The basic idea of SL is to replace the original non-linear system in Equation (4) with an equivalent linear one:

$$\mathbf{M}^{(e)} \ddot{\mathbf{U}}(t) + \mathbf{C}^{(e)} \dot{\mathbf{U}}(t) + \mathbf{K}^{(e)} \mathbf{U}(t) = \mathbf{f}(t) \tag{15}$$

in which the equivalent system matrices $\mathbf{M}^{(e)}$, $\mathbf{C}^{(e)}$ and $\mathbf{K}^{(e)}$ are evaluated by minimizing the difference between the two systems in statistical sense. The expressions of equivalent linear matrices for MDOF systems equipped with several kind of passive control devices, such as Tuned Liquid Column Dampers and Non-linear Energy Sinks, may be found in Navarra et al. (2019a). In the case of FVDs, it can be shown that the equivalent linear mass and stiffness matrices coincide with those of the uncontrolled system (i.e., $\mathbf{M}^{(e)} = \mathbf{M}$ and $\mathbf{K}^{(e)} = \mathbf{K}$), while the equivalent linear damping matrix $\mathbf{C}^{(e)}$ can be obtained as:

$$\mathbf{C}^{(e)} = \mathbf{C} + \mathbf{R}^{\mathrm{T}} \mathbf{D}_{FVD} \mathbf{R} \tag{16}$$

in which $\mathbf{R}$ is the $(m \times n)$ transformation matrix, whereas the diagonal matrix $\mathbf{D}_{FVD}$ can be expressed as (Di Paola et al., 2007; Di Paola and Navarra, 2009):

$$D_{FVD,ij} = \mathrm{E}\left[\frac{\partial f_{d,i}}{\partial \dot{Y}_j} \right] = \alpha\, \hat{C}_{d,j}\, \frac{2^{\alpha/2} \Gamma(\alpha/2)}{\sqrt{2\pi}}\, \sigma_{\dot{Y}_j}^{\alpha-1}\, \delta_{ij}, \quad (i, j = 1, 2, \ldots, m) \tag{17}$$

being $\Gamma(\cdot)$ the Euler Gamma function, δ_{ij} the Kronecker delta and $\sigma_{\dot{Y}_j} = \lambda_{Y_j,2}$ the standard deviation of the j-th relative velocity.

It is to remark that Equation (17) is derived based on a statistical equivalence in terms of damper force and by assuming the Gaussianity of the response process. Recently, other different equivalent damping formulae based on energy equivalency or by assuming other non-Gaussian probability distributions have been proposed (De Domenico and Ricciardi, 2018, 2019). However, in all these approaches the equivalent linear system is completely defined when some response statistics are evaluated. This is, in general, achieved by using an iterative procedure. In the first iteration, it is assumed that the equivalent linear system coincides to the uncontrolled system whereas, at subsequent iterations, the estimations of equivalent linear matrices computed at the previous iteration are considered.

In conclusions, it appears that the optimal design problem into a probabilistic framework requires the evaluation in a efficient way of the first spectral moments of the response process. Furthermore, even assuming that the uncontrolled system, Equation (1), may be considered classically damped, the presence of passive control devices makes the controlled system a non-classically damped one. In this context, in order to determine the response spectral moments, two approaches may be followed. In the most common one the evaluations are carried out through numerical integrations in the geometric space, accordingly to the flowchart reported in **Figure 1A**. In this case, the computational burden required for the analyses increases, even if it is drastically reduced with reference to Monte Carlo simulations. In the second alternative approach, herein proposed, the computations of spectral moments, taking advantage of the analytical model of the seismic action, does not require any numerical integrations, aiming at drastically reducing the computational efforts. A flowchart of this procedure is reported in **Figure 1B** and these two approaches are addressed in the following subsection.

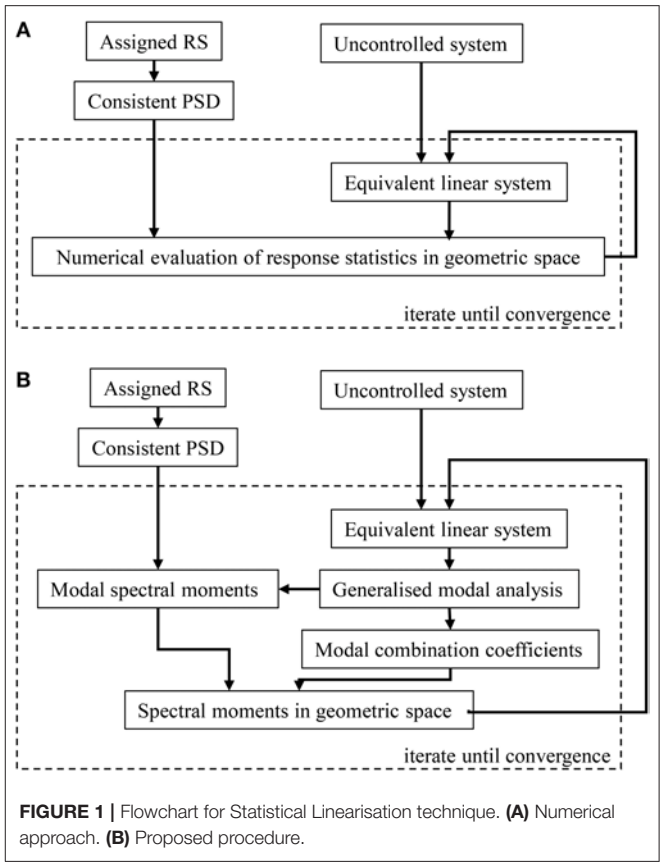

FIGURE 1 | Flowchart for Statistical Linearisation technique. **(A)** Numerical approach. **(B)** Proposed procedure.

3.1. Numerical Approach for the Evaluation of Spectral Moments

The evaluation of the j-th order spectral moment matrix in terms of the response quantity of interest vector $\mathbf{Y}$ may be performed through numerical integration in the geometric space of the response PSD matrix:

$$\Lambda_{\mathbf{Y},j} = \mathbf{R}\left(\int_0^\infty \omega^j \mathbf{G}_{\mathbf{UU}}(\omega)\, d\omega\right)\mathbf{R}^{\mathrm{T}} \tag{18}$$

being $\mathbf{G}_{\mathbf{UU}}(\omega)$ the one-sided PSD matrix of the response:

$$\mathbf{G}_{\mathbf{UU}}(\omega) = \mathbf{H}^*(\omega)\,\mathbf{M}^{(e)}\boldsymbol{\tau}\boldsymbol{\tau}^{\mathrm{T}}\mathbf{M}^{(e)\mathrm{T}}\mathbf{H}^{\mathrm{T}}(\omega)\,G_{\ddot{U}_g}(\omega) \tag{19}$$

in which $\mathbf{H}(\omega) = [-\omega^2\mathbf{M}^{(e)} + i\omega\mathbf{C}^{(e)} + \mathbf{K}^{(e)}]^{-1}$ is the transfer functions matrix, the asterisk denotes complex conjugate and $G_{\ddot{U}_g}(\omega)$ is the seismic load PSD function, whose expression is reported in Appendix for seismic actions consistent with several building codes RS. The spectral moments for the evaluation of the equivalent linear system, for the computation of the cost function and for the determination of the survival probability may be properly extracted from $\Lambda_{\mathbf{Y},j}$.

For lightly damped and flexible systems (large period of vibration), the accuracy of Equation (18) decreases mainly due to an insufficiently long duration assumed for the stationary excitations so that the steady-state conditions are not met. In order to enhance the accuracy, a frequency-dependent corrective damping factor can be adopted (Vanmarcke, 1976a). Spanos and Giaralis (2013) provided numerical results to facilitate the selection of sufficiently long duration of stationary excitation as a function of the structural natural frequency and damping ratio.

Numerical integration of Equation (18) requires large computational efforts and may lead to inaccurate estimations of spectral moments, due to the very sharp functions involved in the case of low damping values. Since numerical integrations are required at each step of the SL, the approach above described is highly time consuming, especially when used into an optimization problem.

3.2. Analytical Evaluation of the Spectral Moments

Generally, the equivalent linear system is not classically damped and a generalized modal analysis needs to be applied. Equations of motion, as customary, can be reformulated into a set of $2n$ first-order differential equations:

$$\dot{\mathbf{Z}} = \mathbf{D}^{(e)}\mathbf{Z} + \mathbf{V}\ddot{U}_g(t) \tag{20}$$

where the state-variables vector $\mathbf{Z}$, the system matrix $\mathbf{D}^{(e)}$ and the load vector $\mathbf{V}$ are defined as:

$$\mathbf{Z}=\begin{bmatrix}\mathbf{U}\\ \dot{\mathbf{U}}\end{bmatrix},\ \mathbf{D}^{(e)}=\begin{bmatrix}\mathbf{0} & \mathbf{I}_n\\ -\mathbf{M}^{(e)-1}\mathbf{K}^{(e)} & -\mathbf{M}^{(e)-1}\mathbf{C}^{(e)}\end{bmatrix},\ \mathbf{V}=-\begin{bmatrix}\mathbf{0}\\ \boldsymbol{\tau}\end{bmatrix} \tag{21}$$

The eigenvalues square roots γ_i and the eigenvectors $\boldsymbol{\psi}_i$ of $\mathbf{D}^{(e)}$ occur in conjugate pairs and they can be collected in such a way that $\gamma_i = \gamma^*_{i+n}$ and $\boldsymbol{\psi}_i = \boldsymbol{\psi}^*_{i+n}$. Moreover, due to the structure of the state-variables vector, the i-th eigenvector and the modal matrix are:

$$\boldsymbol{\psi}_i=\begin{bmatrix}\boldsymbol{\phi}_i\\ \gamma_i\boldsymbol{\phi}_i\end{bmatrix},\ \boldsymbol{\Psi}=\begin{bmatrix}\boldsymbol{\psi}_1 & \boldsymbol{\psi}_2 & \cdots & \boldsymbol{\psi}_{2n}\end{bmatrix}=\begin{bmatrix}\boldsymbol{\Phi} & \boldsymbol{\Phi}^*\\ \boldsymbol{\Gamma}\boldsymbol{\Phi} & \boldsymbol{\Gamma}^*\boldsymbol{\Phi}^*\end{bmatrix} \tag{22}$$

where $\boldsymbol{\Gamma} = diag\{\gamma_1, \gamma_2, \cdots, \gamma_n\}$ and $\boldsymbol{\Phi} = \begin{bmatrix}\boldsymbol{\phi}_1, \boldsymbol{\phi}_2, \cdots, \boldsymbol{\phi}_n\end{bmatrix}$ are the diagonal matrix of the eigenvalues square roots and the reduced modal matrix in terms of only displacements, respectively. Lastly, the modal participation factors vector can be defined as $\mathbf{p} = \boldsymbol{\Psi}^{-1}\mathbf{V}$. The i-th eigenvalue square root can be rewritten as $\gamma_i = -\zeta_i\,\omega_{0i} \pm i\,\omega_{Di}$, where ω_{0i}, ω_{Di} and ζ_i are determined by:

$$\omega_{0i}=|\gamma_i|,\ \zeta_i=-\frac{\mathrm{Re}\left[\gamma_i\right]}{|\gamma_i|},\ \omega_{Di}=\omega_{0i}\sqrt{1-\zeta_i^2} \tag{23}$$

These parameters designate natural frequency, modal damping and damped frequency of the i-th modal oscillator (Igusa et al., 1984), respectively. Taking advantage by the analytical definition of the seismic input PSD function reported in Appendix, it is possible to perform a closed-form approximate evaluation of direct spectral moments in the modal space, without resorting to numerical integrations (Barone et al., 2019). Referring to the i-th modal oscillator response process $Q_i(t)$, the expression of the j-th spectral moment $\lambda_{j,Q_i,k}$ is:

$$\lambda_{j,Q_i,k}=\frac{G_{\ddot{U}_g}(\omega_{0i})}{4\,\zeta_i\omega_{0i}^{3-j}}\varphi_{j,k}+\frac{1}{\omega_i^4}\sum_{s=1}^{k-1}G_{\ddot{U}_g}(\omega_s)\omega_s^{j+1}\gamma_{j,s} \tag{24}$$

when ω_{0i} falls within the k-th branch of the input PSD (see Equation 32), while the dimensionless quantities $\varphi_{j,k}$ and $\gamma_{j,s}$ are defined as follows:

$$\varphi_{j,k}=\pi-\frac{4\zeta_i}{(1+j)(1+j+e_k)}\begin{cases}e_k & j=0,2;\\ 2\,(1+e_k) & j=1;\\ 8+3e_k & j=3;\end{cases}$$
$$\gamma_{j,s}=\frac{e_{s+1}-e_s}{(1+j+e_{s+1})(1+j+e_s)} \tag{25}$$

and the quantities e_i, ω_s and $G_{\ddot{U}_g}(\omega_s)$ are the parameters of the analytical model of the PSD function, whose meaning is detailed in the Appendix. Further details on the derivation and application of Equations (24) to (25) can be found in Barone et al. (2019).

Di Paola and Muscolino (1988) demonstrated that the cross-spectral moments of any order λ_{j,Q_i,Q_k}, if they exist for a given PSD function of the excitation, may be obtained recursively as linear combinations of the direct spectral moments. These analytical expressions are reported in the Appendix for the sake of simplicity. Furthermore, it is noted that equations from (20) to (23) account for unitary values of modal participation factors $\mathbf{p}$. In this way, closed-from expressions for the determination of modal spectral moments—like those in Equation (24)—can be used straightforwardly. Conversely, when analytical expressions are not available for the problem at hand, only a limited number of numerical integrations should be performed in the modal space. Once the cross-spectral moments of the modal oscillators are obtained, the j-th order spectral moment of a set of quantities of interest in the geometric space defined by the vector $\mathbf{Y}$ can be computed as (Igusa et al., 1984):

$$\lambda_{Y_r,j}=\sum_{i=1}^{n}\sum_{k=1}^{n}\left(C_{r,ik}\mathrm{Re}\left[\lambda_{j,Q_i,Q_k}\right]-D_{r,ik}\mathrm{Im}\left[\lambda_{j+1,Q_i,Q_k}\right]+E_{r,ik}\mathrm{Re}\left[\lambda_{j+2,Q_i,Q_k}\right]\right) \tag{26}$$

where the modal combination coefficients $C_{r,ik}$, $D_{r,ik}$, and $E_{r,ik}$, which depend on the modal participating factors, can be determined as:

$$C_{r,ik}=a_{ri}a_{rk},\ D_{r,ik}=a_{ri}c_{rk}-a_{rk}c_{ri},\ E_{r,ik}=c_{ri}c_{rk} \tag{27}$$

being a_{ri} and c_{ri} the entries of the following matrices:

$$\mathbf{a}=-2\mathrm{Re}\left[\mathbf{b}\boldsymbol{\Gamma}^*\right],\ \mathbf{c}=-2\mathrm{Re}\left[\mathbf{b}\right] \tag{28}$$

whereas the matrix $\mathbf{b}=\mathbf{R}\boldsymbol{\Phi}\mathbf{p}_n$, with $\mathbf{p}_n = diag\{p_1, p_2, \cdots, p_n\}$.

It is worth to note that this procedure can be generally applied for both classically and non-classically damped systems and it can be easily implemented in a computer program routine. In general, approximate evaluations of the spectral moments are achieved since analytical closed-form solutions for response statistics are available just for a limited class of problems (Spanos and Miller, 1994; Artale et al., 2017). In these cases, exact analytical evaluation of the direct spectral moments in the modal space may be used in place of the Equation (24), thus obtaining exact results. Ultimately, the evaluation of spectral moments of response quantities of interest needs only the estimation of $4\hat{n}$ direct spectral moments in modal space, if a modal truncation is applied and only $\hat{n} \leq n$ modal contributions are retained. The estimation of the spectral moments $\lambda_{Y_r,j}$ allows for the updating of the linear equivalent system, for the estimation of the cost function and for the evaluation of the survival probability, as described in the previous section 2.

4. NUMERICAL APPLICATIONS

In this section, aiming to show the validity of the proposed approach, the results of numerical applications are reported. Case studies of optimal design of fluid viscous dampers are addressed for a plane five-story shear-type frame and for an irregular three-dimensional building structure.

Firstly, it is to be remarked that the analytical procedure proposed in section 3.2 is based on the approximate evaluation

of the direct modal spectral moments, Equations (24 and 25), by taking advantage of the definition of the probabilistic analytical model of the seismic input reported in Appendix. The same approach would also apply for other environmental hazards, i.e., wind or ocean waves, when a PSD model of the input is available. The issue of accuracy of the seismic PSD analytical model has been investigated in Barone et al. (2019), to which the reader is referred for further details. In **Figure 2**, however, a comparison between first order closed-form spectral moments ($m = 0, 1, 2$) and their numerical counterparts is shown for several values of natural periods and viscous damping ratios. Results are in very good agreement and small differences can be observed for high-order moments at large natural periods and damping ratios.

Therefore, when a specific application needs the evaluation of spectral moments in those cases in which larger errors can be anticipated, an alternative approach may consist in using numerical integration only for the $4n$ first direct modal spectral moments, instead of Equations (24, 25), and in evaluating all other response statistics accordingly to section 3.2. In this way both computational efficiency and high accuracy may be obtained.

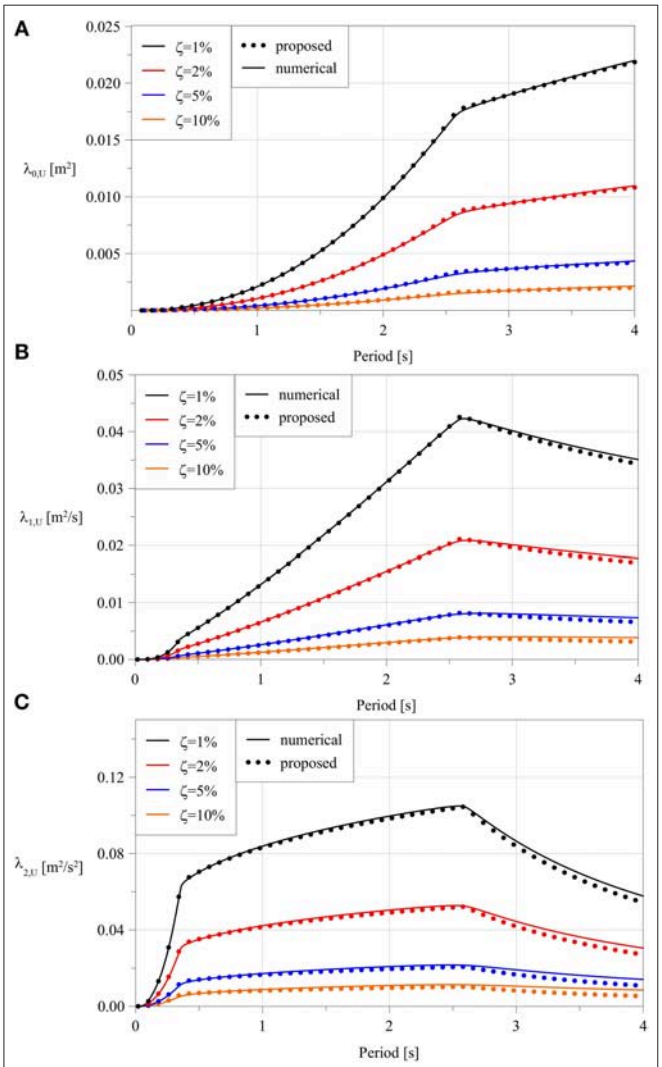

FIGURE 2 | Comparison between the first spectral moments evaluated numerically (solid lines) and by closed-form approximate expressions (dots) against natural period. **(A)** Zero order moments. **(B)** first order moments. **(C)** second order moments.

In all the following numerical applications. the seismic load is modeled accordingly to RS prescribed by Eurocode 8 (UNI ENV 1998:2005, 2005). In particular, it has been modeled as a process having an EC8-compatible PSD function, obtained considering the ground type A and a pseudo-stationary duration $T_s = 20$ s. Nevertheless, similar results can be obtained for a wide range of building codes RS covered by the model adopted (Barone et al., 2015, 2019). In **Table 1**, the parameters used to define the RS and the correspondent values in PSD analytical model, are reported.

Lastly, it is worthwhile noting that, since viscous dampers are usually installed in the braces of the structural frames, the relative displacements at the damper ends constitute a subset of the inter-story drifts at each story and in each direction. Therefore, it is convenient to denote with $\mathbf{Y}(t)$ the vector of all the inter-story drifts, to evaluate $\mathbf{R}$ accordingly, and to set the parameters $C_{d,i} = 0$ for all the locations in which actually there are no dampers.

4.1. Accuracy and Computational Efficiency

In order to investigate the proposed procedure both in terms of accuracy and computational efficiency, a plane five-story shear-type frame, originally proposed in Takewaki (1997) and then modified in Trombetti and Silvestri (2004) has been considered. In this structural system, referred to as *Model 1*, both horizontal stiffness of the columns and the story mass do not vary along the height. In particular, the mass and stiffness at each floor are $m_i = 8 \cdot 10^4$ kg and $k_i = 4 \cdot 10^7$ N/m, respectively. It is also assumed

TABLE 1 | Parameters for the definition of the design earthquake in terms of Response Spectrum and PSD function.

Parameter	Value	Parameter	Value
S_0	0.250 g	G_0	1.8148 10^{-2} g^2/(rad/s)
a	2.50	e_1	2.5688
T_1	2.00 s	e_2	0.7526
T_2	0.40 s	e_3	−1.3247
T_3	0.15 s	e_4	−2.6468

TABLE 2 | Computational times and mean errors for application of numerical and analytical procedures.

	Computational time [ms]		Mean errors [%]	
	Numerical	Analytical	$\bar{e}_U$	$\bar{e}_{\dot{Y}}$
Uncontrolled	380	24	0.12	0.20
FB-G	3,812	31	0.88	1.13
FB-NG	3,841	32	0.92	1.04
EE-G	4,158	30	0.34	1.28
EE-NG	4,035	28	0.91	1.10

a constant modal damping ratio $\zeta_i = 0.02$ and the horizontal displacements U_i at each story have been chosen as degrees of freedom. The location vector is given as $\boldsymbol{\tau} = \begin{bmatrix} 1 & 1 & 1 & 1 & 1 \end{bmatrix}^{\mathrm{T}}$. In this application, the inter-story drifts are obtained as $\mathbf{Y}(t) = \mathbf{R}\mathbf{U}(t)$, where the linear transformation matrix $\mathbf{R}$ is:

$$\mathbf{R} = \begin{bmatrix} 1 & 0 & 0 & 0 & 0 \\ -1 & 1 & 0 & 0 & 0 \\ 0 & -1 & 1 & 0 & 0 \\ 0 & 0 & -1 & 1 & 0 \\ 0 & 0 & 0 & -1 & 1 \end{bmatrix} \tag{29}$$

As a first application, two identical FVDs having $\alpha_i = 0.15$ and $C_{d,i} = 1 \times 10^5$ N/(m/s)$^{\alpha_i}$ and positioned only at the first and third inter-story, are considered. Stochastic linearisation is performed using four statistical equivalences criteria, chosen among those described in De Domenico and Ricciardi (2018). In particular, force-based Gaussian SLT (FB-G), force-based non-Gaussian SLT (FB-NG), equal energy Gaussian SLT (EE-G) and equal energy non-Gaussian SLT (EE-NG) criteria are used. Response statistics are computed for uncontrolled and controlled system and, in the latter case, for each of the aforementioned equivalence criteria. Results are reported in **Table 2** in terms of computational time and of mean relative errors in the evaluation of the displacements, U_i and relative velocity standard deviations $\dot{Y}_i$. The two mean errors are defined as follows:

$$\bar{e}_U = \frac{1}{n}\sum_{i=1}^{n} \frac{\sigma_{U_i,ana} - \sigma_{U_i,num}}{\sigma_{U_i,num}};$$
$$\bar{e}_{\dot{Y}} = \frac{1}{m}\sum_{i=1}^{m} \frac{\sigma_{\dot{Y}_i,ana} - \sigma_{\dot{Y}_i,num}}{\sigma_{\dot{Y}_i,num}} \tag{30}$$

where the subscripts *ana* and *num* stand for analytical and numerical evaluation, respectively.

Outcomes of computational times for uncontrolled system show that a great reduction of more than 90% is achieved for each evaluation of response statistics, whereas the mean errors with respect to numerical integrations, in terms of both displacements and relative velocities, are negligible.

The advantage in using analytical procedure becomes more and more evident when it is used inside a SL procedure. In fact, for the present case, eleven iterations are needed, irrespective of the equivalence criterion adopted; the computational efforts of the numerical approach increase proportionally, while no significant increments of computational time are observed for the analytical procedure. During the iterations, discrepancies due to the use of analytical procedure tend to accumulate, but the mean errors are limited below few percentage points.

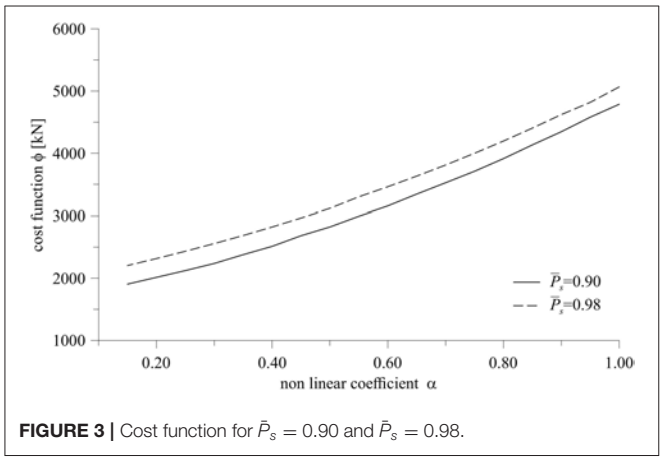

FIGURE 3 | Cost function for $\bar{P}_s = 0.90$ and $\bar{P}_s = 0.98$.

4.2. Optimal Patterns and Optimal Design

In this section, the proposed analytical procedure is applied to determine the optimal pattern of fluid viscous dampers, accordingly to the minimization problem outlined in Equation (3). The minimization procedure is carried out by using the

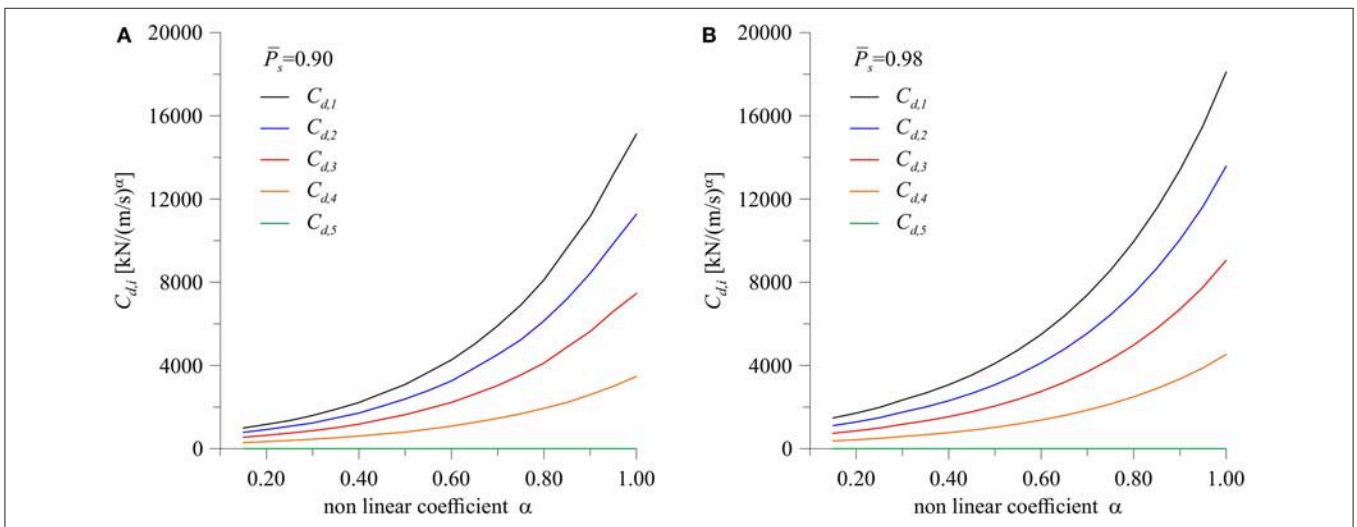

FIGURE 4 | Optimal pattern of viscous dampers. for **(A)** $\bar{P}_s = 0.90$ and **(B)** $\bar{P}_s = 0.98$.

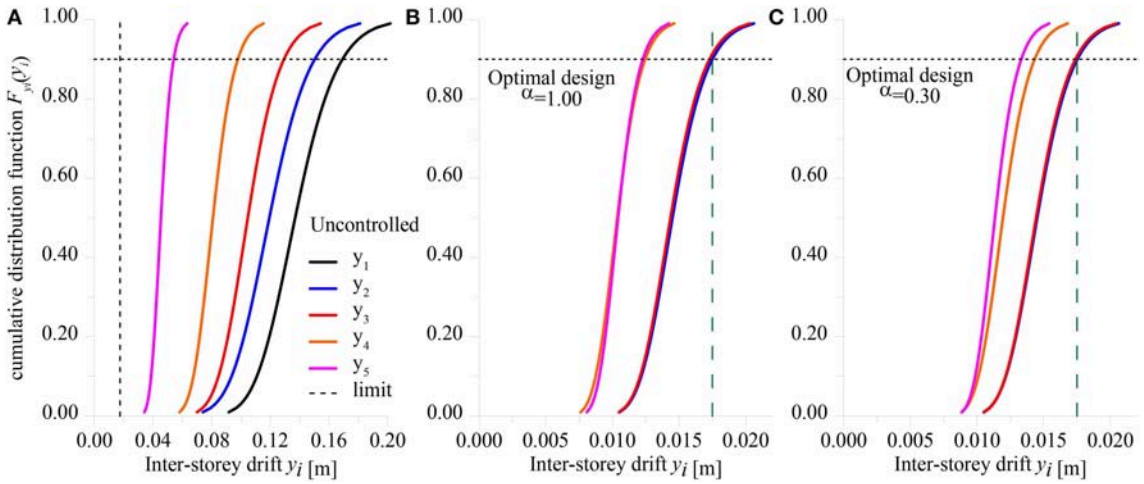

FIGURE 5 | Cumulative distribution functions of inter-story drifts. **(A)** Uncontrolled structure. **(B)** optimal design for $\alpha = 1.00$. **(C)** optimal design for $\alpha = 0.30$. Target survival probability $\bar{P}_s = 0.90$.

routine *fmincon* in MATLAB environment that uses the interior-point algorithm. Following this approach, the constrained minimization is reduced to a sequence of approximate minimization problems (Byrd et al., 2000).

The probabilistic constraint in the optimization loop is defined by assuming that structure fails when the maximum inter-story drift ratio at any story and in any direction exceeds the value of 0.5%, as suggested by Eurocodes. Such a value ensures almost elastic behavior of the structure. The minimum allowable survival probability $\bar{P}_s$ is treated as a parameter and numerical analyses are performed for different values of $\bar{P}_s$.

With reference to the aforementioned *Model 1*, the optimal design of viscous dampers is performed by considering the presence of a device at each floor and assuming a constant story height $h_i = 3.50$ m. Optimal patterns have been evaluated for several values of the dampers coefficient α, ranging from 0.15 to 1.00, and for two values of the target survival probability $\bar{P}_s$, 0.90 and 0.98. **Figure 3** depicts the cost function of Equation (8) against α, whereas the correspondent optimal values of $C_{d,i}$ are shown in **Figure 4**.

It is worth to note that, for every value of α, the optimal pattern remains practically the same and the presence of dampers at fifth inter-story is excluded (i.e., $C_{d,5} = 0$). Moreover, the use of strongly non linear devices has proven to be beneficial as it allows for a great reduction of the maximum forces exerted by dampers, thus reducing their size and, consequently, their cost.

In **Figure 5**, cumulative distribution functions of the inter-story drifts have been computed for probability values from 1% to 99% and compared with the maximum allowable drift (0.5% of the inter-story height). For the uncontrolled structural system (**Figure 5A**), i.e., when no dampers devices are used, all inter-story drifts largely exceed the limit, whereas **Figures 5B,C** depict the configurations correspondent to the optimal deployment of viscous damper devices for $\alpha = 1.00$ and $\alpha = 0.30$, respectively. In the latter configurations, optimal control of structural displacements is achieved, since most of inter-story drifts reach the maximum allowable value at the same time, thus obtaining an almost uniform distribution of deformations and stresses throughout the height of the frame (Connor, 2003).

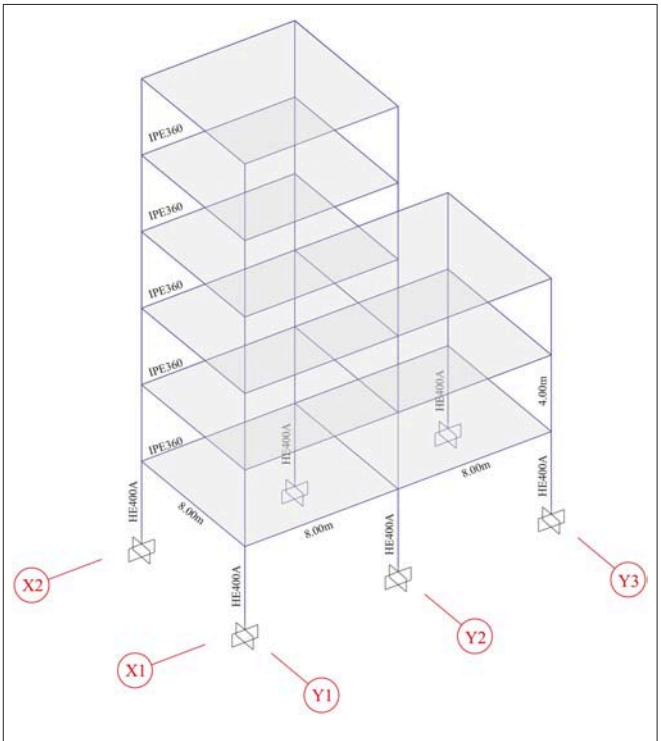

FIGURE 6 | Geometrical characteristics of the six-story three-dimensional building.

The second structural model, denoted as *Model 2*, consists of an irregular three-dimensional six-story building structure, whose geometrical characteristics are illustrated in **Figure 6**.

Each floor height is 4.00 m, the first three floors have an overall dimension of 8.0 m by 16.0 m, while the top three story have plan dimension of 8.0 m by 8.0 m. All the columns are made up by HE400A profiles, whereas beams have IPE360 cross section. An uniform gravity load of $q = 5.5$ kN/m^2 is considered. This structure is representative of a low-to-medium rise civil steel building. Under the assumptions of rigid diaphragms at each floor and of inextensible columns, the

TABLE 3 | Natural frequencies, mass participation ratios and equivalent linear damping of Model 2 system.

Mode	Frequency	Participating mass ratio		Equivalent linear damping [%]			ζ_i/ζ ratio		
	[Hz]	$\theta = 0°$ [%]	$\theta = 90°$ [%]	UNC	OPT-X	OPT-Y	UNC	OPT-X	OPT-Y
1	0.735	0.0	81.1	2.00	2.03	21.03	1.02	1.02	1.00
2	1.585	83.6	0.0	2.00	3.35	2.00	1.00	1.00	1.00
3	1.593	0.0	11.2	2.00	2.48	30.64	1.00	1.00	1.00
4	2.059	0.0	2.6	2.00	2.53	19.14	1.00	1.00	1.00
5	3.103	0.0	3.8	2.00	2.00	3.80	1.00	1.00	1.00
6	3.779	11.3	0.0	2.00	3.28	2.00	1.00	1.00	1.00

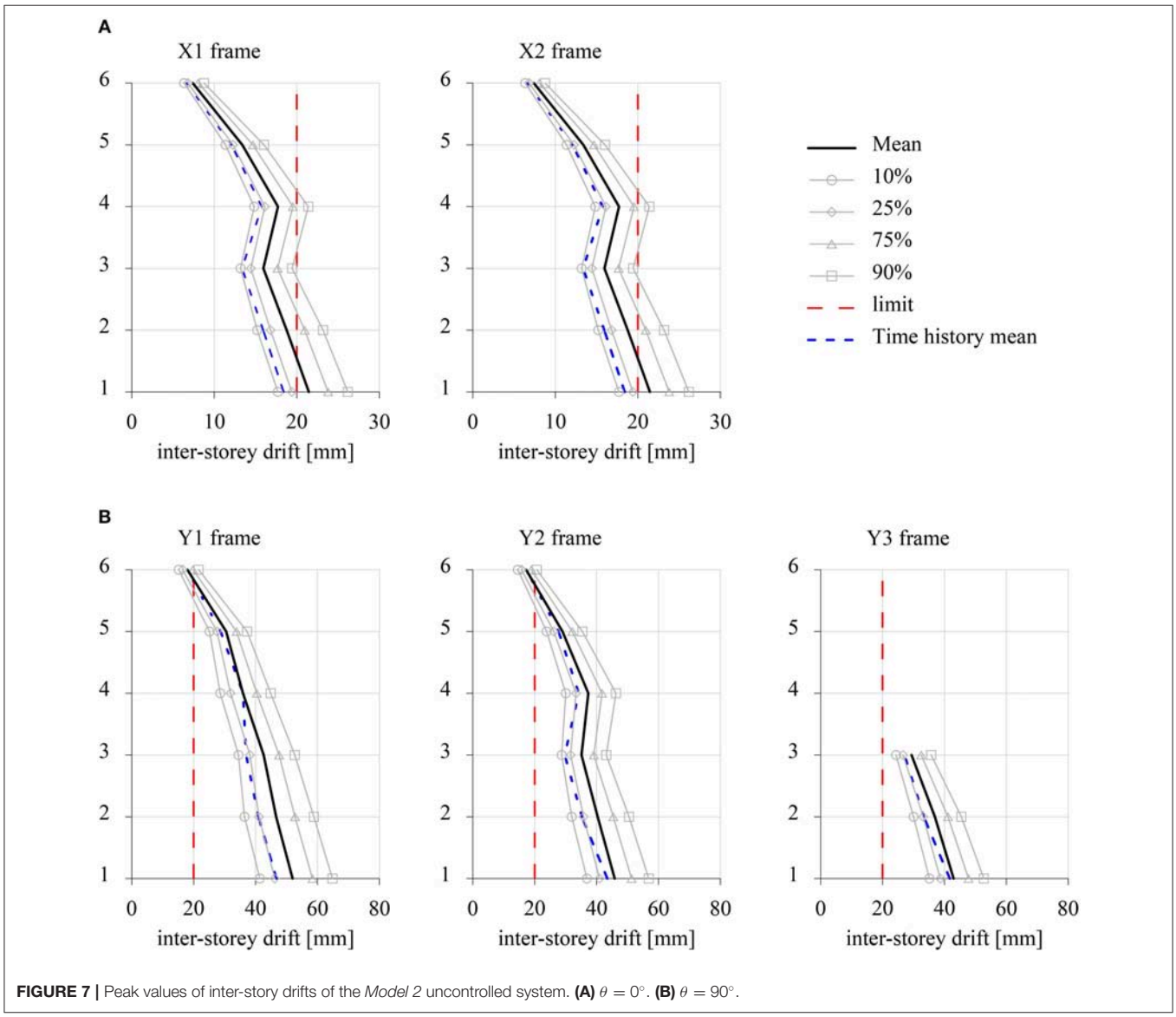

FIGURE 7 | Peak values of inter-story drifts of the *Model 2* uncontrolled system. **(A)** $\theta = 0°$. **(B)** $\theta = 90°$.

dynamically significant degrees of freedom of the i-th floor can be reduced to two translations (u_i and v_i) and a rotation φ_i, for a total of 18 degrees of freedom. A constant modal damping of $\zeta_i = 0.02, (i = 1, \ldots, 6)$ is assumed.

The structure is composed of two frames in x-direction and of three frames in y-direction. In this case, the vector **Y** collects all the 27 inter-story drifts (six for the frames X1, X2, Y1, and Y2 and three for the frame Y3), useful for evaluate the constraint function and the **R** matrix is derived accordingly.

The first columns of the **Table 3** reports the modal parameters of the stiffer modal oscillators in terms of natural frequencies and of mass participating ratios for two epicentral directions of the ground motion, namely $\theta = 0^\circ$ (x-direction) and $\theta = 90^\circ$ (y-direction). For each frame, **Figure 7** depicts the distribution of inter-story drifts peak values along the height computed for 25%, 50% (mean value), 75% and 90% percentiles. It can be observed that the building exhibits inter-story drift ratios that exceed the value of 0.5% for both the epicentral

TABLE 4 | Cost function and characteristic parameters for optimal configurations.

	cost function [kN]	$C_{d,xl}$ [kN/(m/s)$^\alpha$]	$C_{d,xh}$ [kN/(m/s)$^\alpha$]	$C_{d,yl}$ [kN/(m/s)$^\alpha$]	$C_{d,yh}$ [kN/(m/s)$^\alpha$]	$IDR_{\max}$
$\theta = 0^\circ$	89.204	24.04	0.00	0.00	0.00	X1, 1st floor
$\theta = 90^\circ$	292.74	0.00	0.00	100.26	0.00	Y1, 1st floor

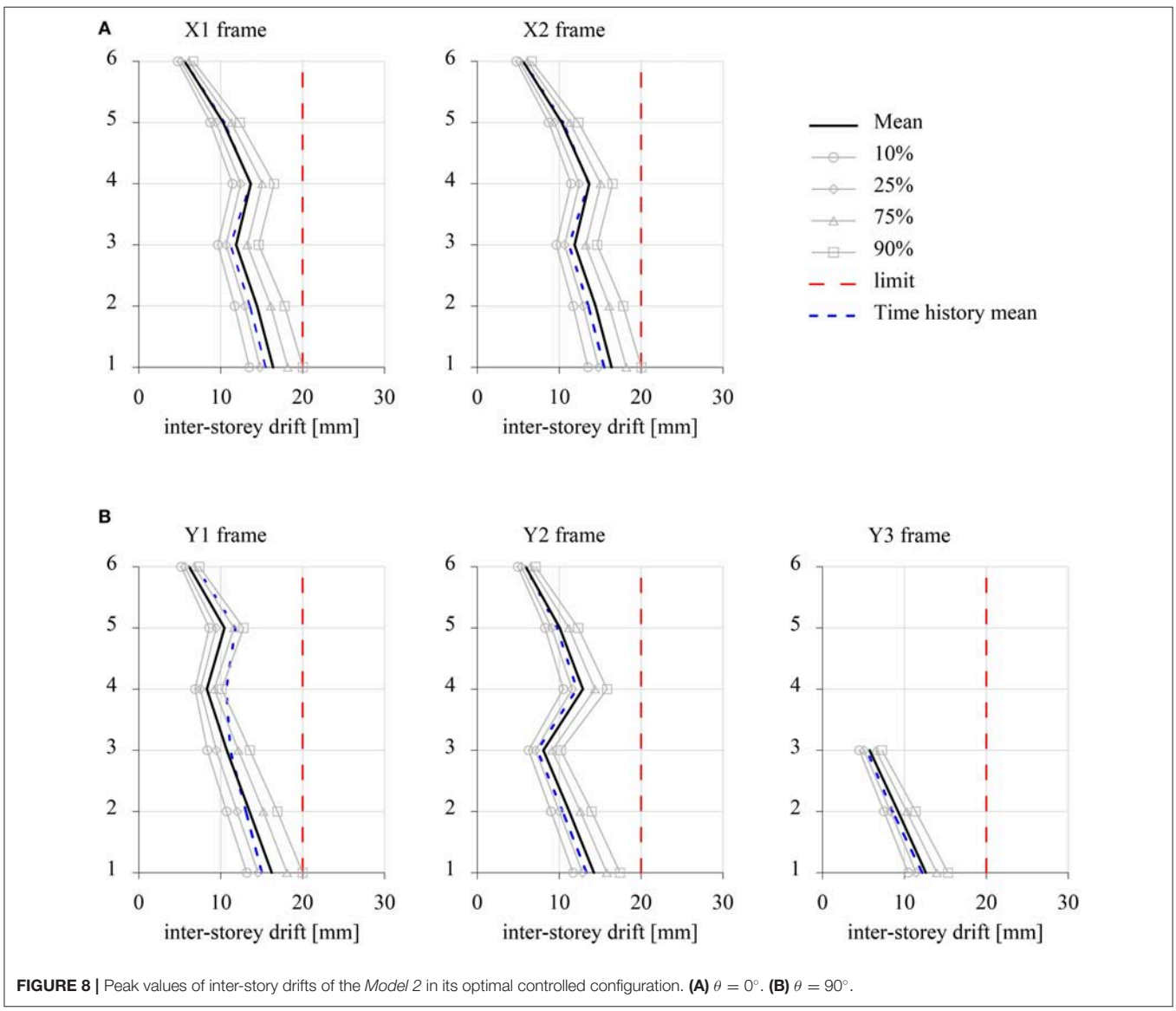

FIGURE 8 | Peak values of inter-story drifts of the *Model 2* in its optimal controlled configuration. **(A)** $\theta = 0^\circ$. **(B)** $\theta = 90^\circ$.

directions, even if these are larger when earthquake strikes in y-direction.

Four typologies of dampers are considered for optimization purposes, all having the non-linear coefficient $\alpha = 0.3$. In particular, the characteristic parameters of the dampers at the three lower floors of x-direction and y-direction frames have been denoted as $C_{d,xl}$ and $C_{d,yl}$, respectively, whereas the correspondent parameters of the dampers at the three higher floors have been denoted as $C_{d,xh}$ and $C_{d,yh}$, respectively.

Two analyses have been performed in order to evaluate the optimal pattern of the viscous dampers for a target survival probability of $\bar{P}_s = 0.90$ and for $\theta = 0^\circ$ (OPT-X) and $\theta = 90^\circ$(OPT-Y). In **Table 4**, the cost function and the values of the characteristic parameters of the four damper typologies are reported for $\theta = 0^\circ$ and $\theta = 90^\circ$. It is to be noted that, irrespective of the epicentral direction, the optimal damper configurations require dampers only at lower floors, since the dynamic behavior of the building structure is dominated by the first bending mode. **Table 4** also shows that the maximum inter-story drift occurred at the first floor of $X1$ frame for $\theta = 0^\circ$ and at the first floor of $Y1$ frame for $\theta = 90^\circ$. Moreover, in the last columns of **Table 3** the values of equivalent linear damping at each of the first six modes are reported for uncontrolled system (UNC) and for the optimal configurations attained for $\theta = 0^\circ$ (OPT-X) and $\theta = 90^\circ$ (OPT-Y). The corrective damping ratios ζ_i/ζ (Spanos and Giaralis, 2013), also reported in **Table 3**, show that, for the problem at hand, the stationarity assumption has negligible effects in the determination of the response statistics. Since optimal design leads to inter-story drifts close to the limit value, larger dampers are required in y-directed frames. This is obviously reflected also in equivalent linear damping values. **Figure 8** depicts the distribution along height of the peak values of the inter-story drifts resulting from the optimal design for the epicentral directions $\theta = 0^\circ$ and $\theta = 90^\circ$.

Since the proposed approach contains several approximations (mainly related to the modeling of the seismic action and on the use of SL), its effectiveness in determining the optimal configuration of dampers is further assessed in the time domain. Aiming at this, a set of seven natural recorded ground motion time-histories has been selected in order to match the EC8 RS used in the previous analyses (Iervolino et al., 2010). Individual ground motion records have been scaled and the spectrum compatibility has been achieved by imposing a ±10% tolerance with respect to the target RS in the period range between 0.10 and 2.5 s. In **Table 5**, all the selected records are listed, together with the main characteristics of the considered earthquakes. The results of the spectrum-compatibility check are shown in **Figure 9** in terms of individual and mean RS together to the target RS and the tolerance zone.

Equations (1) and (4) have been solved by means of a step-by-step fourth-order Runge-Kutta integration scheme in order to evaluate the dynamic response of the *Model 2* building subjected to the selected ground motions for the two epicentral directions $\theta = 0^\circ$ and $\theta = 90^\circ$. Peak values of the inter-story drift have been computed for each record and their mean value has been reported in blue dashed line for comparison purposes in **Figure 7** and **Figure 8** for uncontrolled and optimal controlled configurations, respectively. The comparison in the uncontrolled system shows that, although stochastic analysis tends to overestimate the inter-story drifts, both the methodologies are able to capture the distribution of the inter-story drift along the height of the building. Also for the optimal damper configuration cases, the time-domain analysis shows a good agreement with the results of the stochastic analysis, thus demonstrating the effectiveness of the proposed approach in the optimal design of a passive control system. However, it is to be remarked that the time-domain analysis allows to evaluate only the mean values of the response peaks, whereas the stochastic analysis provides the full probabilistic characterization of the response.

5. CONCLUSIONS

In this paper, a methodology for the optimal design of passive control systems into a probabilistic framework has been described. In this way, uncertainties and response dispersion have been taken into account and, at the same time, a seismic analysis consistent with the Eurocode 8 response spectra has been carried out. The following conclusions can be drawn:

- A general form of Stochastic Linearisation approach for the cases of MDOF structural systems controlled by multi concurrent passive control devices has been presented and an iterative efficient solution, able to avoid any use of numerical integrations, has been proposed for the case of seismic loads.
- Herein, an optimal design procedure for fluid viscous dampers has been formulated. For this purpose, a cost function has been

TABLE 5 | Characteristic of selected ground motion records.

Event	Station ID	Earthquake name	Date	Mw	Fault mechanism	Original PGA [g]	Scaled PGA [g]	Scale Factor
1	ST2557	South Iceland	21/06/2000	6.4	Strike slip	0.127	0.25	1.965
2	ST222	Umbria Marche	26/09/1997	6.0	Normal	0.025	0.25	9.922
3	ST20	Friuli	06/05/1976	6.5	Thrust	0.316	0.25	0.792
4	ST132	Kozani	13/05/1995	6.5	Normal	0.142	0.25	1.757
5	ST3311	Avej	22/06/2002	6.5	Thrust	0.446	0.25	0.561
6	ST2486	South Iceland	17/06/2000	6.5	Strike slip	0.318	0.25	0.787
7	ST93	Campano Lucano	23/11/1980	6.9	Normal	0.181	0.25	1.381

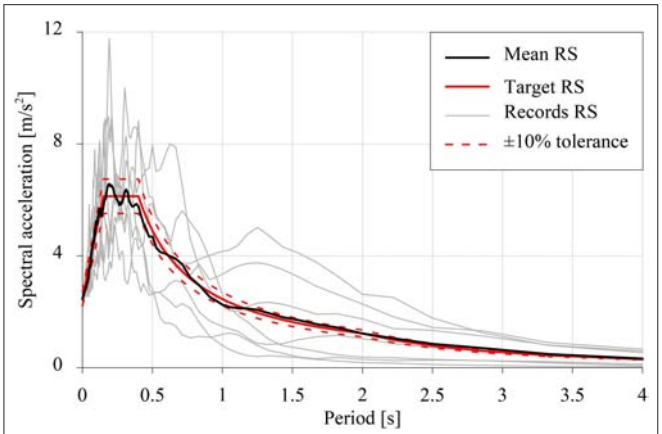

FIGURE 9 | Spectrum compatibility check results.

used as objective function to minimize. This has been defined as the sum of the characteristic values of the forces exerted by the dampers themselves.

- Taking advantage of an analytical model for the computation of response spectra compatible PSD functions as well as of complex modal analysis in state-space, analytical evaluations of the first spectral moments of a set of response quantities of interest have been derived for not-classically damped systems.
- The design problem has been posed in terms of survival probability considering that the failure of the structural system is identified with the over-crossing of a maximum allowable relative displacement.
- The validity of the proposed approach has been investigated in terms of accuracy and computational efficiency and two applications have been presented. The first one is related to a plane shear-type five-story frame, while the second one deals with a six-story three-dimensional building structure. Optimal damper configurations and cumulative distribution functions of inter-story drifts have been evaluated and it is proved that the proposed procedure leads to an accurate evaluation of response statistics.
- The proposed procedure allows for a dramatic reduction of the computational time, especially when is used for those problems that make intensive use of stochastic linearisation technique, as optimal design of passive control device.
- The effectiveness of the proposed approach has been assessed against the results of time-domain analyses by using a set of seven scaled spectrum-compatible natural ground motion records.
- The most recent SL techniques for the hysteretic systems seismic demand evaluation can benefit of the two novel aspects herein presented, namely the analytical model of PSD functions and the algorithm for evaluating spectral moments, in terms of both computational efficiency and accuracy.

DATA AVAILABILITY STATEMENT

The datasets generated for this study are available on request to the corresponding author.

AUTHOR CONTRIBUTIONS

All the authors contributed in an equal manner to the study of the relevant literature, to the derivation of the proposed approach, to the preparation of software routines for the numerical applications and to writing and editing of the manuscript.

REFERENCES

Alibrandi, U., and Ricciardi, G. (2012). *Stochastic Methods in Nonlinear Structural Dynamics*. Vienna: Springer.

Altieri, D., Tubaldi, E., De Angelis, M., Patelli, E., and Dall'Asta, A. (2018). Reliability-based optimal design of nonlinear viscous dampers for the seismic protection of structural systems. *Bull. Earthq. Eng.* 16, 963–982. doi: 10.1007/s10518-017-0233-4

Artale, V., Navarra, G., Ricciardello, A., and Barone, G. (2017). Exact closed-form fractional spectral moments for linear fractional oscillators excited by a white noise. *ASCE-ASME J. Risk Uncertain. Eng. Syst. B Mech. Eng.* 3:030901. doi: 10.1115/1.4036700

Atalik, T. S., and Utku, S. (1976). Stochastic linearization of multi-degree-of-freedom nonlinear system. *Earthq. Eng. Struct. Dyn.* 4, 411–420. doi: 10.1002/eqe.4290040408

Bahnasy, A., and Lavan, O. (2013). "Linear or nonlinear fluid viscous dampers? A seismic point of view," in *Proceedings of the Structures Congress* (Pittsburgh, PA). doi: 10.1061/9780784412848.197

Barone, G., Lo Iacono, F., Navarra, G., and Palmeri, A. (2015). "A novel analytical model of Power Spectral Density function coherent with earthquake Response Spectra," in *Proceedings of the 1st International Conference on Uncertainty Quantification in Computational Sciences and Engineering (UNCECOMP 2015)*, eds G. S. M. Papadrakakis and V. Papadopoulos (Athens: Institute of Structural Analysis and Antiseismic Research School of Civil Engineering National Technical University of Athens (NTUA) Greece), 394–406.

Barone, G., Lo Iacono, F., Navarra, G., and Palmeri, A. (2019). Closed-form stochastic response of linear building structures to spectrum-consistent seismic excitations. *Soil Dyn. Earthq. Eng.* 125:105724. doi: 10.1016/j.soildyn.2019.105724

Byrd, R. H., Gilbert, J. C., and Nocedal, J. (2000). A trust region method based on interior point techniques for nonlinear programming. *Math. Programming* 89, 149–185. doi: 10.1007/PL00011391

Cacciola, P., Colajanni, P., and Muscolino, G. (2004). Combination of modal responses consistent with seismic input representation. *J. Struct. Eng.* 130, 47–55. doi: 10.1061/(ASCE)0733-9445(2004)130:1(47)

Connor, J. J. (2003). *Introduction to Structural Motion Control*. Cambridge, MA: MIT-Prentice Hall Series on Civil, Environmental, and Systems Engineering.

De Domenico, D., and Ricciardi, G. (2018). Improved stochastic linearization technique for structures with nonlinear viscous dampers. *Soil Dyn. Earthq. Eng.* 113, 415–419. doi: 10.1016/j.soildyn.2018.06.015

De Domenico, D., and Ricciardi, G. (2019). Earthquake protection of structures with nonlinear viscous dampers optimized through an energy-based stochastic approach. *Eng. Struct.* 179, 523–539. doi: 10.1016/j.engstruct.2018.09.076

De Domenico, D., Ricciardi, G., and Takewaki, I. (2019). Design strategies of viscous dampers for seismic protection of building structures: a review. *Soil Dyn. Earthq. Eng.* 118, 144–165. doi: 10.1016/j.soildyn.2018.12.024

Der Kiureghian, A. (1980). Structural response to stationary excitation. *J. Eng. Mech. Div.* 106, 1195–1213.

Der Kiureghian, A., and Fujimura, K. (2009). Nonlinear stochastic dynamic analysis for performance-based earthquake engineering. *Earthq. Eng. Struct. Dyn.* 38, 719–738. doi: 10.1002/eqe.899

Di Matteo, A., Lo Iacono, F., Navarra, G., and Pirrotta, A. (2014a). "A novel mathematical model for TLCD: theoretical and experimental investigations," in *Vulnerability, Uncertainty, and Risk: Quantification, Mitigation, and Management - Proceedings of the 2nd International Conference on Vulnerability and Risk Analysis and Management, ICVRAM 2014 and the 6th International Symposium on Uncertainty Modeling* (Liverpool, UK).

Di Matteo, A., Lo Iacono, F., Navarra, G., and Pirrotta, A. (2014b). Experimental validation of a direct pre-design formula for tlcd. *Eng. Struct.* 75, 528–538. doi: 10.1016/j.engstruct.2014.05.045

Di Matteo, A., Lo Iacono, F., Navarra, G., and Pirrotta, A. (2015). Optimal tuning of tuned liquid column damper systems in random vibration by means of an approximate formulation. *Meccanica* 50, 795–808. doi: 10.1007/s11012-014-0051-6

Di Paola, M., La Mendola, L., and Navarra, G. (2007). Stochastic seismic analysis of structures with nonlinear viscous dampers. *J. Struct. Eng.* 133, 1475–1478. doi: 10.1061/(ASCE)0733-9445(2007)133:10(1475)

Di Paola, M., and Muscolino, G. (1988). Analytic evaluation of spectral moments. *J. Sound Vibrat.* 124, 479–488. doi: 10.1016/S0022-460X(88)81389-0

Di Paola, M., and Navarra, G. (2009). Stochastic seismic analysis of MDOF structures with nonlinear viscous dampers. *Struct. Control Health Monit.* 16, 303–318. doi: 10.1002/stc.254

Elishakoff, I. (2000). Stochastic linearization technique: a new interpretation and a selective review. *Shock Vibr. Dig.* 32, 179–188. doi: 10.1177/058310240003200301

Fujimura, K., and Der Kiureghian, A. (2007). Tail-equivalent linearization method for nonlinear random vibration. *Probabilist. Eng. Mech.* 22, 63–76. doi: 10.1016/j.probengmech.2006.08.001

Giaralis, A., and Spanos, P. D. (2010). Effective linear damping and stiffness coefficients of nonlinear systems for design spectrum based analysis. *Soil Dyn. Earthq. Eng.* 30, 798–810. doi: 10.1016/j.soildyn.2010.01.012

Gidaris, I., and Taflanidis, A. A. (2015). Performance assessment and optimization of fluid viscous dampers through life-cycle cost criteria and comparison to alternative design approaches. *Bull. Earthq. Eng.* 13, 1003–1028. doi: 10.1007/s10518-014-9646-5

Housner, G., Bergman, L., Caughey, T., Chassiakos, A., Claus, R., Masri, S., et al. (1997). Structural control: past, present, and future. *J. Eng. Mech.* 123, 897–971. doi: 10.1061/(ASCE)0733-9399(1997)123:9(897)

Iervolino, I., Galasso, C., and Cosenza, E. (2010). REXEL: computer aided record selection for code-based seismic structural analysis. *Bull. Earthq. Eng.* 8, 339–362. doi: 10.1007/s10518-009-9146-1

Igusa, T., Kiureghian, A. D., and Sackman, J. L. (1984). Modal decomposition method for stationary response of non-classically damped systems. *Earthq. Eng. Struct. Dyn.* 12, 121–136. doi: 10.1002/eqe.4290120109

Makris, N., Constantinou, M. C., and Dargush, G. F. (1993). Analytical model of viscoelastic fluid dampers. *J. Struct. Eng.* 119, 3310–3325. doi: 10.1061/(ASCE)0733-9445(1993)119:11(3310)

Melchers, R. (1999). *Structural Reliability Analysis and Prediction, 2nd Edn*. Chichester, UK: John Wiley & Sons Ltd.

Mitseas, I. P., Kougioumtzoglou, I. A., Giaralis, A., and Beer, M. (2018). A novel stochastic linearization framework for seismic demand estimation of hysteretic MDOF systems subject to linear response spectra. *Struct. Safety* 72, 84–98. doi: 10.1016/j.strusafe.2017.12.008

Navarra, G., Lo Iacono, F., and Oliva, M. (2017). "Probabilistic optimal design of passive control devices coherently with seismic codes response spectra," in *Proceedings of the 23rd Conference of the Italian Association of Theoretical and Applied Mechanics (AIMeTA 2017)* (Rome).

Navarra, G., Lo Iacono, F., Oliva, M., and Cascone, D. (2019a). "Speeding up the stochastic linearisation for systems controlled by non-linear passive devices," in *Proceedings of the 24th Conference of the Italian Association of Theoretical and Applied Mechanics (AIMeTA 2019)* (Rome).

Navarra, G., Lo Iacono, F., Oliva, M., and Esposito, A. (2019b). "Design of a NES device via efficient stochastic linearisation," in *Proceedings of ICNAAM 2019 - 17th International Conference on Numerical Analysis and Applied Mathematics*. (Rhodes).

Oliva, M., Barone, G., and Navarra, G. (2017). Optimal design of nonlinear energy sinks for sdof structures subjected to white noise base excitations. *Eng. Struct.* 145, 135–152. doi: 10.1016/j.engstruct.2017.03.027

Pinto, P., Giannini, R., and Franchin, P. (2007). Seismic reliability analysis of structures. *Earthq. Eng. Struct. Dyn.* 36, 2081–2081. doi: 10.1002/eqe.742

Roberts, J., and Spanos, P. (1991). *Random Vibration and Statistical Linearization*. Chichester: John Wiley & Sons Ltd.

Schwann, K., Reinsch, H., and Weber, F. (1988). "Description of the feature of viscous dampers on the goals of equivalent rheological models, presented for pipework dampers," in *Proceedings of the Pressure Vessels and Piping Conference, ASME* (Pittsburgh, PA), 528–538.

Spanos, P. D., and Giaralis, A. (2013). Third-order statistical linearization-based approach to derive equivalent linear properties of bilinear hysteretic systems for seismic response spectrum analysis. *Struct. Safety* 44, 59–69. doi: 10.1016/j.strusafe.2012.12.001

Spanos, P. D., and Miller, S. M. (1994). Hilbert transform generalization of a classical random vibration integral. *J. Appl. Mech.* 61, 575–581. doi: 10.1115/1.2901498

Spencer, B., and Nagarajaiah, S. (2003). State of the art of structural control. *J. Struct. Eng.* 129, 845–856. doi: 10.1061/(ASCE)0733-9445(2003)129:7(845)

Takewaki, I. (1997). Optimal damper placement for minimum transfer functions. *Earthq. Eng. Struct. Dyn.* 26, 1113–1124.

Trombetti, T., and Silvestri, S. (2004). Added viscous dampers in shear-type structures: the effectiveness of mass proportional damping. *J. Earthq. Eng.* 8, 275–313. doi: 10.1080/13632460409350490

Tubaldi, E., Barbato, M., and Dall'Asta, A. (2016). Efficient approach for the reliability-based design of linear damping devices for seismic protection of buildings. *ASCE-ASME J. Risk Uncertain. Eng. Syst. A Civil Eng.* 2:C4015009. doi: 10.1061/AJRUA6.0000858

Tubaldi, E., and Kougioumtzoglou, I. A. (2015). Nonstationary stochastic response of structural systems equipped with nonlinear viscous dampers under seismic excitation. *Earthq. Eng. Struct. Dyn.* 44, 121–138. doi: 10.1002/eqe.2462

UNI ENV 1998:2005 (2005). *Eurocode 8: Design of Structures for Earthquake Resistance Part 1: General Rules, Seismic Actions and Rules for Buildings*. Brussels: Standard, CEN Central Secretariat.

Vanmarcke, E. H. (1972). Properties of spectral moments with applications to random vibration. *J. Eng Mech. Div.* 98, 425–446.

Vanmarcke, E. H. (1975). On the distribution of the first-passage time for normal stationary random processes. *J. Appl. Mech.* 42:215. doi: 10.1115/1.3423521

Vanmarcke, E. H. (1976a). "Chapter 8 - structural response to earthquakes," in *Seismic Risk and Engineering Decisions*, volume 15 of *Developments in Geotechnical Engineering*, eds C. Lomnitz and E. Rosenblueth (Amsterdam: Elsevier), 287–337.

Vanmarcke, E. H. (1976b). *Structural Response to Earthquakes*. Vol. 55. Mexico City: Elsevier Scientific Publishing Company.

Conflict of Interest: The authors declare that the research was conducted in the absence of any commercial or financial relationships that could be construed as a potential conflict of interest.

APPENDIX

Stochastic model of the seismic action consistent with Response Spectra

The procedure for the optimal design of passive control devices into a probabilistic framework requires the modeling of the seismic ground motion as a stochastic process. Generally, international building codes define the seismic action by means of pseudo-acceleration elastic uniform hazard spectra associated with the peak response of linear single-degree-of-freedom systems having viscous damping. A general class of RS can be expressed as in the following four-branches expression:

$$S_a(T) = \begin{cases} S_0\left[1 + (a-1)\dfrac{T}{T_3}\right] & 0 \le T \le T_3 \\ aS_0 & T_3 < T \le T_2 \\ aS_0\left(\dfrac{T_2}{T}\right)^{k_1} & T_2 < T \le T_1 \\ aS_0\left(\dfrac{T_2}{T_1}\right)^{k_1}\left(\dfrac{T_1}{T}\right)^{k_2} & T > T_1 \end{cases} \quad \text{(A1)}$$

where T is the natural period of the SDOF system, S_0 is the peak ground acceleration, a is the dynamic amplification factor, T_1, T_2 and T_3 are the periods that define the various branches, and k_1 and k_2 are shape factors. In this paper we refer only to RS with $k_1 = 1$ and $k_2 = 2$ and in **Figure A1A** a qualitative representation of RS is depicted.

Several building codes allow for an alternative representation of the seismic ground motion by means of artificial accelerograms of nominal duration T_s that can be generated as samples of a zero-mean Gaussian stationary process, fully characterized by its one-sided PSD function $G_{\ddot{U}_g}(\omega)$.

In this work, the RS-consistent PSD was intended as an alternative conventional way to define the seismic action or, in other word, as a mathematical tool to conveniently represent the seismic action and to be used into the linear stochastic dynamic context. With this in mind, the RS-consistent PSD function is determined by solving an inverse stochastic dynamic problem in order to produces the same effects of the target RS, hence in Equation (A2) a value of $\zeta = 0.05$ has been used. Once the PSD function was determined, it completely defines the input process from a probabilistic point of view, irrespective of the characteristics of the superimposed structure (linearity, damping values and so on). It is remarked that in some recent SL approaches (Mitseas et al., 2018) the PSD is updated at each iteration to be consistent with a RS in which damping modification factors are applied.

Seismic codes do not define the process, but require, instead, that it has to be compatible with an assigned RS, by providing the compatibility conditions. For instance, following the provision of Eurocode 8 (UNI ENV 1998:2005, 2005), a ground acceleration PSD function $G_{\ddot{U}_g}(\omega)$ is considered

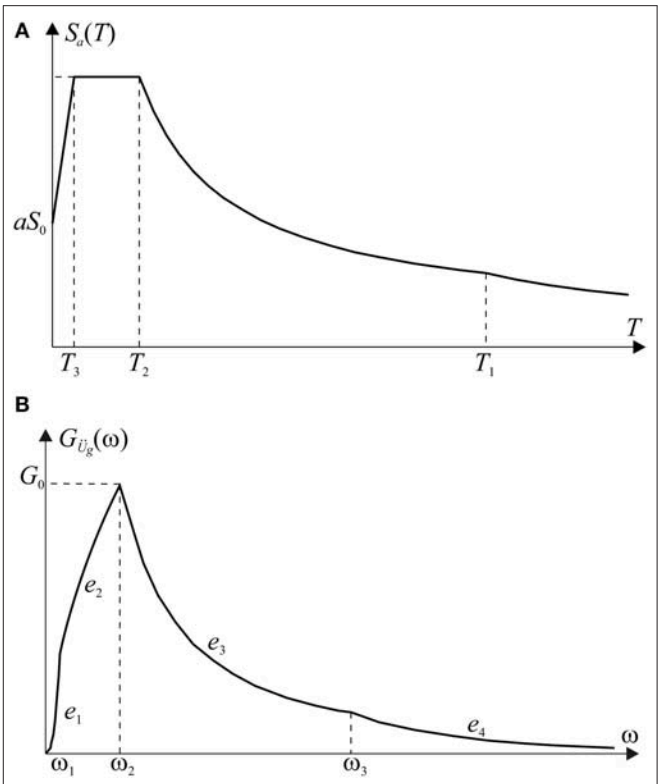

FIGURE A1 | (A) Pseudo-acceleration Response Spectrum; **(B)** Power Spectral Density function coherent with Response Spectrum.

compatible with an assigned acceleration RS, $S_a(T)$, if a SDOF system with an assigned damping ratio (usually $\zeta_0 = 0.05$), subjected to accelerogram samples generated from $G_{\ddot{U}_g}(\omega)$, experiences into a time window of the nominal duration T_s of the earthquake an average absolute peak acceleration larger than 90% of $S_a(T)$ for each value of the natural period T. If the ground motion PSD was known, the corresponding RS could be easily obtained by stochastic analysis. However, the inverse problem (i.e. determining the PSD function corresponding to an assigned RS) is not easy to solve. An approximate recursive solution for this problem has been provided in (Cacciola et al., 2004) in order to obtain an estimate of the PSD function $G_{\ddot{U}_g}(\omega)$ compatible with the assigned RS:

$$G_{\ddot{U}_g}(\omega) = \frac{\gamma}{\omega}\left[\left(\frac{S_a(\omega,\zeta)}{\eta_U(\omega,\zeta)}\right)^2 - \int_0^{\omega} G_{\ddot{U}_g}(\hat{\omega})\, d\hat{\omega}\right] \quad \text{(A2)}$$

where the parameter $\gamma = 4\zeta/(\pi - 4\zeta)$ and the peak factor $\eta_U(\omega,\zeta)$ is computed for 50% probability of non-exceedance. In this choice, a further little approximation is introduced, i.e. by confusing the mean value with the median.

Recently, an analytical model of PSD function, compatible with RS building code defined by Equation (A1), has been

proposed (Barone et al., 2015, 2019) as:

$$G_{\ddot{U}_g}(\omega) = G_0 \begin{cases} \left(\frac{\omega_1}{\omega_2}\right)^{e_2}\left(\frac{\omega}{\omega_1}\right)^{e_1} & 0 \le \omega \le \omega_1 \\ \left(\frac{\omega}{\omega_2}\right)^{e_2} & \omega_1 < \omega \le \omega_2 \\ \left(\frac{\omega}{\omega_2}\right)^{e_3} & \omega_2 < \omega \le \omega_3 \\ \left(\frac{\omega_3}{\omega_2}\right)^{e_3}\left(\frac{\omega}{\omega_3}\right)^{e_4} & \omega > \omega_3 \end{cases} \tag{A3}$$

where $\omega_i = 2\pi/T_i$ $(i = 1, 2, 3)$ is the circular frequencies corresponding to the periods T_i $(i = 1, 2, 3)$ and G_0 represents the peak value of the PSD function that occurs at the frequency $\omega = \omega_2$. The proposed model, whose graphical representation is reported in **Figure A1B**, depends on only five parameters, namely G_0 and the four exponents $e_1, ..., e_4$.

In Barone et al. (2019), the procedure to determine closed-form expressions for all the parameters, starting from those of the assigned RS, is extensively reported, whereas herein only the final expressions are recalled for the sake of brevity.

$$\begin{aligned} e_1 &= 2k_2 - 1 - L(\omega_1) \\ e_2 &= 2k_1 - 1 - L(\omega_2) \\ e_3 &= -1 - \gamma - \beta_2 L(\omega_2) \\ e_4 &= -1 - \gamma - \beta_3\left(L(\omega_3) + 2\frac{a-1}{a}\right) \\ G_0 &= \frac{\gamma}{\beta_2\omega_2}\left(\frac{aS_0}{\eta_U^2(\omega_2)}\right)^2 \end{aligned} \tag{A4}$$

in which the following positions have been made:

$$\begin{aligned} L(\omega) &= 2\omega\frac{d\left(\log\left(\eta_U(\omega)\right)\right)}{d\omega} \\ \beta_2 &= \left(\frac{\omega_1}{\omega_2}\right)^{e_2+1}\frac{\gamma + e_1 + 1}{e_1 + 1} + \left(1 - \left(\frac{\omega_1}{\omega_2}\right)^{e_2+1}\right)\frac{\gamma + e_2 + 1}{e_2 + 1} \\ \beta_3 &= \left(\frac{\omega_2}{\omega_3}\right)^{e_3+1}\beta_2 + \left(1 - \left(\frac{\omega_2}{\omega_3}\right)^{e_3+1}\right)\frac{\gamma + e_3 + 1}{e_3 + 1} \end{aligned} \tag{A5}$$

Lastly, some seismic codes define the ground motion accelerations by means of three-branches (by setting $\omega_1 \to 0$) or two-branches RS ($\omega_1 \to 0$ and $\omega_3 \to \infty$). In these cases, the PSD analytical model is easily obtained by Equations (A4) and (A5), by taking into account the same positions with regards to ω_1 and ω_3.

Analytical expression for evaluating the cross-spectral moments

The proposed analytical procedure to derive the spectral moments of a set of quantity of interest **Y**, requires the following steps: a) execution of the generalised modal analysis; b) evaluation of the direct spectral moments of the modal oscillators; c) determination of the cross-spectral moments in the modal space; d) evaluation of the spectral moments in the geometric space. With reference to the step c), Di Paola and Muscolino (1988) demonstrated that the cross-spectral moments of any order λ_{j,Q_i,Q_k} may be obtained recursively as linear combinations of the direct spectral moments. In particular, real and imaginary parts of even-order cross-spectral moments can be determined as:

$$\begin{aligned} \mathrm{Re}\left[\lambda_{m,Q_j,Q_k}\right] &= \frac{(-1)^{m/2}}{2} \\ &\left(\lambda_{0,Q_j}\gamma_{m,k,j}\omega_{0j}^2 + \lambda_{2,Qj}\delta_{m,k,j} + \lambda_{0,Q_k}\gamma_{m,j,k}\omega_{0k}^2 + \lambda_{2,Q_k}\delta_{m,j,k}\right) \\ \mathrm{Im}\left[\lambda_{m,Q_j,Q_k}\right] &= \frac{(-1)^{m/2}}{2} \\ &\left(\lambda_{1,Q_j}\varepsilon_{m,k,j} - \lambda_{1,Q_k}\varepsilon_{m,j,k} + \lambda_{3,Q_j}\alpha_{m,j,k} - \lambda_{3,Q_k}\alpha_{m,k,j}\right) \end{aligned} \tag{A6}$$

while for the odd-order cross-spectral moments:

$$\begin{aligned} \mathrm{Re}\left[\lambda_{m,Q_j,Q_k}\right] &= \frac{(-1)^{(m+1)/2}}{2} \\ &\left(\lambda_{1,Q_j}\varepsilon_{m,k,j} + \lambda_{1,Q_k}\varepsilon_{m,j,k} + \lambda_{3,Q_j}\alpha_{m,k,j} + \lambda_{3,Q_k}\alpha_{m,j,k}\right) \\ \mathrm{Im}\left[\lambda_{m,Q_j,Q_k}\right] &= \frac{(-1)^{(m-1)/2}}{2} \\ &\left(\lambda_{0,Q_j}\gamma_{m,k,j}\omega_{0j}^2 + \lambda_{2,Q_j}\delta_{m,k,j} - \lambda_{0,Q_k}\gamma_{m,j,k}\omega_{0k}^2 - \lambda_{2,Q_k}\delta_{m,j,k}\right) \end{aligned} \tag{A7}$$

In Equations (A6) and (A7), the following positions have been made:

$$\begin{aligned} \alpha_{m,j,k} &= \alpha_{m-1,j,k} + \omega_{Dk}\beta_{m-1,j,k}; \\ \beta_{m,j,k} &= -\zeta_k\,\omega_{0k}\,\beta_{m-1,j,k} - \omega_{Dk}\alpha_{m-1,j,k}; \\ \gamma_{m,j,k} &= \zeta_k\omega_{0k}\alpha_{m,j,k} + \omega_{Dk}\beta_{m,j,k}; \\ \delta_{m,j,k} &= \zeta_k\omega_{0k}\alpha_{m,j,k} - \omega_{Dk}\beta_{m,j,k}; \\ \varepsilon_{m,j,k} &= 2\zeta_k\omega_k\omega_{Dk}\beta_{m,j,k} + \alpha_{m,j,k}\left(\omega_{0k}^2 - 2\omega_{Dk}^2\right); \end{aligned} \tag{A8}$$

being:

$$\begin{aligned} \alpha_{0,j,k} &= 4\left(\zeta_j\omega_j + \zeta_k\omega_k\right)/K_{jk} \\ \beta_{0,j,k} &= 2\left(\omega_{0j}^2 - \omega_{0k}^2 + 2\zeta_j\zeta_k\omega_{0j}\omega_{0k} + 2\zeta_k^2\omega_{0k}^2\right)/\left(\omega_{Dk}K_{jk}\right) \\ K_{jk} &= \left(\omega_{0j}^2 - \omega_{0k}^2\right)^2 + 4\zeta_j\zeta_k\left(\omega_{0j}^2 + \omega_{0k}^2\right) \\ &\quad \omega_{0j}\omega_{0k} + 4\left(\zeta_j^2 + \zeta_k^2\right)\omega_{0j}^2\omega_{0k}^2 \end{aligned} \tag{A9}$$

frontiers in Built Environment

ORIGINAL RESEARCH
published: 17 April 2020
doi: 10.3389/fbuil.2020.00024

Effectiveness of Seismic Isolation for Long-Period Structures Subject to Far-Field and Near-Field Excitations

Hamidreza Anajafi[1], Kiavash Poursadr[2], Milad Roohi[3] and Erin Santini-Bell[1]*

[1] Department of Civil and Environmental Engineering, University of New Hampshire, Durham, NH, United States, [2] Pars Seismic Co., Tehran, Iran, [3] NIST Center of Excellence for Risk-Based Community Resilience Planning, Department of Civil and Environmental Engineering, Colorado State University, Fort Collins, CO, United States

This study evaluates primarily the effectiveness of seismic isolation for structures with intermediate and relatively long non-isolated periods (e.g., bridges with tall piers) subjected to near-field (NF) and far-field (FF) excitations. The inelastic response spectrum approach is used to systematically evaluate the effects of the two fundamental aspects of seismic isolation, i.e., period lengthening and lateral-strength reduction on the seismic responses (e.g., displacement, acceleration, and base shear) of isolated structures. To validate the results, the real-world isolated Rudshur bridge with a relatively flexible (long-period) substructure is studied. Additional isolated and non-isolated variants of the Rudshur bridge with different initial periods are also developed. 20 FF (non-pulse) and 20 NF (pulse type) ground motions are used for the non-linear response history analyses. The results illustrate that when designed properly, seismic isolation can effectively reduce the *mean* base shear and acceleration responses of structures with relatively long non-isolated periods under FF excitations. For these structures, seismic isolation does not significantly increase the mean displacement responses under FF excitations, and for particular cases, can even reduce them. For NF excitations, seismic isolation can significantly reduce the mean base shear responses of intermediate- to long-period structures. In some cases, this reduction is even more significant than that for FF excitations. However, when the initial period of the isolated structure is relatively long (e.g., greater than 2.5 s), NF excitations can impose significantly large mean displacement demands on the superstructure (i.e., as great as 1.0 m for the studied cases). For NF excitations, a range of initial period (e.g., 1.5–2.5 s for the studied ground motions) and lateral yield-strength (e.g., 10–15% of the seismically effective weight) exists for the isolation system parameters that can noticeably reduce mean acceleration and base shear responses while mean displacement responses of the isolated superstructure remain within ranges used in practice. The inelastic-spectrum approach, as used in this paper, can reasonably predict these isolation system parameters.

Keywords: isolated bridges, long-period structures, inelastic spectra, far-field excitations, near-field excitations, forward rupture directivity effects

OPEN ACCESS

Edited by:
Dario De Domenico, University of Messina, Italy

Reviewed by:
Emanuele Gandelli, Maurer, Germany
Vincenzo Bianco, University of Rome Unitelma Sapienza, Italy

****Correspondence:***
Hamidreza Anajafi
hamid.anajafi@unh.edu

Specialty section:
This article was submitted to Earthquake Engineering, a section of the journal Frontiers in Built Environment

Received: *13 December 2019*
Accepted: *18 February 2020*
Published: *17 April 2020*

Citation:
Anajafi H, Poursadr K, Roohi M and Santini-Bell E (2020) Effectiveness of Seismic Isolation for Long-Period Structures Subject to Far-Field and Near-Field Excitations. Front. Built Environ. 6:24. doi: 10.3389/fbuil.2020.00024

INTRODUCTION

Base isolation (BI) systems were originally applied to short-period structures (e.g., low-rise buildings) subjected to short-period ground excitations such as far-field (FF) earthquakes recorded on firm-soil profiles. In the past decade, BI has been used even for rather tall (long-period) buildings and long-period ground motions such as those present in most near-field (NF) excitations. Examples of isolated tall buildings are the 41-story residential Thousand Tower and the Sendai MTI 18-story building in Japan, and the 33-story Nunoa Capital building in Chile (Komuro et al., 2005; Lagos et al., 2017). Despite these specific examples, consensus does not exist on the effectiveness of the BI technique for long-period (flexible) structures and for long-period ground motions.

The concerns regarding the application of BI systems in flexible structures (e.g., high-rise buildings) subject to FF excitations arise primarily from the relatively long fundamental period of the fixed-base superstructure. For most typical FF earthquake ground motions, spectral acceleration responses are relatively high in short period regions (e.g., periods less than 0.5 s), and as the period increases to intermediate values (e.g., 2.0–3.0 s), the spectral acceleration ordinates significantly decrease. Therefore, increasing the fundamental period of common bridges and short-rise buildings to 2.0–3.0 s, which is feasible by the BI technique, can reduce the seismic force demands under FF ground motions significantly. Conversely, in most typical FF ground motions, for periods greater than 2.0–3.0 s, the absolute values of spectral acceleration responses are already relatively small. Therefore, one might question the use of seismic isolation to further increase the periods of relatively long-period structures to reduce seismic force demands. However, as the results of the present research and a few previous studies illustrate, seismic isolation can considerably reduce the mean acceleration and base shear responses of relatively long-period structures (e.g., up to 50% for the cases studied in this paper). Although these reductions might not be as pronounced as those for short-period structures, they are significant as compared to the improvements achieved in the responses of long-period structures using other well-adopted seismic protection systems. For example, tuned mass dampers with practical mass ratios (e.g., 1–5%) can provide reductions in the base shear and floor acceleration responses of high-rise buildings not greater than 20–30% (e.g., see Soto-Brito and Ruiz, 1999; Bekdaş and Nigdeli, 2013; Anajafi and Medina, 2018; Naderpour et al., 2019). Furthermore, as shown in the present study, for FF excitations, the lateral-strength reduction caused by isolation systems can potentially even reduce the global displacement responses of the structures with relatively long non-isolated periods.

Significant concerns also exist in the application of seismic isolation for NF ground motions. Many (not all) ground motions recorded in NF regions (typically within 15 km of causative faults) are characterized by one or several long-period pulse motions caused by forward-directivity (FD) effects. The long period of these pulse-type motions can coincide with the fundamental periods of flexible structures, such as isolated structures, imposing large spectral acceleration responses on these structures. This may reduce the efficacy of the seismic isolation technique in terms of base-shear response reduction and also cause significant superstructure displacement responses. Numerous studies in the past have illustrated that for the same PGA and duration of shaking, NF ground motions could impose higher seismic demands (e.g., base shear, and global displacement) on flexible structures, as compared to ordinary FF excitations (e.g., see Hall et al., 1995; Malhotra, 1999; Liao et al., 2000, 2004; Shen et al., 2004; Li et al., 2007; Jäger and Adam, 2013; Beiraghi et al., 2016; Güneş and Ulucan, 2019). Specific examples of isolated structures damaged due to NF effects are presented in Li et al. (2008), Wang and Lee (2009), and Jónsson et al. (2010). The abovementioned studies provide significant insight into understanding the behavior of isolated structures subjected to NF excitations. However, when interpreting the results of these studies, several important points should be considered. First, in many cases, the damaged base-isolated structures in NF events presented in these studies were designed without NF considerations (e.g., the examples studied in Li et al., 2008; Wang and Lee, 2009; Jónsson et al., 2010). Therefore, the poor seismic performance of these structures cannot be considered evidence of the inefficacy of the BI technique for structures constructed in NF regions. Second, some of these studies show that the BI technique is, on average, more effective for FF excitations than for NF excitations (e.g., Liao et al., 2004). The present study, while corroborating the validity of this statement for structures with short non-isolated periods, illustrates that this is not always the case for structures with relatively long non-isolated periods. Additionally, a more rational approach to evaluate the effectiveness of seismic isolation for NF excitations should also consider comparing the responses of a base-isolated structure and its non-isolated counterpart rather than a sole comparison with the responses under FF excitations. Last but not least, many of these studies investigated the behavior of isolated structures with relatively short non-isolated periods (e.g., Liao et al., 2004), and as a result, the increase in the displacement responses due to seismic isolation was significant under NF excitations. However, structures with relatively long periods are already influenced by directivity pulses of NF excitations, and it is not trivial that seismic isolation would further increase their displacement responses significantly.

An evaluation of the results of a few previous studies that investigated responses of relatively long-period structures under NF excitations illustrates that the values of the initial periods of the non-isolated and isolated counterparts are key parameters to predict the level of decrease/increase caused by seismic isolation in force and displacement demands (e.g., see examples presented in Takewaki, 2008; Ma et al., 2014; Fujita et al., 2017; Lagos et al., 2017; Anajafi and Medina, 2018; Naderpour et al., 2019). This evaluation shows that seismic isolation for NF excitations can, in many cases, reduce the mean force demands significantly (up to 70–80%). The extent of this reduction depends on the values of the non-isolated and isolated periods. However, the trends observed for displacement responses in these studies suggest establishing limitations for the initial periods and lateral strength of isolated structures. The evaluation of the results of these studies leads to the hypothesis that seismic isolation is effective for

long-period structures subject to NF excitations when the initial periods of the non-isolated and isolated counterparts are both in the range of 2.0–2.5 s. In this case, while mean force demands on the substructure reduce significantly, the mean displacement responses of the isolated superstructure remain within ranges used in practice. In these examples, it is observed that when seismic isolation results in initial periods greater than 3.0–4.0 s, mean displacement demands imposed on the superstructure might significantly increase under NF excitations, although the mean force demands still reduce to some extent.

The present study investigates the effects of seismic isolation on the performance of structures with relatively long non-isolated periods under NF and FF excitations. The primary objective is to evaluate the accuracy of the hypotheses made in the previous expositions based on the results of studies available in the literature.

Following the seminal works of Veletsos in collaboration with Newmark (Veletsos et al., 1965), the inelastic response spectrum concept has been widely used as a promising tool to study the inelastic responses of structures and equipment to dynamic excitations. This study employs this simple yet profound concept to systematically evaluate the effects of the two fundamental aspects of seismic isolation, i.e., period elongation and lateral-strength reduction. The results of inelastic ground response spectra are used to roughly estimate a near-optimum range for the characteristics of seismic isolators for relatively long-period structures. To illustrate the accuracy of the predictions of the implemented approach, isolated and non-isolated bridges with relatively stiff and flexible substructures are studied. The case-study structures are developed based on the real-world isolated Rudshur bridge. This bridge has a relatively flexible substructure and is located in an NF region. Despite being constructed in an NF region, the Rudshur bridge was designed based on a typical ground spectrum that did not consider NF effects. Therefore, an additional objective of this study is to evaluate the performance of the Rudshur bridge for NF ground motions and propose possible required rehabilitations.

The rest of this paper is organized as follows. First, the adopted method of approach is elaborated. This is followed by a section discussing the NF and FF record pair selection for inelastic response history analyses. A next section presents a preliminary evaluation of the effectiveness of seismic isolation for long-period structures using the inelastic spectrum concept. Subsequently, case-study structural models are used to further validate the results of inelastic response spectra. The paper ends with a section proposing a rehabilitation scheme for improving the seismic performance of the isolated Rudshur bridge under NF excitations.

METHOD OF APPROACH

The adopted method of approach consists of using: (1) ground response spectrum concept; and (2) non-linear response history analysis of case-study structures; to evaluate the effectiveness of seismic isolation for long-period structures subjected to FF and NF excitations. The following two subsections discuss these two approaches in more detail.

Ground Response Spectrum Concept

Inelastic response spectra are widely used to understand the effect of the inelastic behavior of structures subject to ground excitations. Ground response spectra illustrate maximum seismic demands (e.g., displacement, force, ductility, etc.) on single-degree-of-freedom (SDOF) systems with predefined viscous damping ratios, initial periods, and force-deformation relationships subject to a given ground excitation. Many studies in the past have developed inelastic spectra for NF and FF ground motions (e.g., see Rahnama and Krawinkler, 1993; Chopra and Chintanapakdee, 2004; Chenouda and Ayoub, 2008; Iervolino et al., 2012). The results of these studies have provided significant insight into understanding the effect of inelastic behavior on the seismic responses of structures. This study re-produces these results to establish a basis for the evaluation of the effectiveness of seismic isolation for long-period structures.

In the literature, different types of inelastic spectra have been developed, including constant ductility, constant damage, constant strength, and constant strength reduction factor (constant-R) spectra. For example, in the constant ductility and constant-R approaches, the inelastic spectra are developed based on a predefined "displacement ductility demand" and "lateral-strength reduction factor," respectively. In principle, the seismic isolation technique causes an increase in the period and a reduction in the lateral-strength of a structure. The constant-R spectrum approach can be used to "systematically" evaluate the influence of the lateral-strength reduction and period shift caused by the seismic isolation technique.

Figure 1A illustrates the bilinear force-deformation relationship of an inelastic SDOF system and the corresponding elastic system used in this study to develop ground response spectra. In this figure, the elastic stiffness is k_s and the post-elastic stiffness is αk_s, where α is the post-yield stiffness ratio. The yield strength is f_y and the yield deformation is u_y. Within the elastic range, the SDOF system has a natural period $T_n = 2\pi\sqrt{m_s/k_s}$, where m_s is the mass of the system. The yield-strength reduction factor, R, is defined by Equation (1) (Chopra and Chintanapakdee, 2004).

$$R = \frac{f_o}{f_y} = \frac{u_o}{u_y} \tag{1}$$

where f_o and u_o are the minimum yield strength and yield deformation required for the system to remain elastic during the ground motion, or the peak response values for the corresponding linear system (Chopra and Chintanapakdee, 2004). f_m and u_m are the peak force and displacement demands on the inelastic system, respectively. In this study, u_m is denoted as the spectral displacement response, S_d.

The inelastic ground response spectra are computed as explained next (Obando and Lopez-Garcia, 2018). SDOF systems are defined by the natural period T_n, the damping ratio ξ, and the response modification (reduction) factor R. For a given SDOF system, first, peak displacement (u_o) and peak force (f_o) demands

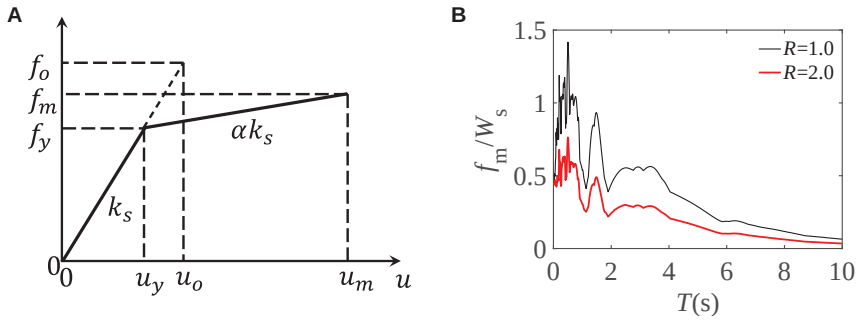

FIGURE 1 | (A) Bilinear force-deformation relationship of inelastic SDOF system and corresponding elastic system (adopted from Chopra and Chintanapakdee, 2004); **(B)** elastic and inelastic normalized force demand spectra for a representative ground motion.

are computed through linear response history analysis under a sample ground acceleration. The parameters yield displacement and yield force are then calculated as $u_y = u_o/R$ and $f_y = f_o/R$, and the sample values S_d and f_m of the same inelastic SDOF system (i.e., same natural period, T_n, and same damping ratio, ξ) are then obtained through non-linear time history analysis under the same sample ground acceleration.

The peak elastic force demand is usually normalized to the SDOF weight (W_s) and is denoted as the elastic pseudo-spectral acceleration response, S_a:

$$S_a = \frac{f_o}{W_s} \tag{2}$$

The S_a parameter is usually used to evaluate the elastic responses of structures to earthquake ground motions. The seismic force demand reduction due to the inelastic behavior of the SDOF system can be quantified using the R^* parameter given by Equation (3):

$$R^* = \frac{f_o}{f_m} \tag{3}$$

Figure 1B illustrates the elastic and constant-R inelastic normalized force spectra, f_m/W_s, for a representative ground motion.

Non-linear Time History Analysis

Non-linear response history analyses are performed on several case-study structural models to further validate the preliminary results obtained from inelastic response spectra. The case-study models are developed based on a real-world isolated bridge. Response history analyses are conducted using two different sets of ground motion records. Full three-dimensional (3D) finite element models of the bridges are developed. The two horizontal components of each record pair are applied to the two principal directions of the bridge deck plane. This analysis approach is referred to as 3D analysis. It is worthwhile noting that an evaluation of the results illustrates that for isolated structures (in general, for long-period structures) subjected to NF excitations, the responses of the two components do not need to be added vectorially to obtain the maximum resultant responses (the term resultant refers to the square root of sum of squares). It is shown that in this case, the maximum resultant responses can be reasonably approximated from a 2D analysis with the forward-directivity component only (see **Supplementary Material Appendix IV** and also Jangid and Kelly, 2001). This approach could eliminate the complexity of a 3D analysis and reduce the computational efforts significantly.

Figure 2 illustrates a summary of the method of approach used in this paper.

NEAR-FIELD AND FAR-FIELD RECORD PAIR SELECTION

Twenty NF record pairs containing forward directivity (FD) pulses are selected from the NGA-West2 database. The detailed characteristics of the NF record pairs can be seen in **Supplementary Tables S1, S3**. These ground motions were classified as pulse-like using the approach proposed by Baker (2007) and Shahi and Baker (2014) that is based on signal processing through wavelet analysis. In this approach, a ground motion is classified as pulse-like if its velocity time-history contains a pulse that is a large portion of the ground motion itself. It is worthwhile noting that a more recent criterion, denoted as pulse-index, was proposed by Quaglini et al. (2017) for the classification of the pulse-like characteristic of earthquake ground motions. The pulse-index was defined based on the ratio between the duration of the ground motion and the time interval during which most of the seismic energy is imparted to a structure. Quaglini et al. (2017) illustrated that the predictions of this approach are in good agreement with those of Baker (2007). The most salient characteristic of many (not all) NF excitations is the occurrence of a large velocity pulse at the beginning of the time history of the record in the FD orientation. This large pulse of motion causes the component in the directivity orientation (denoted as the FD component herein) to be significantly stronger than the component perpendicular to the directivity orientation (denoted as PD herein) at periods usually longer than 0.5 s (Somerville, 2005). This difference is not observed in the two components of ordinary far-field ground motions. Studies of ground motion directionality have shown that the azimuth of the FD component (i.e., the strongest observed pulse)

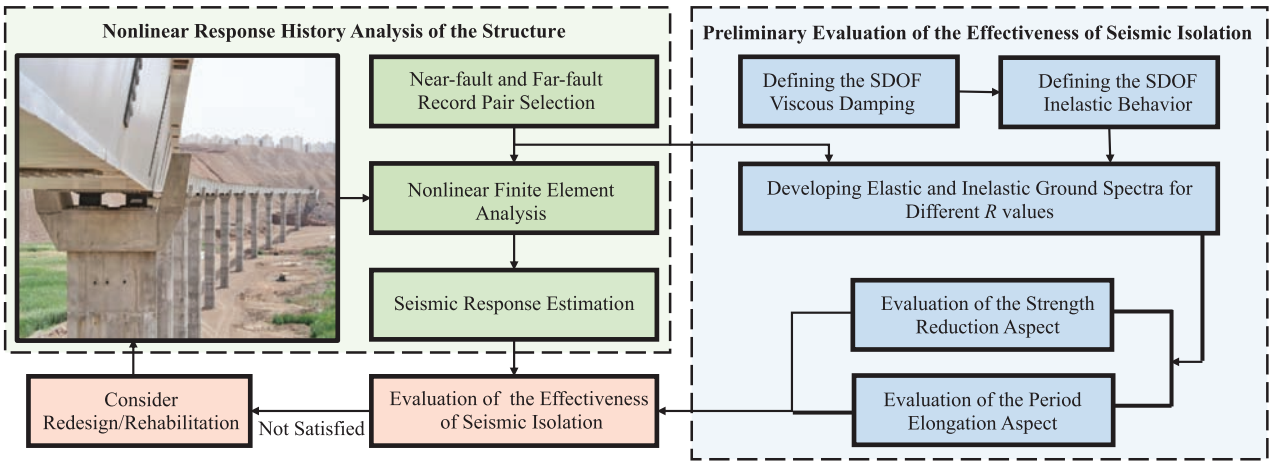

FIGURE 2 | Summary of the adopted method of approach to evaluate the effectiveness of seismic isolation.

is arbitrary for fault distances greater than approximately 3–5 km (Campbell and Bozorgnia, 2008). At closer fault distances, however, the azimuth of this component tends to align with the strike-normal orientation (Huang et al., 2008). Ground motions are usually recorded at two arbitrary orientations that are not necessarily the orientations of the strongest (FD) and weakest (PD) pulses. In this study, each NF pair is rotated to derive its FD and PD components, as illustrated in **Supplementary Material Appendix II**.

Twenty ordinary record pairs without velocity pulses, denoted as far-field (FF), are also selected for this study (see **Supplementary Material Appendix II** for the details of the selection of the FF record pairs and their characteristics). The PGA of each FF and NF record pair is scaled to a design PGA (i.e., 0.45 g). This scaling eliminates the effect of PGA on the conducted evaluations.

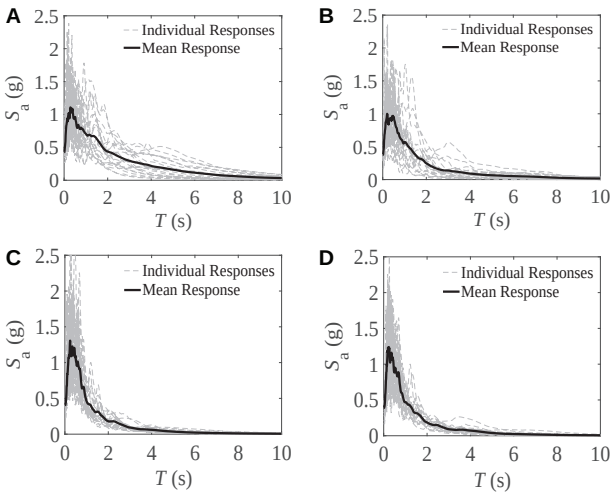

FIGURE 3 | 2.5%-damped pseudo-acceleration response spectra for the: **(A,B)** FD and PD components of the NF excitations; **(C,D)** NS and EW components of the FF excitations.

GROUND SPECTRA TO PRELIMINARY EVALUATE THE EFFECTIVENESS OF SEISMIC ISOLATION

This section presents a preliminary evaluation of the effectiveness of the seismic isolation using the ground response spectrum concept. The characteristics of the SDOF systems to generate ground response spectra are defined in such a way that they represent typical seismic isolators. To this end, the viscous damping ratio of the SDOF oscillators is assumed to be 2.5%; a bilinear model with a 9% post-yielding stiffness ratio represents the inelastic behavior of the SDOF oscillators; it is assumed that the unloading and re-loading of the hysteretic system occur without any deterioration of stiffness or strength. These characteristics are consistent with those of the isolators used in the case-studies of this paper. The initial period of the SDOF systems ranges from 0 to 10.0 s with increments of 0.01 s, and the R factor is varied from 1.0 to 15.0.

Figures 3A,B illustrate, respectively, the 2.5%-damped pseudo-spectral acceleration responses for the FD and PD components of the scaled rotated NF excitations. **Figures 3C,D** present similar graphs for the north-south (NS) and east-west (EW) components of the FF excitations. The terms "scaled" and "rotated" are omitted hereinafter for brevity.

As seen in **Figure 3**:

- In the relatively long-period region (e.g., $T > 2.0$ s), the FD-NF components are, on average, much stronger than the PD-NF components. This difference is not highlighted for the two components of the FF record pairs. These conclusions were reported in many previous studies (e.g., see Archila et al., 2017). For both record suites, the maximum value of the mean acceleration spectra occurs

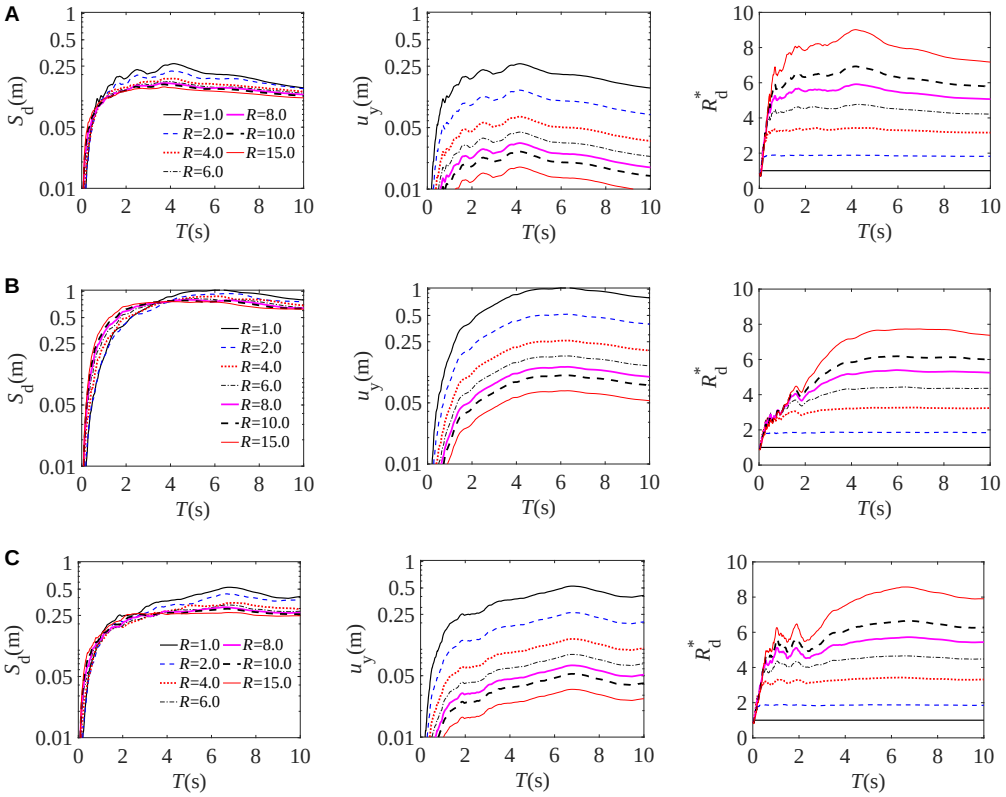

FIGURE 4 | Mean inelastic displacement spectra, yield displacement spectra and force-reduction factor spectra for the **(A)** 40 FF components; **(B)** 20 FD-NF components; **(C)** 20 PD-NF components.

in the short-period region (e.g., $T < 0.5$ s), and with increasing the period, the mean spectral acceleration responses consistently reduce. The reduction rates for the NS-FF and EW-FF components are comparable and larger than those for the NF components.

- Period-elongation is most effective in reducing the mean elastic force demands in the case of relatively short-period structures subject to the FF records. However, it could still significantly reduce mean elastic force demands for all other scenarios, i.e., (i) short-period structures subject to the NF excitations; (ii) relatively long-period structures subject to the FF excitations; and (iii) relatively long-period structures subject to the NF excitations. For example, let SDOF systems with initial periods of 0.3 and 2.0 s represent a relatively short- and long-period non-isolated structure, respectively. Assume that the target initial isolated period is 4.0 s. In this case, increasing the period from 0.3 to 4.0 s reduces the mean S_a under the NS-FF records by 95% (i.e., from 1.17 to 0.06 g). This reduction for the case of the same period-shift under the FD-NF records is 80%; and for the period-shift from 2.0 to 4.0 s under the NS-FF and FD-NF excitations is 67 and 50%, respectively.
- The relatively large S_a values for the FD-NF records at relatively long periods imply that, in this case, the period-elongation due to seismic isolation might result in significant elastic spectral displacement responses.

Figure 4A illustrates the mean inelastic displacement spectra, yield displacement spectra and force-reduction factor spectra for the FF excitations assuming different R-values. Given that the NS-FF and EW-FF components are not significantly different, the mean values of all 40 FF components are computed and shown without differentiating based on the NS and EW directions. **Figures 4B,C** depict similar results for the FD-NF and PD-NF components that are considered separately due to their significance difference.

The most important conclusions of **Figures 4A–C** regarding the effectiveness of seismic isolation for structures with relatively long fixed-base periods are summarized next.

For the FF excitations, it is observed that:

- Consistent with numerous previous studies (e.g., Chopra and Chintanapakdee, 2004; Chenouda and Ayoub, 2008), for intermediate- and relatively long-period SDOF systems (e.g., $T > 1.0$ s), reducing the yield strength can decrease the mean displacement demands. The largest reduction occurs in the period range $3.0 < T < 5.0$ s, suggesting that for structures with initial periods in this range, reducing the lateral strength can significantly reduce the mean displacement demands. The desired low lateral strength in conventional seismic design approaches can be achieved by using low yield-strength material in the lateral-force-resisting systems. However, in many cases, the high

strength required for gravity loads may cause difficulties in achieving this characteristic. Seismic isolation systems by incorporating a relatively low yield-strength seismic fuse (i.e., isolators) at a specific level (e.g., at the base) can effectively provide this characteristic. It is observed that in the relatively large-period region (e.g., $T > 4.0$ s), as the period increases, the inelastic spectral displacement responses consistently reduce.

- For an R-value greater than 4.0, the yield displacement responses are consistently smaller than 0.05 m that is within the practical range of yield displacement for common types of seismic isolators, such as Lead Rubber Bearings.
- For periods greater than the constant acceleration region (e.g., $T > 0.5$ s), the reduction in the force demand (i.e., the value of R^*) due to the inelastic behavior is significant. In this region, the magnitude of R^* for lower R factors is approximately constant and close to the value of R (e.g., assuming $R = 2.0$, this parameter varies between 0.90 and 0.94 R for different periods). For greater R factors, the amplitude of R^* is significantly smaller than the value of R (e.g., for $R = 15.0$, this parameter varies from 0.48 to 0.60 R).
- These results imply that for a structure with a relatively long non-isolated period, seismic isolation (i.e., a simultaneous period-lengthening and lateral-strength reduction), not only reduces force demands significantly but also can reduce the mean global displacement demands with respect to the non-isolated counterpart responses. For example, let an SDOF system with an initial period of 4.0 s and R factor of 1.0 represent a flexible non-isolated structure. Assume that the seismic isolation technique increases the R factor of this system to 8.0 while the initial period remains constant. In this case, the mean spectral displacement response reduces from 0.26 to 0.15 m (i.e., 42% reduction) and the mean force demand reduces by 83% (i.e., an R^* factor of 5.9 is achieved). The validity of these results is investigated in Section "Case-Study Bridges."

For the NF excitations:

- Inelasticity can reduce seismic force demands on relatively long-period structures under the NF excitations; this reduction is as pronounced as that for the FF excitations. For example, for an SDOF system with an initial period of 4.0 s, adopting an R factor of 8.0 reduces the mean force demand under the FD-NF excitations by 81% (i.e., $R^* = 5.15$), whereas, this reduction for the FF excitations is 83% (i.e., $R^* = 5.9$).
- For relatively long periods (e.g., approximately $T > 3.0$ s), the mean elastic displacement responses are significant (i.e., as great as 1.0 m). Although the inelastic behavior can reduce these responses to some extent, they are still relatively large (i.e., up to 0.7 m). The accommodation of these relatively large displacement responses might be challenging in practice. For this period region, yield displacement values associated with smaller R factors are unrealistically large (i.e., much higher than ranges used in practice). In other words, the target R factors cannot be achieved by adopting yield displacements that lie in ranges used in practice (i.e., $u_y < 0.05$ m). Therefore, designing isolation systems with initial periods in this range may prove to be challenging. For the intermediate periods of 1.5–2.5 s, the displacement responses are in ranges used in practice (i.e., $S_d < 0.5$ m). For these periods, assuming $R > 4.0$, the yield displacement values are also within a practical range. For example, adopting an initial period of 2.0 s and R factor of 6.0 results in a u_y value of 0.05 m. However, for these intermediate periods, reducing the lateral strength could considerably increase the displacement demands implying that a relatively low R-value might be preferred in design to limit displacement responses.
- These results suggest that seismic isolation is an effective approach under NF excitations when (i) the initial period of the isolated structure is smaller than approximately 2.5 s (ii) the R factor of the isolation system is roughly between 4.0 and 6.0. The validity of these statements is investigated in Section "Case-Study Bridges."

Bridges with tall and slender piers and high-rise buildings are of common long-period structures to be considered for seismic isolation. For high-rise buildings, additional challenges arise from the P-delta effects, heavy overturning moments, and gravity loads exerted on isolator bearings. In bridges, isolators are installed between the deck and piers as opposed to at the base in buildings. Therefore, the latter concerns are much less pronounced in long-period bridges. In the next section, bridge models with different isolated and non-isolated periods and lateral-strength levels are studied to validate further the preliminary results obtained from studying the ground response spectra. Most importantly, the results of the next section illustrate that with the proper selection of the lateral-strength and stiffness of bearings, the seismic isolation technique can be effectively applied to relatively long-period structures not only for FF excitations but also for NF excitations. It is also shown that the characteristics of isolator bearings can be reasonably approximated based on the results of inelastic ground response spectra.

CASE-STUDY BRIDGES

This section uses the responses of case-study bridges to the selected NF and FF excitations to validate the results of the preliminary investigations conducted in Section "Ground Spectra to Preliminary Evaluate the Effectiveness of Seismic Isolation." The case-study models are developed based on the real-world isolated Rudshur bridge. The initial periods of the Rudshur bridge in the longitudinal and transverse directions are 1.93 and 2.55 s, respectively. The superstructure of the bridge is decoupled from the substructure through Lead Rubber Bearings (LRBs) having an overall lateral yield strength, Q_y, equal to 0.06 of the seismically effective weight of the bridge deck. Assuming that the FD-NF and PD-NF are applied to the longitudinal and transverse directions, respectively, the mean resultant (SRSS) elastic S_a for the NF excitations is 0.50 g. For the FF excitations, assuming that the

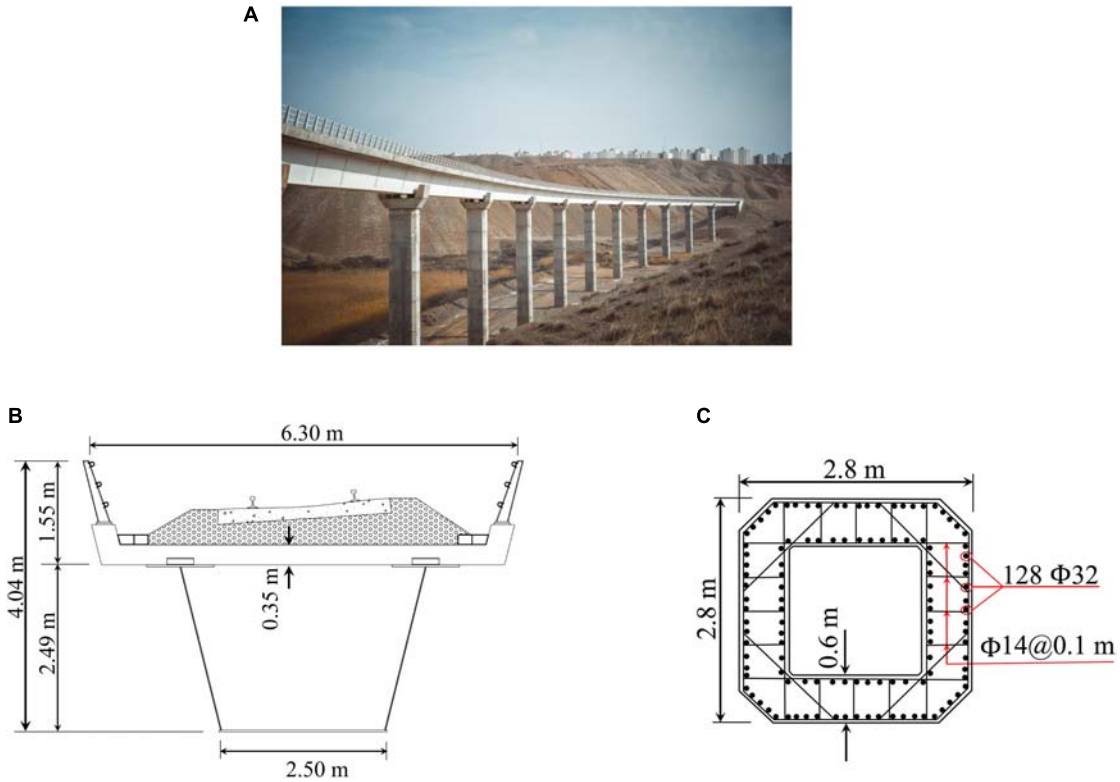

FIGURE 5 | (A) The isolated Rudshur bridge; **(B)** typical cross-section of the deck; **(C)** typical reinforcement of the piers at the critical section.

NS-FF and EW-FF are applied to the longitudinal and transverse directions, respectively, the mean resultant (SRSS) elastic S_a is 0.24 g. Using Equations (1) and (2), the R factor for the NF and FF excitations is 8.3 and 4.0, respectively. The bridge piers are relatively tall and slender resulting in a relatively large initial period of 2.22 s for the non-isolated counterpart. Based on the results of the preliminary investigations of Section "Ground Spectra to Preliminary Evaluate the Effectiveness of Seismic Isolation," seismic isolation of this bridge can be an effective design scheme for the FF excitations. As of the NF excitations, the initial isolated and non-isolated periods of the bridge are in the desired range of 1.5–2.5 s obtained in Section "Ground Spectra to Preliminary Evaluate the Effectiveness of Seismic Isolation." However, the existence of the relatively large R factor of 8.3 might result in relatively large displacement responses. The accuracy of these predictions is investigated in this section. To evaluate the effect of the substructure flexibility on the performance of the isolation system, a variant of the bridge with a relatively stiff substructure is also developed.

Rudshur Bridge

Rudshur bridge (**Figure 5A**) spans the Parand valley in the Tehran–Hamadan railway in Iran and was opened to traffic in 2013. According to the American Association of State Highway and Transportation Officials [AASHTO] (2017), this bridge is categorized as an essential structure as it provides an emergency link in an interstate transportation network connecting the historical province of Hamedan to Tehran, the capital city of Iran. The 600-m-long superstructure of the bridge is a composite steel box-girder (**Figure 5B**) that is continuous over the 12 spans of equal length. The width of the seismic gaps provided at the deck two ends is 0.40 m. The bridge substructure is composed of 11 intermediate single-column piers and two abutments. The bridge piers are of different heights ranging from 19.0 to 26.0 m. Considering their slenderness, the piers are relatively flexible. All pier types have a reinforced concrete square hollow cross-section with external dimensions 2.8 m × 2.8 m (**Figure 5C**). The thickness of both the flange and the web is 0.6 m. The longitudinal reinforcement at the bottom 6.0 m of the piers is 128Φ32 (i.e., a total of 128 rebars with a diameter of 32 mm), resulting in a volumetric ratio of 2.1%. The longitudinal reinforcement for the next 9.0 m decreases to 1.6% (i.e., 64Φ32 + 64Φ25) and for the rest of the pier length to 1.2% (i.e., 128Φ25). The typical confining reinforcement is 7Φ14@0.1 m and 2Φ14@0.1 m in the long and short directions of the pier walls, respectively. The expected compressive strength and the ultimate strength of the unconfined concrete are 39 and 25 MPa, respectively. These values for the confined concrete are 50 and 35 MPa, respectively. The compressive strain corresponding to the maximum compressive strength and the ultimate compressive strength for the unconfined concrete is 0.002 and 0.005, respectively. These quantities for the confined concrete are 0.007 and 0.030, respectively. The expected yield strength and the

ultimate strength of the reinforcing rebars are 460 and 600 MPa, respectively. The ultimate strain capacity of the rebar material is assumed to be 0.05.

At the top of each pier, a rectangular concrete cap-beam with a plan dimension of 4.5 m × 3.2 m and a thickness of 1.0 m was constructed. Above the cap-beam of each pier and above each abutment, two LRBs with a plan dimension of 0.67 m × 0.67 m, a height of 0.37 m, and a lead core of 0.17 m diameter were installed. The seismically effective weight of the deck (i.e., dead load plus 0.50 live load), W_{eff}, is approximately 100 MN. The lateral yielding force, yielding displacement, and post-elastic hardening ratio of a single LRB is 225 kN, 23 mm, and 9%, respectively. The lateral elastic stiffness of the rubber and the lead material is 0.88 and 8.91 kN/m, respectively. The lateral displacement capacity of the LRBs is 0.40 m, which is the minimum value obtained from different damage states, including the break of the rubber compound due to shear strain, and the buckling and overturning thresholds (Skinner et al., 2011). The elastic compressive stiffness of each LRB is 934.5 kN/mm. The behavior of the rubber material in tension is assumed to be bilinear with an initial stiffness of 24.4 kN/mm and a stiffness hardening ratio of 4%.

The site-specific seismic hazard studies illustrate that the closest fault to the Rudshur bridge is an inferred fault with a length of 30 km at a distance of 4.5 km (according to the Joyner–Boore criterion). Two faults are also located within 50–70 km of the site. Although the bridge was constructed in an NF region, it was designed assuming a typical response spectrum per the third edition of the Iranian seismic design code (Building and Housing Research Center, 2005) with no considerations for the NF effects. The design PGA of the spectrum was selected as 0.45 g. Note that the design PGA is equivalent to $0.4S_{\text{DS}}I_{\text{P}}$, where I_{P} is the bridge importance factor, and S_{DS} is the short-period pseudo-spectral acceleration for the site. The elastic 0.05-damped design spectral acceleration for periods smaller and greater than 0.70 s was considered to be 2.50 PGA and 2.75 PGA $(0.70/T)^{2/3}$, respectively, where T is the structural period in the direction of interest. For designing the bridge substructure, the elastic force demands were reduced by a factor of $R_{\text{iso}}(\xi_{\text{equiv.}}/0.05)^{0.3}$, where $\xi_{\text{equiv.}}$ is the equivalent viscous damping ratio provided by the LRBs, and R_{iso} is the response modification factor that is 1.5 for an isolated bridge with single-column piers (American Association of State Highway and Transportation Officials [AASHTO], 2010).

Additional Bridge Models

To evaluate the efficacy of the seismic isolation technique for the Rudshur bridge, a baseline non-isolated (NI) variant of the bridge with the same geometry and gravity loading but a different bearing condition and pier reinforcement is developed. In this model, it is assumed that the bridge deck is supported by ordinary elastomeric bearings (i.e., low-damping bearings with a relatively small height) that allow for the rotation of the deck with respect to the piers. It is assumed that shear keys are installed between the deck and piers to prevent the relative translational movements between the deck and piers. This bearing condition is equivalent to a pinned connection meaning that only shear forces and gravity loads can be transmitted from the deck to the piers. In this model, to provide a consistent lateral-yielding mechanism in the substructure, each abutment is replaced by a pier with the same characteristics as the side piers. Spectral analysis is conducted, and the bridge piers are redesigned for the updated forces per the AASHTO LRFD provisions. The seismic force-resisting system of this NI scheme in the transverse and longitudinal directions consists of single-column piers. Hence, in this case, an R factor of 3.0 is used for the flexural design of piers. The longitudinal reinforcement at the bottom 6.0 m of the piers (i.e., the critical section for flexural design) is obtained as 160Φ36 with a volumetric ratio of 3%. The longitudinal reinforcement for the next 9.0 m decreases to 2.3% (80Φ36 and 80Φ25) and for the rest of the pier's length to 1.5% (160Φ25). The confining reinforcement is 14Φ14@0.1 m and 2Φ14@0.1 m in the long and short directions of the pier walls, respectively. The maximum and ultimate compressive strength of the concrete and corresponding strain values are updated for the concrete material based on the new confinement details. The shear reinforcing is performed following the capacity design philosophy meaning that the design shear force is determined based on the pier overstrength moment resistance.

A second substructure scenario is also adopted in which the heights of all piers are reduced to 7.5 m. For this scenario, which represents a relatively short-period substructure, an isolated model with the same LRBs as those used in the as-built bridge and an NI counterpart are developed. In both bridge models, the piers are designed using the response spectrum method. For this substructure scheme, all piers have a reinforced concrete square hollow cross-section with dimensions of 2.2 m × 2.2 m × 0.5 m. The longitudinal reinforcing rebars of the piers for these NI and isolated models are obtained to be 2 and 1%, respectively. The confining rebar is 5Φ14@0.1 m and 2Φ14@0.1 m in the long and short directions of the pier walls and remains the same for both models.

In summary, this section considers four different bridge models: (i) the isolated long-pier (ILP) model that corresponds to the as-built condition of the Rudshur bridge, (ii) the non-isolated long-pier (NLP) model, (iii) the isolated short-pier model (ISP), and (iv) the non-isolated short-pier (NSP) model. The most salient characteristics of the four considered models are summarized in **Table 1**. To determine the initial fundamental periods, the cracked moment of inertia of the piers is considered to be $0.35I_{\text{g}}$, where I_{g} is the gross moment of inertia of the cross-section; for the isolated models, the initial stiffness of the LRBs is used.

Finite Element Modeling and Analysis

The primary finite element modeling and analysis are conducted using OpenSees (McKenna et al., 2000). Independent modeling is carried out in SAP2000 (Computers and Structures Inc., 2019) for verification purposes. The detail of finite element modeling is provided in **Supplementary Material Appendix III**.

Each record pair, including perpendicular components A and B, is used twice for the 3D non-linear response history analyses performed on a given bridge model. First, component A of a record pair is applied in the longitudinal direction of the bridge, and component B is applied in the transverse direction. Then,

TABLE 1 | The most salient characteristics of different structural models studied in this section.

		Bridge model			
Acronym*		**NLP**	**ILP**	**NSP**	**ISP**
Pier height (m)		19.0–26.0	19.0–26.0	7.5	7.5
Deck-to-pier connection		Pin	LRB	Pin	LRB
Initial period (s)	Longitudinal	1.66	1.93	0.62	1.44
	Transverse	2.22	2.55	0.56	1.35
Critical volumetric ratio of the vertical reinforcement of the piers		3%	2%	2%	1%

**ILP, isolated long-pier (the as-built condition); NLP, non-isolated long-pier; ISP, isolated short-pier; NSP, non-isolated short-pier.*

the components are swapped. Therefore, for each model, 40 non-linear response history analyses are performed using the NF record pairs and 40 analyses using the FF record pairs. For the FF set, the loading condition in which the SN and EW components of a record pair are applied to the longitudinal and transverse directions of the bridge, respectively, is referred to as Loading Condition 1 (LC 1). The loading condition in which the components are swapped is denoted as LC 2. For the NF excitations, the LC 1 implies the loading condition in which the FD and PD components are applied to the longitudinal and transverse directions, respectively. In the next sections, unless otherwise mentioned, the results are presented for LC 1.

Seismic Performance of Different Bridge Models Subject to Near-Field and Far-Field Excitations

Figure 6A illustrates the time history of the resultant displacement of the deck at the location of pier P_7 for the long-pier models under an FF record pair from the 1995 Kobe earthquake [record pair No. 20 in **Supplementary Table S2** (**Supplementary Material Appendix I**)]. Note that in this context, the resultant response is the square root of the sum of squares of the longitudinal and transverse responses. **Figure 6B** presents similar graphs for the short-pier models. As it can be observed from **Figure 6A**, for the long-pier models, the maximum displacement responses of the isolated and non-isolated deck are 0.28 and 0.32 m, respectively, implying that in this case, seismic isolation has reduced the maximum displacement response by 13%. This observation can be interpreted based on the trend observed in non-linear displacement response spectra of the FF ground motions in Section "Ground Spectra to Preliminary Evaluate the Effectiveness of Seismic Isolation." For relatively long-period structures, such as the NLP model studied herein, reducing the lateral yield strength can lead to a reduction in global displacement responses subject to the FF excitations. Given that the yield strength of the isolator bearings in the ILP model is much smaller than that of the concrete piers in the NLP model, in this case, seismic isolation can reduce the deck displacement responses. On the contrary, for the short-pier models, as shown in **Figure 6B**, the maximum displacement response of the isolated deck with a relatively long period is significantly higher than that of the non-isolated deck with a relatively short period (i.e., 0.28 m versus 0.11 m). This latter observation has been reported in numerous studies available in the literature (e.g., see Liao et al., 2004). It is important to note that in this case, the displacement responses of the isolated deck, although greater than those of the non-isolated deck, are within practical ranges and can be accommodated using typical LRBs and seismic gaps.

Figures 6C,D show, respectively, the time history of the resultant base-shear for the long-pier and short-pier models under the FF record pair referred above. As seen, seismic isolation in the long-pier model reduces the maximum resultant base shear from 52 MN to 30 MN (i.e., 42% reduction) and in the short-pier model from 70 MN to 10 MN (i.e., 86% reduction). As seen, the number of strong cycles in the base-shear responses of the isolated models is less than that of the corresponding non-isolated ones.

Figures 7A,B illustrate the mean values of the maximum resultant displacement responses at the locations of piers P_1 to P_{13} for different components (i.e., deck, piers, and LRBs) of the four models under the 20 FF record pairs. As seen in **Figure 7A**, for the long-pier model (i.e., the case with a flexible substructure), seismic isolation under the FF excitations does not cause a significant increase in the mean deck displacement responses. For the case with a stiff substructure shown in **Figure 7B**, seismic isolation leads to a significant increase in the mean deck displacement responses, although these responses are still within practical range.

Figures 8A,B illustrate the time history of the resultant displacement response of the deck at the location of pier P_7 under a representative NF record pair [record pair No. 3 in **Supplementary Table S1** (**Supplementary Material Appendix I**)] for the long-pier and short-pier structural models, respectively. As seen, the deck displacement response in both isolated models and also the non-isolated model with a relatively long period is characterized by a relatively large pulse that appears at the beginning of the response. This displacement pulse is analogous to the velocity pulse observed in the time history of the FD component of the NF record pair shown in **Figure 9**. This observation, which is consistent with the results of many previous studies (e.g., see Jónsson et al., 2010), reiterates the significant effect of forward directivity pulses on flexible structures.

Figures 8C,D illustrate, respectively, the time history of the resultant base-shear for the long-pier and short-pier models subjected to the NF record pair No. 3. As seen, under this NF excitation, seismic isolation reduces the maximum resultant base-shear response of the long-pier model from 52 MN to 33 MN

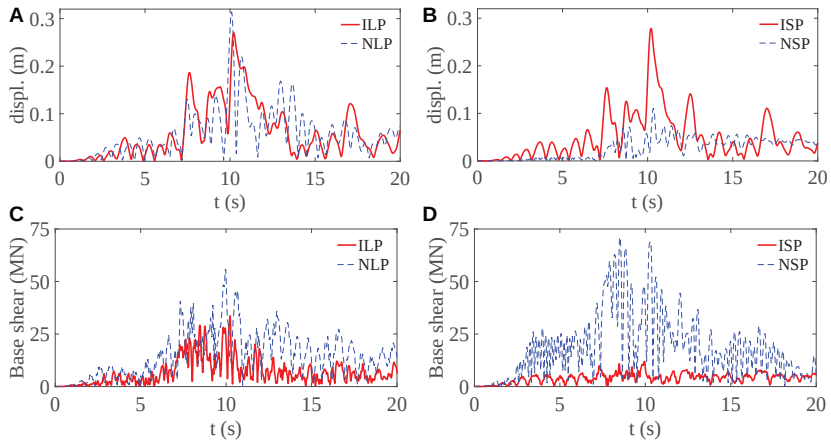

FIGURE 6 | Time history of the resultant responses of different bridge models under an FF record pair from the 1995 Kobe earthquake: **(A,B)** the deck resultant displacement at the location of pier P_7; **(C,D)** the bridge resultant base-shear.

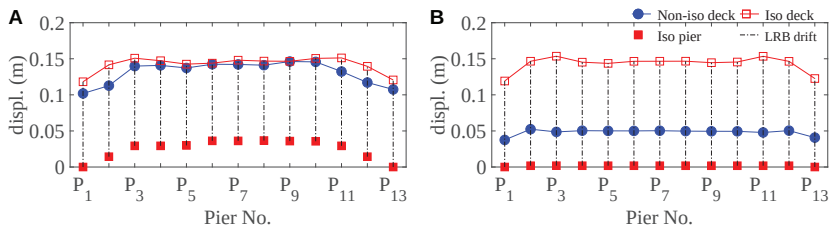

FIGURE 7 | The mean value of the maximum resultant displacement responses under the FF record pairs at piers P_1 to P_{13}: **(A)** long-pier models; **(B)** short-pier models.

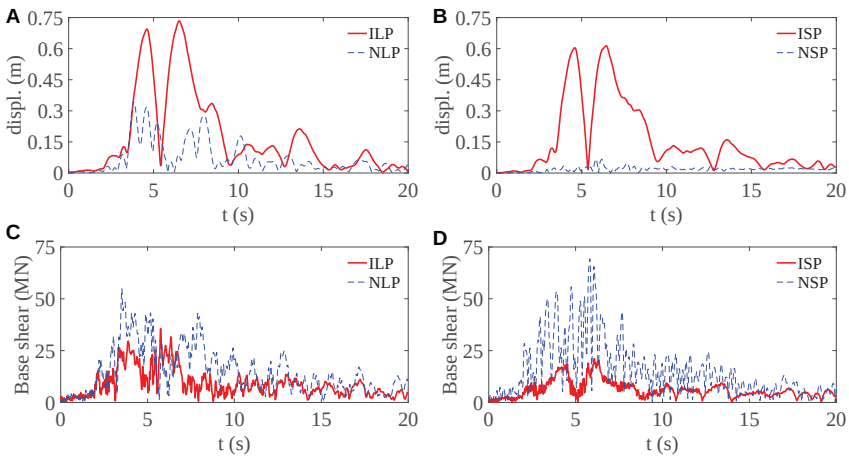

FIGURE 8 | Time history of the resultant responses of different bridge models under an NF record pair from the 1979 Imperial Valley earthquake: **(A,B)** the deck resultant displacement at the location of pier P_7; **(C,D)** the bridge resultant base-shear.

(i.e., 34% reduction) and of the short-pier model from 65 MN to 20 MN (i.e., 69% reduction). As an important observation, the number of strong cycles in the base-shear response of the isolated models is less than that of the corresponding non-isolated ones.

Figures 10A,B illustrate the mean values of the maximum resultant displacement responses at the locations of piers P_1 to P_{13} for different components of the four models under the 20 NF record pairs. As seen, for the NF excitations, seismic isolation leads to a significant increase in the deck displacement

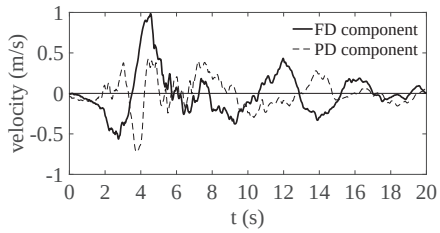

FIGURE 9 | The velocity time history of the FD and PD components of an NF record pair from the 1979 Imperial Valley event.

responses. This increase is less pronounced in the case of the flexible substructure scenario. This is relevant because the non-isolated counterpart of the flexible substructure scenario, unlike that of the stiff substructure scenario, is itself long-period and hence, experiences relatively large displacement responses under the NF excitations. As a result, in this case, the difference between the displacement responses of the isolated and non-isolated models is smaller. For example, the increase in the mean deck displacement at pier P_7 for the long-pier model (flexible substructure scenario) is 0.28 m, whereas for the short-pier model (stiff substructure scenario) is 0.45 m. As seen, the LRBs' drift responses in the isolated short-pier model are more significant.

The adverse effect of seismic isolation under the NF excitations is the relatively large mean displacement responses of the isolated deck that can be as great as 0.55 m. Further evaluation of the results illustrates that for the as-built Rudshur bridge model, almost under half of the NF excitations, the LRBs' drift responses exceed their failure threshold. These observations show that for the isolated Rudshur bridge, which was designed only for ordinary FF excitations, the main problem under the NF excitations is the relatively large displacement responses of the isolated deck.

Further Evaluation of the Effectiveness of Seismic Isolation for the Long-Period Model

This section aims to further (1) clarify the extent to which seismic isolation is effective in improving the performance of the long-period bridge model (i.e., the as-built model of the Rudshur bridge) with respect to the short-period one; (2) evaluate the effectiveness of the seismic isolation for the long-period model under the NF excitations with respect to that under the FF excitations. To this end, for a given earthquake excitation, the maximum resultant response of an isolated model is normalized to that of its non-isolated counterpart. As mentioned earlier in this section, a total of 40 NF and 40 FF excitations are used in the response history analyses. Therefore, for a given structural response of an isolated model, the adopted approach results in 40 normalized values under each ground motion set. These values (i.e., response ratios) are used to determine the probability of exceedance of the maximum resultant response of an isolated model from its non-isolated counterpart. **Figure 11** illustrates such analysis results for the four analysis cases considered herein: the ILP model subject to the NF records; the ILP model subject to the FF records; the ISP model subject to the NF records; the ISP model subject to the FF records. In this figure, "the probability of exceedance equal to 0.5" is the median value of a response ratio.

An evaluation of the results shown in **Figure 11** illustrates that, in terms of the substructure response reduction, seismic isolation is most effective for the bridge model with the short-period

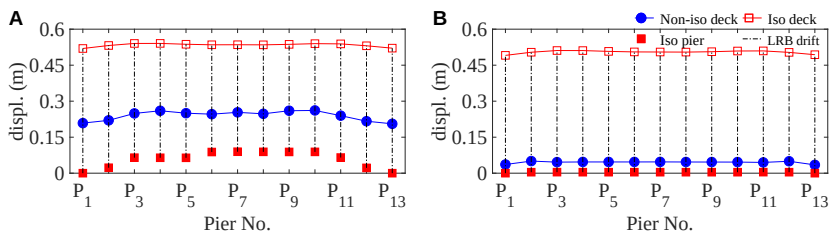

FIGURE 10 | The mean value of the maximum resultant displacement responses under the NF record pairs at piers P_1 to P_{13} **(A)** long-pier models; **(B)** short-pier models.

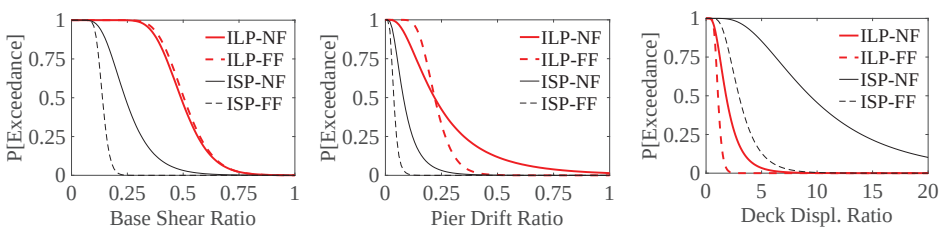

FIGURE 11 | Probability of exceeding the ratio of the maximum resultant responses of the isolated models from a given value.

substructure under the FF excitations (i.e., the ISP-FF analysis case) as the smallest base-shear and pier-drift ratios are obtained for this case. As seen, the median base-shear response for this case is decreased by 86% (a response ratio of 0.14). However, seismic isolation is still an effective method to reduce the seismic demands on the substructure in the three other cases. As seen, the median base-shear reduction for the ISP-NF, ILP-FF, and ILP-NF cases is 76, 49, and 51%, respectively (i.e., still significant). The base-shear and pier-drift ratios for these analysis cases are always smaller than unity (with different extents), implying a consistent performance improvement due to seismic isolation. In summary, seismic isolation is effective in reducing mean force demands for all four cases considered. However, it is observed that this approach:

(i) subject to the FF excitations, is to some extent more effective for stiff structures than for flexible structures;
(ii) for stiff structures, is more effective under the FF excitations than under the NF excitations; this latter conclusion is consistent with the results presented in Liao et al. (2004);
(iii) for flexible structures, is approximately equally effective under the NF and FF excitations;

These observations are consistent with the effects of the period-shift caused by isolation system on the spectral acceleration demands for the NF and FF excitations.

In terms of the superstructure displacement response, for the cases ILP-NF, ISP-FF, and ISP-FF, the deck displacement ratios are always greater than 1.0 (with different extent) meaning that seismic isolation consistently increases the deck displacement response. However, for the ILP-FF case, the probability of the displacement ratio being smaller than 1.0 is 55% meaning that under 22 out of the 40 FF excitations, the maximum resultant displacement response of the isolated deck is smaller than that of the non-isolated deck. It is observed that the effect of the NF records on the maximum displacement responses of the isolated superstructure is more highlighted for the short-pier bridge model than for the long-pier one. Indeed, in the first case, the median displacement ratio can be as great as 9.34, while in the latter case, this quaintly is only 1.80. This observation is related to the frequency content of the NF ground motions (i.e., pulse period). As previously discussed, the non-isolated long-pier model is already long-period and more affected by the pulse motions of the NF records. Therefore, in this case, the difference between the displacement responses of the isolated and non-isolated superstructure is smaller.

The results of the previous sections illustrate that for the isolated Rudshur bridge (the ILP model with a relatively flexible substructure) subject to the FF excitations, seismic isolation is not only effective in reducing the substructure seismic demands but also can reduce the median (and mean) deck displacement responses; although, in this case, the substructure demand reduction might not be as pronounced as that in the stiff-substructure model. As of the NF excitations, seismic isolation provides significant reduction in the substructure responses of this bridge, however, due to the relatively small lateral strength of the LRBs, the deck displacement responses become relatively large. These results verify the accuracy of the predictions made in the outset of Section "Case-Study Bridges" based on the results of the inelastic ground response spectra. The next section proposes a retrofit scheme to reduce the deck displacement responses of the Rudshur bridge without much altering (deteriorating) the substructure seismic demands.

Improving the Performance of the Isolated Rudshur Bridge for Near-Field Excitations

The normalized yield strength of the LRBs, Q_y/W_{eff}, used is the Rudshur bridge is relatively low (i.e., 6%) as the bridge was designed for ordinary FF (non-pulse) ground motions. This normalized yield strength for the NF excitations is equivalent to an R factor of 8.3. As illustrated in Section "Ground Spectra to Preliminary Evaluate the Effectiveness of Seismic Isolation" and verified in Section "Further Evaluation of the Effectiveness of Seismic Isolation for the Long-Period Model," for NF excitations, this low yield strength (i.e., relatively large R-value) causes relatively large superstructure displacement responses under the NF excitations. Assume that a target superstructure displacement response of 0.30 m is desired. The results of Section "Ground Spectra to Preliminary Evaluate the Effectiveness of Seismic Isolation" suggest that for the range of the initial period of the isolated Rudshur bridge, the use of an R-value between 4.0 and 6.0 (i.e., a Q_y/W_{eff} ratio of 12–15%) can limit the maximum displacement response of the superstructure to this target value. This prediction is consistent with the results of Jangid (2007). Jangid performed parametric studies on a few numerical models subject to six NF excitations and illustrated that a Q_y/W_{eff} value in the range 10–15% can result in an optimum design meaning that acceleration and force demands are significantly reduced and bearing displacement responses are within ranges used in practice. In this section, the normalized yield strength of the LRBs is increased from the existing value of 6% to 12% to examine the accuracy of these predictions. The other characteristics of the LRBs, including their elastic and post-elastic stiffness values, remain unchanged. 3D non-linear response history analyses are conducted on the isolated Rudshur bridge (ILP model) with the new LRBs subject to the 20 NF and 20 FF record pairs (for LC1).

The maximum resultant responses of the ILP models with Q_y/W_{eff} values of 6 and 12% are normalized to those of the baseline non-isolated counterpart (NLP model). These normalized values are used to evaluate the probability of exceedance of the responses of the ILP models from those of the NLP model. This evaluation can illustrate whether the seismic isolation technique with the new LRBs can improve the seismic behavior of the Rudshur bridge subject to the NF and FF excitations. **Figure 12A** shows the probability of exceedance of the normalized responses of the ILP models from a given value for the FF excitations. **Figure 12B** presents a similar evaluation for the NF excitations. As seen, increasing the yield strength of the LRBs to 12% can significantly improve the performance of the isolated model under the NF excitations in terms of the deck displacement responses. For example, for the case with $Q_y/W_{eff} = 6\%$, the

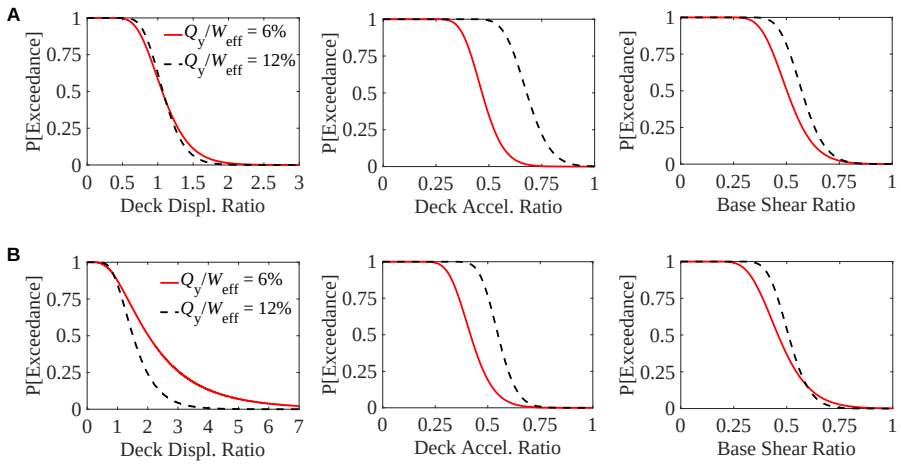

FIGURE 12 | Probability of exceeding the ratio of the maximum resultant responses of the isolated long-pier models from a given value for the **(A)** FF; **(B)** NF excitations.

probability that the displacement ratio of the isolated deck exceeds 2.0 is 51%, whereas for the case with $Q_y/W_{eff} =$ 12%, this quantity reduces to 24%. The performance of the ILP model under the FF excitations has remained almost unaffected in terms of the deck displacement response. Increasing the yield strength of the LRBs degrades the performance of the ILP model in terms of the base-shear and acceleration response reduction. The most highlighted adverse effect of increasing the LRBs' yield strength is the increase of the deck acceleration responses under the FF excitations. For example, the probability that the acceleration ratio of the isolated deck under the FF and NF excitations exceeds 0.50, for the case with $Q_y/W_{eff} = 6\%$ is 35 and 20%, respectively, whereas these quantities for the case with $Q_y/W_{eff} = 12\%$ are 98 and 77%, respectively. However, these increased acceleration responses (and base shear responses) are still quite below those of the non-isolated counterpart. This is further investigated next.

Table 2 presents the values of the maximum resultant seismic responses of the ILP model with $Q_y/W_{eff} = 6\%$ and 12% and also of the NLP model. As seen, using the higher-strength LRBs reduces the mean deck displacement responses under the NF excitations from 0.53 to 0.33 m (i.e., 38% reduction) that is smaller than the LRBs' drift capacity and also than the width of seismic gaps at the two ends of the deck. This conclusion verifies the prediction made at the outset of this section regarding the use of an R factor of 4.0 to limit the superstructure displacement response to 0.30 m. As an adverse effect, the mean deck acceleration response under the FF excitations increases from 0.23 to 0.28 g and under the NF excitations from 0.22 to 0.33 g. However, these increased acceleration responses are still 42 and 38% below the responses of the non-isolated counterpart, respectively. Furthermore, while in building structures, a primary objective of seismic isolation is to minimize the superstructure acceleration responses to protect acceleration-sensitive equipment and non-structural components, most bridges do not contain such components. Therefore, the slight deterioration in the performance of the isolated bridge in terms of the superstructure acceleration response cannot be considered a significant drawback of increasing LRBs' yield strength, especially when these responses are still quite below the responses of the non-isolated counterpart. These results, consistent with those of studying inelastic ground response spectra in Section "Ground Spectra to Preliminary Evaluate the Effectiveness of Seismic Isolation," illustrate that when designed properly (i.e., initial period and lateral strength of the isolation system are within certain ranges), seismic isolation can be an effective approach for intermediate- and relatively long-period structures subjected to both FF and NF excitations.

It is worthwhile noting that a few other studies have also proposed solutions for the relatively large responses of isolated superstructures, including an adaptive semi-active control system (Rabiee and Chae, 2019), gap hysteretic dampers operating in

TABLE 2 | The mean value of the maximum resultant seismic responses under the NF and FF record pairs for the LC 1.

		Normalized base shear response		Deck displacement response		Pier drift ratio		Deck absolute acceleration response	
Model		V_{FF}/W_{eff}	V_{NF}/W_{eff}	d_{FF} (m)	d_{NF} (m)	θ_{FF} (%)	θ_{NF} (%)	a_{FF} (g)	a_{NF} (g)
NLP		0.34	0.46	0.13	0.24	0.57	1.03	0.48	0.51
ILP; Q_y/W_{eff}	6%	0.17	0.21	0.142	0.53	0.12	0.28	0.23	0.22
	12%	0.19	0.23	0.144	0.33	0.17	0.27	0.28	0.33

parallel to the isolation system (De Domenico et al., 2020), and tuned-mass-damper inerters (De Domenico and Ricciardi, 2018; De Domenico et al., 2019), among others. In future studies, the use of these control systems for reducing the displacement responses of the superstructure of isolated structures with long non-isolated periods subjected to NF excitations can be investigated.

CONCLUSION

It is well established that seismic isolation is effective for short-period (stiff) structures exposed to short-period ground excitations such as ordinary far-field (FF) motions. However, the use of this technique for structures with relatively long non-isolated periods and also for pulse-like motions, such as many near-field (NF) excitations, has remained controversial. This study addresses this controversy. Constant-*R* inelastic ground response spectra are used to systematically evaluate the effects of the two fundamental aspects of seismic isolation, i.e., period lengthening and lateral-strength reduction, on the responses of relatively long-period structures. To verify the results, non-linear response history analyses are conducted on isolated and non-isolated case-study bridges with different periods and lateral strength. These bridge models are developed based on the real-world isolated Rudshur bridge. In the as-built condition, the piers are relatively tall and flexible, resulting in a relatively long non-isolated period of 2.22 s. This bridge, which is located in the Tehran–Hamadan railway in Iran, is categorized as an essential infrastructure according to the AASHTO LRFD provisions. With the length of 600 m, the continuous deck of the bridge is decoupled from the substructure by Lead Rubber Bearing (LRBs) installed between the deck and substructure. In spite of the existence of a major fault within 10 km of the site, this structure was designed for ordinary FF ground motions without NF considerations. This design resulted in LRBs with relatively low yield strength (i.e., equal to 6% of the seismic weight of the deck). An additional objective of this study is to assess the seismic performance of the Rudshur bridge and propose a rehabilitation scheme, if necessary.

A set of 20 NF record pairs containing forward directivity (FD) pulses and a set of 20 ordinary FF (non-pulse) record pairs are used in the response history analyses. To investigate the FD effects, each NF record pair is rotated to the FD/PD directions, where the FD is the orientation that dominates the seismic hazard at the recording site, and the PD is the orientation perpendicular to the FD. Peak ground acceleration (PGA) of all FF and NF record pairs is scaled to the design value of 0.45 g. Elastic/inelastic acceleration and displacement response spectra are developed for the selected ground motions. Non-linear response history analyses are also conducted on the case-study bridges.

The effectiveness of seismic isolation is investigated for four different scenarios: short-period structures subject to FF excitations, short-period structures subject to NF excitations, long-period structures subject to FF excitations, and long-period structures subject to NF excitations. The structural responses used to evaluate this effectiveness are superstructure displacement and acceleration responses, and substructure drift and shear force demands. The most salient results of the present study are summarized next:

(1) Inelastic constant-*R* ground spectra, including the spectral displacement, yield displacement, and force-reduction spectra together, can be used for the preliminary design of seismic isolation systems. It is shown that they can reasonably predict the global displacement responses of isolated structures.
(2) In terms of the superstructure acceleration response reduction and substructure force demand reduction, it is observed that:

- Seismic isolation is most effective for short-period structures subject to FF excitations but still significantly effective for the other three cases. In general, subject to FF excitations, seismic isolation is to some extent more effective for stiff structures than for flexible structures; for stiff structures, this approach is more effective under FF excitations than under NF excitations; for flexible structures, is approximately equally effective under NF and FF excitations. For example, for the case-study bridge models, the reduction in the median value of the maximum base-shear responses due to seismic isolation for the stiff-FF, stiff-NF, flexible-FF and flexible-NF cases is 86, 76, 49, and 51%, respectively. These results are consistent with the frequency contents of the NF and FF excitations and their significant different effects on structures with short and long periods.
- Reducing the yield strength of isolator bearings can consistently reduce mean seismic force and acceleration demands under both NF and FF excitations.
- For structures with relatively long non-isolated periods, the mean force demand reduction under NF excitations can be even more highlighted than that under FF excitations. This observation is opposite to that for structures with short non-isolated periods.

(3) In terms of superstructure displacement response, it is observed that:

- Seismic isolation does not result in a significant increase of the mean responses of the superstructure in long-period structures under FF excitations, and in some cases, can even reduce these responses. However, for NF excitations, when the initial period of the isolated structure is relatively large (approximately greater than 2.5 s), seismic isolation can impose relatively large superstructure displacement demands (e.g., as great as 1.0 m for the studied cases). In this case, if the initial isolated period lies in the intermediate region (e.g., 1.5–2.5 s), and the lateral strength of the isolators is relatively high (e.g., the *R* factor is 4.0–6.0), the displacement responses remain within ranges used in practice.

(4) The isolated Rudshur bridge was designed for ordinary ground motions resulting in isolator bearings with a relatively low yield strength that is equal to 6% of the deck seismic weight (i.e., the design resulted in the relatively large equivalent *R* factor of 8.3). This design causes relatively large deck displacement responses under NF excitations. The results illustrate that for many individual NF excitations, the drift demands on LRBs exceed their failure capacity. Increasing the LRBs' lateral yield strength from 6 to 12% of the deck seismic weight while reducing the superstructure displacements under the NF excitations to acceptable values, only slightly increases base shear and acceleration responses. It is shown that these increased values are still quite smaller than those of the non-isolated counterpart.

Tall buildings and bridges with tall/slender piers are of common long-period structures. The important challenges of applying base isolation to tall buildings are the P-delta effects, and heavy overturning moments and gravity loads exerted on bearings that may cause difficulties in the operation and design of isolator bearings. In bridges, isolators are installed between the deck and piers as opposed to at the base in buildings. Therefore, the concerns arising from the heavy overturning moments and gravity loads of tall buildings are much less pronounced in bridges. This statement, combined with the results of the conducted numerical studies, suggests that seismic isolation is an effective approach for bridges with relatively flexible piers (i.e., relatively long non-isolated periods).

DATA AVAILABILITY STATEMENT

The datasets generated for this study are available on request to the corresponding author.

AUTHOR CONTRIBUTIONS

HA developed the research idea, performed the literature review, designed the bridge models, performed finite element modeling and analysis, processed the results, drafted the article, and addressed the review comments. KP contributed to the finite element modeling, record selection, and design of the bridge models. MR contributed to the finite element modeling, analysis and writing the first two sections of the article. ES-B supervised and proofread the article.

SUPPLEMENTARY MATERIAL

The Supplementary Material for this article can be found online at: https://www.frontiersin.org/articles/10.3389/fbuil.2020.00024/full#supplementary-material

REFERENCES

American Association of State Highway and Transportation Officials [AASHTO] (2010). *Guide Specifications for Seismic Isolation Design*. Washington, DC: AASHTO.

American Association of State Highway and Transportation Officials [AASHTO] (2017). *AASHTO LRFD Bridge Design Specifications*. Washington, DC: AASHTO.

Anajafi, H., and Medina, R. A. (2018). Partial mass isolation system for seismic vibration control of buildings. *Struct. Control Health Monit.* 25:e2088. doi: 10.1002/stc.2088

Archila, M., Ventura, C. E., and Liam Finn, W. (2017). New insights on effects of directionality and duration of near-field ground motions on seismic response of tall buildings. *Struct. Des. Tall Spec. Build.* 26:e1363. doi: 10.1002/tal.1363

Baker, J. W. (2007). Quantitative classification of near-fault ground motions using wavelet analysis. *Bull. Seismol. Soc. Am.* 97, 1486–1501. doi: 10.1785/0120060255

Beiraghi, H., Kheyroddin, A., and Kafi, M. A. (2016). Forward directivity near-fault and far-fault ground motion effects on the behavior of reinforced concrete wall tall buildings with one and more plastic hinges. *Struct. Des. Tall Spec. Build.* 25, 519–539. doi: 10.1002/tal.1270

Bekdaş, G., and Nigdeli, S. M. (2013). Mass ratio factor for optimum tuned mass damper strategies. *Int. J. Mech. Sci.* 71, 68–84. doi: 10.1016/j.ijmecsci.2013.03.014

Building and Housing Research Center (2005). *Iranian Code of Practice for Seismic Resistant Design of Buildings (Standard No. 2800)*, 3rd Edn. Tehran: BHRC Publication.

Campbell, K. W., and Bozorgnia, Y. (2008). NGA ground motion model for the geometric mean horizontal component of PGA, PGV, PGD and 5% damped linear elastic response spectra for periods ranging from 0.01 to 10 s. *Earthq. Spectra* 24, 139–171. doi: 10.1193/1.2857546

Chenouda, M., and Ayoub, A. (2008). Inelastic displacement ratios of degrading systems. *J. Struct. Eng.* 134, 1030–1045. doi: 10.1061/(asce)0733-9445(2008)134:6(1030)

Chopra, A. K., and Chintanapakdee, C. (2004). Inelastic deformation ratios for design and evaluation of structures: single-degree-of-freedom bilinear systems. *J. Struct. Eng.* 130, 1309–1319. doi: 10.1061/(asce)0733-9445(2004)130:9(1309)

De Domenico, D., Deastra, P., Ricciardi, G., Sims, N. D., and Wagg, D. J. (2019). Novel fluid inerter based tuned mass dampers for optimised structural control of base-isolated buildings. *J. Franklin Inst.* 356, 7626–7649. doi: 10.1016/j.jfranklin.2018.11.012

De Domenico, D., Gandelli, E., and Quaglini, V. (2020). Effective base isolation combining low-friction curved surface sliders and hysteretic gap dampers. *Soil Dyn. Earthq. Eng.* 130:105989. doi: 10.1016/j.soildyn.2019.105989

De Domenico, D., and Ricciardi, G. (2018). An enhanced base isolation system equipped with optimal tuned mass damper inerter (TMDI). *Earthq. Eng. Struct. Dyn.* 47, 1169–1192. doi: 10.1002/eqe.3011

Fujita, K., Yasuda, K., Kanno, Y., and Takewaki, I. (2017). Robustness evaluation of elastoplastic base-isolated high-rise buildings subjected to critical double impulse. *Front. Built Environ.* 3:31. doi: 10.3389/fbuil.2017.00031

Güneş, N., and Ulucan, Z. Ç (2019). Nonlinear dynamic response of a tall building to near-fault pulse-like ground motions. *Bull. Earthq. Eng.* 17, 2989–3013. doi: 10.1007/s10518-019-00570-y

Hall, J. F., Heaton, T. H., Halling, M. W., and Wald, D. J. (1995). Near-source ground motion and its effects on flexible buildings. *Earthq. Spectra* 11, 569–605. doi: 10.1193/1.1585828

Huang, Y. N., Whittaker, A. S., and Luco, N. (2008). Maximum spectral demands in the near-fault region. *Earthq. Spectra* 24, 319–341. doi: 10.1193/1.2830435

Iervolino, I., Chioccarelli, E., and Baltzopoulos, G. (2012). Inelastic displacement ratio of near-source pulse-like ground motions. *Earthq. Eng. Struct. Dyn.* 41, 2351–2357.

Jäger, C., and Adam, C. (2013). Influence of collapse definition and near-field effects on collapse capacity spectra. *J. Earthq. Eng.* 17, 859–878. doi: 10.1080/13632469.2013.795842

Jangid, R., and Kelly, J. (2001). Base isolation for near-fault motions. *Earthq. Eng. Struct. Dyn.* 30, 691–707. doi: 10.1016/j.heliyon.2016.e00069

Jangid, R. S. (2007). Optimum lead-rubber isolation bearings for near-fault motions. *Eng. Struct.* 29, 2503–2513. doi: 10.1016/j.engstruct.2006.12.010

Jónsson, M. H., Bessason, B., and Haflidason, E. (2010). Earthquake response of a base-isolated bridge subjected to strong near-fault ground motion. *Soil Dyn. Earthq. Eng.* 30, 447–455. doi: 10.1016/j.soildyn.2010.01.001

Komuro, T., Nishikawa, Y., Kimura, Y., and Isshiki, Y. (2005). Development and realization of base isolation system for high-rise buildings. *J. Adv. Concr. Technol.* 3, 233–239. doi: 10.3151/jact.3.233

Lagos, R., Boroschek, R., Retamales, R., Lafontaine, M., Friskel, K., and Kasalanati, A. (2017). "Seismic Isolation of the Nunoa Capital Building, the Tallest Base Isolated Building in the Americas," in *Proceedings of the 16th World Conference on Earthquake Engineering*, Santiago.

Li, J., Peng, T., and Xu, Y. (2008). Damage investigation of girder bridges under the Wenchuan earthquake and corresponding seismic design recommendations. *Earthq. Eng. Eng. Vib.* 7, 337–344. doi: 10.1007/s11803-008-1005-6

Li, X., Dou, H., and Zhu, X. (2007). Engineering characteristics of near-fault vertical ground motions and their effect on the seismic response of bridges. *Earthq. Eng. Eng. Vib.* 6, 345–350. doi: 10.1007/s11803-007-0723-5

Liao, W. I., Loh, C. H., and Lee, B. H. (2004). Comparison of dynamic response of isolated and non-isolated continuous girder bridges subjected to near-fault ground motions. *Eng. Struct.* 26, 2173–2183. doi: 10.1016/j.engstruct.2004.07.016

Liao, W. I., Loh, C. H., Wan, S., Jean, W. Y., and Chai, J. F. (2000). Dynamic responses of bridges subjected to near-fault ground motions. *J. Chin. Inst. Eng.* 23, 455–464. doi: 10.1080/02533839.2000.9670566

Ma, C., Zhang, Y., Tan, P., and Zhou, F. (2014). Seismic response of base-isolated high-rise buildings under fully nonstationary excitation. *Shock Vib.* 2014:401469.

Malhotra, P. K. (1999). Response of buildings to near-field pulse-like ground motions. *Earthq. Eng. Struct. Dyn.* 28, 1309–1326. doi: 10.1002/(sici)1096-9845(199911)28:11<1309::aid-eqe868>3.0.co;2-u

McKenna, F., Fenves, G., and Scott, M. (2000). *Open System for Earthquake Engineering Simulation*. Berkeley, CA: University of California.

Naderpour, H., Naji, N., Burkacki, D., and Jankowski, R. (2019). Seismic response of high-rise buildings equipped with base isolation and non-traditional tuned mass dampers. *Appl. Sci.* 9:1201. doi: 10.3390/app9061201

Obando, J., and Lopez-Garcia, D. (2018). Inelastic displacement ratios for nonstructural components subjected to floor accelerations. *J. Earthq. Eng.* 22, 569–594. doi: 10.1080/13632469.2016.1244131

Quaglini, V., Gandelli, E., Dubini, P., and Limongelli, M. P. (2017). Total displacement of curved surface sliders under nonseismic and seismic actions: a parametric study. *Struct. Control Health Monit.* 24:e2031.

Rabiee, R., and Chae, Y. (2019). Adaptive base isolation system to achieve structural resiliency under both short-and long-period earthquake ground motions. *J. Intell. Mater. Syst. Struct.* 30, 16–31. doi: 10.1177/1045389x18806403

Rahnama, M., and Krawinkler, H. (1993). *Effects of soft soil and hysteresis model on seismic demands, John A. Blume Earthquake Engineering Center Standford*. Stanford, CA: Stanford University.

Shahi, S. K., and Baker, J. W. (2014). An efficient algorithm to identify strong-velocity pulses in multicomponent ground motions. *Bull. Seismol. Soc. Am.* 104, 2456–2466. doi: 10.1785/0120130191

Shen, J., Tsai, M. H., Chang, K. C., and Lee, G. C. (2004). Performance of a seismically isolated bridge under near-fault earthquake ground motions. *J. Struct. Eng.* 130, 861–868. doi: 10.1061/(asce)0733-9445(2004)130:6(861)

Skinner, R. I., Kelly, T. E., Robinson, W. H., Robinson Seismic, L., and Holmes Consulting, G. (2011). *Seismic Isolation for Designers and Structural Engineers*. Wellington: Robinson Seismic Ltd.

Somerville, P. G. (2005). "Engineering characterization of near fault ground motions," in *Proceedings of the 2005 NZSEE Conference*, (Pasadena, CA: URS Corporation), 1–8.

Soto-Brito, R., and Ruiz, S. E. (1999). Influence of ground motion intensity on the effectiveness of tuned mass dampers. *Earthq. Eng. Struct. Dyn.* 28, 1255–1271. doi: 10.1002/(sici)1096-9845(199911)28:11<1255::aid-eqe865>3.0.co;2-c

Takewaki, I. (2008). Robustness of base-isolated high-rise buildings under code-specified ground motions. *Struct. Des. Tall Spec. Build.* 17, 257–271. doi: 10.1002/tal.350

Veletsos, A., Newmark, N., and Chelapati, C. (1965). "Deformation spectra for elastic and elastoplastic systems subjected to ground shock and earthquake motions," in *Proceedings of the 3rd World Conference on Earthquake Engineering*, Wellington, 663–682.

Wang, Z., and Lee, G. C. (2009). A comparative study of bridge damage due to the Wenchuan, Northridge, Loma Prieta and San Fernando earthquakes. *Earthq. Eng. Eng. Vib.* 8, 251–261. doi: 10.1007/s11803-009-9063-y

Conflict of Interest: KP was employed by the company Pars Seismic Co.

The remaining authors declare that the research was conducted in the absence of any commercial or financial relationships that could be construed as a potential conflict of interest.

frontiers in Built Environment

ORIGINAL RESEARCH
published: 28 April 2020
doi: 10.3389/fbuil.2020.00050

A Resilience and Robustness Oriented Design of Base-Isolated Structures: The New Camerino University Research Center

Andrea Dall'Asta[1], Graziano Leoni[1], Fabio Micozzi[1]*, Laura Gioiella[1] and Laura Ragni[2]*

[1] School of Architecture and Design, University of Camerino, Camerino, Italy, [2] Department of Civil and Building Engineering and Architecture, Università Politecnica delle Marche, Ancona, Italy

This paper analyses the new Research Centre designed for the University of Camerino and entirely financed by the national Civil Protection Department (DPC), following the seismic events in Central Italy in 2016. The building has been designed to guarantee speed of execution as well as a high level of safety, especially regarding seismic actions. The structural solution was to create an isolated system with a steel braced super-structure with pinned joints and r.c. sub-structures able to adapt to the complex morphology of the area. As described in the first part of the paper, design choices have been made to achieve a high level of resilience and robustness, i.e., to limit damage to structural and non-structural components and equipment under moderate and design seismic actions and to avoid disproportionate consequences in the event of extreme actions, larger than the design ones. In the second part of the paper, specific risk analyses have been carried out to evaluate the real performance of the building under increasing intensity levels, with reference to both serviceability and ultimate conditions. To this purpose a site-specific hazard study was first conducted, then non-linear analyses were performed using a hazard-consistent set of records with return periods ranging from T_R = 60 years to T_R = 10000 years. The main demand parameters of both the isolation system and the super-structure were recorded and capacity values corresponding to different ultimate and damage limit conditions were defined. The results obtained in terms of demand hazard curves show that the building performances in terms of robustness and resilience are very high, confirming the efficacy of the strategies adopted in the design.

Keywords: base isolation, high damping rubber bearings, hybrid isolation system, seismic risk analysis, hazard demand curves

OPEN ACCESS

Edited by:
Solomon Tesfamariam, The University of British Columbia, Canada

Reviewed by:
Yongbo Peng, Tongji University, China
Giuseppe Ricciardi, University of Messina, Italy

****Correspondence:***
Dall'Asta Andrea
andrea.dallasta@unicam.it
Fabio Micozzi
fabio.micozzi@unicam.it

Specialty section:
This article was submitted to Earthquake Engineering, a section of the journal Frontiers in Built Environment

Received: *13 December 2019*
Accepted: *30 March 2020*
Published: *28 April 2020*

Citation:
Dall'Asta A, Leoni G, Micozzi F, Gioiella L and Ragni L (2020) A Resilience and Robustness Oriented Design of Base-Isolated Structures: The New Camerino University Research Center. Front. Built Environ. 6:50. doi: 10.3389/fbuil.2020.00050

INTRODUCTION

Since the seismic events in Central Italy in 2016, which severely damaged the city of Camerino, several buildings are under reconstruction or are to be rebuilt. One of these is the new University of Camerino Research Centre, which is entirely financed by the national Civil Protection Department (DPC). The structure, as required by the funding body, was conceived by privileging solutions guaranteeing the speed of execution (and possible dismantling) and a high level of safety, especially with regard to seismic actions.

The structural solution was therefore to create an isolated system with a steel braced super-structure with pinned joints and r.c. sub-structures able to adapt to the complex morphology of the area. In particular, a hybrid isolation system was adopted, comprising High Damping Rubber (HDR) bearings and low-friction sliders able to provide a high period of isolation. The choice of this isolation system is mainly due to their good behavior for both low-medium and strong intensity earthquakes. In fact, the hazard of the site does not lead to excessive displacements for strong earthquakes, which can be faced with a moderate damping. Thus, high dissipative solutions, such as lead rubber bearings (LRBs) or curved surface sliders (CSSs) are not required in this case. Moreover, the solution with HDR bearings is better in providing resilience to the building for frequent earthquakes, i.e., no damage or downtime. In fact, for lower displacements the stiffness and damping of this kind of bearings only slightly increase. Differently, devices such LRBs or CSSs are characterized by high level of damping and stiffness for small displacements, which could lead to larger floor accelerations for frequent events (Yang et al., 2010). This would be very dangerous for the Research Centre object of this paper, given the potentially high risk activities in the chemistry and physics laboratories, where dangerous substances and expensive equipment sensitive to floor accelerations will be housed. Moreover, since the building is intended for public use with the possibility of accommodating large crowds and may even be used as coordination center in the organization of civil protection post-earthquake activities in the case of possible future seismic events, two complementary strategies have been adopted to also ensure adequate structural robustness against extreme actions, larger than the design ones. The first consists of a safety margin adopted for the displacement capacity of both the devices composing the isolation system and the seismic gaps on the upstream side of the building. For both of them a capacity limit greater than the maximum design displacement at the Collapse Limit State (CLS, characterized by the return period of T_R = 950 years) has been required to avoid anomalous behaviors, such as the exit of the sliders out of the sliding surface or the impact of the building with neighboring structures. The second strategy consists of adopting a steel super-structure equipped with elasto-plastic braces, able to limit disproportionate consequences in the case of even more large horizontal actions. This aspect is guaranteed by the over-strength of the diagonal brace, which is important in the case of extreme horizontal actions causing an increase in the stiffness of the HDR bearings (due to their hardening behavior) or the closure of the gaps. Finally, the robustness under exceptional scenario (such as fire events or explosions) leading to the loss of vertical bearing of isolators is ensured by adopting safety supports around the device.

In this paper a description of the building is first presented, then the design procedure of the base-isolated building is illustrated and finally a specific risk analysis is reported to demonstrate the achievement of the design objectives, i.e., a very low seismic risk in terms of the attainment of both damage and ultimate limit states. In particular, the last part of the paper reports a site-specific hazard study carried out with the Reasses v.2.0 software (Chioccarelli et al., 2019) providing a conditioned spectrum of the site for different return periods of the seismic action. Based on the obtained mean conditioned spectra and relevant dispersions, procedures as described in the literature (Baker, 2011; Baker and Lee, 2018) have been applied to obtain set of records to be used for the non-linear analyses under increasing intensity levels characterized by return periods ranging from T_R = 60 years to T_R = 10000 years. The main demand parameters of both the isolation system and the super-structure have been recorded and capacity values corresponding to different ultimate and damage conditions have been defined. Finally, the demand hazard curves of the monitored demand parameters have been evaluated to quantify the exceedance probability of each limit state considered.

BUILDING DESCRIPTION AND DESIGN

The structural system of the university research center was conceived around a design solution suitable for the complex morphology of the area and for the speed of execution and able to guarantee a high level of resilience and robustness to the construction. In particular, the foundations and the lower parts of the building have been designed to reduce the impact on the ground profile, which is characterized by a remarkable slope. The characteristics of the soil and the variability of the thickness of the deformable layer led to the adoption of deep foundations (**Figure 1**). The isolation system, consisting of high-damping elastomeric isolators and low-friction flat sliders, have been placed at the horizontal level above the sub-structure r.c. elements. The upper part of the building (super-structure) is made of steel elements and is developed by assuming a 7.2 m × 7.2 m modular system, for a total of 7 modules along each direction, and a 1.9 m long cantilever along the entire perimeter of building (**Figure 2**). The steel elements have been optimized in terms of dimensions and connection systems based on the single module, resulting in a significant saving on materials and a significant reduction in construction times.

Sub-Structures

The building is founded on a multi-level pile system, with piles of 0.8 m diameter and 14 m long. The foundation system on the head of the piles is composed of a set of plinths, of variable shapes and a height of 1.2 m, mutually connected by r.c. beams with a 0.4 m × 0.8 m cross section. All the elements are made of C25/30 concrete with B450C steel reinforcement bars. The columns of the sub-structures have a circular section of 1.2 m diameter or a 1 m × 1 m square section and they are only in the downstream part of the building (**Figure 1**). All the elements are made of C28/35 concrete with B450C steel reinforcement bars. At the head of each column, a capital allows for the easy maintenance and the replacement of seismic support systems (HDR bearings or sliders). These capitals are of two distinct types: (a) as a support for the elastomeric and (b) as support for the sliders to compensate for the different heights and to allow for vertical alignment of the top of all the devices (**Figure 3**). It is worth noting that the capitals are designed with specific reinforcements to withstand the forces acting on the super-structure during

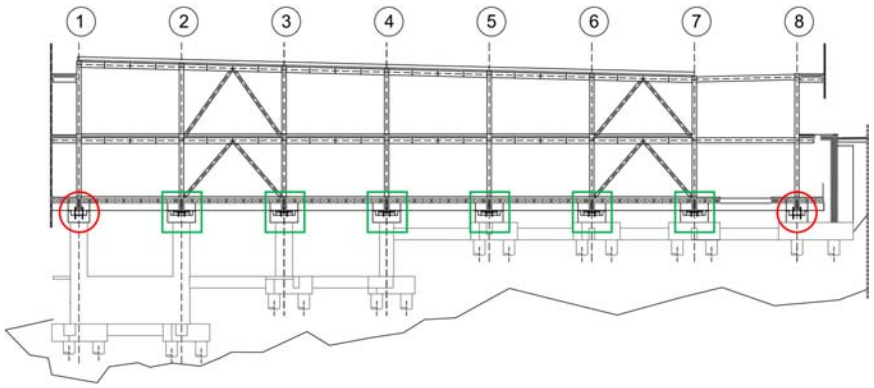

FIGURE 1 | Longitudinal section of the building (red circles represent HDR bearings and green squares represent flat sliders).

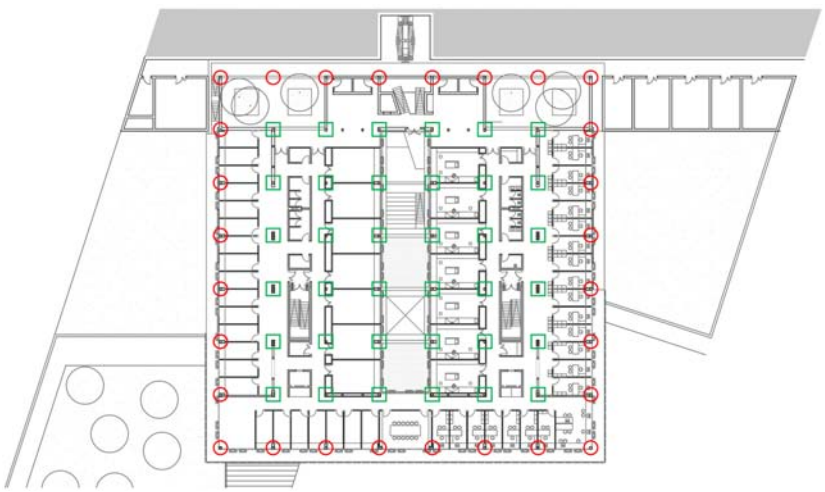

FIGURE 2 | Plan view of the building (red circles represent HDRB bearings and green squares represent flat sliders).

lifting for possible removing and replacement of the devices. Finally, they are all equipped with 4 safety supports (one on each corner) to ensure the transfer of vertical loads in cases of emergency (loss of support capacity of one or more devices).

Isolation System

The isolation system has been designed considering a target period of T_{is} = 3.5 s at the design intensity earthquake, able to guarantee a significant reduction of the actions transferred to the super-structure in the case of a seismic event. In particular, the solution adopted to guarantee this period involves the use of a hybrid isolation system with HDR bearings arranged on the perimeter in order to maximize torsional stiffness, and flat sliding supports in the central part to support higher vertical loads. HDR bearings commonly used in Italy have a damping ratio ranging from 10% to 15% (FIP, 2016), which is lower than HDR bearings used in other countries with higher seismicity areas, such as Japan (Bridgestone, 2017). In the design of the isolation system the lower limit of 10% at the design shear strain was assumed. However, according to EN15129 (2009), this rubber compound can still be classified as high damping, because the damping ratio is larger than the lower bound of 6% (at 100% of shear strain) fixed by the code. Moreover, a shear stiffness equal to 0.4 MPa was assumed at the design shear strain, typical of a soft rubber. For the flat sliding bearings, a friction coefficient of less than 1% was required. In a preliminary phase, the bearings were dimensioned by assuming a rigid super-structure and sub-structures to obtain a 1-DOF (degree of freedom system) and by neglecting the slider friction. Thus, the elastic response spectra have been used, reduced for all the periods $T \geq 0.8\ T_{is}$ by the equivalent damping of the HDR bearings. **Figure 4** shows the elastic displacement spectra and the pseudo-acceleration spectra for the considered site (Camerino, soil type B) at the different limit states: the Operational Limit State (OLS), the Damage Limit State (DLS), the Ultimate Limit State (ULS) and the Collapse Limit State (CLS), characterized by the return periods respectively equal to T_R = 60 years, T_R = 100 years, T_R = 950 years, and T_R = 1950 years, according to the national seismic code (NTC, 2018) for the use class IV. According to that code, the design was carried out by deriving the maximum

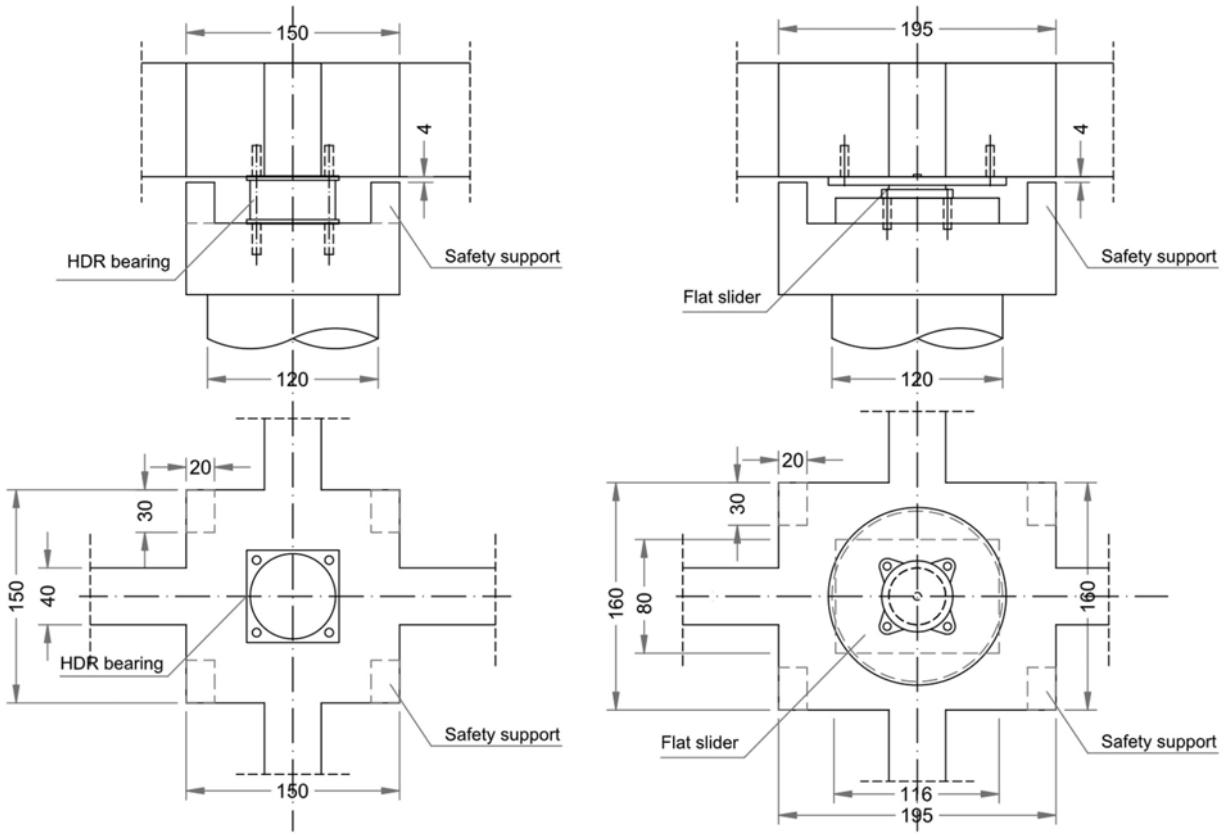

FIGURE 3 | Capitals for the isolation system devices (HDR bearings and flat sliders).

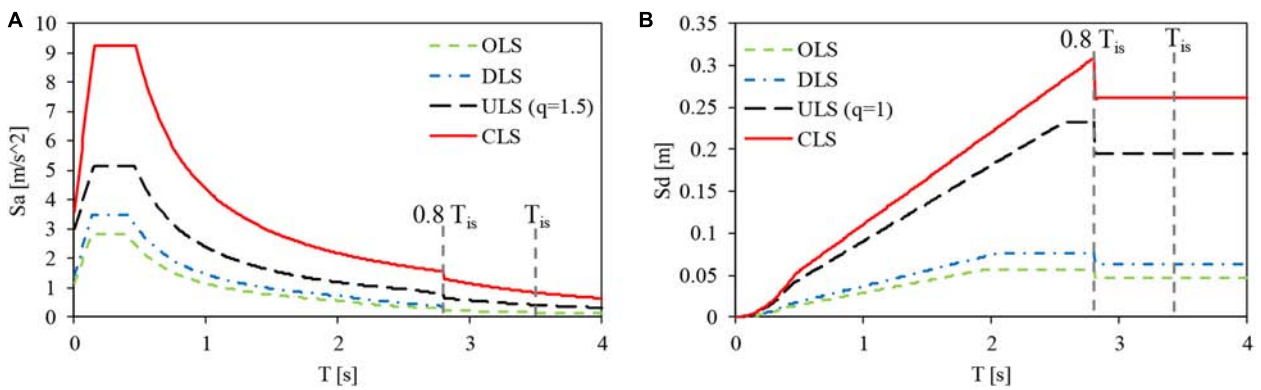

FIGURE 4 | Displacement **(A)** and pseudo-acceleration **(B)** spectra at the different limit states.

displacement of the isolators from the displacement spectrum at the CLS corresponding to the isolation period of 3.5 s, which is about 0.27 m. An average design shear strain equal to 1.5 is assumed, ensuring a significant safety margin against possible shear failure, even in the presence of accidental torsional effects. In fact, by assuming an amplification of 1.2 (Dolce et al., 2013) for torsional effects, the maximum deformation is equal to 1.8, which is still lower than the maximum value allowed by the European standard on anti-seismic devices (EN15129, 2009) equal to 2.5. Based on the obtained displacement and the design shear strain of bearings the total height of rubber of the bearings is h_{is} = 0.27/1.5 = 0.18 m. The total area of rubber (A_{is}) able to guarantee the target isolation period can be deduced through the following relationship:

$$\frac{GA_{is}}{h_{is}} = \left(\frac{2\pi}{T_{is}}\right)^2 M \tag{1}$$

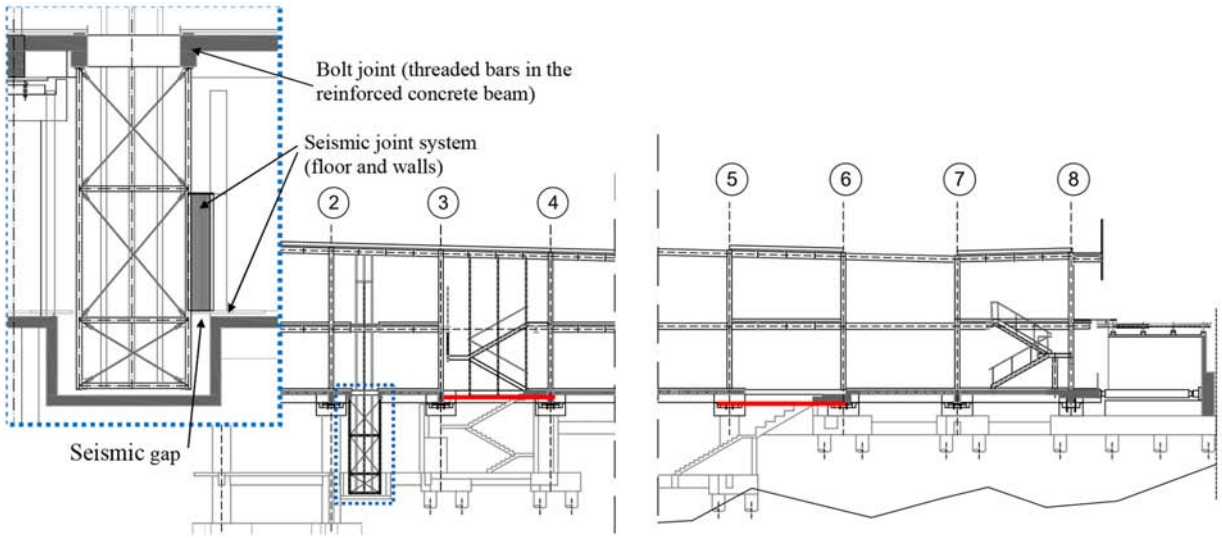

FIGURE 5 | Sections of the building (the red line highlights the seismic cut of staircases whereas the blue dotted area highlights the steel frame of the hanged elevator).

The total mass of the system is equal to M = 6173 kNms^{-2} therefore the total area obtained is equal to A_{is} = 9,087 m^2. Based on the total rubber area obtained and on the devices available on the market, the following types of devices have been chosen: (i) elastomeric isolators with a diameter of 600 mm, total height of rubber 184 mm, with horizontal rigidity 0.62 kN/mm and maximum displacement 350 mm, (ii) sliding supports with a maximum displacement of 400 mm and friction coefficient lower than 1%. The final choice of devices led to a slightly higher isolation period equal to T_{is} = 3.60 s. It should be noted that the displacement capacity of both the devices is larger than the maximum displacement at the CLS accounting for torsional effects (270 * 1.2 = 324 mm), especially for slider devices. As already highlighted in the introduction, this safety assumption guarantees the absence of anomalous behaviors due for example to the exit of the sliders for actions greater than those considered in the design. An adequate dimension has also been assumed for the seismic gaps placed in the upstream part of the building at the road level. In particular, high-performance floor gaps have been installed in the entrance areas, able to absorb the entire movement without damage and maintaining a horizontal surface even during the earthquake, while in the other areas standard gaps have been arranged, able to absorb the entire displacement but with damage to the rubber inserts beyond a certain threshold. In both cases, the displacement capacity assumed is equal to 350 mm. Similar precautions have been taken with regard to facilities, piping and installations, which must absorb the entire design displacement without damage or loss of functionality.

Super-Structure

As already mentioned, the super-structure is articulated on two levels (for a total of three decks) and the structural system is made of steel. In particular, the structural system consists of beams and columns with pinned joints, that take on gravitational actions, while the resistance to horizontal actions is ensured by the diagonal tension-compression braces, arranged in a reverse V and placed in the two main directions of the building. HE300B type profile columns are used, for both elevations, whereas the main beams are made of HE400A type profiles and the secondary ones are made of IPE360 profiles. Braces have a hollow circular section with 193.6 mm diameter and 16 mm thickness. The first floor above the isolation plane is made of precast r.c. slabs (H = 5 + 20 + 5 cm) and beams of 40 × 80 cm sections arranged in both directions and designed by accounting for moments induced by P-Δ effects due to the large displacements of HDR bearings and sliders during the earthquake motion. The second and third floors are made of corrugated steel sheets and r.c. slabs (H = 75 + 55 mm), supported by secondary steel beams. For the external cantilever, present in all three levels, the structural systems of the respective floors are used. All the elements are made using S355 steel. Finally, twin staircases guarantee the vertical connection of the building. Since the staircases cross the isolation layer, a seismic gap has been placed below the first floor slab, and the arrival ramp has been cut to guarantee a relative displacement of 400 mm (**Figure 5**). There are other staircases in the building: a reinforced concrete staircase connecting the sub-structure to the first floor (also provided with a seismic cut to allow the relative displacement of the adjacent reinforced concrete beams and plinths in the arrival area) and two other steel staircases connecting the super-structure. There are also three elevators in the building, two of which reach the sub-structure. For these lifts, the part of the structure being under the isolation level is hanged on the floor just above the isolation system. In this way, the absence of any interference with the isolation system or the fixed parts of the sub-structure is ensured. At the underground level high-performance seismic floor gaps have been used to permit access to the lift and avoid impact between the hanged lift-case and the sub-structure during an earthquake.

LINEAR DYNAMIC ANALYSES UNDER SERVICE AND DESIGN CONDITIONS

For design purposes, seismic analyses of the building was carried out by modeling all the structural system components (the super-structure, the sub-structure and the isolation system) as linear elastic elements, having satisfied the conditions reported in NTC for the linear modeling of isolation systems (NTC, 2018). In particular, the isolation devices were modeled by means of linear elastic springs (HDR bearings) and sliding supports (sliders). For the bearings, the horizontal stiffness is assumed consistent with the level of displacement reached at each considered limit state. This was iteratively estimated based on the displacement spectra of the different limit states and the expressions available in the technical literature about rubber equivalent parameters (G and ξ) as a function of the obtained shear strain (FIP, 2016). It should be noted that the vertical deformability of the HDR bearings was also taken into account, despite the ratio between their vertical stiffness and horizontal stiffness being greater than 800, to verify the effect of the different vertical stiffness of sliders and bearings. Finally, all the decks are considered as rigid. The Sap 2000 software has been used for the analyses (Computer and Structures, 1995).

First, a modal analysis was carried out on the model, and the results, in terms of the three main vibration periods of the building, are presented in **Table 1**, together with mean values of the shear strains of bearings at the different limit states and the corresponding equivalent parameters. Thereafter, a spectral analysis was carried out by using elastic spectra reduced, for all periods $T \geq 0.8\ T_{is}$, of the equivalent damping of the isolation system, as illustrated in **Figure 4**. Only for the resistance verifications of the super-structure at the ULS, a behavior factor equal to q = 1.5 was assumed, in accordance with NTC (2018). However, as better explained later, the braces have been dimensioned based on a request for rigidity adequate for the isolation system, rather than for resistance. In this way, the structure is also insensitive to the second order effects and the effect of global imperfections in resistance verifications can be neglected. Finally, the over-strength of the braces provides a strategy to ensure adequate structural robustness, i.e., limited consequences in the case of exceptional horizontal actions causing an increase in the stiffness of the HDR bearings (due to their hardening behavior) or the closure of the gaps. **Table 2** summarizes the base shear and displacement of the isolation system for the different limit states. For each limit state, the maximum and minimum axial load acting on the bearings, including the increase in axial load due to seismic actions, is also reported.

TABLE 1 | Shear strain, stiffness and damping ratio of isolation bearings at different limit states and relevant vibration periods.

	γ_{is}	K_{is} kN/m	ξ_{is} %	1st mode (Y) s	2nd mode (X) s	3rd mode (Θ) s
CLS	1.40	618	9.15	3.60	3.58	2.86
ULS	1.27	617	9.37	3.60	3.58	2.86
DLS	0.33	836	12.07	3.10	3.09	2.46
OLS	0.25	966	12.57	2.90	2.89	2.29

TABLE 2 | Maximum base shear, maximum displacements of the isolation system and maximum compression forces on the isolation devices.

	V_x	V_y	d_x	d_y	N_{max} sliders	N_{min} sliders	N_{max} HDRBs	N_{min} HDRBs
	kN	kN	mm	mm	kN	kN	kN	kN
OLS_X	1277	379	51	19	716	1204	647	1034
OLS_Y	383	1265	19	51	780	1215	648	1033
DLS_X	1477	439	68	25	689	1225	647	1035
DLS_Y	443	1465	26	68	758	1238	648	1034
ULS_X (q = 1)	2287	685	212	77	594	1313	647	1025
ULS_Y (q = 1)	686	2284	80	212	665	1336	647	1026
CLS_X	4576	1364	284	104	329	1560	645	1043
CLS_Y	1373	4545	107	284	412	1605	646	1041

Firstly, it can be observed that the maximum displacements at the CLS are lower than the displacement capacity of the selected devices and no tensile forces occur on any devices (no cavitation for HDR bearings or uplift of sliders). Regarding maximum compression forces, the maximum values obtained in the seismic condition are about 1040 kN for the bearings and 1600 kN for the sliders. Under the static condition (the ultimate limit state without seismic action, not reported in this paper) the maximum axial loads are about 2100 kN for the bearings and 2400 kN for the sliders. The buckling capacity of the selected HDR bearings is sufficiently larger than the demand. In fact, given the primary shape factor S_1 = D/4t (where D is the bearing diameter and t the thickness of a single rubber layer), the buckling load capacity at zero displacement can be computed through the following expression, as suggested by the European code for anti-seismic devices (EN15129, 2009):

$$P_{CR} = \frac{1.1 G A_r D' S_1}{T_q} \tag{2}$$

where D' is the effective diameter of the bearing (i.e., the diameter of steel plates without the rubber cover), A_r is the effective area of the device and T_q is the total rubber thickness called h_{is} in Eq. 1. Supposing that the selected HDR bearings are composed by 23 rubber layers of thickness 8 mm, the primary shape factor is S_1 = 18.75 and the buckling load capacity is about 6640 kN. For the code, the maximum admissible compressive load at zero displacement is $P_{CR}/2$ = 3320 kN, while the maximum admissible compressive load at the maximum admissible displacement equal to $d_{max,b} = 0.7D'$ is $P_{CR}/4$ = 1660 kN. For the bearings selected $d_{max,b} = 0.7D' = 0.7 \cdot 580$ = 406 mm. Since the maximum axial load under static conditions is lower than the corresponding limit, and the fact that the maximum displacement and the maximum axial load obtained from the seismic analysis are both lower than the respective admissible values, the stability of the bearings is ensured. For the sliders, the diameter of the internal pad has been chosen, by assuming a maximum contact pressure on the elastomeric pad of about 60 MPa (EN 1337-5, 2005). By

TABLE 3 | Maximum inter-storey drift and maximum floor acceleration for different limit states.

	d_x mm	d_y mm	a_x m/s^2	a_y m/s^2
OLS_X	0.62	0.25	0.22	0.06
OLS_Y	0.27	0.60	0.07	0.21
DLS_X	0.72	0.28	0.26	0.08
DLS_Y	0.30	0.70	0.08	0.25
ULS_X (q = 1)	1.67	0.66	0.40	0.12
ULS_Y (q = 1)	0.71	1.63	0.13	0.39
CLS_X	2.21	0.85	0.80	0.23
SLC_Y	0.924	2.135	0.26	0.78

adopting a diameter of 270 mm and partial safety factor of γ_m = 1.3 (EN 1337-5, 2005) the maximum axial load is about $N_{b,Rd}$ = 2640 kN, which is lower than the maximum axial load acting on the sliders. With regard to the super-structure and the sub-structures, all the elements have been checked for resistance (r.c. and steel elements) and stability (steel elements) at the ULS, moreover inter-storey drifts and absolute floor accelerations of the super-structure have been estimated for the different limit states (**Table 3**). It must be emphasized that the designed isolation system and the choice adopted for the non-structural elements (vertical closure panels) ensure the absence of any significant damage up to the CLS and therefore allow the construction to be operative immediately after the occurrence of a high intensity earthquake without any loss of functionality or downtime.

NON-LINEAR DYNAMIC ANALYSES AND SEISMIC RISK EVALUATION

In order to accurately estimate the risk level of the base-isolate building, a probabilistic seismic risk analysis has been carried out, following a probabilistic framework already used for base-isolated structures as well as for other kinds of code-conforming structures (Iervolino et al., 2018; Ragni et al., 2018a). In particular, a hazard analysis of the site was first conducted, then non-linear dynamic analyses were carried out under increasing seismic intensities in order to assess the attainment of damage and ultimate conditions. Finally, linking information about the site hazard and the vulnerability of the building made it possible to estimate the seismic risk. Hereafter is reported a description of the procedure followed.

Hazard Analysis and Record Selection

Probabilistic seismic hazard analysis (PSHA) is generally recognized as the rational method to quantify the seismic input in a probabilistic way, i.e., define the probability of exceedance (or the annual rate of exceedance) of a measure of the seismic intensity (IM). In order to make the implementation of this procedure less demanding for engineers dealing with practical applications, a practice-oriented software, namely REASSESS V2.0 (REgionAl, Single-SitE and Scenario-based Seismic hazard analysis) has recently been developed (Chioccarelli et al., 2019) and was used in the analyses of Camerino site. The software allows the user to define the input of the analysis in terms of: site coordinates, the Ground Motion Prediction Equation (GMPE) selected from an embedded database, the intensity measure (IM) of interest (according to the GMPE), the seismic sources (user-defined three-dimensional faults, seismic sources areal zones or sources selected from embedded databases), and structure of logic tree, if any. When these input elements are set, REASSESS is able to provide classical results of PSHA such as hazard curves, even in terms of advanced ground motion IM. Moreover, uniform hazard and conditional mean spectra (UHS and CMS), together with disaggregation distributions given the occurrence or the exceedance of the IM threshold, can be computed.

In this application the pseudo-acceleration spectral ordinate at the isolated period has been selected as the IM. With regard to the seismic zones and the GMPE, it is known that the seismic hazard study of Italy (Stucchi et al., 2011), at the basis of the current Italian building code, considers the seismic source model of the thirty-six areal zones defined by Meletti (Meletti et al., 2008) and the GMPE by Ambraseys (Ambraseys et al., 1996). In this study, the same source model has been considered, but a recently developed GMPE has been assumed (Lanzano et al., 2019). This GMPE is based on updated data including later events (i.e., 2012 Emilia, Northern Italy; 2016–2017 Central Italy), which allowed the magnitude range to be extended beyond 6.9 and the vibration period to be increased up to 10 s. Thus, it can also be used for long period structures, such as base-isolated structures. It should also be noted that this GMPE uses as IM the median of orientation independent amplitudes (RotD50) instead of the maximum component in the two directions, as in Ambraseys (Ambraseys et al., 1996). **Figure 6A** shows the computed hazard curves for different spectral ordinates and for the site of interest with soil classes B (v_s = 400 m/s). The Uniform Hazard Spectrum (UHS) for different return periods is indicated in **Figure 6B**. Note that **Figure 6B** also illustrates the UHS given by the Italian seismic code (NTC, 2018) for the same site and for the CLS (T_R = 1950 years). Although the source model considered in this paper for the hazard assessment lies at the basis of the hazard map used by the code, the latter is based on a different GMPE. Furthermore, a logic tree was considered for the hazard map definition, while only one branch has been considered in this study. Therefore, the UHS obtained for T_R = 1950 years is different from the code UHS, in particular it is larger for short periods but lower for long periods typical of base-isolated structures. However, it should be noted that this comparison is only qualitative, because the code spectrum is referred to a different IM (maximum component instead of RotD50).

In this study, for the non-linear analyses reported in the next section the return periods of the design limit states (T_R = 60 years for the OLS, T_R = 100 years for the DLS, T_R = 950 years for the ULS, T_R = 1950 years for the CLS) have been considered together with a larger return period of T_R = 10000 years. For each return period, a hazard consistent seismic input has been chosen for non-linear dynamic analysis. Practically, this means that records were selected to be consistent with the hazard-based spectral shape and variability obtained for each return period, by using the methods available in the technical

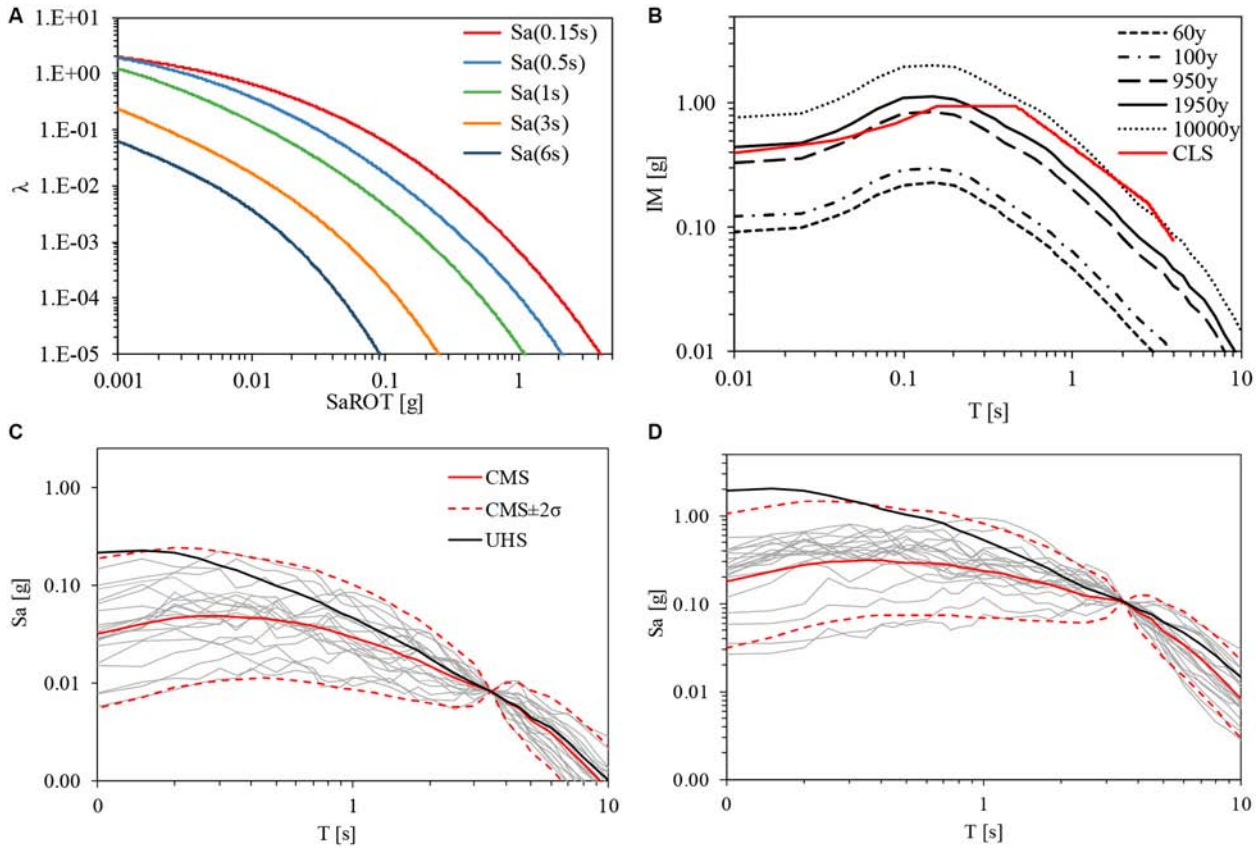

FIGURE 6 | Hazard Curves for the Camerino site with v_s = 400 m/s **(A)**, UHS at different hazard periods **(B)**, CMS and spectra of the selected set of records for T_R = 60 years **(C)**, and T_R = 10000 years **(D)**.

literature (Baker, 2011; Baker and Lee, 2018). In particular, for each intensity level a set of 20 records was selected by extracting them from the ESM database (Luzi et al., 2016). **Figures 6C,D** illustrate the pseudo-acceleration spectra of the selected record for returns periods of T_R = 60 years and T_R = 10000 years. The CMS is also shown together with an interval corresponding to twice the standard deviation (σ) in which almost all the records are included. A specific study with only pulse-like motions is not carried out, according to EC8 indications (EN 1998-1, 2005), since a fault closer than 15 Km and with a Magnitude larger than 6.5 is not known for the Camerino site.

Non-linear Dynamic Analyses and Seismic Risk Assessment

For the non-linear dynamic analyses a non-linear numerical model has been developed, starting from the linear model used in the design phase. In particular, linear springs representing the HDR bearings have been replaced by non-linear elements adopting the HDR isolator (Masaki et al., 2017) available in the Sap 2000 software (Computer and Structures, 1995). This model is bidirectional and accounts for non-linear phenomena, such as the strain-dependent behavior of the HDR bearings, but neglects other aspects, such as the strain hardening at large shear strains (larger than 250%) or the effect of the vertical load on the horizontal response of the bearings (Ishii and Kikuchi, 2018). This may be important for large axial loads close to the buckling capacity of the bearing in the deformed configuration (Kelly, 1997). The load history dependence characterizing some HDR bearings has also been neglected. This last aspect concerns bearings made of natural rubber with a large amount of filler, causing progressive damage to the rubber microstructure as the strain history progresses. Although there are numerical models accounting for this phenomenon in scientific literature (Grant et al., 2004; Tubaldi et al., 2017; Ragni et al., 2018b), it has been neglected in this study and the numerical model adopted for the bearings has been calibrated based on third cycle data available in the technical literature (FIP, 2016). More in details, model parameters have been calibrated to obtain target stiffness and damping data at each shear deformation. The cyclic behavior obtained is reported in **Figure 7A** and the equivalent linear parameters are illustrated in **Figures 7B,C**. The hardening at large shear strains as well as the effect of the vertical load on the horizontal response of the bearings were also neglected in these analyzes, due to the limited maximum shear strain and maximum axial load experienced by the bearings, even in very rare events. With reference to the sliding supports, these have been modeled as friction elements with constant friction coefficient equal to

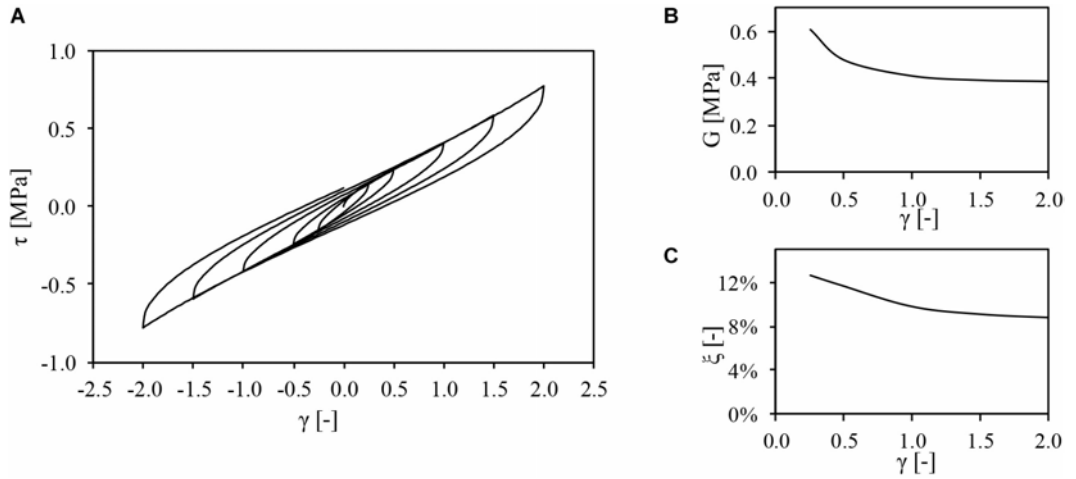

FIGURE 7 | Cyclic behavior of the HDR model of the Sap 2000 software **(A)** and trends pf equivalent stiffness **(B)** and equvalent damping **(C)**.

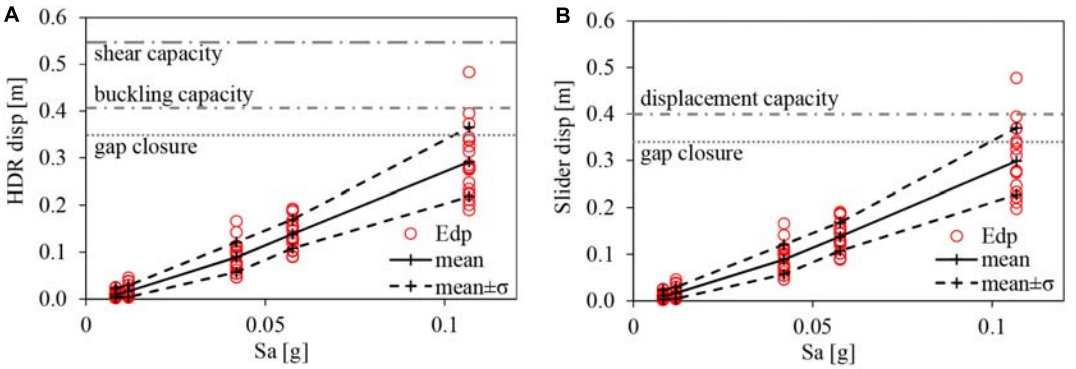

FIGURE 8 | Maximum displacement of HDR bearings **(A)** and sliders **(B)** and the corresponding capacity limits.

0.5% (typical of dimpled lubricated PTFE sheet on austenitic steel, EN 1337-5, 2005), neglecting its dependency on sliding velocity, contact pressure or heating during repeated cycles. This choice is supported by the expected low effect on the global behavior of the hybrid system of the variation of the friction coefficient. More sophisticated models, based on available numerical and experimental studies accounting for these three effects (Lomiento et al., 2013; De Domenico et al., 2018, 2019; Furinghetti et al., 2019), should be used to analyze the response of base-isolated buildings equipped with high or medium friction CSSs, where the primary function is to support vertical loads and to provide energy dissipation. The elastic behavior of the super-structure has been maintained by checking that the elastic limit of the diagonal braces has not been exceeded for each time history. Finally, seismic gaps have not been included in the model, but for each time history it has been checked whether displacements were smaller or larger than the gap amplitude.

Figures 8, **9** show the results of the non-linear analyses carried out for the different intensity levels considered. In particular, **Figure 8** shows the seismic demand on the isolation system, in terms of the maximum displacement attained by the HDR bearings (**Figure 8A**) and the sliding supports (**Figure 8B**). First, it can be observed than mean values are lower than those expected from the design, for all the design limit states (OLS with T_R = 60 years, DLS with T_R = 100 years, ULS with T_R = 950 years, and CLS with T_R = 1950 years). This is due to the different hazards assumed in the design and seismic risk assessment phases, but also to the different structural models and types of analysis used in the two phases. An important role is played by the slider friction (neglected in the design but considered in seismic risk assessment) which reduces the displacement demand of the isolation system while slightly increasing accelerations transferred to the super-structure. The second remark is about the dispersion of the monitored repose parameters due to the record-to-record variability, which is particularly evident at IM5. The reason of this variability can be explained by **Figure 10**, where displacement spectra of the records selected at IM5 are illustrated in terms of RotD100 ($Sd_{RotD100}$), i.e., the maximum spectral value over all the rotation angles of the bidirectional signal. In order to simulate displacements sustained by the isolated building, spectra are computed by assuming a damping ratio equal to ξ = 10%. It can be observed that even though

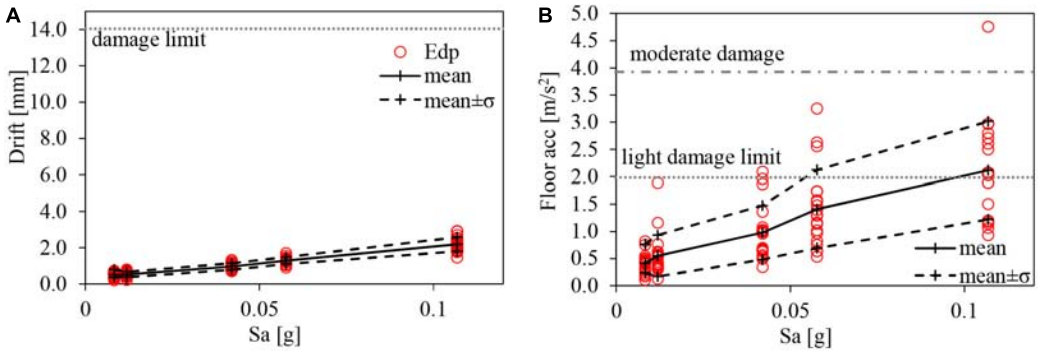

FIGURE 9 | Maximum inter-storey drifts **(A)** and maximum floor absolute acceleration **(B)**.

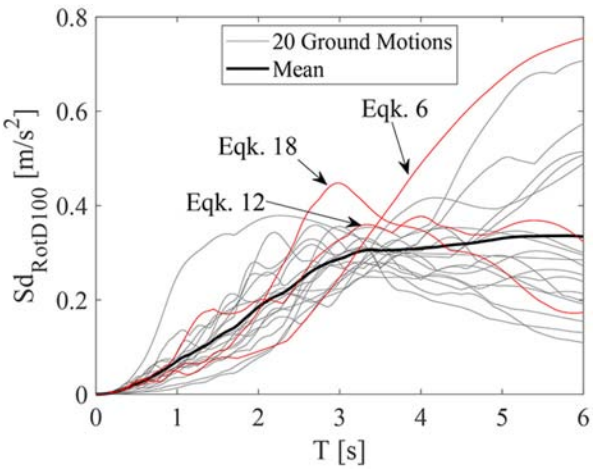

FIGURE 10 | Displacement spectra in terms of RotD100 of the selected set of records for T_R = 10000 years.

records are scaled to obtain the same intensity measure in terms of RotD50 at the isolation period (as shown in **Figure 7**), a significant record-to-record variability is obtained at the same period for spectral displacement in terms of RotD100, due the different record directivity. The three earthquakes leading to the highest displacements of the isolation system are the same earthquakes with the highest values around the isolation period.

The capacity limits corresponding to different limit states are also highlighted in **Figures 8**, **9**. In particular, for HDR bearings (**Figure 8A**) the gap amplitude equal to 350 mm is reported as well as the maximum admissible displacement for the buckling stability equal to $d_{max,b} = 0.7D' = 0.7 \cdot 580 = 406$ mm. The maximum displacement corresponding to the shear failure ($d_{max,s}$) of the bearings is also reported, assuming a shear capacity equal to 300% ($d_{max,s} = 3 \cdot h_{is} = 546$ mm). This limit corresponds to the maximum value at which an HDR bearing may be tested to verify its horizontal displacement capacity, according to the code on anti-seismic devices (EN15129, 2009). In fact, for the code the maximum admissible shear strain due to the horizontal displacement is 2.5 and the partial factor to be used in the test is 1.15 for elastomeric isolators. Thus, the maximum tested strain would be $2.5 \cdot 1.15 = 2.9$. Experimental and numerical evidence (Montuori et al., 2016; Brandonisio et al., 2017; Ragni et al., 2019) shows larger shear capacity limits, but these depend heavily on the rubber compound, on the isolator shape as well as on the manufacturer, thus a conservatory value of 300% has been assumed in this study. Notwithstanding, as observed in **Figure 8A**, the shear capacity limit assumed is never attained, not even for the largest return period. Differently, for the largest IM with T_R = 10000 years the gap amplitude is exceeded in three time histories whereas the maximum admissible displacement for the buckling stability only once. However, actually the impact is reached only once (for earthquake n°6), because maximum displacements are not along the direction orthogonal to the retaining walls and for the other two time-histories the displacement components in these directions are both lower than the gap amplitude. Since the maximum axial load is lower than $P_{CR}/4$ = 1660 kN for all the time histories carried out at that IM, only for one record the buckling requirement was not satisfied. Regarding the sliders (**Figure 8B**), also in this case the maximum axial loads obtained are always lower than the vertical capacity assumed for the sliders ($N_{b,Rd}$ = 2640 kN) and their displacement capacity is only reached once, for the same time history leading to the maximum admissible displacement for the buckling stability of HDR bearings. However, it should be noted that attainment of the gap closure is not a collapse condition, it only makes necessary a more accurate model of the base-isolation system, where contact elements for the gaps are included to investigate the effects of their closure on the super-structure. With this model, displacement larger than the gap amplitude will be still possible in the direction opposed to the gap (placed only at the upstream side of the building), thus advanced models of bearings (accounting for their post-buckling behavior) and sliders (accounting for their over-stroke behavior) should also be included in the more accurate model. In fact, according to the most recent research outcomes, HDR bearings are able to show a post-buckling behavior up to a maximum displacement equal to the effective diameter of the bearing (Montuori et al., 2016) and sliders can reach an ultimate displacement almost equal to the capacity of the slider increased by half of the internal pad diameter (Ragni et al., 2018a).

With reference to the super-structure, maximum inter-storey drifts are illustrated in **Figure 9A**, while absolute floor accelerations are shown in **Figure 9B**. It is evident that, due to the high degree of stiffness of the super-structure, inter-storey drifts remain limited up to the largest IM, whereas absolute accelerations become significant for the largest return periods. In this case, the mean values obtained are lower than the design ones for the inter-storey drifts but are larger for the floor absolute accelerations. Differences can be ascribed to the same reasons explained for the isolation system displacements. According to technical literature, damage limits for displacement-sensitive elements may be assumed equal to 0.33% of the story height, equal to 0.0033·4300 = 14.2 mm (Okazaki et al., 2007; Scozzese et al., 2017, 2018). For the acceleration-sensitive components a limit of 0.2 and 0.4 g is assumed for slight and moderate damage, respectively (Hazus-MH 2.1, 2001). It is evident from the results that the displacement limit is never reached. Similarly, the acceleration limit corresponding to moderate damage is exceeded only in one case at the largest IM, whereas the light damage level is also reached at lower IM, but excluding the first two intensity levels. Displacements and flexural moments of the sub-structure columns have not been reported, because they are very small and far from their resistance limit. The obtained results confirm that only in one case at the largest IM (record n.6) the moderate damage limit is exceeded. However, in this case maximum displacements and accelerations would be even larger than registered values, because of the impact with the retaining wall. Also the axial force acting on the diagonal steel braces (about 800 kN for record n.6) could be larger and could exceed the buckling capacity of the brace equal to $N_{b,Rd}$ = 1630 kN. However, to estimate exact values of these response parameters a gap element should be included in the model. Different contact models are available in the technical literature (Pant and Wijeyewickrema, 2014), however stiffness and damping capacity of the model must properly selected in order to obtain reliable results.

Figures 11, **12** illustrate the hazard curves relevant to the demand parameter described above and expressing the mean rate of annual exceedance (λ) for each level of the demand parameter considered. These curves have been computed by combining the results obtained in the seismic hazard assessment and in the non-linear dynamic analyses using the total probability theorem. Since these results are available only as discrete values, this calculation is not solvable in closed form. The procedure followed in this study to compute these hazard curves starting from discrete values is that one suggested by Porter (2019). Observing the demand hazard curves obtained for the maximum displacement of the isolation system it is evident that the mean annual rate of exceedance of the gap closure is very low. The obtained value is about $2{\cdot}10^{-5}$, which is significantly lower than $2{\cdot}10^{-4}$ suggested by the American seismic code (ASCE 7 16) and the draft annex of the new Eurocode 8 (Fajfar, 2018), as maximum value for the structural safety. Furthermore, the mean annual frequency of exceedance of the ultimate conditions corresponding to the buckling capacity of HDR bearings and the displacement capacity of the sliders is lower than 10^{-5}. This confirming the high level of safety and robustness of the building. Regarding the super-structure performance, the hazard curves obtained for the

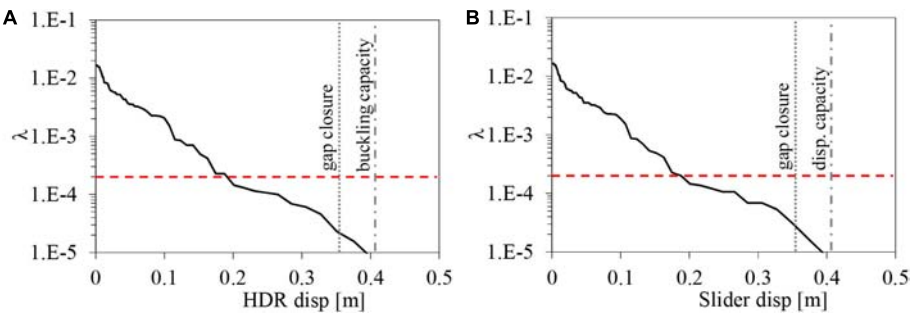

FIGURE 11 | Hazard curve of the maximum displacement of HDR bearings **(A)** and sliders **(B)**.

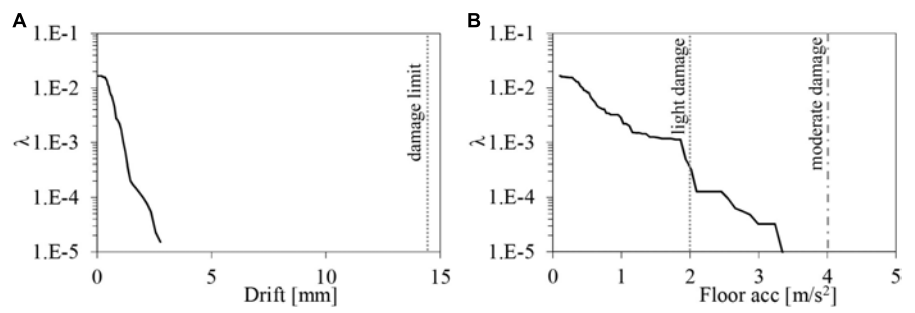

FIGURE 12 | Hazard curve of the maximum inter-storey drift **(A)** and the maximum floor absolute acceleration **(B)**.

inter-storey drift and the floor acceleration show that only the light damage state of acceleration-sensitive components has an exceedance probability larger than 10^{-5}, confirming the high level of resilience of the building, i.e., a very low probability of a damage level causing the downtime of the building.

It should be noted that the procedure followed to build the hazard curves accounts for the variability of the seismic input, i.e., the record-to-record variability (Scozzese et al., 2020). In this study this variability is due to the selection of the natural records according to the conditional spectrum of the site; alternatively it could be simulated by using a stochastic model of the input, as already done for different structural systems (Chen et al., 2007; Peng et al., 2013; Altieri et al., 2018). Furthermore, the variability of the properties of the isolation devices could also be considered. A more complete probabilistic framework accounting for both the variability sources should be applied in this case, as already carried out for structural systems with seismic isolation or dissipative devices (Dall'Asta et al., 2017; Franchin et al., 2018; Scozzese et al., 2019).

CONCLUSION

In this paper the new research center of the Camerino University has been described and analyzed. The building was designed to achieve speed of execution as well as a high level of safety, especially with regard to seismic activity. The structural solution was to create an isolated system with a steel braced super-structure with pinned joints and r.c. sub-structures able to adapt to the complex morphology of the area. In particular, a hybrid isolation system was adopted, comprising High Damping Rubber (HDR) bearings and low-friction sliders, able to provide a high period of isolation and thus to drastically reduce actions in the super-structure for both low intensity earthquakes and very severe seismic events. The first part of the paper focuses on the building description and the linear analyses carried out during the design phase, while in the second part the paper addresses specific risk analyses aimed at demonstrating the very low exceedance probability of damage and ultimate limit conditions, as defined for the structural system. To this purpose a site-specific hazard study was first carried out, then non-linear analyses were performed using a hazard-consistent set of records selected from the European strong motion database. The main demand parameters of both the isolation system and the super-structure were recorded, then capacity values corresponding to ultimate and damage limit conditions were assumed. Then, as final result, the demand hazard curves have been computed for the isolation system and for the super-structure. The obtained curves show that the mean annual rate of exceedance of the gap closure is significantly lower than the code prescription and the mean annual rates of exceedance of the limit states corresponding to the buckling capacity of HDR bearings and the displacement capacity of the sliders are even lower. Regarding the super-structure, the hazard curves obtained for the inter-storey drift and the floor acceleration show that only the light damage state of acceleration-sensitive components has an exceedance probability larger than 10^{-5}. These results confirm the high level of safety and robustness of the building as well as the high level of resilience, i.e., a very low probability of disproportioned consequences due to seismic action larger than the design ones as well as a low probability of a damage level causing the downtime of the building. Finally, it is worth noting that the seismic risk assessment carried out in this paper is based on conservative hypotheses. Further analysis should be carried out with a more advanced model, including contact elements for seismic gaps as well as advanced non-linear models able to describe the post-buckling behavior of the HDR bearings and the extra-stroke behavior of the sliders, to more accurately estimate the real collapse probability of the building. Furthermore, a more complete probabilistic framework should be applied, also including a local site hazard analysis as well as the uncertainty affecting the structural system. Finally, floor response spectra should be also evaluated in order to assess the damage risk of possible flexible acceleration-sensitive components inside the building.

DATA AVAILABILITY STATEMENT

The datasets generated for this study are available on request to the corresponding author.

AUTHOR CONTRIBUTIONS

AD and GL designed base-isolated building with the contribution of FM and LG. LG, FM, and LR performed the numerical analyses and processed the analytical results. All authors have contributed to the manuscript revision, read, and approved the submitted version.

REFERENCES

Altieri, D., Tubaldi, E., De Angelis, M., Patelli, E., and Dall'Asta, A. (2018). Reliability-based optimal design of nonlinear viscous dampers for the seismic protection of structural systems. *Bull. Earthq. Eng.* 16, 963–982. doi: 10.1007/s10518-017-0233-4

Ambraseys, N. N., Simpson, K. A., and Bommer, J. J. (1996). Prediction of horizontal response spectra in Europe. *Earthq. Eng. Struct. Dyn.* 25, 371–400. doi: 10.1002/(SICI)1096-9845(199604)25:4<371::AID-EQE550>3.0.CO;2-A

Baker, J. W. (2011). Conditional mean spectrum: tool for ground-motion selection. *J. Struct. Eng.* 137, 322–331. doi: 10.1061/(ASCE)ST.1943-541X.0000215

Baker, J. W., and Lee, C. (2018). An improved algorithm for selecting ground motions to match a conditional spectrum. *J. Earthq. Eng.* 22, 708–723. doi: 10.1080/13632469.2016.1264334

Brandonisio, G., Ponzo, F., Mele, E., and De Luca, A. (2017). "Prove sperimentali di isolatori elastomerici: influenza del carico verticale V e del fattore di forma secondario S2," in *Proceedings of the XIV Convegno ANIDIS "L'ingegneria Sismica in Italia". 17–21 Settembre*, Pistoia.

Bridgestone (2017). *Seismic Isolation Product Line-up*. Available online at: www.bridgestone.com (October, 2019).

Chen, J., Liu, W., Peng, Y., and Li, J. (2007). Stochastic seismic response and reliability analysis of base-isolated structures. *J. Earthq. Eng.* 11, 903–924. doi: 10.1080/13632460701242757

Chioccarelli, E., Cito, P., Iervolino, I., and Giorgio, M. (2019). REASSESS V2.0: software for single- and multi-site probabilistic seismic hazard analysis. *Bull. Earthq. Eng.* 17, 1769–1793. doi: 10.1007/s10518-018-00531-x

Computer and Structures (1995). *SAP2000, Structural Analysis Program*. Berkeley, CA: University Ave., Berkeley.

Dall'Asta, A., Scozzese, F., Ragni, L., and Tubaldi, E. (2017). Effect of the damper property variability on the seismic reliability of linear systems equipped with viscous dampers. *Bull. Earthq. Eng.* 15, 5025–5053. doi: 10.1007/s10518-017-0169-8

De Domenico, D., Ricciardi, G., and Benzoni, G. (2018). Analytical and finite element investigation on the thermo-mechanical coupled response of friction isolators under bidirectional excitation. *Soil Dyn. Earthq. Eng.* 106, 131–147. doi: 10.1016/j.soildyn.2017.12.019

De Domenico, D., Ricciardi, G., Infanti, S., and Benzoni, G. (2019). Frictional heating in double curved surface sliders and its effects on the hysteretic behavior: an experimental study. *Front. Built Environ.* 5:74. doi: 10.3389/fbuil.2019.00074

Dolce, M., Arleo, G., Di Cesare, A., and Ponzo, F. C. (2013). *Progetto di Edifici con Isolamento Sismico (Italiano)*. Pavia: IUSS Press.

EN 1337-5 (2005). *"EN 1337-5: Structural Bearings – Part 5: Pot Bearings"*. Brussels: European Committee for Standardization.

EN 1998-1 (2005). *Eurocode 8: Design of Structures for Earthquake Resistance – Part 1: General Rules, Seismic Actions and Rules for Buildings*. Brussels: European Committee for Standardization.

EN15129 (2009). *"UNI EN 15129: "Antiseismic Devices"*. Brussels: European Committee for Standardization.

Fajfar, P. (2018). Analysis in seismic provisions for buildings: past, present and future. *Bull. Earthq. Eng.* 16, 2567–2608. doi: 10.1007/s10518-017-0290-8

FIP (2016). *S02-Isolatori Elastomerici Serie SI (italian)*. Available online at: www.fipindustriale.it (October, 2019).

Franchin, P., Ragni, L., Rota, M., and Zona, A. (2018). Modelling uncertainties of Italian code-conforming structures for the purpose of seismic response analysis. *J. Earthq. Eng.* 22, 1964–1989. doi: 10.1080/13632469.2018.1527262

Furinghetti, M., Pavese, A., Quaglini, V., and Dubini, P. (2019). Experimental investigation of the cyclic response of double curved surface sliders subjected to radial and bidirectional sliding motions. *Soil Dyn. Earthq. Eng.* 117, 190–202. doi: 10.1016/j.soildyn.2018.11.020

Grant, D. N., Fenves, G. L., and Whittaker, A. (2004). Bidirectional modelling of high-damping rubber bearings. *J. Earthq. Eng.* 8, 161–185. doi: 10.1080/13632460409350524

Hazus-MH 2.1 (2001). *Multi-hazard Loss Estimation Methodology*. Washington, DC: FEMA.

Iervolino, I., Spillatura, A., and Bazzurro, P. (2018). Seimic structural reliability of code-conforming Italian buildings. *J. Earthq. Eng.* 22(Suppl. 2), 5–27. doi: 10.1080/13632469.2018.1540372

Ishii, K., and Kikuchi, M. (2018). Improved numerical analysis for ultimate behavior of elastomeric seismic isolation bearings. *Earthq. Eng. Struct. Dyn.* 48, 65–77. doi: 10.1002/eqe.3123

Kelly, J. M. (1997). *Earthquake-Resistant Design with Rubber*. London: Springer. doi: 10.1007/978-1-4471-0971-6

Lanzano, G., Luzi, L., Pacor, F., Felicetta, C., Puglia, R., Sgobba, S., et al. (2019). A revised ground−motion prediction model for shallow crustal earthquakes in Italy. *Bull. Seismol. Soc. Am.* 109, 525–540. doi: 10.1785/0120180210

Lomiento, G., Bonessio, N., and Benzoni, G. (2013). Friction model for sliding bearings under seismic excitation. *J. Earthq. Eng.* 17, 1162–1191. doi: 10.1080/13632469.2013.814611

Luzi, L., Puglia, R., Russo, E., and Orfeus WG5. (2016). *Engineering Strong Motion Database, Version 1.0*. Rome: Istituto Nazionale di Geofisica e Vulcanologia, Observatories & Research Facilities for European Seismology. doi: 10.13127/ESM

Masaki, N., Mori, T., Murota, N., and Kasai, K. (2017). "Validation of hysteresis model of deformation-history integral type for high damping rubber bearings," in *Proceedings of the 16th World Conference on Earthquake, Santiago Chile, January 9th to 13th 2017*, Santiago.

Meletti, C., Galadini, F., Valensise, G., Stucchi, M., Basili, R., Barba, S., et al. (2008). A seismic source zone model for the seismic hazard assessment of the Italian territory. *Tectonophysics* 450, 85–108. doi: 10.1016/j.tecto.2008.01.003

Montuori, G. M., Mele, E., Marrazzo, G., Brandonisio, G., and De Luca, A. (2016). Stability issues and pressure–shear interaction in elastomeric bearings: the primary role of the secondary shape factor. *Bull. Earthq. Eng.* 14, 569–597. doi: 10.1007/s10518-015-9819-x

NTC (2018). *"Norme Tecniche per le Costruzioni", Decreto Ministeriale del 17 Gennaio 2 (ItalianBuilding Code, 2008)*. Lugano-Paradiso: NTC.

Okazaki, T., Nakashima, M., Suita, K., and Matusmiya, T. (2007). Interaction between cladding and structural frame observed in a full-scale steel building test. *Earthq. Eng. Struct. Dyn.* 36, 35–53. doi: 10.1002/eqe.618

Pant, D. R., and Wijeyewickrema, A. C. (2014). Performance of base-isolated reinforced concrete buildings under bidirectional seismic excitation considering pounding with retaining walls including friction effects. *Earthq. Eng. Struct. Dyn.* 43, 1521–1541. doi: 10.1002/eqe.2409

Peng, Y., Ghanem, R., and Li, J. (2013). Generalized optimal control policy for stochastic optimal control of structures. *Struct. Control Health Monitor.* 20, 187–209. doi: 10.1002/stc.483

Porter, K. (2019). *A Beginner's Guide to Fragility, Vulnerability, and Risk*. Boulder, CO: University of Colorado Boulder, 119.

Ragni, L., Cardone, D., Conte, N., Dall'Asta, A., Di Cesare, A., Flora, A., et al. (2018a). Modelling and seismic response analysis of Italian code-conforming base-isolated buildings. *J. Earthq. Eng.* 22(Suppl. 2), 198–230. doi: 10.1080/13632469.2018.1527263

Ragni, L., Micozzi, F., Brandonisio, G., Dall'Asta, A., De Luca, A., Di Cesare, A., et al. (2019). "Comportamento dei dispositivi HDRB sotto grandi spostamenti ed elevati carchi assiali," in *Proceedings of the XV Convegno ANIDIS "L'ingegneria Sismica in Italia". 15–19 Settembre*, Ascoli Piceno.

Ragni, L., Tubaldi, E., Dall'Asta, A., Ahmadi, H., and Muhr, A. (2018b). Biaxial shear behaviour of HDNR with Mullins effect and deformation-induced anisotropy. *Eng. Struct.* 154, 78–92. doi: 10.1016/j.engstruct.2017.10.060

Scozzese, F., Dall'Asta, A., and Tubaldi, E. (2019). Seismic risk sensitivity of structures equipped with anti-seismic devices with uncertain properties. *Struct. Safety* 77, 30–47. doi: 10.1016/j.strusafe.2018.10.003

Scozzese, F., Terracciano, G., Zona, A., Della Corte, G., Dall'Asta, A., and Landolfo, R. (2017). "Rintc project: nonlinear dynamic analyses of Italian code-conforming steel single-storey buildings for collapse risk assessment," in *Proceedings of the 6th International Conference on Computational Methods in Structural Dynamics and Earthquake Engineering (COMPDYN 2017) – Rhodes Island, Greece, 15–17 June 2017*, Rhodes. doi: 10.7712/120117.5513.17301

Scozzese, F., Terracciano, G., Zona, A., Della Corte, G., Dall'Asta, A., and Landolfo, R. (2018). Analysis of seismic non-structural damage in single-storey industrial steel buildings. *Soil Dyn. Earthq. Eng.* 114, 505–519. doi: 10.1016/j.soildyn.2018.07.047

Scozzese, F., Tubaldi, E., and Dall'Asta, A. (2020). Assessment of the effectiveness of Multiple-Stripe Analysis by using a stochastic earthquake input model. *Bull Earthquake Eng.* doi: 10.1007/s10518-020-00815-1

Stucchi, M., Meletti, C., Montaldo, V., Crowley, H., Calvi, G. M., and Boschi, E. (2011). Seismic hazard assessment (2003–2009) for the Italian building code. *Bull. Seismol. Soc. Am.* 101, 1885–1911. doi: 10.1785/0120100130

Tubaldi, E., Ragni, L., Dall'Asta, A., Ahmadi, H., and Muhr, A. (2017). Stress-softening behaviour of HDNR bearings: modelling and influence on the seismic response of isolated structures. *Earthq. Eng. Struct. Dyn.* 46, 2033–2054. doi: 10.1002/eqe.2897

Yang, T. Y., Konstantinidis, D., and Kelly, J. M. (2010). The influence of isolator hysteresis on equipment performance in seismic isolated buildings. *Earthq. Spectra* 26, 275–293. doi: 10.1193/1.3276901

Conflict of Interest: The authors declare that the research was conducted in the absence of any commercial or financial relationships that could be construed as a potential conflict of interest.

frontiers in Built Environment

ORIGINAL RESEARCH
published: 28 April 2020
doi: 10.3389/fbuil.2020.00037

An Experimental Study on Scale Effect in Dynamic Shear Properties of High-Damping Rubber Bearings

Nobuo Murota and Takahiro Mori*

Bridgestone Corporation, Seismic Isolation and Vibration Control Products Development Department, Yokohama, Japan

High-damping rubber bearing (HDRB) is one of the most popular devices used for seismic isolation of structures. In order to clarify the mechanical characteristics of HDRB, various loading tests have been conducted on the bearings and obtained data have been applied to practical design of isolation systems. In this study, in order to investigate the scale effect on the physical characteristics of HDRB, dynamic loading tests were conducted with full scale and scaled model isolators, which have diameters of 1,000 and 225 mm, respectively. The test program covers shear strain dependence tests, frequency dependence tests, and repeated loading dependence tests. Special attention is paid in the differences of shear characteristics caused by the specimen scale. Repeated loading test was conducted only with a scaled model, and the relationship of temperature increase of the specimen and shear characteristics was evaluated. In parallel, finite element analysis (FEA) of the isolator under repeated loading was conducted. After the constitutive model of FEA was identified by the results, the FEA was extrapolated to simulate repeated loading of 1,000- and 1,600-mm-diameter isolators, which cannot be tested realistically by dynamic loading. Change of properties along the increasing number of cycles and temperature distribution of full scale and scaled down isolators were investigated. Necessity of consideration for the scale effect in the evaluation of HDRB properties by dynamic testing is discussed.

Keywords: seismic isolation, high-damping rubber bearing, full scale, dynamic loading, scale effect

OPEN ACCESS

Edited by:
Enrico Tubaldi,
University of Strathclyde,
United Kingdom

Reviewed by:
Laura Ragni,
Marche Polytechnic University, Italy
Stergios Aristotle Mitoulis,
University of Surrey, United Kingdom
Daniele Losanno,
Construction Technologies Institute,
Italian National Research Council, Italy

****Correspondence:***
Nobuo Murota
nobuo.murota@bridgestone.com

Specialty section:
This article was submitted to Earthquake Engineering, a section of the journal Frontiers in Built Environment

Received: *22 November 2019*
Accepted: *11 March 2020*
Published: *28 April 2020*

Citation:
Murota N and Mori T (2020) An Experimental Study on Scale Effect in Dynamic Shear Properties of High-Damping Rubber Bearings. Front. Built Environ. 6:37. doi: 10.3389/fbuil.2020.00037

INTRODUCTION

Seismic isolation technology has gained popularity in the recent decades as one of the measures for seismic protection of structures (Murota, 2009; Nishi and Murota, 2012). Seismic isolation is an aseismic design concept to reduce the seismic force transmitted to the structure by supporting it with a flexible support member to elongate the natural period of the structure and thereby decouples it from the ground effects. Basically, seismic isolation systems provide functions of restoring force and energy dissipation. The seismic isolation bearing (SIB), made up with layers of alternating rubber and steel plates, is the most popular device for providing restoring force and damping characteristics. In addition to conventional SIB, innovation of new types of SIB has been progressed by many researchers (Losanno et al., 2019; Madera Sierra et al., 2019).

Many kinds of SIB testing, such as shear strain dependence, temperature dependence, frequency dependence, vertical loading force dependence (Tubaldi et al., 2016; Kalfas et al., 2017), aging effect (Hamaguchi et al., 2009), and ultimate properties (Nishi et al., 2019), have been conducted and useful data have been obtained for the design of the isolation systems. In order to evaluate realistic isolator characteristics, full scale isolator testing under dynamic loading is desired (Infanti et al., 2004; Yamamoto et al., 2012; Kato et al., 2014). However, in the case of dynamic loading of such specimens, a substantial capacity of hydraulic systems including the number of accumulators, high-level control devices, and high-precision measurement systems are required for the test setup. Therefore, full scale testing is generally conducted under quasi-static loading conditions, and rate-dependent characteristics are evaluated using a scaled model by a relatively small capacity dynamic testing machine. As an example, in ASCE 7–16, chapter 17 (American Society of Civil Engineers [ASCE], 2017), it is permitted to use a scaled model for the test of isolators that has rate-dependent properties, considering practical reasons caused by the limitation of the number of facilities, which provides sufficient capacity for dynamic tests of full scale specimens. In ISO 22762 "Elastomeric seismic-protection isolators" (ISO 22762, 2018a,b), the allowable scaling for each test type is specified. Basically, rubber material itself has frequency dependency in its restoring force characteristics. High-damping rubber bearing (HDRB) is one of the types of SIB that has relatively large frequency dependence in terms of shear properties. Generally, the rubber material of HDRB is filled with carbon or other ingredients, and interaction occurring between the polymer and the filler under stretching condition dissipates kinetic energy as heat builds up. Increasing temperature of rubber results in the decrease in shear stiffness and damping ratio. The thermal conductivity of rubber is much lower than that of metals, and the build-up heat in rubber radiates from the surface of SIB. Therefore, the accumulation of heat inside rubber is affected by the scale of length, which is considered as the main reason of scale effect on the physical properties of SIB.

In this study, firstly, the scale effect on the fundamental shear properties of HDRB is investigated by dynamic loading tests with two types of specimen: full scale and scaled-down specimens with a scale ratio of 1/4.44. Specimen diameters are 1,000 and 225 mm. The measured properties are shear strain dependence and frequency dependence. Secondly, dynamic repeated loading test with 200 cycles is conducted on isolator specimens with a diameter of 225 mm.

After the 2003 Tokachi-Oki earthquake, long-period and long duration ground motions have become one of the most highlighted topics in earthquake engineering in Japan. A long duration ground motion may continue for over 5 min. and in the case of a seismically isolated structure, isolation devices are subjected to vibration for a long period (Building Research Institute Japan, 2016). On this background, this study deals with the subject of scale effect on isolator characteristics under repeated cyclic loading. During the repeated loading, the properties of isolators are changed according to the increasing number of cycles. This property change firstly occurred by loading history (Tubaldi et al., 2017) for first several cycles, and then the increase in temperature is mostly influenced by the large number of cycles. During the tests, the surface temperature of the specimens is measured, and the relationship between the change of mechanical properties and the temperature according to the increase in the number of cycles is investigated. Additionally, finite element analyses (FEAs) are carried out under identical conditions with the tests, where parameter identification is conducted. After confirming the accuracy of the FEA model, the dynamic repeated loading characteristics with 1,000- and 1,600-mm-diameter isolators are investigated with this model and compared with the test results.

DYNAMIC LOADING TEST

Definition of Shear Properties

The shear characteristics, such as effective shear stiffness K_{eq}, equivalent shear modulus G_{eq}, equivalent damping ratio H_{eq}, and dissipated energy E_d, of HDRB are defined in **Figure 1**. K_{eq} is defined as the slope of the straight line from the point of (maximum load, maximum displacement) to the point of (minimum load, minimum displacement). Under sinusoidal loading, the force at maximum displacement has generally small difference from the maximum force. In the definition of the viscoelastic characteristics, the force at maximum displacement is generally used for the estimation of effective stiffness. However, the maximum displacement point, where the shear force drops sharply, is very difficult to identify and sometimes causes loss of accuracy in the calculation of characteristics when the time step for data acquisition is not precise enough. For this reason, effective stiffness is defined as mentioned above in this study. In frequency dependence test and shear strain dependence test, shear properties at the third cyclic loop are used for evaluation.

Test Specimens

The dimensional characteristics, performance specifications, and material properties of full scale and scaled-down models are shown in **Table 1** and **Figure 2**. The full scale and scaled model isolators have consistency of important parameters such as unit rubber layer thickness, number of layers, and first and second shape factors. However, because of the manufacturing process, there are slight differences for each parameter, which are indicated in **Table 1**. For reinforcing plates and flanges, it is challenging to follow an exact scale. Furthermore, full scale isolator has an inner hole with a diameter of 25 mm for manufacturing purpose. The authors considered these differences in the scale as negligible in this study. Full scale and scaled model isolators are identified as scale-I and scale-II, respectively. Two different types of high-damping rubber materials are used in the specimens. They are identified as rubber-A and -B, which have equivalent shear modulus G_{eq} of 0.392 and 0.620 MPa at 100% shear strain, respectively. The equivalent damping ratio H_{eq} of both rubber materials is 24% at 100% shear strain. These two high-damping rubber materials had been improved in terms of load history dependence. A stress softening behavior, known

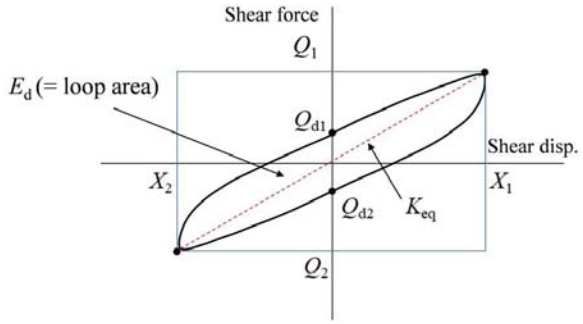

$$K_{eq}=(Q_1-Q_2)/(X_1-X_2)$$

$$G_{eq}=K_{eq}\cdot h_r/A_r$$

$$H_{eq}=2/\pi\cdot E_d/[K_{eq}\cdot(X_1-X_2)^2]$$

where,

A_r : Effective area

H_r : Effective area and total rubber height

K_{eq} : Equivalent shear stiffness

G_{eq} : Equivalent shear modulus

H_{eq} : Equivalent damping ratio

Q_{d1}, Q_{d2}: Characteristic strength

Q_1, Q_2 : Maximum and minimum shear force

E_d : Area of hysteresis loop= Dissipated energy

FIGURE 1 | Definition of shear properties of HDR.

TABLE 1 | Dimensional characteristics and material properties of test specimens.

Isolator Type		**I (Full scale)**		**II (Scaled model)**	
Outer diameter (mm)		1000		225 (0.225)*1	
Inner diameter (mm)		25		0 (0.00)*1	
Thickness of rubber (mm)		6.7		1.6 (0.239)*1	
Number of lamination		30		28	
Total thickness of rubber (mm)		201		44.8 (0.223)*1	
Thickness of reinforcing plate (mm)		4.4		1.0 (0.227)*1	
First shape factor		36.4		35.2	
Second shape factor		4.98		5.02	
ID of rubber material	A		B	A	B
Design value of shear modulus G_{eq} (MPa)*2	0.392		0.620	0.392	0.620
Design value of equivalent damping ratio H_{eq}*2	0.240		0.240	0.240	0.240
Number of specimens*3	2		2	2+1	2+1

Rubber compound	**Elongation at break (%)*4**	**Tensile strength (MPa)*4**	**100% modulus (MPa)*4**
A	min. 840	min. 7	0.43+/−0.2
B	min. 780	min. 8.5	0.73+/−0.2

**1 Value in () is the ratio of the dimension of each part to those of 1,000-mm-dia. isolator. *2 Design values are for shear strain 100%, loading frequency (sinusoidal) 0.33 Hz, temperature 20 degrees Celsius, and third cycle of the hysteresis loop. *3 Type-II specimens: two for frequency dependence, shear strain dependence, and one for repeated loading test. *4 Specified by JIS K 6251: Japanese Industrial Standards "Rubber, vulcanized or thermoplastics-Determination of tensile stress-strain properties."*

as the Mullins effect, is improved compared with conventional high-damping rubber materials (Murota et al., 2007).

Each test specimen is named according to size, rubber material, and specimen no. as follows: [size: I or II]-[rubber: A or B]-[No.: 1, 2, or 3].

Shear strain γ is defined as X_{max}/h_r, where X_{max} is the maximum horizontal displacement at a cycle of shear loading and h_r is the total rubber height in an isolator unit. The shear strain of 100% corresponds to the shear displacement equivalent to the total rubber height. Each test specimen was manufactured from a different lot of rubber material and vulcanization conditions. Therefore, the variation of the modulus of used rubber material and the cure state of rubber by vulcanization may affect the shear properties of isolators. Especially, the cure state of scale-I and

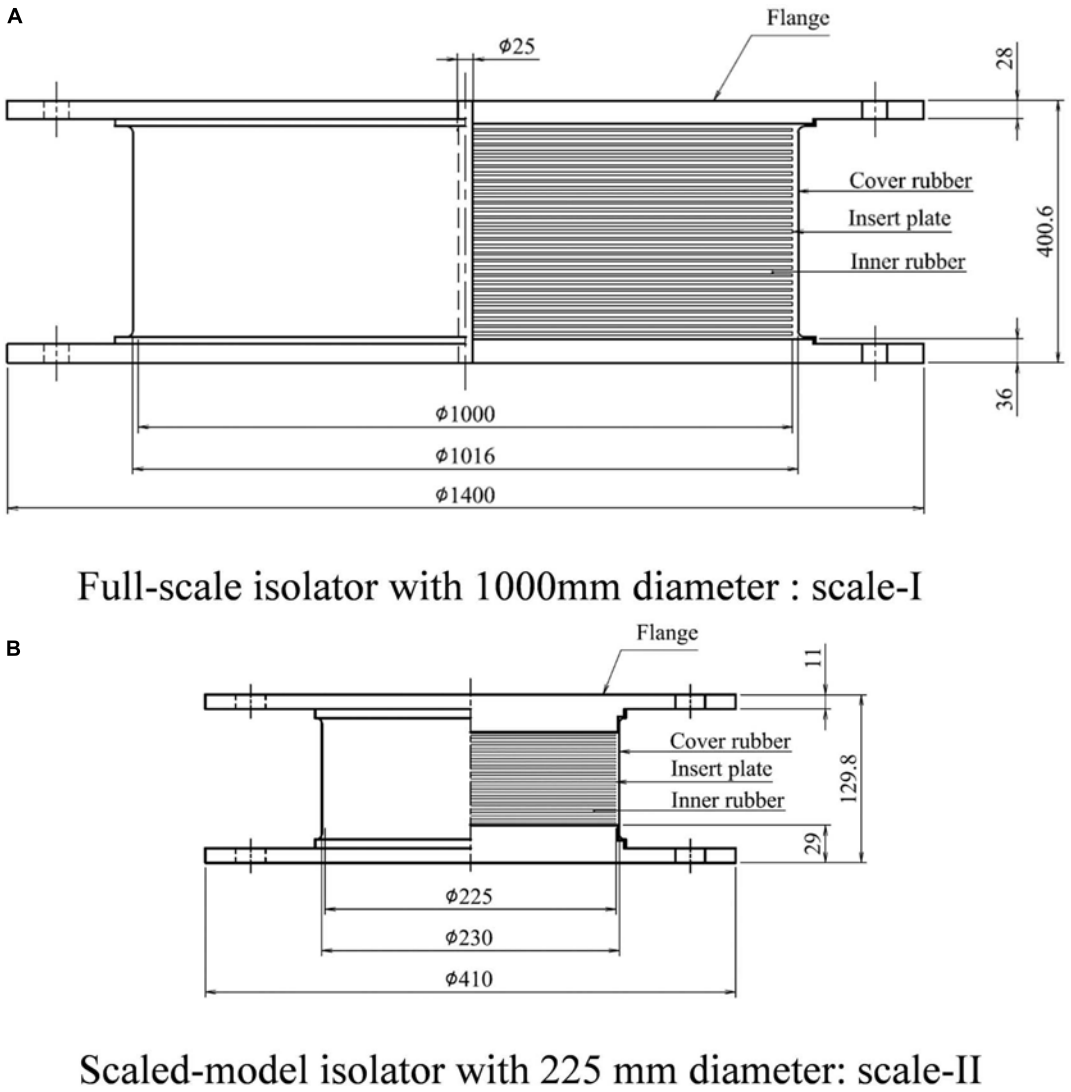

FIGURE 2 | Test specimens.

scale-II may have significant difference in network structures of polymer, sulfur, and fillers. This may be also considered as a scale effect.

Test Facility

The dynamic loading tests of the scale-I specimen were carried out by "Seismic Response Modification Device (SRMD) Test Machine" (Seible et al., 2000) in the University of California at San Diego. The loading plate of the test device, where the isolator is installed, slides over low-friction hydrostatic bearings. The generated friction force during dynamic loading was deducted from the raw data during data analysis. The friction force was measured by the UCSD laboratory in advance. The inertia force is calculated by acceleration and weight of mobile parts of the test device and was also deducted from the raw data. All test procedures were operated by the staff of the SRMD test facility in the UCSD.

The tests of scale-II were carried out by dynamic loading test machine in Bridgestone Corporation Technical Center, Yokohama, Japan. The maximum vertical load is 1,000 kN, and the maximum horizontal load and maximum strokes of the horizontal actuator is 200 kN and ± 0.3 m, respectively. The load cell, for measurement of shear and compression load, was installed just beneath the specimen. Therefore, the shear force obtained by the load cell does not include the friction force generated in the slide guide of the test machine. The inertia force is included but it is considered as negligibly small.

Test Conditions

Correspondence between the specimen number and the test type is shown in **Table 2** along with test frequency and no. of cycles incorporated. Benchmark test was conducted to investigate the fundamental performance of isolators at a shear strain of 100% under a compressive stress of

TABLE 2 | Summary of test conditions.

Test item	Specimen no.	Compressive stress (MPa)	Shear strain (%)	Number of cycle	Frequency (Hz)
Benchmark	I-A, II-A	A: 13	100	3	0.33
	I-B, II-B	B: 15			
Frequency dependence	I-A-1, I-B-1		100	3	0.01, 0.033, 0.1, 0.33
	II-A-1, II-B-1				
Shear strain dependence	I-A-2, I-B-2		10, 20, 50, 100	3	0.33
	II-A-2, II-B-2		150, 200, 270		
Repeated loading dependence	II-A-3, II-B-3		200	200	0.33

Wave form: Sinusoidal wave. Sequence of benchmark test [BT(N), N is the set number of the test] in the frequency dependence test: BT(1), BT(2), 0.01 Hz, BT(3), 0.033 Hz, BT(4), 0.1 Hz, BT(5) (=0.33 Hz).

13 MPa for material A and 15 MPa for material B, which is the test condition of the isolator used for determining the nominal shear modulus and the damping ratio by the manufacturer (**Table 2**). In frequency dependence tests, the benchmark tests were conducted repeatedly between each test at specific frequency in order to evaluate the influence of loading history on the results, which should be properly considered at evaluation. The change of the properties measured by the benchmark tests is an indicator of the fatigue by numerous loadings to the specimen. Ambient temperature during the testing of the scaled model was controlled at 20 ± 5 degree Celsius. The temperature of scale-I in the UCSD was not controlled, but the measured temperature ranges between 20 and 26 degrees Celsius during the test. Therefore, the authors consider the influence of ambient temperature to the properties as insignificant and negligible.

In frequency dependence test, the shear strain is 100%, the wave form is sinusoidal, and the number of cycles is three. A frequency of 0.33 Hz is considered as the standard vibration frequency in this study. The series of frequency is 0.01, 0.033, 0.1, and 0.3 Hz. Benchmark test was conducted between each test at a specific frequency as prescribed. In this study, frequency dependence is defined as the ratio of G_{eq}, H_{eq}, and E_d at each frequency level to those of 0.33-Hz frequency.

In the shear strain dependence test, its series is 10, 25, 50, 100, 150, 200, and 270%. The test frequency is fixed as 0.33 Hz, and the wave form is sinusoidal. The benchmark test is conducted at the beginning and end of the test series. In this study, shear strain dependence is defined as the ratio of G_{eq}, H_{eq}, and E_d at each shear strain to those of 100% shear strain.

In the repeated loading test, the specimen was subjected to a compressive load according to the corresponding nominal stress of 13 and 15 MPa for materials A and B, respectively. Under the controlled compressive load, the cyclic loading was conducted in the shear direction for a shear strain of 200%, with a frequency of 0.33 Hz. The total number of cycles was 200. The cumulative displacement was 72 m, which corresponds to 320 m for a full scale isolator unit assuming a total rubber height of 200 mm. The ratio of shear properties, G_{eq} and H_{eq}, at each cycle was computed by normalizing each value with that of the third cyclic loading. During testing, the surface temperature of the specimen was measured by a radiation thermometer.

Verification of Initial Properties of Test Specimens

Initial properties of test specimens were evaluated by the first set of benchmark tests. Comparing the nominal value of each property, all results were within the range of ± 20%, concluding that all test specimens were properly manufactured within designated margins. In the tests, scale-I specimens gave higher stiffness and a lower damping ratio than those of scale-II specimens. **Figure 3** shows a comparison of the shear stress-strain relationship of I-A-1 and II-A-1, I-B-1, and I-B-1, for all three cycles. The factors that have possible influence on the difference

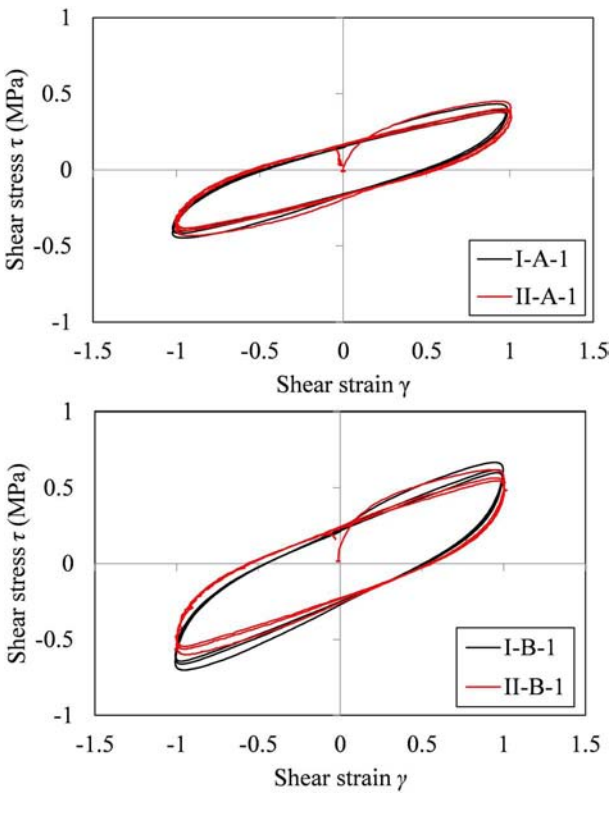

FIGURE 3 | Shear stress-strain relationship of scale-I and-II of rubber-A and -B for all three cycles.

in properties between scale-I and -II are the difference in the rubber material lot, vulcanization conditions, and the test device. Here, the difference in stiffness may be caused by the rubber material. The difference in the dissipated energy is quite small between scale-I and scale-II specimens, while the difference in stiffness is larger, which is attributed to the difference of the material lot and/or vulcanization conditions.

Although there is some difference in measured properties between scale-I and -II specimens, all specimens satisfy the standard deviation, ± 15% of the design value, which is generally considered as the acceptance criterion of isolators in practical use.

Results of Frequency Dependence and Shear Strain Dependence Tests

The comparison of shear stress–strain relationships under frequency of 0.01, 0.033, 0.1, and 0.33Hz for scale-I and -II with rubber-A and -B at the third cycle is shown in **Figure 4**. Shear properties, G_{eq}, H_{eq}, and E_d at each frequency, normalized by the value at 0.33 Hz are shown in **Figure 5**. As it was expected, the shear modulus becomes higher for increasing values of the frequency. The shear modulus at 0.01-Hz frequency, which is considered as quasi-static, is more than 25% lower than that at the 0.33-Hz level. The damping ratio and dissipated energy values also show similar tendency. The difference in the frequency dependence between scale-I and -II is relatively small. Especially, for E_d, results almost agree with each other. These results indicate that the test results of the scale-I isolator conducted by quasi-static test conditions can be corrected to the results of dynamic test conditions by applying frequency dependence obtained by dynamic test of the scaled model.

Figure 6 shows the transition of each property in benchmark tests conducted before each test at each frequency. The first benchmark test [BT(1), number in () : set number of the test] is conducted for verification of the initial performance of the specimens as prescribed in 2.5. The total number of sets was 5, and their sequence is

$$\text{BT(1)} \rightarrow \text{BT(2)} \rightarrow \text{0.01Hz test} \rightarrow \text{BT(3)} \rightarrow \text{0.033Hz} \rightarrow \text{BT(4)} \rightarrow \text{0.1Hz test} \rightarrow \text{0.33Hz test}(= \text{BT(5)})$$

The absolute value of each BT was normalized by the value at BT(1). All properties in each test specimen decrease as the number of sets increases. Also, it can be observed that scale-II shows more reduction of stiffness and constant reduction in dissipated energy. However, correlation with scaling is not obvious. The change ratio varies approximately between −10 and −20%. The results indicate that during the prototype test of isolators, effects of fatigue by accumulated loading should be adequately considered when making judgments according

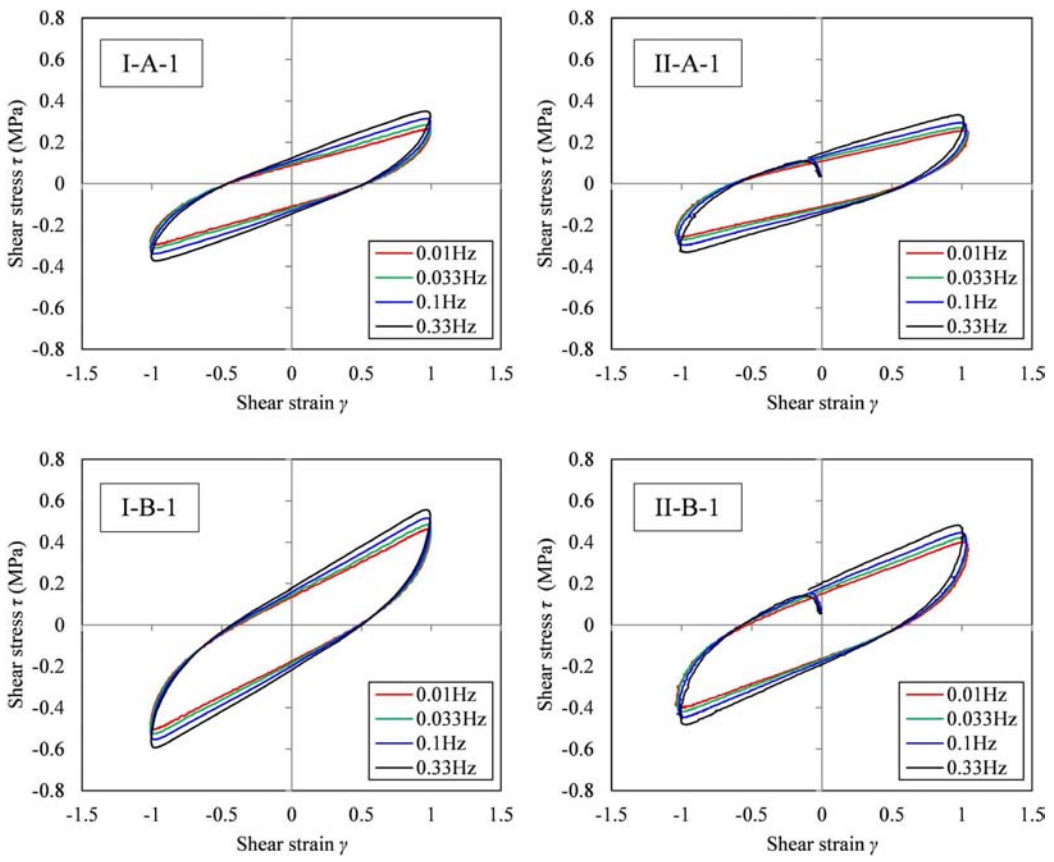

FIGURE 4 | Shear stress-strain relationship of scale-I and -II in frequency dependence test at 3rd cycle.

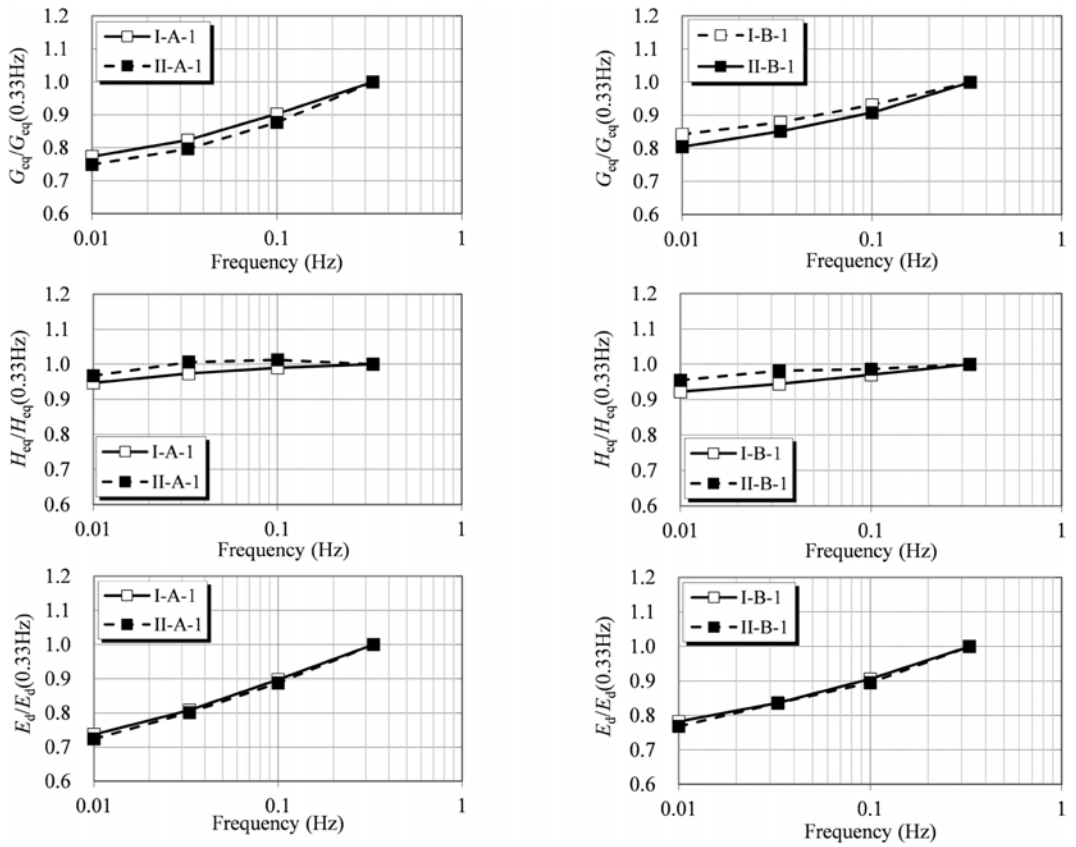

FIGURE 5 | Comparison of shear properties in frequency dependency of-Scale-I and -II at 3rd cycle.

to design criteria. It is suggested that when the frequency dependence test will be conducted, fatigue effect should be measured by the benchmark test between each test as conducted in this study, and adequate correction of the results should be carried out such as deduction of the decreased amount of properties by fatigue from the results.

The shear stress–strain relationships for all cycles and each property normalized by the value at a shear strain of 100% for both rubber-A and -B with scale-I and II at the third cycle of each shear strain are shown in **Figures 7**, **8**. Significant difference in the absolute value of shear stress is observed in the shear stress–strain relationship for scale-I and II, which is shown in **Figure 7**. The authors consider that the difference in stress is caused by the variation of rubber material and vulcanization process in scale-I and II specimens. However, it is noteworthy that the normalized value shows good agreement in scale-I and -II as indicated in **Figure 8**. Deviation in shear modulus, ± 10 to 20% for example, does not affect the shear strain dependence. This result suggests that the shear strain dependence can be effectively evaluated using scaled models instead of full scale similar to frequency dependence.

The results in frequency and shear strain dependence tests show that even when there is significant difference in the absolute value of shear properties in scale-I and -II, the normalized trends with frequency and shear strain amplitude were not affected by the scale. In both tests, loading was conducted in three cycles. The temperature on the rubber surface on scale-I isolators increased only 4 to 5 degrees Celsius at the end of the test compared to the initial condition. Benchmark test results indicate effective stiffness and dissipated energy decrease as loading experience increases. Appropriate consideration should be made in the evaluation of the results in continuous sets of loading.

Results of Repeated Loading Test

Figure 9 shows the shear force–displacement relationship of each specimen in repeated loading tests for the entire cyclic loading protocol. It is observed that the shear force and E_d are decreased by the increased number of cycles. The change of G_{eq}, H_{eq}, and E_d under repeated loading is indicated in **Figure 10**. The change of properties by repeated loading is considered as a combination of fatigue and temperature effect. For the first few cycles, fatigue effect, also called as "Mullins's effect" (Mullins, 1969) is dominant in the change of properties. After a few cycles, properties are majorly affected by temperature increase. At the 200th cycle, G_{eq} decreased for approximately 40% in II-A-3 and 30% in II-B-3. There is no significant difference in the change ratio of G_{eq} and E_d for both rubber-A and -B. The increase in the surface temperature along the increase in the number of loading cycle, and the relationship between volumetric E_d of rubber in specimens (V_r) and surface temperature for both rubber materials are shown

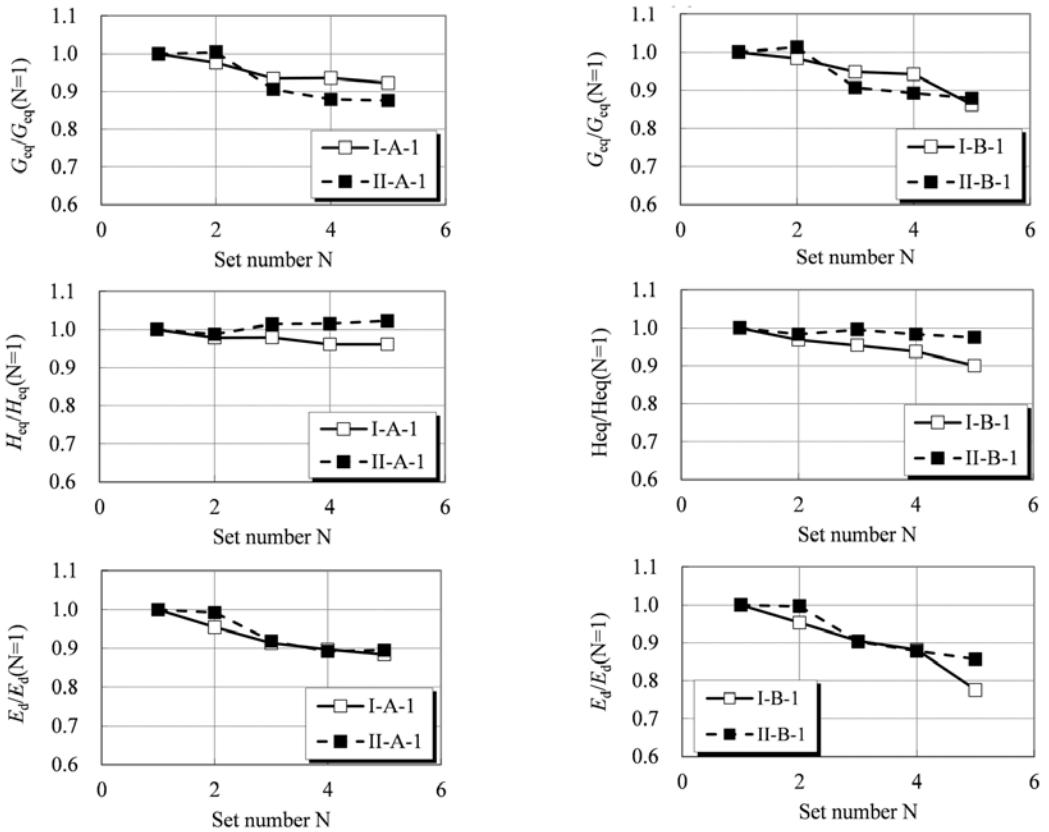

FIGURE 6 | Change of characteristics in benchmark test [BT(1) to BT(5)] of scale-I and -II at 3rd cvcle.

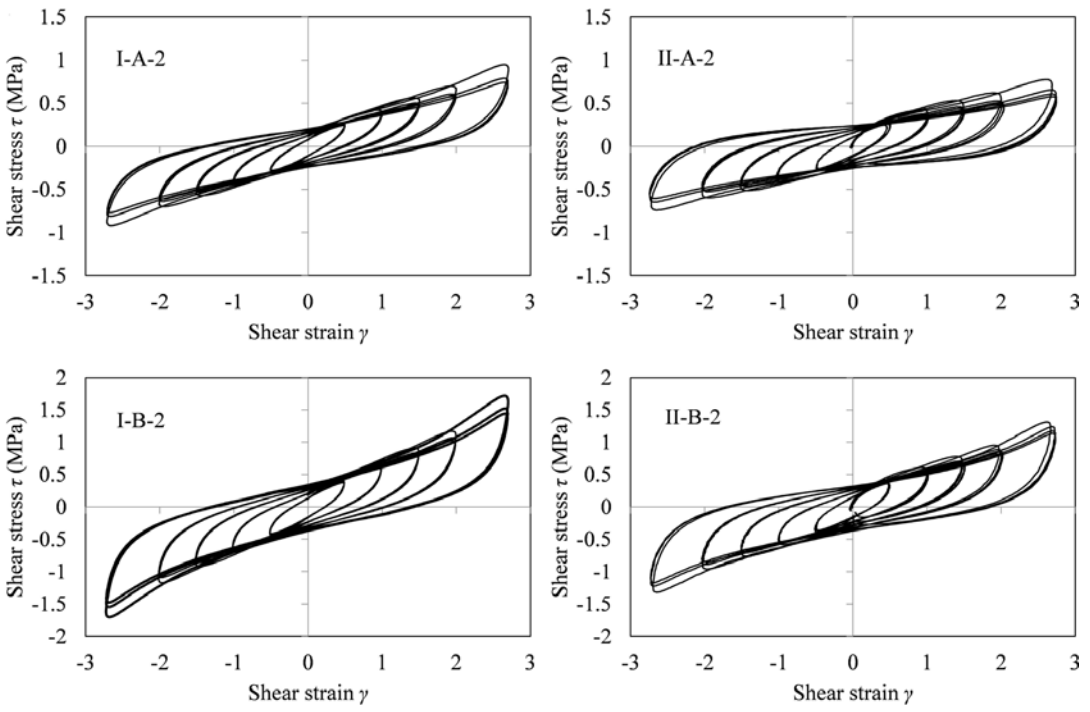

FIGURE 7 | Comparison of shear stress-strain relationship in shear strain dependence test of scale-I and -II for all three cycles.

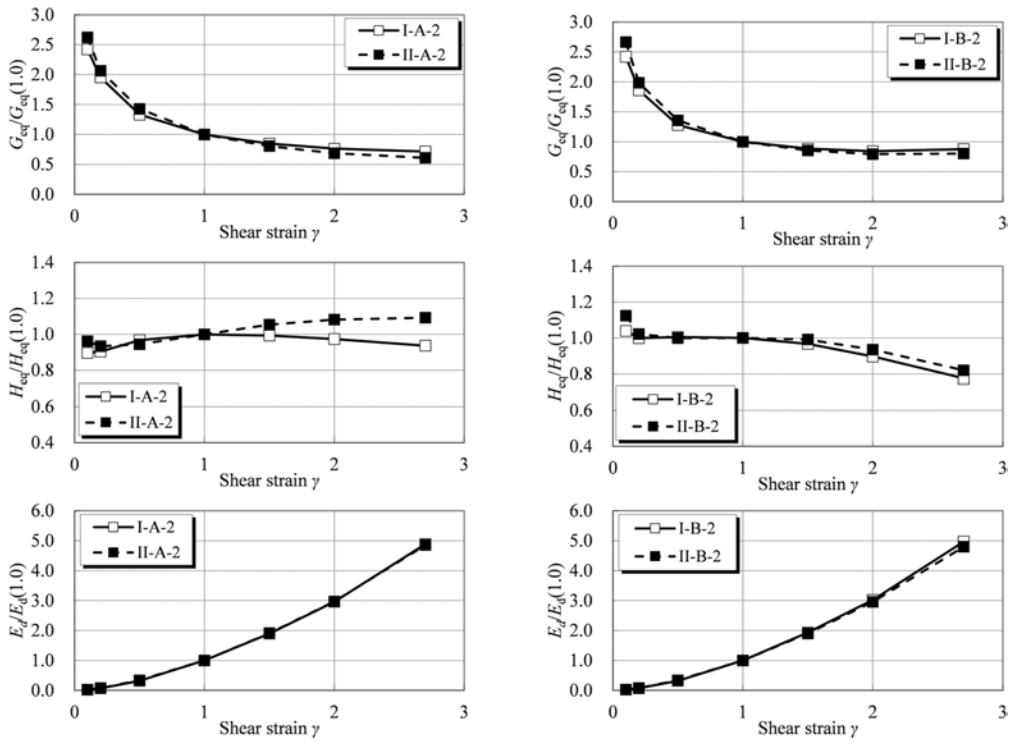

FIGURE 8 | Comparison of shear strain dependency of scale-I and -II at 3rd cycle.

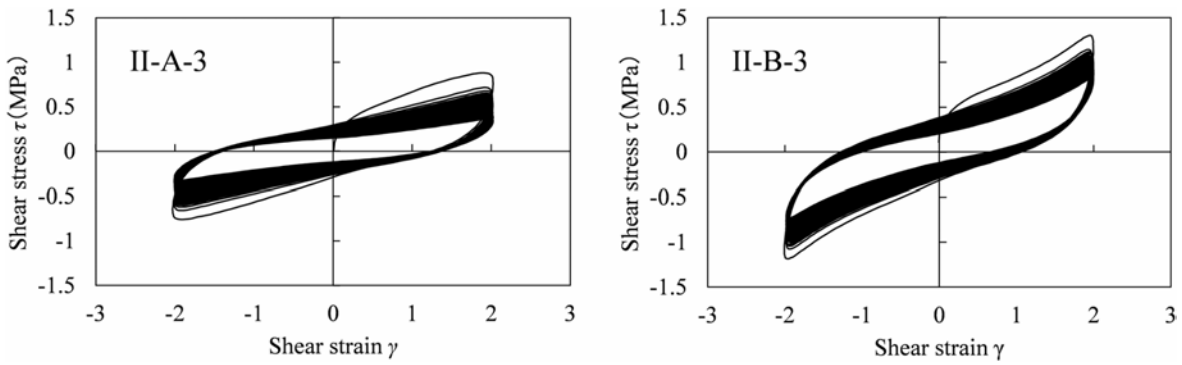

FIGURE 9 | Shear stress-strain relationship of scale- II-A and -II-B under repeated loading for shear strain 200% × 200 cycles.

in **Figure 11**. The temperature increases from 20 degrees to a maximum of 80 degrees Celsius in the case of specimen B, which has higher shear modulus and energy dissipation. The result indicates that the specific heat capacities of rubber-A and -B have no significant difference. Therefore, the difference of temperature increase in A and B is simply caused by the difference in accumulated energy dissipation during repeated loading.

Finite Element Analysis for Evaluation of Scale Effect in Repeated Loading

As repeated loading tests on full scale specimens are quite challenging in existing test machines, FEA was conducted to predict the scale effect on the repeated loading by extrapolation to a large size isolator test case. FEA code named as the "Deformation History Integral Type (DHI)" model (Mori et al., 2012; Masaki et al., 2017) was implemented for the study. The function of the code is a heat-mechanics coupled analysis, which consists of hyper elastic stress–strain analysis and heat-transfer analysis. The constitutive law of the mathematical model (Mori et al., 2012) involves parameters for temperature affect and fatigue affect. Using both parameters, the properties of isolators during repeated loading are reproduced. The conceptual flow of the heat-mechanics coupled FEA and the comparison of the test results and FEA results for scaled model II-B-3 are shown in **Figure 12**.

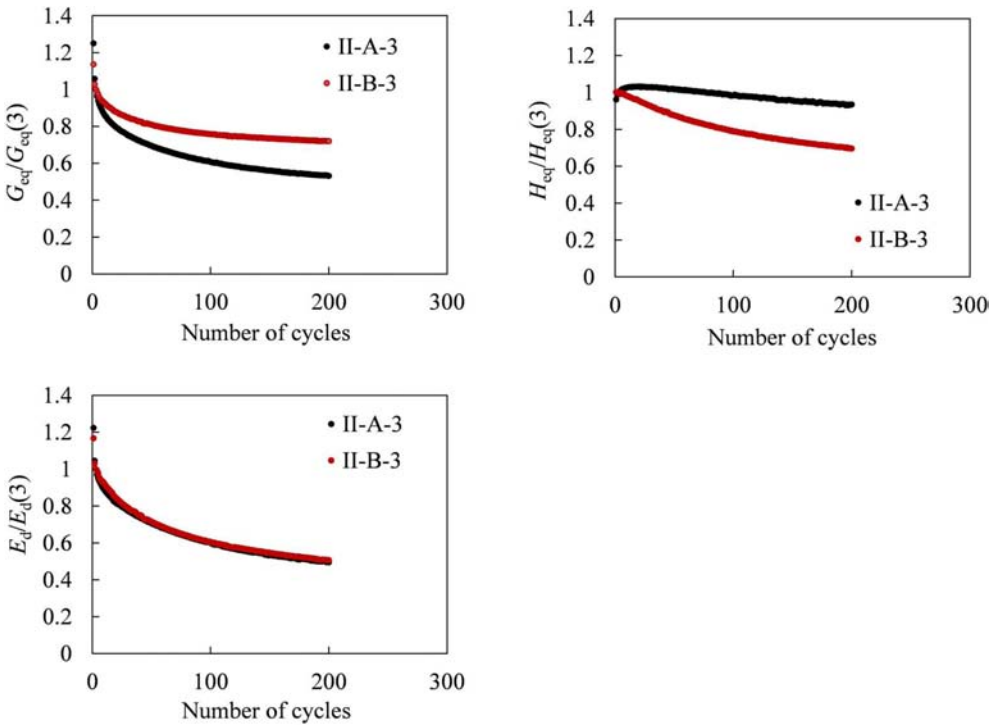

FIGURE 10 | Relationship of change of properties and number of cycles in scale-II-A and -II-B.

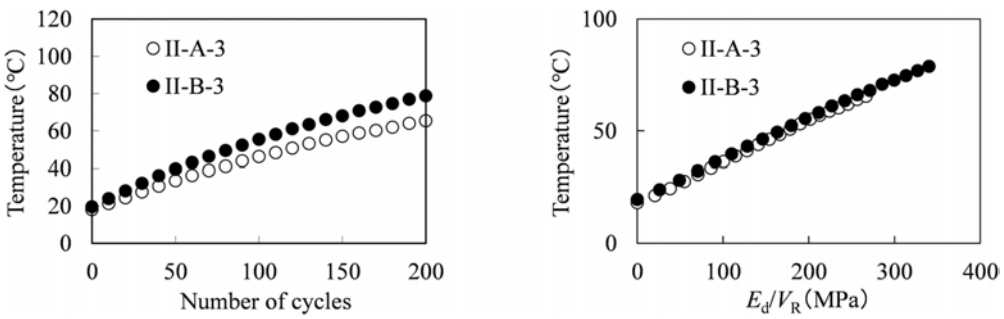

FIGURE 11 | Change of temperature by increase of loading cycle and E_d/V_r in scale-II-A, and -II-B.

Heat transfer boundary is set surrounded by isolators, and the coefficient of heat transfer was identified so as to agree with the surface temperature of the model. As explained in a previous publication (Mori et al., 2012), parameters were identified by the results of scaled models and shear-block specimens. Firstly, the parameters for temperature effect on the change of properties were identified by the test conducted with shear-block specimen, which was conditioned in constant temperature under −10, 0, 10, 20, 30, and 40 degrees Celsius. The number of loading cycles was three, and the properties at the third cycle was measured and recorded. Property change in the temperature range over 40 degrees Celsius was assumed by extrapolation with curve fitting. Parameters related to fatigue were identified using data of property change obtained during repeated loading dependency tests with 200 cycles.

Using these parameters, the repeated loading for full scale isolators with a diameter of 1,000 mm, which was used in this study as specimen I-B, and 1,600-mm-diameter was simulated by an FEA model, and the results were compared with II-3. The analysis was conducted based on 50 cycles. The dimensional characteristics of 1,600-mm isolators are as follows:

- outer diameter = 1,600 mm, inner diameter = 80 mm
- thickness of unit rubber layer = 10.4 mm, number of lamination = 19, total rubber thickness = 198 mm
- thickness of reinforcing plate = 5.8 mm, rubber material = B.

Figure 13 shows a comparison of normalized analysis results for G_{eq}, H_{eq}, and E_d with respect to the number of loading cycles,

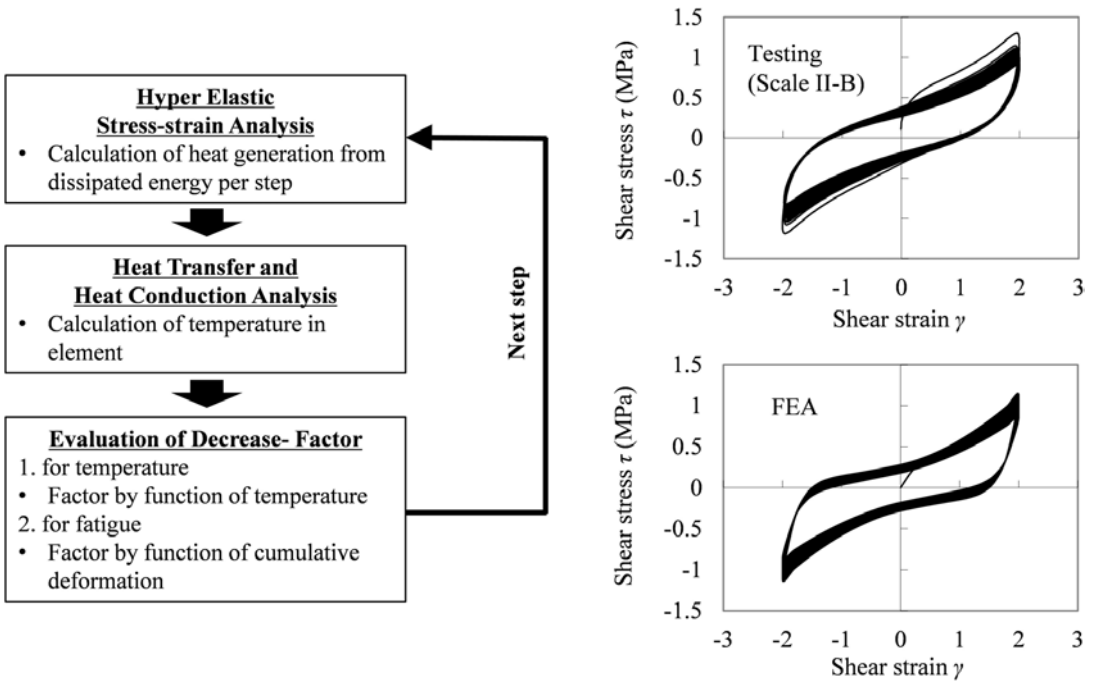

FIGURE 12 | Concept of heat-mechanics coupled FEA and comparison of shear stress-strain relationship of Testing (Scale II-B) and FEA results.

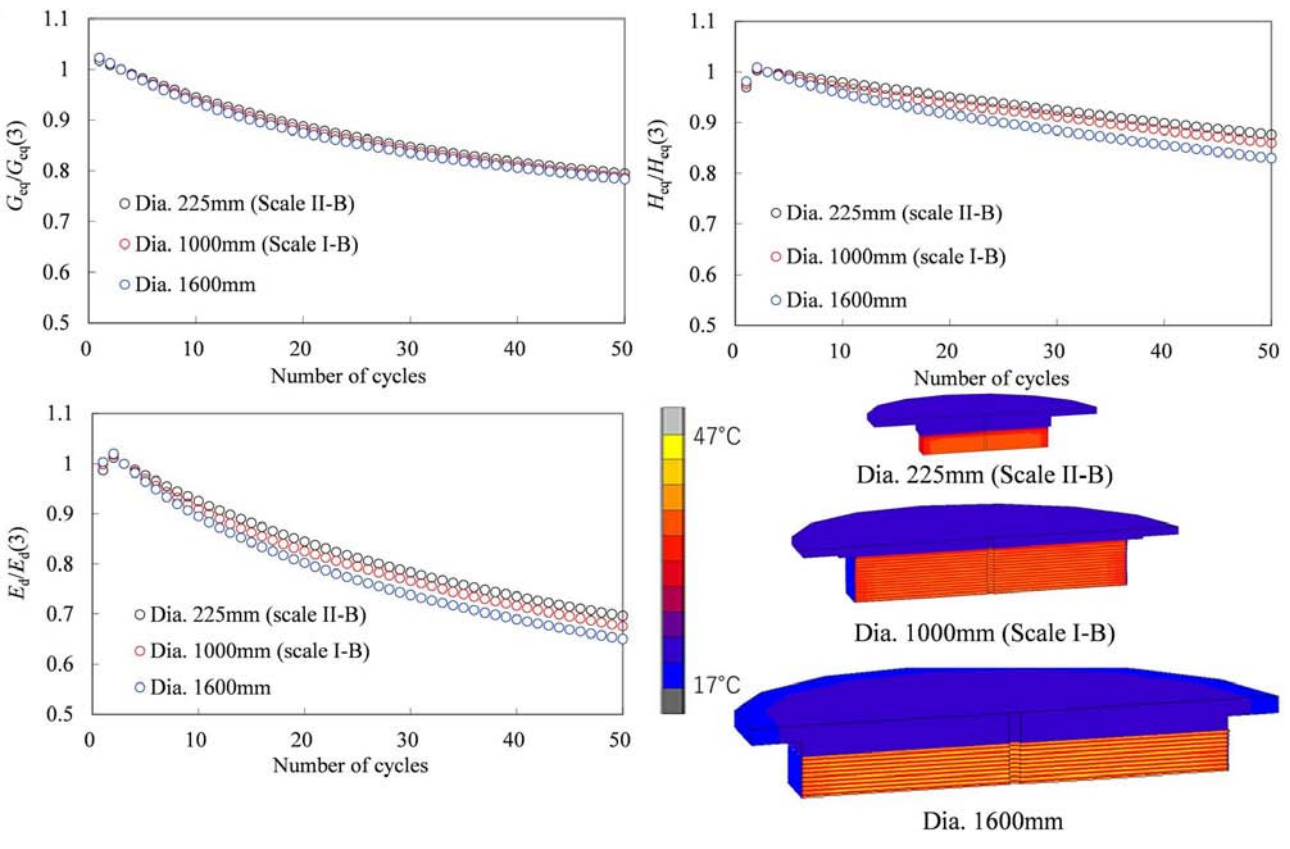

FIGURE 13 | Comparison of change in G_{eq}, H_{eq}, and E_d of isolators with diameter of 225 mm (scale-II-B). 1000 mm (scale I-B), and 1600 mm in repeated loading by FEA.

where values are normalized according to the results of the third cycle. The temperature distribution in all three isolator models at the final step is also shown in **Figure 13**. The results show the scale effect on the dynamic characteristics under repeated loading, which was not observed in frequency and shear strain dependence tests conducted for the three cycles. Analyses have shown that the effect of increasing repeated cycles on the shear modulus is almost the same for each diameter. However, in terms of dissipated energy E_d, there are significant differences between scaled model II-B and the largest size of the 1,600-mm-diameter isolator as the number of cycles increases. Obviously, the difference comes from the different temperature levels inside isolators, as the heat generation by high-damping rubber is proportional to the cube of the size (volume), whereas heat dissipation from the surface of the isolator is proportional to the square of the size (surface area).

CONCLUSION

The scale effect on the dynamic shear properties of HDRB was investigated by dynamic loading tests on full scale specimens with a diameter of 1,000 mm, and scaled model with 225 mm, using two different types of rubber material with soft and hard shear moduli.

Firstly, the nominal shear properties at 100% shear strain were measured and the manufacturing conformity of all specimens was verified. Then, dynamic loading tests of frequency and shear strain dependence were conducted. In both types of rubber materials, although there is some degree of difference between shear stress–strain relationship of full scale and scaled specimens, no significant difference was observed in neither dependences.

During the frequency dependence test, the change of fundamental properties was evaluated by the benchmark test, which was conducted between each test at a specific frequency. The stiffness and dissipated energy vales were decreased as the number of test cases increased. This fact suggests that when the continuous test is conducted, such as the prototype test of an actual project, the fatigue condition of the specimen should be appropriately considered in the evaluation of the results.

Next, repeated dynamic loading for 200 cycles of 200% shear strain with a scaled isolator specimen was conducted, and the relationship between the change of shear properties, temperature increase, and the number of loading cycles was investigated. As the number of cycles increases, the temperature of the isolator increased and stiffness and dissipated energy decreased.

The FEA model, which was developed in a previous study by authors for heat-mechanics coupled analysis, was implemented in order to investigate the cyclic characteristics of 1,000- and 1,600-mm-diameter isolators. The parameters in the constitutive law of the FEA was identified with test results of the scaled model with the diameter of 225 mm. The results show a significant difference in the change of shear properties by the number of repeated cycles. The results indicate that when the isolator is subjected to repeated loading over three cycles, the scale effect on shear properties is significant.

It is concluded that the scale effect on shear properties under a limited number of cycles, such as fewer than 10 cycles, can be neglected. It can be fed back to the practical case of the isolator test. In the prototype tests, if the frequency dependence is evaluated in advance, testing with a scaled model can be accepted. However, when long duration seismic input is considered, which has been a current issue since recent major earthquakes in Japan, the isolators may be subjected to an extreme repeated number of shear loading cycles. Considering these cases, the scale effect on the dynamic properties should be properly considered.

In this study, investigation of the scale effect is limited to the properties between 100 and 200% shear strain. The scale effect of HDRB isolators on ultimate properties such as shear breaking or buckling is under consideration as future subjects. Furthermore, investigation of the scale effect on other types of isolators, especially lead-core rubber bearing (LRB), is also considered in the next step. Energy dissipation is concentrated in the lead core where the thermal diffusion is considered to be affected by the dimension of the isolator.

DATA AVAILABILITY STATEMENT

The datasets generated for this study are available on request to the corresponding author.

AUTHOR CONTRIBUTIONS

All authors listed have made a substantial, direct and intellectual contribution to the work, and approved it for publication.

ACKNOWLEDGMENTS

The authors would like to express great appreciation to all the members of the University of California at San Diego for their contribution to the dynamic loading test of full scale isolators.

REFERENCES

American Society of Civil Engineers [ASCE], (2017). "Chapter 17 seismic design requirements for seismically isolated structures," in *Minimum Design Loads and Associated Criteria for Buildings and Other Structures American Society of Civil Engineering*, Bombai: American Society of Civil Engineers.

Building Research Institute Japan, (2016). "Study on repeated loading characteristics of seismic isolation devices and its influence to seismically isolated structures," in *Building Research Report, No.170*, 2016.4, Japanese.

Hamaguchi, H., Samejima, Y., and Kani, N. (2009). "A study of aging effect on rubber bearings after about twenty years in use," in *11the World Conference on Seismic Isolation, Energy Dissipation and Active Vibration Control of Structures*, Guangzou, 7–21.

Infanti, S., Papanikolas, P., Benzoni, G., and Castellano, M. G. (2004). "Rion-antirion bridge: design and full scale testing of the seismic protection devices," in *13th World Conference on Earthquake Engineering*, Vancouver.

Iso 22762, (2018a). "Elastomeric seismic-protection isolators," in *Part-1 Test methods International Organization for Standardization*, Geneva: ISO.

Iso 22762, (2018b). "Elastomeric seismic-protection isolators," in *Part-3 Applications of buildings - specifications, International Organization for Standardization*, Geneva: ISO.

Kalfas, K., Mitoulis, S., and Katakalos, K. (2017). Numerical study on the response of steel-laminated elastomeric bearings subjected to variable axial loads and development of local tensile stresses. *Eng. Struct. Col.* 134, 346–357. doi: 10.1016/j.engstruct.2016.12.015

Kato, H., Akutsu, S., Mori, T., Nakamura, M., and Murota, N. (2014). "Development of large-scale elastomeric seismic isolation bearings for buildings," in *5th Asia Conference on Earthquake Engineering*, Taiwan.

Losanno, D., Dierra, I. E., Spizzuoco, M., Marulanda, J., and Thomson, P. (2019). Experimental assessment and analytical modeling of novel fiber-reinforced isolators in unbounded configuration. *Composize Struct.* 212, 66–82. doi: 10.1016/j.compstruct.2019.01.026

Madera Sierra, I. E., Losanno, D., Srano, S., Marulanda, J., and Thomson, P. (2019). Development and experimental behavior of HDR seismic isolators for low-rise residential buildings. *Eng. Struct.* 183, 894–906. doi: 10.1016/j.engstruct.2019.01.037

Masaki, N., Mori, T., Murota, N., and Kasai, K. (2017). "Validation of hysteresis model of deformation-integral type of high damping rubber bearings," in *16WCEE, proceedings of 12th World Conference of Earthquake Engineering*, Santiago.

Mori, T., Kato, H., and Murota, N. (2012). Modeling for analysis of high damping rubber bearings with effects of fatigue and temperature increase due to repeated deformation. *Struct. Constr. Eng.* 77, 1517–1526. doi: 10.3130/aijs.77.1517

Mullins, L. (1969). Softening of rubber by deformation. *Rubber Chem. Technol.* 42, 339–362. doi: 10.5254/1.3539210

Murota, N. (2009). Earthquake protection materials – reviews and future directions of elastomeric isolators. *Soc. Polym. Sci.* 58,

Murota, N., Nishimura, K., Kikuchi, T., Okutsu, N., Kuwamoto, K., and Suzuki, S. (2007). "Development of new high-damping rubber bearings with improved material for load-history dependence," in *Summaries of Technical Papers of Annual Meeting Architectural Institute of Japan*, Japanese, 879–880.

Nishi, T., and Murota, N. (2012). Elastomeric seismic-protection isolators for buildings and bridges. *Chin. J. Polym. Sci.* 31, 50–57.

Nishi, T., Suzuki, S., Aoki, M., Sawada, T., and Fukuda, S. (2019). International investigation of shear displacement capacity of various elastomeric seismic-protection isolators for buildings. *J. Rubber Res.* 22, 33–41. doi: 10.1007/s42464-019-00006-x

Seible, F., Benzoni, G., Filiatrault, A., Post, T., and Mellon, D. (2000). "Performance validation of large seismic response modification devices," in *Proceedings of 12th World Conference of Earthquake Engineering*, Auckland.

Tubaldi, E., Mitoulis, S., Ahmadi, H., and Muhr, A. (2016). A parametric study on the axial behaviour of elastomeric isolators in multi-span bridges subjected to horizontal excitation. *Bull. Earthqu. Eng.* 14, 1285–1310. doi: 10.1007/s10518-016-9876-9

Tubaldi, E., Ragni, L., Dall'Asta, A., Ahmadi, H., and Muhr, A. (2017). stress softening behavior of HDNR bearings: modelling and influence on the seismic response of isolated structures. *Earthq. Eng. Struct. Dyn.* 46, 2033–2054.

Yamamoto, M., Minewaki, S., Yoneda, H., and Higashino, M. (2012). Nonlinear behavior of high-damping rubber bearings under horizontal bidirectional loading: full scale tests and analytical modeling. *Earthq. Eng. Struct. Dyn.* 41, 1845–1860. doi: 10.1002/eqe.2161

Conflict of Interest: NM and TM were employed by the company Bridgestone Corporation.

frontiers in Built Environment

ORIGINAL RESEARCH
published: 09 June 2020
doi: 10.3389/fbuil.2020.00062

Hysteretic–Viscous Hybrid Damper System for Long-Period Pulse-Type Earthquake Ground Motions of Large Amplitude

*Shoki Hashizume and Izuru Takewaki**

Department of Architecture and Architectural Engineering, Graduate School of Engineering, Kyoto University, Kyoto, Japan

This paper aims to develop a hysteretic–viscous hybrid (HVH) damper system for long-period pulse-type earthquake ground motions of large amplitude. Long-period pulse-type earthquake ground motions of large amplitude have been recorded recently (Northridge, 1994; Kumamoto, 2016). It is well-known that these ground motions could cause severe damage to high-rise and base-isolated buildings with long natural period. To mitigate the damage caused by such ground motion, a new viscous–hysteretic hybrid damper system is proposed here, which consists of a viscous damper with large stroke and a hysteretic damper including a gap mechanism. A double impulse is employed as a representative of long-period pulse-type earthquake ground motions of large amplitude and a closed-form maximum response to this double impulse is derived for an elastic–plastic SDOF system including the proposed HVH system. To reveal the effectiveness of the proposed HVH system, time-history response analyses are performed for an amplitude modulated double impulse and a recorded ground motion at Kumamoto (2016). The performance comparison with the previous dual hysteretic damper (DHD) system consisting of small-amplitude and large-amplitude hysteretic dampers in parallel is also conducted to investigate the effectiveness of the proposed HVH system.

Keywords: damping, viscous damper, hysteretic damper, hybrid use, gap mechanism, double impulse, long-period motion, pulse-type motion

OPEN ACCESS

Edited by:
Ehsan Noroozinejad Farsangi, Graduate University of Advanced Technology, Iran

Reviewed by:
Abbas Sivandi-Pour, Graduate University of Advanced Technology, Iran
Aleksandra Bogdanovic, Institute of Earthquake Engineering and Engineering Seismology (IZIIS), North Macedonia

****Correspondence:***
Izuru Takewaki
takewaki@archi.kyoto-u.ac.jp

Specialty section:
This article was submitted to Earthquake Engineering, a section of the journal Frontiers in Built Environment

Received: *21 January 2020*
Accepted: *15 April 2020*
Published: *09 June 2020*

Citation:
Hashizume S and Takewaki I (2020) Hysteretic–Viscous Hybrid Damper System for Long-Period Pulse-Type Earthquake Ground Motions of Large Amplitude. Front. Built Environ. 6:62. doi: 10.3389/fbuil.2020.00062

INTRODUCTION

In the field of structural engineering of buildings and infrastructures, the resilience of structures is attracting many researchers and being treated as one of the targets of structural design (Bruneau et al., 2003; Cimellaro et al., 2010; Takewaki et al., 2011; Noroozinejad et al., 2019). The resilience consists of two phases, i.e., the resistance to disturbances and the recovery from damages. While the resistance can mostly be dealt with properly by the structural engineering technology, the recovery is related to various multidisciplinary fields including non-structural engineering fields.

Up to now, various innovative methodologies for upgrading the level of resilience have been exploited. The structural control is a well-accepted reliable strategy in terms of cost and implementability (Aiken et al., 1993; Hanson, 1993; Nakashima et al., 1996; Soong and Dargush, 1997; Hanson and Soong, 2001; Takewaki, 2009; Lagaros et al., 2013). The control of earthquake response by passive dampers certainly enables the upgrade of earthquake resilience levels and the

continuous use of buildings (Taniguchi et al., 2016a). In the 2016 Kumamoto earthquake (Japan), severe shakings were observed repeatedly within 2 days and JMA (Japan Metheorological Agency) seismic intensity 7 (the highest level in the JMA scale; approximately X–XII in Mercalli scale) was recorded. As a result, unprecedented large-amplitude ground motions, called long-period pulse-type ground motions, were recorded. Even for such large-amplitude ground motions, the suppression of plastic deformations is strongly recommended in view of the resistance and recovery as the measure of earthquake resilience (Kojima and Takewaki, 2016; Ogawa et al., 2017).

It is well-recognized that the sophisticated and smart use of passive dampers is extremely important because their effectiveness strongly depends on the quantity and location. For responding properly to this requirement, various innovative methods have been proposed (see, for example, Xia and Hanson, 1992; Inoue and Kuwahara, 1998; Quagliarella et al., 1998; Uetani et al., 2003; Aydin et al., 2007; Takewaki, 2009; Aittokoski and Miettinen, 2010; Lavan and Levy, 2010; Adachi et al., 2013a,b; Lagaros et al., 2013; Fujita et al., 2014). As for the design of linear and non-linear viscous dampers, various useful, and effective methods have been proposed (Uetani et al., 2003; Attard, 2007; Aydin et al., 2007; Takewaki, 2009; Lavan and Levy, 2010; Adachi et al., 2013a,b; Noshi et al., 2013). To overcome the cost problem of viscous dampers (Murakami et al., 2013a), hysteretic dampers, such as buckling-restrained ones, have often been used in many buildings. At the same time, a problem is discussed recently resulting from their complex characteristics (Uetani et al., 2003; Murakami et al., 2013a,b). The non-linear characteristics of hysteretic dampers are similar to those of friction-damped types (Pall and Marsh, 1982; Austin and Pister, 1985; Filiatrault and Cherry, 1990; Cherry and Filiatraut, 1993; Ciampi et al., 1995). In addition, since hysteretic dampers exhibit residual deformation, complex hysteretic rules are required in the response evaluation.

As for hysteretic dampers, Inoue and Kuwahara (1998) treated a single-degree-of-freedom (SDOF) model and established a criterion on the optimal hysteretic damper quantity in terms of the equivalent viscous damping (Caughey, 1960; Jacobsen, 1960). Furthermore, Lavan and Levy (2010) developed an optimal design method by taking advantage of a newly derived optimality condition. Murakami et al. (2013a,b) proposed a general and stable sensitivity-based approach applicable to various kinds of dampers. Sivandi-Pour et al. (2014) investigated the equivalent modal damping ratios for non-classically damped hybrid steel concrete buildings.

Because hysteretic dampers possess abovementioned peculiar characteristics, most past researches on hysteretic dampers required numerical optimization algorithms including time-history response analysis for response evaluation and tremendous amount of computational effort was required to reveal special properties of the optimal damper location and quantity. On the other hand, Shiomi et al. (2016) proposed a novel design method for hysteretic dampers using an explicit expression of the maximum elastic–plastic response of an SDOF system with hysteretic dampers under the critical near-fault ground motion that is modeled by "the double impulse" (Kojima and Takewaki, 2015; Taniguchi et al., 2016b). Then, an explicit optimization was performed using this explicit expression. However, the performance comparison with other-type passive dampers has never been conducted under earthquake ground motions with broad amplitude.

In this paper, a hysteretic–viscous hybrid (HVH) damper system is proposed for long-period pulse-type earthquake ground motions of large amplitude, which consists of a viscous damper and a hysteretic damper with a gap mechanism (Tagawa and Hou, 2008; Asakawa et al., 2017). It is demonstrated that HVH is effective for large-amplitude input motions expressed by the double impulse.

DOUBLE IMPULSE AS REPRESENTATIVE OF MAIN PART OF NEAR-FAULT GROUND MOTION

Kojima and Takewaki (2015) demonstrated that the double impulse is a good substitute of the main part of a near-fault ground motion. They introduced the double impulse based on the motivation such that, while the normal input, such as a sinusoidal input or earthquake ground motions, requires the combination of a free-vibration component and a forced-vibration component for their elastic linear responses, the double impulse induces only a free-vibration component. This enables the avoidance to encounter the transcendental equation for finding the maximum response and the efficient use of the energy balance law for deriving the maximum response without time-history response analysis. In the introduction of the double impulse, the principal part of a near-fault ground motion is first modeled by a one-cycle sine wave $\ddot{u}_{g\sin}(t)$ as shown in Equation (1) (see **Figure 1A**) and then transformed into a double impulse $\ddot{u}_{gimp}(t)$ expressed by Equation (2) (see **Figure 1B**).

$$\ddot{u}_{g\sin}(t) = A_p \sin \omega_p t \tag{1}$$

$$\ddot{u}_{gimp}(t) = V\delta(t) - V\delta(t - t_0) \tag{2}$$

In Equations (1) and (2), A_p, ω_p, V, and t_0 indicate the acceleration amplitude of the one-cycle sine wave, the circular frequency of the one-cycle sine wave, the velocity amplitude of the double impulse, and the time interval of the two impulses, respectively. Kojima and Takewaki (2015) employed the condition of the same maximum Fourier amplitude in this transformation.

PROPOSED HVH DAMPER

A new HVH damper system is proposed in this paper. In this system, a hysteretic damper with a gap mechanism in series and a viscous damper are used in parallel. The gap mechanism plays a role to give a trigger function to the hysteretic damper. As a result, this hysteretic damper with a gap mechanism possesses a function as a stopper.

Mechanical Model

The model of a building structure including the proposed HVH system is shown in **Figure 2**. It is assumed that the

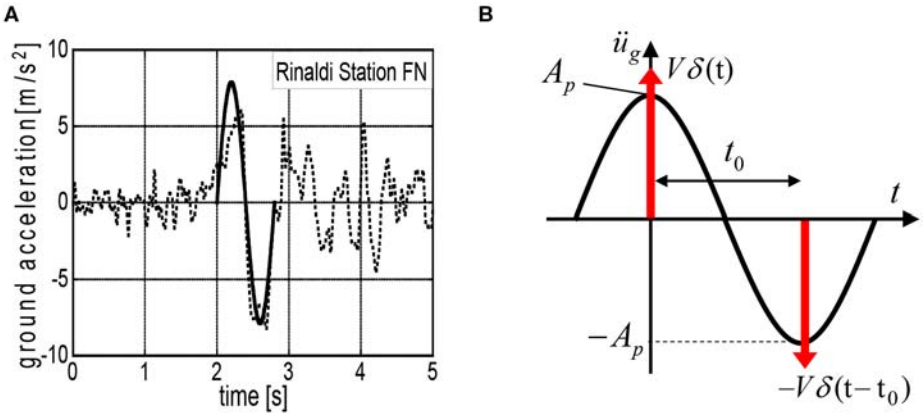

FIGURE 1 | Transformation of ground motion into double impulse. **(A)** Modeling of principal part of Rinaldi station FN motion (Northridge, 1994) into one-cycle sinusoidal wave; **(B)** Re-modeling into double impulse (Shiomi et al., 2018).

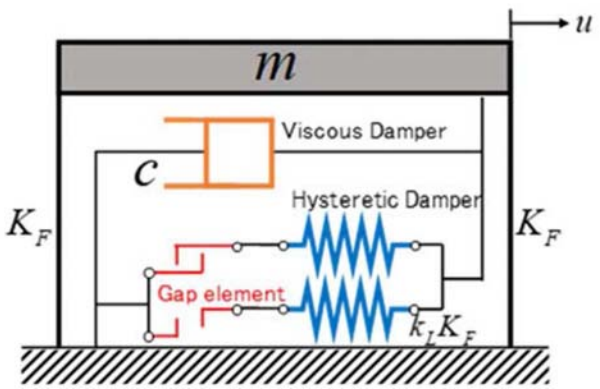

FIGURE 2 | Elastic–perfectly plastic SDOF system with HVH damper system.

building structure and the hysteretic damper have the elastic–perfectly plastic restoring-force characteristics. In this figure, K_F, k_L, c denote the frame stiffness, the stiffness ratio of the hysteretic damper to the frame, and the damping coefficient of the viscous damper.

Mechanism of Response Reduction

The viscous damper is aimed at resisting for broad-amplitude range vibration and the hysteretic damper with a gap mechanism is expected to play as a stopper for large-amplitude range vibration.

CLOSED-FORM CRITICAL ELASTIC–PLASTIC RESPONSE OF BUILDING MODEL WITH HVH

Kojima and Takewaki (2015) derived a closed-form expression of the maximum deformation of an elastic–perfectly plastic SDOF system under the critical double impulse by using an energy balance approach. This energy balance approach can be applied to more general models with broader class of restoring-force characteristics (see Shiomi et al., 2016, 2018). In this paper, a more general case is treated where a hysteretic damper with a gap mechanism and a viscous damper are used in parallel in an elastic–perfectly plastic SDOF system.

TABLE 1 | Classification of closed-form expressions on maximum deformation of the elastic–perfectly plastic SDOF system with HVH damper system under critical double impulse.

	After first impulse		After second impulse	
	Frame	**Hysteretic damper**	**Frame**	**Hysteretic damper**
Case 1	Elastic		Plastic	Elastic
Case 2	Elastic		Plastic	Plastic
Case 3	Plastic		Plastic	Elastic
Case 4	Plastic		Plastic	Plastic
Case 5	Plastic	Elastic	Plastic	
Case 6	Plastic	Elastic	Plastic	Elastic
Case 7	Plastic	Elastic	Plastic	Plastic
Case 8	Plastic	Plastic	Plastic	
Case 9	Plastic	Plastic	Plastic	Elastic
Case 10	Plastic	Plastic	Plastic	Plastic

Two types exist depending on the state in the unloading process after the first impulse.
Type A: The hysteretic damper becomes inactive before the frame re-yields.
Type B: The frame re-yields before the hysteretic damper becomes inactive.
Furthermore, two types exist depending on the state at the zero overall restoring force in the unloading process after the first impulse.
1. Both the frame and hysteretic damper have elastic stiffnesses.
2. Either one of the frame and the hysteretic damper has an elastic stiffness. (A-2: Only the frame has an elastic stiffness, B-2: Only the hysteretic damper has an elastic stiffness).

The model used in this paper is the SDOF model. Therefore, the effect of higher modes on the response of buildings is not considered. Since only the critical input of double impulse resonant to the elastic–plastic building with the HVH damper system is treated, the lowest-mode response governs most components of the total response of the building. This is because the long-period pulse-type earthquake ground motion possesses a clear predominant period and the treatment of the resonant input to the building is considered to be important in the investigation of the safety of the building.

The closed-form expressions are classified into several cases depending on the input level and structural parameters

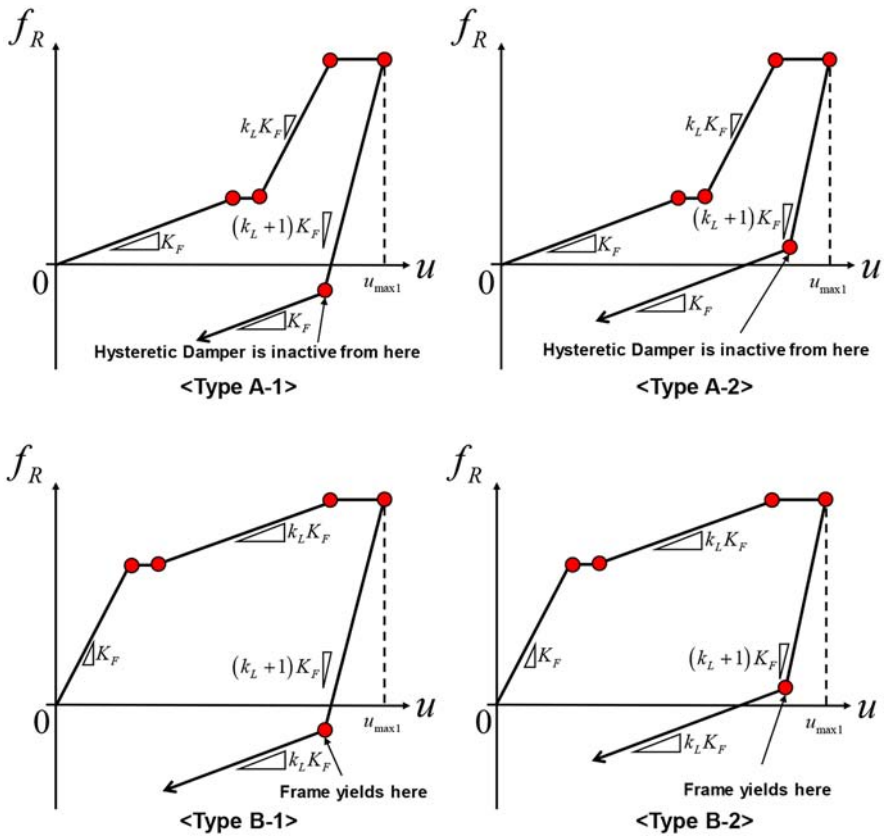

FIGURE 3 | Classification depending on the state in the unloading process after the first impulse and the state at the zero overall restoring force in the unloading process after the first impulse (Cases 5–10).

(see **Table 1**). In this case, the maximum displacement $u_{\max 1}$ after the first impulse, the velocity v_c at the zero restoring force (frame plus hysteretic damper) after the first impulse, and the maximum displacement $u_{\max 2}$ after the second impulse can be derived.

In the present model, an example of the restoring-force characteristic is presented in **Figure 3** and the same energy balance approach can be applied by referring to the restoring-force and damping-force diagrams as shown in **Figure 4**, i.e., Cases 1–4 in **Figure 4A**, Case 5 in **Figure 4B**, Case 6 in **Figure 4C**, Case 7 in **Figure 4D**, Case 8 in **Figure 4E**, Case 9 in **Figure 4F**, and Case 10 in **Figure 4G**. When a viscous damper exists, an extended energy balance approach by Kojima et al. (2018) can be used for closed-form expressions.

The closed-form expressions of the maximum displacement $u_{\max 1}$ after the first impulse, the velocity v_c at the zero restoring force (frame plus hysteretic damper) after the first impulse, and the maximum displacement $u_{\max 2}$ after the second impulse for Cases 1–4 are as follows.

[Case 1]

$$u_{\max 1} = \frac{-2cV + \sqrt{4c^2V^2 + 9K_F m V^2}}{3K_F}$$

$$v_c = \frac{-2cu_{\max 1} + \sqrt{4c^2u_{\max 1}^2 + 9mK_F u_{\max 1}^2}}{3m}$$

$$u_{\max 2} = \frac{-\left\{2c\left(v_c+V\right) - 3k_L K_F d_{gh} + 3K_F d_y\right\} + \sqrt{\left\{2c\left(v_c+V\right) - 3k_L K_F d_{gh} + 3K_F d_y\right\}^2 - 3k_L K_F\left\{-3K_F d_y^2 + 3k_L K_F d_{gh}^2 - 3m(v_c+V)^2\right\}}}{3k_L K_F}$$

[Case 2]

$$u_{\max 1} = \frac{-2cV + \sqrt{4c^2V^2 + 9K_F m V^2}}{3K_F}$$

$$v_c = \frac{-2cu_{\max 1} + \sqrt{4c^2u_{\max 1}^2 + 9mK_F u_{\max 1}^2}}{3m}$$

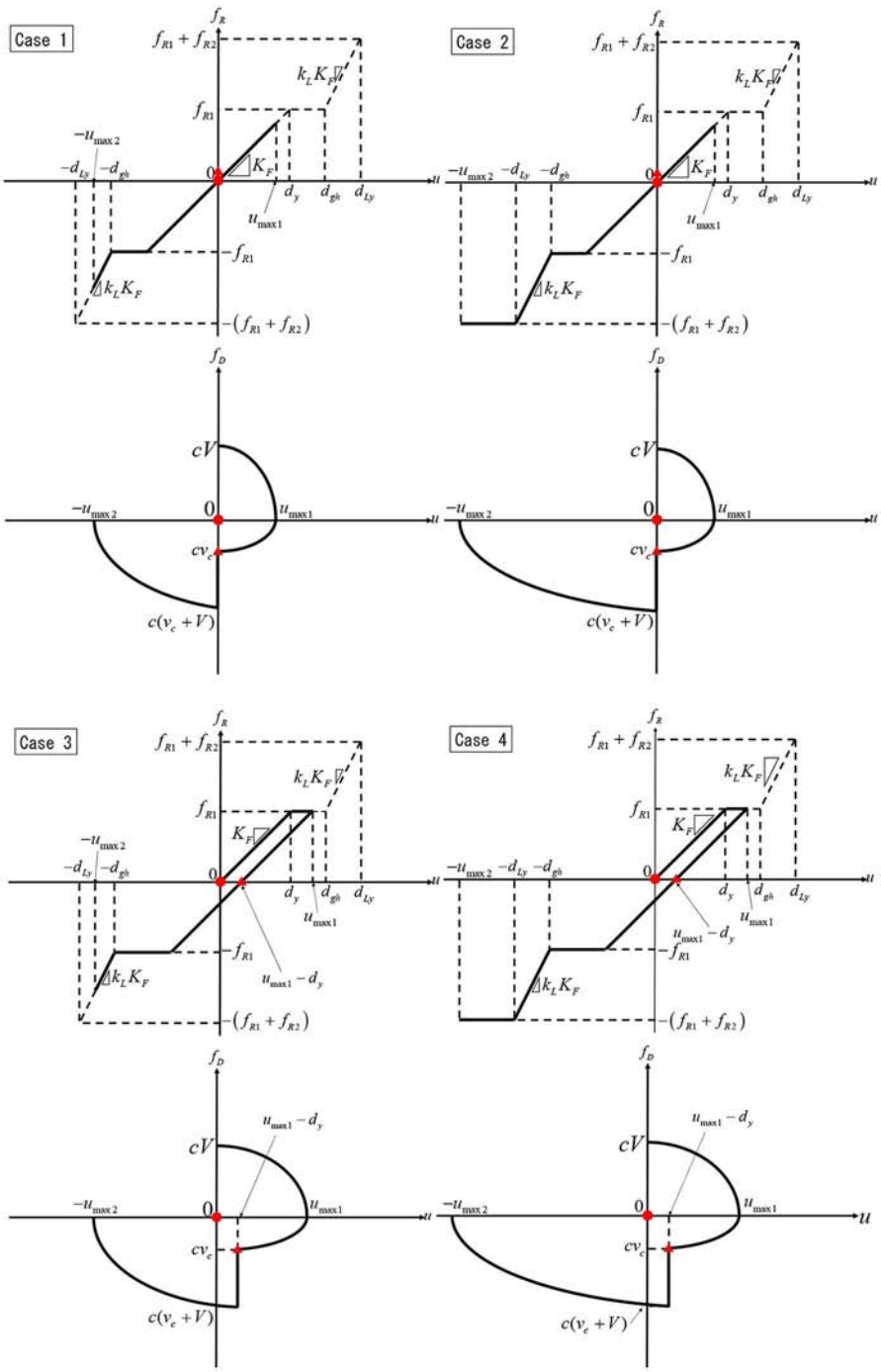

FIGURE 4A | Case 1–4.

$$u_{\max 2} = \frac{3m(v_c+V)^2 + 3K_F d_y^2 + 6k_L K_F d_{Ly}(d_{Ly}-d_{gh}) - 3k_L K_F (d_{Ly}-d_{gh})^2}{6k_L K_F (d_{Ly}-d_{gh}) + 6K_F d_y + 4c(v_c+V)}$$

[Case 3]

$$u_{\max 1} = \frac{3mV^2 + 3K_F d_y^2}{4cV + 6K_F d_y} \qquad v_c = \frac{-2cd_y + \sqrt{4c^2 d_y^2 + 9mK_F d_y^2}}{3m}$$

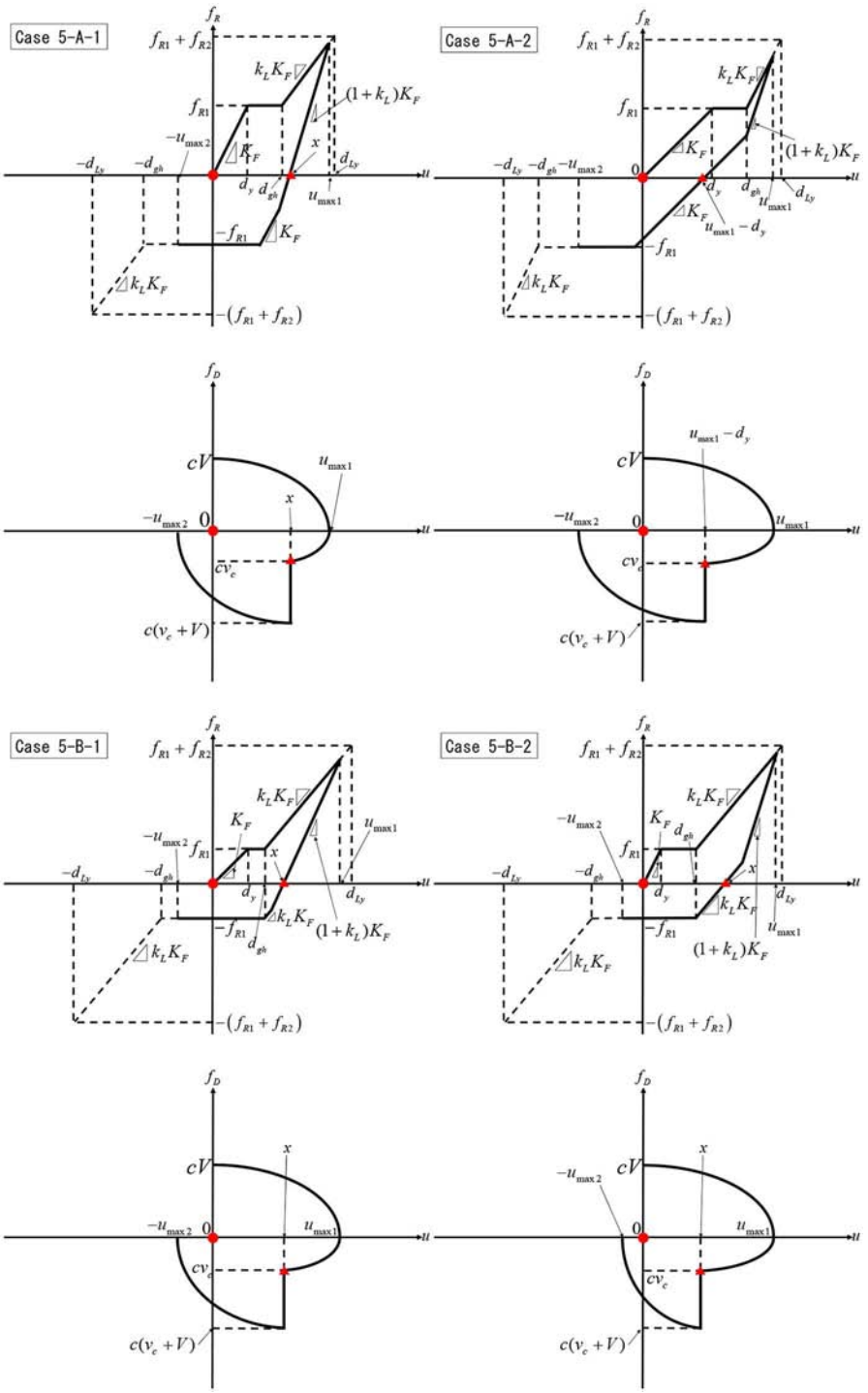

FIGURE 4B | Case 5.

$$= \frac{-\left\{3K_F d_y - 3k_L K_F d_{gh} + 2c(V+v_c)\right\} + \sqrt{\begin{array}{l}\left\{3K_F d_y - 3k_L K_F d_{gh} + 2c(V+v_c)\right\}^2 \\ -3k_L K_F \left\{\begin{array}{l} 3k_L K_F d_{gh}^2 + 4c(V+v_c)\left(u_{\max 1} - d_y\right) \\ +6K_F d_y\left(u_{\max 1} - 2d_y\right) + 3K_F d_y^2 - 3m(V+v_c)^2 \end{array}\right\}\end{array}}}{3k_L K_F} \quad u_{\max 2}$$

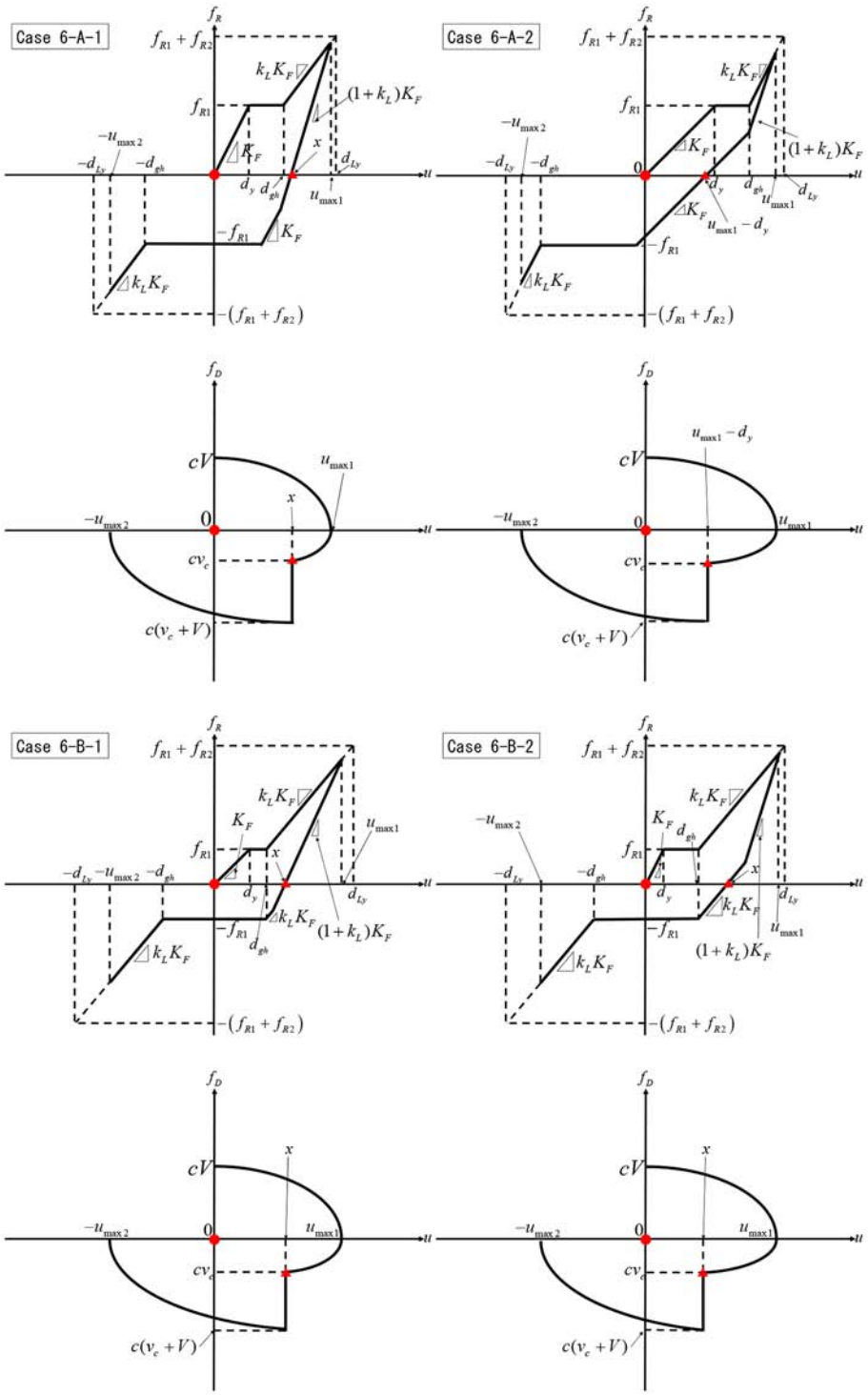

FIGURE 4C | Case 6.

[**Case 4**]

$$u_{\max 1} = \frac{3mV^2 + 3K_F d_y^2}{4cV + 6K_F d_y}$$

$$v_c = \frac{-2cd_y + \sqrt{4c^2 d_y^2 + 9mK_F d_y^2}}{3m}$$

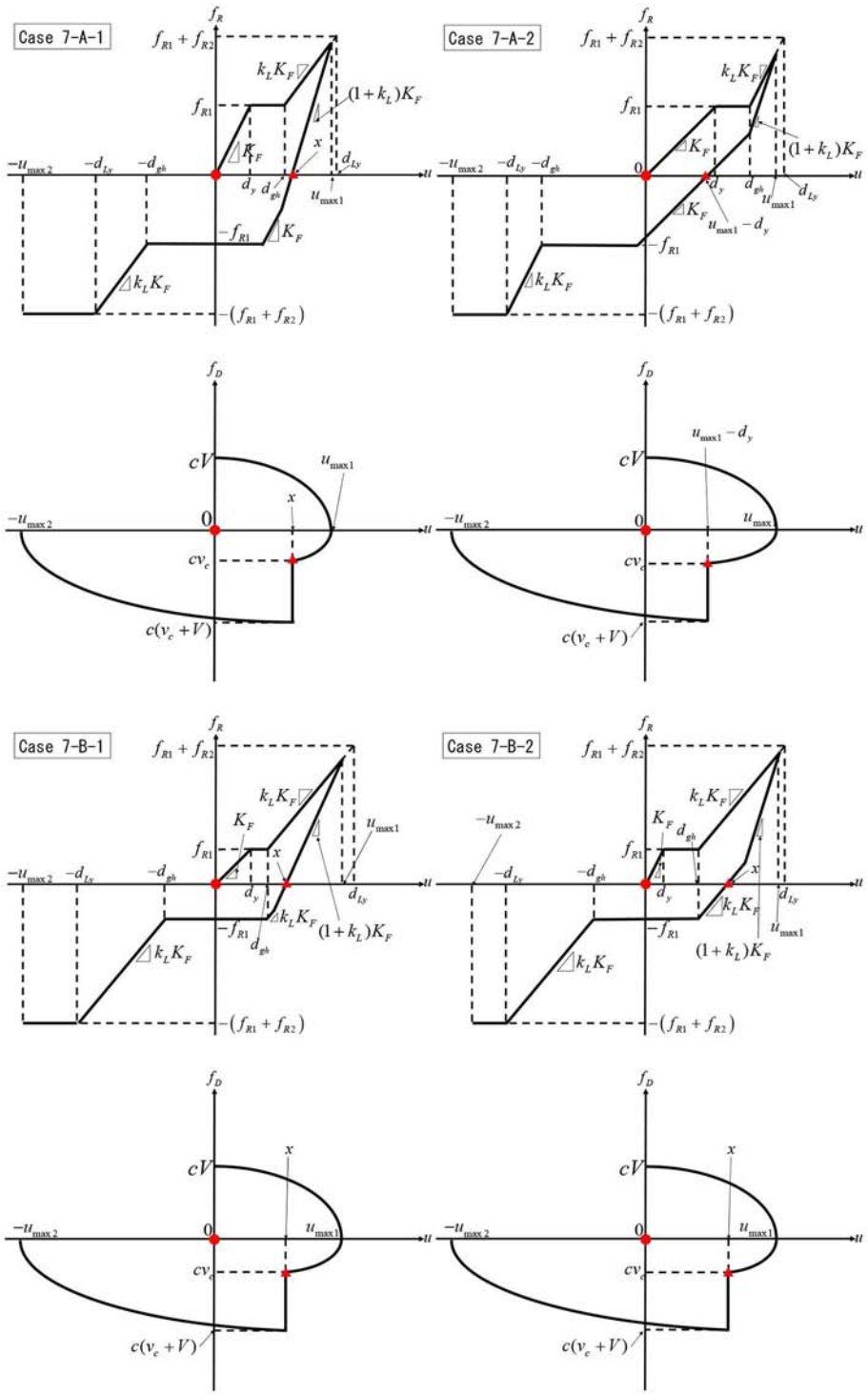

FIGURE 4D | Case 7.

$$u_{\max 2} = \frac{3m(V+v_c)^2 - 4c\,(v_c+V)\left(u_{\max 1}-d_y\right) - 3K_F d_y^2 - 6K_F d_y(u_{\max 1}-2d_y) - 3k_L K_F\left(d_{Ly}-d_{gh}\right)^2 + 6k_L K_F d_{Ly}\left(d_{Ly}-d_{gh}\right)}{4c\,(v_c+V) + 6K_F d_y + 6k_L K_F\left(d_{Ly}-d_{gh}\right)}$$

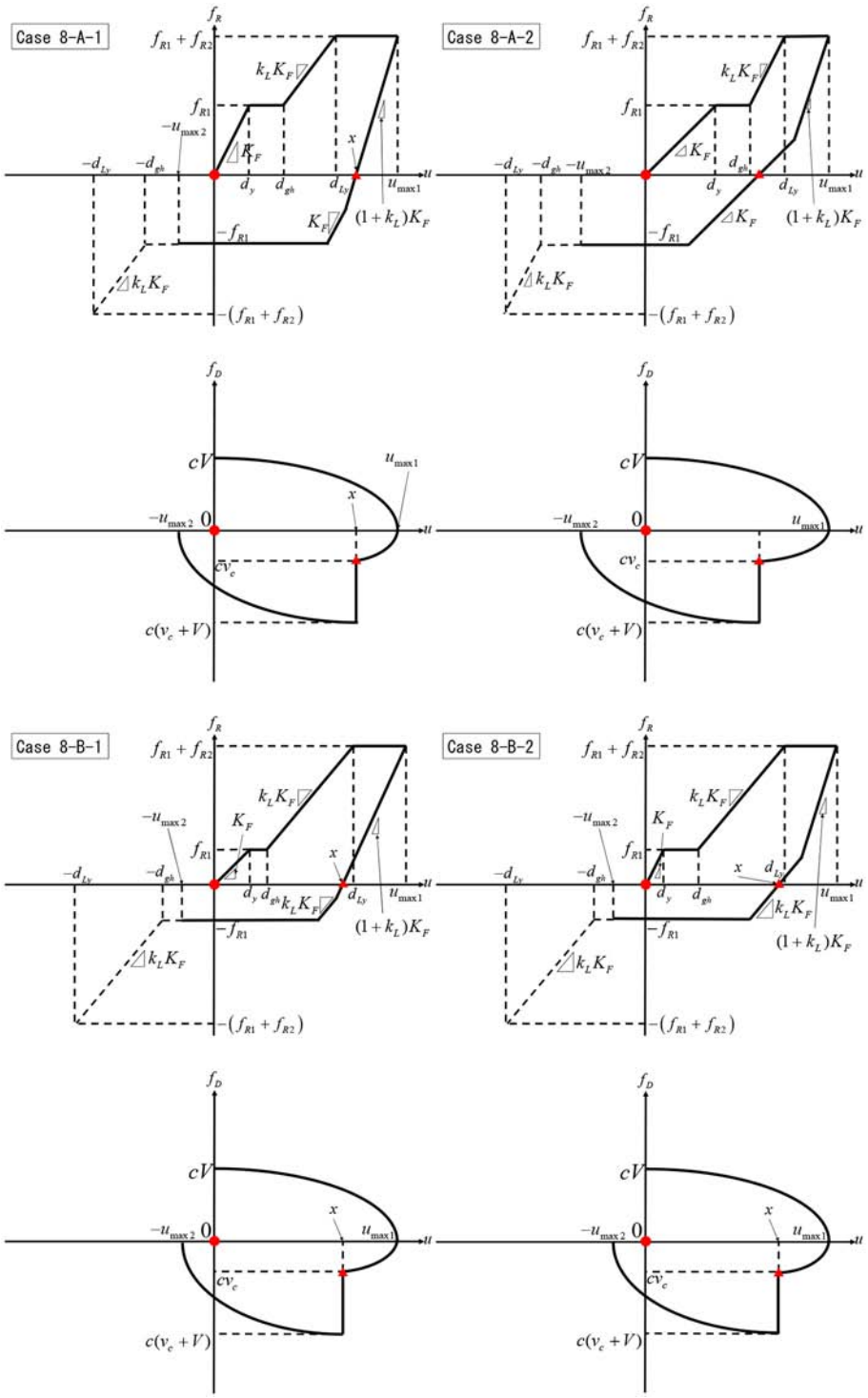

FIGURE 4E | Case 8.

The closed-form expressions for Case 5 [A-1]–Case 10 [B-1] are shown in **Appendix** (**Supplemental file**). Since Case 10 [B-2] is a case including a general restoring-force characteristic, a detailed derivation for Case 10-B-2 is shown below to explain the derivation process of the closed-form expressions.

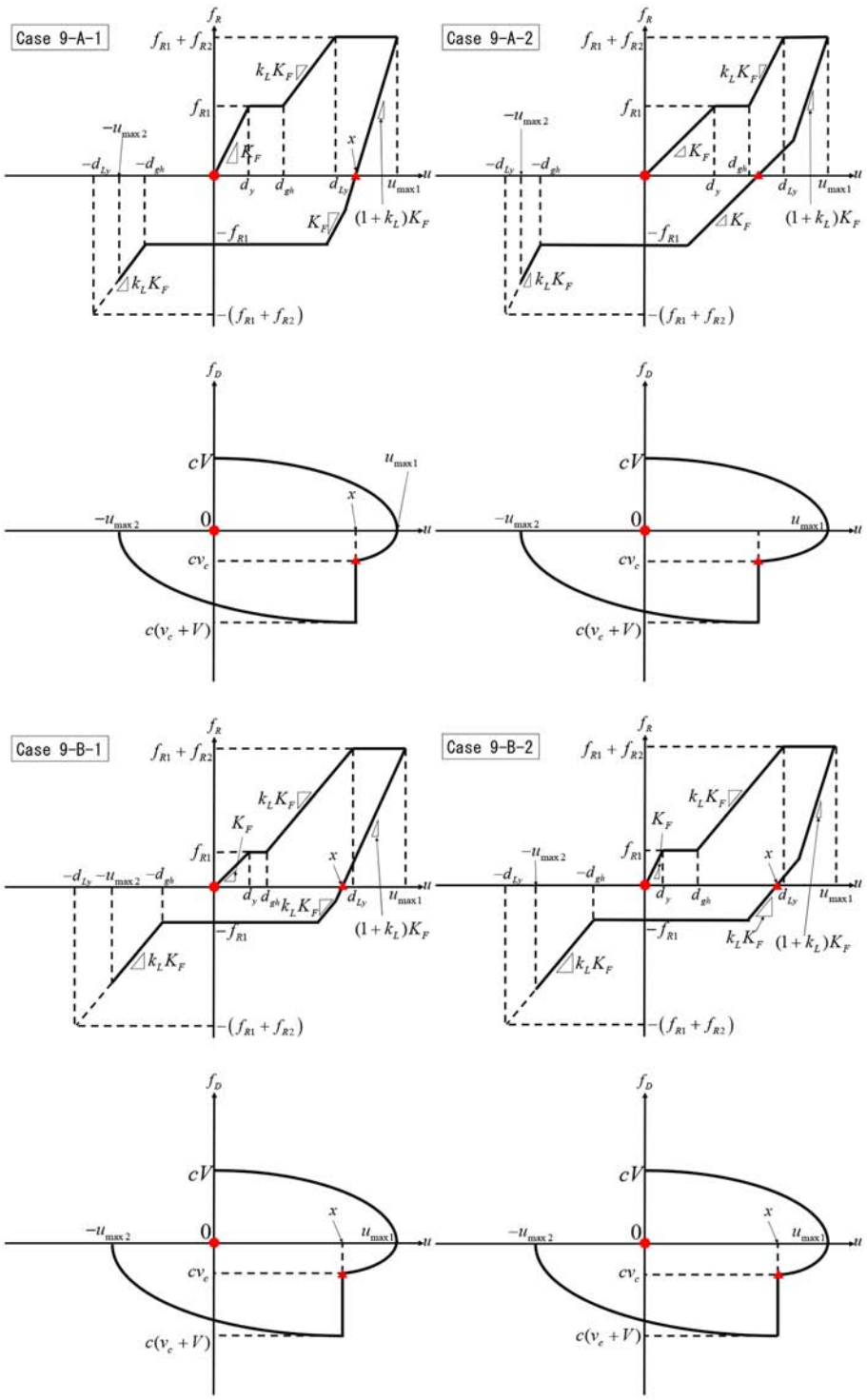

FIGURE 4F | Case 9.

[Case 10] [B-2]

Consider the case where the frame and the hysteretic damper with a gap mechanism yield after both the first impulse and the second impulse.

Evaluate the work done by the viscous damper by approximating the damping force–deformation relation as a quadratic function. The damping force–deformation relation after the first impulse can be approximated by a quadratic

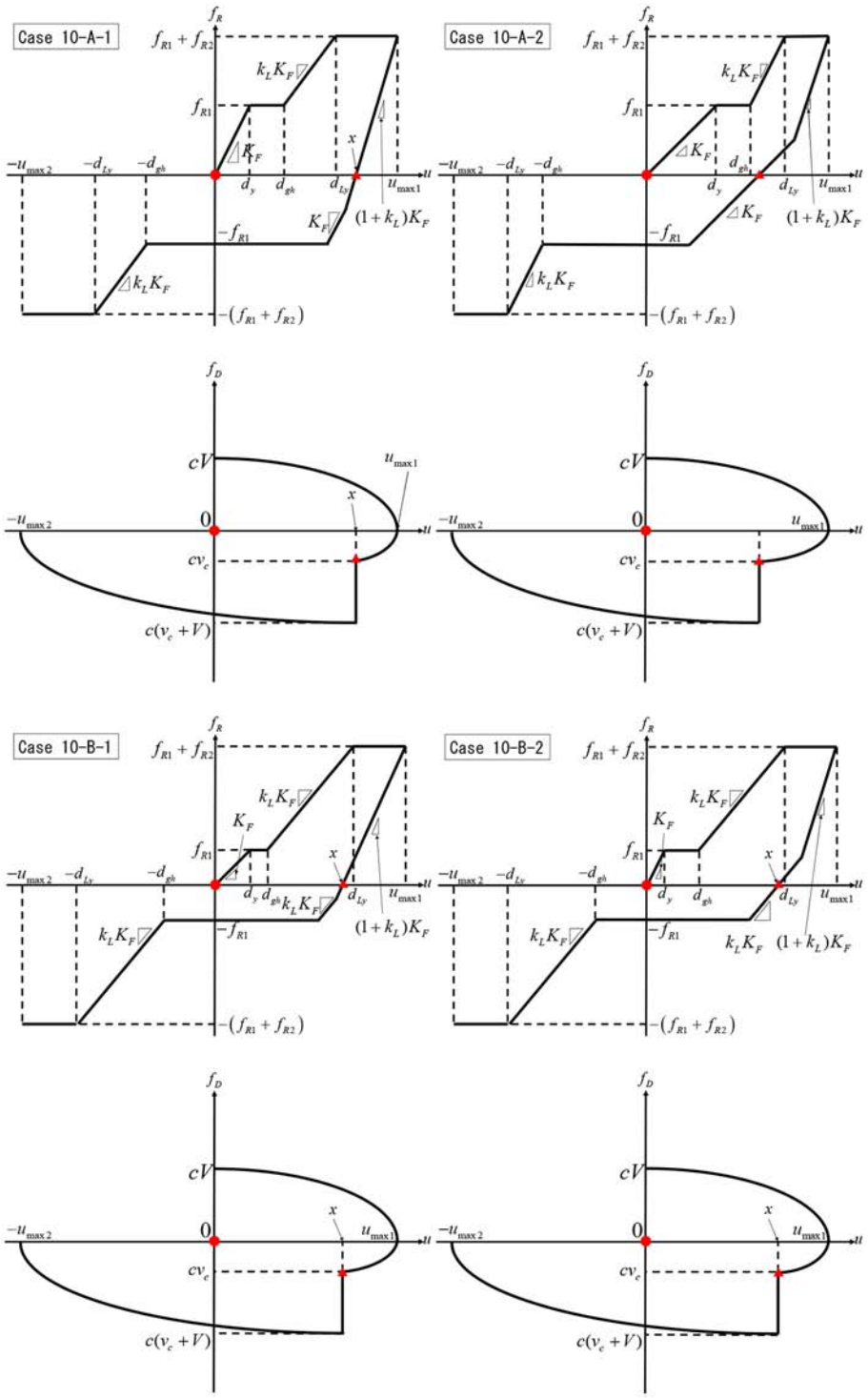

FIGURE 4G | (A) Restoring-force and damping-force diagrams for various closed-form expressions (Cases 1–4) on maximum deformation of elastic–perfectly plastic SDOF system with HVH damper system under critical double impulse (●: 1st impulse; ▲: 2nd impulse). **(B)** Restoring-force and damping-force diagrams for various closed-form expressions (Case 5) on maximum deformation of elastic–perfectly plastic SDOF system with HVH damper system under critical double impulse (●: 1st impulse; ▲: 2nd impulse). **(C)** Restoring-force and damping-force diagrams for various closed-form expressions (Case 6) on maximum deformation of elastic–perfectly plastic SDOF system with HVH damper system under critical double impulse (●: 1st impulse; ▲: 2nd impulse). **(D)** Restoring-force and damping-force diagrams for various closed-form expressions (Case 7) on maximum deformation of elastic–perfectly plastic SDOF system with HVH damper system under critical double impulse (●: 1st impulse; ▲: 2nd impulse). **(E)** Restoring-force and damping-force diagrams for various closed-form expressions (Case 8) on maximum deformation of

(Continued)

FIGURE 4G | elastic–perfectly plastic SDOF system with HVH damper system under critical double impulse (●: 1st impulse; ▲: 2nd impulse). **(F)** Restoring-force and damping-force diagrams for various closed-form expressions (Case 9) on maximum deformation of elastic–perfectly plastic SDOF system with HVH damper system under critical double impulse (●: 1st impulse; ▲: 2nd impulse). **(G)** Restoring-force and damping-force diagrams for various closed-form expressions (Case 10) on maximum deformation of elastic–perfectly plastic SDOF system with HVH damper system under critical double impulse (●: 1st impulse; ▲: 2nd impulse).

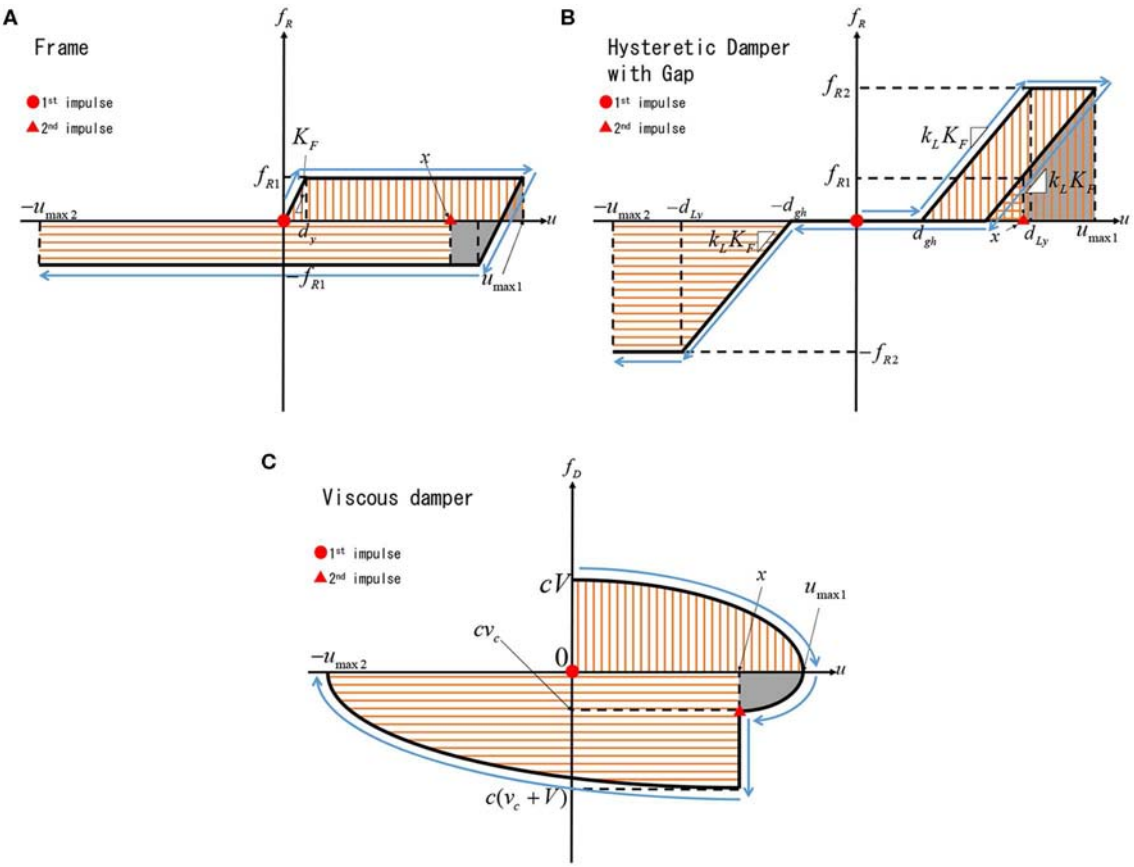

FIGURE 5 | Diagrams for Case 10-B-2. **(A)** Restoring force–deformation relation of frame; **(B)** Restoring force–deformation relation of hysteretic damper with gap mechanism; **(C)** Damping force–deformation relation of viscous damper.

function with vertex $(u, f_D) = (u_{\max 1}, 0)$ and passing through the point $(u, f_D) = (0, cV)$. f_D can then be obtained as follows.

$$f_D = cV\sqrt{1-(u/u_{\max 1})} \tag{3}$$

The work done by the damping force after the first impulse can be obtained by integrating Equation (3) from $u = 0$ to $u = u_{\max 1}$.

$$\int_0^{u_{\max 1}} f_D du = \int_0^{u_{\max 1}} \left\{cV\sqrt{1-(u/u_{\max 1})}\right\} du = (2/3)\, cV u_{\max 1} \tag{4}$$

By using Equation (4), the energy balance law after the first impulse (see **Figure 5**) leads to

$$\begin{aligned} mV^2/2 &= K_F d_y^2/2 + K_F d_y(u_{\max 1} - d_y) \\ &+ k_L K_F (d_{Ly} - d_{gh})^2/2 + k_L K_F (d_{Ly} - d_{gh})(u_{\max 1} - d_{Ly}) \\ &+ (2/3)\, cV u_{\max 1} \end{aligned} \tag{5}$$

From Equation (5), $u_{\max 1}$ can be evaluated by

$$u_{\max 1} = \frac{3mV^2 + 3K_F d_y^2 - 3k_L K_F (d_{Ly} - d_{gh})^2 + 6k_L K_F d_{Ly}(d_{Ly} - d_{gh})}{4cV + 6K_F d_y + 6k_L K_F (d_{Ly} - d_{gh})} \tag{6}$$

Derive the velocity v_c at the timing of the second impulse based on the assumption that the critical timing of the second impulse (the timing of the second impulse maximizing the maximum response $u_{\max 2}$ after the second impulse with respect to a variable impulse timing) is the timing when the overall story shear force becomes zero.

Designate the deformation at the time when the overall story shear force becomes zero after the achievement of $u_{\max 1}$ as x. Then, Case 10 B-2 in **Figure 4G** for the restoring-force characteristic provides the following relation.

$$\begin{aligned} K_F d_y + k_L K_F \left(d_{Ly} - d_{gh}\right) &= 2\left(1 + k_L\right) K_F d_y \\ &+ k_L K_F \left(u_{\max 1} - 2d_y - x\right) \end{aligned} \tag{7}$$

From Equation (7), the deformation x at the time when the overall story shear force becomes zero after the achievement of $u_{\max 1}$ can be expressed by

$$x = u_{\max 1} - \frac{k_L\left(d_{Ly} - d_{gh}\right) - d_y}{k_L} \tag{8}$$

As in the previous case, the work done by the damping force is derived by using the quadratic function approximation. The damping force–deformation relation after achieving $u_{\max 1}$ is approximated by a quadratic function with vertex $(u, f_D) = (u_{\max 1}, 0)$ and passing through the point $(u, f_D) = (x, cv_c)$. f_D can be obtained as follows.

$$f_D = -cv_c\sqrt{(u_{\max 1} - u)/(u_{\max 1} - x)} \tag{9}$$

By integrating Equation (9) from $u = x$ to $u = u_{\max 1}$, the work done by the damping force can be evaluated by

$$\begin{aligned}\int_x^{u_{\max 1}}\left(-f_D\right)du &= \int_x^{u_{\max 1}}\left(cv_c\sqrt{(u_{\max 1} - u)/(u_{\max 1} - x)}\right)du \\ &= (2/3)\,cv_c\,(u_{\max 1} - x)\end{aligned} \tag{10}$$

Equation (10) and the energy balance law lead to

$$\begin{aligned}&K_F d_y^2/2 + k_L K_F\left(d_{Ly} - d_{gh}\right)^2/2 \\ &= mv_c^2/2 + (2/3)\,cv_c\,(u_{\max 1} - x) + K_F d_y^2/2 \\ &+K_F d_y\left(u_{\max 1} - 2d_y - x\right) + k_L K_F\left(x - u_{\max 1} + d_{Ly} - d_{gh}\right)^2/2\end{aligned} \tag{11}$$

From Equation (11), the velocity v_c at the time when the overall shear force becomes zero can be expressed by

$$v_c = \frac{-2c\,(u_{\max 1} - x) + \sqrt{4c^2(u_{\max 1} - x)^2 - 9mk_L K_F\,(x - u_{\max 1})\left(x - u_{\max 1} + 2d_{Ly} - 2d_{gh}\right)}}{3m} \tag{12}$$

As in the above case, the damping force–deformation relation after the second impulse is approximated by a quadratic function with vertex $(u, f_D) = (-u_{\max 2}, 0)$ and passing through the point $(u, f_D) = (x, -c(v_c + V))$. f_D can be obtained as follows.

$$f_D = -c\,(v_c + V)\,\sqrt{(u_{\max 2} + u)/(u_{\max 2} + x)} \tag{13}$$

By integrating Equation (13) from $u = -u_{\max 2}$ to $u = x$, the work done by the damping force can be evaluated by

$$\int_{-u_{\max 2}}^{x}\left(-f_D\right)du = \int_{-u_{\max 2}}^{x}\left\{c\,(v_c + V)\,\sqrt{(u_{\max 2} + u)/(u_{\max 2} + x)}\right\}du = (2/3)\,c\,(v_c + V)\,(u_{\max 2} + x) \tag{14}$$

Equation (14) and the energy balance law lead to

$$\begin{aligned}&m(V + v_c)^2/2 + k_L K_F\left(x - u_{\max 1} + d_{Ly} - d_{gh}\right)^2/2 \\ &= (2/3)\,c\,(V + v_c)\,(u_{\max 2} + x) + K_F d_y\,(x + u_{\max 2}) \\ &+k_L K_F\left(d_{Ly} - d_{gh}\right)^2/2 + k_L K_F\left(d_{Ly} - d_{gh}\right)\left(u_{\max 2} - d_{Ly}\right)\end{aligned} \tag{15}$$

From Equation (15), $u_{\max 2}$ can be evaluated by

$$u_{\max 2} = \frac{\left\{\begin{array}{r}3m(V + v_c)^2 + 3k_L K_F\left(x - u_{\max 1} + d_{Ly} - d_{gh}\right)^2 - 4c\,(V + v_c)\,x \\ -6K_F d_y x - 3k_L K_F\left(d_{Ly} - d_{gh}\right)^2 + 6k_L K_F d_{Ly}\left(d_{Ly} - d_{gh}\right)\end{array}\right\}}{6K_F d_y + 6k_L K_F\left(d_{Ly} - d_{gh}\right) + 4c\,(V + v_c)} \tag{16}$$

INVESTIGATION ON ACCURACY OF CLOSED-FORM EXPRESSIONS FOR MAXIMUM DEFORMATION OF SDOF BUILDING MODEL INCLUDING HVH SYSTEM WITH VARIOUS PARAMETERS

Consider an SDOF building model including the HVH system with various parameters. **Figure 6** shows the comparison of the maximum deformation by the proposed closed-form expressions including an approximate damping force–deformation relation and by the time-history response analysis for the quantity $k_L = 1$ of hysteretic dampers and the damping ratios $h = 0, 0.05, 0.1, 0.2$ of viscous dampers. V_y in the horizontal axis indicates the input velocity level of the double impulse such that the undamped model just reaches the yield level after the first impulse. In **Figure 6**, the maximum deformations after the first and second impulses are also plotted for reference. It should be remarked that, while the maximum deformation $u_{\max 1}$ after the first impulse becomes the maximum deformation $u_{\max}$ in larger input velocity levels, the maximum deformation $u_{\max 2}$ after the second impulse becomes the maximum deformation $u_{\max}$ in smaller input velocity levels. It can also be observed that the proposed closed-form expressions provide fairly accurate results for various damping levels and input levels.

Figure 7 indicates the same comparison for the quantity $k_L = 2$ of hysteretic dampers and the damping ratios $h = 0, 0.05, 0.1, 0.2$ of viscous dampers. It can also be seen that the proposed closed-form expressions possess fairly good accuracy. However, as the damping level becomes larger, a little difference appears.

RESPONSE COMPARISON OF SDOF BUILDING MODEL INCLUDING HVH SYSTEM WITH MODEL INCLUDING DHD (DUAL HYSTERETIC DAMPER) SYSTEM UNDER DOUBLE IMPULSE

Figure 8A shows the elastic–perfectly plastic SDOF system with HVH damper system and one with DHD system that was proposed by Shiomi et al. (2018). In this figure, K_F, k, α denote the frame stiffness, the stiffness ratio of DSA (hysteretic damper for small-amplitude control) to the frame, and the stiffness ratio of DLA (hysteretic damper for large-amplitude control) to DSA. It should be remarked that $\alpha k = k_L$ in the model with HVH.

In comparing the response reduction performances by the HVH system and the DHD system, it is necessary to adjust the quantities of both systems. In this paper, $cV = kK_F d_{sy}$

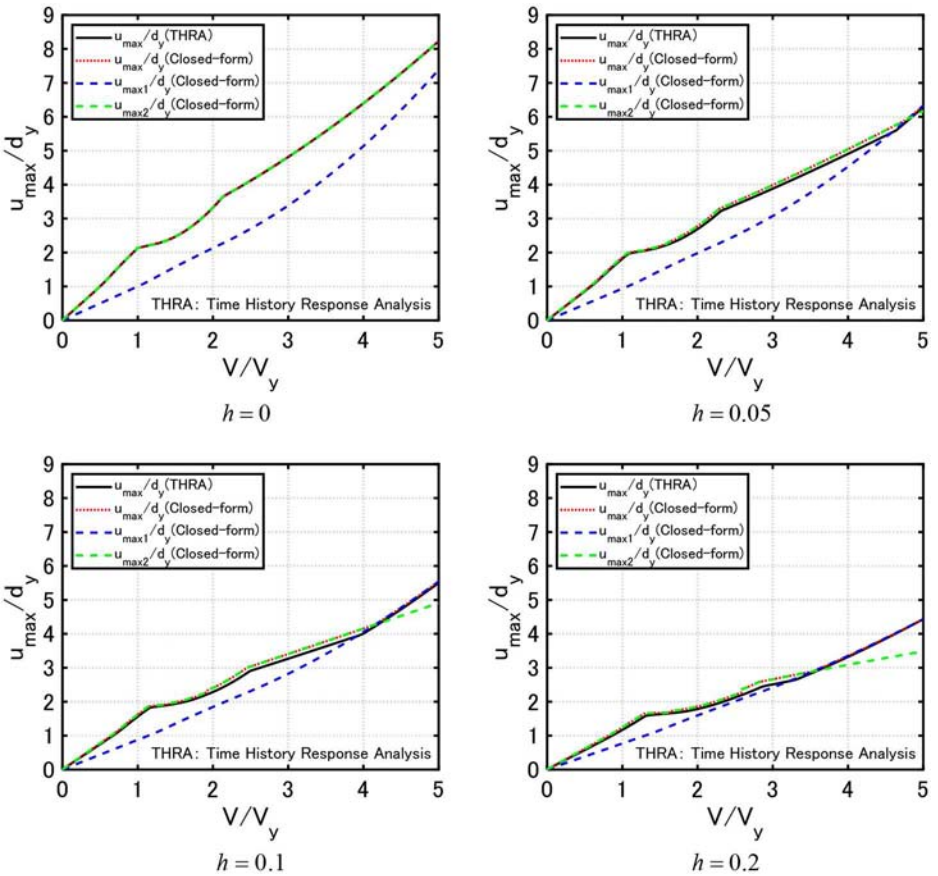

FIGURE 6 | Comparison of maximum deformation under critical double impulse between time-history response analysis and closed-form expression ($k_L = 1$).

is employed as shown in **Figure 8B**. From this relationship, it can be understood that, as the parameter V becomes larger, the quantity of hysteretic dampers in the HVH and DHD systems increases for a given damping coefficient c of viscous dampers in the HVH system.

Figure 9 shows the comparison of the maximum deformations under the critical double impulse between the elastic–perfectly plastic SDOF system with HVH and one with DHD ($\alpha = 0$) for $h = 0.05, 0.1, 0.2, 0.3$. The quantitative changes of the response of the model with HVH from that of the model with DHD are indicated in percent at the two input levels $V/V_y = 2, 4$. It should be reminded that, since $\alpha k = k_L$, $\alpha = 0$ indicates the SDOF models with only the viscous damper in HVH and the short-amplitude hysteretic damper in DHD. It can be seen that the viscous damper is effective for the input of smaller level ($V/V_y < 3$). In addition, the quantity of the short-amplitude hysteretic damper in DHD is specified by using the relation $cV = kK_F d_{sy}$ explained above. The good response reduction performance of the DHD system in $V/V_y > 3$ is due to the fact that, as the parameter V becomes larger, the quantity of hysteretic dampers in the DHD systems increases for a given damping coefficient c of viscous dampers in the HVH system. On the other hand, **Figure 10** presents the same comparison for $\alpha = 1$ and **Figure 11** illustrates the comparison for $\alpha = 3$. It can be observed that the HVH has a good response reduction performance in the broad range of input levels compared with the DHD.

RESPONSE COMPARISON OF SDOF BUILDING MODEL INCLUDING THE HVH SYSTEM WITH MODEL INCLUDING DHD SYSTEM UNDER RECORDED GROUND MOTION

The effectiveness of the HVH system under a recorded ground motion of long-period pulse-type is shown in this section. **Figure 12A** and **B** show a ground acceleration and its velocity of JMA Nishiharamura–Komori(EW) wave during the Kumamoto earthquake in 2016, which is known as a long-period pulse-type ground motion of a very large velocity amplitude. The displacement, velocity, and acceleration response spectra are presented in **Figures 12C–E**. It can be found that this wave has a large velocity response around 0.7, 3.0(s).

Figure 13 indicates the comparison of the maximum deformation under the JMA Nishiharamura–Komori(EW) wave

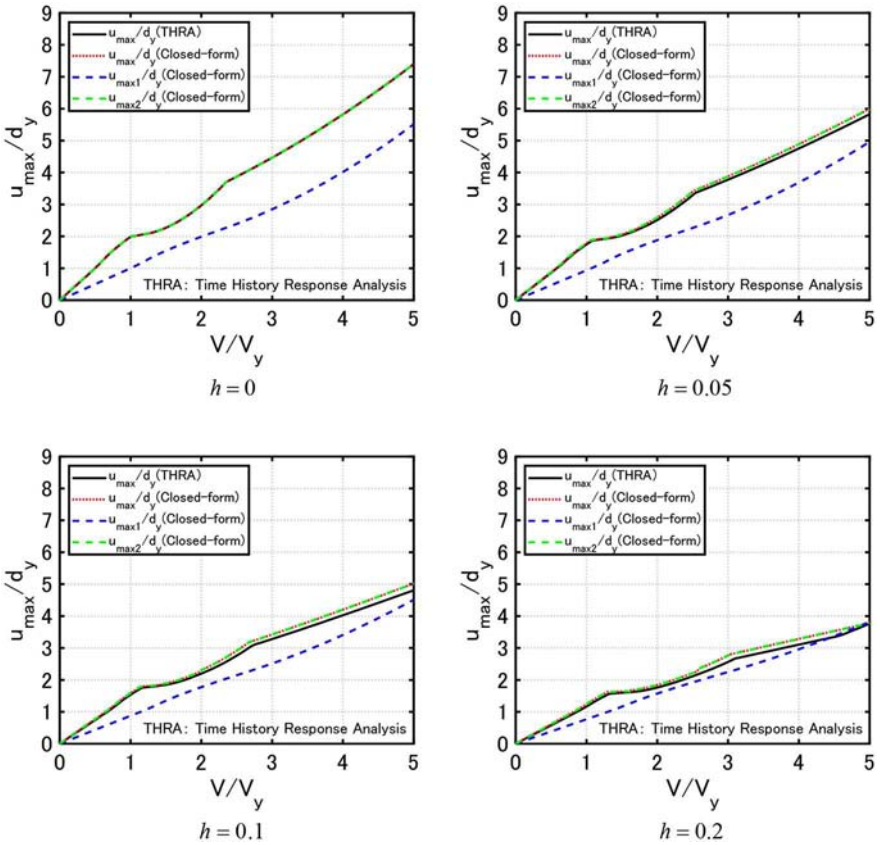

FIGURE 7 | Comparison of maximum deformation under critical double impulse between time-history response analysis and closed-form expression ($k_L = 2$).

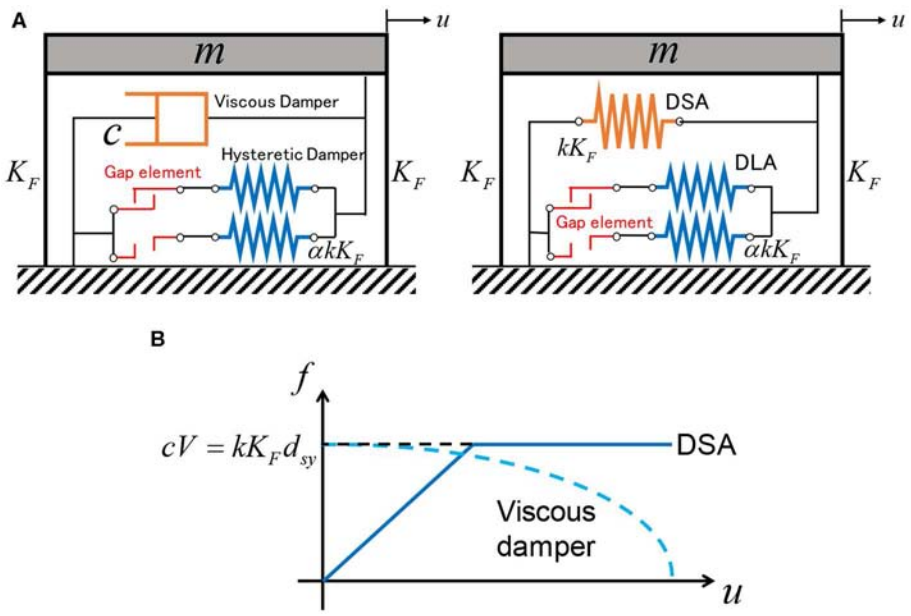

FIGURE 8 | Proposed model and comparison with previously developed model. **(A)** Elastic–perfectly plastic SDOF system with HVH damper system and one with DHD system; **(B)** Parameter adjustment between HVH and DHD.

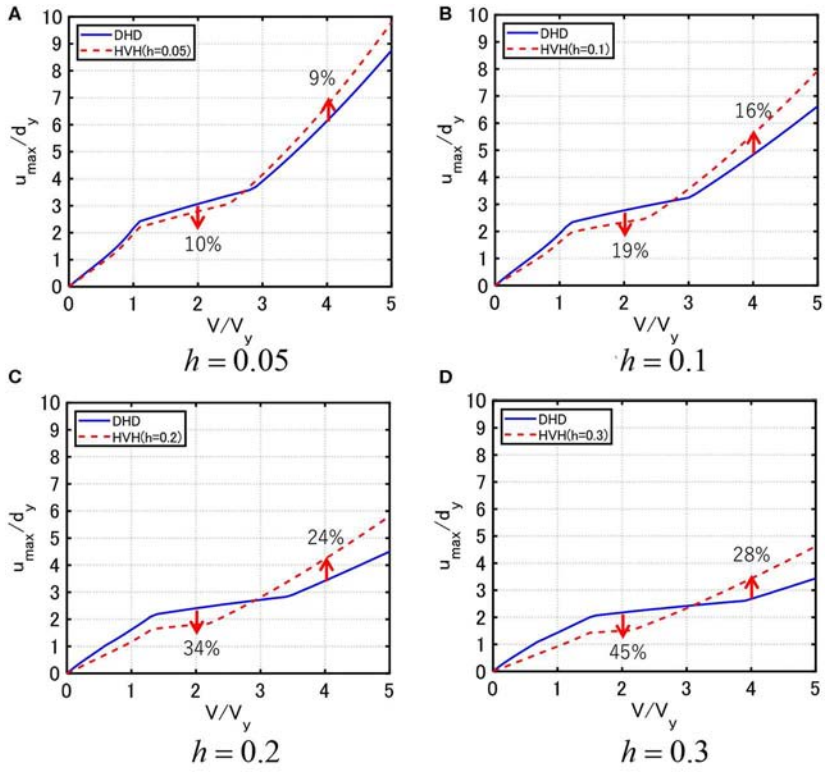

FIGURE 9 | Comparison of maximum deformation under critical double impulse between elastic–perfectly plastic SDOF system with HVH and one with DHD ($\alpha = 0$) **(A)** $h = 0.05$, **(B)** $h = 0.1$, **(C)** $h = 0.2$, **(D)** $h = 0.3$.

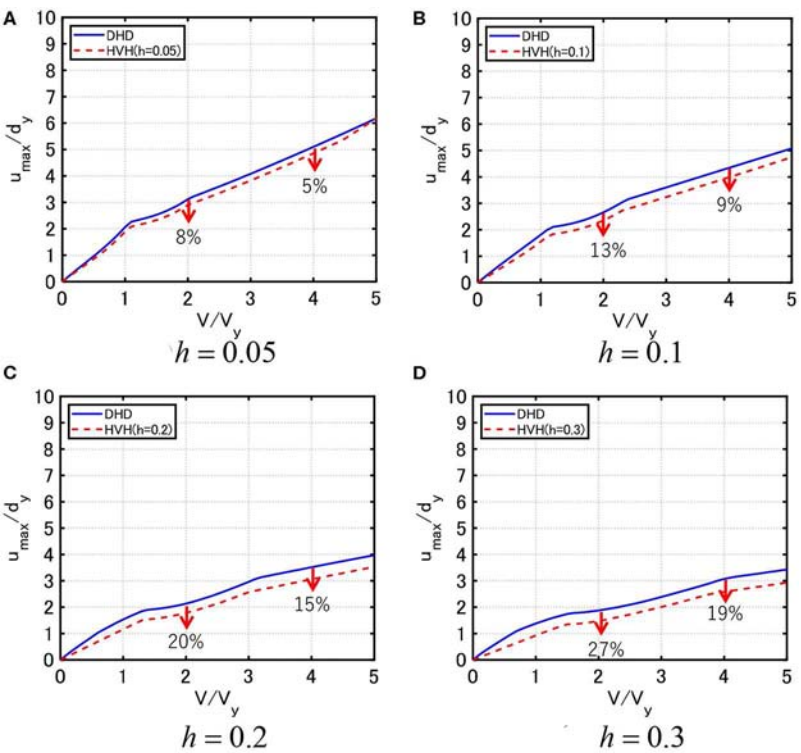

FIGURE 10 | Comparison of maximum deformation under critical double impulse between elastic–perfectly plastic SDOF system with HVH and one with DHD ($\alpha = 1$) **(A)** $h = 0.05$, **(B)** $h = 0.1$, **(C)** $h = 0.2$, **(D)** $h = 0.3$.

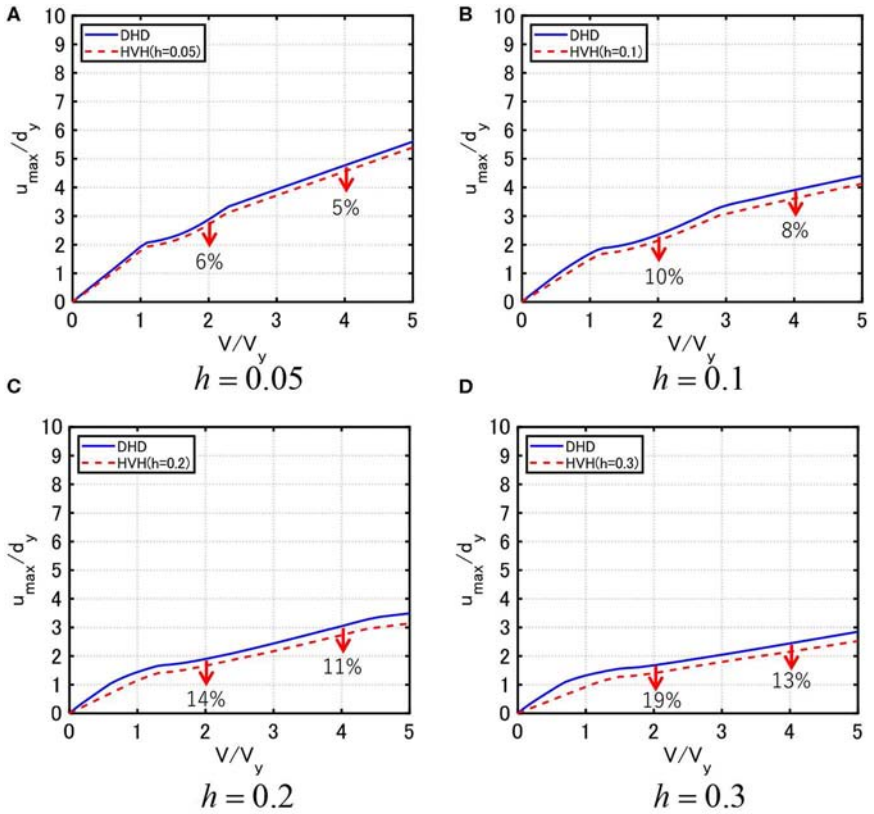

FIGURE 11 | Comparison of maximum deformation under critical double impulse between elastic–perfectly plastic SDOF system with HVH and one with DHD ($\alpha = 3$) **(A)** $h = 0.05$, **(B)** $h = 0.1$, **(C)** $h = 0.2$, **(D)** $h = 0.3$.

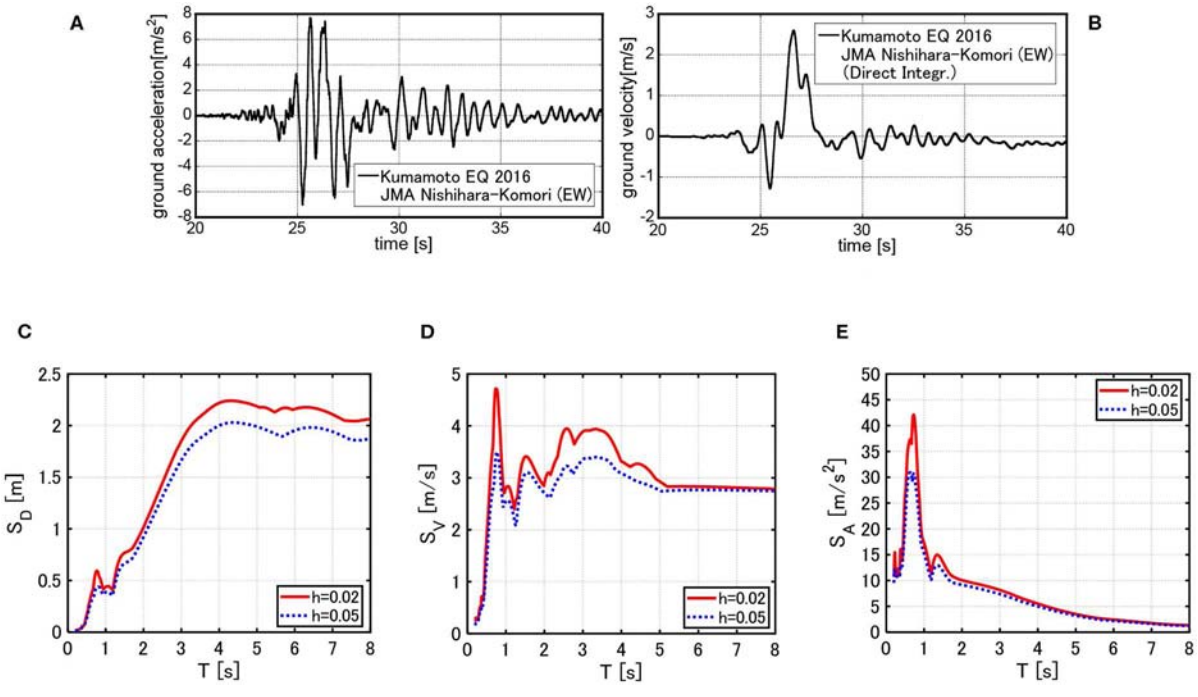

FIGURE 12 | Long-period pulse-type ground motion. **(A)** Ground acceleration of JMA Nishiharamura-Komori (EW) wave; **(B)** Ground velocity of JMA Nishiharamura–Komori(EW) wave; **(C)** Displacement response spectrum; **(D)** Velocity response spectrum; **(E)** Acceleration response spectrum.

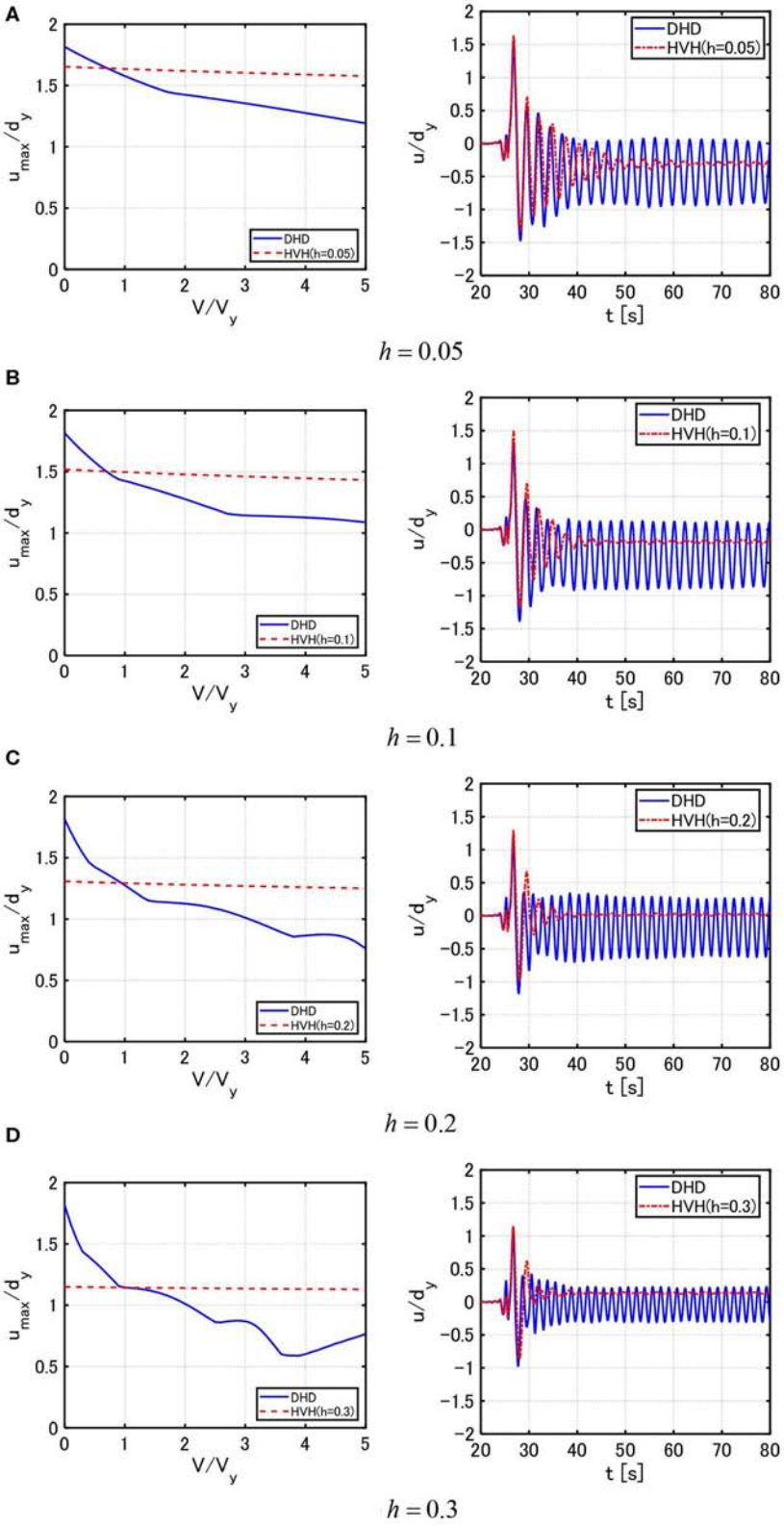

FIGURE 13 | Comparison of maximum deformation under JMA Nishiharamura–Komori(EW) wave between elastic–perfectly plastic SDOF system with HVH and one with DHD (structural damping ratio = 0) **(A)** $h = 0.05$, **(B)** $h = 0.1$, **(C)** $h = 0.2$, **(D)** $h = 0.3$.

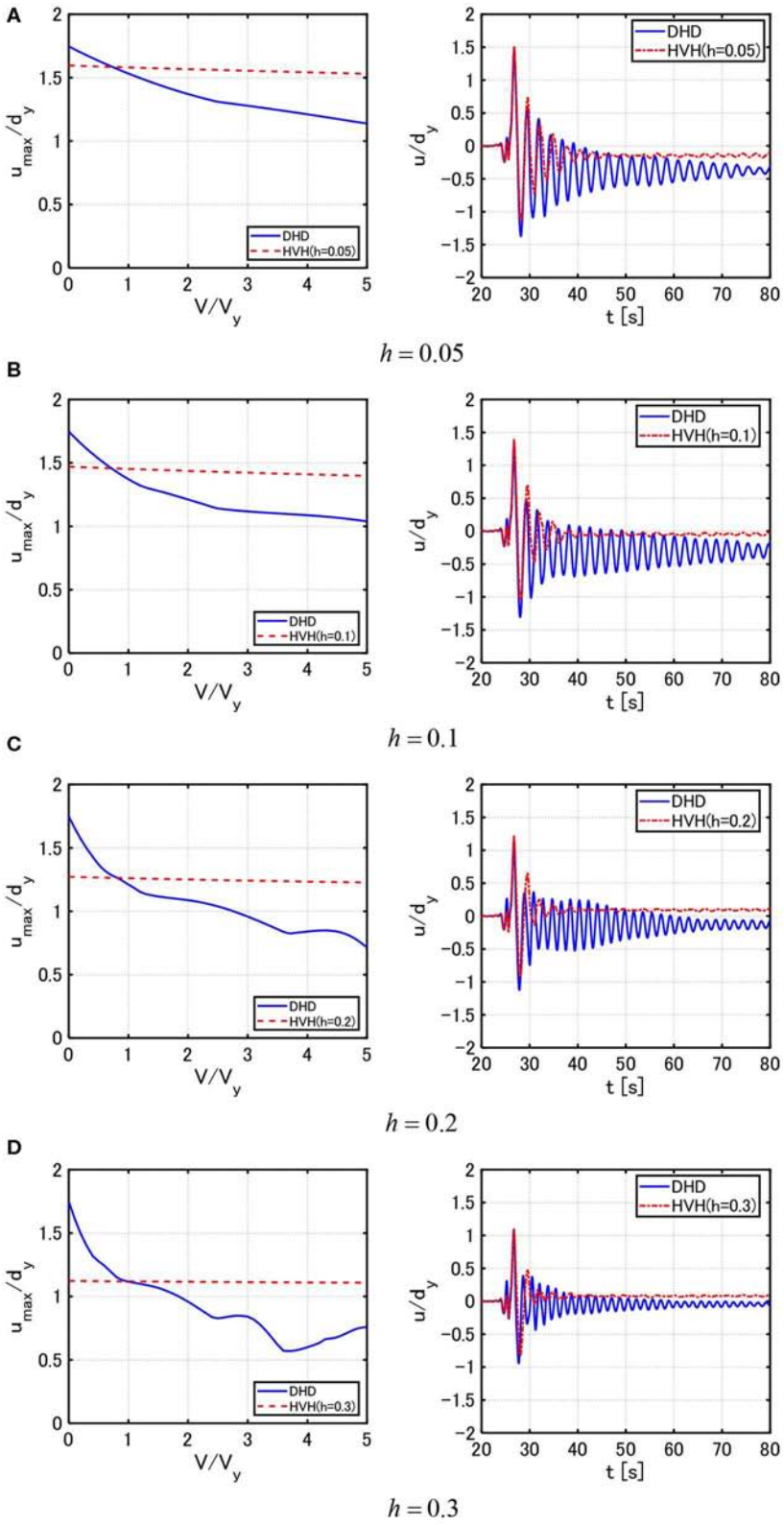

FIGURE 14 | Comparison of maximum deformation under JMA Nishiharamura–Komori(EW) wave between elastic–perfectly plastic SDOF system with HVH and one with DHD (structural damping ratio = 0.02) **(A)** $h = 0.05$, **(B)** $h = 0.1$, **(C)** $h = 0.2$, **(D)** $h = 0.3$.

between the elastic–perfectly plastic SDOF system with HVH (structural damping ratio = 0) and one with DHD (structural damping ratio = 0) for the damping ratio $h = 0.05, 0.1, 0.2, 0.3$ of the viscous damper. V in the horizontal axis indicates the parameter used for $cV = kK_F d_{sy}$, which specifies the quantity of hysteretic dampers in DHD. Furthermore, the quantities of large-amplitude hysteretic dampers in DHD and hysteretic dampers in HVH are also given by this parameter V. The frame damped fundamental natural period = 2.7[s]. The deformation time histories are also plotted for reference ($V/V_y = 1.3, V = 2.0[m/s], V_y = 1.57[m/s]$). Furthermore, **Figure 14** shows the same comparison for the structural damping ratio = 0.02. The frame damped fundamental natural period = 2.7005[s]. The deformation time histories are also plotted again for reference ($V/V_y = 1.3$, $V = 2.0[m/s]$, $V_y = 1.57[m/s]$).

It can be seen from **Figures 13**, **14** that the HVH system exhibits a stable performance compared to the DHD system. The good response reduction performance of the DHD system in the larger level of V/V_y is due to the fact that, as the parameter V becomes larger, the quantity of hysteretic dampers in the DHD systems increase for a given damping coefficient c of viscous dampers in the HVH system. It can also be observed that, while the SDOF system with DHD exhibits a fairly large residual deformation, the SDOF system with HVH does not induce large residual deformation.

The HVH damper system consists of viscous dampers (oil dampers) and hysteretic dampers with gap mechanism in parallel. Each damper has already been used in actual buildings in many countries. Therefore, it seems possible to use the HVH damper system in actual buildings.

CONCLUSIONS

A new HVH damper system has been proposed for long-period pulse-type earthquake ground motions of large amplitude. The proposed system includes a viscous damper and a hysteretic damper with a gap mechanism. The following conclusions have been derived.

Although the structural control system is generally understood to be rather ineffective for impulsive earthquake ground motions, the viscous damper is aimed at resisting for broad-amplitude range vibration and the hysteretic damper with a gap mechanism is expected to play as a stopper for large-amplitude range vibration in the proposed damper system.

A closed-form maximum response to the critical double impulse with the impulse timing maximizing the response has been derived for an elastic–perfectly plastic SDOF system with a HVH damper system. The closed-form expression depends on the input level (i.e., the deformation level) and structural parameters.

The performance comparison with the previous DHD system has been conducted to investigate the effectiveness of the proposed HVH system. It has been observed that the viscous damper is effective for the input of smaller level ($V/V_y < 3$). Furthermore, it can be observed that the HVH with an appropriate quantity of hysteretic dampers has a good response reduction performance in the broad range of input levels compared with the DHD.

To reveal the effectiveness of the proposed HVH system, time-history response analyses have been performed for a long-period pulse-type recorded ground motion at Kumamoto (2016). It has been revealed that the HVH system exhibits a stable response reduction performance compared to the DHD system. The good response reduction performance of the DHD system in the larger level of V/V_y is due to the fact that, as the parameter V becomes larger, the quantity of hysteretic dampers in the DHD systems increases for a given damping coefficient c of viscous dampers in the HVH system. It can also be observed that, while the SDOF system with DHD exhibits a fairly large residual deformation, the SDOF system with HVH does not induce large residual deformation.

AUTHOR CONTRIBUTIONS

All authors listed have made a substantial, direct and intellectual contribution to the work, and approved it for publication.

ACKNOWLEDGMENTS

Part of the present work is supported by the Grant-in-Aid for Scientific Research (KAKENHI) of Japan Society for the Promotion of Science (No. 15H04079). This support is greatly appreciated.

SUPPLEMENTARY MATERIAL

The Supplementary Material for this article can be found online at: https://www.frontiersin.org/articles/10.3389/fbuil.2020.00062/full#supplementary-material

REFERENCES

Adachi, F., Fujita, K., Tsuji, M., and Takewaki, I. (2013b). Importance of interstory velocity on optimal alongheight allocation of viscous oil dampers in super highrise buildings. *Eng. Struct.* 56, 489–500. doi: 10.1016/j.engstruct.2013.05.036

Adachi, F., Yoshitomi, S., Tsuji, M., and Takewaki, I. (2013a). Nonlinear optimal oil damper design in seismically controlled multi-story building frame. *Soil Dyn. Earthq. Eng.* 44, 1–13. doi: 10.1016/j.soildyn.2012.08.010

Aiken, I. D., Nims, D. K., Whittaker, A. S., and Kelly, J. M. (1993). Testing of passive energy dissipation systems. *Earthq. Spectra* 9, 335–370. doi: 10.1193/1.1585720

Aittokoski, T., and Miettinen, K. (2010). Efficient evolutionary approach to approximate the Pareto-optimal set in multiobjective optimization. UPS-EMOA. *Optim. Methods Softw.* 25, 841–858. doi: 10.1080/10556780903548265

Asakawa, T., Yamakawa, M., and Uetani, K. (2017). "Optimum design of displacement-restraint PC steel bar brace for moment-resisting steel frames," in *Proc. of 7th International Conference on Mechanics and Materials In Design, Albufeira, Portugal, 11–15 June* 2017.

Attard, T. L. (2007). Controlling all interstory displacements in highly nonlinear steel buildings using optimal viscous damping. *J. Struct. Eng. ASCE* 133, 1331–1340. doi: 10.1061/(ASCE)0733-9445(2007)133:9(1331)

Austin, M. A., and Pister, K. S. (1985). Design of seismic-resistant friction-braced frames, *J. Struct. Eng. ASCE* 111, 2751–2769. doi: 10.1061/(ASCE)0733-9445(1985)111:12(2751)

Aydin, E., Boduroglub, M. H., and Guney, D. (2007). Optimal damper distribution for seismic rehabilitation of planar building structures. *Eng. Struct*. 29, 176–185. doi: 10.1016/j.engstruct.2006.04.016

Bruneau, M., Chang, S. E., Eguchi, R. T., Lee, G. C., O'Rourke, T. D., Reinhorn, A. M., et al. (2003). A framework to quantitatively assess andenhance the seismic resilience of communities. *Earthq. Spectra.* 19, 733–752. doi: 10.1193/1.1623497

Caughey, T. K. (1960). Sinusoidal excitation of a system with bilinear hysteresis, *J. Appl. Mech*. 27, 640–643. doi: 10.1115/1.3644075

Cherry, S., and Filiatraut, A. (1993). Seismic response control of buildings using friction damper. *Earthq. Spectra* 9, 447–466. doi: 10.1193/1.1585724

Ciampi, V., Angelis, M. D., and Paolacci, F. (1995). Design of yielding or friction-based dissipative bracings for seismic protection of buildings. *Eng. Struct*. 17, 381–391. doi: 10.1016/0141-0296(95)00021-X

Cimellaro, G., Reinhorn, A., and Bruneau,. M. (2010). Framework for analytical quantification of disaster resilience. *Eng. Struct*. 32, 3639–3649. doi: 10.1016/j.engstruct.2010.08.008

Filiatrault, A., and Cherry, S. (1990). Seismic design spectra for friction-damped structure. *J. Struct. Eng. ASCE* 116, 1334–1355. doi: 10.1061/(ASCE)0733-9445(1990)116:5(1334)

Fujita, K., Kasagi, M., Lang, Z. Q., Guo, P. F., and Takewaki, I. (2014). Optimal placement and design of nonlinear dampers for building structures in the frequency domain. *Earthq. Struct.* 7, 1025–1044. doi: 10.12989/eas.2014.7.6.1025

Hanson, R. D. (1993). Supplemental damping for improved seismic performance. *Earthq. Spectra.* 9, 319–334. doi: 10.1193/1.1585719

Hanson, R. D., and Soong, T. T. (2001). *Seismic Design With Supplemental Energy Dissipation Devices*. EERI, Oakland, CA.

Inoue, K., and Kuwahara, S. (1998). Optimum strength ratio of hysteretic damper. *Earthq. Eng. Struct. Dyn*. 27, 577–588. doi: 10.1002/(SICI)1096-9845(199806)27:6<577::AID-EQE743>3.0.CO;2-U

Jacobsen, L. S. (1960). Damping in composite structures. *Proc. 2nd WCEE*. Tokyo, 1029–1044.

Kojima, K., Saotome, Y., and Takewaki, I. (2018). Critical earthquake response of an SDOF elastic-perfectly plastic model with viscous damping under double impulse as a substitute for near-fault ground motion, Japan architectural review. *Int. J. Jpn. Arch. Rev. Eng. Design Wiley* 1, 207–220. doi: 10.1002/2475-8876.10019

Kojima, K., and Takewaki, I. (2015). Critical earthquake response of elastic-plastic structures under near-fault ground motions (Part 1: Fling-step input). *Front. Built. Environ.* 1:12. doi: 10.3389/fbuil.2015.00012

Kojima, K., and Takewaki, I. (2016). A simple evaluation method of seismic resistance of residential house under two consecutive severe ground motions with intensity 7. *Front. Built. Environ.* 2:15. doi: 10.3389/fbuil.2016.00015

Lagaros, N., Plevris, V., and Mitropoulou, C. C. (eds) (2013). *Design Optimization of Active and Passive Structural Control Systems*. Hershey, PA: Information Science. doi: 10.4018/978-1-4666-2029-2

Lavan, O., and Levy, R. (2010). Performance based optimal seismic retrofitting of yielding plane frames using added viscous damping. *Earthq. Struct.* 1, 307–326. doi: 10.12989/eas.2010.1.3.307

Murakami, Y., Noshi, K., Fujita, K., Tsuji, M., and Takewaki, I. (2013a). Simultaneous optimal damper placement using oil, hysteretic and inertial mass dampers. *Earthq. Struct.* 5, 261–276. doi: 10.12989/eas.2013.5.3.261

Murakami, Y., Noshi, K., Fujita, K., Tsuji, M., and Takewaki, I. (2013b). "Optimal placement of hysteretic dampers via adaptive sensitivity-smoothing algorithm," in *Engineering and Applied Sciences Optimization*, eds N. Lagaros and M. Papadrakakis (Cham: Springer), 1821–1835.

Nakashima, M., Saburi, K., and Tsuji, B. (1996). Energy input and dissipation behaviour of structures with hysteretic dampers. *Earthq. Engng. Struct. Dyn*. 25, 483–496. doi: 10.1002/(SICI)1096-9845(199605)25:5<483::AID-EQE564>3.0.CO;2-K

Noroozinejad, E., Takewaki, I., Yang, T. Y., Astaneh-Asl, A., and Gardoni, P. (eds.). (2019). *Resilient Structures and Infrastructures.* Singapore: Springer.

Noshi, K., Yoshitomi, S., Tsuji, M., and Takewaki, I. (2013). Optimal nonlinear oil damper design in seismically controlled multi-story buildings for relief forces and damping coefficients. *J. Struct. Eng. AIJ*, 49B, 299–307. doi: 10.1016/j.soildyn.2012.08.010

Ogawa, Y., Kojima, K., and Takewaki, I. (2017). General evaluation method of seismic resistance of residential house under multiple consecutive severe ground motions with high intensity. *Int. J. Earthq. Impact Eng.* 2, 158–174. doi: 10.1504/IJEIE.2017.089055

Pall, A. S., and Marsh, C. (1982). Response of friction damped braced frames. *J. Struct. Div. ASCE* 108, 1313–1323.

Quagliarella, D., Periaux, J., Poloni, C., and Winter, G. (1998). *Genetic Algorithms and Evolution Strategies in Engineering and Computer Science Recent Advances and Industrial Applications.* Chichester: John Wiley & Sons.

Shiomi, T., Fujita, K., Tsuji, M., and Takewaki, I. (2016). Explicit optimal hysteretic damper design in elastic-plastic structure under double impulse as representative of near-fault ground motion. *Int. J. Earthq. Impact Eng.* 1, 5–19. doi: 10.1504/IJEIE.2016.080029

Shiomi, T., Fujita, K., Tsuji, M., and Takewaki, I. (2018). Dual hysteretic damper system effective for broader class of earthquake ground motions. *Int. J. Earthquake Impact Eng.* 2, 175–202. doi: 10.1504/IJEIE.2018.093391

Sivandi-Pour, A., Gerami, M., and Khodayarnezhad, D. (2014). Equivalent modal damping ratios for non-classically damped hybrid steel concrete buildings with transitional storey. *Struct. Eng. Mechan.* 50, 383–401. doi: 10.12989/sem.2014.50.3.383

Soong, T. T., and Dargush, G. F. (1997). *Passive Energy Dissipation Systems in Structural Engineering*. Chichester: JohnWiley & Sons. doi: 10.1201/9781439834350.ch27

Tagawa, H., and Hou, X. (2008). Wire-rope bracing system of displacement-control-type considering seismic response property of moment-resisting frames. *J. Struct. Construct. Eng.* 73, 843–850. doi: 10.3130/aijs.73.843

Takewaki, I. (2009). *Building Control With Passive Dampers: Optimal Performance-Based Design for Earthquakes*. Singapore: John Wiley & Sons Ltd. doi: 10.1002/9780470824931

Takewaki, I., Fujita, K., Yamamoto, K., and Takabatake, H. (2011). Smart passive damper control for greater building earthquake resilience in sustainable cities. *Sustain. Cities Soc.* 1, 3–15. doi: 10.1016/j.scs.2010.08.002

Taniguchi, M., Fujita, K., Tsuji, M., and Takewaki, I. (2016a). Hybrid control system for greater resilience using multiple isolation and building connection, *Front. Built Environ.* 2:26. doi: 10.3389/fbuil.2016.00026

Taniguchi, R., Kojima, K., and Takewaki, I. (2016b). Critical response of 2DOF elastic-plastic building structures under double impulse as substitute of near-fault ground motion. *Front. Built Environ.* 2:2. doi: 10.3389/fbuil.2016.00002

Uetani, K., Tsuji, M., and Takewaki, I. (2003). Application of optimum design method to practical building frames with viscous dampers and hysteretic dampers. *Eng. Struct.* 25, 579–592. doi: 10.1016/S0141-0296(02)00168-2

Xia, C., and Hanson, R. D. (1992). Influence of ADAS element parameters on building seismic response. *J. Struct. Eng. ASCE* 118, 1903–1918. doi: 10.1061/(ASCE)0733-9445(1992)118:7(1903)

Conflict of Interest: The authors declare that the research was conducted in the absence of any commercial or financial relationships that could be construed as a potential conflict of interest.

frontiers in Built Environment

ORIGINAL RESEARCH
published: 26 June 2020
doi: 10.3389/fbuil.2020.00092

Tuned Mass Dampers for Response Reduction of a Reinforced Concrete Chimney Under Near-Fault Pulse-Like Ground Motions

Said Elias, Rajesh Rupakhety and Simon Ólafsson*

Earthquake Engineering Research Centre, Faculty of Civil and Environmental Engineering, School of Engineering and Natural Science, University of Iceland, Reykjavik, Iceland

The article investigates response mitigation of a reinforced concrete (RC) chimney subjected to pulse-like near-fault ground motions using tuned mass damper (TMD) schemes. The total height of the chimney is 265 m with a mass of 11,109 ton. Three TMD schemes are used: single tuned mass damper (STMD), multiple TMDs having equal stiffness (w-MTMDs) and multiple TMDs having equal masses (e-MTMDs). The STMD is tuned to the fundamental frequency of the chimney while both w-MTMDs and e-MTMDs have three TMDs for controlling each of the first and second modes (total of six TMDs) of vibration. Response of the uncontrolled and controlled structures is calculated for 69 recorded ground motions containing a dominant velocity pulse. Displacement and acceleration at top node of the RC chimney are the response of interest for performance assessment. It is found that e-MTMDs are more effective and robust than other schemes. It is also found that the pulse period of ground motion plays a very important role in how effective the control schemes are. There is a large variability in the reduction of response across these ground motions, and optimization methods independent of ground motion are not robust. There is a need for more advanced optimization methods incorporating information about local seismic sources.

Keywords: chimney, earthquake, reinforced concrete (RC), tuned mass dampers, vibration, near-fault ground motion

OPEN ACCESS

Edited by:
Dario De Domenico, University of Messina, Italy

Reviewed by:
Chunxiang Li, Shanghai University, China
Sinan Melih Nigdeli, Istanbul University-Cerrahpasa, Turkey
Hugo Hernandez Barrios, Michoacana University of San Nicolás de Hidalgo, Mexico

****Correspondence:***
Said Elias
said@hi.is

Specialty section:
This article was submitted to Earthquake Engineering, a section of the journal Frontiers in Built Environment

Received: *23 December 2019*
Accepted: *26 May 2020*
Published: *26 June 2020*

Citation:
Elias S, Rupakhety R and Ólafsson S (2020) Tuned Mass Dampers for Response Reduction of a Reinforced Concrete Chimney Under Near-Fault Pulse-Like Ground Motions. Front. Built Environ. 6:92. doi: 10.3389/fbuil.2020.00092

INTRODUCTION

Reinforced concrete (RC) chimneys are tall structures. They are very sensitive to earthquake ground motion Wilson (2003) explained that seismic response of a tall chimney is not adequately described by a single degree of freedom (SDOF) model, and that significant contribution from higher modes can be expected, especially in acceleration response. Distribution of shear force and moment demands along the height of such chimneys, is therefore, not as is implied by many design standards which typically rely on the mode shape of the fundamental normal mode.

Seismic vibration mitigation of tall structures has been an active area of research. Longarini and Zucca (2014) studied a 50 m tall masonry chimney and found that tuned mass damper (TMD) can be used to reduce its seismic response. Multiple TMDs (MTMDs) could be more beneficial to control a range of frequencies, which provides robustness

against detuning caused by variations of the frequencies of the structure (Wang and Shi, 2019). Elias et al. (2016) showed that multiple TMDS tuned to different vibration modes and distributed over the structure (d-MTMDs) are superior to a single TMD tuned to the fundamental mode of vibration in controlling seismic response of tall chimneys. Application of d-MTMDs for wind response control of a chimney is presented in Elias et al. (2017, 2019a). The concept of d-MTMDs is well-established and defined for response control of different structures subjected to different loading conditions (Gill et al., 2017; Elias, 2018, 2019; Elias and Matsagar, 2019; Elias et al., 2019b; Matin et al., 2019; Nigdeli and Bekdas, 2019). Etedali et al. (2019) demonstrated that friction TMDs (FTMDs) can mitigate structural response better than TMDs. Other solutions such as inerter TMDs or particle dampers (Greco and Marano, 2013; Reggio and Angelis, 2015; De Domenico and Ricciardi, 2018a,b; De Domenico et al., 2018; Lu et al., 2018; Rezaee and Aly, 2018; Cao and Li, 2019) have also been proposed in the vibration control literature. Different optimization techniques are used by researchers to improve the performance of TMDs (Nigdeli and Bekdas, 2013, 2017; Bekdas et al., 2018; Yucel et al., 2019). Huergo and Hernández (2019a,b) presented a structural model using coupled shear and flexural beams incorporating an arbitrary number of TMDs along the height. A detailed literature survey on passive TMDs is provided by Elias and Matsagar (2017).

Ground motions close to an earthquake source are often impulsive. Forward-rupture directivity results in constructive interference of seismic waves radiated by different sections of a rupturing fault as they arrive at a station, and this is manifest as a strong, short duration velocity pulse (see, for example, Rupakhety et al., 2011). Such dominant pulses have been found to be demanding on tall and flexible structures. For example, Sigurðsson et al. (2019) have shown that near-fault pulse-like ground motions are more demanding than far-fault non-pulse-like ground motion of same peak acceleration to a utility-scale land-based wind turbine. Since the strong shaking in these pulse-like ground motions is impulsive in nature, TMD masses do not have enough time to respond to the excitation and thereby control structural response effectively. This has been generally acknowledged in the literature (see for example Chen and Wu, 2001). Matta (2013), however, showed that TMDs can be used to control response of structures to pulse-like ground motion, provided the TMD has a large enough mass. The potential effectiveness of TMDs also depends on the structure being considered. For example, effectiveness of TMDs might be better for tall and flexible structures, which are very susceptible to pulse-like ground motions, than for very stiff structures. Effectiveness of TMDs in controlling response of tall structures like chimneys when subjected to pulse-like ground motions is missing in the literature. This work investigates this important issue using numerical simulation of response of a tall reinforced concrete chimney subjected to many near-fault pulse-like ground motions recorded during past earthquakes. To quantify the effect of such ground motions, a set of 69 recorded earthquake ground motions are selected from the database given in Sigurðsson et al. (2019), and further described in Rupakhety (2010).

Three TMD schemes namely single TMD (STMD); MTMDs with equal stiffness (w-MTMDs); and MTMDs with equal masses (e-MTMDs) are considered in this study. The STMD is tuned to the fundamental frequency of the chimney, while w-MTMDs and e-MTMDs are designed to control the response around two modes.

MATHEMATICAL MODELING

A 265 m high reinforced concrete (RC) chimney which has been studied by several investigators and originally reported by Melbourne et al. (1983) is considered as the case-study structure. Inelastic deformations and soil-structure interaction are ignored in this study. Schematic representation of the chimney with and without TMDs is presented in **Figure 1**. Further details about the structure can be found in Melbourne et al. (1983). **Figure 1A** shows the basic geometry of the structure. A typical cross section of the chimney and a schematic of a typical tuned mass damper is shown in **Figure 1B**. The structure is modeled with 30 2-dimensional uniform Euler-Bernoulli beam elements The geometrical details of these 30 sections are given in **Table 1**.

Each node has one translational and one rotational degree of freedom, which is statically condensed. The base of the chimney is assumed to be fixed. A lumped mass matrix formulation is used. The statically condensed stiffness matrix is denoted as $[K_N]$ and the corresponding diagonal mass matrix is denoted by $[M_N]$. The damping matrix ($[C_N]$) is constructed in such a way that damping ratio in all the modes of vibration is 5% of critical damping.

Three different TMD schemes are considered. In the STMD scheme, a single TMD is placed at the top of the chimney. In the MTMD scheme, multiple TMDs are placed at the top of the chimney. The mass, stiffness, and damping coefficient of the i^{th} TMD are denoted by m_i, k_i, and c_i, respectively. The structural matrices with the TMDs incorporated into them are denoted by $[K_s]$, $[C_s]$, and $[M_s]$, and are of order $(N+n)\times(N+n)$ where N is 30 and n represents the number of TMDs used.

The equations of motion for the coupled system, under ground motion can be stated as,

$$[M_s]\{\ddot{x}_s\} + [C_s]\{\dot{x}_s\} + [K_s]\{x_s\} = -[M_s]\{r\}\ddot{x}_g \tag{1}$$

where the displacement, velocity, and acceleration vectors are denoted by $\{x_s\}$, $\{\dot{x}_s\}$, and $\{\ddot{x}_s\}$; $\ddot{x}_g$ is the ground acceleration and $\{r\}$ is the influence coefficient vector populated by 1. The system of equations is solved by the Newmark's integration method.

The optimum parameters (frequency tuning ratio and damping ratio) of the TMDs are based on a detailed parametric study explained in the following sections. Two different types of MTMDs are considered: e-MTMDs where all the TMDs have the same mass, and w-MTMDs where all the TMDs have the same stiffness.

The multiple TMDs are tuned to the first two modes of vibration, and their frequencies are uniformly distributed around the corresponding modal frequencies. The natural frequency of each TMD (ω_i) is expressed by (Li, 2000; Li and Qu, 2006; Han and Li, 2008),

$$\omega_i = \omega_T \left[1 + \left(i - \frac{n+1}{2}\right)\frac{\beta}{n-1}\right] i = 1 \text{ to } n \tag{2}$$

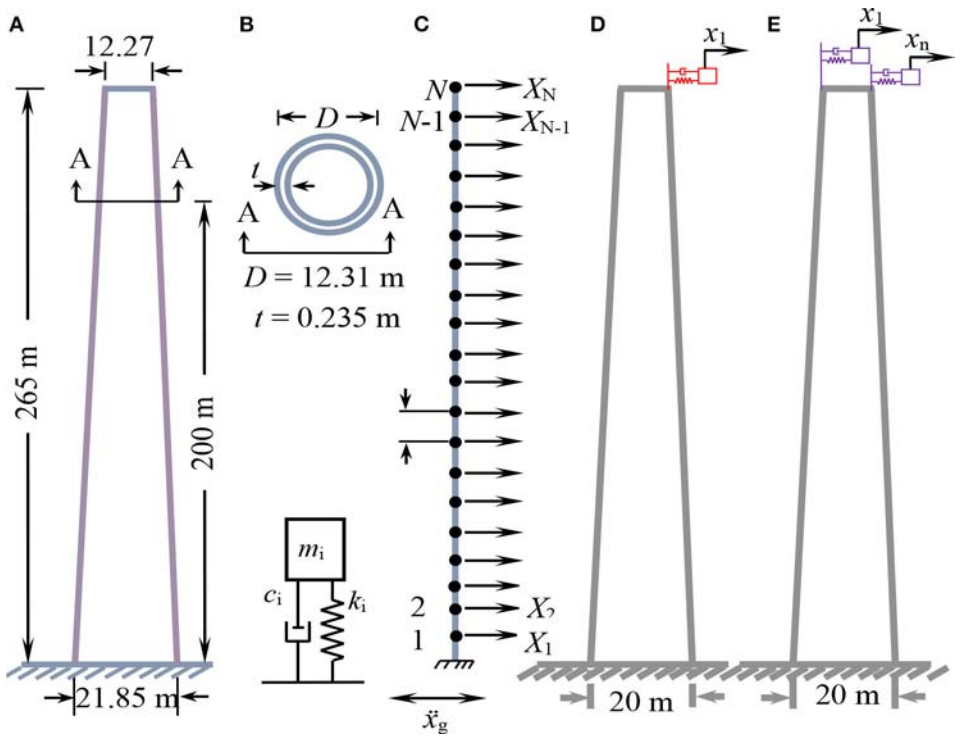

FIGURE 1 | (A) Geometry of the chimney, **(B)** schematic diagram of TMD and section A-A **(C)** lumped mass idealization model **(D)** representation of a STMD, and **(E)** representation of MTMDs.

and

$$\omega_T = \sum_i^n \frac{\omega_i}{n} \tag{3}$$

$$\beta = \frac{\omega_n - \omega_1}{\omega_T} \tag{4}$$

where ω_T is the average frequency of MTMDs and β is the non-dimensional frequency bandwidth of the MTMDs systems (for more details see Li, 2000). The average frequency of the MTMDs are tuned to the first two frequencies of the structure, and are denoted as ω_{T1}, ω_{T2} and n is equal to 6, implying that 3 TMDS are used to control each mode. For e-MTMDs, the mass of each TMD $m_\mathrm{i} = \frac{m_t}{n}$. where m_t, is the total mass of the TMDs. The stiffness (k_i) is then given by,

$$k_i = m_i\,\omega_i^2 \;\; i = 1 \; to \; n. \tag{5}$$

For w-TMDs, the stiffness of each TMD is given by

$$k_i = \frac{m_t}{\left(\frac{1}{\omega_1^2} + \frac{1}{\omega_2^2} + \cdots \frac{1}{\omega_n^2}\right)} i = 1 \; to \; 6 \tag{6}$$

$$m_i = \frac{k_i}{\omega_i^2} \tag{7}$$

The damping ratio ($\zeta_\mathrm{d} = \zeta_1 = \zeta_2 = \cdots = \zeta_\mathrm{n}$) of the TMDs is kept the same and the damping coefficients (c_i) of the TMDs is calculated as follows:

$$c_\mathrm{i} = 2\zeta_d m_i \omega_i \quad i = 1 \; to \; n \tag{8}$$

The total mass of the TMDs is assumed to be 3% of the total mass of the chimney, which is 11,109 ton. The resulting design parameters of the different TMD schemes are shown in **Table 2**. The first three frequencies of the uncontrolled chimney are 1.6798 rad/sec (0.267 Hz), 6.816 rad/sec (1.085 Hz) and 16.090 rad/sec (2.562 Hz). The corresponding modal mass participation for the three modes are 0.321, 0.193, and 0.112, respectively. Optimal frequency tuning ratio and damping ratio for STMD are 0.85 and 0.3, respectively. In case of w-MTMDs, the optimal frequency tuning ratio is found to be the same as STMD, but the optimal damping ratio is 0.18. Also, the frequency bandwidth of the three TMDs tuned to fundamental mode is 0.2 and that of those tuned to the second mode is 0.1. Frequency tuning ratio and damping ratio of the e-MTMDs 0.95 and 0.11, respectively. In this case, the bandwidth of all the TMDs is 0.3. These parameters were obtained by a detailed parametric study discussed in the next section.

NUMERICAL STUDY

Numerical simulation of response of the Chimney without and with different TMD schemes are carried using 69 near-fault pulse-like ground motions recorded during different past earthquakes. These ground motions were all affected by forward

TABLE 1 | Geometric details of the RC chimney.

Node number	Distance from base (m)	*l* (m)	Outer Diameter, *D* (m)	Thickness, *t* (m)	Mass, *m* (ton)
30	265	10	12.27	0.235	106.622
29	255	15	12.27	0.235	266.554
28	240	10	12.27	0.235	266.554
27	230	10	12.27	0.235	213.243
26	220	10	12.27	0.235	213.243
25	210	5	12.27	0.235	159.932
24	205	5	12.27	0.235	106.710
23	200	5	12.31	0.235	107.065
22	195	5	12.39	0.235	107.773
21	190	5	12.51	0.235	108.836
20	185	5	12.67	0.235	110.789
19	180	6	12.85	0.24	125.330
18	174	14	13.15	0.24	237.233
17	160	10	13.85	0.24	294.136
16	150	10	14.35	0.243	259.557
15	140	10	14.85	0.25	274.718
14	130	10	15.35	0.255	291.693
13	120	10	15.85	0.265	311.489
12	110	10	16.35	0.275	333.400
11	100	10	16.85	0.285	358.540
10	90	4	17.35	0.303	267.735
9	86	16	17.85	0.322	440.438
8	70	10	18.35	0.348	609.216
7	60	10	18.85	0.38	525.330
6	50	10	19.35	0.4	571.699
5	40	10	19.85	0.42	611.848
4	30	15	20.35	0.43	959.347
3	15	3	21.1	0.7	806.209
2	12	6	21.25	0.7	489.853
1	6	6	21.55	0.7	660.262
0	0	0	21.85	0.7	334.000

TABLE 2 | Design parameters of TMDs.

Schemes	TMDi	Frequency (rad/sec)	Mass (ton)	Stiffness 10^4 (N/m)	Damping 10^4 (N-sec/m)
STMD	TMD1	1.428	333.270	67.944	28.551
w-MTMDs	TMD1	1.285	126.531	20.895	5.854
	TMD2	1.428	102.490		5.268
	TMD3	1.571	84.703		4.789
	TMD4	4.925	8.615		0.764
	TMD5	5.794	6.224		0.649
	TMD6	6.663	4.707		0.564
e-MTMDs	TMD1	1.197	55.545	7.957	0.798
	TMD2	1.596		14.145	1.064
	TMD3	1.995		22.102	1.330
	TMD4	4.857		131.012	3.237
	TMD5	6.475		232.911	4.316
	TMD6	8.094		363.923	5.395

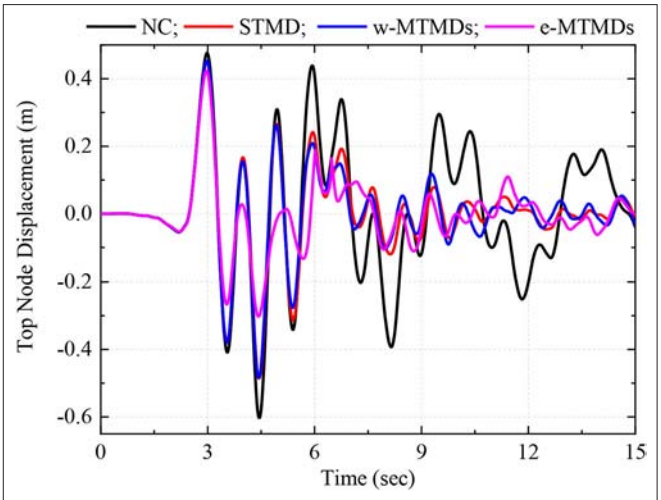

FIGURE 2 | Time history of top node displacement response of chimney with and without TMD schemes.

directivity effect and contain a dominant velocity pulse. Some salient features of the ground motions relevant for this study are given in **Table A1**.

Parameters of the TMDs were optimized through a parametric study. In the first step, tuning frequency was assumed to be equal to 1, and damping ratio of the TMD was varied from 0.01 to 0.5, with an increment of 0.01. The damping ratio corresponding to the best average response reduction across the 69 ground motions was selected as the optimal solution. Once the damping ratio is fixed, the frequency tuning ratio was varied between 0.85 and 1.15 with an increment of 0.01. The optimal solution was selected as the one that provided the best average response reduction across the 69 ground motions. Performance of TMDs

An example from one of the ground motions is presented here. The ground motion is from the 2004 Parkfield earthquake, 2004 earthquake recorded at the fault zone 12 station. The time variation of top node displacement of the uncontrolled (NC) and controlled structures is shown in **Figure 2**.

The peak top node displacement is 0.602, 0.486, 0.484, and 0.42 m respectively for NC, STMD, w-MTMDs, and e-MTMDs. The STMD, w-MTMDs and e-MTMDs reduce the top node displacement by 19, 19.6, and 30%, respectively. The time history of top node acceleration is presented in **Figure 3**. Response reduction in acceleration is 11.6, 10.5, and 49.6% respectively for STMD, w-MTMDs, and e-MTMDs.

The difference in the performance of the different schemes can be understood by inspecting the response in the frequency domain. Fourier amplitude spectra (FAS) of the top node displacement and top node acceleration are plotted in **Figures 4A**, **5A**. The corresponding transfer functions are shown in **Figures 4B**, **5B**. These transfer functions relate ground acceleration to top node displacement and acceleration, respectively. For ease of visualization, the transfer functions are normalized by the peak of the transfer function of the uncontrolled structure.

Figure 4 shows that the displacement response is mainly contributed by the first and the second modes of vibration. All the TMD schemes are equally effective in controlling the response due to the first mode. However, e-MTMDs outperform the other schemes in controlling the second mode. In this also evident from the transfer functions shown in **Figure 4B**. Because there is significant contribution from the second vibration mode, the e-MTMDs is more effective in controlling overall displacement response. Although the w-MTMDs are also intended to control the second mode, they are not as effective as the e-MTMDs because the TMD masses tuned to the second mode are rather low. Second mode contribution is even higher in acceleration response as shown in **Figure 5A**. The second mode contributes a lot more than the first in the acceleration response. The pulse period of this ground motion is about 1 Hz which resonates with the second mode of the structure. Therefore, the e-MTMDs, which control the second mode the best, are the most effective in controlling the overall response. Apart from the pulse, high frequency part of the near-fault ground motion can also have significant impact on structure response (Rupakhety and Sigbjörnsson, 2011).

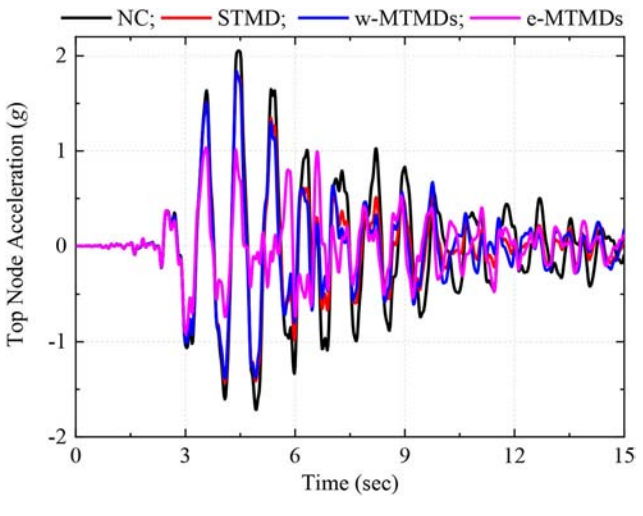

FIGURE 3 | Time history of top node acceleration response of chimney with and without TMD schemes.

Next we discuss a scenario when the pulse period of the ground motion is close to the fundamental period of vibration of the chimney. Ground motion from the 1992 Landers earthquake recorded at the LUC station has a dominant pulse frequency of about 0.25 Hz. Top node displacement and acceleration due to this ground motion are shown in **Figure 6**. The TMDs are effective in controlling the displacement response, but not so effective in controlling acceleration. Unlike in the previous case where the e-MTMDs were found to be the best scheme, the w-MTMDs perform the best against this ground motion. This is because the w-MTMDs control the first vibration mode the best as a lot of mass is provided to those TMDs that are tuned to this mode. From the FAS of the response presented in **Figure 7**, it is clear that the displacement response is dominated by the first mode of vibration while the third mode has significant contribution in the acceleration response. These results show that the pulse period of near-fault ground motion relative to the vibration frequencies of the structure plays an important role in the structural response. This effect is further investigated in the next section.

Effect of Frequency Content of Ground Motions

To study the effect of pulse period response reduction ratios are plotted against the first mode period of the chimney normalized by the pulse period of 69 near-fault ground motions is shown in **Figure 8**. In controlling the peak displacement, the TMD schemes are, in general, not very effective, except when the ground motion pulse resonates with the structure. In a narrow

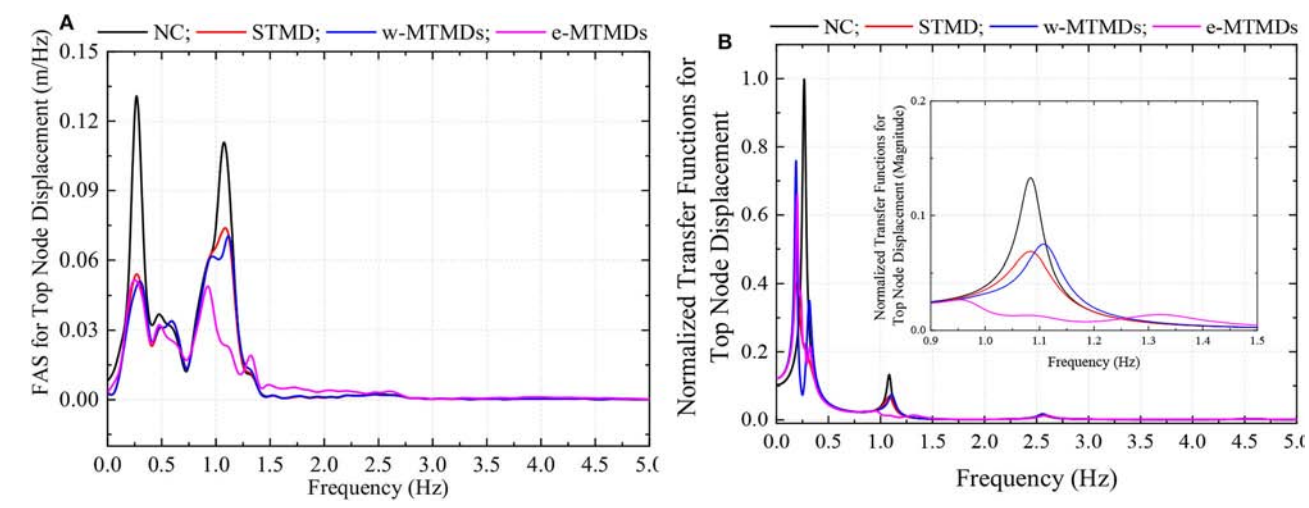

FIGURE 4 | FAS **(A)** and normalized transfer function **(B)** of top node displacement.

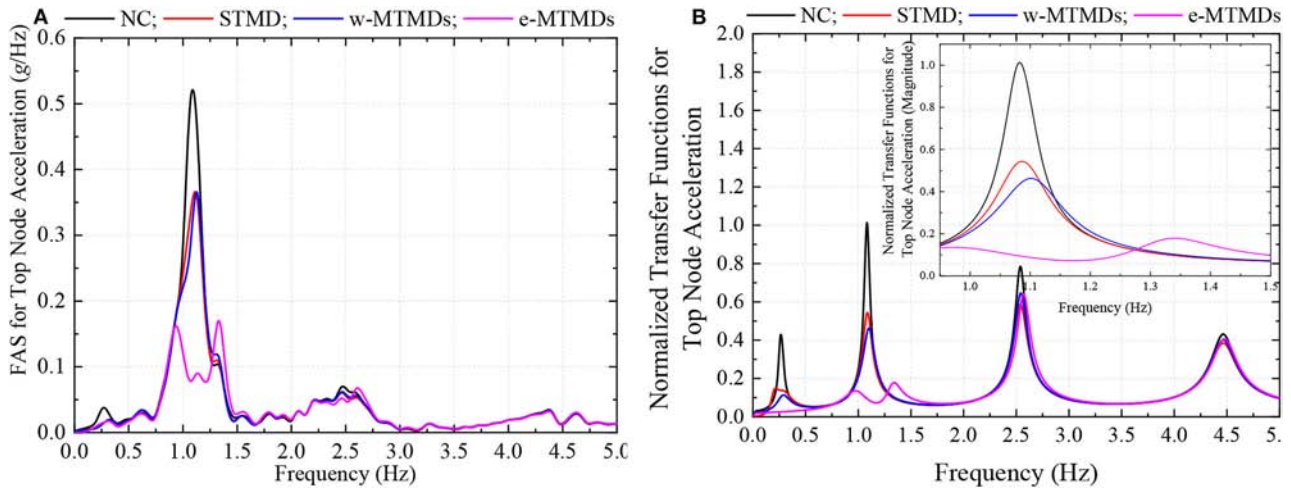

FIGURE 5 | FAS **(A)** and normalized transfer function **(B)** of top node acceleration.

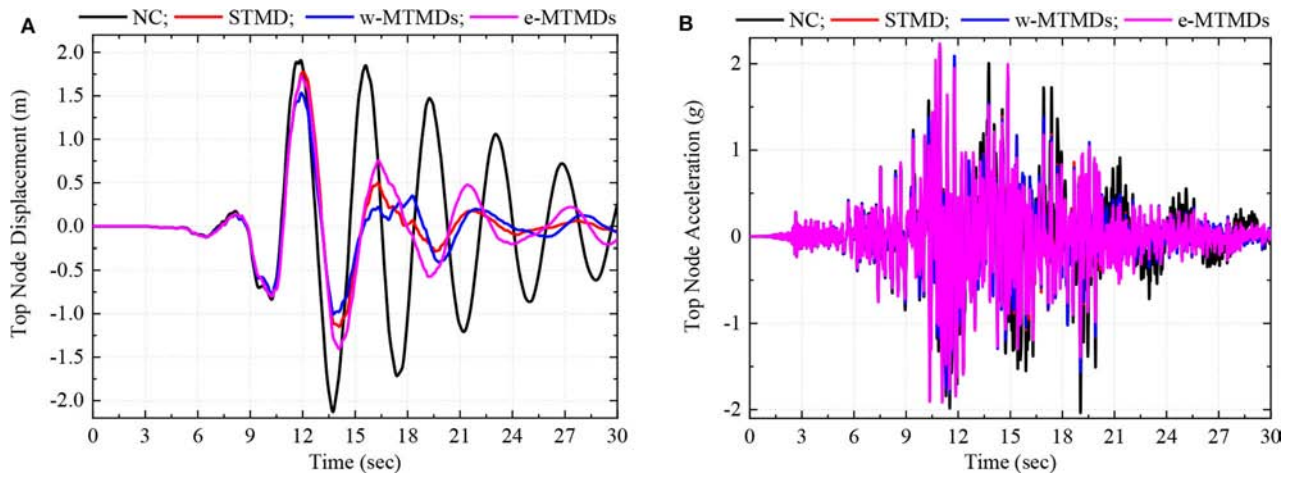

FIGURE 6 | Time history of top node displacement **(A)** and acceleration **(B)** response of chimney with and without TMD schemes.

band around resonance with the first mode, the effectiveness is higher. In this band, there is no significant difference between the STMD and MTMDs. When the second mode period is close to the pulse period, the TMDs reduce the displacement by up to 40%, and the e-TMDs outperform the other schemes. It is noted that the structural experiences the highest displacement demand, and in such cases, response reduction is in the range of 15–30%. In general, the e-MTMD seems to be the most effective scheme. Similar observations can be made in **Figure 8B** which shows response reduction in acceleration. In this case, the e-MTMDs are clearly superior to the other schemes.

These results highlight that some degree of response reduction can be achieved in tall chimneys subjected to near-fault pulse-like ground motions by passive control schemes using TMDs. The effectiveness of the control schemes, however, differs a lot of ground motion characteristics, most importantly on its frequency content relative to the vibration frequencies of the structure. Since a structure, during its useful life, might face ground motions with different frequency contents, such control schemes are not expected to be beneficial in all cases. However, the most critical cases which require control are those when the fundamental mode of the structure resonates with the ground motion pulse. In such cases, TMDs can be effective in controlling structural displacement demand. The TMDs presented in this research are optimized by maximizing their average performance against all the ground motions. The large variability in response reduction observed from the results presented here, a more focused optimization scheme might be more beneficial. For example, the TMDs can be optimized for a sub-set of ground motions which impose the largest demands on the uncontrolled structure. This and other advanced optimization schemes need further research, and might potentially provide better control, but it is clear that optimization schemes that are independent of ground motions, for example, that of Sadek et al. (1997) are not expected to be robust enough when the structure is subjected to near-fault ground motions.

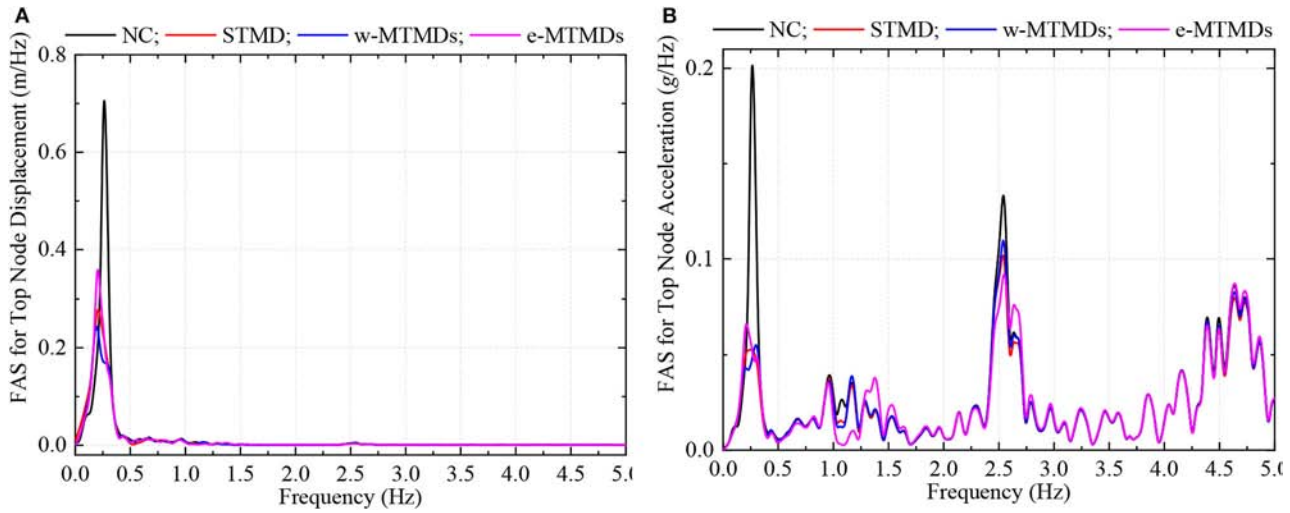

FIGURE 7 | FAS of top node displacement **(A)** and acceleration **(B)** response of chimney with and without TMD schemes.

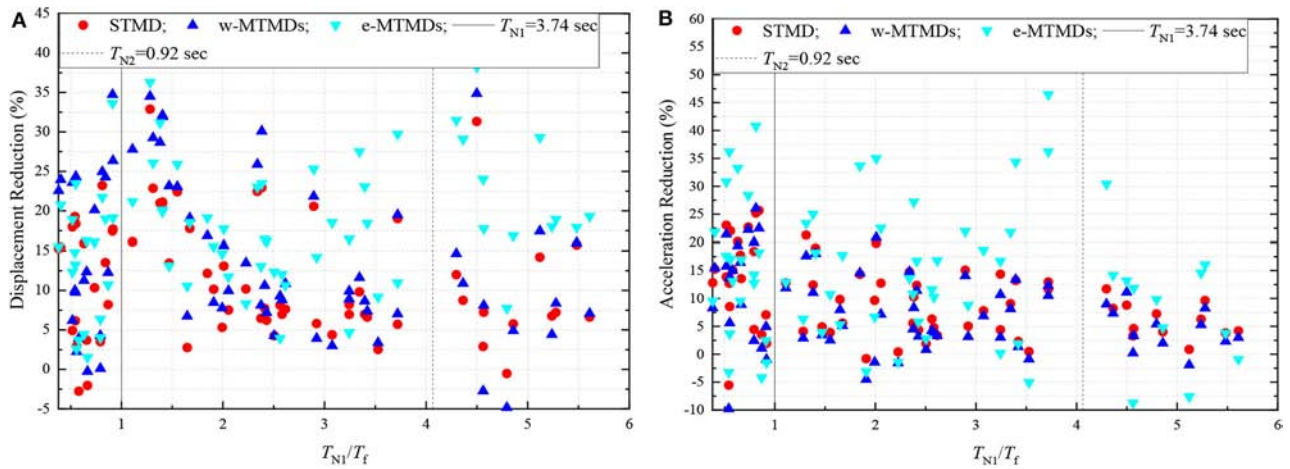

FIGURE 8 | (A,B) Variation of displacement and acceleration reduction with the normalized period. The results correspond to 69 near-fault ground motions.

CONCLUSIONS

The results discussed above lead to the following conclusions.

1. Passive TMDs optimized by maximizing average response reduction across a set of ground motions show large variability in control performance and offer limited effectiveness against most of the ground motions.
2. In the critical cases when the fundamental mode of the structure resonates with the ground motion pulse, structural displacements can be controlled by 10–35%.
3. Multiple TMDs, especially the e-MTMDs tuned to the first two modes of vibration provide more robust control than STMDs. This is more the case in acceleration control.
4. When the pulse period is much larger than the fundamental period of the structure, the TMDs don't provide effective control.
5. Traditional methods of optimization which are independent of ground motion do not provide effective and robust vibration control against near-fault ground motions. In this regard, the optimization needs to be target to a certain type of ground motions that are the most critical for the structure. This corresponds to situations when the first and the second vibration mode of the structure resonates with the pulse period. For such situations, e-MTMDs optimized for only those ground motions that resonate with the first and the second mode of the structure, might provide better control of displacement and acceleration demand. For

practical applications, this requires a good understanding of the impending hazard and the critical seismic sources near the construction site. The pulse period is dependent on earthquake magnitude (see Rupakhety et al., 2011) and can be estimated empirically. With such estimates, a more targeted optimization can be carried out so that the TMDs provide superior performance when subjected to the most critical ground motions.

DATA AVAILABILITY STATEMENT

The datasets generated for this study are available on request to the corresponding author.

AUTHOR CONTRIBUTIONS

All authors listed have made a substantial, direct and intellectual contribution to the work, and approved it for publication.

FUNDING

We acknowledge support from University of Iceland Research Fund.

SUPPLEMENTARY MATERIAL

The Supplementary Material for this article can be found online at: https://www.frontiersin.org/articles/10.3389/fbuil.2020.00092/full#supplementary-material

REFERENCES

Bekdas, G., Nigdeli, S. M., and Yang, X. S. (2018). A novel bat algorithm based optimum tuning of mass dampers for improving the seismic safety of structures. *Eng. Struct.* 159, 89–98. doi: 10.1016/j.engstruct.2017.12.037

Cao, L., and Li, C. (2019). Tuned tandem mass dampers-inerters with broadband high effectiveness for structures under white noise base excitations. *Struct. Con. Health Monit.* 26:e2319. doi: 10.1002/stc.2319

Chen, G., and Wu, J. (2001). Optimal placement of multiple tune mass dampers for seismic structures. *J. Struct. Eng.* 127, 1054–1062. doi: 10.1061/(ASCE)0733-9445(2001)127:9(1054)

De Domenico, D., Deastra, P., Ricciardi, G., Sims, N. D., and Wagg, D. J. (2018). Novel fluid inerter based tuned mass dampers for optimised structural control of base-isolated buildings. *J. Franklin Inst.* 356, 7626–7649. doi: 10.1016/j.jfranklin.2018.11.012

De Domenico, D., and Ricciardi, G. (2018a). Optimal design and seismic performance of tuned mass damper inerter (TMDI) for structures with nonlinear base isolation systems. *Earthq. Eng. Struct. Dyn.* 47, 2539–2560. doi: 10.1002/eqe.3098

De Domenico, D., and Ricciardi, G. (2018b). Earthquake-resilient design of base isolated buildings with TMD at basement: application to a case study. *Soil Dyn. Earthq. Eng.* 113, 503–521. doi: 10.1016/j.soildyn.2018.06.022

Elias, S. (2018). Seismic energy assessment of buildings with tuned vibration absorbers. *Shock Vibrat.* 2018:2051687. doi: 10.1155/2018/2051687

Elias, S. (2019). Effect of SSI on vibration control of structures with tuned vibration absorbers. *Shock Vibrat.* 2019:7463031. doi: 10.1155/2019/7463031

Elias, S., and Matsagar, V. (2017). Research developments in vibration control of structures using passive tuned mass dampers. *Annu. Rev. Control* 44, 129–156. doi: 10.1016/j.arcontrol.2017.09.015

Elias, S., and Matsagar, V. (2019). Seismic vulnerability of non-linear building with distributed multiple tuned vibration absorbers. *Struct. Infrastruct. Eng.* 15, 1103–1118. doi: 10.1080/15732479.2019.1602149

Elias, S., Matsagar, V., and Datta, T. K. (2016). Effectiveness of distributed tuned mass dampers for multi-mode control of chimney under earthquakes. *Eng. Struct.* 124, 1–16. doi: 10.1016/j.engstruct.2016.06.006

Elias, S., Matsagar, V., and Datta, T. K. (2017). Distributed tuned mass dampers for multi-mode control of benchmark building under seismic excitations. *J. Earthq. Eng.* 23, 1137–1172. doi: 10.1080/13632469.2017.1351407

Elias, S., Matsagar, V., and Datta, T. K. (2019a). Along-wind response control of chimneys with distributed multiple tuned mass dampers. *Struct. Control Health Mon.* 26:e2275. doi: 10.1002/stc.2275

Elias, S., Matsagar, V., and Datta, T. K. (2019b). Dynamic response control of a wind-excited tall building with distributed multiple tuned mass dampers. *Intern. J. Struct. Stab. Dyn.* 19:1950059. doi: 10.1142/S0219455419500597

Etedali, S., Akbari, M., and Seifi, M. (2019). MOCS-based optimum design of TMD and FTMD for tall buildings under near-field earthquakes including SSI effects. *Soil Dyn. Earthq. Eng.* 119, 36–50. doi: 10.1016/j.soildyn.2018.12.027

Gill, D., Elias, S., Steinbrecher, A., Schröder, C., and Matsagar, V. (2017). Robustness of multi-mode control using tuned mass dampers for seismically excited structures. *Bull. Earthq. Eng.* 15, 5579–5603. doi: 10.1007/s10518-017-0187-6

Greco, R., and Marano, G. C. (2013). Optimum design of tuned mass dampers by displacement and energy perspectives. *Soil Dyn. Earthq. Eng.* 49, 243–253. doi: 10.1016/j.soildyn.2013.02.013

Han, B., and Li, C. (2008). Characteristics of linearly distributed parameter-based multiple-tuned mass dampers. *Struct. Control Health Mon.* 5, 839–856. doi: 10.1002/stc.222

Huergo, I. F., and Hernández, H. (2019a). Coupled shear-flexural model for dynamic analysis of fixed-base tall buildings with tuned mass dampers. *Struct. Des. Tall Spec. Build.* 28:e1671. doi: 10.1002/tal.1671

Huergo, I. F., and Hernández, H. (2019b). Coupled-two-beam discrete model for dynamic analysis of tall buildings with tuned mass dampers including soil–structure interaction. *Struct. Des. Tall Spec. Build.* 29:e1683. doi: 10.1002/tal.1683

Li, C. (2000). Performance of multiple tuned mass dampers for attenuating undesirable oscillations of structures under the ground acceleration. *Earthq. Eng. Struct. Dynam.* 29, 1405–1421. doi: 10.1002/1096-9845(200009)29:9<1405::AID-EQE976>3.0.CO;2-4

Li, C., and Qu, W. (2006). Optimum properties of multiple tuned mass dampers for reduction of translational and torsional response of structures subject to ground acceleration. *Eng. Struct.* 28, 472–494. doi: 10.1016/j.engstruct.2005.09.003

Longarini, N., and Zucca, M. (2014). A chimney's seismic assessment by a tuned mass damper. *Eng. Struct.* 79, 290–296. doi: 10.1016/j.engstruct.2014.05.020

Lu, Z., Li, K., and Zhou, Y. (2018). Comparative studies on structures with a tuned mass damper and a particle damper. *J. Aerosp. Eng.* 31:04018090. doi: 10.1061/(ASCE)AS.1943-5525.0000878

Matin, A., Elias, S., and Matsagar, V. (2019). Distributed multiple tuned mass dampers for seismic response control in bridges. *Proc. Instit. Civil Eng. Struct. Build.* 173, 217–234. doi: 10.1680/jstbu.18.00067

Matta, E. (2013). Effectiveness of tuned mass dampers against ground motion pulses. *J. Struct. Eng.* 139, 188–198. doi: 10.1061/(ASCE)ST.1943-541X.0000629

Melbourne, W. H., Cheung, J. C., and Goddard, C. R. (1983). Response to wind action of 265-m Mount Isa stack. *J. Struct. Eng.* 109, 2561–2577. doi: 10.1061/(ASCE)0733-9445(1983)109:11(2561)

Nigdeli, S.M., and Bekdas, G. (2017). Optimum tuned mass damper design in frequency domain for structures. *KSCE J. Civil Eng.* 21, 912–922. doi: 10.1007/s12205-016-0829-2

Nigdeli, S. M., and Bekdas, G. (2013). Optimum tuned mass damper design for preventing brittle fracture of RC buildings. *Smart Struct. Syst.* 12, 137–155. doi: 10.12989/sss.2013.12.2.137

Nigdeli, S. M., and Bekdas, G. (2019). Optimum design of multiple positioned tuned mass dampers for structures constrained with axial force capacity. *Struct. Design Tall Spec. Build.* 28:e1593. doi: 10.1002/tal.1593

Reggio, A., and Angelis, M. D. (2015). Optimal energy-based seismic design of non-conventional Tuned Mass Damper (TMD) implemented via inter-story isolation. *Earthq. Eng. Struct. Dyn.* 44, 1623–1642. doi: 10.1002/eqe.2548

Rezaee, M., and Aly, A.M. (2018). Vibration control in wind turbines to achieve de-sired system-level performance under single and multiple hazard loadings. *Struct. Control Health Mon.* 25:e2261 doi: 10.1002/stc.2261

Rupakhety, R. (2010). *Contemporary issues in earthquake engineering research: processing of accelerometric data, modelling of inelastic structural response, and quantification of near-fault effects* (Doctoral dissertation). University of Iceland, Reykjavik, Iceland.

Rupakhety, R., and Sigbjörnsson, R. (2011). Can simple pulses adequately represent near-fault ground motions?. *J. Earthq. Eng.* 15, 1260–1272. doi: 10.1080/13632469.2011.565863

Rupakhety, R., Sigurdsson, S. U., Papageorgiou, A. S., and Sigbjörnsson, R. (2011). Quantification of ground-motion parameters and response spectra in the near-fault region. *Bull. Earthq. Eng.* 9, 893–930. doi: 10.1007/s10518-011-9255-5

Sadek, F., Mohraz, B., Taylor, A. W., and Chung, R. M. (1997). A method of estimating the parameters of tuned mass dampers for seismic applications. *Earthquake Engineering and Structural Dynamics*, 26, 617–635.

Sigurðsson, G. Ö., Rupakhety, R., Rahimi, S. E., and Olafsson, S. (2019). Effect of pulse-like near-fault ground motions on utility-scale land-based wind turbines. *Bull. Earthq. Eng.* 18, 1–16. doi: 10.1007/s10518-019-00743-9

Wang, C., and Shi, W. (2019). Optimal design and application of a multiple tuned mass damper system for an in-service footbridge. *Sustainability* 11:2801. doi: 10.3390/su11102801

Wilson, J. L. (2003). Earthquake response of tall reinforced concrete chimneys. *Eng. Struct.* 25, 11–24. doi: 10.1016/S0141-0296(02)00098-6

Yucel, M., Bekdaş, G., Nigdeli, S. M., and Sevgen, S. (2019). Estimation of optimum tuned mass damper parameters via machine learning. *J. Build. Eng.* 26:100847. doi: 10.1016/j.jobe.2019.100847

Conflict of Interest: The authors declare that the research was conducted in the absence of any commercial or financial relationships that could be construed as a potential conflict of interest.

Advantages of publishing in Frontiers

OPEN ACCESS
Articles are free to read for greatest visibility and readership

FAST PUBLICATION
Around 90 days from submission to decision

HIGH QUALITY PEER-REVIEW
Rigorous, collaborative, and constructive peer-review

TRANSPARENT PEER-REVIEW
Editors and reviewers acknowledged by name on published articles

Frontiers
Avenue du Tribunal-Fédéral 34
1005 Lausanne | Switzerland

Visit us: www.frontiersin.org
Contact us: info@frontiersin.org | +41 21 510 17 00

REPRODUCIBILITY OF RESEARCH
Support open data and methods to enhance research reproducibility

DIGITAL PUBLISHING
Articles designed for optimal readership across devices

FOLLOW US
@frontiersin

IMPACT METRICS
Advanced article metrics track visibility across digital media

EXTENSIVE PROMOTION
Marketing and promotion of impactful research

LOOP RESEARCH NETWORK
Our network increases your article's readership